

AD-A215 353



DTIC  
ELECTF  
DEC 14 1989  
S B D

SILICON HYBRID WAFER SCALE  
INTEGRATION INTERCONNECT EVALUATION

THESIS

James C. Lyke  
Captain, USAF

AFIT/ENG/GE/89D-27

DEPARTMENT OF THE AIR FORCE  
AIR UNIVERSITY

**AIR FORCE INSTITUTE OF TECHNOLOGY**

Wright-Patterson Air Force Base, Ohio

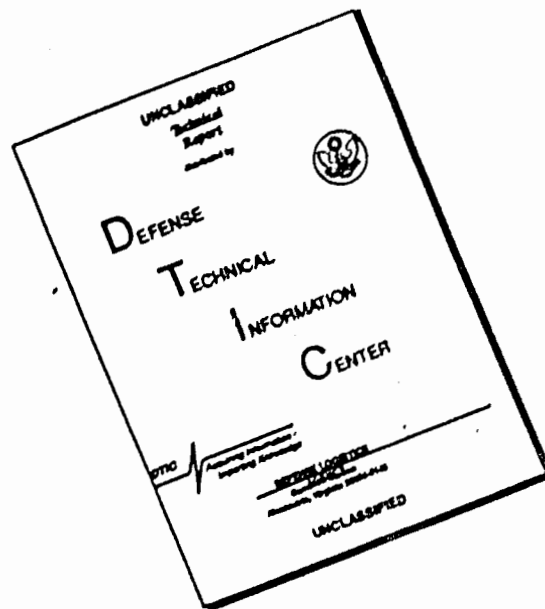
**DISTRIBUTION STATEMENT A**

Approved for public release;  
Distribution Unlimited

89 12 14 030

PII Redacted

# DISCLAIMER NOTICE



THIS DOCUMENT IS BEST QUALITY AVAILABLE. THE COPY FURNISHED TO DTIC CONTAINED A SIGNIFICANT NUMBER OF PAGES WHICH DO NOT REPRODUCE LEGIBLY.

AFIT/ENG/GE/89D-27

SILICON HYBRID WAFER SCALE  
INTEGRATION INTERCONNECT EVALUATION

THESIS

James C. Lyke  
Captain, USAF

AFIT/ENG/GE/89D-27

DTIC  
ELECTE  
DEC 14 1989  
S B D

Approved for public release; distribution unlimited

AFIT/ENG/GE/89D-27

SILICON HYBRID WAFER SCALE  
INTEGRATION INTERCONNECT EVALUATION

THESIS

Presented to the Faculty of the School of Engineering  
of the Air Force Institute of Technology

Air University

In Partial Fulfillment of the  
Requirements for the Degree of  
Master of Science

James C. Lyke, BSEE

Captain, USAF

December 1989

Approved for public release; distribution unlimited



## *Preface*

I am indebted to several of the faculty at the Air Force Institute of Technology and am grateful for the assistance they have provided. Dr. Mark Oxley of the Mathematics Department was particularly helpful and essentially responsible for the derivation of the solutions of the lossless version of the multi-conductor telegrapher's equations given in Appendix F. I would also like to acknowledge Dr. Gregory Warhola, also of the Mathematics Department, for his suggestions regarding the simulation of floating conductors with finite difference methods. I feel that my role was primarily implementational with respect to this simulation. Finally, I especially want to acknowledge the overall contribution of my academic advisor, Dr. Edward Kolesar, whose seemingly inordinate level of support throughout this research effort was instrumental to its completion.

I am particularly glad for the opportunity to acknowledge the sacrifices my wife and children have unselfishly made in order for me to complete this document. Mere words are inadequate in expressing my gratitude for their support.

I dedicate this thesis to the memory of my precious son, Jefferson Samuel Lyke.

James C. Lyke

<b>Accession For</b>	
NTIS GRA&I	<input checked="checked" type="checkbox"/>
DTIC TAB	<input type="checkbox"/>
Unannounced	<input type="checkbox"/>
Justification	
By	
Distribution/	
Availability Codes	
Dist	Avail and/or Special
A-1	

## *Table of Contents*

	Page
Preface . . . . .	ii
Table of Contents . . . . .	iii
List of Figures . . . . .	vii
List of Tables . . . . .	xiii
Abstract . . . . .	xv
 I. Introduction . . . . .	 1-1
Overview . . . . .	1-1
Background . . . . .	1-1
Problem Statement . . . . .	1-9
Scope . . . . .	1-9
Assumptions . . . . .	1-13
Approach . . . . .	1-14
Equipment . . . . .	1-16
Order of Presentation . . . . .	1-18
Summary . . . . .	1-18
 II. Review of the Current Literature . . . . .	 2-1
Overview . . . . .	2-1
Transmission Line Effects in Wafer Scale Interconnections . . . . .	2-1
Wafer Scale Integration Interconnection Structures. . . . .	2-3
Elements of Transmission Line Theory. . . . .	2-13
Microstrip Transmission Line Analysis Techniques. . . . .	2-29
The Application of Transmission Line Concepts to Wafer Scale Interconnections. . . . .	2-34
Other Wafer Scale Interconnection Issues . . . . .	2-62
Yield of Wafer Scale Interconnections. . . . .	2-62
Discontinuities. . . . .	2-64
Materials. . . . .	2-65
Summary . . . . .	2-71

	Page
III. Experimental and Computational Methodology . . . . .	3-1
Overview . . . . .	3-1
Test Wafers . . . . .	3-2
Physical Design Description. . . . .	3-3
Interconnect Configurations. . . . .	3-14
Experimental Arrangement . . . . .	3-17
Specific Measurement Equipment Configurations. . .	3-22
Experimental Measurement Techniques . . . . .	3-29
Continuity Measurements. . . . .	3-29
Characteristic Impedance Measurements . . . . .	3-29
Transmission and Coupling Measurements. . . . .	3-32
Pulsed Signal Measurements. . . . .	3-33
Computational Methodology . . . . .	3-35
Characteristic Impedance Determination. . . . .	3-35
Coupled Signal Waveform Determination. . . . .	3-43
Pulsed-Signal Response Processing Methodology. . .	3-49
Summary . . . . .	3-55
IV. Results and Analysis . . . . .	4-1
Overview . . . . .	4-1
Physical and Continuity Measurement Findings . . . . .	4-2
Physical Observations. . . . .	4-2
Continuity Measurement Results. . . . .	4-9
Frequency-Domain Computational and Measurement Findings	4-15
Characteristic Impedance Results. . . . .	4-17
Coupling Results. . . . .	4-45
Transmission Results. . . . .	4-58
Analysis. . . . .	4-59
Isolation Results. . . . .	4-60
Time-Domain Measurement Findings . . . . .	4-64
De-Cabling Technique Results. . . . .	4-64
Input Signal Waveforms. . . . .	4-70
Meander Structure Results. . . . .	4-70
Dual-Line Structure Results. . . . .	4-79
Triple-Line Structure Results. . . . .	4-83

	Page
Coplanar Waveguide Results. . . . .	4-83
Summary . . . . .	4-84
V. Conclusions and Recommendations . . . . .	5-1
Overview . . . . .	5-1
Summary of the Research Effort . . . . .	5-1
Research Objectives. . . . .	5-3
Research Methodology. . . . .	5-3
Research Findings. . . . .	5-5
Conclusions . . . . .	5-8
Transmission Line Behavior and Modeling. . . . .	5-8
Coupling Effects. . . . .	5-9
Pulsed-Signal Performance. . . . .	5-9
Recommendations for future research . . . . .	5-10
Extension of Current Research. . . . .	5-10
WSIC Design Support. . . . .	5-14
Recommendations Regarding Future Hybrid WSI Sys- tems. . . . .	5-18
Summary . . . . .	5-21
Appendix A. Numerical Simulation Programs and Data . . . . .	A-1
Characteristic Impedance Formulas . . . . .	A-1
Program Listing. . . . .	A-1
Telegrapher's Equation Solver. . . . .	A-10
Digital Signal Processing (DSP) Routines. . . . .	A-14
Appendix B. LIBRA Program Listing. . . . .	B-1
Program Listing. . . . .	B-1
Appendix C. Detailed Measurement Procedures . . . . .	C-1
Continuity Measurements . . . . .	C-1
Impedance Measurements . . . . .	C-3
Coupling, Transmission, and Isolation Measurements . . . .	C-5
Pulse Measurement Procedure . . . . .	C-7
Appendix D. Control Programs for the Test Equipment . . . . .	D-1

	Page
Appendix E.      Finite Difference Method (FDM) Calculation Utilizing a Spreadsheet . . . . .	E-1
Extension of Semi-Infinite Regions . . . . .	E-1
Treatment of Floating Conductors . . . . .	E-12
Appendix F.      Solutions to the Matrix Representation of the Telegrapher's Equations . . . . .	F-1
Two-Conductor Backward Coupling Gain . . . . .	F-4
Two-Conductor Configuration with Generalized Termination Conditions. . . . .	F-7
Three-Conductor Configuration with Generalized Termination Conditions. . . . .	F-8
Appendix G.      Characteristic Impedance Results. . . . .	G-1
Characteristic Impedance Measurement Results. . . . .	G-1
Estimation of "Good" Measurement Frequencies . . . . .	G-3
Linearized Impedance Approximations. . . . .	G-3
Appendix H.      Gain Phase Measurement Results. . . . .	H-1
Appendix I.      Pulsed-Signal Measurement Responses. . . . .	I-1
Bibliography . . . . .	BIB-1
Vita . . . . .	VITA-1

## *List of Figures*

Figure	Page
1.1. Silicon hybrid-wafer integration approach. . . . .	1-4
1.2. An example interconnect structure. . . . .	1-5
1.3. Photograph of a test wafer. . . . .	1-11
1.4. Close-up view of a test wafer, revealing several groupings of interconnections. . . . .	1-12
1.5. Typical conductor geometries on a test wafer scale integrated circuit. . . . .	1-15
2.1. Representative planar transmission line structures. . . . .	2-5
2.2. Several non-traditional transmission lines. . . . .	2-10
2.3. Multi-wire transmission line . . . . .	2-12
2.4. Lumped parameter transmission-line model . . . . .	2-19
2.5. A two-line transmission line. . . . .	2-20
2.6. The coupled transmission line pair. . . . .	2-26
2.7. Even- and odd-mode circuit configurations. . . . .	2-26
2.8. Even-and odd-mode field configurations. . . . .	2-27
2.9. Wheeler's conformal transformation technique. . . . .	2-59
2.10. Probability distribution of defect density as a function of size. . . . .	2-64
3.1. High Density Multilayer Interconnect Process . . . . .	3-4
3.2. Two-line, edge-coupled stripline. . . . .	3-6
3.3. Stripline. . . . .	3-6
3.4. Three-line, edge-coupled stripline. . . . .	3-7
3.5. Meander line. . . . .	3-7
3.6. Coplanar waveguide. . . . .	3-14
3.7. Three-line stripline. . . . .	3-15
3.8. Measurement configurations. . . . .	3-16
3.9. Illustration of plate extension modification for the probing station. . . . .	3-19
3.10. Low-impedance probes for high-frequency work. . . . .	3-21
3.11. Configuration used to determine the continuity. . . . .	3-23
3.12. Configuration used to measure the characteristic impedance. . . . .	3-24
3.13. Configuration used to measure coupling. . . . .	3-25
3.14. Configuration used for the pulse measurements. . . . .	3-26

Figure	Page
3.15. Use of a probe tip for the short-circuit measurements. . . . .	3-32
3.16. Traditional coupler and coupling measurement configuration. . . .	3-34
3.17. Example spreadsheet display for an electrostatics problem. . . . .	3-39
3.18. The fundamental finite-difference node. . . . .	3-41
3.19. Schematic representation of characteristic impedance problem formulation. . . . .	3-42
3.20. LIBRA model of a two-conductor transmission line structure. . . .	3-46
3.21. Block diagrams depicting the "de-cabing" filter technique. . . . .	3-51
4.1. Detailed view of coplanar waveguide, revealing definition of lithography. . . . .	4-4
4.2. Leakage defect from one of the test wafers. . . . .	4-5
4.3. Appearance of the contact pad "blackened" surfaces of the BCB wafer compared to those of normal (PIQ) wafer. . . . .	4-7
4.4. Depiction of problem encountered during probing. . . . .	4-9
4.5. Example of the physical (destructive) removal of the dielectric region between contact pads. . . . .	4-10
4.6. Leakage model for structures on first PIQ wafer. . . . .	4-12
4.7. Finite-difference model cross-sections. . . . .	4-20
4.8. Voltage distribution in a convergent FDM simulation (odd-mode) for an ECS structure. . . . .	4-23
4.9. Transverse cross-section of the 65th structure from the PIQ wafer. . . . .	4-29
4.10. Magnitude and phase of the characteristic impedance measured from the 36th structure of PIQ wafer. . . . .	4-33
4.11. Results of two lossless simulations of the 36th structure. . . . .	4-36
4.12. Results of a lossy simulation of the 36th structure compared with the measured values. . . . .	4-37
4.13. Comparisons between simulated and measured driving point impedances in open-circuit and short-circuit configurations. . . . .	4-38
4.14. The reference LIBRA simulation . . . . .	4-47
4.15. Variations of the reference simulation which considered the omission of discontinuities and a lossless model. . . . .	4-50
4.16. Other analytic estimates of the 42nd structure. . . . .	4-51
4.17. Results of lossless and lossy solutions to the telegrapher's equation. . . . .	4-52
4.18. Coupling measurement of the 48th structure from the second PIQ wafer compared with two LIBRA simulations. . . . .	4-53

Figure	Page
4.19. Maximum coupling gain spanning 1–100 MHz of the simulated two-conductor ECS structures as a function of lateral spacing between conductors. . . . .	4-56
4.20. Extended frequency simulation of the 48th structure from the PIQ wafer. . . . .	4-57
4.21. Predicted worst case coupling noise levels for 10 $\mu\text{m}$ and 25 $\mu\text{m}$ structures. . . . .	4-58
4.22. Simple transmission gain model. . . . .	4-59
4.23. Measured transmission gain of structure 50. . . . .	4-61
4.24. Measured transmission gain of structure 63. . . . .	4-62
4.25. Measured transmission gain of structure 93. . . . .	4-63
4.26. Representative pulsed-signal measurement of a 10 $\mu\text{m}$ wide meander structure at 5 MHz. . . . .	4-66
4.27. Short-cable, pulsed-signal measurement at 5 MHz . . . . .	4-67
4.28. Long-cable, pulsed signal measurement at 5 MHz. . . . .	4-68
4.29. Signal after de-cabling processing. . . . .	4-69
4.30. Pulsed-signal input for the short-cable configuration at 5 KHz. . . . .	4-71
4.31. Pulsed-signal input for the short-cable configuration at 50 KHz. . . . .	4-71
4.32. Pulsed-signal input for the short-cable configuration at 500 KHz. . . . .	4-72
4.33. Pulsed-signal input for the short-cable configuration at 50 MHz. . . . .	4-72
4.34. Pulsed-signal input for the short-cable configuration at 200 MHz. . . . .	4-73
4.35. Pulsed signal response of meander structure, revealing small pedestal in waveform's leading edge. . . . .	4-74
4.36. Pulsed signal response of meander line at 5 KHz. . . . .	4-75
4.37. Pulsed signal response of the meander line at 50 KHz. . . . .	4-76
4.38. Pulsed signal response of the meander line at 500 KHz. . . . .	4-77
4.39. Pulsed signal response of the meander line at 50 MHz. . . . .	4-78
4.40. Pulsed signal response of the meander line at 200 MHz. . . . .	4-80
4.41. Pulsed-signal response of the 62nd structure from the PIQ wafer at 50 KHz. . . . .	4-84
4.42. Pulsed-signal response of the 62nd structure from the PIQ wafer at 500 KHz. . . . .	4-85
4.43. Pulsed-signal response of the 62nd structure from the PIQ wafer to 5 MHz. . . . .	4-85
4.44. Pulsed-signal response of the 62nd structure from the PIQ wafer at 50 MHz. . . . .	4-86



Figure	Page
5.1. Suggested additional standards for future test wafers. . . . .	5-16
5.2. Ring and linear resonators. . . . .	5-17
5.3. Application and configuration of a matching buffer-driver. . . . .	5-20
E.1. Problem domain. . . . .	E-2
E.2. Simple FDM model. . . . .	E-4
E.3. Simple FDM model with an extended horizontal domain. . . . .	E-5
E.4. FDM simulation with virtual boundaries. . . . .	E-5
E.5. One-dimensional point source example. . . . .	E-6
E.6. One-dimensional point source distributions. . . . .	E-7
E.7. Voltage profile along the $x$ -axis for $y=0$ . . . . .	E-10
E.8. Detail of the FDM simulation cells required to simulate a floating conductor. . . . .	E-13
F.1. Schematic of the general two-conductor configuration. . . . .	F-7
F.2. Schematic of the general two-conductor configuration. . . . .	F-9
G.1. Measured characteristic impedance of structure 33 from the PIQ wafer. . . . .	G-4
G.2. Measured characteristic impedance of structure 36 from the BCB wafer. . . . .	G-5
G.3. Measured characteristic impedance of structure 62 from the PIQ wafer. . . . .	G-6
G.4. Measured characteristic impedance of structure 65 from the PIQ wafer (left conductor). . . . .	G-7
G.5. Measured characteristic impedance of structure 65 from the PIQ wafer (center conductor). . . . .	G-8
G.6. Measured characteristic impedance of structure 91 from the BCB wafer. . . . .	G-9
G.7. Measured characteristic impedance of structure 91 from the PIQ wafer. . . . .	G-10
G.8. Measured characteristic impedance of structure 100 from the BCB wafer. . . . .	G-11
G.9. Measured characteristic impedance of structure 100 from the PIQ wafer. . . . .	G-12
G.10. Measured characteristic impedance of structure 101 from the PIQ wafer. . . . .	G-13

Figure	Page
G.11.Measured characteristic impedance of structure 109 from the BCB wafer. . . . .	G-11
H.1. Measured coupling gain of structure 36 from the BCB wafer. . . .	H-3
H.2. Measured coupling gain of structure 36 and 37 from the PIQ wafers.	H-4
H.3. Measured coupling gain of structure 50 (a-b terminals) from the PIQ wafer. . . . .	H-5
H.4. Measured coupling gain of structure 50 (a-c terminals) from the PIQ wafer. . . . .	H-6
H.5. Measured coupling gain of structure 51 (a-b terminals) from the PIQ wafer. . . . .	H-7
H.6. Measured coupling gain of structure 51 (a-c terminals) from the PIQ wafer. . . . .	H-8
H.7. Measured coupling gain of structure 55. . . . .	H-9
H.8. Measured coupling gain of structure 100. . . . .	H-10
H.9. Measured coupling gain of structure 100. . . . .	H-11
H.10.Measured coupling gain of structure 101. . . . .	H-12
H.11.Measured coupling gain of structure 109. . . . .	H-13
H.12.Measured transmission gain of structure 50. . . . .	H-14
H.13.Measured isolation gain of structure 50. . . . .	H-15
H.14.Measured isolation gain of structure 50. . . . .	H-16
H.15.Measured isolation gain of structure 50. . . . .	H-17
I.1. Pulsed-signal response of structure 62 at 5 KHz. . . . .	I-2
I.2. Pulsed-signal response of structure 91 at 5 KHz. . . . .	I-3
I.3. Pulsed-signal response of structure 91 at 5 KHz. . . . .	I-4
I.4. Pulsed-signal response of structure 100 at 5 KHz. . . . .	I-5
I.5. Pulsed-signal response of structure 109 at 5 KHz. . . . .	I-6
I.6. Pulsed-signal response of structure 36 at 50 KHz. . . . .	I-7
I.7. Pulsed-signal response of structure 36 at 50 KHz. . . . .	I-8
I.8. Pulsed-signal response of structure 91 at 50 KHz. . . . .	I-9
I.9. Pulsed-signal response of structure 100 at 50 KHz. . . . .	I-10
I.10. Pulsed-signal response of structure 109 at 50 KHz. . . . .	I-11
I.11. Pulsed-signal response of structure 36 at 500 KHz. . . . .	I-12
I.12. Pulsed-signal response of structure 49 at 500 KHz. . . . .	I-13

Figure	Page
I.13. Pulsed-signal response of structure 49 at 500 KHz from isolated conductor. . . . .	I-14
I.14. Pulsed-signal response of structure 91 at 500 KHz. . . . .	I-14
I.15. Pulsed-signal response of structure 100 at 500 KHz. . . . .	I-15
I.16. Pulsed-signal response of structure 109 at 500 KHz. . . . .	I-15
I.17. Pulsed-signal response of structure 36 at 5 MHz. . . . .	I-16
I.18. Pulsed-signal response of structure 36 at 5 MHz. . . . .	I-17
I.19. Pulsed-signal response of structure 36 at 5 MHz. . . . .	I-18
I.20. Pulsed-signal response of structure 49 at 5 MHz. . . . .	I-19
I.21. Pulsed-signal response of structure 54 at 5 MHz. . . . .	I-20
I.22. Pulsed-signal response of structure 62 at 5 MHz. . . . .	I-21
I.23. Pulsed-signal response of structure 91 at 5 MHz. . . . .	I-22
I.24. Pulsed-signal response of structure 91 at 5 MHz. . . . .	I-23
I.25. Pulsed-signal response of structure 100 at 5 MHz. . . . .	I-24
I.26. Pulsed-signal response of structure 100 at 5 MHz. . . . .	I-25
I.27. Pulsed-signal response of structure 109 at 5 MHz. . . . .	I-26
I.28. Pulsed-signal response of structure 36 at 50 MHz. . . . .	I-27
I.29. Pulsed-signal response of structure 36 at 50 MHz. . . . .	I-28
I.30. Pulsed-signal response of structure 54 at 50 MHz. . . . .	I-29
I.31. Pulsed-signal response of structure 62 at 50 MHz. . . . .	I-30
I.32. Pulsed-signal response of structure 91 at 50 MHz. . . . .	I-31
I.33. Pulsed-signal response of structure 100 at 50 MHz. . . . .	I-32
I.34. Pulsed-signal response of structure 100 at 50 MHz. . . . .	I-33
I.35. Pulsed-signal response of structure 109 at 50 MHz. . . . .	I-34
I.36. Pulsed-signal response of structure 36 at 200 MHz. . . . .	I-35
I.37. Pulsed-signal response of structure 36 at 200 MHz. . . . .	I-36
I.38. Pulsed-signal response of structure 54 at 200 MHz. . . . .	I-37
I.39. Pulsed-signal response of structure 91 at 200 MHz. . . . .	I-38
I.40. Pulsed-signal response of structure 100 at 200 MHz. . . . .	I-39
I.41. Pulsed-signal response of structure 109 at 200 MHz. . . . .	I-40
I.42. Pulsed-signal response of structure 109 at 200 MHz. . . . .	I-41

## *List of Tables*

Table	Page
1.1. WSI Implementation Issues. . . . .	1-7
2.1. Desirable features in wafer scale interconnections. . . . .	2-11
2.2. Typical impedance ranges for several microstrip-like structures. . . . .	2-37
2.3. Effective permittivity models. . . . .	2-61
2.4. Properties of materials considered for WSIC substrates. . . . .	2-67
2.5. Properties of dielectrics considered for use in WSICs. . . . .	2-67
2.6. Properties of selected conductors. . . . .	2-68
3.1. Materials used in the test wafers. . . . .	3-4
3.2. Design specifications of the 10 cm long transmission lines. . . . .	3-8
3.3. Design specifications of the 10 cm long transmission lines (continued). . . . .	3-9
3.4. Design specifications of the 10 cm long transmission lines (continued). . . . .	3-10
3.5. Design specifications of the 10 cm long transmission lines (continued). . . . .	3-11
3.6. Design specifications of the 10 cm long transmission lines (continued). . . . .	3-12
3.7. Design specifications of the 10 cm long transmission lines (concluded). . . . .	3-13
4.1. Continuity measurement outcomes. . . . .	4-14
4.2. Results of the continuity and leakage measurements. . . . .	4-16
4.3. Structures for which characteristic impedance measurements were performed. . . . .	4-18
4.4. Quantity definitions used in the finite-difference simulations. . . . .	4-21
4.5. Analytic characteristic impedance results for certain 10 $\mu\text{m}$ the ECS structures from the PIQ wafer. . . . .	4-24
4.6. Analytic characteristic impedance results for certain 25 $\mu\text{m}$ wide ECS structures from the PIQ wafer. . . . .	4-25
4.7. Analytic characteristic impedance results for certain 10 $\mu\text{m}$ wide ECS structures from the BCB wafer. . . . .	4-26
4.8. Analytic characteristic impedance results for certain 25 $\mu\text{m}$ wide ECS structures from the BCB wafer. . . . .	4-27
4.9. Results of the FDM simulations for the three-conductor structures. . . . .	4-29

Table	Page
4.10. Analytic characteristic impedance results for coplanar waveguide structures. . . . .	4-31
4.11. Results of the characteristic impedance measurements after processing. . . . .	4-42
4.12. Analysis of coupling sensitivity to various factors. . . . .	4-48
4.13. Measured maximum coupling gain spanning 1-100 MHz for the WSIC structures. . . . .	4-55
G.1. List of characteristic impedance plots by structure and wafer type.	G-2
G.2. Linearized models of the characteristic impedance. . . . .	G-15
II.1. List of coupling measurement plots by structure and wafer type. .	II-2

### *Abstract*

This thesis considered the electrical characteristics of interconnections that have been proposed for use in silicon hybrid wafer scale integration (WSI) approaches. The study was based on a set of five-inch test wafers, containing various interconnection structures previously designed at AFIT. Two test wafers used a special polyimide dielectric, while a third was composed of a benzocyclobutene (BCB). The investigated structures represented 10 cm length aluminum, coupled, stripline-like transmission lines. The metrics used included continuity measurements, ac measurement of the characteristic impedance and coupling levels, and pulsed-signal response measurements. Continuity results indicated transmission and leakage failures in all wafers, although the failure mechanisms were sometimes wafer-specific. The characteristic impedance measurement technique was flawed, but revealed interesting information concerning the driving-point impedances of the structures. Most coupled structures manifested coupling responses which were consistent in shape with theoretical estimates, but higher in magnitude by 10-20 dB. All structures revealed coupling levels lower than -25 dB. Despite correlation difficulties, the results implied that transmission line behavior is manifested in WSIC interconnections. The measured coupling was determined to be sufficiently low to implement digital systems with adequate noise margins. Time domain performance indicated that pulsed signals up to 250 MHz could be propagated in certain WSIC structures. Proper termination of signals was found to be vital in achieving any semblance of signal fidelity at the higher frequencies. However, such terminations created great signal attenuation in 0.1 m length structures, even with 25  $\mu$ m linewidths. Recommendations for further research included: more in-depth and higher frequency evaluations of particular WSIC structures; design enhancements for future test wafers; and the development of special drivers with high gain and low input impedance for hybrid WSI systems.

# SILICON HYBRID WAFER SCALE INTEGRATION INTERCONNECT EVALUATION

## *I. Introduction*

### *Overview*

Wafer scale integration (WSI) is a promising research area which, when perfected, could have a similar effect on the microelectronics industry comparable to the introduction of the first integrated circuit. WSI cannot be truly realized until the challenges of yield, thermal management, packaging, and electrical performance are surmounted. The objective of this research was to explore a particular facet of the electrical performance area, namely, that involving the high frequency characterization of the interconnections that will be used to achieve wafer scale integrated circuits (WSICs).

### *Background*

The desire to achieve electronic systems that are smaller and more capable is ever-present, even as newer, faster, and denser integrated circuit (IC) technologies emerge. These emergent technologies predominantly lead to the realization of better IC "chips". Typically, an IC "chip" packages a single integrated circuit die. These die are separated from a single integrated circuit wafer. Contemporary electronic systems often use a set of individually packaged die — the IC "chips" — along with other discrete components to achieve a specific level of electronic performance when appropriately packaged and connected.

An examination of such systems in detail, even those regarded as being particularly compact, reveals that a large amount of the space inside the "black boxes" and on the printed circuit boards (PCBs) is wasted. Most of this space is devoted

to the interconnections from the integrated circuit die to the package, from the die package to the PCB, along the surface of the PCB between IC packages, and even from PCB to PCB. This wasted space translates into a larger physical size and mass, less reliability, and a limited electrical performance compared to that which could be obtained if this space were reduced.

An obvious alternative to building systems from packaged IC "chips" and discrete components on printed circuit boards is to increase the size of the integrated circuit die so that an entire electronic system may be accommodated. A convenient size increment for consideration and, presently, the largest feasible is that of an entire IC silicon wafer (from one to six inches in diameter). Rather than using a silicon wafer only as a fabrication media, it is plausible that this wafer might also be used as a substrate which contains and interconnects all the components that would be mounted on a PCB. Fabrication approaches which attempt to use a planar substrate the size of a wafer to realize a single, operational system are aptly termed wafer scaled integration (WSI) approaches (52).

The development of the capability to perform Wafer Scale Integration on a routine basis is being vigorously pursued by a number of interests in military, academic, and commercial sectors. Historically, WSI research interest has fluctuated over the past 20 years, although a recent resurgence has been observed [(3),(50),(62),(66:3128),(70)]. WSI approaches will have several important advantages over discrete, printed-circuit board implementations. Not only can WSI approaches achieve the highest component densities in a planar circuit, but by virtue of the resulting compactness, these approaches can also achieve a higher operating speed, lower power consumption, and improved reliability. The higher speed of operation is possible, since the required length of interconnections is decreased overall and, hence, the transit time of signals is reduced. Correspondingly, the power consumption is reduced, because the need for large package-to-package signal drivers is eliminated. These drivers were necessary in non-WSI approaches to overcome signal



attenuation in the larger geometry signal lines connecting two or more separate packages on a PCB. The intrinsic reliability of the system is also improved, since fewer connections are required outside of the wafer-sized package, which means fewer connections are subject to potentially unreliable electro-mechanical interconnections. Another advantage of WSI implementation is the potential cost reduction, as compared to conventional printed-circuit board approaches. A WSI system realizes a cost advantage since many of the additional tooling, fabrication, and evaluation processes required to implement a printed-circuit board system are eliminated [(52),(63)].

The advantages of a WSI system over a discrete IC system favor their application in military systems where space for component placement is highly valued. Specific examples include space-borne electronics systems in satellites and embedded avionics subsystems in aircraft (52). In such systems, especially the space-borne systems, the mass reduction afforded by WSI approaches is a particularly salient advantage in terms of performance as well as cost.

The WSIC application focus is primarily on high-performance digital systems, but this perspective will undoubtedly broaden to cover the more general class of analog systems. One would usually regard the former category as being the easier to implement, since digital logic generally has well defined noise margins, which are more technology dependent (for example, TTL, ECL, CMOS, etc.) than application dependent.

WSI technologies are dichotomized as either *monolithic* or *hybrid* approaches (70). The monolithic approach treats the wafer as an oversized die, and the processes used to achieve a wafer-sized circuit are basically the same as those used to achieve normal (die-sized) integrated circuits. In the hybrid approach (Figure 1), a single silicon host wafer is used as a receptacle for a variety of IC die that were previously fabricated on other silicon wafers. The host wafer in this case serves as a miniaturized PCB. After all the IC die are mounted into specially-etched receptacle holes in the host wafer, the entire assembly is then subjected to further processing,

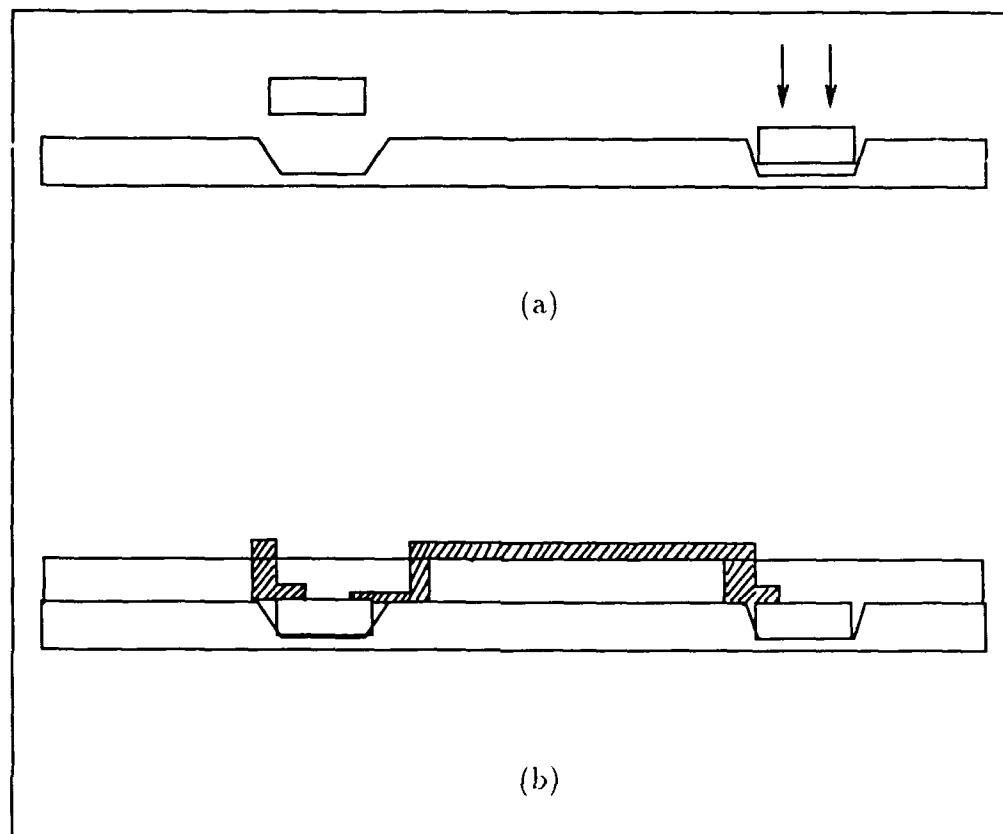


Figure 1.1. Silicon hybrid-wafer integration approach. (a) Silicon wafer substrate and receptacle structure into which integrated circuit die are mounted. (b) Subsequent structuring used to fabricate interconnections to the die and external environment. After (94).

including the formation of contacts and interconnections between the discrete die (52). The techniques for achieving die-to-die interconnections in the hybrid WSI approach are analogous to those used in the monolithic approach to internally interconnect various components. The monolithic and hybrid approaches need not be mutually exclusive, although most current research efforts tend to focus on either monolithic WSI methods or hybrid WSI methods.

A typical WSI layering scheme consists of two or more layers of signal conductors, separated vertically by layers of dielectric material. The gaps between conductors on the same plane would similarly be filled by dielectric. Finally, this

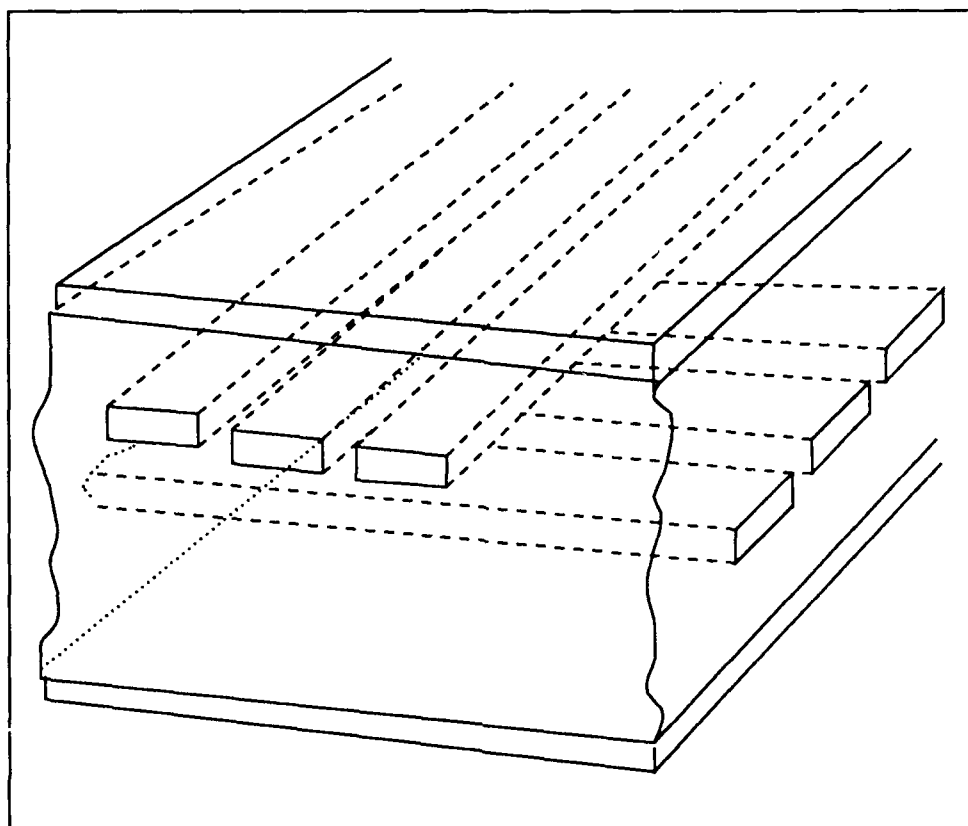


Figure 1.2. Example interconnect structure illustrating the use of multiple dielectric and conductor layers. From (71).

conductor-dielectric assembly would be sandwiched between two horizontal ground planes. Among other things, the ground planes would serve as an electrical shield, protecting the circuitry inside from electrical interference, while presumably reducing the amount of electrical interference created by the interconnections themselves. Such an interconnect assembly is shown in Figure 1.2. Wafer-scaled approaches are not without problems, which is part of the reason why little success has been achieved during the past 20 years [(70),(94)].

In the monolithic approach, the problems of integrated circuit yield are especially exasperating. The yield problem, that of producing a defect-free circuit, becomes particularly tenacious when the area of interest is increased from the size

of an IC die to the size of an entire wafer. The success of the monolithic approach hinges upon the circumvention of the yield problem (among other things) and, as such, a number of creative responses have been elicited from researchers (70).

With the hybrid approach, circuit yield problems are reduced, since the resident circuit die are pre-selected. The most significant yield problems involved with the hybrid approach concerns the interconnections between discrete die. However, other problems affect the hybrid scale WSI technology. First, the planarity of the entire wafer's surface after the die are mounted in their etched cavities has been difficult to achieve. If the surface of the wafer is not planar, the ability to achieve interconnections between die are jeopardized. Second, micron-level deviations in the size of the die relative to their receptacles in the host wafer can result in misalignment and contribute to interconnection problems (63).

Many of the problems in achieving WSI afflict both the monolithic and the hybrid approaches. In both approaches, the yield of the interconnections themselves is an area of concern. Other fabrication and design issues common to both approaches are shown in Table 1.1 (71:95). To be considered successful, WSI must surmount these problems [(28),(52)].

Due to the large amount of interconnection wiring (a recent study estimated that a typical hybrid WSIC would require a kilometer length (71)), the electrical performance of WSICs merits particular consideration. Even if all other obstacles are surmounted, WSI cannot truly be regarded as successful if only low frequency systems can be realized. The electrical performance area is often neglected by the designer, who, by tradition, relies on established design methodologies to realize die-sized IC circuits. These standard practices or design methodologies, especially as they apply to silicon microcircuits, do not consider the effects of transmission line behavior. Transmission line effects, in particular, the phenomena of coupling, loss, dispersion, and reflections due to impedance mismatches, have usually been relegated to the designers of PCBs, as evidenced by the body of literature available (84).

Table 1.1. WSI Implementation Issues. After (71:95)

Yield	The yield of fabricated WSI interconnections (opens, shorts, leakage in dielectric, via faults)
Design	Producing wafer-scale layouts
Reliability	Dependability of Interconnects under physical stresses
Testing	Testability of wafer, including accessibility of components for diagnostic exercise and fault isolation capability
Packaging	Achieving adequate packaging Hermeticity
Thermal	Power dissipation Heat removal
Electrical	Transmission line effects (ringing, coupling, dispersion) Power and ground planes

The reason for the apparent oversight is that the wavelengths of the frequencies involved in silicon microcircuits are much greater than any spatial dimension of or inside the die. A one-centimeter sized die, for example, has a free-space wavelength corresponding to a frequency of approximately 30 GHz. As such, transmission line effects may be neglected for die-size IC circuits, since they are only significant when the wavelengths of concern approach the physical size of the die. However, with a wafer-sized circuit, and the potentially higher operating frequency, a more serious consideration of transmission line effects is warranted. The chances of undesired transmission line effects are now greater, since the wavelengths of concern approach the size of the wafer substrate. Since these transmission line effects are a consequence of physical dimensions, they obviously are common to both WSI approaches.

The predominant transmission line effects include wave reflection (also called "ringing"), dispersion, and coupling (also called "crosstalk"). Wave reflections occur as a result of impedance mismatches in a system and are a direct consequence of the energy conservation principle which also applies to electrical systems. Loss

mechanisms, such as conductor attenuation, dielectric losses, radiative losses, and skin effect losses, cause undesired attenuation of a signal's amplitude. Wave dispersion, related both to frequency-dependent material properties and to geometric dispersive effects, results in signal distortion due to the change of propagation velocity with respect to frequency. Since dispersion is generally frequency dependent, a broadband signal will become distorted, since its higher frequency components will be attenuated differently than its lower frequency components. Finally, coupling problems occur when multiconductor transmission lines have significant field interactions which result in the "bleeding through" of signals from one line to another.

In the "mainstream" of microwave applications, the effects associated with transmission line behavior are well-defined. The interconnections of an integrated circuit are usually equivalent to either *microstrip* transmission lines or *stripline* transmission lines, a classification that is based on the geometries involved (45). In addition to geometric considerations, much of the design work is accomplished by knowing the fundamental material parameters, such as relative permittivity ( $\epsilon_R$ ), relative permeability ( $\mu_R$ ), and conductivity ( $\sigma$ ), which usually give the analyst and designer the ability to estimate important transmission line quantities such as the characteristic impedance, the degree of coupling, and the loss and dispersion mechanisms of the transmission media. The transmission media in this case is a set of conductors, rectangular in shape, which are usually embedded in a dielectric material suspended over a ground plane of conducting material and a substrate of semiconducting bulk material. Many design approximations and rules of thumb have evolved for the design and analysis of microstrip and stripline transmission lines [(29),(42)]. However, most of these design guidelines were developed for transmission lines with physical dimensions that are large compared to those in a WSIC (roughly a 100:1 to 1000:1 difference in linewidths, for example). It is likely that some of these design rules will not be applicable to WSI technology.

Analysis and experimental verification of the transmission line phenomena that

can affect WSICs is needed. Analyses of these problems exist; most of the treatments presented in the literature are very specific. Most authors deal with only one facet of the overall transmission line problem as it relates to microcircuits. In almost all cases, the discussions are purely theoretical, and, in some cases, the conclusions are contradictory. Any experimental verification, for the most part, is performed on large scale models, if addressed at all. A cohesive and comprehensive treatment of transmission line effects in WSI circuits, which would include some experimental support, does not exist in the present literature.

### *Problem Statement*

This thesis addresses the electrical performance issues focused on the transmission line phenomena that will affect high-frequency WSICs. Specifically, the analysis and measurements of the influence of transmission line effects on the interconnections of wafer-scaled systems with silicon substrates have been pursued. The particular high-frequency measurements and analyses addressed the following questions:

1. Do currently established and proposed models for calculating characteristic impedance, coupling, dispersion, and attenuation adequately characterize WSI interconnects so that designers may continue to use them?
2. Are the electrical coupling phenomena present in representative WSI interconnects so severe as to render them useless in digital and analog system applications?
3. What performance can be expected from a typical WSI network when digital signals are impressed upon it?

### *Scope*

This research effort explored the electrical properties of several conductor and dielectric combinations intended for use in future WSI developments. The subjects

for evaluation included a set of specially designed wafers, manufactured by Polycon (Ventura, CA) with various test interconnect patterns. This thesis report addresses:

1. Transmission-line properties of the WSI interconnects
2. Pulsed waveform performance of the WSI interconnects.

The primary emphasis of this report concerns transmission line effects, especially the characteristic impedance and mutual coupling parameters which affect WSICs. Additionally, the effects of WSI interconnections on pulses are investigated, since these results are of interest for digital applications. Finally, the yield of WSI interconnections is analyzed.

Since yield quantities are not deterministic, the yield results of this research cannot be generalized, due to the small sample population studied. Furthermore, certain of the yield phenomena unique to hybrid WSI will not be addressed by this effort. In particular, the yield problems due to non-planarity and mis-alignment of die cannot be explored, since no die were involved in this interconnect-only study (81).

The focus of work in this thesis addresses the hybrid WSI approach, reflecting the emphasis at the Air Force Institute of Technology (AFIT) concerning this approach (52). Most of the pertinent results, however, are equally applicable to monolithic WSI systems. Problems peculiar to monolithic systems, such as adaptive discretionary wiring, will not be addressed in this thesis [(63), (28)].

The WSI technology evaluated in this study were three, five-inch diameter wafers fabricated by arrangement through Polycon, Inc. (Ventura, CA) (Figure 1.3). Structurally, these wafers consist of a silicon substrate, onto which layers of dielectric and conductor materials are alternately patterned. These wafers do not incorporate active devices, but they contain various proposed WSI interconnection schemes. Approximately ten blocks or groupings of interconnection structures are present on each wafer; a slight magnification of Figure 1.3, shown in Figure 1.4, reveals several such groupings (82). The resulting wafer structures are physically arranged in a manner



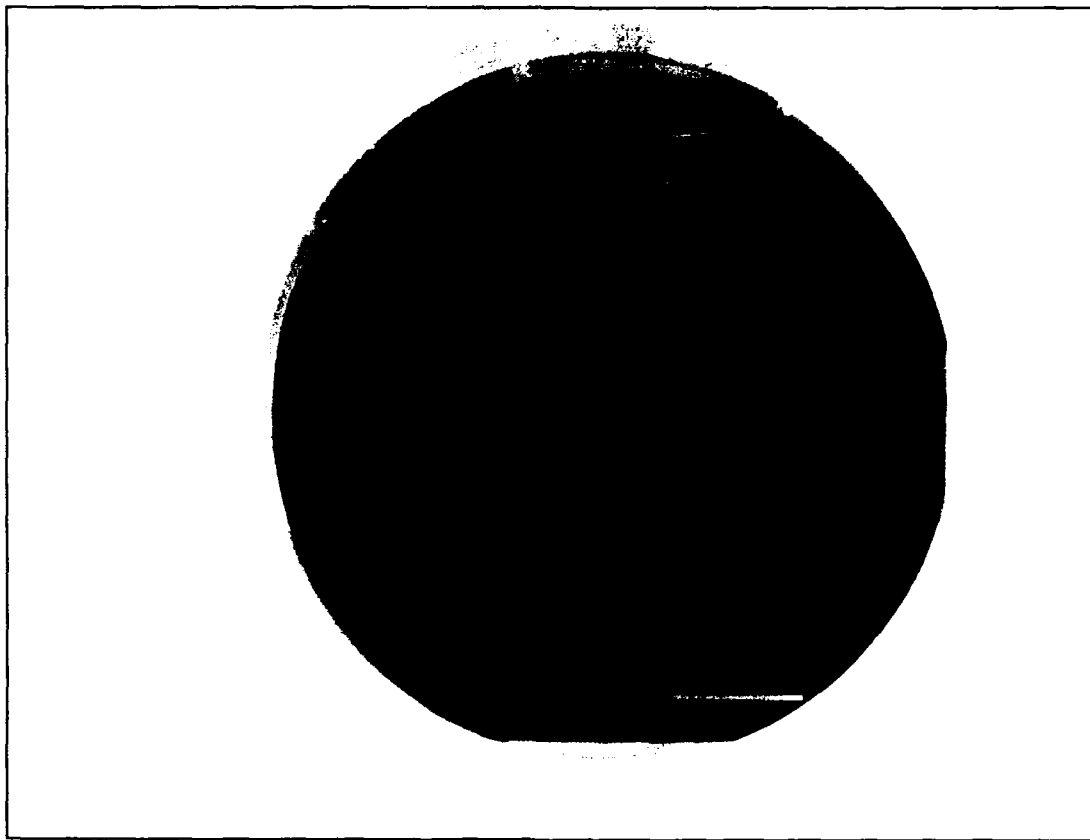


Figure 1.3. Photograph of a test wafer.

similar to that shown in Figure 1.2 and represent the electrical links which would be used to connect WSI circuit elements to each other and to the external environment. The design of the interconnection patterns were based on earlier work accomplished by Capt (Ret.) Brian Donlan at AFIT and Rensselaer Polytechnic Institute (RPI) for three-inch diameter WSI systems. The final interconnection designs were modified by Polycon, Inc. (Mr. John Reche, President) to take advantage of the larger five-inch diameter wafer size which became available during the study [(27),(81)].

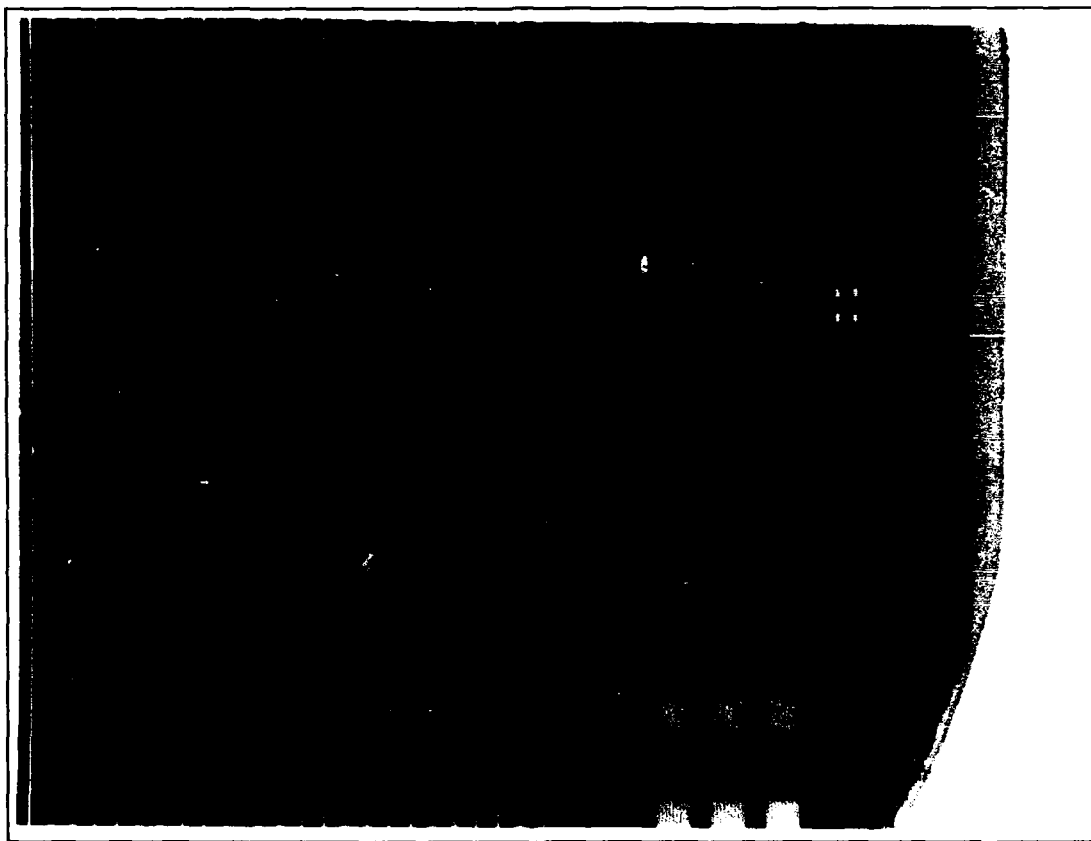


Figure 1.4. Close-up view of a test wafer, revealing several groupings of interconnections.

### *Assumptions*

1. The material properties of dielectrics and conductors used in this study were assumed to be linear, homogeneous, and isotropic. This assumption was made as a simplifying approximation, and, in general, such materials will exhibit some degree of non-linearity, inhomogeneity, and anisotropy. Ignoring these anomalous effects for the particular materials studied in this thesis was believed to have introduced only a slight error over the frequency ranges investigated (1-100 MHz for gain-phase measurement and 1-700 MHz for impedance measurement). Furthermore, the magnetic permeability of all materials involved in this study were assumed to be equal to that of free space.
2. The experimental work in this research was based on the availability of two types of WSI dielectric and conductor material combinations. The first type was a silicon substrate, overlayed with a special polyimide (polyimide iso-indroquinazolinedione, abbreviated PIQ) dielectric and aluminum conductors. The second type, which also consists of a silicon substrate, utilizes a benzocyclobutene (BCB) dielectric and aluminum conductors [(27),(81)].
3. The measurements were accomplished with special-purpose wafer probes. These probes had either a known characteristic impedance at their tip ( $50\ \Omega$ ), or a relatively high impedance, that is, greater than one million ohms ( $1\ \text{M}\Omega$ ). The WSI wafers (with unknown characteristic impedance) were assumed to be electrically unaffected by the high impedance probes.
4. The frequency ranges used in this research spanned 1-100 MHz for the gain-phase measurements and 1-700 MHz for the impedance measurements. In the pulse measurements, square-waves were used with rise times on the order of 1-6 ns.
5. The limitations of time prevented an in-depth study of all available structures on the test wafers. In particular, the study focussed on only five types of

transmission line structures, as outlined in Chapter 3. Hence, a many other structures remain to be explored.

### *Approach*

To approach each problem category, except for the pulsed waveform evaluation, a three-step method was implemented. The first step, a modeling effort, was used to characterize the WSI interconnects by analytical and numerical techniques. The second step involved collecting actual WSI interconnection measurements in the laboratory. The final step in the methodology involved the analysis of the measurement results and a comparison with the theoretical predictions, with an anticipation of achieving reasonable correlation.

Ideally, the wafer scale lines could be characterized by transmission line parameters at high frequencies. The primary parameters include the characteristic impedance and the attenuation and propagation constants. These parameters, along with the material and geometrical properties upon which they depend, determine the electrical properties of the associated transmission lines. The models selected for characterizing the electrical performance of WSI interconnections were based on existing theoretical developments, some for transmission lines of larger sizes, as reported in the available literature.

The literature review process facilitated the identification of such models and the determination of their applicability to wafer scale geometries. The treatments presented in currently existing literature are widely varied and often must be carefully interpreted and adapted for wafer scale use. In some cases, especially for arbitrary multi-conductor transmission line network arrangements, numerical modeling approaches are required, since appropriate closed form expressions do not exist. In the tradition of engineering approximation, simpler, lossless models and simplified closed form expressions were used extensively in attempts to achieve correlation with measurements. More sophisticated models were also used; presumably, these models would work better in this respect, if the simpler expressions were too inaccurate.

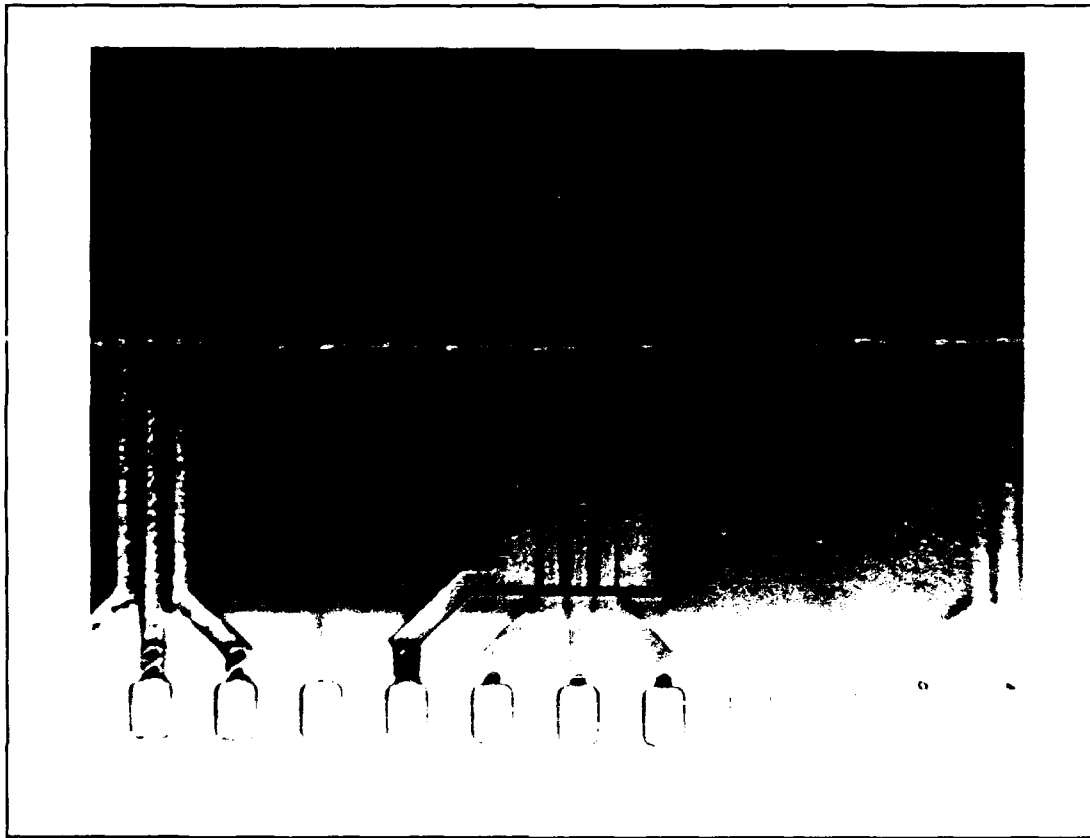


Figure 1.5. Typical conductor geometries on a test wafer scale integrated circuit.

Development of the measurement configurations and procedures followed from a knowledge of suitable metrics, which were identified in the literature review. To characterize a physical wafer scale interconnection network in terms of transmission line parameters, so that they could then be compared to the theoretical models, it was necessary to measure the characteristic impedance, attenuation, and coupling factors of individual wafer-scale interconnections. These measurements were made on a variety of wafer scale transmission structures, such as those shown in Figure 1.5, over a frequency range of 6–100 MHz. All measurements were conducted in the Cooperative Electronics Materials and Processing Laboratory in Building 125, Room 1065, in Area B of Wright-Patterson AFB, Ohio.

The impedance measurements were obtained using an impedance analyzer, and the attenuation and coupling measurements were acquired with an oscilloscope and gain-phase analyzer. The equipment used was computer controlled to simplify data gathering. Through the use of a Z-248 class personal computer and an IEEE-488 accessory interface card, the calibration, measurement, and data collection activities for most of the research involved were coordinated. Of course, the development of appropriate software was required, and the modification of existing software developed and successfully used for previous master's thesis efforts fulfilled this requirement.

In addition to the electrical material property measurements, the responses of the interconnections to pulsed square wave signals were observed. This particular investigation was more qualitative and was undertaken because of the widespread use of integrated circuits for digital applications. It is, in fact, expected that WSICs will be used for digital circuitry before more general analog applications are developed.

To minimize the problems of perturbing probe interactions, the use of special probes of controlled impedance and high impedance were used for the quantitative impedance and coupling measurement and for the pulsed-signal measurements, respectively. The low impedance probes minimized the transition circuits which are usually formed when transmission line measurements are made (36). The high-impedance probes, on the other hand, which also manifested a low capacitance (less than 1 pF) were used to sample signals from a measured line as a non-perturbing observation tool. These probes allowed for the reduction of loading effects by the probe and receiving cable, thus isolating the loading effects to those produced by the cable, the subject line, and, in the case of terminated lines, the electrical load placed at the end of the line.

### *Equipment*

The following instrumentation list summarizes the critical resources necessary to accomplish this thesis. The items listed below were used in the experimental configuration located in the Cooperative Electronics Materials and Processing

Laboratory in Building 125, Room 1065:

1. Beckman, Inc., digital ohmmeter, model no. 3010UL, Fullerton, CA.
2. International Scientific Instruments, scanning electron microscope, model no. WB-6, Milpitas, CA.
3. Hewlett-Packard, Inc., RF impedance analyzer, HP 4191A, Colorado Springs, CO.
4. Hewlett-Packard, Inc., frequency-tunable impedance bridge, HP 4192A, Colorado Springs, CO.
5. Hewlett-Packard, Inc., gain-phase analyzer, HP 4194A, Colorado Springs, CO.
6. Micromanipulator Co., VLSI sub-micron probing station with video camera, monitor, and probing accessories, model no. 6200, Carson City, NV.
7. Micromanipulator Co., ultrasonic cutting probe, model no. 7000-MUC, Carson City, NV.
8. Micromanipulator Co., high-impedance ( $>1\text{ M}\Omega$ ), low-capacitance ( $0.2\text{ pF}$ ) probes equipped for high frequency work (up to  $1\text{ GHz}$ ), model no. FET-1, Carson City, NV (six were required).
9. Micromanipulator Co., low-impedance ( $50\Omega$ ) probes with ground plane connection, equipped for high-frequency work (up to  $1\text{ GHz}$ ), model no. 44-7000-GP, Carson City, NV (four were required).
10. Micromanipulator Co., Kelvin measurement probes ( $50\Omega$  impedance) with ground plane connection, equipped for high-frequency work ( $1\text{ GHz}$ ), model no. 44-7000-D, Carson City, NV (two were required).
11. Zenith Data Systems, personal computer configured to function as an automatic laboratory data acquisition system, model no. Z-248/150 PC, St. Joseph, MI.
12. Hewlett-Packard, Inc., pulse generator, HP 8082A, Colorado Springs, CO.

13. Hewlett-Packard, Inc., digitizing oscilloscope, HP 54100A, Colorado Springs, CO.

### *Order of Presentation*

This thesis report documents the research accomplished concerning the problem statement discussed above. This thesis achieves this objective by presenting an analysis of WSI interconnections and their high frequency electrical performance, outlining the proposed experimental techniques to verify the theoretical projections, and discussing the results of the proposed measurements. Chapter 2 will provide a review of current work in WSI electrical characterization, compiled from recent literature. The wafers that were evaluated are discussed Chapter 3, along with the experimental measurement techniques and numerical computation approaches used in the analysis. The results of the measurement exercises and computer simulations are presented in Chapter 4. Chapter 5 summarizes the relevant findings and provides recommendations for the continuation of this research.

### *Summary*

The objective of this thesis was to explore the electrical performance of wafer scale interconnections. To be considered a viable technology, wafer scale integration must be able to achieve acceptable and predictable performance, even at frequencies where transmission line effects become significant. As discussed, the potential interconnection schemes which could be used in working WSI designs will behave as multiconductor transmission lines. As such, it is important to understand the transmission line effects which will affect wafer scale systems, to predict their impact, and to experimentally verify the projections given by existing theory. Due to the small physical size involved, the fundamentals of existing theory must be examined to further justify its use for the special geometries involved in WSI.

This thesis addresses these concerns. First, it examines the existing theory in depth, in order to determine where it may fall short in correctly characterizing



the WSI interconnections at high frequencies. In particular, the transmission line effects of coupling, dispersion, loss, and reflections are examined. Another important parameter, the characteristic impedance, is explored. When possible, available software packages (Mathematica, LINECALC, and LIBRA) are used to supplement the theoretical predictions. Second, this thesis used actual WSI networks fabricated on a silicon substrate to experimentally measure certain quantities. These quantities include the characteristic impedance and coupling between interconnections. Pulsed-signal response behavior is also examined, as this area is of special concern to the digital VLSI design community. All experimental activities over the frequency range of interest were accommodated with available resources. Finally, of course, a correlation between the theoretical projections and experimental measurements is sought, and deviations between the two are critically examined. Ultimately, the most desirable outcome of this research would be to show not only that existing theory will support WSI interconnections, but that the problems of these closely-spaced connections are not so severe as to render WSI approaches impractical, and, consequently, that most of the existing computer-aided design software will still be useful for WSI work.

## II. Review of the Current Literature

A theory is not an absolute truth but a self-consistent analytical formulation of the relations governing a group of natural phenomena.

— Julius Stratton, *Electromagnetic Theory*

### *Overview*

This chapter considers the electrical performance of the interconnections of proposed WSI systems, and it attempts to reconcile their performance relative to established and proposed theoretical projections. In particular, the important concepts of transmission line and full-wave analyses are regarded as they apply to WSI interconnections. It is necessary to adequately characterize WSI systems electrically, and part of this characterization involves the assessment of the current state-of-the-art in electromagnetic analyses to determine its applicability to WSI interconnections. Weak links or potential inaccuracies must be identified. The ultimate goal and hope for WSI advocates is that this theory will apply and, furthermore, that high electrical wiring densities can be achieved.

To accomplish this goal, the transmission line effects that can affect the interconnections are examined first. After the presentation of transmission line theory in somewhat general terms, more specific results that apply to wafer scale interconnections are considered. In particular, results found in the existing literature relevant to the analysis of characteristic impedance, attenuation, dispersion, and coupling in wafer scale transmission line structures are presented and discussed. Next, other relevant issues, such as the yield of wafer scale interconnections and the performance of interconnections in pulsed-signal environments, are examined.

### *Transmission Line Effects in Wafer Scale Interconnections*

In introductory circuit theory, a wire or conductor connecting points *A* and *B* in a circuit is regarded as a zero-resistance, zero-reactance, zero-time-delay conduit

for electrons. It is also assumed that two adjacent signal lines are electrically independent; that is, that the electrical performance of a given conductor is not influenced by the presence of neighboring conductors (no mutual reactance). These statements, in general, do not apply to a high-frequency system, because the interconnections between circuit elements themselves must be regarded as circuit components which may significantly alter the performance of a system (as projected from analyses which do not consider their presence). As a result, circuit theory breaks down when the transverse dimensions of a circuit approach the wavelength of the driving source (55:368).

These higher frequency effects are often referred to as *transmission line effects*. A dividing line between the regions where the simpler, lower frequency circuit theory (sometimes called "lumped-circuit" theory) and the higher frequency transmission line theory are applicable is difficult to establish. A common rule of thumb states that transmission line effects are clearly exhibited when the physical length of any component of an electrical system (include interconnections) is greater than 1/15th of the wavelength of any signal which may be impressed on the component (84); these effects are manifested to a lesser degree as the wavelength increases. For sufficiently long wavelengths, the system operates in the *lumped parameter* regime, which is adequately characterized by the simpler circuit theory mentioned above.

The length of interconnections of WSICs, in particular, can approach or exceed the frequency limit where simple circuit theory alone cannot characterize their electrical performance. Even in integrated circuits of smaller size, it is clear that such a frequency limit can be attained. For example, as reported by Goosen *et al.* and Hasegawa *et al.*, lumped circuit models are inadequate for representing interconnections when the signal switching time is faster than 100 picoseconds (39).

The analysis of interconnections in these cases may be accomplished through various modeling techniques, ranging from more sophisticated extensions of lumped circuit models and multi-port analyses to elaborate full-wave field analysis approaches

(41). An analysis approach of intermediate complexity involves the use of transmission line theory, which is a specialized form of the more-involved, full-wave treatment. While not as general as a full-wave analysis, transmission line techniques provide more versatility than simple lumped-element circuit theory.

Assuming that a transmission line approach is adequate for considering wafer scale interconnections, several concerns must be addressed. The transmission line effects of primary concern in the study of wafer scale interconnections include: *reflections* or ringing, which are the result of impedance mismatches at an interconnection; *coupling*, which refers to the influence on an interconnection by neighboring components, due to an electromagnetic field interaction; and *losses*, which cause attenuation and dispersion of the signals impressed upon an interconnection. These effects are usually undesired, and sometimes they occur due to designer negligence or due to inadequate modeling techniques. The first problem can be reduced by increasing designer awareness, whereas the second problem is more difficult and will require the re-evaluation and refinement of existing models.

This section explores the existing literature, which reveals many attempts to rectify the latter deficiency. The goal of this section is to document the most significant results that pertain to transmission line effects in wafer scale interconnections. To accomplish this goal, the structures involved in wafer scale interconnections will be examined. Next, the pertinent elements of transmission line theory will be discussed in somewhat general terms. The more specific and detailed results which apply to this study will then follow.

*Wafer Scale Integration Interconnection Structures.* If transmission line behavior exists in WSIC's at a given frequency, it is important to identify the types of transmission line structures that they represent. Since the evolution of transmission line structures has not been completely deliberate, one may also wish to address a more important question: What are the desirable qualities of a wafer scale transmission line? Obviously, if existing wafer scale interconnections are *bad* transmission

lines, it would seem prudent to identify their weaknesses and identify more suitable candidates.

As it turns out, the interconnections of integrated circuits are predominantly *microstrip-like* structures by coincidence (7:348), if not by design. A primary difference between the interconnections of typical integrated circuits and those proposed in some WSI projects is that the former display an RC-like characteristic, whereas the latter manifest an LC-like behavior, approximating those of traditional transmission lines (66). The term "microstrip" has two separate meanings in the literature. As a class of transmission lines, "microstrip" lines will be used to refer to any of the several planar transmission line types which are to be described. A "microstrip" transmission line also refers to a specific type of planar transmission line. When the denotation of the term "microstrip" is not clear by context, the term "microstrip-like" will be used to denote the class of planar transmission lines. Several representative planar transmission line types are shown in Figure 2.1.

Following is a brief discussion of these transmission lines. In all of these structures, a relative permeability ( $\mu_R$ ) equal to that of free-space is assumed for conductors and dielectrics. Furthermore, all geometric distances are assumed to be uniform, unless otherwise stated. This assertion implies, for example, that the width of a microstrip-like structure is constant along its length.

*Microstrip.* The microstrip transmission line (Figure 2.1a) consists of a solid rectangular conductor, resembling a long plank, affixed to the top surface of a flat dielectric slab which is covered on its bottom surface with a conducting ground plane. The beam-like conductor is the *active* line in the sense that it is usually the one upon which signals of interest are impressed. The width ( $w$ ) of the top conductor is usually much greater than its thickness ( $t$ ) or height ( $h$ ), which is an important relationship in some design approximations. The top surface of the microstrip is usually uncovered, but, in general, another passivating dielectric medium may protect the exposed surfaces of the conductor and dielectric (41:2).

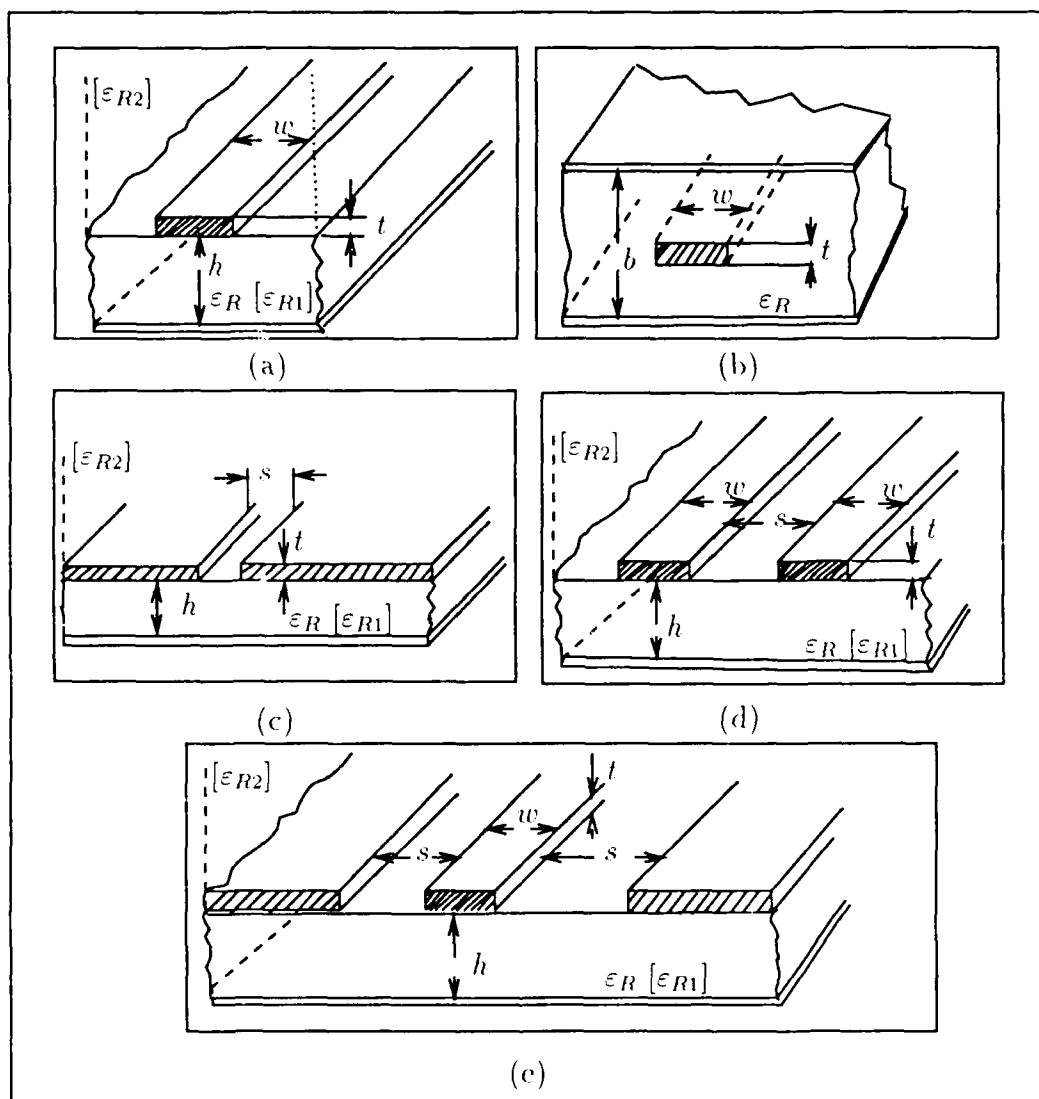


Figure 2.1. Representative planar transmission line structures. Bracketed [ ] quantities denote alternate representations for the case where the superficial dielectric has a relative permittivity not equal to that of free-space ( $\epsilon_R \neq 1$ ). (a) Microstrip. (b) Stripline. (c) Slotline. (d) Coplanar strip. (e) Coplanar waveguide. After (41).

In addition to the geometric parameters already mentioned, the microstrip is characterized by the vertical separation of the active conductor relative to the ground plane and the material parameters associated with the dielectric and conductor materials. The ground plane is almost always treated as dimensionally infinite in analyses, but it is, of course, finite in practice. The material parameters of the microstrip structure include the relative permittivity and loss tangent of the dielectrics and the conductivity of the active conductor and ground plane. For a microstrip assembly covered by a free-space dielectric, the electric permittivity of the substrate is denoted by  $\epsilon = \epsilon_R \epsilon_0$ , where  $\epsilon_R$  is the relative permittivity of the substrate dielectric. When the assembly is not covered by a non free-space dielectric ( $\epsilon \neq \epsilon_0$ ), then the electric permittivity of the two dielectrics are denoted by  $\epsilon_{R1}$  for the substrate and  $\epsilon_{R2}$  for the superficial dielectric. The loss tangent ( $\delta_L$ ) is a property of dielectrics which manifest leakage conductance. For lossless dielectrics,  $\delta_L = 0$ . The most important material property of the active conductor is its conductivity ( $\sigma$ ). The ground plane is generally treated as a perfect conducting medium; that is, the ground plane is assumed to have an infinite conductivity (41:2).

*Stripline.* The stripline transmission line (Figure 2.1b) is similar to the microstrip line, except that its top surface is covered by the same dielectric material that isolates it from the lower ground plane. Additionally, a conducting ground plane is placed on the top surface of the added dielectric. In other words, the rectangular conductor is embedded in a dielectric which is sandwiched between two conducting planes. This structure is characterized in a similar manner as the microstrip line, except that  $\epsilon_{R1} = \epsilon_{R2}$ , and an additional geometric parameter is required to specify ground plane separation ( $b$ ).

*Slotline.* The slotted transmission line or slotline structure (Figure 2.1c) may be physically regarded as a dielectric covered above by a conducting ground plane, with a rectangular strip of metal removed from the top ground plane, forming a trench which exposes the dielectric beneath (41:195). With this physical

conductor separation, the top ground plane becomes a transmission line. The electrical properties of the slotline are determined by the gap spacing ( $s$ ), the vertical separation between the active conductors and the ground plane ( $h$ ), and the material properties of the dielectric ( $\epsilon_R$ ). As with the microstrip and stripline, the ground plane is usually assumed to possess infinite conductivity.

*Coplanar Strip.* The coplanar strip (CPS) transmission line (Figure 2.1d) resembles two microstrip lines placed in parallel, which lie on the same dielectric, separated by a gap ( $s$ ) (41:287). The generic structure does not possess a conducting ground plane beneath the two conductors. For this case, one conductor is arbitrarily considered to be the active conductor, and the remaining conductor serves as the ground. The associated material parameters are the permittivity of the dielectric ( $\epsilon_R$ ) and the conductivity ( $\sigma$ ) of the two conductors.

The applicable geometric parameters include the thickness and width of the conductors and the spacing between them. For symmetric assemblies, the thickness of both conductors and the width of both conductors are identical, and they are denoted by ( $t$ ) and ( $w$ ), respectively. When either the thickness or width of the conductors differ, these quantities are distinguished with subscripts. The spacing between the two conductors is denoted by the variable ( $s$ ).

*Edge-Coupled Microstrip.* When the coplanar strip structure is affixed below with a ground plane, the assembly is referred to as an *edge-coupled microstrip* (ECM) assembly (42:77). In this case, both conductors are active conductors. In addition to the geometric parameters used to describe the coplanar strip, the ECM assembly must additionally specify the height of each conductor relative to the ground plane. In a symmetric assembly, the height of each conductor above ground is specified by the single variable ( $h$ ). Otherwise, separate heights ( $h_1$  and  $h_2$ ) are specified for each conductor. In practical WSICs, configurations of edge-coupled microstrips may be encountered with more than two conductors. For such configurations, the nomenclature used to describe the dual-line configuration is extended



as necessary to accommodate the extra conductors. For example, the third line of a three-line ECM may be characterized by a width ( $w_3$ ), height ( $h_3$ ) above ground, and thickness ( $t_3$ ). Alternately, when these geometric parameters are the same for each conductor in the system, the width, height, and thickness of all conductors are denoted by the single variables ( $w$ ), ( $h$ ), and ( $t$ ), respectively. Multi-conductor structures with identical widths, heights, and inter-conductor lateral spacings are referred to as *symmetric* structures.

*Edge-Coupled Stripline.* When the ECM assembly is covered by the same dielectric above and below the conductor assembly ( $\epsilon_{R1} = \epsilon_{R2}$ ), and when a ground plane is affixed on top of the superficial dielectric, the assembly is referred to as an *edge-coupled stripline* (ECS) assembly. As in the case of a single-conductor stripline, the specification of an additional geometric factor, the ground plane separation ( $b$ ), is required. As with ECM configurations, ECS configurations with more than two conductors may be encountered in practice.

*Coplanar Waveguide.* The coplanar waveguide (Figure 2.1c) resembles a set of three parallel microstrip conductors. In this configuration, the center conducting strip is the active line, and the conductors on either side are ground conductors. In most cases of practical interest, the center conductor is centered between the ground conductors. In this case, the gap spacing is symmetric and its value is denoted by the variable ( $s$ ). Coplanar waveguides sometimes occur with a conducting ground plane affixed below. In this case, the vertical separation between the three conductors and ground is denoted by the variable ( $h$ ) (41:258).

Of the planar transmission lines discussed, the most frequently encountered types in the integrated circuit technology are the microstrip and stripline transmission lines. For designs involving low frequency (lumped-parameter) operation, this occurrence is coincidental, since integrated circuit interconnections are fabricated as rectangular metal strips because of geometric necessity. However, at higher operating frequencies, these interconnections behave as planar transmission lines.

Designers who take advantage of this knowledge may intentionally utilize any of the aforementioned transmission line types in a design.

Unfortunately, these transmission line classifications do not comprehensively categorize every possible transmission line structure that occurs in integrated circuits. For example, the transmission line structures shown in Figure 2.2, which represent those which can occur in an integrated circuit or wafer scale design, cannot be strictly classified into any of the above categories. Some of these structures appear to be approximately equivalent to some of the previously defined types, while others bear little resemblance. A great number of such non-standard structures may be encountered. They are not intentionally designed this way, per se, but simply result from the connection of many circuit elements together in an integrated circuit wafer. Obviously, the analysis of such structures can become considerably more complicated.

The first structure in Figure 2.2 resembles an asymmetric ECS, but the structure does not possess a superficial ground plane. For purposes of classification, this structure could be denoted as an *edge-coupled semi-stripline (ECCS)*. The same nomenclature used in the ECS would apply to this structure, except that the ground plane separation ( $b$ ) would be used to represent the total dielectric layer thickness. This structure is also referred to in the literature as an *embedded microstrip*. Unlike the first structure, the second and third structures in Figure 2.2 defy standard classification schemes.

Since some interconnections of wafer scaled circuits can be at least tentatively associated with one class of existing transmission lines, the next obvious point to consider is the adequacy of this class of transmission lines. The salient qualities of good integrated circuit interconnections for frequency regions where transmission line effects become significant are summarized in Table 2.1. The entries in this table are numbered for purposes of reference only (7).

As highlighted previously, integrated circuit interconnections, in general, are

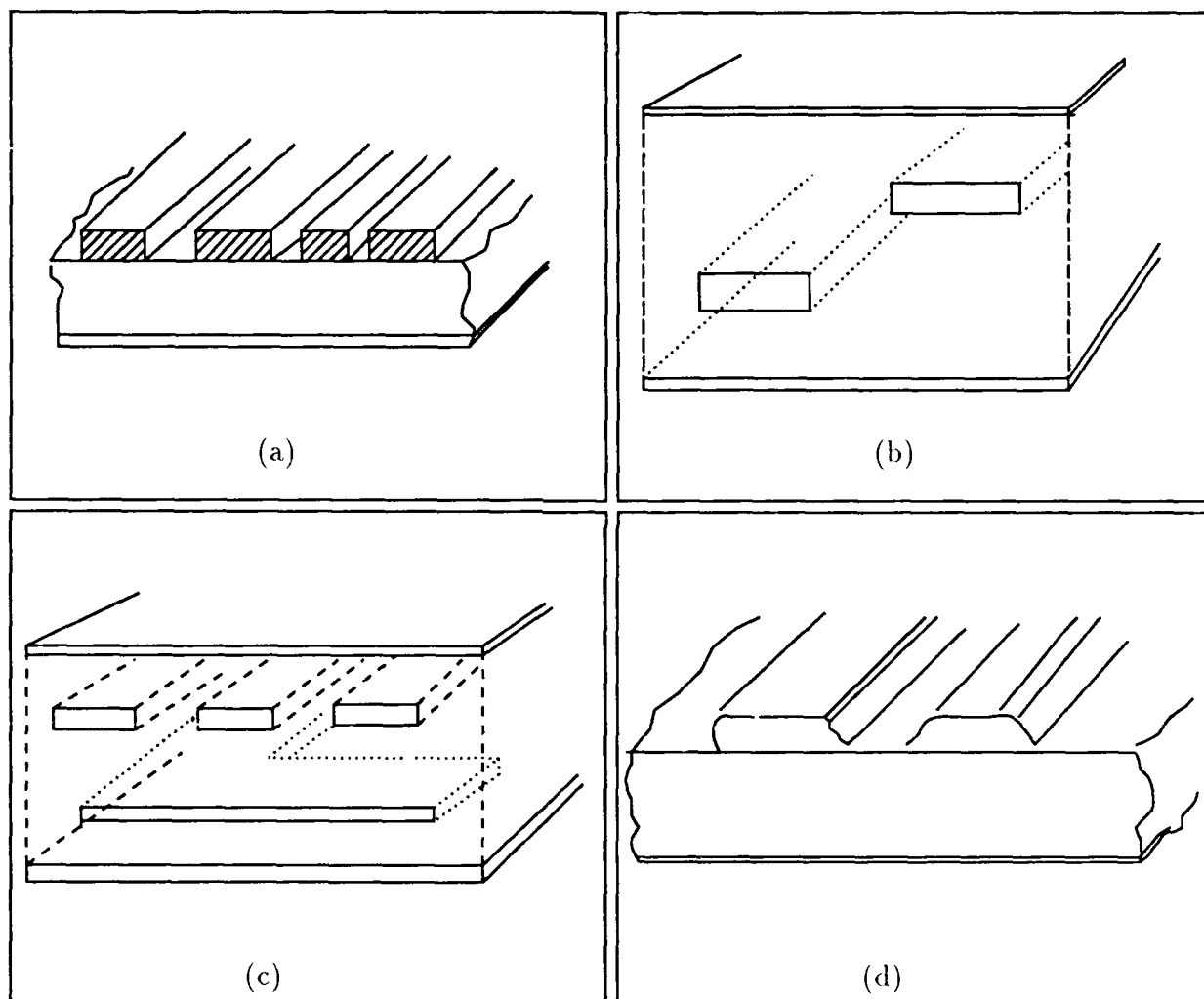


Figure 2.2. Several non-traditional transmission lines.

Table 2.1. Desirable features in wafer scale interconnections. After (7).

1.	Low insertion loss
2.	Electrically independent
3.	Wide bandwidth
4.	Ease of bondability
5.	Reproducibility
6.	RF matching
7.	Small size
8.	Easily and economically fabricated
9.	Reliability

microstrip-like structures. Bhasi *et al.* noted their advantages; they are easily fabricated with established methods and have wide bandwidths. The reliability (item 9) is difficult to deterministically establish, but, by using structures and materials similar to those used in established integrated circuit technologies, it is expected to be high. Hence, items 3, 4, 5, 7, 8 and 9 in Table 2.1 can be satisfied by existing and well-established technologies. However, the problems associated with microstrip interconnections include their inefficiency when compared to waveguide interconnections at the higher operating frequencies ( $> 18$  GHz) and the analytic problems associated with characterizing their electrical behavior (7:348). Further complicating the analysis of planar transmission lines are the discontinuities in conductor shapes (for example, corners and steps) that occur on an integrated circuit. If these analytical problems are significant, then the predictable design of RF matching networks (item 6) will become even more difficult. Hence, items 1 and 6 from Table 2.1 are questionable for existing interconnections. The electrical independence, item 2, is directly gleaned from the knowledge of signal coupling in the WSIC.

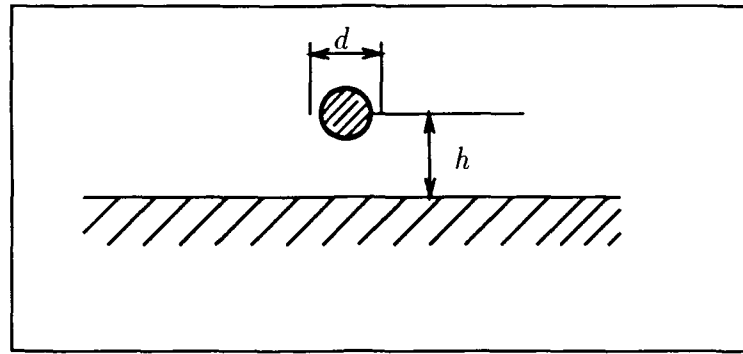


Figure 2.3. The multi-wire transmission line. After (53).

Despite the problems with microstrip-like lines, few other alternatives for wafer scale interconnections seem practical. As a possible alternative, Kozuch has suggested the use of *multi-wire* transmission lines in lieu of microstrip lines in printed circuit boards (53). Multi-wire transmission lines (Figure 2.3) consist of circular wire conductors, embedded in a dielectric and supported by a ground plane, and, as such, can be regarded as circular versions of microstrip lines. Since these multi-wire transmission lines sometimes use polyimide as the dielectric (which is a candidate dielectric for WSI), it seems conceptually plausible that the multi-wire technology might also be extensible to wafer scale circuitry. As advantages, Kozuch asserts that multi-wire transmission lines do not require vias, avoid discontinuous corner turns, achieve higher wiring densities compared to microstrip structures, and have very predictable impedance and coupling characteristics (53). However, the use of multi-wire transmission lines in WSICs does not seem likely in the near future, since processes to fabricate these lines into integrated circuits, and techniques to smoothly transition their interconnections with active semiconductor elements are not yet well-defined.

Thus, by virtue of availability, microstrip-like structures are the primary candidates for consideration as transmission line structures in wafer scale integrated circuits. However, to justify their use, it is necessary to consider the electrical properties of these structures in depth, so that more of the desired features listed in

Table 2.1 can be validated. For purposes of this evaluation, the transmission lines in Figure 2.1 will be considered, especially the microstrip and stripline structures. Since WSI interconnection structures do not always lend themselves to an unambiguous identification classification within the generalized class of microstrip lines, it will be necessary, in some cases, to apply approximations to certain results so that these structures can be examined.

*Elements of Transmission Line Theory.* Transmission line theory is a specialized topic in electromagnetic theory, as is the simple lumped-element analysis in network theory. In researching the applicability of existing theory to wafer scale microstrip-like transmission line structures, it is beneficial to retrace the critical conceptual concepts. As manifested in most pedagogical discussions involving electromagnetics, Maxwell's equations establish the starting point (79:234):

$$\nabla \cdot \overline{D} = \rho \quad (2.1)$$

$$\nabla \cdot \overline{B} = 0 \quad (2.2)$$

$$\nabla \times \overline{E} = -\frac{\partial \overline{B}}{\partial t} \quad (2.3)$$

$$\text{and } \nabla \times \overline{H} = \overline{J} + \frac{\partial \overline{D}}{\partial t}. \quad (2.4)$$

where  $\overline{D}$  is the electric flux density,  $\rho$  is the charge density,  $\overline{B}$  is the magnetic flux density,  $\overline{E}$  is the electric field intensity,  $\overline{H}$  is the magnetic field intensity, and  $\overline{J}$  is the current density. These equations, along with the following point-form and constitutive relationships, form a basis for most practical work (55:373):

$$\overline{J} = \sigma \overline{E} \quad (2.5)$$

$$\nabla \cdot \overline{J} = -\frac{\partial \rho}{\partial t} \quad (2.6)$$

$$\overline{D} = \epsilon \overline{E} \quad (2.7)$$

$$\text{and } \overline{B} = \mu \overline{H}. \quad (2.8)$$

In these expressions,  $\sigma$  is the conductivity,  $\epsilon$  is the electrical permittivity, and  $\mu$  is the magnetic permeability. These quantities are tensors in general, but here they will be treated as scalars. As such, for the discussions which follow, it is necessary to enforce the condition that materials exhibit isotropic molecular properties. It will further be assumed that the materials discussed are also homogeneous.

In the electrostatic case, when the electromagnetic fields do not vary with time, Equations 2.3 and 2.4 become (91:161):

$$\nabla \times \overline{E} = 0 \quad (2.9)$$

$$\text{and } \nabla \times \overline{H} = \overline{J}. \quad (2.10)$$

Since  $E = \nabla\phi$  in static fields (55:77), where  $\phi$  is the electrostatic potential, Equation 2.1 is rewritten as:

$$\nabla \cdot (-\epsilon \nabla \phi) = -\epsilon \nabla^2 \phi - \nabla \epsilon \cdot \nabla \phi = \rho. \quad (2.11)$$

Since homogeneity is assumed, then  $\nabla \epsilon = 0$  and the potential satisfies (91:161):

$$\nabla^2 \phi = -\frac{\rho}{\epsilon} \quad (2.12)$$

which is Poisson's equation. When the region is source-free, Equation 2.12 reduces to Laplace's equation:

$$\nabla^2 \phi = 0. \quad (2.13)$$

For the time-varying case, such simplifications cannot be made in general. That is, assuming perfect conductors, Maxwell's equations simplify to a wave equation of the form [(15:83),(79:254)]:

$$\nabla^2 \overline{E} = \mu \epsilon \frac{\partial^2 \overline{E}}{\partial t^2} + \sigma \mu \frac{\partial \overline{E}}{\partial t}. \quad (2.14)$$

*Modes of Propagation.* In guided wave structures, the solution to Equation 2.14 is comprised of one or more of three mode types: transverse magnetic (TM), transverse electric (TE), or transverse electromagnetic (TEM). Transverse magnetic (TM) modes are so named because the magnetic field configuration has no longitudinal components; that is, TM modes only have transverse magnetic components. The electrical field, however, can have longitudinal components. The converse of the TM mode is the transverse electric (TE) mode, which has no longitudinal electric-field components (55:368). Kraus identifies TEM waves as waves which have neither longitudinal electric nor magnetic components. He also asserts that the TEM field configuration is the only one which can exist under steady-state conditions (55:367). Adler *et al.* further point out that waves in the TEM case have the same field configurations as in the electrostatic case (4:493-499).

The solution for a particular wave problem can be expressed, in general, as a linear combination of the TE, and TM modes, although in many cases, only one mode type will be dominant. The most important case for the study of transmission lines is the TEM case. Adler *et al.* point out that only TEM solutions exist in ideal transmission lines (4:493-499).

One of the most important advantages of TEM structures, a term referring to structures which only support TEM modes, is that their analysis may be performed using static potential analysis methods. In the static case, as shown previously, Maxwell's equations (Equations 2.1-2.4) can be reduced to Poisson's equation (Equation 2.12) and Laplace's equation (Equation 2.13) in source regions and source-free regions, respectively (79:397-398), except at frequencies which are sufficiently high for skin effects to exist. This conversion, when possible, is an advantage, since many powerful techniques can be applied to the analysis of these equations. Clearly, Equation 2.13 is more easily solved than Equation 2.14, and, therefore, TEM-only propagation is usually assumed when possible to simplify the analysis. As implied by the name of the term, a "transverse electromagnetic" wave possesses electric and



magnetic field components which exist in a plane that is perpendicular to the direction of propagation. For a TEM structure, this statement is true for *all* such cross sections, which implies that whatever solution can be found will be independent of the dimension along which propagation occurs. This condition reduces the wave equation by one dimension. If any longitudinal electric or magnetic field component exists, the resulting wave solution would bear some type of dependence on the direction of propagation, and the analysis of potential distributions would become considerably more complicated (4).

For a transmission line structure to support the TEM propagation mode, the electric and magnetic fields must reside in homogeneous dielectric regions [(23),(40),(54)]. As such, most microstrip-like structures are not truly TEM in nature, due to the geometric discontinuities resulting from the interface formed by different dielectric media. For example, the microstrip in Figure 2.1a has two different dielectric media; their interface results in discontinuous field configurations. Since, as Green points out, the field discontinuities resulting from this interface are frequency dependent, it seems plausible on a qualitative basis to treat microstrip structures as "TEM-like" at lower frequencies. As the frequency approaches the dc limit, the field configurations asymptotically approach a TEM configuration [(23),(40)]. Treatments which approximate structures having inhomogeneous dielectric compositions as possessing only a TEM mode are referred to as *quasi-static* or *quasi-TEM* approximations [(54),(103)]. In some cases, the quasi-TEM approximation is inappropriate. In these cases, the alternative and more involved, *full wave* analysis must be implemented to investigate the effects of the higher-order hybrid modes (TE and TM) (38).

The choice as to whether to utilize the quasi-TEM or full wave analysis approach is dependent on the application. For integrated circuit applications, in what could pessimistically be called a highly coupled system of multiconductor guided wave structures, Gilbert *et al.* claimed that the quasi-static approximations apply

only for digital systems where signal rise times are on the order of one nanosecond. When rise times are less than 100 ps, they felt that "a full-wave analysis of multiconductor microstrip transmission lines becomes necessary" (38:307). Although not all authors agree on a precise frequency-domain threshold to separate the quasi-TEM and full-wave regimes, they generally concur that quasi-TEM approaches are inadequate above *some* threshold. Several physical indicators reinforce this position. First, the same rules of thumb which roughly delimit WSI analyses into either lumped element or transmission line can be applied to the smaller geometric features of the structures involved (84). Examples of such features on WSIC structures include their vertical distance from ground plane ( $h$ ) and their lateral separation between neighboring structures ( $s$ ). At these higher frequencies, TE and TM modes can be supported. Pramanick *et al.* reported that several workers have considered high-frequency analyses based on the existence of low-order TE and TM surface wave modes (77). Another indicator of the non-TEM nature of microstrip structures stems from their inhomogeneous dielectric composition. These structures experience dispersive effects due to phase velocity differences in the dissimilar dielectrics. The dispersion and, hence, the difference in phase velocity between the media increases from zero at dc (the electrostatic case) to larger values at higher frequencies. The discontinuity results from the generation of electric fields which are non-TEM in nature. In fact, as Wu states, these field configurations are not even TE or TM in nature [(23),(162)]. A more quantitative treatment of the quasi-TEM concept was considered by Lindell *et al.* (59). However, even this treatment does not provide a definitive threshold between the quasi-static and full-wave regions.

*The Transmission Line Equations.* While full-wave analyses for higher frequency designs on a routine basis will most closely approach the exact values predicted by electromagnetic theory, it is not always practical or even sensible to pursue them. On the other hand, as implied earlier, simple circuit theory may also be inadequate. Fortunately, in many instances, an intermediate solution may be achieved

through *transmission line analysis* techniques. Transmission line theory is based on one-dimensional TEM structures, although it can be approximately applied in cases where longitudinal electric and magnetic fields are small in magnitude relative to their projection in the transverse directions.

The fundamental transmission line equations can be derived directly from the evaluation of a TEM wave solution to Equation 2.14, assuming it exists (4:493-551). It is important to remember that the equations are only completely correct for TEM transmission modes, subject to the other applicable assumptions regarding material properties. The material assumptions include linearity, homogeneity, and the isotropic behavior of the material parameters, which include electrical conductivity, permittivity, and magnetic permeability. Linearity implies that Equations 2.5-2.8 are applicable. The homogeneity assumption permits the material parameters to be regarded as spatially invariant. Finally, the isotropic assumption simplifies the consideration of material parameters from the general anisotropic case, where they must be treated as tensors.

The general form for the transmission line equations, or telegrapher's equations as they are sometimes called, are [(16),(43:260)]:

$$C \frac{\partial V}{\partial t} + GV + \frac{\partial I}{\partial z} = 0 \quad (2.15)$$

$$\text{and} \quad L \frac{\partial I}{\partial t} + RI + \frac{\partial V}{\partial z} = 0 \quad (2.16)$$

where  $R$ ,  $L$ ,  $G$ , and  $C$  are the distributed series resistance, inductance, shunt conductance, and capacitance, respectively, expressed on a per unit length basis. Although Equations 2.15 and 2.16 can be derived from Maxwell's equations, they were, interestingly, developed by Lord Kelvin, long before Maxwell's equations were written. The alternate method of deriving the telegrapher's equations is based on a distributed lumped-parameter model, shown in Figure 2.4. With this model, the distributed quantities of inductance ( $L$ ), resistance ( $R$ ), capacitance ( $C$ ), and conductance ( $G$ )

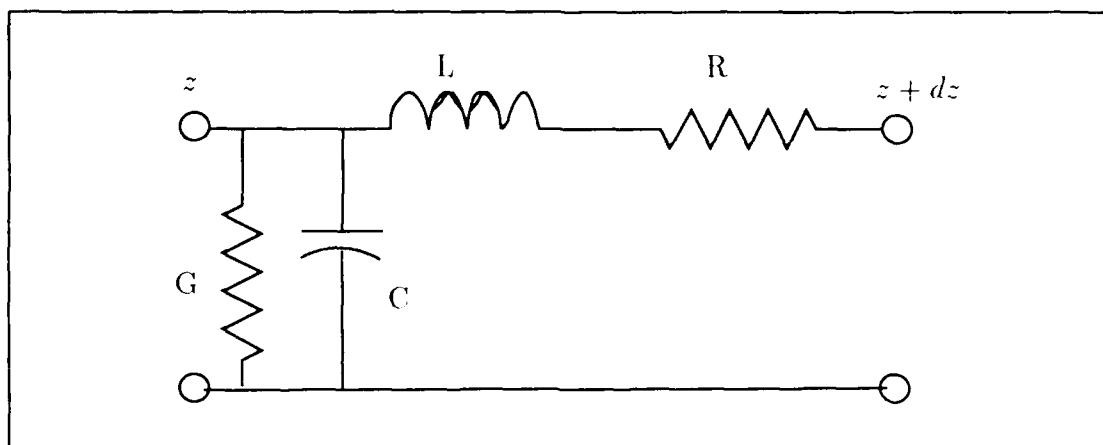


Figure 2.4. A lumped-parameter circuit model of a transmission line. After (15:86).

are analyzed on an incremental length ( $dz$ ) basis associated with the  $\hat{z}$ -directed transmission line. When the increments are evaluated in the limit as  $dz$  approaches zero, the transmission line equations are formed. The two different derivation techniques serve to demonstrate the consistency of Maxwell's equations with circuit theory in the special case of TEM fields (15:186–187).

By substituting a time-harmonic expression into Equations 2.15 and 2.16 (that is, the phasor representation of a sinusoidal signal), some concepts very useful to transmission line analysis can be developed. If  $V(z)$  and  $I(z)$  represent the steady-state voltage and current, respectively, of the transmission line in Figure 2.5, then the phasor solution forms of Equations 2.15 and 2.16 become (18):

$$V(z) = V_+ e^{-jz} + V_- e^{jz} \quad (2.17)$$

$$\text{and } I(z) = \frac{V_+}{Z_0} e^{-jz} - \frac{V_-}{Z_0} e^{jz} \quad (2.18)$$

where  $V_+$  and  $V_-$  are the amplitudes of the forward (incident) and backward

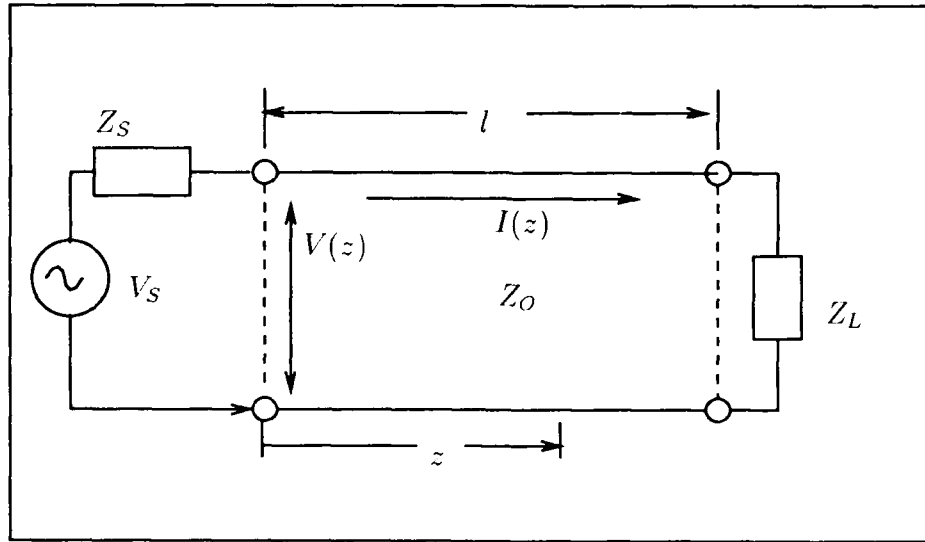


Figure 2.5. A two-line transmission line.

(reflected) voltage wave components, and  $Z_O$  is the characteristic impedance, sometimes defined as (18):

$$Z_O = \sqrt{\frac{R + j\omega L}{G + j\omega C}} \quad (2.19)$$

where  $\omega$  is the angular frequency (radians/second). An alternative definition of the characteristic impedance which is often used for lossless lines is [(29:5),(87)]:

$$Z_O = \frac{1}{v_p C} \quad (2.20)$$

where  $v_p$ , the wave's phase velocity, is defined as (29:4):

$$v_p = \frac{c}{\sqrt{\epsilon_R}} \quad (2.21)$$

where  $c$  is the velocity of light and the relative magnetic permeability ( $\mu_R$ ) is assumed to be unity. This definition is adequate for homogeneously filled structures, such as striplines or coaxial cable transmission lines. For structures with non-homogeneous

dielectric compositions, this definition is slightly modified (40):

$$Z_O = \frac{1}{c\sqrt{C_1C}} \quad (2.22)$$

where  $C$  is the capacitance per unit length of the structure, and  $C_1$  is the capacitance per unit length of the same structure without the dielectric (that is, the dielectric material is replaced by a vacuum). The phase velocity is not explicitly shown for this definition, but it is defined separately as (40):

$$v_p = c\sqrt{\frac{C_1}{C}}. \quad (2.23)$$

The propagation constant ( $\beta$ ) in Equations 2.17 and 2.18 is defined as a complex number in general, with the real part ( $\alpha$ ) referred to as the attenuation constant and the imaginary part ( $\gamma$ ) is referred to as the phase constant (18):

$$\beta = \alpha + j\gamma. \quad (2.24)$$

Another important quantity in transmission line work is the reflection coefficient ( $\Gamma$ ), defined by the ratio of the forward to the backward voltage components, or in terms of  $Z_O$  and the load impedance ( $Z_L$ ) (18):

$$\Gamma = \frac{V_-}{V_+} = \frac{Z_L - Z_O}{Z_L + Z_O}. \quad (2.25)$$

A necessary condition for eliminating reflections in a transmission line is to match the source and load impedances to the characteristic impedance of the line. Matching is always desired but difficult to establish in practice due to discontinuities in the transitions between the transmission line and other system components, the difficulty of controlling system impedances, and, in the case of microstrip-like structures, being able to predict the characteristic impedance of the transmission line [(9),(18),(36)]. As Izadian pointed out, even a perfect impedance match will not prevent reflections

in a transmission line unless a continuous field transition can be provided across media transitions. The requirement of continuous field transitions is almost nearly equivalent to the requirement of smooth physical or geometric transitions across media (47).

The transmission coefficient ( $\tau$ ), the portion of wave transmitted at a junction, is simply related to the reflection coefficient (79:28):

$$\tau = 1 + \Gamma. \quad (2.26)$$

The characteristic impedance, propagation constant, and reflection and transmission coefficients allow complete characterization of uncoupled transmission line networks. Also, adopting a phasor representation is not overly restrictive in the context of transmission line work; that is, choosing a sinusoidal waveform does not affect the generality of the results, except in cases where the input waveform cannot be expressed as a Fourier series (for example, non-periodic waveforms) (18).

*Multiconductor Transmission Lines.* The theory of multiconductor transmission lines is an extension of the concepts used in the more basic two-conductor transmission line. Multiconductor transmission line networks are of special importance in WSI research, since many of the transmission line structures contained within a WSIC which are intended by design to be isolated are, in fact, potentially a part of a multiconductor transmission line system. The undesired coupling effects of adjacent circuit lines are exacerbated as they are brought closer together (64). In general, the amount of coupling also depends on other parameters, including the operating frequency, the materials, and the geometry of the conductors in a circuit. The degree of coupling which can be tolerated may very well establish a limitation with respect to the minimum spacing between conductors in a WSIC, which implies a physical density limitation.

The transmission line equations for  $n$ -conductors are (37:446):

$$\frac{\partial[v(z,t)]}{\partial z} = - \left( [R] + [L] \frac{\partial}{\partial t} \right) [i(z,t)] \quad (2.27)$$

$$\text{and} \quad \frac{\partial[i(z,t)]}{\partial z} = - \left( [G] + [C] \frac{\partial}{\partial t} \right) [v(z,t)] \quad (2.28)$$

where  $[v]$  and  $[i]$  represent  $N$ -element column vectors, and  $[R]$ ,  $[L]$ ,  $[G]$ , and  $[C]$  are  $[N \times N]$  matrices. These equations are coupled, partial differential equations. The mathematical coupling of these equations is directly related to the physical coupling of the electric fields between the structures in a given system. Non-zero, off-diagonal elements in the  $[R]$ ,  $[L]$ ,  $[G]$ , and  $[C]$  matrices indicate the presence of coupling.

By adopting phasor-represented sinusoidal waveforms, these coupled partial differential equations become coupled ordinary differential equations (97:955):

$$\frac{d[v]}{dz} = -([R] - jw[L])[i] \quad (2.29)$$

$$\text{and} \quad \frac{d[i]}{dz} = -([G] - jw[C])[v]. \quad (2.30)$$

The analysis of an arbitrary system of transmission lines may be thought of as a two-phase process. The first analysis examines the conductor-dielectric system geometry and extracts the  $[R]$ ,  $[L]$ ,  $[G]$ , and  $[C]$  matrices; the second considers solutions to Equations 2.29 and 2.30.

A fundamental analysis of a particular configuration is required to obtain the  $[R]$ ,  $[L]$ ,  $[G]$ , and  $[C]$  matrices. For the lossless case, where  $[R]=[G]=0$ , the analysis is considerably simpler. For example, some authors perform their initial analyses using only the capacitance matrix [(44),(99)]. For this case, a set of simultaneous equations can be obtained for the capacitive coefficients (99):

$$[q] = [C][v]. \quad (2.31)$$

where  $[q]$  and  $[v]$  are  $[N \times 1]$  column vectors representing charge and voltage, respectively.



When the elements of the voltage matrix  $[v]$  are defined with respect to a ground, the off-diagonal capacitance elements ( $c_{ij}, i \neq j$ ) are referred to as coefficients of induction, whereas the diagonal elements ( $c_{ij}, i = j$ ) are referred to as coefficients of capacitance (30). The inductance matrix  $L$  is obtained by (31:20):

$$L = \mu\epsilon[C]^{-1}. \quad (2.32)$$

The coupled transmission line equations (Equations 2.29 and 2.30) are then solved at individual frequencies. At any single frequency, the solution to Equations 2.29 and 2.30 can be obtained with conventional linear analysis techniques. One common method seeks diagonalized versions of the  $[N \times N]$  matrices:  $[Z] = [R] - j\omega[L]$  (which can be thought of as a characteristic impedance matrix), and  $[Y] = [G] - j\omega[C]$  (a characteristic admittance matrix). Consequently, the solution matrices may be formed [(37:449),(73:631)]. However, the problems associated with determining the coefficient matrices  $[R]$ ,  $[L]$ ,  $[G]$ , and  $[C]$  and solving the coupled transmission line equations are difficult in the general case. In fact, analytic treatments to determine these matrices of coefficients do not exist for even the simplest physical configurations of microstrip-like structures. Some authors have considered numerical approaches to extract these values [(97),(30),(99)]. The analysis of Equations 2.29 and 2.30, on the other hand, is that of a coupled eigenvalue problem (56). Similarly, many treatments of coupled transmission lines and their solutions exist in the literature [(26),(31),(73)]. Since both facets of the multi-conductor transmission line problem are somewhat involved, it is not surprising to find very few treatments in the literature which consider them at the same time. At least two in-depth treatments do exist which consider the synthesis of three-line microstrip couplers [(73),(96)], but more commonly, the end-to-end coupling analyses only investigate two-line conductor configurations [(29),(41),(42)].

#### *Dual-Conductor Transmission Line Structures as a Special Case.*

In the special case of dual-conductor transmission line structures located above a

common ground (Figure 2.6), many analyses have been reported which characterize *even-mode* and *odd-mode* configurations. For such a system, an even-mode configuration implies that the two conductors have currents and voltages of the same magnitude and phase, as shown in Figure 2.7a. In the odd-mode configuration (Figure 2.7b), the voltages and currents have the same magnitude, but their phases differ by 180 degrees. This representation is flexible in that any TEM signal may be expressed as a linear combination of even- and odd-mode signals (95:397). However, for non-TEM signals, the odd-mode and even-mode analyses become more complicated, since the phase velocities may be different, unlike the situation characterizing the TEM case (29:131). The different phase velocities complicate the analysis, since the electrical length of the transmission line structure becomes dependent on the mode of propagation. The odd- and even-mode field configurations on a coupled stripline structure are shown in Figure 2.8 for a transverse cross-section of an ECS. (33:260). Since different voltage and current configurations are defined for each mode, it follows that other dependent quantities, such as the characteristic impedance, have values that differ, depending on the mode. Edwards (29:134) and Gupta *et al.* (41:339) defined the odd-mode and even-mode characteristic impedances for lossless lines as:

$$Z_{Oe} = \frac{1}{c\sqrt{C_{1e}C_e}} \quad (2.33)$$

$$\text{and } Z_{Oo} = \frac{1}{c\sqrt{C_{1o}C_o}} \quad (2.34)$$

where  $c$  is the velocity of light;  $C_{1e}$  is the capacitance of the lines in the even-mode configuration and in the presence of the dielectric;  $C_e$  is the even-mode line capacitance evaluated with the dielectric removed; and  $C_{1o}$  and  $C_o$  have corresponding definitions for the odd-mode configuration. This particular definition often facilitates the computation of these characteristic impedances by numerical methods (60).

Howe noted that the even-mode characteristic impedance ( $Z_{Oe}$ ) is always greater than or equal to the odd-mode characteristic impedance ( $Z_{Oo}$ ) (46). For loosely

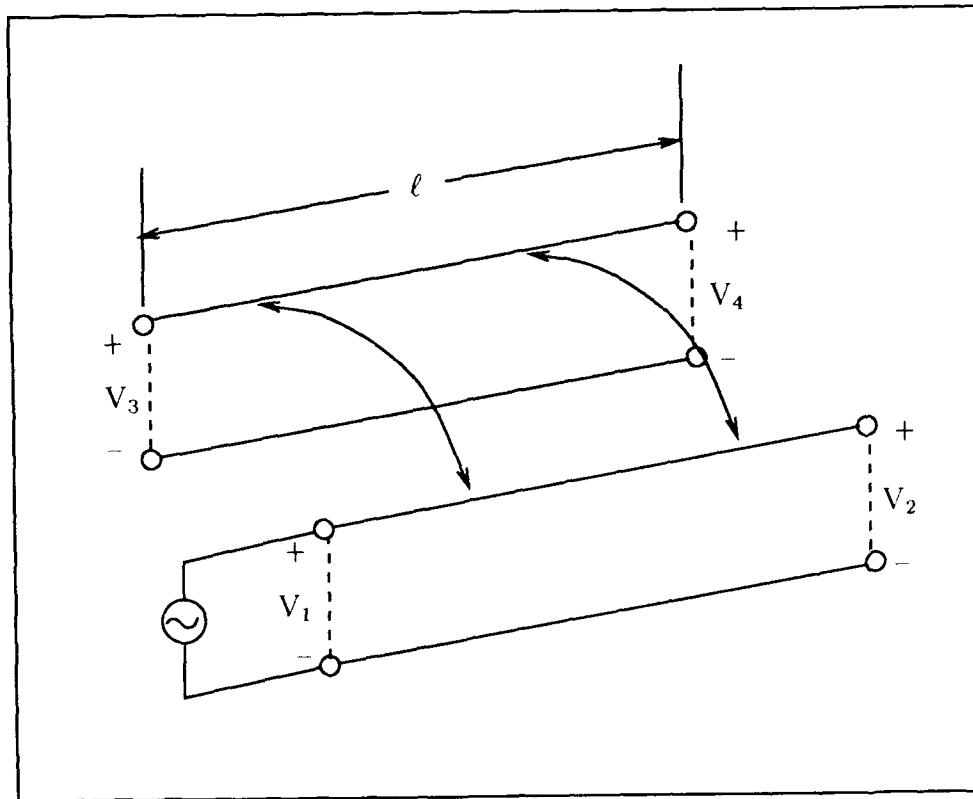


Figure 2.6. The coupled transmission line pair. After (29).

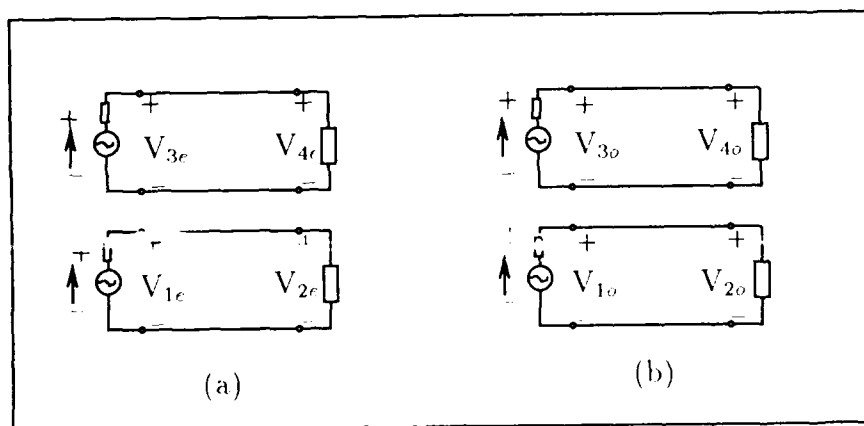


Figure 2.7. Even- and odd-mode circuit configurations. (a) Even-mode. (b) Odd-mode. After (29).

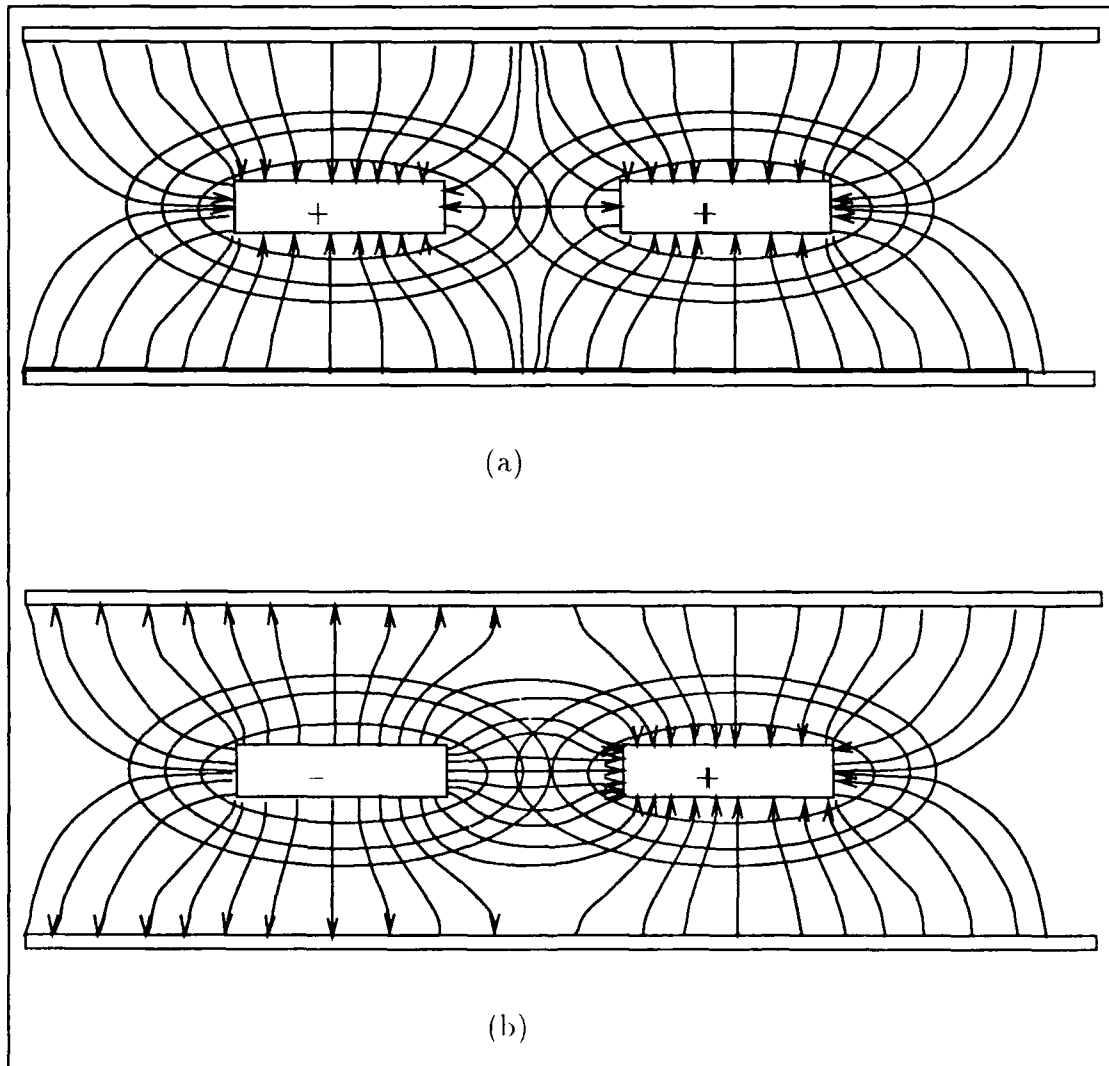


Figure 2.8. Even- and odd-mode field configurations. (a) Even-mode. (b) Odd-mode. After (33).

coupled lines, Edwards provides the following relationship between the odd-mode, even-mode, and design specification characteristic impedances (29:134):

$$Z_O = \sqrt{Z_{Oe}Z_{Oo}}. \quad (2.35)$$

This relationship can be directly verified by enforcing impedance match conditions at the source and load of both configurations in Figure 2.7 (29). This relationship is useful for showing the effects of coupling for the characteristic impedance of a given line evaluated without assuming that a coupling effect is present. That is, it provides a measure by which single-conductor microstrip lines can be compared to dual-conductor microstrip lines.

The odd- and even-mode impedance definition promotes the introduction of a special transmission line constant. This constant is termed the *coupling factor*, defined by (29:167):

$$C_F = \frac{Z_{Oe} - Z_{Oo}}{Z_{Oe} + Z_{Oo}}. \quad (2.36)$$

This coupling factor is distinct from other coupling-related quantities, such as the coupling voltage or coupling gain, as they are generally discussed. Rather, the coupling factor may be thought of as a metric which reflects the proximity of two transmission lines and as a fundamental property of a coupled transmission line system, similar to the characteristic impedance or propagation constant. Other coupling related terms include *crosstalk*, *mutual capacitance*, and *mutual inductance* [(30),(99)]. Ghione *et al.* define *far-end* crosstalk as a voltage appearing on the load of an inactive line when an adjacent line is impressed with a voltage, while *near-end* crosstalk refers to the voltage induced on the source end of an inactive line (37). The mutual inductance and capacitance of a coupled system are properties of a transmission line, independent of excitation, as is the coupling factor, but with definitions extensible to multiconductor systems which have more than two lines. The definitions of these quantities are not completely standard in the literature, although the mutual

capacitance and inductance are often described in terms of farads and henries, respectively, per unit length [(66),(73)].

As a specific example for a typical proposed WSIC, McDonald *et al.* considers a two-conductor transmission line system, with an inter-line spacing of  $10\text{ }\mu\text{m}$ . Using  $10\text{ }\mu\text{m}$  wide and  $5\text{ }\mu\text{m}$  thick aluminum conductors with a  $10\text{ }\mu\text{m}$  thick polyimide dielectric, they estimated a mutual capacitance of  $0.2\text{ pF/cm}$  and a mutual inductance of  $0.4\text{ nH/cm}$  for this WSIC structure (66).

*Microstrip Transmission Line Analysis Techniques.* Most transmission line analyses evaluate networks of transmission line structures using Equations 2.17-2.18 for uncoupled networks and Equations 2.29-2.30 for coupled networks. The tendency to use one-dimensional, time-independent expressions more readily facilitates the design and analysis of larger networks; such simplifications are practically mandatory in WSICs. These transmission line formulations reduce most of the electromagnetic analytical difficulties compared to those involved in obtaining the propagation constant and characteristic impedance of the desired transmission line structures. In turn, the determination of the characteristic impedance involves determining the coefficients for  $[R]$ ,  $[L]$ ,  $[G]$ , and  $[C]$  in Equations 2.29-2.30. However, to evaluate these coefficients, it is necessary to consider the electrostatic formulation of Equation 2.12, at least, and the time-varying formulations of Equations 2.1-2.8, in general. The latter, more involved analyses are required, especially at higher frequencies, in order to be able to compare the true electromagnetic solution of quasi-TEM structures with idealized solutions obtained by electrostatic approximations.

Several numerical and analytical techniques have been formulated, including conformal mapping techniques, moment methods, finite difference methods, and finite element methods. Most of these methods are also extensible to the full wave solutions of Equation 2.14. The next four sub-sections present a brief survey of the techniques, methods, and concepts which have been applied to microstrip analysis.

*Conformal Mapping Techniques.* A technique which has been very popular in the past for evaluating the capacitance of certain transmission line configurations is the conformal mapping approach. The conformal mapping approach, simply stated, solves an electrostatic problem by mapping geometries into different domains to alter their apparent configuration into a form which can be more easily solved. Thus, the analytically-awkward geometries are mapped from their original domain to a domain where the geometries are simpler to analyze. The geometry transformation is achieved by applying a certain function to each point in the original domain. The respective output or result of each functional evaluation maps into the new domain. Together, when the functional evaluations are applied to all points corresponding to geometries in the original domain, a mapping into different geometries in a new domain is created. The function involved in this transformation is specially chosen. The primary restriction on the selection of this function is that it must satisfy the Cauchy-Riemann conditions. Functions which satisfy the Cauchy-Riemann conditions are called "analytic functions", and transformations involving analytic functions are called "analytic transformations" (20). When an analytic transformation is used, the solution of Laplace's equation in the new domain is, in fact, a transformation of the solution in the original domain.

One significant disadvantage of the conformal mapping technique is that the formulas required to transform arbitrary configurations must be found through trial and error. This limitation is evidenced in the literature by the distinct shortfall of conformal mapping analyses for thick microstrip-like structures and multiconductor microstrip-like structures. An additional drawback with this technique is that, sometimes, the resultant expressions are cumbersome in appearance and are not particularly insightful.

*Moment Method Techniques.* The moment method techniques are a popular class of methods used to solve electromagnetics problems. They address the solution of an unknown function  $f$  operated upon by the linear operator  $L$  in

the following generalized problem (72):

$$\mathcal{L} \cdot f = y. \quad (2.37)$$

With the moment technique,  $f$  is approximated by the summation of basis functions (72):

$$f = \sum_N \alpha_j f_j. \quad (2.38)$$

By invoking the principle of linearity, Equations 2.37-2.38 become:

$$\sum_N \alpha_j \mathcal{L} f_j = y. \quad (2.39)$$

Through the introduction of a weighting function ( $w_i$ ) against which the inner product of Equation 2.39 is formulated, Equation 2.39 becomes (72):

$$\sum_M \sum_N L_{ij} \alpha_j = [L][\alpha] \quad (2.40)$$

where  $[\alpha]$  is a column vector comprised of the  $N$ -unknown  $\alpha_j$  coefficients, and the elements of  $[L]$  are given by:

$$L_{ij} = \langle w_i, f_j \rangle \quad (2.41)$$

The notation " $\langle \rangle$ " denotes the inner product of  $w_i$  with the basis function  $f_j$  over the appropriate region. As reported by Ney, this notation is necessarily general to accommodate the different moment method techniques. For example, if  $w_i = f_i$ , then the method is known as a *Galerkin* technique, which is a moment method technique popularized by Harrington. The resulting  $[L]$  matrix (not to be confused with the inductance matrix described earlier) is algebraic, and the unknown coefficient vector  $[\alpha]$  is solved through matrix inversion (72):

$$[\alpha] = [L]^{-1} y. \quad (2.42)$$



Consequently, the solution of Equation 2.42 approximates  $f$  (72:973).

In electrostatics, the moment method formulation can be applied to the solution of Laplace's equation. A popular method for solving Laplace's equation in electrostatics problems involves the use of Green's functions. This technique can be applied in two dimensions to a transverse cross-section of a transmission line, or it may be extended to three dimensions to solve for potential distributions in a volume. Given a charge distribution  $\rho(x, y)$  and the corresponding Green's function  $G(x, y; x', y')$ , the potential distribution is specified in the two dimensional problem as (19):

$$\phi(x, y) = \int_R G(x, y; x', y') \rho(x', y') dx' dy' \quad (2.43)$$

where  $\phi(x, y)$  is the potential at  $(x, y)$ . The Green's function  $G(x, y; x', y')$  is the solution of Poisson's equation, forced by a delta function, and subject to homogeneous boundary conditions in the Dirichlet (specified boundary potential) problem (41:15):

$$\nabla^2 G(x, y; x', y') = \frac{1}{\epsilon_0 \epsilon_R} \delta(x - x') \delta(y - y'). \quad (2.44)$$

Besides the obvious problem of mechanizing a numerical solution to Equation 2.43, the determination of the appropriate Green's function may be quite difficult. Furthermore, since the Green's function is highly dependent on the geometry of the problem, including the boundary conditions of the problem, it may be necessary to determine several Green's functions in order to achieve the desired generality of a particular solution.

*Finite Difference Method (FDM) Techniques.* With the method of finite differences, a discrete solution of an appropriate differential equation is sought. In this method, the spatial and, if necessary, temporal regions of interest, which must be bounded, are subdivided into a large number of grid points or nodes. These nodes are programmed with a discrete representation of a differential equation which, as the name of the method implies, represents a finite forward or backwards differential

in the appropriate variable. Solution methods may be either algebraic, equivalent to matrix inversion, or iterative, which is algorithmically simpler. Algebraic inversion implementations are computationally intensive, especially for large meshes. Problems with iterative finite difference approaches, which require substantially fewer calculations than algebraic matrix inversions, include inefficiency and slowness to converge, or even failure to converge. Several types of differential equations, most notably Laplace's equation, are readily solved with this technique. Most FDM approaches consider only Dirichlet boundary conditions (voltages specified on boundaries), and they require bounded solution regions. One approach used to effectively increase the size of a bounded region is to increase the mesh size. The differential increments of size need not be constant. For example, in order to improve accuracy in a bounded region, Corr used a graded finite mesh, which, in effect, allows the simulation of a large enclosure while reducing the number of nodes required to achieve accurate results [(23),(38:829),(40),(55),(60),(58)].

A few authors have implemented another approach to improve accuracy in regions of very large or infinite extent. This approach involves the selection of a fictitious boundary coinciding with the physical boundary limit of the simulation. At this boundary, the potential is chosen, usually by iteration, to correspond with the correct potential at the imaginary boundary to a problem with a large or infinite extent. When the selected potentials at the fictitious boundaries are correct, the potential distribution in the region enclosed by the artificial boundary more closely approximates the correct values (85).

Although FDM applications have primarily focused on the solution of Laplace's equation (applicable to electrostatics problems), some researchers have extended them to time-varying problems. For example, Corr utilized a FDM to analyze the hybrid wave (TE plus TM) components of a microstrip structure. Gupta *et al.* stated that these hybrid methods separately solve the hybrid components and then combine them through superposition [(23:41), (41:50-64)].

*Finite Element Method (FEM) Techniques.* The finite element method is similar to the finite difference method, except that it uses an integral formulation; in particular, a variational formulation is used, whereas the finite difference method uses a differential formulation. A potential advantage that has been demonstrated with the finite element method is that solutions can be extended to an unbounded domain, through the use of boundary elements. With the boundary element method (BEM), an arbitrarily-sized but bounded domain is modeled with traditional finite element techniques, and area surrounding the bounded region is subdivided into boundary elements, which approximate regions of infinite spatial extent. By appropriately matching the boundary conditions between the two regions, a solution valid over all space is possible (65). It has been remarked that finite element approaches sometimes encounter a problem with spurious solutions (38:830), although, in this respect, they are really not much different from some of the finite difference formulations, as evidenced in Corr's work (23). However, Corr, who relied exclusively on finite difference techniques, found no particular merit in the utility of the finite element method to perform the hybrid wave analysis of a microstrip structure. It should be remarked that, in general, integral evaluations provide better accuracy than differential formations, since it is possible to integrate a finite number of certain types of discontinuities, whereas it is not usually possible to differentiate a discontinuity (23).

*The Application of Transmission Line Concepts to Wafer Scale Interconnections.* Many techniques may be applied in the transmission line analysis of microstructures which seem far-removed from the special restrictions of transmission line behavior. The goal of most approaches is to obtain specific parameters, such as the characteristic impedance and propagation constant of transmission lines and their mutual capacitances. To be more accurate, the rigorous full-wave analysis approaches may be applied to larger spatial domains of interest. However, the obvious complexity of wafer-scale interconnection networks demand treatments which are

simple, quick, but yet approximate. Performing a full-wave analysis for every conductor in a WSI system is out of the question, just as performing a SPICE simulation on every transistor in a VLSI design would be. However, the full wave analyses do serve a useful purpose. The insights afforded from the more involved analyses provide the designer with the necessary confidence to make correct assumptions that lead to the simpler treatments.

The following specializations of transmission line theory apply directly to the microstrip-like structures which will undoubtedly comprise wafer scale interconnections. These specializations include: the prediction of characteristic impedances, which are a fundamental property of the interconnections; the attenuation effects or losses, which will allow the maximum length of interconnections to be surmised; and dispersion, which will consider the frequency-dependencies of the interconnections.

*Characteristic Impedance.* Originally, the concept of impedance was defined as the ratio of "force per unit area" to "flow per unit area" (86:18), a definition which seems completely general to mechanical systems as well as electrical systems (9:80). It appears that the characteristic impedance might be thought of as a unique quantity of a particular system (for example, a transmission line or waveguide). This philosophy, in general, does not hold, and the fallacy of the viewpoint is clearly demonstrated by considering one of the widely used definitions of  $Z_O$  for a  $\hat{z}$ -directed propagating wave at a fixed angular frequency  $\omega$  [(4:341),(35)]:

$$Z_O = \frac{E_x}{H_y} \quad (2.45)$$

where  $E_x$  is the  $\hat{x}$ -component of the electric field, and  $H_y$  is the  $\hat{y}$ -component of the magnetic field. By observing that  $E_x/H_y$  is stationary only for TEM structures (as in the electrostatic case) (4:524), it is apparent that  $Z_O$  depends on the wave, in addition to the transmission line system, as concluded by Schelkunoff (86:18). As such, Brillouin discouraged extending the notion of  $Z_O$  beyond one-dimensional

structures, stating that attempts to do so seemed somewhat "artificial" (9:93). Adler *et al.* also cautioned more generally about the extension of transmission line concepts, such as  $Z_O$ , to higher-dimensional structures, such as waveguides. It should be noted, as pointed out by Adler *et al.*, that voltage, current, and dependent quantities including  $Z_O$ , are uniquely defined only for TEM structures (4:524). Unfortunately, in transmission line work, it is not always practical to adopt Brillouin's suggestion to work with quantities "such as energy flow, energy density, energy velocity, and group velocity, in addition to ... phase velocity" (9:93), which are well-established for two- and three-dimensional systems.

Since microstrip structures do not strictly support the TEM mode of propagation, then it is logical to conclude that  $Z_O$  may not be uniquely defined [(8),(35),(29:80)]. Some contention concerning the appropriate expression for  $Z_O$  is apparent (35), and many different expressions exist. Brews summarized that the origins of most definitions of  $Z_O$  can be traced to Schelkunoff's original work [(8),(86)]:

$$Z_O = V/I \quad \text{(voltage-current definition)} \quad (2.46)$$

$$Z_O = |V|^2/(2P^*) \quad \text{(power-voltage definition)} \quad (2.47)$$

$$\text{and } Z_O = 2P/|I|^2 \quad \text{(power-current definition)} \quad (2.48)$$

where  $P$  is power,  $P^*$  is the complex conjugate of power, and  $I$  is the current. Brews noted that although controversy existed over which definition of  $Z_O$  was appropriate, it could be shown that they were all equivalent by enforcing the power requirement in transmission lines (8):

$$P = I^*V/2. \quad (2.49)$$

where  $I^*$  is the complex conjugate of the current  $I$ . Despite the problems associated with defining  $Z_O$  and its ambiguity where non-TEM structures are concerned, the use of the characteristic impedance is important for practical work with microstrip

Table 2.2. Typical impedance ranges for several microstrip-like structures. After (29).

Type	Impedance Range ( $\Omega$ )
Microstrip	20-125
Slotline	60-200
Coplanar Waveguide	40-150

and is, therefore, continued today. The errors involved in neglecting the deviations from TEM behavior in microstrips are deemed to be small (less than one per cent) at frequencies below several gigahertz, according to Green (40).

Edwards summarized typical impedance ranges of several microstrip-like structures, as shown in Table 2.2 (29:23). Royle indicates that the characteristic impedance changes over a relatively small range despite large changes in the physical dimensions. For example, the characteristic impedance of circuit-board traces typically varies from 15 to 140  $\Omega$ , and the characteristic impedance of stray interconnections on ground planes typically spans 100 to 200  $\Omega$  (84:136). Even though higher impedance lines are desirable for matching the output impedances of active devices, Gilbert *et al.* remarked that increasing the characteristic impedance of signal lines above 100  $\Omega$  increases the problems associated with coupling (38:821).

*Formulae for Characteristic Impedance.* Unfortunately, it is not completely clear which of the many existing formula for characteristic impedance are appropriate for WSI interconnections. To worsen matters, many of the "non-standard" transmission line structures will not have a closed-form expression to predict the characteristic impedance. The following survey of characteristic impedance formulae provides a representative compilation that will form a basis for subsequent numerical and experimental work. These formula are characterized by structure and

applicability to thick conductors. In all cases, the nomenclature in the formula will be consistent with that in Figure 2.1.

Most of the formula will be oriented to microstrip and stripline structures in particular, but other structures can be analyzed either through judicious approximations using the closed-form expressions, or by appropriate application of the generalized formula. Not represented among these formula are expressions for the characteristic impedance of slotlines or coplanar strips. The slotline case was not represented since this configuration is not believed to be useful in WSI work below 1 GHz. Slotlines will be of limited use at lower frequencies since they cannot support TEM modes. The coplanar strip is not represented due to the presence of ground planes in existing and proposed WSI schemes. As discussed previously, the coplanar strip can be analyzed with ECM or ECS expressions when one or two ground planes are present.

Expressions are provided, when possible, for structures with non-zero thickness. Cohn noted that the thickness of a microstrip-like structure could not always be neglected: "Even a small thickness may affect the characteristic impedance substantially"(22). This case is particularly important in WSI, since relatively thick conductors have been proposed.

Almost without exception, the formulae for microstrip-like structures are derived through conformal transformations. These conformal techniques are based primarily on the Equation 2.20 definitions of characteristic impedance and the Equation 2.21 definition of phase velocity. When Equation 2.20 is used, the capacitance is solved utilizing a conformal transform technique, as previously described. Equation 2.21 is then applied to approximate the phase velocity. Although this expression requires the specification of a relative permittivity ( $\epsilon_R$ ), an *effective permittivity* ( $\epsilon_{R,eff}$ ) is often used instead of a relative permittivity for structures with inhomogeneous dielectric compositions, such as a microstrip. This effective permittivity is used to model the dispersion effects which occur in certain microstrip-like structures.

For purposes of discussion, expressions for conductors having non-zero thickness are classified into two categories. The first category or type refers to expressions which are based on structures having zero-thickness, but use empirical corrections to account for thickness effects. The second type refers to expressions which are based on direct conformal transformations of *thick* structures; that is, these expressions do not require correction terms.

*Microstrip-Zero Thickness-Conformal Mapping.* One technique used to develop an expression for  $Z_O$  in microstrip lines is to use the conformal mapping techniques to map the transverse geometries of the structures in a new complex domain. This new domain retains the analytic properties of the original domain and, thus, if a simple geometry can be formed, it may be analyzed with existing formulae for that geometry.

Several popular expressions exist for estimating the characteristic impedance in microstrip structures which are infinitesimally thin. One of the first formulae developed for estimating  $Z_O$  for a microstrip was Wheeler's formula [(29:45),(45:145)]:

$$Z_O \cong \begin{cases} \frac{120}{\sqrt{2(\epsilon_R+1)}} \left[ \ln \left\{ \frac{4h}{w} + \sqrt{16 \left( \frac{h}{w} \right)^2 + 2} \right\} - \frac{\epsilon_R-1}{2(\epsilon_R+1)} \left\{ \ln \left( \frac{\pi}{2} \right) + \frac{\ln(4/\pi)}{\epsilon_R} \right\} \right], & (w/h) \leq 3.3 \\ \frac{60\pi}{\sqrt{\epsilon_R}} \left[ \frac{w}{2h} + \frac{\ln 4}{\pi} + \frac{\epsilon_R+1}{2\pi\epsilon_R} \left\{ \ln \left( \frac{\pi\epsilon}{2} \right) + \ln \left( \frac{w}{2h} + 0.91 \right) \right\} + \frac{(\epsilon_R-1)\ln(c\pi^2/16)}{2\pi\epsilon_R^2} \right]^{-1}, & (w/h) > 3.3. \end{cases} \quad (2.50)$$

Other conformal mapping techniques have been used to model zero-thickness microstrip lines. Goossen reports the following formula for the characteristic impedance, which was developed by Schneider (39):



$$Z_O \cong \begin{cases} 60 \ln [8h/w + w/(4h)] \sqrt{\varepsilon_{R,eff}}, & \text{for } (w < h) \\ 120\pi / [w/h + 2.42 - 0.44h/w + (1 - h/w)^6] \sqrt{\varepsilon_{R,eff}}, & \text{otherwise} \end{cases} \quad (2.51)$$

where  $\varepsilon_{R,eff}$  is the effective permittivity, defined originally as [(39:470),(88:1430)]:

$$\varepsilon_{R,eff} = \varepsilon_{R,eff}(0) = \frac{1}{2} \left( \frac{(\varepsilon_R + 1) + (\varepsilon_R - 1)}{\sqrt{(1 + 10h/w)}} \right) \quad (2.52)$$

and extended for frequency dependence by Goossen through Yamashita's approximation (39):

$$\varepsilon_{R,eff} = \varepsilon_{R,eff}(f) = \sqrt{\varepsilon_{R,eff}(0)} + \left[ \sqrt{\varepsilon_R} - \sqrt{\varepsilon_{R,eff}(0)} / (1 + 4F^{-3/2}) \right] \quad (2.53)$$

where

$$F = 4fh\sqrt{\varepsilon_R - 1} \left\{ 1/2 + 2\log_{10}(1 + w/h) \right\}^2 / c$$

$f$  is the frequency, and  $c$  is the velocity of light. Schneider based this definition of  $Z_O$  on the following asymptotic expressions [(39),(87)]:

$$Z_O \cong \begin{cases} 60 \ln(8h/w), & \text{for } w \ll h \\ 120\pi/w, & \text{for } w \gg h. \end{cases} \quad (2.54)$$

The asymptotic expressions resulted from a Schwarz-Christoffel transform involving theta functions, based on a zero thickness microstrip conductor. Schneider maintained that the original closed-form formulation was exact, but stated that the effective permittivity factor is not exact and introduces an approximation error as large as two percent (88:1430).

Another popular expression for the zero-thickness microstrip was developed by Hammerstad *et al.* This expression also uses an approximation of a conformal

transformations (45:149):

$$Z_0 \cong \frac{120\pi}{2\pi\sqrt{\varepsilon_{R,eff}}} \ln \left( F_1 \frac{h}{w} + \sqrt{1 + \left( \frac{2h}{w} \right)^2} \right) \quad (2.55)$$

where  $\varepsilon_{R,eff}$  is the effective permittivity and:

$$F_1 = 6 + (2\pi - 6) \exp \left[ -(30.666h/w)^{0.7528} \right]. \quad (2.56)$$

Along with this expression, Hoffman reported an associated expression for the effective permittivity (45:149):

$$\varepsilon_{R,eff} = \frac{\varepsilon_R + 1}{2} + \varepsilon_R - 12 \cdot \left( 1 + \frac{10h}{w} \right)^{-a \cdot b} \quad (2.57)$$

where:

$$\begin{aligned} a &= 1 + \frac{1}{49} \ln \left[ \frac{(w/h)^4 + [w/(52h)]^2}{(w/h)^4 + 0.432} \right] + \frac{1}{18.7} \ln \left[ 1 + \left( \frac{w}{18.1h} \right)^3 \right] \\ b &= 0.564 \cdot [(\varepsilon_R - 0.9)/(\varepsilon_R + 3)]^{0.053}. \end{aligned}$$

This expression is based on functional approximations of numerically calculated values. The numerical values were based on solutions using Green's functions in the associated electrostatics problem.

*Microstrip-Non-zero Thickness.* For modeling the characteristic impedance of microstrips with non-zero thickness, two possibilities exist. The first technique uses the expressions developed for a zero-thickness microstrip. However, to account for the thickness of the microstrip, the width, and sometimes other parameters are adjusted. Hence, an *effective* width is specified instead of the actual physical width, and so on. The second technique considers a conformal transformation of the thick microstrip structures. Expressions of the second type were not

found for microstrip structures.

Representative applications of the first approach are reported by Edwards, based on Getsinger's work. In this case, effective width and effective permittivity adjustments are given (29:58):

$$Z_O \cong \begin{cases} \frac{60}{\sqrt{\epsilon_{R,eff}}} \ln \left( 8 \frac{h}{w_{eff}} + 0.25 \frac{w_{eff}}{h} \right), & \text{for } (w/h) \leq 1 \\ \frac{120\pi}{\sqrt{\epsilon_{R,eff}}} \left[ \frac{w_{eff}}{h} + 1.393 + 0.667 \left( \frac{w_{eff}}{h} + 1.444 \right) \right]^{-1}, & \text{otherwise} \end{cases} \quad (2.58)$$

where  $w_{eff}$  is the effective width, defined by:

$$\frac{w_{eff}}{h} = \begin{cases} \frac{w}{h} + \frac{1.25t}{\pi h} \left( 1 + \ln \frac{4\pi w}{t} \right), & \text{for } (w/h) \leq (1/2)\pi \\ \frac{w}{h} + \frac{1.25t}{\pi h} \left( 1 + \ln \frac{2h}{t} \right), & \text{otherwise.} \end{cases} \quad (2.59)$$

In this case, the effective permittivity ( $\epsilon_{R,eff}$ ) must be modulated by a perturbation term which accounts for the thickness of the strip; that is:

$$\epsilon_{R,eff} = \epsilon_{R,eff}(t) = \epsilon_{R,eff} - \Delta\epsilon_{R,eff}(t) \quad (2.60)$$

where  $\epsilon_{R,eff}$  is evaluated using an appropriate formula for effective permittivity (for example, Equation 2.52), and  $\Delta\epsilon_{R,eff}$  is a correction term to the effective permittivity due to thickness, given by (29:58):

$$\Delta\epsilon_{R,eff}(t) = \frac{(\epsilon_R - 1)t/h}{4.6\sqrt{w/h}}. \quad (2.61)$$

No application of the second technique (conformal transforms for thick, inhomogeneous microstrip) was found in the literature.

#### *Embedded Microstrips Non-Zero Thickness Conformal Mapping.*

Although no techniques which apply conformal mapping to thick, inhomogeneous microstrips were found in the literature, at least one approach is recorded for *embedded* microstrips (as described before, embedded microstrips feature a homogeneous

dielectric fill and a single, conducting ground plane located beneath it). Chang (13) applied a conformal mapping technique to achieve a closed form solution for the capacitance of single, embedded microstrip lines above a ground plane and for the case of conducting planes above and below (stripline). The difference between Chang's conformal method and the other efforts previously attempted, is that rectangles, not lines, were transformed into linear representations in a complex plane. With this technique, Chang converted the analysis of rectangular strips over a ground plane into a much simpler problem: that of a parallel plate capacitor. Though somewhat awkward, the following closed-form approximations required modest computational resources compared to most numerical methods (13). For the case of a single microstrip conductor of non-zero width ( $w$ ), thickness ( $t$ ), positioned at height ( $h$ ) above a single ground plane, and embedded in a homogeneous dielectric of thickness ( $b$ ), Chang estimated the capacitance as:

$$C = \frac{2\varepsilon_0\varepsilon_R}{\pi} \ln \left( \frac{2R_b}{R_a} \right) \quad (2.62)$$

where

$$\begin{aligned} \ln R_a &= -1 - \frac{\pi w}{2h} - [(p+1)/p^{1/2}] \cdot \tanh^{-1} p^{-(1/2)} - \ln \left[ \frac{p-1}{4p} \right] \\ P_b &= \eta + [(p+1)/2p^{(1/2)}] \ln \Delta \\ \eta &= p^{(1/2)} \left( \frac{\pi w}{2h} + [(p+1)/(2p^{(1/2)})] \left[ 1 + \ln \left( \frac{4}{p-1} \right) \right] - 2 \tanh^{-1} p^{-(1/2)} \right) \\ \Delta &= \max(\eta, p) \\ p &= 2b^2 - 1 + \sqrt{(2b^2 - 1)^2 - 1} \end{aligned}$$

$$\text{and } b = 1 + t/h.$$

An accuracy of within one percent is reported for Equation 2.62 when  $(w/h) \geq 1$ . With the capacitance known, the characteristic impedance can be found using Equation 2.21.

*Stripline-Zero Thickness-Conformal Mapping.* Several researchers have achieved an exact, closed form solution for an infinitesimally thin stripline structure (15:147). The expressions were developed using conformal mapping techniques (Schwarz-Christoffel transformations). Chatterjee reports that Oberhettinger *et al.* originated the following expression in 1949 [(15:147),(42:56)]:

$$Z_0 = \frac{30\pi K(k)}{\sqrt{\epsilon_R} K(k')} \quad (2.63)$$

where  $K(k)$  is the complete elliptic integral of the first kind, tabulated in (1), where  $k$  and  $k'$  are defined as:

$$k = \operatorname{sech}\left(\frac{\pi w}{2b}\right) \quad k' = \tanh\left(\frac{\pi w}{2b}\right).$$

and ( $w$ ) is the conductor's width, and ( $b$ ) is the ground plane separation distance.

*Stripline-Non-Zero Thickness.* For non-coupled microstrips, a number of expressions have been developed that accommodate conductors which have non-zero thicknesses. As in the microstrip, these expressions are primarily of two types. The first type uses an expression developed for striplines with zero thickness. To account for the conductor thickness, corrections are made to the width (and possibly other parameters) which, in effect, simulate the thick stripline as another stripline with a different width but zero thickness. The second type of expression is more direct and is based on a conformal transformation of the actual structure (and not the approximated structure, which has zero thickness).

Chatterjee presents a closed-form expression for a stripline with a non-zero thickness as (15:148):

$$Z_0 = \frac{91.15}{\sqrt{\epsilon_R}[w/(b-t) + 0.45 + 1.18(t/w)]}, \quad 0.05 < (t/w) < 0.5. \quad (2.64)$$

Chatterjee does not explicitly state the origin of this expression, but it is most

likely to be based on the first type of expressions (corrected version of zero-thickness conformal mapping).

Another approximation for thick striplines, developed by Wheeler, is reported by Gupta *et al.* as (42:57):

$$Z_0 = \frac{30}{\sqrt{\epsilon_R}} \ln \left\{ 1 + \frac{4}{\pi} \frac{b-t}{w'} \left[ \frac{8}{\pi} \frac{b-t}{w'} + \sqrt{\left( \frac{8}{\pi} \frac{b-t}{w'} \right)^2 + 6.27} \right] \right\} \quad (2.55)$$

where

$$\frac{w'}{b-t} = \frac{w}{b-t} + \frac{\Delta w}{b-t}$$

$$\frac{\Delta w}{b-t} = \frac{x}{\pi(1-x)} \left\{ 1 - \frac{1}{2} \ln \left[ \left( \frac{x}{2-x} \right)^2 + \left( \frac{0.0796x}{w/b + 1.1x} \right)^m \right] \right\}$$

$$m = 2 \left[ 1 + \frac{2}{3} \frac{x}{1-x} \right]^{-1}$$

$$\text{and } x = t/b.$$

This expression is valid to within .5 percent for  $w'/(b-t) < 10$ , and it is clearly of the first type.

Chang developed an expression of the second type for thick striplines. The expression he developed actually estimates the capacitance of the stripline structure. Of course, the characteristic impedance can be evaluated from Equation 2.20 after the capacitance is determined. For single striplines with grounded conducting planes above and below, Chang proposed that (13):

$$C = \frac{2\epsilon_0\epsilon_R}{\pi} \ln(R_b/R_a) \quad (2.66)$$

where

$$\begin{aligned}\ln R_a &= \pi w/(2h) - 2\alpha \tanh^{-1} \sqrt{(p+q)/\gamma(1+q)} + 2\gamma \tanh^{-1} p^{-1/2} \\ &\quad + \ln[4p/(p-1)] \\ \ln R_b &= \gamma^{-1}[\pi w/(2h) + 2\alpha \tanh^{-1} \sqrt{(1+q)/(p+q)} + \gamma \ln(p-1)/4 \\ &\quad - 2 \tanh^{-1} p^{-1/2}]\end{aligned}$$

$$\alpha = b/h$$

$$\gamma = (b-h-t)/h$$

$$p = q^2/\gamma^2$$

$$\text{and } q = \frac{1}{2}[\alpha^2 - \gamma^2 - 1 + \sqrt{(\alpha^2 - \gamma^2 - 1)^2 - 4\gamma^2}].$$

An accuracy to within one percent is reported for Equation 2.66 when  $(w/h) \geq 0.5$  and  $(d/h) \geq 0.5$ .

*Coplanar Waveguide-Zero Thickness.* Gupta *et al.* and Hoffman reported the following expression for the characteristic impedance of coplanar waveguides which have infinitesimally thin conductors [(42:69),(45)]:

$$Z_0 = \frac{30\pi}{\sqrt{\epsilon_{R,eff}}} \frac{K'(k)}{K(k)} \quad (2.67)$$

where:

$$k = w/(w+2s) \quad (2.68)$$

$\epsilon_{R,eff}$  is the effective permittivity, which is related to the relative permittivity ( $\epsilon_R$ ) by (45):

$$\epsilon_{R,eff} = \frac{\epsilon_R + 1}{2} \quad (2.69)$$

and  $s$  is the gap spacing between either conductor and the coplanar ground plane conductors. Of course, the assembly is assumed to be symmetric; that is, the gap spaces  $s_1$  and  $s_2$  are assumed to be equal. Furthermore, as evidenced by Equation 2.67, the

dielectric substrate is assumed to be infinitely thick.

For dielectric substrates of finite thickness, Hoffman recommended using Equation 2.67 with an alternate expression for the effective permittivity. For a dielectric substrate thickness of  $h$ , the resultant expression becomes:

$$\epsilon_{R,eff} = 1 + \frac{(\epsilon_R - 1)K(k'_1) + K(k')}{2K(k_1)K(k)} \quad (2.70)$$

where

$$\begin{aligned} k &= \text{Equation 2.68} \\ k' &= \sqrt{1 - k^2} \\ k_1 &= \sqrt{1/(1 + q)} \\ k'_1 &= \sqrt{1 - k'^2} \\ \text{and } q &= \frac{\sinh [\pi w/(4h)]^2}{\sinh [\pi s/(2h)] \sinh [\pi(w + s)/(2h)]} \end{aligned}$$

Gupta *et al.* recommended a simpler expression (41:275):

$$\begin{aligned} \epsilon_{R,eff} &= \frac{\epsilon_R + 1}{2} \{ \tanh[1.785 \ln(h/2) + 1.75] \\ &\quad + (kw)/h[0.01 - 0.7k + 0.01(1 - 0.1\epsilon_R)(0.25 + k)] \} \end{aligned} \quad (2.71)$$

*Coplanar Waveguide Non-Zero Thickness.* For coplanar waveguides with non-zero thickness, Gupta *et al.* recommended Equation 2.67 with modified forms of the effective permittivity  $\epsilon_{R,eff}$  and the parameters  $k$  and  $k'$  to account for conductor thickness (42):

$$Z_0 = \frac{30\pi}{\sqrt{\epsilon_{R,eff}(th/k)}} \frac{K(k'_{eff})}{K(k_{eff})} \quad (2.72)$$



where

$$\begin{aligned}
 k &= \text{Equation 2.68} \\
 k_{eff} &= s_{eff}/(s_{eff} + 2w_{eff}) \\
 k'_{eff} &= \sqrt{1 - k_{eff}^2} \\
 w_{eff} &= w + \Delta \\
 s_{eff} &= s - \Delta \\
 \Delta &= 1.25 \frac{t}{\pi} \left( 1 + \ln \left[ \frac{4\pi w}{t} \right] \right) \\
 \varepsilon_{R,eff} &= \text{Equation 2.71} \\
 \varepsilon_{R,eff(thick)} &= \varepsilon_{R,eff} - 1.4(\varepsilon_{R,eff} - 1)t / [s(x + 1.4t/s)] \\
 \text{and } x &= \frac{K(k')}{K(k)}.
 \end{aligned}$$

This expression is reportedly accurate to within 1.5 per cent for  $\varepsilon_R > 9$ ,  $(h/w) > 1$ , and  $0 < k < 0.7$  for zero thickness lines.

*Edge-Coupled Microstrips (ECM).* Expressions for estimating the characteristic impedance have been developed for ECMs with conductors which have both zero and non-zero thicknesses. The expressions are quite extensive and are not presented here. For zero-thickness ECMs, Hoffman reported an approach for estimating the characteristic impedance which is based on functional approximations to Green's function solutions to the electrostatic problem, similar to the approach of Equation 2.55 (45:242-245). Gupta *et al.* presented a different approach for zero-thickness ECMs. This approach uses the definitions given in Equations 2.33 and 2.34 to calculate the characteristic impedance for the even- and odd-modes. To supply the capacitance estimate required by these defining equations, the partial capacitances between each conductor and ground, between the conductors themselves, and those capacitances associated with fringing are calculated through functional

approximations for both even- and odd-modes. The capacitances appropriate to the even-mode are then combined to form the total even-mode capacitance, and those appropriate to the odd-mode are combined to form the total odd-mode capacitance. For ECMs with non-zero thickness, the approach reported by Gupta *et al.* is used, except that an effective width is used instead of the physical width. As in Equation 2.59, this effective width is a function of thickness. Thus, through the use of an effective width, an ECM with non-zero thickness is described by the same formulae used for ECMs with zero-thickness conductors (42:76-82).

*Edge-Coupled Striplines-Zero Thickness-Conformal Mapping.* A number of expressions for ECS structures have been reported. Most of these expressions are based on the same conformal transformations used for coplanar strips. These transformations, in turn, are quite similar to those used for the coplanar waveguide (42:67-73). For zero-thickness ECS structures, Hoffman reported the following expressions for the even- and odd-mode characteristic impedances (45:346):

$$Z_{O,even} = \frac{30\pi}{\sqrt{\epsilon_R}} \frac{K(k'_{even})}{K(k_{even})} \quad (2.73)$$

$$Z_{O,odd} = \frac{30\pi}{\sqrt{\epsilon_R}} \frac{K(k'_{odd})}{K(k_{odd})} \quad (2.74)$$

where

$$k_{even} = \tanh \left( \frac{\pi w}{2b} \right) \tanh \left[ \frac{\pi(w+s)}{2b} \right]$$

$$k'_{even} = \sqrt{1 - (k_{even})^2}$$

$$k_{odd} = \tanh \left( \frac{\pi w}{2b} \right) \coth \left[ \frac{\pi(w+s)}{2b} \right]$$

$$k'_{odd} = \sqrt{1 - (k_{odd})^2}.$$

As before, ( $w$ ) is the width of the conductors, ( $s$ ) is the lateral spacing between conductors, and ( $b$ ) is the ground plane separation distance.

*Edge-Coupled Striplines-Non-Zero Thickness.* Gupta *et al.* report the following closed-form expressions for ECS structures which have non-zero conductor thickness (42:74):

$$Z_{O,even} = \frac{30\pi(b-t)}{\sqrt{\epsilon_R} [w + bC_F/(2\pi)A_{even}]} \quad (2.75)$$

$$Z_{O,odd} = \frac{30\pi(b-t)}{\sqrt{\epsilon_R} [w + bC_F/(2\pi)A_{odd}]} \quad (2.76)$$

where

$$\begin{aligned} A_{even} &= 1 + \ln \left[ 1 + \tanh \left( \frac{\pi s}{2b} \right) \right] / \ln 2 \\ A_{odd} &= 1 + \ln \left[ 1 + \coth \left( \frac{\pi s}{2b} \right) \right] / \ln 2 \\ \text{and } C_F &= 2 \ln \left( \frac{2b-t}{b-t} \right) - \frac{t}{b} \ln \left[ \frac{t(2b-t)}{(b-t)^2} \right]. \end{aligned} \quad (2.77)$$

The parameters ( $s$ ) and ( $w$ ) are as defined previously, and ( $t$ ) is the conductor thickness. These expressions are reportedly most accurate when  $(t/b) < 0.1$  and  $(w/b) \geq 0.35$  (42:74).

*Loss and Distortion Mechanisms.* Several important loss and distortion mechanisms are active in WSICs, including (25):

1. Conductor resistive losses
2. Conductor skin effect losses
3. Dielectric leakage losses
4. Radiation losses
5. Dispersion due to material and geometric sources.

The various contributions to the attenuation factor in the frequency-independent case (non-dispersive) are often modeled in transmission lines in a simple manner (2:11):

$$\alpha = \alpha_C + \alpha_D \quad (2.78)$$

where  $\alpha_C$  is the attenuation factor due to conductor losses, and  $\alpha_D$  is the attenuation factor due to dielectric losses. When a transmission line satisfies the conditions:

$$\frac{\omega L}{R} \gg 1 \quad (2.79)$$

$$\text{and } \frac{\omega C}{G} \gg 1 \quad (2.80)$$

the attenuation factor ( $\alpha$ ) can be further simplified by the following approximation (16):

$$\alpha = \frac{R}{2Z_0} + \frac{G}{2Z_0} \quad (2.81)$$

where the first term is the conductor loss and the second term is the dielectric loss.

Bhasil *et al.* noted that the loss of microstrip structures is higher than that of other waveguide types at higher frequencies. However, Denlinger commented that coplanar waveguides and possibly slotlines experienced greater losses than microstrip lines (25). The following sections consider the various loss and dispersion mechanisms which may be encountered in microstrip-like lines.

*Attenuation Due to Resistive Losses.* Resistive losses in the wire conductors typically used in integrated circuits create a resistance-capacitance (RC)-like transmission line behavior in the conductor lines. RC transmission lines are notoriously sluggish in their response time and manifest high signal attenuation. For this reason, some WSI approaches alter the configuration of conductor geometries, such that the conductors more closely approximate inductor-capacitor (LC)-like transmission line behavior. This modification, for example, can be effected by increasing the thickness of the interconnections. Compounding the resistive losses in interconnections due to materials, the skin-effect present at high frequencies further increases the resistance of interconnections and may contribute to losses in signal transmission. The dielectrics used in WSI will be naturally dispersive, and the geometries of microstrip-like structures introduce a dispersive effect, as well (36). Furthermore, dispersion will be aggravated in materials that absorb moisture [(66),(80)].

If the dielectric has a finite conductance, this mechanism will also create losses in an interconnection. Yield imperfections, such as pinholes (66) and partially broken conductors, can cause conduction losses or complete electrical failure. An in-depth consideration of these effects is warranted, since, if severe enough, they will negate any benefit that might be afforded by a WSI approach (66).

The attenuation in a slightly lossy transmission line is often approximated by the first term of Equation 2.81 as [(25),(66)]:

$$A = e^{-R/(2Z_0)} \quad (2.82)$$

where  $R$  is the total resistance per unit length of the line, and  $Z_0$  is the characteristic impedance of the same line treated as being lossless. Obviously, attenuation effects due to conductor loss increases as the interconnection line length increases. McDonald *et al.* stated that the following constraint should be met in order to minimize signal degradation on lines which are to be used in WSI (66):

$$th \gg \frac{1}{\sigma} \epsilon_0 \sqrt{\epsilon_R} \ell c \quad (2.83)$$

where  $\ell$  is the length of the interconnection; ( $t$ ) and ( $h$ ) are the metal and dielectric thicknesses (as shown in Figure 2.1), respectively;  $\sigma$  is the conductivity of the metal;  $\epsilon_R$  is the relative permittivity of the insulating medium; and  $c$  is the velocity of light. McDonald *et al.* observed that for a polyimide dielectric ( $h = 10 \mu\text{m}$ ) and aluminum conductors ( $t = 5 \mu\text{m}$ ) this constraint is satisfied, even for wafer interconnections 20 cm in length (66).

More detailed conductor loss models have been proposed. For example, Edwards reports a more detailed model, developed by Hammerstad, which accounts for the frequency dependence as (29:90):

$$\alpha_c = 0.672 \frac{\sqrt{f}}{w Z_0} \lambda_g \quad (2.84)$$

where  $\alpha_c$  represents the conductor loss in decibels per microstrip wavelength,  $f$  is the frequency in gigahertz,  $w$  is the conductor width, and  $\lambda_g$  is the microstrip wavelength, defined as (29:70):

$$\lambda_g = \frac{c}{f\sqrt{\epsilon_{R,eff}(f)}} \quad (2.85)$$

and  $\epsilon_{R,eff}(f)$  is the effective permittivity of the microstrip structure. An even more exacting model, reported by Edwards, uses Equation 2.84 as a multiplicative factor in an expression which accounts for the rms surface roughness of the substrate (29):

$$\alpha_{C'} = \alpha_C \left[ 1 + \frac{2}{\pi} \tan^{-1} \left\{ 1.4 \left( \frac{\Delta}{\delta} \right)^2 \right\} \right] \quad (2.86)$$

where  $\alpha_{C'}$  is the attenuation in dB/wavelength,  $\Delta$  is the rms surface roughness (unit length),  $\delta = 1/(R_s\sigma)$  is the skin depth (unit length),  $R_s$  is the surface resistance, and  $\sigma$  is the conductor's conductivity.

*Skin Effect Losses.* The *skin effect* refers to the tendency of electric and magnetic fields to "seek" the outer surface of a conductor at higher frequencies. The *classical* skin depth is defined by Ramo *et al.* as (79:252):

$$\delta = \frac{1}{\pi f \mu \sigma} \quad (2.87)$$

where  $\delta$  is the skin depth,  $\mu = \mu_0 \mu_R$  is the magnetic permeability, and  $f$  is the frequency (in hertz). The skin depth represents the distance measured from a conductor's surface to its interior at which electromagnetic fields are attenuated by a factor of  $(1/exp)$ . Derivation of this quantity is instructive; the field penetration in conductors of electric fields is easily demonstrated by forming the curl of Equation 2.3 (79:234):

$$\nabla \times \nabla \times E = \nabla(\nabla \cdot E) - \nabla^2 E = \nabla \times \frac{\partial B}{\partial t} \quad (2.88)$$

Since, for a good conductor,  $\sigma \rightarrow \infty$  and:

$$\nabla \cdot E = 0 \quad (2.89)$$

then, using Equations 2.4, 2.7, and 2.8, Equation 2.88 reduces to:

$$\nabla^2 E = \sigma \mu \frac{\partial E}{\partial t} \quad (2.90)$$

or, equivalently, for time-harmonic signals:

$$\nabla^2 E = j\omega\sigma\mu E. \quad (2.91)$$

The skin depth is found by solving Equation 2.91 for a semi-infinite solid conductor whose surface is the  $xy$ -plane (57:202). With the  $x$  and  $y$  dependency removed, the solution to this second-order differential equation is:

$$E_z = C_1 e^{-\delta x} + C_2 e^{\delta x} \quad (2.92)$$

where  $(\delta)$  is the skin depth. For the field to remain finite,  $C_1$  must be chosen to be identically zero [(57),(79)]. Hence,

$$E_z = E_0 e^{-\delta x}. \quad (2.93)$$

An obvious problem with applying the normally defined  $\delta$  is that, for conductors with small thicknesses,  $C_2$  in Equation 2.92 need not be chosen to be zero, and, consequently, the classical skin depth no longer reflects the point of  $(1/erp)$  attenuation. Therefore, Equation 2.87 only defines skin depth exactly for semi-infinitely deep conductors.

However, the classical skin depth can often be taken as the true skin depth without appreciable error. Cangelaris observed that when the skin depth of a conductor

is much less than its physical dimensions, useful relations, such as Wheeler's incremental inductance rule may be applied (12:197). As Wheeler noted, the incremental inductance calculations are only approximate when the classical skin depth ( $\delta$ ) is much less than any transverse dimension of a conductor (100:11). Unfortunately, the transverse dimensions of contemporary interconnections are sufficiently small to invalidate the use of Wheeler's incremental inductance rule at frequencies as low as 500 MHz (12:197). In addition to its dependence on the physical size of a conductor, the skin effect is dependent on the shape of a conductor. For a conductor to be considered "flat" with respect to skin effects, the surface curvature must be several times greater than the skin depth (75:205). Hence, even large microstrip-like structures will have irregular skin-depths near corners and other discontinuities.

For "admissible" interconnection geometries, that is, structures which have transverse dimensions much greater than their classical skin depth, approximations for skin resistance loss have been developed. Hill *et al.* arrived at an approximation for the lower bound on conductor transverse dimensions, such that the skin impedance is negligible; that is (44:315):

$$d \gg \frac{400}{Z_0} \sqrt{\frac{\tau_r}{\epsilon_R}} \quad (2.91)$$

where  $d$  is the diameter of the round conductor,  $Z_0$  is the characteristic impedance,  $\tau_r$  is the switching transition time, and  $\epsilon_R$  is the relative permittivity. As an example, Hill *et al.* showed that for a material with a characteristic impedance of 50  $\Omega$ , and a relative permittivity of 4, that signals as fast as 200 ps could be analyzed on a conductor whose transverse dimensions were no smaller than 57  $\mu\text{m}$ .

*Dielectric Leakage Losses.* The conductance parameter ( $G$ ) in Equations 2.15 and 2.30 refers to the leakage current which flows from a conductor to the substrate and other conductors through the dielectric medium. This loss is characterized by the loss tangent ( $\tan \delta_L$ ), a material parameter. Deulinger



characterized the loss in microstrip lines using an effective loss tangent in the following approximation (25):

$$\alpha_D = \frac{27.3}{\lambda_g} (\tan \delta_{L,eff}) \quad (\text{dB/unit length}) \quad (2.95)$$

where  $\lambda_g$  is the microstrip wavelength, as defined before, and  $\tan \delta_{L,eff}$  is the *effective* loss tangent, defined as (29:91):

$$\tan \delta_{L,eff} = \frac{1 - 1/\epsilon_{R,eff}}{\epsilon_R - 1} \tan \delta_L. \quad (2.96)$$

*Radiation Losses.* The radiative losses in a microstrip are geometry-dependent and occur at discontinuities in the conductor, such as at corner bends, T-junctions, and impedance changes. Even matched terminations can produce radiative losses (25). Radiation losses, which are exploited for antenna design, are clearly undesired in WSI systems.

*Dispersion of Dielectric Medium.* In transmission lines, *dispersion* refers to a frequency-dependent time delay experienced by waves traveling on the line (4:179). In microstrip lines, dispersive effects can be attributed to material properties or to the geometric anomalies of the quasi-TEM structures. The general discussion of dispersion motivates a consideration of the electrical permittivity of these structures.

The material-dependent dispersive effects are characterized by the frequency dependent behavior of the supporting dielectric media; that is,  $\epsilon_R = \epsilon_R(f)$ . The permittivity of some materials has little variance over a wide frequency range; for these materials,  $\epsilon_R$  may be approximated as a constant. Other materials, such as polyimide, for example, which is often used in integrated circuit fabrication, can display significant fluctuations in  $\epsilon_R$ , due to its non-hermeticity (66:3133), among other reasons. Another source of dispersion is inherent in materials. Landau *et al.* reported that at sufficiently high frequencies, the permittivity of all materials approaches

that of free-space ( $\epsilon_R$ ) (57:267). No analytic expressions exist for the frequency-dependency of the permittivity in materials; it is usually modeled empirically, if at all.

The geometrically-dependent dispersion phenomenon in microstrip lines, in particular, has been studied extensively [(77),(34),(51),(88)]. Most of these workers have concluded that the non-TEM nature of the microstrip structures causes dispersion. Additionally, Goossen proposed that dispersive effects in microstrip lines occur because of the nonlinear dependency of the propagation constant on the width of the microstrip line. As such, non-uniformities in the conductivity of the line with frequency, such as skin-effect losses, affect the dispersion (39:470). Getsinger developed an expression for effective permittivity ( $\epsilon_{R,eff}$ ), based on the analysis of a structurally altered model of a microstrip line which is forced to electrically behave like a microstrip line in the lower limit (29:72-74).

Wheeler was apparently the first researcher to apply the concept of a geometrically-based dispersion formula to account for the frequency-dependent behavior of microstrip lines. In his conformal transformation, a microstrip is mapped from the  $z$ -plane (Figure 2.9a) to a parallel plate capacitor in another complex plane (Figure 2.9b). However, the space between the parallel plates in the new complex plane is inhomogeneously filled, and in Wheeler's analysis, the microstrip is modeled by an *effective* permittivity, which accounts for the incomplete filling of the parallel plate capacitor in Figure 2.9b (41:8-11). One author defines this effective permittivity as (29:40):

$$\epsilon_{eff} = \left( \frac{C}{C_1} \right) \quad (2.97)$$

where  $C$  is the capacitance of the configuration shown in Figure 2.9b, and  $C_1$  is the capacitance of the configuration shown in Figure 2.9c. In the latter configuration, the supporting dielectric medium is replaced by a vacuum. An alternate definition

can be obtained from Equation 2.97 as (29:40):

$$\epsilon_{R,eff} = \left( \frac{c}{v_p} \right)^2 \quad (2.98)$$

where  $c$  is the velocity of light, and  $v_p$  is the phase velocity.

These definitions lead to the approximations expressed in Equations 2.52 and 2.53, for example. These definitions are based on microstrip lines which are covered by a vacuum (or air, as an approximation) on its top surface. For use with other dielectrics coverings, it is possible to develop expressions with the filling factor concept (based on (41:10)):

$$\epsilon_{R,eff} = (1 - q)\epsilon_{R2} + q\epsilon_{R1} \quad (2.99)$$

where  $\epsilon_{R1}$  is the relative permittivity of the dielectric below the microstrip ( $\epsilon_R$  in Figure 2.1a),  $\epsilon_{R2}$  is the relative permittivity of the superficial dielectric medium, and ( $q$ ) is the filling factor ( $0 \leq q \leq 1$ ), which corresponds to the fraction of the area in Figure 2.9b occupied by  $\epsilon_{R1}$  (41:10). Wheeler reported a simple empirical approximation for ( $q$ ), developed by Getsinger, which is useful in thin microstrip lines (100):

$$q = \frac{1}{2} \left( 1 + 1/\sqrt{1 + 10h/w} \right). \quad (2.100)$$

One of the more common expressions for the zero-frequency effective permittivity ( $\epsilon_{R,eff}(0)$ ) in microstrip lines is provided in Equation 2.52. Some expressions for effective permittivity require an  $a$ , or  $h$ , determination of the characteristic impedance ( $Z_0$ ) [(29):(45:147,44-45)], while others operate over a limited range of relative permittivities (45:146). Other closed form expressions for effective permittivity which are useful over large ranges of relative permittivity are divided into narrow strip approximations (41:10):

$$\epsilon_{R,eff}(0) = \frac{\epsilon_R + 1}{2} + \frac{\epsilon_R - 1}{2} \frac{\ln \pi}{2} + (1/\epsilon_R) \ln \frac{4}{\pi} \ln \frac{8h}{w}, \quad (w/h) < 2 \quad (2.101)$$

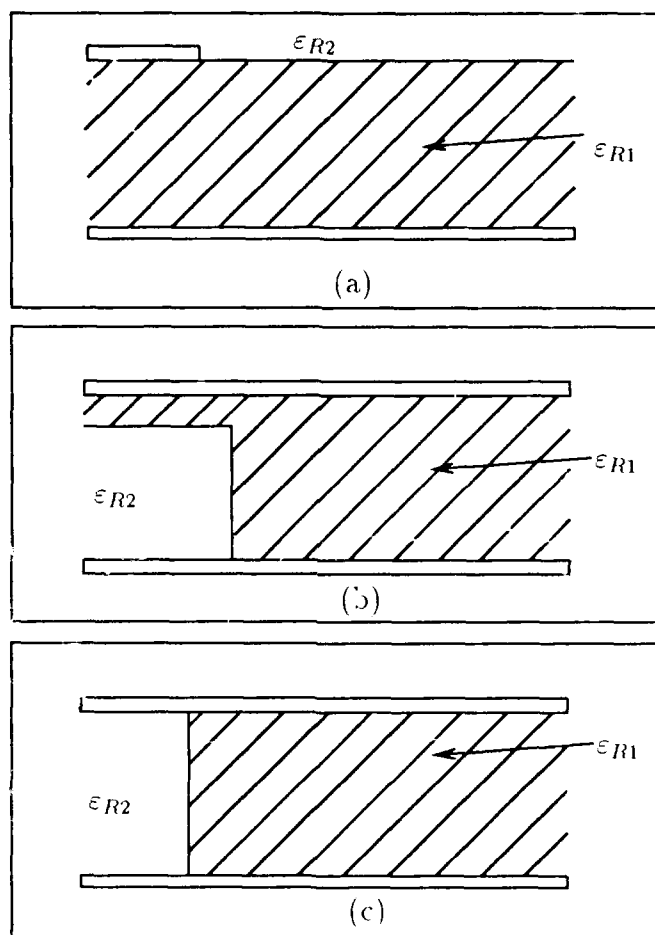


Figure 2.9. A simplified illustration of Wheeler's conformal transformation technique. (a) Configuration of microstrip. (b) Approximate conformally transformed representation. (c) Alternate transformed representation, filled with a single dielectric. After (41).

and for wide strip approximations (29:45):

$$\varepsilon_{eff}(0) = \frac{\varepsilon_R + 1}{2} + \frac{\varepsilon_R - 1}{2} \left( 1 + 10 \frac{h}{w} \right)^{-0.555} \quad (w/h) > 1.3. \quad (2.102)$$

The frequency-dependence of the effective permittivity has been investigated extensively [(88),(34),(77)]. Pramanick *et al.* summarized these efforts as sharing in common the form:

$$\varepsilon_{R,eff}(f) = \varepsilon_R - \frac{\varepsilon_R - \varepsilon_{R,eff}(0)}{1 + G(f/f_c)} \quad (2.103)$$

where  $\varepsilon_{R,eff}(0)$  is the effective permittivity evaluated at zero frequency,  $f_c$  is a "critical" frequency, and  $G(f/f_c)$  is a function. The latter two quantities vary between the several analytic efforts [(77),(41)]; most of these were summarized by Gupta *et al.* and later by Pramanick *et al.* [(41:21),(77:28)]. Specifically, they noted that Jain *et al.* defined the critical frequency to occur where the TEM mode and lowest order TM mode (TM<sub>0</sub>) have equal phase velocities. They pointed out that Schneider and Carlin, on the other hand, created an expression for effective permittivity which considered  $f_c$  to occur at the cutoff of the lowest order TE mode. In the latter case, Carlin actually considered the TEM and TE modes as two separate transmission lines which possessed a frequency-dependent coupling factor. Gupta *et al.* and Pramanick *et al.* also observed that Getsinger's expressions for effective permittivity were based on a structural transformation analysis combined with experimental data, yielding a semi-empirical model, while Edwards *et al.* further modified this result empirically for alumina substrates [(41:21),(77:28)]. Pramanick *et al.* favored the model which considered the coupling between the quasi-TEM mode and the lowest order TE mode in their own development (77). Another approach was forwarded by Kirschling *et al.*, involving the generation of empirical expressions based on the computer-modeling of interactions between the TEM mode and certain frequency-dependent hybrid modes (51). Several formula for the frequency-dependent dispersion of permittivity are tabulated in Table 2.3.

Table 2.3. Effective permittivity models. From [(41),(51),(77),(45)].

$\varepsilon_{R,eff} = \varepsilon_{R,eff}(f) = \varepsilon_R - \frac{\varepsilon_R - \varepsilon_{R,eff}(0)}{1 + G(f/f_c)}$		
Author	$G(f/f_c)$	$f_c$
Getsinger	$(0.6 + 0.009Z_0)(f/f_c)^2$	$\frac{Z_0}{2\mu_0 b}$
Yamashita	See Equation 2.53	
Pramanick <i>et al.</i>	$f/f_c$	$\frac{C}{2(w + \Delta w)\sqrt{\varepsilon_R}}$
Kirsching	$P_1 P_2 [(0.1844 + P_3 P_4) 10 f h]^{1.5763}$	1
<p>where</p> $\Delta w = h \sqrt{\varepsilon_{eff}} / (Z_0 C \varepsilon_0 \varepsilon_R) - w;$ $P_1 = 0.27488 + [(0.6315 + 0.525 / (1 + 0.157 f h)^{20}) u - 0.065683 \exp(-8.7513 u)];$ $P_2 = 0.33622 [1 - \exp(-0.03442 \varepsilon_R)];$ $P_3 = 0.036 \exp(-4 \cdot 6 u) \times \{1 - \exp[-(f h / 3.87)^{4.97}]\}$ $P_4 = 1 + 2.751 \{1 - \exp[-(\varepsilon_r / 15.916)^8]\};$ <p>and <math>u = w/h</math>.</p>		

### *Other Wafer Scale Interconnection Issues*

*Yield of Wafer Scale Interconnections.* The yield of WSI must be high, especially for the hybrid approach. Of course, high yield is desired in monolithic approaches, but monolithic WSI designs are expected to feature redundancy schemes sufficiently robust to survive a number of random yield faults. Thus, monolithic designs are expected to have functional configurations which differ from wafer to wafer as a result of this capability. However, hybrid systems are expected to have reliable and identical electrical configurations from wafer to wafer.

One of the advantages of hybrid WSI relative to monolithic WSI systems from a yield perspective, is in area reduction. Yield projections are usually cast as increasing functions of area. One example is the following yield model, given by McDonald *et al.* (66:3128):

$$Y = [1/(1 + D_O A_C/\alpha)]^{\alpha} \quad (2.104)$$

where  $Y$  is the yield fraction, indicating the percentage of good wafers per lot;  $D_O$  is the defect density;  $A_C$  is the chip or wafer area; and  $\alpha$  is "an empirical parameter with a value close to unity" (66:3128). Since parts of a hybrid WSIC are vacated to accommodate IC die, the area of a hybrid WSIC is less than that corresponding to a monolithic WSIC of the same size. Thus, the number of defects are expected to be less for a hybrid WSIC than for a monolithic WSIC. However, even this comparison is not adequate. Since a monolithic WSIC houses active devices, the defect density ( $D$ ) of this wafer will be comparable to that for a typical VLSI circuit based on the same technology. On the other hand, a hybrid WSIC will have a different defect density. Since the technology base of hybrid WSIC is primarily concerned with interconnections rather than active devices, the feature sizes as well as the primary failure mechanisms, are different. Thus, the defect densities used to analyze the yield of hybrid WSICs will generally be different compared to those used to analyze monolithic WSICs. Almost certainly, one could conclude that the defect densities for hybrid WSICs will be lower compared to monolithic WSICs [(66),(67)].

For batches of hybrid WSICs, McDonald *et al.* considered a simple yield model (67:65):

$$Y_b = e^{-\lambda_b} \quad (2.105)$$

where  $\lambda_b$  is the average number of yield failures in a lot or batch of wafers. McDonald *et al.* identified three components of  $\lambda_b$  [(66:3135),(67:65)]:

$$\lambda_b = \lambda_O + \lambda_S + \lambda_P \quad (2.106)$$

where  $\lambda_O$  is the number of faults due to electrical opens;  $\lambda_S$  is the number of faults due to electrical shorts; and  $\lambda_P$  is the number of faults due to pinholes in the dielectric. Thus, the overall yield model is the product of three Poisson probability distributions: one based on  $\lambda_O$ , one based on  $\lambda_S$ , and one based on  $\lambda_P$  [(66),(67)].

McDonald *et al.* stipulated that  $\lambda_P \cong 0$  for processes which fabricate the dielectric layers through the application of multiple thin layers. The applications of polyimide, for example, can be performed with several successive spin-on and cure cycles. The likelihood that any overall pinhole failure would occur through the alignment of pinhole failures in the constituent layers would be sufficiently small to be neglected, according to McDonald *et al.* [(66:3135),(67:65)].

The remaining defect parameters  $\lambda_O$  and  $\lambda_S$  are defined as [(66:3136),(67:65)]:

$$\lambda_O = A_{open} D_{open} \quad (2.107)$$

$$\text{and } \lambda_S = A_{short} D_{short} \quad (2.108)$$

where  $A_{open}$  and  $A_{short}$  are the average critical areas for opens and shorts, respectively, and  $D_{open}$  and  $D_{short}$  are the defect densities for opens and shorts. The critical areas are evaluated using:

$$A_{open} = A_w \frac{X_O^2}{2w(2w + s)} \quad (2.109)$$



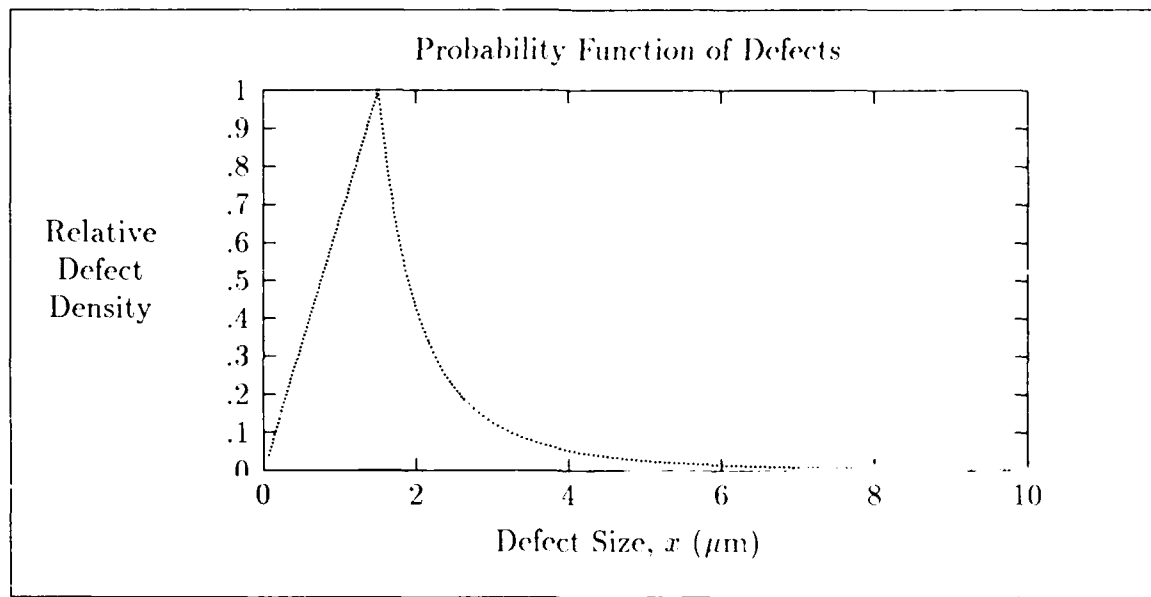


Figure 2.10. Probability distribution of defect density as a function of size. In this example,  $X_O = 1.5\mu\text{m}$ . From (66).

$$\text{and } A_{short} = A_w \frac{X_O^2}{2s(2s + w)} \quad (2.110)$$

where ( $w$ ) is the width of the conductors, ( $s$ ) is lateral separation distance,  $A_w$  is the wafer area available for interconnections; and  $X_O$  is the lithographic resolution. The characteristic probability model for defects shown in Figure 2.10 indicates that this lithographic feature size is that associated with the highest average defect density  $\bar{D}$ . An analysis, performed by McDonald *et al.*, predicted the batch yield for a candidate hybrid WSI approach. They only considered a WSIC with conductor widths of  $10\mu\text{m}$  with inter-conductor spacings of  $15\mu\text{m}$ . The results of the study indicated that a 97% yield could be expected for a defect density of 0.1 defects/ $\text{cm}^2$ , decreasing to 88% for a defect density of 0.5 defects/ $\text{cm}^2$  [(66:3136),(67:65)].

**Discontinuities** A discontinuity in a microstrip-like line refers to virtually any geometric deviation from an infinite length of line of homogeneous shape and composition. Analyses which consider physical discontinuities in microstrip-like transmission structures are abundant in the literature [(41),(42)]. Examples of discontinuities

typically encountered in these systems include bends, step width changes, and T-junctions (69). These discontinuities can be analyzed with the same techniques used to analyze the transmission lines themselves. Similar to the transmission line case, electrostatic approximations may be applied, or time-varying analyses may be conducted. In a celebrated paper, Sylvester *et al.* considered right-angle bends, cross-overs, and T-junctions with static analyses (92). In another related paper, Sylvester *et al.* analyzed microstrip gaps and step width changes (93). In each case, Sylvester *et al.* developed formulations that approximate each discontinuity as a capacitive lumped element.

*Materials.* The particular materials used to fabricate the transmission structures of a wafer scale system obviously influence its electrical performance. The selection of suitable materials from which the conductors, supporting dielectrics, and substrates are to be fabricated involves a careful consideration of the trade-offs between the electrical, structural, and thermal properties characteristic of available candidate materials.

Electrically, good interconnections require minimal resistivity in a conductor and minimal leakage conductivity in a dielectric. The electrical permittivities of dielectrics should be sufficiently low to reduce the mutual capacitances and inductances in conductors which lead to crosstalk. Jayaraj *et al.* observed that lower permittivities are also desired for improved signal speed, since propagation delays are proportional to the square root of the permittivity (48). The use of dielectric materials with low leakage conductances is, of course, preferred. The roughness of the substrate, another material property that is usually specified by feature size (29:26), should also be small in a conductor to further reduce conductor losses. Edwards indicated that the surface roughness of the substrate can affect the calculated value of the conductor loss ( $\alpha_C$ ) by as much as 60 percent (29:91).

Structurally, the interconnection network must provide the WSI system with a high degree of mechanical integrity, since this network serves the same packaging

function as a PCB. The structural compliance of semiconductors is typically taken for granted, as most often implied by terms such as "solid state" electronics. Among the various denotations of this term, the solidness or ruggedness of semiconductor components is often taken as a "given". However, WSI will literally press this interpretation, since semiconductors have never before been impressed with the task of mechanical support to such a degree. Excessively brittle materials, as well as excessively flexible materials, though adequate for die-sized dimensions, may be unacceptable for wafer-sized dimensions.

Thermally, WSI materials must adequately handle the heat generated in wafer-size regions which have high component densities. Furthermore, the thermal coefficients of expansion (TCEs) for the dielectric materials must track reasonably well with those for the substrates, since large differences can create structural problems due to the delamination of these dielectrics from the supporting substrate (66).

In addition to the electrical, mechanical, and thermal considerations, the cost and ease of fabricating WSI interconnections must be considered. If WSICs can only be realized from rare materials or with exceedingly difficult fabrication methods, they will remain as laboratory curios with an otherwise limited usage. Fortunately, several combinations of substrate, dielectric, and conductor materials for fabricating WSICs have been explored and which are, for the most part, compatible with existing fabrication methods and, furthermore, offer reasonably good performance in the aforementioned areas. Tables 2.4-2.6 summarize the various substrate, dielectric, and conductor materials, respectively, which have been considered for wafer scale interconnections. Those materials which are of current research interest in wafer scale interconnections are denoted in the tables by an asterick (\*), while those actually used in this study for measurement are denoted by a dagger symbol (†).

*Substrates.* Of the materials shown in Table 2.4, silicon is the most obvious and practical choice for WSI work. A simple reason for this assertion is that

Table 2.4. Properties of materials considered for WSIC substrates. From [(3),(29)].

Material	Thermal Conductivity (W/cm °C)	Surface Roughness ( $\mu$ )	$\epsilon_R$ at 1 MHz
silicon *†	1.47	1	11.9
alumina	0.17	2-8	10.2
beryllia	2.18		6.9
silicon carbide	2.7		40.
silicon nitride	0.15		7.5
aluminum nitride	1.5		10.0
epoxy (silica loaded)	0.01		5.0

Table 2.5. Properties of dielectrics (at 10 KHz) considered for use in WSICs. From [(3),(5),(76),(6),(49)]

Material	$\epsilon_R$	Loss tangent
Polyimide *†	3.4	.002
Polyphenylquinoxaline (PPQ)	< 2.9	.007
Benzocyclobutene *†	2.75	.002
Silicon Oxide *	3.9	
Teflon	1.9	

Table 2.6. Properties of selected conductors. From (3).

Material	Resistivity ( $\times 10^{-6}$ ohm-cm)	Thermal Conductivity (W/cm $^{\circ}$ C)
Copper *	1.7	16.6
Gold	2.4	14.2
Aluminum *†	2.8	25
Tungsten	5.5	4.5
Nickel	7.8	13
Tantalum	12.4	6.5
Solder	17.0	24.5

none of the other materials listed in Table 2.4 have well-defined processes for creating wafer scale interconnections, with the possible exception of alumina, which is widely used for thick film and thin film hybrids (89). As such, it seems plausible, at first, that an alumina interconnection network could be used in a WSIC to form the electrical connections in a silicon-based die assembly after planarization. However, due to the large mismatch in TCE between alumina and silicon, the fabrication of such a structure cannot be regarded as practical.

Another desirable property of substrates is a smooth surface. One metric used to quantify this smoothness is the *rms surface roughness* ( $\Delta$ ). this metric provides an indication of the amount of fluctuation in the profile of a flat surface. These surface variations are assumed to be periodic within some interval ( $x_p$ ). For a flat substrate surface parallel to the  $x$ -axis, the surface roughness is defined as (45:198-199):

$$\Delta = \sqrt{\frac{1}{x_p} \int_0^{x_p} f(x) dx} \quad (2.111)$$

where  $x_p$  is the assumed interval of periodicity for surface variations and  $f(x)$  is the surface profile as a function of distance along the surface in the  $x$ -direction.

*Dielectrics.* The choice of dielectrics in WSIC's is important, since the characteristic impedance and coupling of the resident transmission line structures are strongly dependent on the relative permittivity of the dielectrics used. Materials with lower dielectric constants are preferred; the dielectrics in Table 2.5 have relative permittivities below five. In conjunction with larger spatial separation, the lower permittivities serve to reduce crosstalk between wafer scale interconnections and, thus, improve their electrical isolation. To create large spatial separations in the vertical dimension, dielectrics which can exhibit structural integrity when they are deposited with a thickness greater than ten microns are required. To minimize leakage conduction losses, the dissipation factors in candidate WSI dielectrics must also be low. Finally, dielectrics must exhibit predictable behavior over a wide frequency range and under various environmental conditions. Small variations in material permittivity over the useful ranges from several megahertz to several gigahertz are preferred to prevent excessive dispersions in the already-dispersive microstrip geometries [(38),(104)].

Although low permittivity dielectrics are generally preferred, Gilbert *et al.* suggested that high permittivity materials should be used between power and ground planes, while low permittivity dielectrics between signal lines should be retained. The high permittivity in this case would promote improved switching performance through charge storage which could help supply current for instantaneous switching (38).

Each of the dielectrics in Table 2.5 have certain qualities which are desired in WSICs, but some possess disadvantages which preclude their use altogether in presently defined WSIC approaches. The following paragraphs discuss the advantages and disadvantages of the particular dielectrics shown in Table 2.5.

*Silicon Dioxide.* Silicon dioxide ( $\text{SiO}_2$ ), which is a traditional intermetal dielectric in many integrated circuits, cannot be deposited at thicknesses much larger than  $1\text{ }\mu\text{m}$  without cracking (80). Since the distances between metal

layers are on the order of 5  $\mu\text{m}$  or more, it appears that  $\text{SiO}_2$  alone is inadequate as an interlayer dielectric.

*Polyimides.* Polyimides have often been considered in WSI approaches due to its low permittivity, ease in fabrication, and excellent planarization properties. Some researchers do not recommend the use of polyimides, despite their low permittivity and desirable thickness properties because of its tendency to form pinholes in monolayers. This material also has the tendency to absorb moisture (66). Other researchers counter these disadvantages by creating polyimide structures which are hermetically sealed to minimize water penetration and by depositing the polyimide in multiple layers to minimize the possibility of a pinhole completely penetrating between two metal layers. Materials research has produced superior types of polyimides. One example is polyphenylquinoxaline (PPQ), which possesses a water absorption factor of 0.9%, compared to the 2.5% water absorption of a typical polyimide (76).

*Benzocyclobutenes.* A promising candidate for wafer scale interlayer dielectrics is the class of plastics known as benzocyclobutenes (BCBs). Recent studies of the electrical properties of BCBs indicate that they have permittivities that are reasonably stable over a wide frequency range (decreasing from 2.8 at 500Hz to 2.5 at 35GHz), with a mean value below that of polyimide. Another advantage of the BCBs is that they are not hygroscopic, which indicates that they will have stable electrical performance under widely varying humidity conditions [(5),(6)].

*Teflon.* Polytetrafluoroethylene (PTFE), or teflon, has very desirable electrical and mechanical properties. The typical PTFE fiber has a dielectric constant of 2.3, and recently developed expanded PTFE fibers have achieved relative permittivities of approximately 1.9. However, the temperature coefficient mismatch between PTFE and silicon is sufficiently severe to render impractical the manufacture of wafer structures which utilize both materials. The primary problem with using

the two materials together is that internal mechanical stresses will develop between the materials as temperature shifts occur, leading to the eventual delamination of PTFE layers from the silicon substrate [(38),(49)].

### *Summary*

This chapter considered the current state-of-the art in WSI interconnections through exposition of current treatments on the subject of microstrip-like transmission line structures. This approach was chosen since WSI interconnections are primarily microstrip-like in physical structure. The adequacy of applying these treatments to WSI transmission lines, with respect to their relatively small physical size, was addressed.

Microstrip structures are not truly TEM in nature, which presents a problem in transmission-line analysis, where the theory is typically one-dimensional and based on TEM structures. Though the definitions of transmission line parameters are ambiguous when the structures are not completely TEM in nature, most analyses treat microstrip lines as one-dimensional transmission lines. Deviations from this behavior are often modeled as frequency-dependent perturbations of ideal behavior.

Design with microstrip structures is a routine practice with larger dimensions, and the techniques seem equally applicable to WSICs. To validate this assumption, a re-examination of these formula was undertaken in this chapter to investigate any shortcomings in applying them to WSI interconnections.

The most significant limitations in the literature appear to be regarding the accurate calculation of skin effect losses and coupling. Skin-effect losses and pronounced dispersive effects are not very severe below 1 GHz in the applicable geometries of microcircuits, as concluded by most researchers. The significance of skin-effect loss is not clearly regarded but it is acknowledged by most authors. A lack of accurate formula for micro-circuit applications is evident. On the other hand, dispersion formula are well-developed and seem applicable to WSI interconnections. The effects of coupling appear to present the more serious problem, especially with



respect to the proximity of wafer scale interconnections. No "canned" formulae exist for the various non-standard configurations described, and numerical approaches are required for the general calculation of these quantities.

### *III. Experimental and Computational Methodology*

The strongest arguments prove nothing so long as the conclusions are not verified by experience. Experimental science is the queen of sciences and the goal of all speculation. -- Roger Bacon, *Opus Tertium*

#### *Overview*

It is prudent to undertake experimental verification, when possible, to validate theoretical projections. CAD systems, for example, that assist in the layout of VLSI circuits require a set of guidelines or rules which permit the proper placement of interconnections between circuit elements. The specific rules, such as line-to-line spacing and maximum connection lengths, must be determined. If the determination is made by unverified theoretical projections, then an obvious risk is involved, and the safety factors are educated guesses, at best.

The use of existing design programs for *testing layout schemes* should be exploited, if possible. Many programs exist (examples include SPICE and LIBRA), and if their accuracy can match experimentally determined values, then the need for additional CAD programs are reduced.

This chapter addresses the experimental measurement configurations used with the test wafers and the specific numerical methods used for this research effort. Descriptions of the test wafers are also included in this chapter, since they are of direct pertinence in the experimental configuration and numerical computations. Next, the test equipment configurations are described for the following measurement categories:

1. Continuity
2. Characteristic impedance
3. Coupling and transmission
4. Pulsed-signal response.

The continuity measurements were chosen as a basic measurement category to provide simple, practical information concerning conductivity and leakage mechanisms on the wafers. The characteristic impedance measurements were accomplished because of the critical importance of this parameter in the associated transmission line analysis. Additionally, the characteristic impedance can be determined by analytic and numeric means. The coupling measurements were selected because of their importance in practical applications. Finally, the pulsed-signal response measurements were selected as a qualitative means for examining the signals impressed on representative wafer scale interconnections.

To complement these measurement schemes, a number of analytic checks were developed. The analytic techniques used are highlighted in this chapter. For the characteristic impedance measurements, several methods were used for comparison with values measured from the wafers, including some of the closed form expressions outlined in Chapter 2, as well as projections based on the LINECALC program and a numerical finite-difference method. For coupling measurements, models were developed for use with the LIBRA program to provide data for comparison with the actual measurements. Additionally, two other numerical approaches are outlined. For the pulsed-signal response, no simulations were attempted, since accurate simulations would be difficult with the available resources, and since the measurements were primarily qualitative in nature. However, some digital signal processing techniques were applied to the measurements to reduce the effects of the test measurement configuration on the measured subject. The digital signal processing techniques used for signal refinement are outlined in this chapter.

### *Test Wafers*

The measurements in this research effort were performed using several different test wafers. The various interconnections on these wafers were designed to exploit the transmission line effects of coupling, dispersion, and attenuation. Not all networks were intended to be representative of actual wafer scale systems; rather,

these interconnections were designed as test structures that might lend themselves to accurate characterization and measurement. In an actual wafer scale network, the shapes and lengths of the interconnections would probably be irregular to a degree that would render accurate analyses even more difficult or even impractical. Of equal importance to the physical conductor-dielectric configurations of the interconnections are the measurement configurations. In particular, the source and load characteristics must be representative of those used in actual digital integrated circuits. If the source and load characteristics of present digital systems prove to be inadequate for WSI approaches, alternatives need to be considered in order to exploit improved electrical performance.

*Physical Design Description.* The WSI test structures evaluated were fabricated on five-inch diameter silicon wafers. The test wafers, fabricated by the Polycon Corporation, were based on a High Density Multilayer Interconnect (HDMI) technology. The wafer interconnection patterns were based on an AFIT design, originally intended for three-inch diameter wafers. After the design was adapted for five-inch diameter wafers, it was not changed from wafer to wafer. Thus, for reference and comparative purposes, the design was not varied among the different test wafers (only the type of materials used in the fabrication was changed). The general structural arrangement of the conductors and dielectric layers used in this technology is shown in Figure 3.1. Each intermetal layer is filled with a dielectric, in particular those dielectrics which are presumed to provide superior fabrication precision, electrical properties, and yield performance. In general, The HDMI process is designed to accommodate a total of six metal layers, although the test wafers in this study contained only four metal layers. In these wafers, the top and bottom layers, termed "Metal 1" and "Metal 4", respectively, were designed as ground planes, while "Metal 2" and "Metal 3" were usually reserved for signal transmission lines, as is typically done in other proposed WSI approaches (82).

The material used for the dielectric was varied such that the relative performance

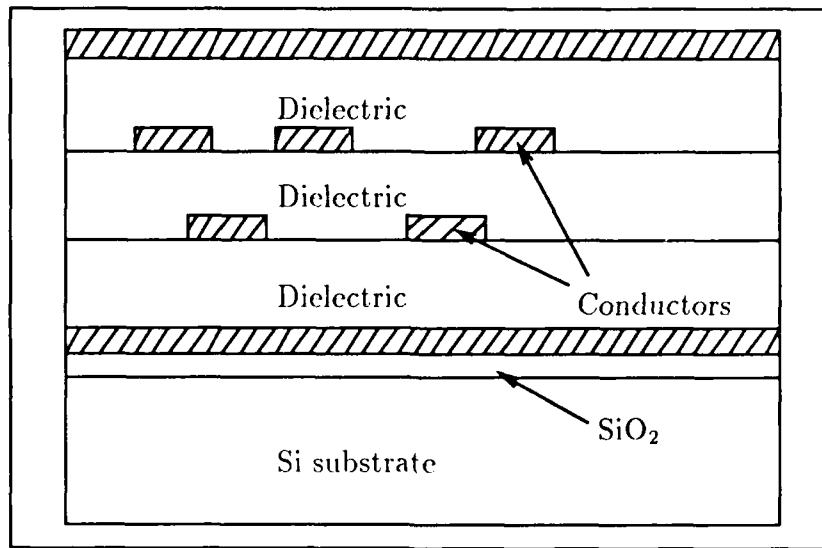


Figure 3.1. General arrangement of signal conductors, dielectric layers, and ground planes in the High Density Multilayer Interconnect (HDMI) process implemented by the Polycon Corporation (Ventura, CA). Based on (80).

of the common WSI interconnection design could be compared. The material combinations used are summarized in Table 3.1.

The wafers, designed specifically for basic electrical characterization, contained ten definite groupings or "blocks" of structures, including 123 different 10 cm transmission line structures, 40 different 2 cm transmission line structures, and 40 different 1 cm transmission line structures (82). Additional transmission line structures were placed along the periphery of the wafer, but the electrical performance evaluation

Table 3.1. Materials used in the test wafers.

Qty.	Conductor	Dielectric
1	aluminum	polyimide
3	aluminum	polyimide iso-indroquinazolinedione (PIQ)
1	aluminum	benzocyclobutene (BCB)

of these special structures was considered to be beyond the scope of this study. In fact, only a subset of the 123, 10 cm long structures were studied in depth for this thesis. All transmission line structures are summarized in Tables 3.2-3.7. In these tables, four basic types of transmission line structures are represented: two-line, edge-coupled striplines; three-line, edge-coupled striplines; meander lines; and coplanar waveguides. These representative transmission line structures are shown in Figures 3.2-3.6. The remaining scaling details for each structure are summarized in Figure 3.7, as well as the nomenclature used to identify and classify the different measurements for a particular structure. All transmission line structures were fabricated in both 10  $\mu\text{m}$  and 25  $\mu\text{m}$  linewidths. The variation of spacing between conductors and height above ground planes account for the large number of variations associated with these structures.

The nominal design thickness of the conductors was 2.5  $\mu\text{m}$ , and the vertical separation between metal layers was nominally designed to be 6  $\mu\text{m}$ . Some lines are closely spaced, to exploit their coupling phenomenon. The use of grounding in the transmission line structures was varied. Three primary ground plane variants were used. The first type was the usual solid ground plane, upon which most theoretical work is based. The second type utilized was the gridded-mesh structure, in which the directions of the grid lines were parallel and perpendicular to those of the transmission lines. The third type was also a gridded-mesh structure, but the directions of the grid lines were rotated 45 degrees with respect to the length of the transmission lines (only the 1 cm structures were fabricated with this ground plane type). The use of gridded structures was proposed for two reasons. First, the fabrication of large, solid ground planes have been regarded as impractical, due to the enhanced possibility of defects. The second reason for the proposed gridded structures was that the physical stresses caused by the thermal coefficient of expansion mismatch between the ground plane material, the dielectric, the substrate, and the active conductors would be lessened by a gridded mesh (82).

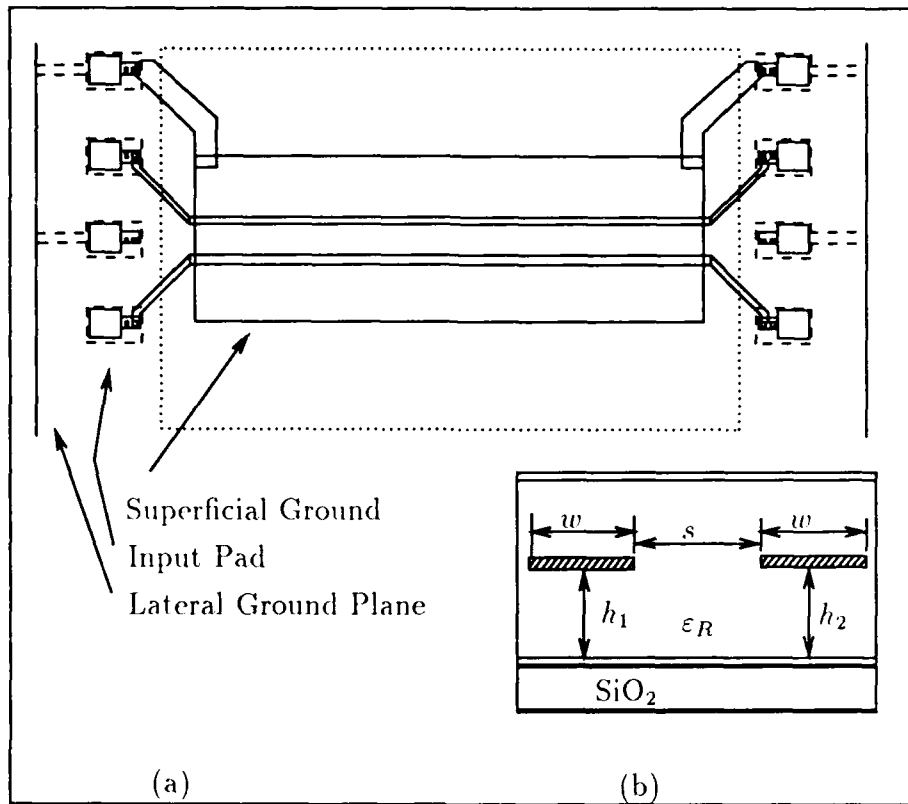


Figure 3.2. Two-line, edge-coupled stripline. (a) View from above. (b) Transverse cross-section. From (82).

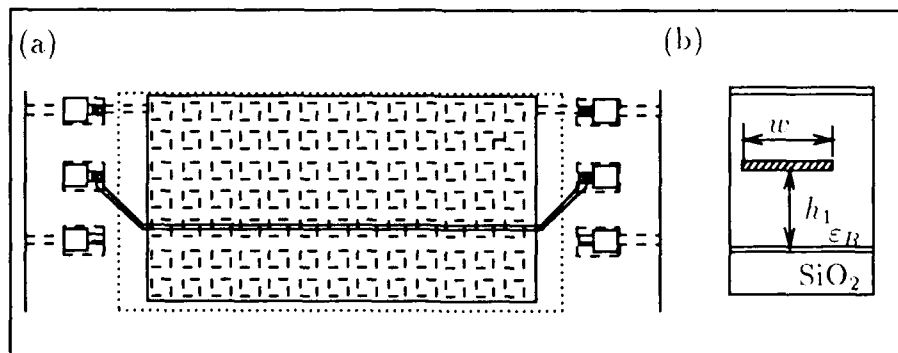


Figure 3.3. Stripline. (a) View from above. (b) Transverse cross-section. From (82).

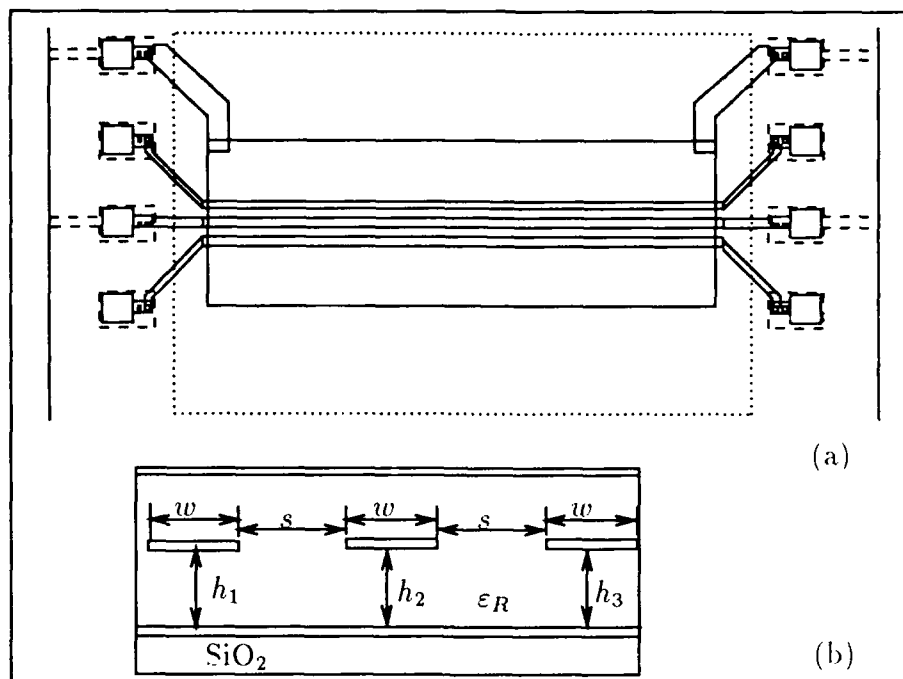


Figure 3.4. Three-line, edge-coupled stripline. (a) View from above. (b) Transverse cross-section. From (82).

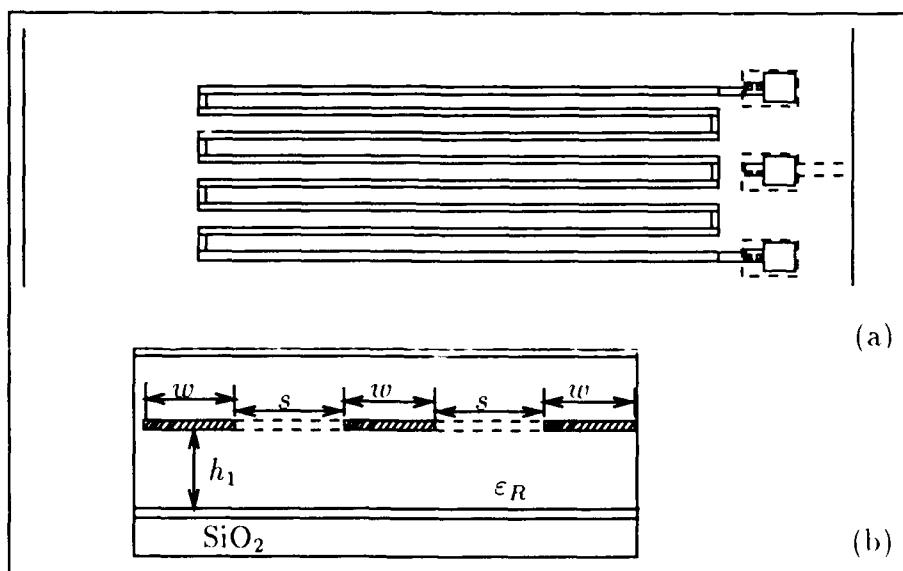


Figure 3.5. Meander line. (a) View from above. (b) Transverse cross-section. From (82).



Table 3.2. Design specifications of the 10 cm long transmission lines. From (82).

Line No.	Figure	No. of Conductors	Ground Above	Ground Below	$h_1$ ( $\mu\text{m}$ )	$h_2$ ( $\mu\text{m}$ )	$h_3$ ( $\mu\text{m}$ )	$s$ ( $\mu\text{m}$ )	$w$ ( $\mu\text{m}$ )
1	3.2	2	Mesh	Mesh	12	12	n/a	46	26
2	3.3	1	n/a	Mesh	6	n/a	n/a	—	26
3	3.2	2	Mesh	Mesh	6	6	n/a	30	26
4	3.2	2	n/a	Mesh	6	12	n/a	30	26
5	3.2	2	Solid	Solid	12	12	n/a	45	26
6	3.2	2	n/a	Solid	12	12	n/a	45	26
7	3.2	2	Solid	Solid	6	6	n/a	45	26
8	3.2	2	n/a	Solid	6	6	n/a	45	26
9	3.2	2	Mesh	Mesh	12	12	n/a	45	26
10	3.2	2	n/a	Mesh	12	12	n/a	45	26
11	3.2	2	Mesh	Mesh	6	6	n/a	45	26
12	3.2	2	n/a	Mesh	6	6	n/a	45	26
13	3.2	2	Solid	Solid	12	12	n/a	38	26
14	3.2	2	n/a	Solid	12	12	n/a	38	26
15	3.2	2	Solid	Solid	6	6	n/a	38	26
16	3.2	2	n/a	Solid	6	6	n/a	38	26
17	3.2	2	Mesh	Mesh	12	12	n/a	38	26
18	3.2	2	n/a	Mesh	12	12	n/a	38	26
19	3.2	2	Mesh	Mesh	6	6	n/a	38	26
20	3.2	2	n/a	Mesh	6	6	n/a	38	26
21	3.4	3	Solid	Solid	12	12	12	22	26
22	3.4	3	n/a	Solid	12	12	12	22	26

Table 3.3. Design specifications of the 10 cm long transmission lines (continued).  
From (82).

Line No.	Figure	No. of Conductors	Ground Above	Ground Below	$h_1$ ( $\mu\text{m}$ )	$h_2$ ( $\mu\text{m}$ )	$h_3$ ( $\mu\text{m}$ )	$s$ ( $\mu\text{m}$ )	$w$ ( $\mu\text{m}$ )
23	3.4	3	Solid	Solid	6	6	6	22	26
24	3.4	3	n/a	Solid	6	6	6	22	26
25	3.4	3	Mesh	Mesh	12	12	12	22	26
26	3.4	3	n/a	Mesh	12	12	12	22	26
27	3.4	3	Mesh	Mesh	6	6	6	22	26
28	3.4	3	n/a	Mesh	6	6	6	22	26
29	3.4	3	n/a	n/a	6	6	6	22	26
30	3.4	3	n/a	n/a	0	0	0	22	26
31	3.5	1	n/a	n/a	18	n/a	n/a	22	26
32	3.5	1	n/a	n/a	6	n/a	n/a	26	26
33	3.6	1	n/a	n/a	0	0	0	26	26
34	3.2	2	Solid	Solid	12	12	n/a	38	10
35	3.2	2	n/a	Solid	12	12	n/a	38	10
36	3.2	2	Solid	Solid	6	6	n/a	38	10
37	3.2	2	n/a	Solid	6	6	n/a	38	10
38	3.2	2	Mesh	Mesh	12	12	n/a	38	10
39	3.2	2	n/a	Mesh	12	12	n/a	38	10
40	3.2	2	Mesh	Mesh	6	6	n/a	38	10
41	3.2	2	n/a	Mesh	6	6	n/a	38	10
42	3.2	2	Solid	Solid	12	12	n/a	18	10
43	3.2	2	n/a	Solid	12	12	n/a	18	10
44	3.2	2	Solid	Solid	6	6	n/a	18	10

Table 3.4. Design specifications of the 10 cm long transmission lines (continued).  
From (82).

Line No.	Figure	No. of Conductors	Ground Above	Ground Below	$h_1$ ( $\mu\text{m}$ )	$h_2$ ( $\mu\text{m}$ )	$h_3$ ( $\mu\text{m}$ )	$s$ ( $\mu\text{m}$ )	$w$ ( $\mu\text{m}$ )
45	3.2	2	n/a	Solid	6	6	n/a	18	10
46	3.2	2	Mesh	Mesh	12	12	n/a	18	10
47	3.2	2	n/a	Mesh	12	12	n/a	18	10
48	3.2	2	Mesh	Mesh	6	6	n/a	18	10
49	3.2	2	n/a	Mesh	6	6	n/a	18	10
50	3.4	3	Solid	Solid	12	12	12	20	10
51	3.4	3	n/a	Solid	12	12	12	20	10
52	3.4	3	Solid	Solid	6	6	6	20	10
53	3.4	3	n/a	Solid	6	6	6	20	10
54	3.4	3	Mesh	Mesh	12	12	12	20	10
55	3.4	3	n/a	Mesh	12	12	12	20	10
56	3.4	3	Mesh	Mesh	6	6	6	20	10
57	3.4	3	n/a	Mesh	6	6	6	20	10
58	3.4	3	n/a	n/a	6	6	6	20	10
59	3.4	3	n/a	n/a	0	0	0	20	10
60	3.5	1	n/a	n/a	18	n/a	n/a	10	10
61	3.5	1	n/a	n/a	6	n/a	n/a	10	10
62	3.6	1	n/a	n/a	0	0	0	18	10
63	3.5	1	n/a	n/a	0	n/a	n/a	10	10
64	3.5	1	n/a	n/a	12	n/a	n/a	10	10
65	3.4	3	n/a	n/a	0	0	0	10	10
66	3.4	3	n/a	n/a	6	6	6	10	10

Table 3.5. Design specifications of the 10 cm long transmission lines (continued).  
From (82).

Line No.	Figure	No. of Conductors	Ground Above	Ground Below	$h_1$ ( $\mu\text{m}$ )	$h_2$ ( $\mu\text{m}$ )	$h_3$ ( $\mu\text{m}$ )	$s$ ( $\mu\text{m}$ )	$w$ ( $\mu\text{m}$ )
67	3.4	3	n/a	Mesh	6	6	6	10	10
68	3.4	3	Mesh	Mesh	6	6	6	10	10
69	3.4	3	n/a	Mesh	12	12	12	10	10
70	3.4	3	Mesh	Mesh	12	12	12	10	10
71	3.4	3	n/a	Solid	6	6	6	10	10
72	3.4	3	Solid	Solid	6	6	6	10	10
73	3.4	3	n/a	Solid	12	12	12	10	10
74	3.4	3	Solid	Solid	12	12	12	10	10
75	3.2	2	n/a	Mesh	6	6	n/a	10	10
76	3.2	2	Mesh	Mesh	6	6	n/a	10	10
77	3.2	2	n/a	Mesh	12	12	n/a	10	10
78	3.2	2	Mesh	Mesh	12	12	n/a	10	10
79	3.2	2	n/a	Solid	6	6	n/a	10	10
80	3.2	2	Solid	Solid	6	6	n/a	10	10
81	3.2	2	n/a	Solid	12	12	n/a	10	10
82	3.2	2	Solid	Solid	12	12	n/a	10	10
83	3.2	2	n/a	Mesh	6	6	n/a	30	10
84	3.2	2	Mesh	Mesh	6	6	n/a	30	10
85	3.2	2	n/a	Mesh	12	12	n/a	30	10
86	3.2	2	Mesh	Mesh	12	12	n/a	30	10
87	3.2	2	n/a	Solid	6	6	n/a	30	10

Table 3.6. Design specifications of the 10 cm long transmission lines (continued).  
From (82).

Line No.	Figure	No. of Conductors	Ground Above	Ground Below	$h_1$ ( $\mu\text{m}$ )	$h_2$ ( $\mu\text{m}$ )	$h_3$ ( $\mu\text{m}$ )	$s$ ( $\mu\text{m}$ )	$w$ ( $\mu\text{m}$ )
88	3.2	2	Solid	Solid	6	6	n/a	30	10
89	3.2	2	n/a	Solid	12	12	n/a	30	10
90	3.2	2	Solid	Solid	12	12	n/a	30	10
91	3.6	1	n/a	n/a	0	0	0	18	10
92	3.4	1	n/a	n/a	0	0	0	14	26
93	3.5	1	n/a	n/a	12	12	12	14	26
94	3.4	3	n/a	n/a	0	0	0	14	26
95	3.4	3	n/a	n/a	6	6	6	14	26
96	3.4	3	n/a	Mesh	6	6	6	14	26
97	3.4	3	Mesh	Mesh	6	6	6	14	26
98	3.4	3	n/a	Mesh	12	12	12	14	26
99	3.4	3	Mesh	Mesh	12	12	12	14	26
100	3.4	3	n/a	Solid	6	6	6	14	26
101	3.4	3	Solid	Solid	6	6	6	14	26
102	3.4	3	n/a	Solid	12	12	12	14	26
103	3.4	3	Solid	Solid	12	12	12	14	26
104	3.4	3	n/a	Mesh	6	6	6	22	26
105	3.4	3	Mesh	Mesh	6	6	6	22	26
106	3.4	3	n/a	Mesh	12	12	12	22	26
107	3.4	3	Mesh	Mesh	12	12	12	22	26
108	3.4	3	n/a	Solid	6	6	6	22	26
109	3.4	3	Solid	Solid	6	6	6	22	26
110	3.4	3	n/a	Solid	12	12	12	22	26

Table 3.7. Design specifications of the 10 cm long transmission lines (concluded).  
From (82).

Line No.	Figure	No. of Conductors	Ground Above	Ground Below	$h_1$ ( $\mu\text{m}$ )	$h_2$ ( $\mu\text{m}$ )	$h_3$ ( $\mu\text{m}$ )	$s$ ( $\mu\text{m}$ )	$w$ ( $\mu\text{m}$ )
111	3.4	3	Solid	Solid	12	12	12	22	26
112	3.4	3	n/a	Mesh	6	6	6	30	26
113	3.4	3	Mesh	Mesh	6	6	6	30	26
114	3.4	3	n/a	Mesh	12	12	12	30	26
115	3.4	3	Mesh	Mesh	12	12	12	30	26
116	3.2	2	n/a	Solid	6	6	n/a	30	26
117	3.2	2	Solid	Solid	6	6	n/a	30	26
118	3.2	2	n/a	Solid	12	12	n/a	30	26
119	3.2	2	Solid	Solid	12	12	n/a	30	26
120	3.2	2	n/a	Mesh	6	12	n/a	30	26
121	3.2	2	Mesh	Mesh	?	?	n/a	30	26
122	3.3	1	n/a	Mesh	6	n/a	n/a		26
123	3.2	2	Mesh	Mesh	12	12	n/a	16	26

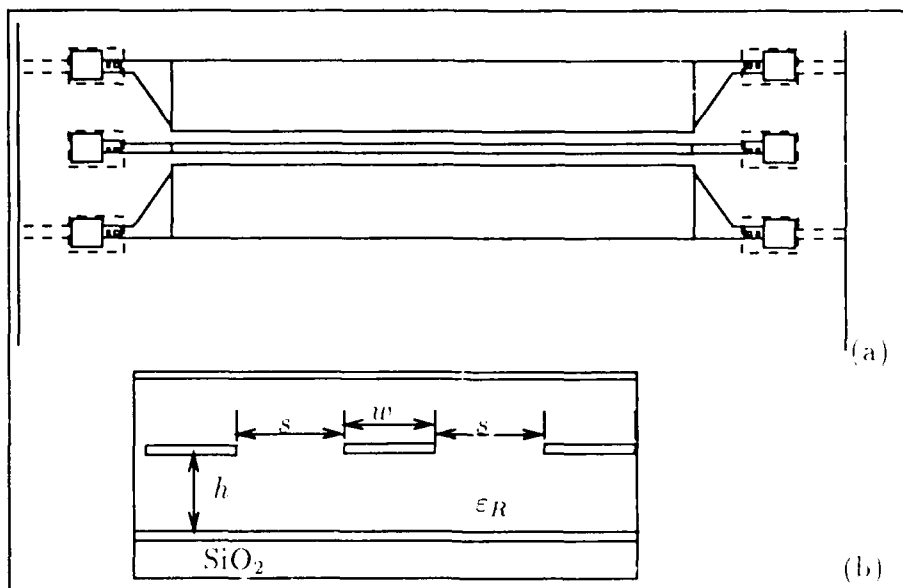


Figure 3.6. Coplanar waveguide. (a) View from above. (b) Transverse cross section. From (82).

The designs for the various structures were originally based on AFIT designs (Capt Brian Donlan (Ret.), AFIT/ENG) for use with three-inch diameter substrates. The designs were subsequently modified by Polycon (Mr. John Reche, President) for use with the larger, five-inch diameter substrates.

*Interconnect Configurations.* A measurement nomenclature was devised to identify the measurement configurations which were performed on the various structures. As shown in Figure 3.7, each terminal of a structure was designated by a lower case letter ("a" - "g"). The three terminals at the near-end were designated "a", "b", and "c", starting at the left. The three terminals at the far-end were labeled "d", "e", and "f". The ground terminal was denoted by the letter "g". Two-terminal measurements were designated by the letters of the corresponding measurements. For example, an impedance measurement between the left and right terminals at the near-end of the 43rd structure was denoted as "Z043AC", where "Z" represents impedance, the numbers "043" represent the 43rd structure, and "AC" implies that

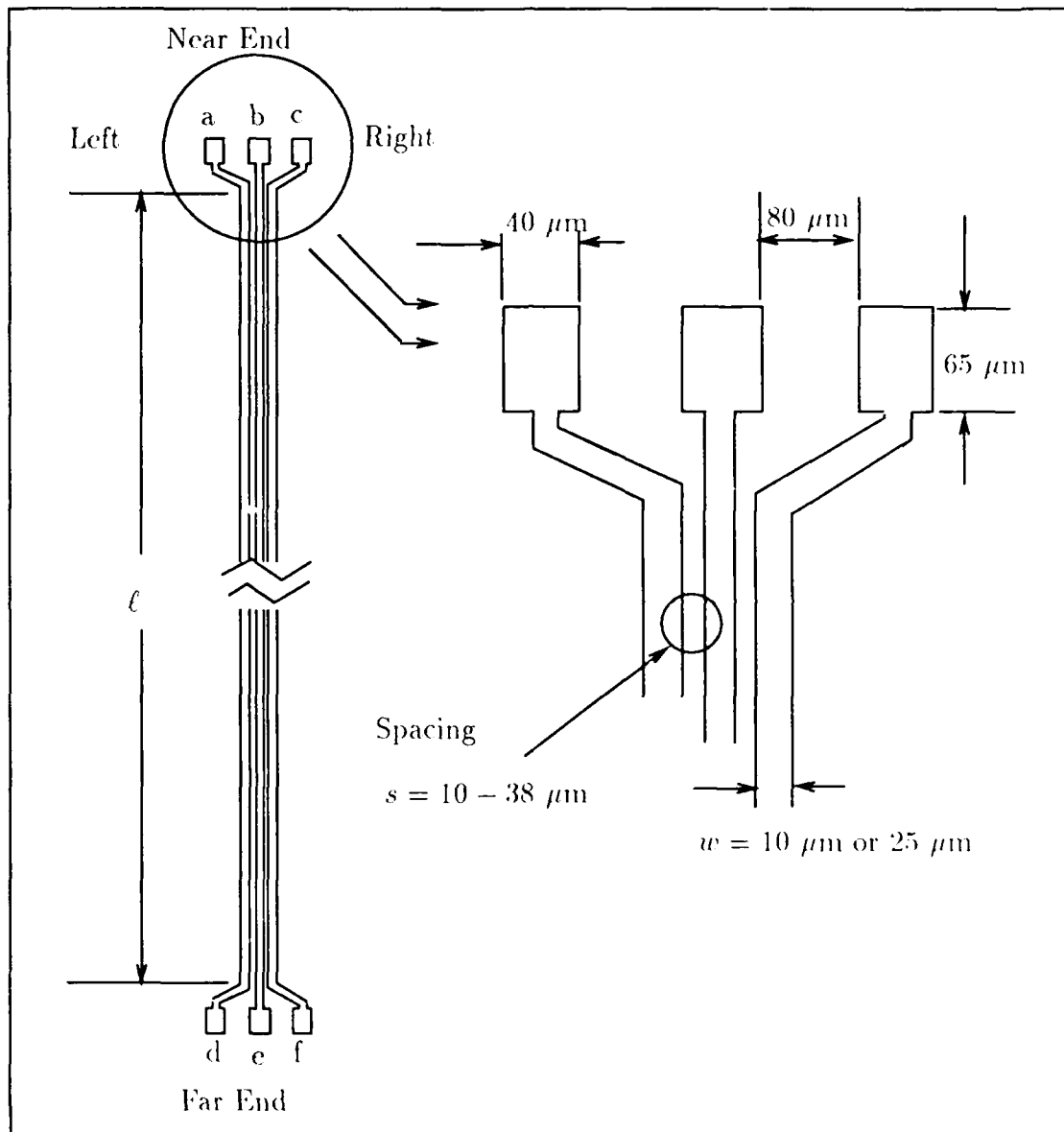


Figure 3.7. Example of a three-line stripline-like structure illustrating scaling details and the measurement nomenclature conventions.



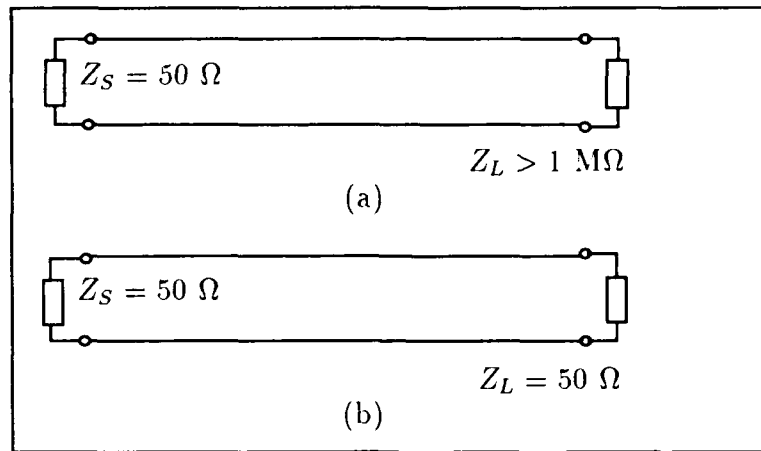


Figure 3.8. Measurement configurations. (a) Measurement configuration which approximates CMOS operating conditions. (b) Measurement configuration which simulates a low-impedance input.

the measurement is taken between the left and right terminals at the near-end of the wafer. This nomenclature was used to record the filenames for the types of measurements made.

The interconnections were measured under two different loading configurations. The first configuration created a source and load configuration approximate to that of a digital CMOS system for a driver in the “on” condition. This condition is simulated by driving a transmission line structure with a Micromanipulator low-impedance electrical probe (model number 44) as the driver, and terminating the end of the transmission line with an open circuit or a Micromanipulator high-impedance, active electrical probe (model number FET-1). This condition is schematically represented in Figure 3.8(a). The second configuration approximated a low impedance input source. Although contemporary logic circuits do not use low impedance inputs, the need to develop them may arise as a result of the undesired transmission line effects, such as reflections which occur with high impedance loads. This condition is schematically represented in Figure 3.8(b).

### *Experimental Arrangement*

The experimental arrangement for wafer measurements was established after consideration of the subject wafer, measurement types, and frequency ranges involved. The equipment and measurement arrangement details are discussed in the next subsection.

*Electrical Measurement Instrumentation.* The primary instruments used to accomplish the impedance analysis were the Hewlett-Packard model IIP 4191A (RF-impedance analyzer) and the IIP 4194A (gain-phase analyzer). The HP 4194A provides frequency coverage from 1 KHz-100 MHz for transmission (two-port) measurements and provides BNC connections for the test and reference channels. The HP 4191A covers the frequency range spanning 1-1000 MHz and uses a type APC-7 connector to perform two-terminal measurements. Since no type APC-7 connector cabling was available for the probes used in this research, an adapter from the type APC-7 to the BNC connector was formed from a type APC-7 to type N connector which was in series with a type N to BNC connector series adaptor combination. All time-domain measurements were performed with a dual-channel, 1 GHz sampling oscilloscope (Hewlett-Packard, model IIP 54100). Both analyzers and the oscilloscope were controlled externally through GPIB (IEEE-Std-488) bus connections. Direct current resistance/continuity measurements were performed with an ordinary volt-ohmmeter (Beckman, Inc., model number 3010UL).

*Electrical Signal Generation Equipment.* Each of the analyzers provided an internal electrical reference signal, automatically adjusted by the analyzer for swept-frequency measurements across the required frequency range. In addition to these signal sources, two waveform generators were utilized in the measurement process. The first, a function generator (Hewlett-Packard, model IIP 4133), provided the capability for generating an arbitrary waveform with a 20 MHz periodicity limit. This generator was useful in performing single frequency measurements, as well as

pulse measurements. The second signal source utilized was a dedicated pulse generator (Hewlett-Packard, model IIP 8082). This pulse generator is designed to drive digital systems and is presettable to six discrete frequencies (near 5 KHz, 50 KHz, 500 KHz, 5 MHz, 50 MHz, and 250 MHz).

*Test Apparatus Controller.* Control of the gain-phase and impedance analyzers, along with the sampling oscilloscope were facilitated by the instruments' IEEE-Std-488 (HPIB) interfaces which were connected to a Zenith Z-248-PC (IBM-AT "clone") configured as a data acquisition system and controller. The configuration included a HPIB controller card (Digital Equipment Corporation) and appropriate software for the specific control routines. Software routines specific to the measurements performed are discussed in Appendix D.

*Wafer-Probing.* In all measurement configurations, a wafer-probing station (Micromanipulator, model number 6200) was utilized to accomplish the microscopic probing connections and to maintain a steady surface. The measurements of each structure were made from either the "near-end" or the "far-end", as illustrated in Figure 3.7. The physical size of the subject wafer complicated the probe measurement arrangement, since the optical microscope could not independently traverse the entire five inch diameter of the wafer. The "far end" measurements were much more difficult to make on the 10 cm long structures, due to the inability of the optical microscope mounted in the wafer probing station to traverse the entire 10 cm length of the transmission line structures. To overcome this obvious difficulty, a special attachment was constructed. This attachment, shown in Figure 3.9, was affixed to the circular vacuum stage of the wafer probing station. Thus, a large, planar working surface was provided which moved along with the stage. Probes on micromanipulator arms could then be placed on the extended working surface, within a convenient distance from a test wafer or sample. Since the motion of the entire extension tracked with that of the stage, the positional stage adjustments could be used to bring all regions of the wafer within view of the optical microscope *without*

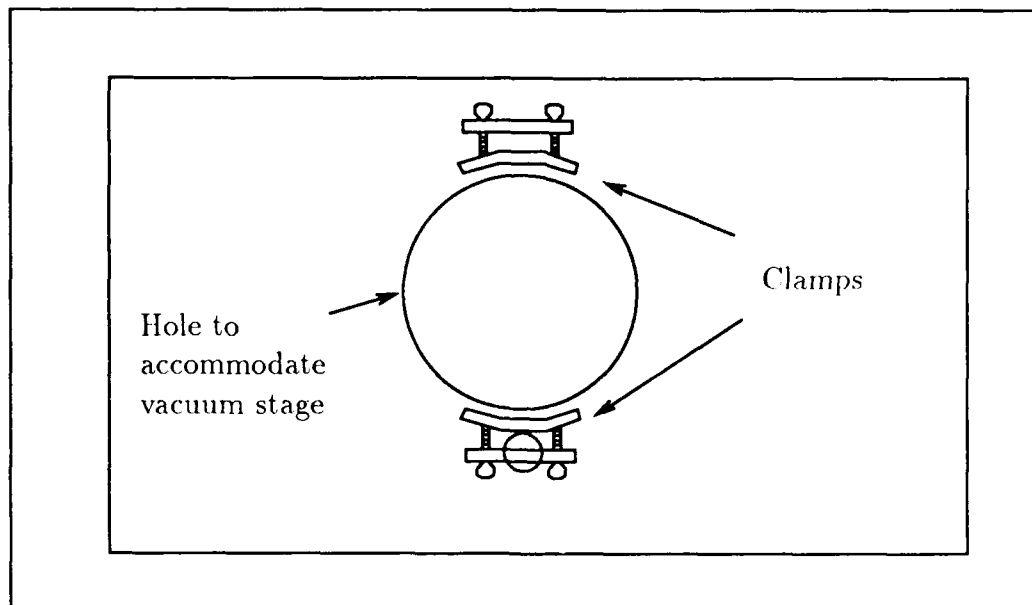


Figure 3.9. Illustration of plate extension modification for the probing station.

excessively disturbing probe placement. In practice, this extension was slightly sensitive to motion and possessed slight non-planarities. These problems were minor and were readily circumvented.

*Wafer Probes.* Low impedance probes (with controlled impedance values) and high-impedance probes were used in this research effort. The term “controlled impedance” refers to the intentional design of a probe’s characteristic impedance to be some specific value, usually  $50\ \Omega$ . High-impedance probes, on the hand, are usually terminated into the input port of an active amplifying device, such as a FET. The input impedance of such a device is usually high, but it is a dynamic impedance, which is not as well-regulated in value as is the impedance of probes in the former category.

*Low-Impedance Probes.* Rabjohn *et al.* classify low-impedance probes as coaxial probes, microstrip probes, and coplanar waveguide probes (78:850).

The coaxial probes (Figure 3.10a) provide a controlled impedance to within a few millimeters of the probe's tip. As implied by its name, the coaxial probe is fabricated from a length of coaxial line. The characteristic impedance of this coaxial line is the same as the design impedance of the probe. The needle tip extends outward from the coaxial line, forming the probing tip. However, these probes usually have relatively high self-inductance and provide poor grounding (78:850).

The microstrip probes (Figure 3.10b) are similar to the coaxial probes, except that they use a microstrip transmission line medium instead of a cylindrical coaxial line. Similar to the coaxial probe, the needle transition from the microstrip to the device under test becomes less useful at high frequencies (78:850).

Coplanar waveguide probes (Figure 3.10c) are fabricated as a transmission line system with a known, controlled impedance that characterizes the test measurement connection along its entire length, as well as to the device under test. The obvious disadvantage of the probe's physical size creates difficulty when using more than four probes at one time (78:850).

The low-impedance probes used for this research were the coaxial variant with needle probes (based upon the Micromanipulator, model number 44 probe) having a tip sharpness of  $1\text{ }\mu\text{m}$  and which were modified for ground plane connections. The probes were designed for a nominal  $50\text{ }\Omega$  impedance. According to the manufacturer, this type of probe has been successfully used up to 3 GHz.

*High-Impedance Probes.* To make non-perturbing measurements, high-impedance, low-capacitance probes are preferred. These probes use active devices, usually FETs, to achieve their high input impedance. However, they also have a more limited bandwidth when compared to the lower impedance probes.

The high-impedance probes used in this research (Micromanipulator, model number FET-1) were designed for an input impedance of at least  $1\text{ M}\Omega$  and a minimum capacitance of  $0.2\text{ pF}$ , and they are reported by the manufacturer to have a bandwidth of 0-1 GHz.

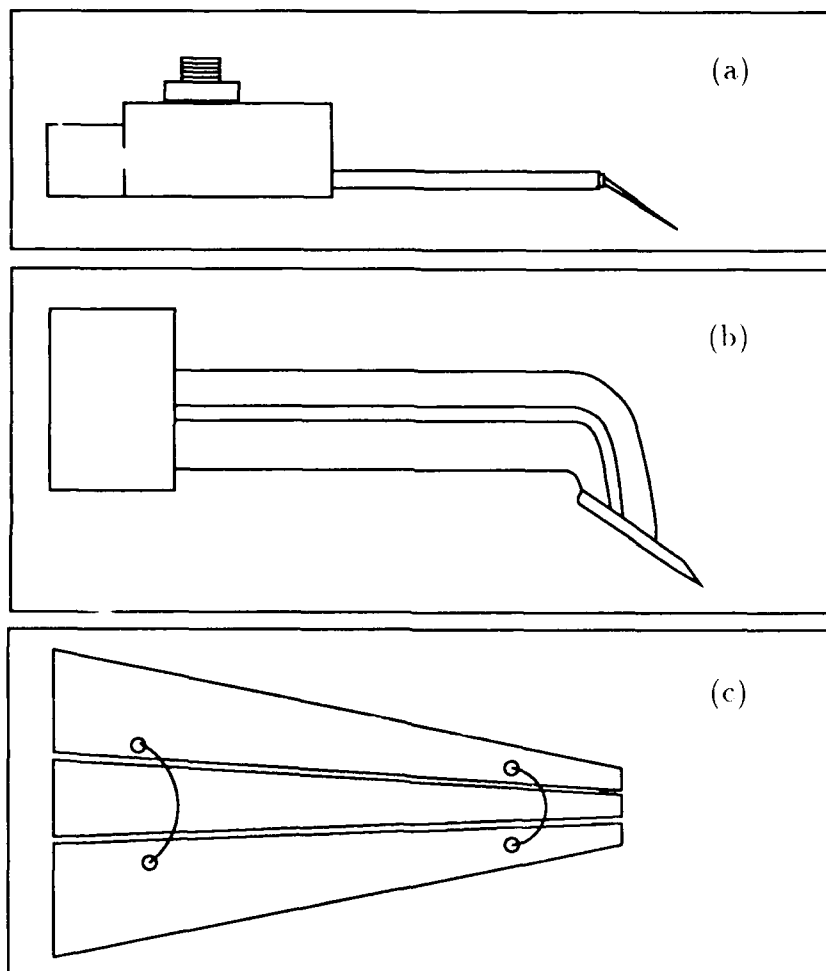


Figure 3.10. Low-impedance probes for high-frequency work. (a) Coaxial probe. (b) Microstrip probe. (c) Coplanar waveguide probe. After (78).

*Specific Measurement Equipment Configurations.* Four primary measurements were performed in this research:

1. Continuity measurements
2. Characteristic impedance measurements
3. Coupling measurements
4. Pulse response measurements.

The equipment configurations used to perform each of these measurements are shown schematically in Figures 3.12–3.14. The use of automated measurement techniques was employed as much as possible. All measurements were accomplished in the AFIT Cooperative Electronics Materials and Processing Laboratory in Building 125, Room 1065.

*Continuity Measurement Configuration.* The continuity measurement configuration (Figure 3.11) consisted of: (1) an ordinary volt-ohmmeter (for example, a Beckman multimeter, model number 3010UL); (2) a Micromanipulator wafer probing station, model number 6200; (3) two Micromanipulator probe arms, model number 550; (4) two Micromanipulator, model number 44 probes (or any ordinary, non-active electrical probes); and (5) suitable cabling between the electrical probes and the volt-ohmmeter.

*Characteristic Impedance Measurement Configuration.* The characteristic impedance measurement configuration (Figure 3.12) employed: (1) a Hewlett-Packard, model HP 4191A, RF impedance analyzer; (2) a Zenith personal computer, model number Z-248, configured as described above for test equipment control and data acquisition; (3) a Micromanipulator wafer probing station, model number 6200; (4) a Micromanipulator electrical probe with ground plane connection, model number 44-7000-GP; (5) a Micromanipulator probe arm, model number 550; (6) a type APC-7 to BNC connector adapter, synthesized from a type APC-7 to type N adaptor in series with a type N to BNC adaptor; (7) a connecting cable between the

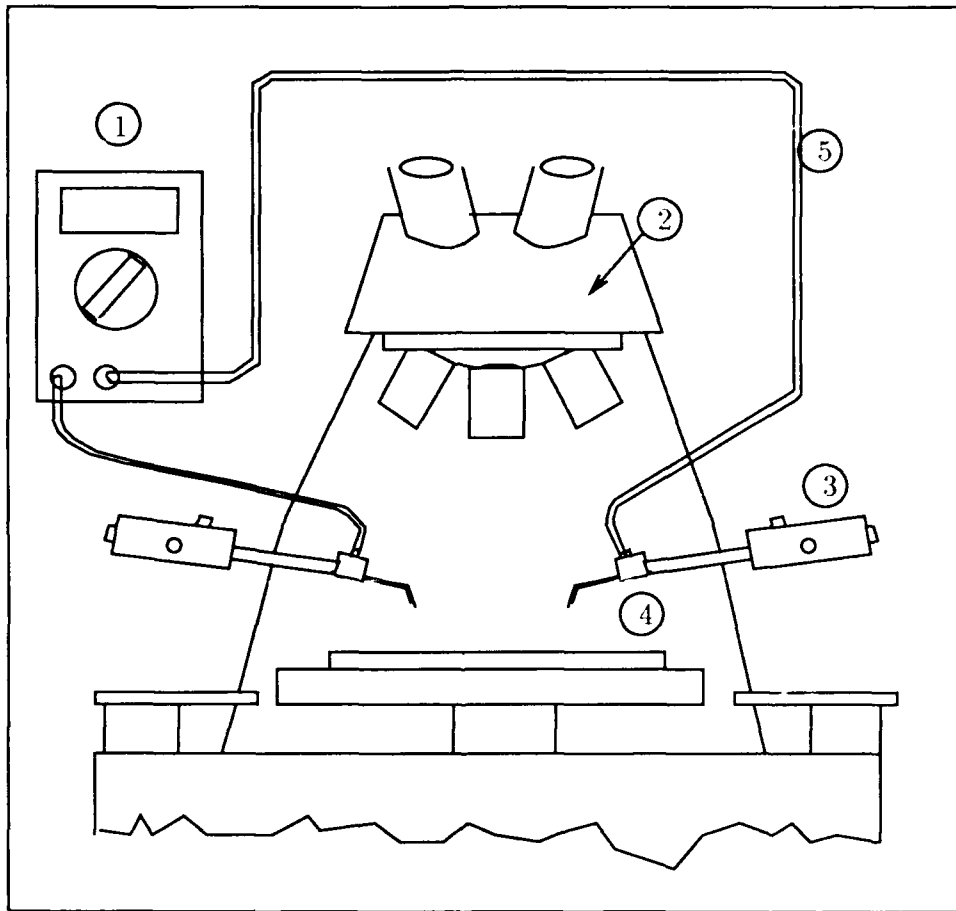


Figure 3.11. Configuration used to determine the continuity: (1) multimeter; (2) wafer probing station; (3) micro-manipulator arm; (4) low-impedance passive probe; and (5) interconnecting cable.



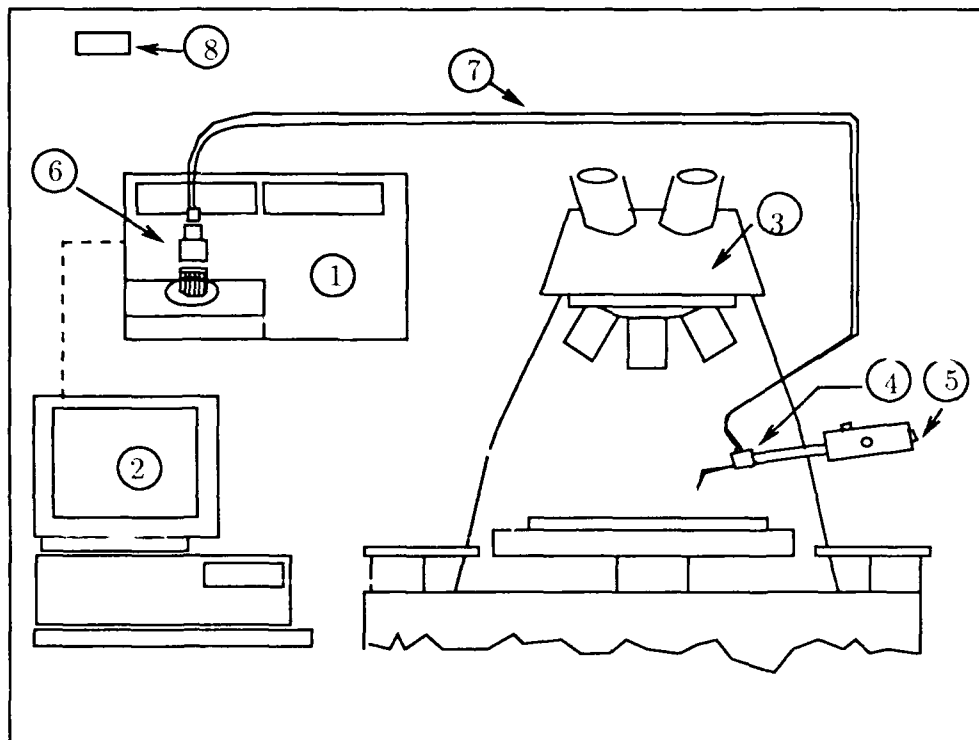


Figure 3.12. Configuration used to measure the characteristic impedance: (1) HP 4191A RF impedance analyzer; (2) personal computer equipped with HP-IB interface card; (3) wafer probing station; (4) model 44 micro-probe; (5) micro-manipulator arm; (6) type APC-7 to BNC adaptor; (7) one-meter length of interconnecting coaxial cable; (8) 50  $\Omega$  reference standard.

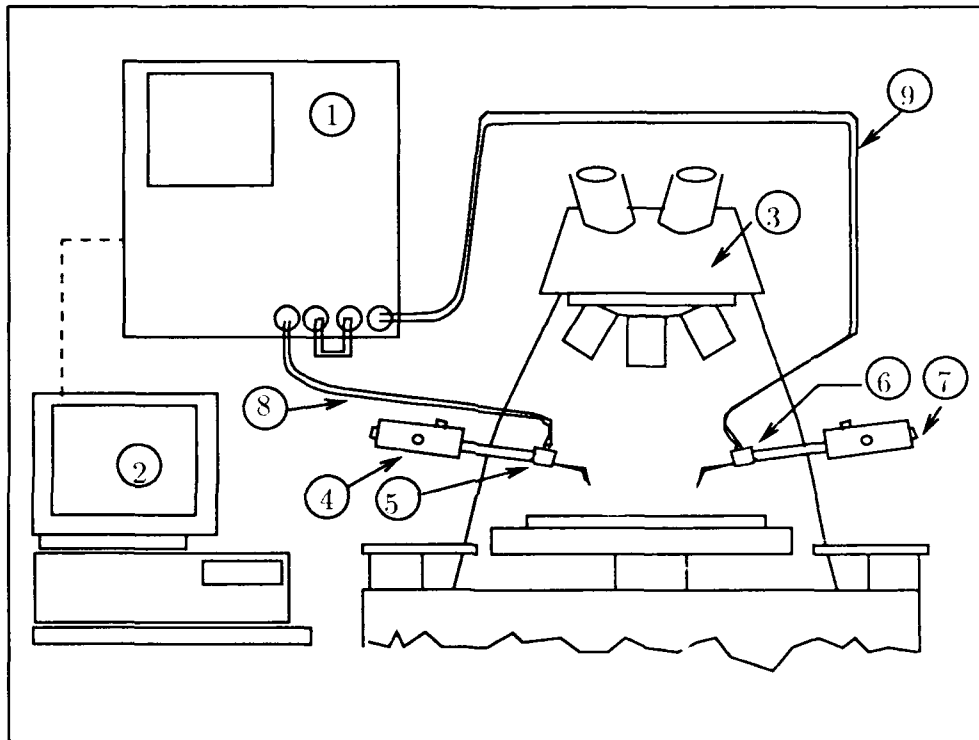


Figure 3.13. Configuration used to measure coupling: (1) HP 4194A gain-phase analyzer; (2) personal computer equipped with HP-IB interface card; (3) wafer probing station; (4) micro-manipulator arm; (5) "source" probe; (6) "load" probe; (7) micro-manipulator arm; (8) "source" probe interconnecting coaxial cable; (9) "load" probe interconnecting coaxial cable.

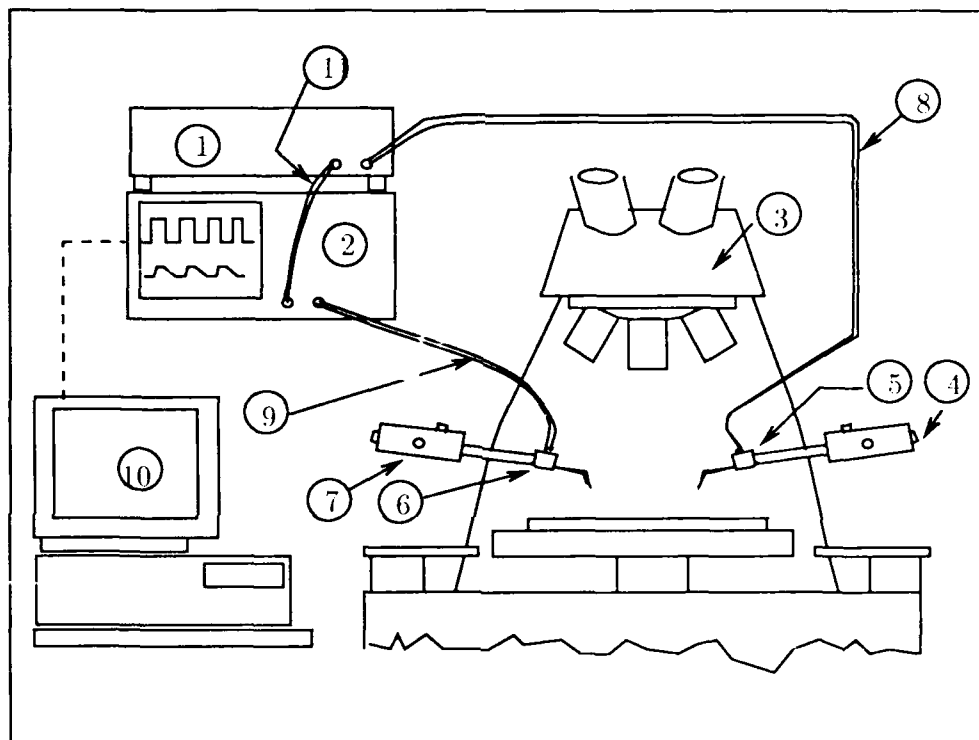


Figure 3.14. Configuration used for the pulse measurements: (1) pulse generator; (2) digital sampling oscilloscope; (3) wafer-probing station; (4) micro-manipulator arm; (5) "source" micro-probe; (6) "load" micro-probe; (7) micro-manipulator arm; (8) "source" probe interconnecting coaxial cable; (9) "load" probe interconnecting coaxial cable; (10) personal computer equipped with HP-IB interface card; (11) optional short coaxial cable connecting the pulse generator to the oscilloscope.

HP 4191A to the probe (designed for a total physical length of 1 meter measured from the BNC connector at the HP 4191A to the tip of the electrical probe) and (8) a  $50\ \Omega$  termination standard. The  $50\ \Omega$  measurement standard was, in fact, a different Model 44 probe, onto which a  $50\ \Omega$  fixed resistor was permanently affixed. For consideration of low frequencies (5 KHz-13 MHz), the impedance measurement section of the HP 4191A was used.

*Coupling Measurement Configuration.* The coupling measurement configuration, shown in Figure 3.13, was comprised of the following: (1) a Hewlett-Packard, model HP 4191A gain-phase analyzer; (2) a Zenith personal computer, model number Z-248, configured as described above; (3) a Micromanipulator wafer probing station, model number 6200; (4) a Micromanipulator model number 550 or equivalent micro-manipulator arm; (5) a Micromanipulator low impedance micro-probe, model number 44, connected to the output of the HP 4191A test channel as a "source" probe; (6) a second probe, connected to the input of the HP 4191A test channel as a "load" probe (to be described); (7) a second Micromanipulator micro-manipulator arm, model number 550; (8) a connecting cable between the HP 4191A to the probe, designed for a total physical length of 1 meter, measured from the BNC connector at the HP 4191A to the tip of the electrical probe; and (9) an appropriate cable for the "load" probe (to be described). To simulate both Figure 3.8 configurations, different probes were used to simulate different impedance loading conditions. The microprobe connected to the output of the HP 4191A test channel was termed a "source probe", corresponding to the source impedance ( $Z_S$ ) of Figure 3.8. The source probe did not change between the two configurations. However, the second probe, corresponding to the load impedance ( $Z_L$ ), varied between the two configurations. Due to its electrical connection relative to Figure 3.8, this second probe was referred to as a "loading" probe. To achieve the Figure 3.8a (high impedance-load) configuration, a Micromanipulator probe, model number FET 1, was used. The probe specifications reveal that this probe provides a load impedance

greater than  $1\text{ M}\Omega$  over the frequency range 0-1000 MHz. Alternately, to achieve the Figure 3.8b loading condition, a Micromanipulator probe, model number 44, was used. The associated "load" probe cable was selected according to the probe configuration utilized. For the model 44 probes, the measured cable, identical to that used for the source probe, was selected. However, for the FET-1 probe, the interconnecting cable supplied with the probe was used.

To facilitate a gain-phase measurement connection, the dual-channel capability of the HP 4194A was employed. The dual-channels, reference and test, provide signals of identical amplitude and phase at their outputs. The gain-phase analysis performed by the HP 4194A is based on the difference of the test and reference channels detected at the test and reference channel inputs. Each of the four connections (an input and output connection for both the test and reference channels) was accessed through a BNC connector on the front panel of the HP 4194A. For all gain-phase measurements performed in this research effort, the reference channel's output and input were directly tied together through a short cable with BNC connectors on both ends. The test channel's output was then connected to the source probe (8), and the test channel's input was connected to the loading probe.

*Pulse Measurement Configuration.* The pulse measurement configuration (Figure 3.14) consisted of the following equipment: (1) a Hewlett-Packard pulse generator, model HP 8082A; (2) a Hewlett-Packard digital sampling oscilloscope, model HP 54100A; (3) a Micromanipulator wafer probing station, model number 6200; and (4-9) the electrical cabling, probes, and micro-manipulator arm combinations described in the coupling configuration. For pulse measurements, the source probe (4, 5, and 8) was connected to the BNC output connection of the HP 8082 pulse generator, and the loading probe (6, 7, and 9) was connected to the HP 54100A oscilloscope. Finally, as in the other measurement configurations, a Zenith personal computer, model Z-248 was used for instrument control and data collection.

### *Experimental Measurement Techniques*

The applications of the four previously described equipment configurations used to perform the measurements in this research effort are addressed in this section. More detailed measurement procedures are provided in Appendix C.

*Continuity Measurements.* The purpose of performing continuity measurements was to verify the electrical connection of a conductor path or to determine if a conduction leakage path existed between two presumably isolated conductors. The continuity measurement technique was accomplished by the positioning of each of the two microprobes onto the test structure of interest. Continuity was verified by a low ohmic reading on the volt-ohmmeter which was electrically connected to the two microprobes. Besides providing the capability of performing basic conductor continuity or leakage measurements, the continuity measurement procedure was executed as a part of the other three measurement procedures to verify electrical connections of the test measurement configuration.

*Characteristic Impedance Measurements* The characteristic impedance measurement technique was based on simple formulas which allow the magnitude and phase of the characteristic impedance between two lines to be determined by open-circuit and short-circuit measurements; that is (14):

$$|Z_o| = \sqrt{|Z_{open}| \cdot |Z_{short}|} \quad (3.1)$$

$$\text{and } Phase(Z_o) = \frac{1}{2} (Phase(Z_{open}) - Phase(Z_{short})) \quad (3.2)$$

where  $|Z_{open}|$  and  $Phase(Z_{open})$  corresponds to the magnitude and phase of the transmission line, measured in the open-circuit configuration, and  $|Z_{short}|$  and  $Phase(Z_{short})$  corresponds to the measurements in the short-circuit configuration.

A BASIC computer program, compiled on the Z 248 PC with the equipment configured as shown in Figure 3.12, facilitated the swept-frequency measurement

used to determine the characteristic impedance. Of course, this technique did not directly measure the characteristic impedance. Rather, this technique measured the *driving point impedance* or input impedance of two transmission line configurations: the first one, short-circuited, and the second one, open-circuited (4:220-231). The control program gathered the data from both the open-circuit and the short-circuit measurements, and then calculated the characteristic impedance, based on Equations 3.1 and 3.2.

Prior to executing the program, an equipment calibration was performed on the HP 4191A. Calibrations were performed by measuring three known test standards (47:104). These calibration measurements were designed to eliminate the systematic measurement uncertainties in a given measurement configuration. For an impedance analyzer, most systematic measurement uncertainties can be reduced to three unknowns, which can be resolved at each frequency by applying three correct calibration measurements (98:185).

The obvious purpose of calibration is to *de-embed* the measurement environmental effects from the measurement subject. Izadian *et al.* distinguishes two types of de-embedding approaches: two-tier and one-tier. The two-tier de-embedding method first requires a localized calibration of an analyzer, followed by a subject measurement made through an extension of the test fixture. Relative to the HP 4191A impedance analyzer, this process can be accomplished by performing calibrations directly at the output of the type APC-7 connector. The second tier of the two-tier method refers to the accessory cabling and probes (test fixture extensions) used to physically contact the test structure of interest. Of course, at first glance, the effects of the second-tier measurement apparatus seems inseparable from the measurement subject itself. The true characteristics of the test structure cannot be distinguished or *unterminated* from the test fixture extension until the effects of the test fixture extension are determined. In a one-tier calibration, the entire test fixture (including extensions) is first calibrated without a wafer test structure in place,

followed by a test structure measurement. The unterminating process is, therefore, not required, and the measured characteristics of the test structure are measured directly (47:107-110).

A one-tier measurement technique was developed for the HP 4191A. The HP 4191A accomplishes calibration corrections automatically after the calibration measurements are performed. In particular, the short-circuit (zero ohm), open-circuit, and 50  $\Omega$  standards are required for calibration. Such calibration techniques are sometimes referred to as open, short, and load (OSL) calibrations (47:106). For the HP 4191A, the short-circuit calibration seeks measurements of minimum resistance, the open-circuit measurement seeks minimum conduction, and the 50  $\Omega$  measurement seeks minimum reflection (the HP 4191A is matched to 50  $\Omega$  impedances). With this calibration data stored within the HP 4191A, the correct adjustments can be applied to remove the effects of the test fixture (the equipment which requires calibration) from an arbitrary wafer test structure positioned at the end of the test fixture.

The calibration and measurement procedure was straightforward. The short-circuit calibrations were performed with the wafer probes placed on the same pad. The open-circuit calibrations were accomplished with the probes suspended in air approximately 1/16th inch above the wafer. To accomplish the 50  $\Omega$  calibrations, the special 50  $\Omega$  standard probe was substituted. Since this probe was of the same type as the one being calibrated, the substitution introduced minimal error. The most difficult step in the procedure was to perform the short-circuit impedance measurement, which required connecting the load ends of the test transmission lines together on the wafer with as accurate a representation of a short as possible. The shorting was approximately achieved with a model 44 probe, modified by the placement of a shorting clip on the end of the probe. To accomplish the short to ground, the probe was placed such that one side contacted the pad of the desired transmission line, while the other contacted the ground plane beside the pads, as shown in Figure 3.15. Alternately, the bond pads could be wire-bonded with the ground plane;



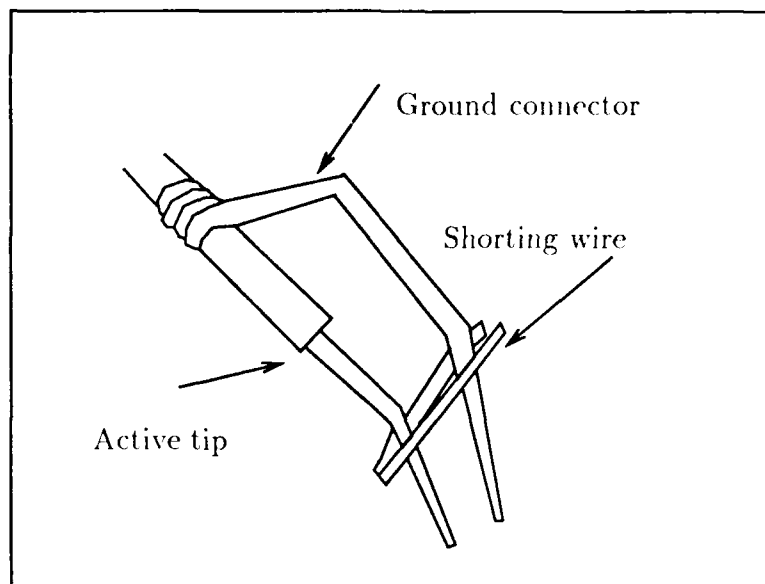


Figure 3.15. Use of a probe tip for the short-circuit measurements.

this possibility was verified experimentally. In practice, the latter method was not used, since the ability to repeat the measurement was limited, due to the destructive nature of the ultrasonic bonding technique that was explored. In either case, stray inductance and capacitance introduces a small error in the calculated value of characteristic impedance.

*Transmission and Coupling Measurements.* The swept-frequency measurement of the coupling voltage was performed using the Figure 3.13 instrument configuration. The measurement operations were coordinated with a BASIC computer program, executed on the Zenith Z-248 personal computer. In this measurement, only a single calibration was required to correct the gain response of the HP 4194A. The type of calibration required is termed a *through*-calibration, which attempts to adjust the transmission path of a given measurement configuration to indicate an effective gain of unity at 400 discrete points over the frequency range of 1-100 MHz. In this manner, the forward transmission gain of any test structure inserted into the calibrated measurement transmission path is accurately measured. To accomplish this

measurement, the output of the test channel (signal source) is electrically connected to the source of a transmission line structure, and the load terminus of the transmission line structure is electrically connected to the input of the test channel through a FET-1 probe, thus simulating the Figure 3.8a circuit configuration. To simulate the 50  $\Omega$  load, the model 44 probe was substituted for the FET-1 probe.

The discussion of coupling measurements is facilitated by the nomenclature and conventions shown in Figure 3.16a. In this figure, the *directivity* of a coupler refers to the voltage gain between ports one and two, which was necessarily a near-end measurement. Due the physical arrangement required for the measurement, this quantity was also referred to as a *backward coupling gain* measurement. The *isolation gain* measurement refers to the voltage gain between ports one and three. Semantically, the isolation gain could also be called the *forward coupling gain*. The measurement between ports one and four is termed *transmission gain*, which is less than unity for passive structures (29).

For the dual-line coupling structures on the test wafers, the backward-coupling and forward-coupling configurations were considered, with more emphasis on the former, since the near-end measurement was simpler to perform. The effective configuration for the backward-coupling measurement is shown in Figure 3.16b, while that for the forward-coupling measurement is shown in Figure 3.16c. For completeness, the configuration used to measure the transmission gain is shown in Figure 3.16d.

*Pulsed Signal Measurements.* The pulse response measurements were accomplished with the Figure 3.14 equipment configuration. Using a Hewlett-Packard pulse generator, model HP 8082, one of the six frequencies available between 5 KHz and 250 MHz were selected (5 KHz, 50 KHz, 500 KHz, 5 MHz, 50 MHz, and 250 MHz). The HP 8082 was chosen as a primary signal source due to its fast rise time (1 ns). The Zenith Z-248 personal computer was then loaded with the appropriate software. To accomplish the pulse measurement, the pulsed signal source was electrically connected to the source end of a transmission line structure, and the load end of the

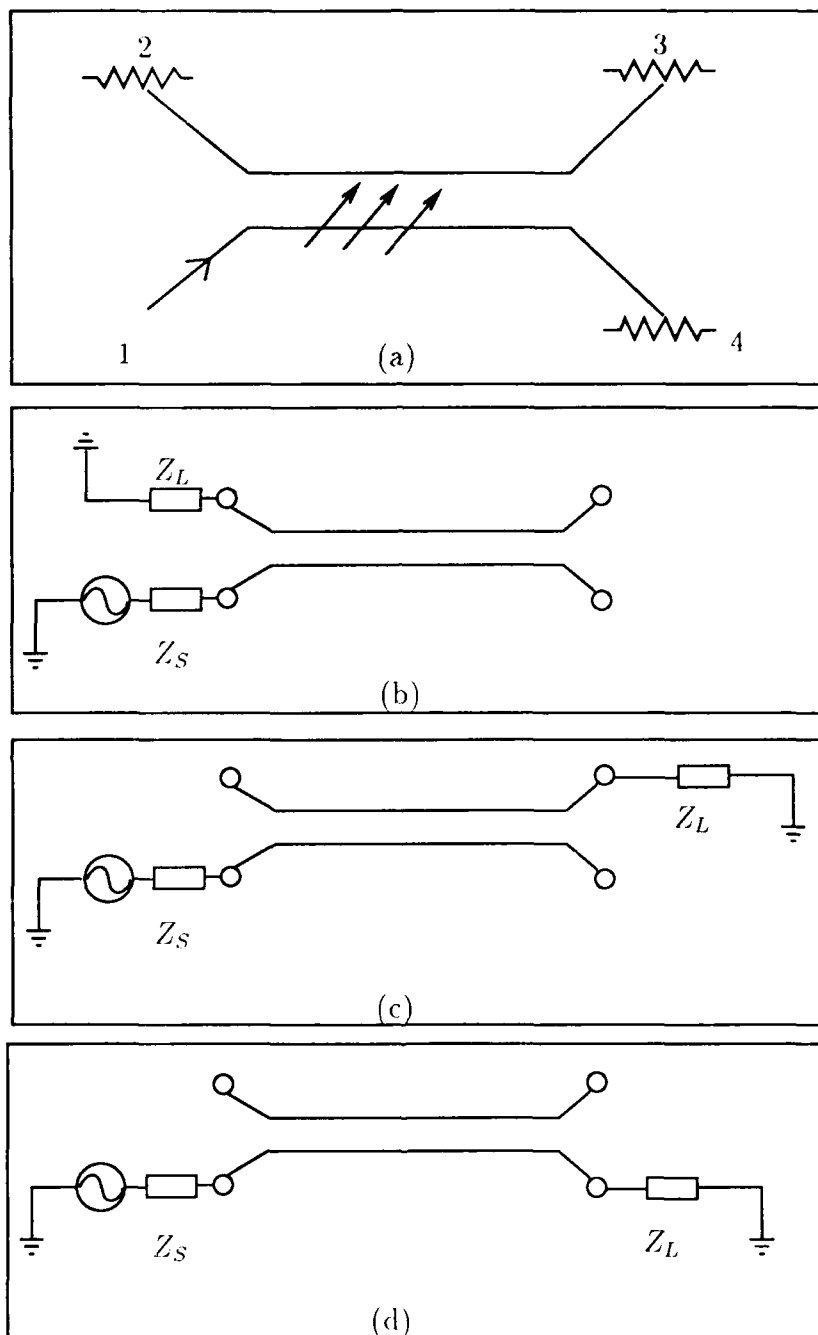


Figure 3.16. Traditional coupler and coupling measurement configuration. (a) Traditional coupler. (b) Backward coupling gain measurement configuration. (c) Isolation gain measurement. (d) Transmission gain measurement. After (29).

transmission line structure was electrically connected to the oscilloscope through a suitable probe to simulate the Figure 3.8a or Figure 3.8b circuit configuration. The pulsed signal response was sampled, digitized, and uploaded to the Zenith Z-248 personal computer.

### *Computational Methodology*

To complement the previously described measurement techniques, a number of analytic methods were devised to provide methods of comparison between theoretical and experimental results. Some of these methods relied on computer-aided design (CAD) application programs. The CAD packages used for this work included the LIBRA and LINECALC programs. These programs are part of an ensemble of programs for microwave network analysis developed by EESof, Inc. Other computer software used for analytic work in this thesis included: MATRIXX, a general matrix manipulation program; Mathematica and MathCad, general mathematics application programs; and Lotus 1-2-3, a spreadsheet program.

The discussion of analysis methods in this section follows the same sequence used to describe the measurement equipment and techniques. First, the analysis methods used for calculating the characteristic impedance are presented. Next, a discussion of the methods used to estimate coupling are presented. Finally, an outline of the digital signal processing techniques applied to the pulsed-signal response measurements are provided.

*Characteristic Impedance Determination.* As discussed in Chapter 2, the characteristic impedance of a transmission line depends on the geometry of the structure and the materials which compose the conductor and dielectric media. Several closed-form expressions, also discussed in Chapter 2, provide the means for determining the characteristic impedance of common structures, such as striplines, slotlines, and microstrip transmission lines. As described earlier in this chapter, many of the transmission line structures on the test wafers fall into one of these categories. However, a

large number of the structures deviated in some respect from the idealized geometries for which the Chapter 2 impedance expressions were developed. For example, many structures were fabricated with a meshed ground plane, which deviates from the solid ground plane structure assumed by most characteristic impedance formulae. Furthermore, the ground planes of the stripline structures were of a finite extent, which deviates from the infinite ground planes assumed by most characteristic impedance formulae. Some of the microstrip-like structures on the subject wafers resembled stripline structures, but with the top ground plane removed. Consequently, this type of structure represents a significant deviation from the structures described by the standard formulae used to estimate the characteristic impedance.

Despite these departures from the ideal case, several of the formulae in Chapter 2 were used as a metric against which the measurement of the characteristic impedance was compared. As discussed in Chapter 1, the question as to the validity of these formulae for even ideal WSI structures had not been resolved. Nevertheless, the Chapter 2 formulae, by virtue of their widespread acceptance by the microwave design community, were selected as one of the bases of comparison.

A second comparative metric chosen for measurement collaboration was the LINECALC program estimates for the characteristic impedance. The LINECALC program is an interactive analysis-synthesis program which estimates the characteristic impedance of a transmission line structure, as well as the attenuation and effective relative permittivity. The LINECALC program appears to rely on closed-form expressions to provide this information, and some of these formulae have been modified in a proprietary manner by the EESof developers. In the analysis mode, the user interactively provides the program with known transmission line specifications. As input parameters, the user may input the material parameters of conductor resistivity (normalized to gold in microstrips, and to copper in striplines), the relative electrical permittivity ( $\epsilon_R$ ) and loss tangent ( $\delta_L$ ) of the dielectric, and the various geometric parameters pertaining to the transmission line structure. The program

boasts a variety of standard planar transmission line types, including single and dual edge-coupled microstrip and striplines, coplanar waveguides with and without ground planes below, and coplanar strip structures. However, LINECALC does not model finite or gridded-mesh ground planes, nor does it treat non-standard versions of striplines, such as those without superficial ground planes (embedded microstrips). An additional limitation of the LINECALC program is its inability to treat coupled versions of any of the previous structures which have more than two conductors.

A third metric chosen to estimate the characteristic impedance used a finite-difference model of a transverse cross-section of particular transmission line structures under consideration. The finite-difference method (FDM) simulates physical models which behave in a mathematically predictable manner. This simulation, which is simply an iterative solution of Laplace's equation in a finite domain with Dirichlet boundary conditions, provides a direct estimate of the scalar potential in the regions modeled. Knowledge of the scalar potential at any point in the simulation's domain permits the electric fields to be determined, from which the other quantities of interest, such as charge, capacitance, and characteristic impedance can be obtained. The FDM approach used for the comparative work discretized two orthogonal spatial coordinates into increments which were typically less than one micron in each dimension. Conductor and dielectric interfaces and regions in this and other FDM approaches can usually be introduced arbitrarily into the model by physical placement into the appropriate region inside the domain of the model. By virtue of this generality, a wide variety of planar structures can be modeled, including those structures which do not have closed form expressions available.

The finite difference method is one of the most common methods used to solve electrostatics problems [(23),(40),(87)]; the discussion which follows outlines a less commonly used implementation of a finite difference scheme. To implement the finite difference algorithm, a Lotus 1-2-3 spreadsheet was created, with the appropriate internode relationships written *en masse* to a large planar array of cells using

traditional Lotus data manipulation commands, a technique which was described by Lockyear (60). A spreadsheet implementation for a FDM solution has been demonstrated by at least two researchers [(43),(60)], and it was selected because of its directness and simplicity.

A typical spreadsheet implementation for a single stripline is shown in Figure 3.17. As in most calculator displays, the displayed precision is more coarse than the true resolution. Since the spreadsheet provides a planar representation of data, it lends itself well to the role of representing a rectangular discretization of quantities with simple inter-element relationships. The spatial positions of nodes in the cross-section roughly map into corresponding spatial positions on the visual display of the spreadsheet.

The inter-element relationships are those commonly employed in traditional finite difference schemes [(40),(87)]. The inter-node or inter-cell relationships for Laplacian-Dirichlet problems are straightforward. An excellent summary of these relationships for the most commonly encountered dielectric-to-conductor and dielectric-to-dielectric interfaces is presented in (40). Transmission line conductors with known potentials and ground planes represent Dirichlet boundary conditions. These structures are represented by entering the appropriate potential values into the cells of the planar array which correspond to their spatial position. By selecting the appropriate scale of values and formatting the worksheet display properly, the executed program provides a visually intuitive representation of equipotentials after a reasonable convergence of the solution is attained.

To improve the accuracy of this finite difference approach and to speed convergence of the solution, two modifications of Lockyear's basic approach were introduced. The first modification introduced floating Dirichlet boundary conditions at the horizontal ends of the finite spatial region to simulate a horizontal region of infinite extent. This method, which is described in more detail in Appendix E, iteratively establishes more approximate estimates of the potential at the boundary than

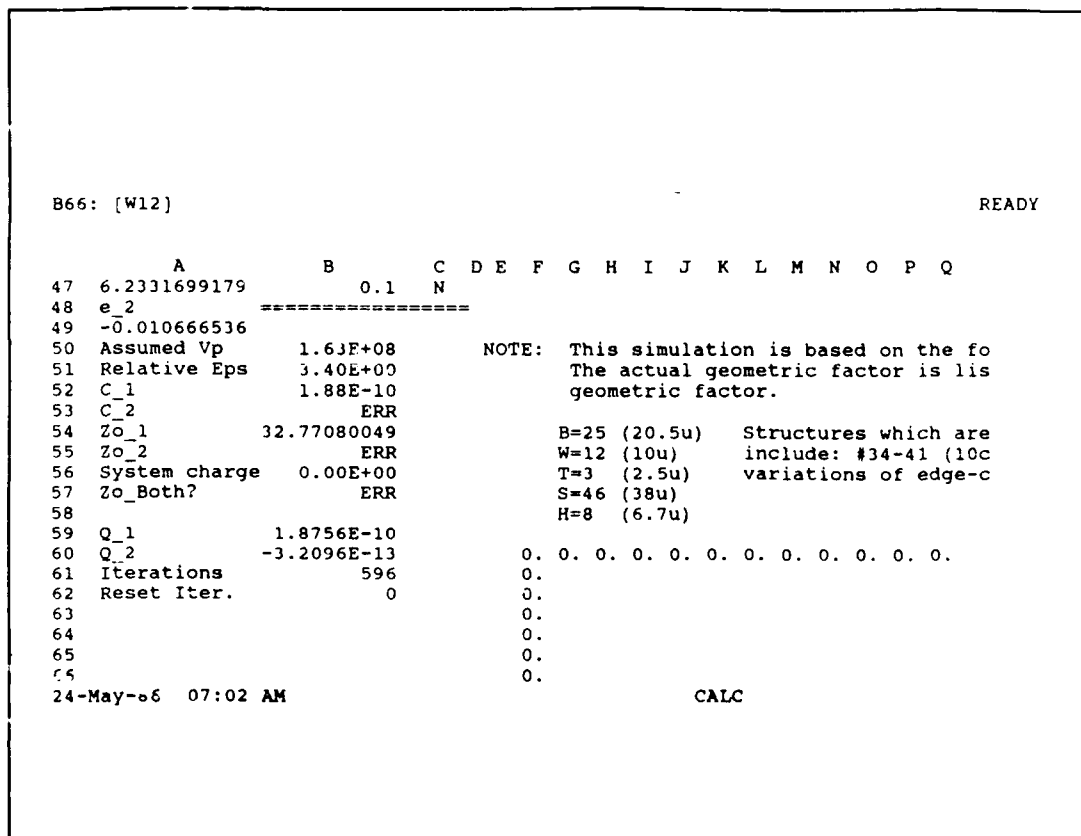


Figure 3.17. Example spreadsheet display for an electrostatics problem.

would be afforded by assuming a zero potential at the sidewalls of the simulation. When the correct potential is established there, the accuracy of the potential estimates of other nodes within the region of interest are improved, since the potential distribution inside the domain of interest is, in fact, more representative of a horizontally infinite domain. This approach is similar, in some respect, to that reported by Sandy *et al.* (85), which relied upon an approximation of the appropriate free-space Green's function to establish the sidewall potential rather than the approach described in Appendix E. The second modification to the FDM approach used by Lockyear includes over-relaxation factors in the inter-node relationships, identical to those used by Green and Schneider [(40),(87)].



A typical problem formulation is schematically illustrated in Figure 3.19, which illustrates: (1) a source-free region, (2) active conductor Dirichlet boundaries, (3) grounded surface Dirichlet boundaries, and (4) floating sidewall Dirichlet boundaries. Also shown on the diagram is a closed contour  $\gamma_1$  and path contour  $\Gamma_1$ . The contour  $\gamma_1$  encircles an active conductor, is confined to the interior (the source-free region), and is otherwise arbitrary. Similarly, the contour  $\Gamma_1$  may connect any single active conductor to ground through an arbitrary path in the source-free region. Corresponding contours  $\gamma_i$  and  $\Gamma_i$  are defined for each active conductor inside the simulation domain. The example in Figure 3.19 models the transversal cross-section of an edge-coupled stripline, a structure which occurs commonly on the test wafer. The spatial domain of the cross-section maps into a simulation similar to that displayed in Figure 3.17.

The “atomic” or cell level of the simulation is schematically represented in Figure 3.18. The cell represents the scalar potential of the simulation space at a point. The simulation is comprised of two-dimensional iterations of such cell schemes. Not all cells contain the same inter-cell relationships, but should bear functional representations consistent with the intended model. The inter-cell relationships are particularly simple for the example problem. For cells of region (1), a familiar voltage averaging relationship is used to obtain the value of the potential at node  $x$  for the  $(N + 1)$ st iteration; that is:

$$V_x^{N+1} = \frac{1}{4}(V_A^N + V_B^N + V_C^N + V_D^N) \quad (3.3)$$

where the nodal voltages  $V_A$ ,  $V_B$ ,  $V_C$ , and  $V_D$  represent the potential values during the  $N$ th iteration at the spatial points represented by the respective nodes. To include over-relaxation, this expression is slightly modified as:

$$V_x^{N+1} = \alpha(V_A^N + V_B^N + V_C^N + V_D^N) + (1 - \alpha)V_x^N \quad (3.4)$$

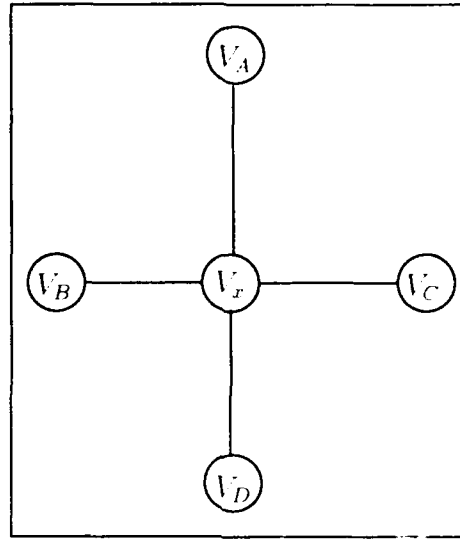


Figure 3.18. The fundamental finite-difference node.

where  $V_x^N$  represents the old value of  $V_x$ , and  $\alpha$  is an empirical relaxation factor, which can range from 0 to 1/2. Of course,  $\alpha = 0.25$  yields Equation 3.3 (no relaxation), while  $\alpha < 0.25$  represents under-relaxation, and  $\alpha > 0.25$  represents over-relaxation. Over-relaxation is used to reduce convergence time in a finite difference scheme. The relaxation factor is usually guessed initially and changed during the course of the simulation. The best relaxation profiles are not predictable in general for a particular simulation, but are developed through trial and error [(40), (87)]. In the case of a spreadsheet simulation, the previous two equations are slightly modified. For example, Equation 3.3 becomes:

$$V_x^{N+1} = V_A^{N+1} + V_B^{N+1} + V_C^N + V_D^N \quad (3.5)$$

while Equation 3.4 becomes:

$$V_x^{N+1} = \alpha(V_A^{N+1} + V_B^{N+1} + V_C^N + V_D^N) + (1 - \alpha)V_x^N. \quad (3.6)$$

These modifications are required because of the raster-scan method which spreadsheet

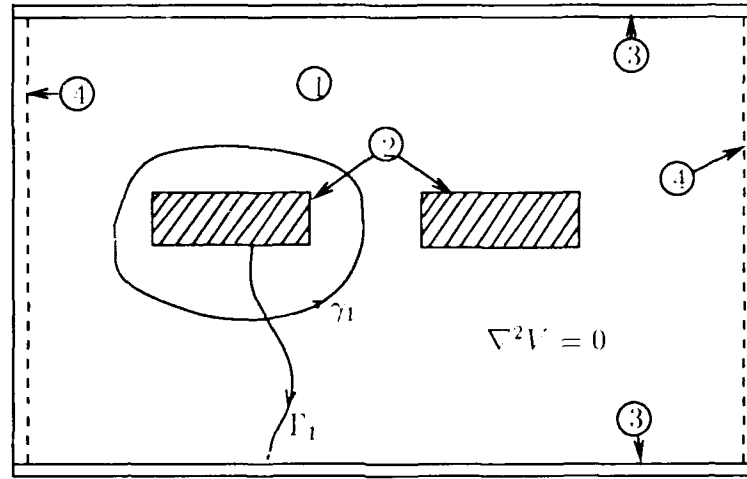


Figure 3.19. Schematic representation of characteristic impedance problem formulation.

programs use to update cells. No changes in overall speed of convergence, ability to achieve convergence, or incremental accuracy have been reported due to this modification, nor were any observed in the simulations performed in this research effort.

After a simulation is encoded into the spreadsheet, the dependent quantities of capacitance and impedance can be obtained. For the capacitance of the  $i$ th conductor, Equation 2.1 is integrated around  $\gamma_i$  to determine the charge enclosed by the  $i$ th conductor. An application of the divergence theorem and Equation 2.7 yields [(60),(87)]:

$$q_i = \varepsilon \oint_{\gamma_i} (\vec{E} \cdot \hat{n}) d\ell. \quad (3.7)$$

Dividing Equation 3.7 by the voltage of the  $i$ th conductor with respect to ground yields:

$$V_i = \int_{\Gamma_i} \vec{E} \cdot \vec{d\ell} \quad (3.8)$$

Consequently, the capacitance of the  $i$ th conductor is given as:

$$C_i = \frac{\varepsilon \oint_{\gamma_i} (\vec{E} \cdot \hat{n}) d\ell}{\int_{\Gamma_i} \vec{E} \cdot \vec{d\ell}}. \quad (3.9)$$

In the finite difference simulation, the electric field  $\overline{E}$  in the direction  $\hat{n}$  or  $E \cdot \hat{n}$  is evaluated as the first forward finite difference of the potential in the direction  $\hat{n}$ ; that is:

$$\overline{E} \cdot \hat{n} = \frac{V(x, y) - V(x + \Delta x, y + \Delta y)}{\sqrt{\Delta x^2 + \Delta y^2}} \quad (3.10)$$

where  $\Delta x$  and  $\Delta y$  correspond to the incremental changes in the directions  $\hat{x}$  and  $\hat{y}$  made in transversing an incremental distance in the direction  $\hat{n}$  [(4:499-505), (55:69)].

Applying Equations 2.20 and 2.21 to the capacitance defined in Equation 3.9, the characteristic impedance of the  $i$ th conductor can be determined [(60), (87)] as:

$$Z_O = \sqrt{\frac{\mu}{\epsilon_R \epsilon_0}} \frac{\int_{\Gamma_i} \overline{E} \cdot d\ell}{\oint_{\Gamma_n} (\overline{E} \cdot \hat{n}) d\ell} \quad (3.11)$$

Equation 3.11 serves as a definition of characteristic impedance for transmission line structures with one or two conductors. For two-conductor transmission line structures, the characteristic impedance is calculated twice: once for the even-mode configuration and once for the odd-mode configuration, as indicated by Equation 2.22. In transmission line structures having more than two conductors, a different scheme must be employed, since the even- and odd-mode dichotomy does not work for generalized multi-conductor systems. For an  $n$ -conductor system, the coefficient matrices  $[C]$  and  $[L]$  of Equations 2.29 and 2.30 can be solved with FDM, using Equation 2.31 to establish the voltage definitions required to extract the elements of the partial capacitance matrix  $[C]$ , and then by using Equation 2.32 to form the partial inductance matrix. Obviously, this approach neglects losses, since the conductance and resistance matrices  $[G]$  and  $[R]$  are not computed. With the  $[C]$  and  $[L]$  matrices and suitable boundary conditions, Equations 2.29 and 2.30 can be solved as a coupled system of first-order, ordinary differential equations at a given frequency.

*Coupled Signal Waveform Determination.* To provide a means for comparing theory to experiment in the coupling measurements, three techniques were used.

These comparisons were carried out on a number of the dual-line, edge-coupled test structures. The first technique involved LIBRA simulations of the structures, using the backward-coupled circuit configuration (Figure 3.16). The LIBRA simulations modeled discontinuities, as well as the expected transmission line sections. The second technique was theoretically less refined and involved the use of a set of equations presented by Edwards (29:161) for dual-line structures with coupling. A third method involved the solution of the multi-conductor telegrapher's equations (Equations 2.29–2.30) based on a set of capacitance coefficients computed using a finite difference model.

*The LIBRA Model.* The LIBRA program provides the capability to simulate a wide variety of pre-defined and user-defined electrical elements. Select transmission lines on the test wafers were approximately represented with combinations of elements from LIBRA's built-in element library, such as coplanar waveguide and dual-line ECS structures. However, none of LIBRA's resident library models could accommodate three-line ECS structures, two-line or three-line edge-coupled embedded microstrip structures, or meander structures. Discontinuity models for corner bends and step width changes were also part of the library of available elements. The available library elements were used to model several of the 10 cm long, dual-line, ECS structures. The resulting representations were simulated in the backward coupled configuration (Figure 3.16) with LIBRA over the frequency range spanning 1 MHz to 100 MHz, thereby matching the range of measurements used with the HP 4194A gain-phase analyzer.

The specific model used to represent the 10 cm long transmission line structures numbered 34–41, 42–49, and 101–111 is shown in Figure 3.20. The LIBRA input program listing used is presented in Appendix B. Each discontinuity of the structure is modeled with corresponding LIBRA library elements. The main section of the model, the 10 cm long transmission line section, is modeled as an ECS with the appropriate geometry and material combinations. The input pads and shorter line

sections of the structure were similarly modeled with shorter lengths of edge-coupled striplines. The equivalent circuit of the transitions between the probe tips and the input pads were not included in the model because of the calibration method used to compensate for their effects. That is, since the HP 4194A provides a through-calibration, any effect of the probe transition would be compensated for during the measurement process.

Of the structures modeled, those in the numbered range 42–49, which possessed an interline spacing of approximately 18  $\mu\text{m}$ , closely representing the 400 line/cm wirability goal cited by McDonald *et al.* for WSI (66). Each structure in this range was represented by the same LIBRA model, since each structure within this range possessed the same width, length, and thickness, and since LIBRA does not include provisions to model differences between the structures, such as gridded or missing superficial ground planes.

*Simplified Analytic Approach.* For a two-line coupled structure, an additional, simpler analytic technique was considered. This technique can be employed for striplines and microstrips, given a knowledge of the odd- and even-mode impedances and the effective relative permittivity. Edwards presented several equations which describe the terminal relationships of a coupled two-line transmission line system. In terms of the electrical length ( $\theta = \beta\ell$ ) and the odd- and even-mode impedances of the coupled line pair, the steady-state terminal relationships of backward coupling gain ( $A_C$ ), isolation ( $A_I$ ), and transmission gain ( $A_T$ ) are given by the following relationships (29:170):

$$A_C = \frac{V_3}{V_1} = \frac{jC_F \sin \theta}{\sqrt{1 - C_F^2 \cos \theta + j \sin \theta}} \quad (3.12)$$

$$A_I = \frac{V_4}{V_1} = 0 \quad (3.13)$$

$$\text{and } A_T = \frac{V_2}{V_1} = \frac{j\sqrt{1 - C_F^2}}{\sqrt{1 - C_F^2 \cos \theta + j \sin \theta}} \quad (3.14)$$

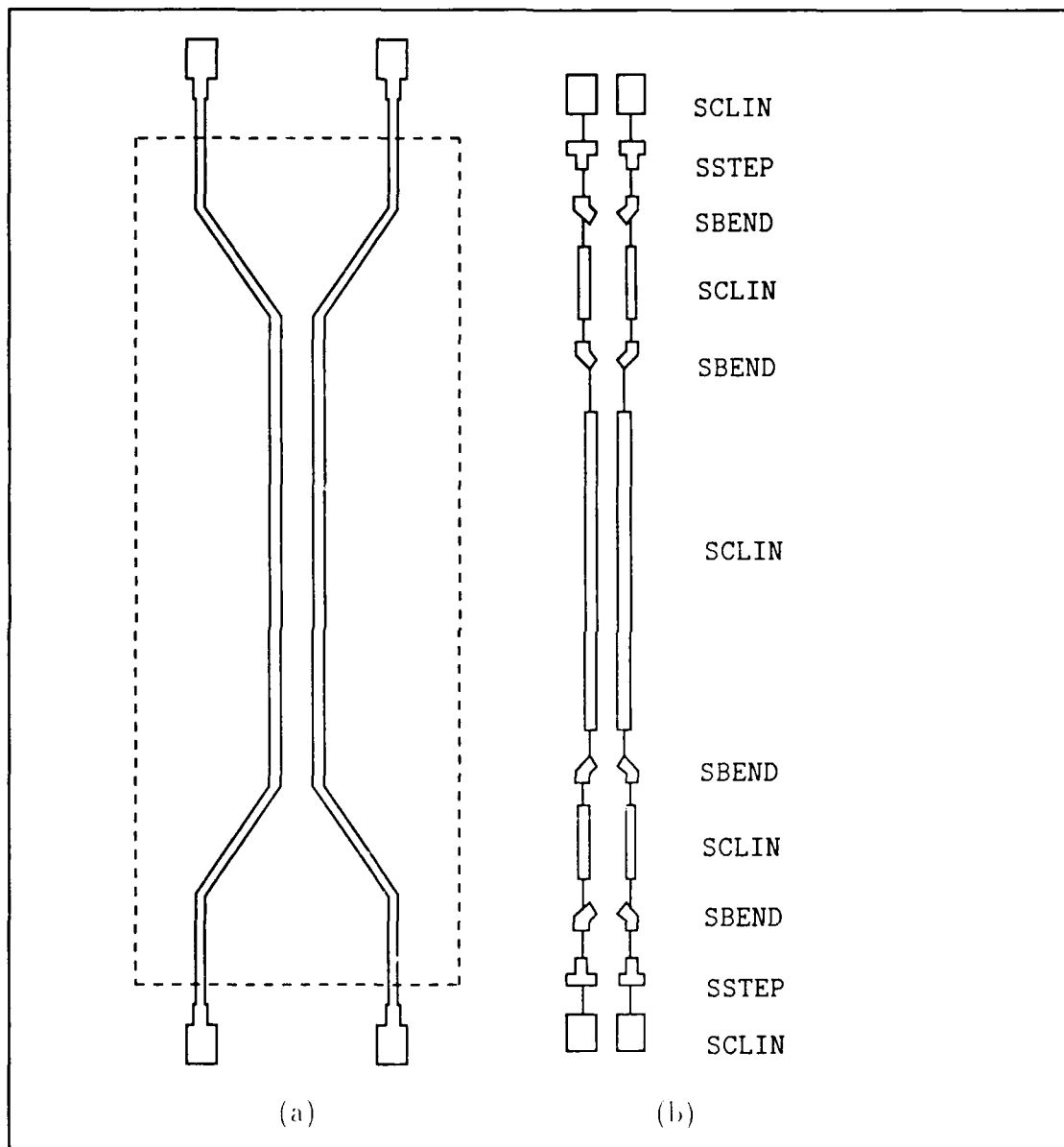


Figure 3.20. LIBRA model of a two-conductor, 10 cm long transmission line structure (#012) on the PIQ test wafer. (a) Physical representation. (b) LIBRA model composed of coupled line sections and discontinuities.

where  $C_F$  is the coupling factor, described in Equation 2.36,  $\theta = \beta\ell$  is the electrical length, and  $\beta$  is the propagation constant. To obtain these expressions, Edwards assumed that all four transmission line ports were terminated in a matched impedance ( $Z_0$ ), given by Equation 2.35. Unfortunately, the four ports of a coupled transmission line pair are generally not matched in practice. Therefore, the resulting values of the terminal relationships are not identically provided by Equations 3.12–3.14. Furthermore, the program does not treat conductor or dielectric losses. However, as an approximation, these expressions find application in coupler analysis and design work.

A simple MathCad program, based on Equations 3.12–3.14, was written to provide an estimate of backward coupling and transmission gain over the frequency range spanning 1 MHz–100 MHz for the 10 cm long, dual transmission lines. As inputs, the program required only the relative permittivity of the dielectric media ( $\epsilon_R$ ) and the even- and odd-mode characteristic impedances ( $Z_{odd}$  and  $Z_{even}$ ). A listing of this program is provided in Appendix B.

*Telegrapher's Equation Approach.* The third method used to achieve a theoretical estimate of the coupling gain of the transmission line structures measured involved the solution of the telegrapher's equations for multi-conductor transmission lines (Equations 2.29–2.30). Considering a two-line coupled, symmetric structure as an example, the charge per unit length on the conductors are related by Equation 2.31:

$$q_1 = c_{11}V_1 + c_{12}V_2 \quad (3.15)$$

$$\text{and } q_2 = c_{21}V_1 + c_{22}V_2. \quad (3.16)$$



By choosing  $V_1 = 1$  volt and  $V_2 = 0$  volts, these equations simplify to:

$$q_1 = c_{11} \quad (3.17)$$

$$\text{and } q_2 = c_{21}. \quad (3.18)$$

By the reciprocity principle,  $c_{12} = c_{21}$ , and by symmetry,  $c_{22} = c_{11}$ . Hence, by evaluating  $q_1$  and  $q_2$  with Equation 3.9 in an appropriate FDM simulation, all four coefficients of  $[C]$  are determined. From Equation 2.32, the system of Equations 2.29 and 2.30 for this problem become:

$$\begin{bmatrix} \frac{di(z)}{dz} \\ \frac{dv(z)}{dz} \end{bmatrix} = \begin{bmatrix} 0 & j\omega\mu\varepsilon[C]^{-1} \\ j\omega[C] & 0 \end{bmatrix} \begin{bmatrix} i(z) \\ v(z) \end{bmatrix}. \quad (3.19)$$

The boundary conditions corresponding to the backward coupling gain measurement configuration (Figure 3.16) are:

$$V_1(0) = Z_{L1}I_1(0) \quad (3.20)$$

$$V_2(0) = Z_{L2}I_2(0) \quad (3.21)$$

$$I_1(\ell) = 0 \quad (3.22)$$

$$\text{and } I_2(\ell) = 0 \quad (3.23)$$

where  $Z_{L1}$  and  $Z_{L2}$  are the load impedances at  $\ell = 0$  for transmission lines one and two, respectively. A solution to the system in Equation 3.19, based on the boundary conditions of the measurement configuration, was developed and mechanized as a Mathematica program. The program used the solution of Equation 3.19 to provide an estimate of the coupling gain. Implementations, of course, are possible in other programs, such as MATRIXX. The Mathematica program solves Equation 3.19 at 100 discrete, equally-spaced frequencies between 1 MHz and 100 MHz. The data sets produced were plotted for comparison with the results of other analyses, simulations,

and measurements. The details of the solution to Equation 3.19 are provided in Appendix F; the Mathematica program listing is given in Appendix A.

*Pulsed-Signal Response Processing Methodology.* To remove the effects of the test equipment environment from the samples tested for pulse response, a set of digital signal processing manipulations were performed on most of the pulsed-signal measurement data. A block diagram of the overall approach selected is shown in Figure 3.21. The goal of this approach was to filter out the effects of the long cables which connected the test wafers (shown in Figure 3.14). By synthesizing a digital filter with a response equal to the inverse of the cable response, a greater insight could be attributed to the actual wafer response characteristics. To extract the wafer response, the output waveforms associated with the test structure measurements were fed through this "de-cabling" filter. Through elementary frequency-domain analysis techniques, the output spectrum of the filter is simply the scalar products of the spectra of all linear sub-units in the transmission path, where each spectrum  $Y(\omega)$  represents the Fourier transform of the equivalent time-domain signal  $y(t)$ . The time-domain signal  $y(t)$  is assumed to be approximated by a Fourier series; the transformed signal  $Y(\omega)$  is represented by:

$$Y(\omega) = \sum_{n=1}^{1024} a_n \delta(\omega - \omega_n) \quad (3.24)$$

where the  $a_n$  constants are the Fourier coefficients of  $y(t)$ . The upper limit of 1024 in the summation is shown to reflect the number of coefficients used in the fast Fourier transform (FFT) algorithms associated with the digital signal processing techniques. Due to the sifting nature of the delta function, the products of spectra become functions with a representation similar to Equation 3.24, but with different Fourier coefficients. Each of the new Fourier coefficients is the scalar product of the same-indexed Fourier coefficients of each inline signal of the transmission paths shown in Figure 3.21. The filtered spectrum can then be converted to a new time-domain

representation through inverse Fourier transformation. Therefore, based on this technique, it is plausible to extract a measurement from the test environment by creating a virtual filter which cancels the effects of the measurement environment. The synthesis of the de-cabing filter is accomplished by manipulating the spectra of two signals. The first signal required is that measured in the Figure 3.14 configuration without a wafer test structure; that is, the cabling of the measurement configuration is measured alone. This particular type of measurement is referred to as the "long-cable" measurement (Figure 3.21c). This measurement is taken with a pulsed-signal input using the normal configuration (Figure 3.14), and both measurement probes are shorted together through a common (non-grounded) conducting surface, such as an input pad on one of the test structures. The resulting spectra of the measured signal is the product spectra  $X(\omega)C(\omega)$ , where  $X(\omega)$  is the spectra of the pulsed-signal input, and  $C(\omega)$  is the impulse response of the cable used in the measurement configuration. The second signal required for the de-cabing filter is the pulsed-signal input, which possesses the spectrum  $X(\omega)$ . Since the pulsed-signal waveform cannot be truly measured, an approximate version is obtained by measuring the direct output of the function generator through the shortest available cable (with length no greater than one foot). This measurement is referred to as a "short-cable" measurement (Figure 3.21b). The spectrum of this approximated measurement of the input waveform is denoted as  $\tilde{X}(\omega)$ . With the spectra of the two measurements,  $X(\omega)C(\omega)$  and  $\tilde{X}(\omega)$ , an approximation of the cable impulse response can be formed:

$$C(\omega) \cong \frac{C(\omega)X(\omega)}{\tilde{X}(\omega)}. \quad (3.25)$$

The de-cabing filter is then defined to be the signal with a spectrum  $C^{-1}(\omega)$ , such that:

$$C(\omega)C^{-1}(\omega) = 1 \quad (3.26)$$

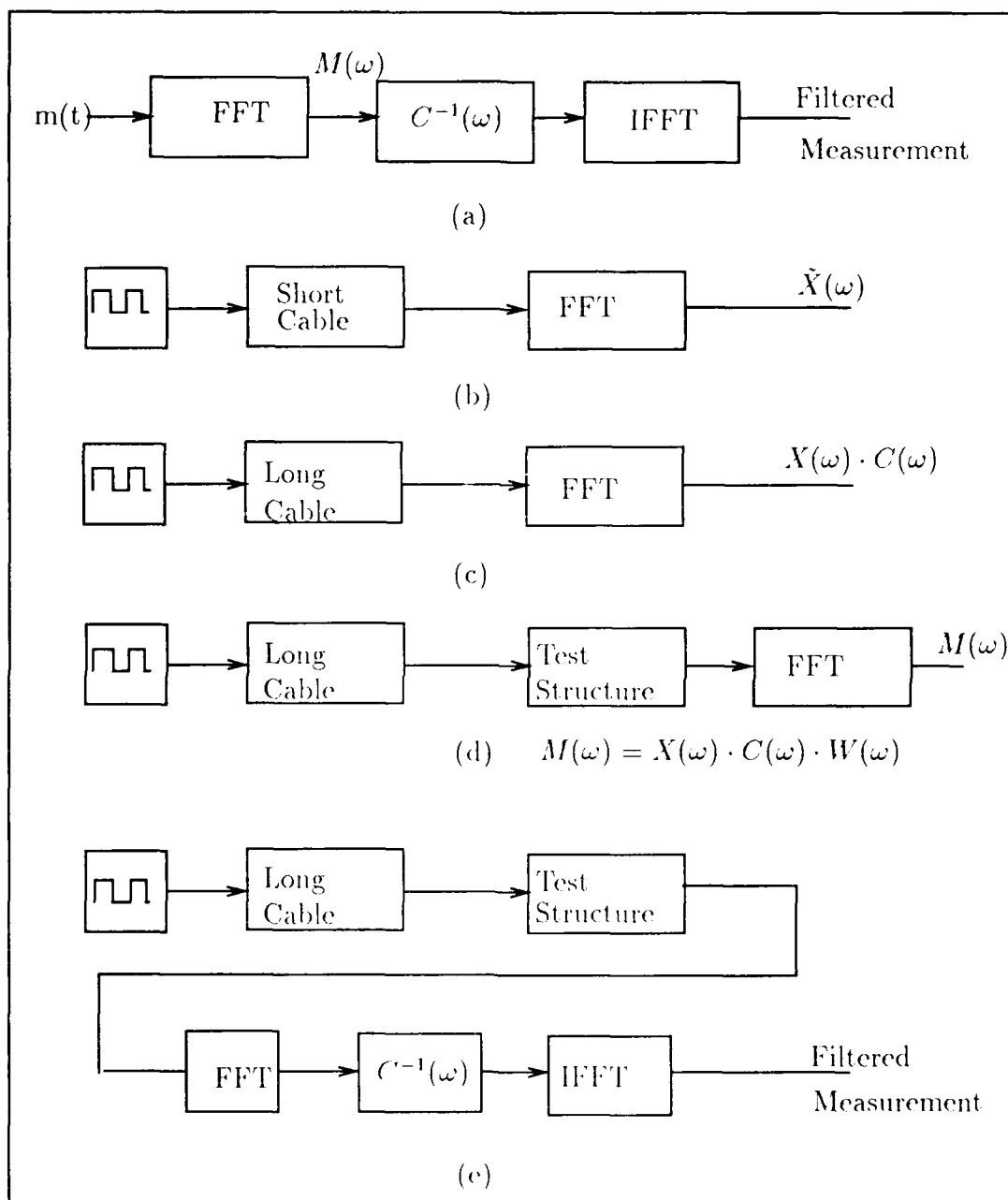


Figure 3.21. Block diagrams of the "de-cabled" filter technique. (a) Overall approach. (b) Short cable system diagram. (c) Long cable system diagram. (d) Sample measurement diagram. (e) Application of de-cabling filter.

for all  $\omega$ . This relationship is satisfied by a function of the form given by Equation 3.24, with Fourier coefficients specified by:

$$a_n = \frac{1}{c_n x_n} \quad (3.27)$$

where  $x_n c_n$  represents the  $n$ th-Fourier coefficient in the long-cable configuration, and  $\tilde{x}_n$  is the  $n$ th-Fourier coefficient in the short cable configuration.

The measurement signal  $m(t)$  (Figure 3.21d) is also affected by the cable measurement. Its Fourier spectrum,  $M(\omega)$ , is represented by the function in Equation 3.24, except that the Fourier coefficient  $m_n$  replace  $c_n$ . Buried in the measurement is the true impulse response  $W(\omega)$  of the subject; simple algebra reveals that these coefficients can be represented by:

$$w_n = \frac{m_n}{c_n x_n} \quad (3.28)$$

where  $m_n$  is the  $n$ th-Fourier coefficient of the measurement signal, and  $c_n x_n$  is the  $n$ th-Fourier coefficient of the signal measured through the cables, as before, in the absence of a wafer test structure.

To extract the pulsed-signal response of the wafer test structure, which is the primary goal of this analysis, the product of the measured signal and the de-cabled signal are formed:

$$P(\omega) = M(\omega)C^{-1}(\omega) = \sum_{n=1}^{N=1024} \frac{w_n c_n x_n}{a_n} \delta(\omega - \omega_n) \cong \sum_{n=1}^{N=1024} w_n x_n \delta(\omega - \omega_n). \quad (3.29)$$

In other words, the Fourier coefficients of the filtered signal (the true pulsed-signal response) are formed by the scalar product of the Fourier coefficients of the measured signal and the Fourier coefficients of the inverse cable filter of like indices.

Of course, this idealized discussion of the "de-cabling" and the impulse extraction technique does not consider several practical problems of implementation.

The problems are not computational, as the signals involved are already in a digital representation from the sampling oscilloscope, and many commercial software programs, such as MATRIXX, Mathematica, and MathCad can perform the necessary transformations outlined above. Rather, the problems in implementing this approach are include:

1. The signals must have identical periodicity. If the sampling intervals in the time-domain are different, the resulting transforms for two signals  $a(t)$  and  $b(t)$  become:

$$A(\omega) = \sum_{n=1}^{N=1024} a_n \delta(\omega - \omega_n) \quad (3.30)$$

$$\text{and } B(\omega) = \sum_{m=1}^{M=1024} b_m \delta(\omega - \omega_m) \quad (3.31)$$

which, when multiplied together, yield:

$$A(\omega)B(\omega) = \sum_{n=1}^{N=1024} a_n \delta(\omega - \omega_n) \cdot \sum_{m=1}^{M=1024} b_m \delta(\omega - \omega_m) = 0. \quad (3.32)$$

In general, Equation 3.32 does not hold unless the Fourier coefficients of the two signals are formulated at the same frequency. Unfortunately, the aforementioned computer programs will provide the following *incorrect* result when this operation is requested:

$$A(\omega)B(\omega) = \sum_{n=1}^{N=1024} a_n b_n \delta(\omega - \omega_n). \quad (3.33)$$

2. The leading edges of the signals must be aligned; that is, the phase of the signals must be identical. If the signal period is given by  $\tau$ , then the Fourier transform of a signal taken from  $t = 0$  to  $t = \tau$  is not the same as the Fourier transform of the signal taken from time  $t = \tau/2$  to  $t = (3/2)\tau$ , in general.
3. The fast Fourier transform technique, the usual numerical technique used to

perform digital or discrete Fourier transforms, assumes infinite periodicity of the input waveform. The Fourier coefficients of a signal of one period duration will differ from the Fourier coefficients of a signal which is based on a time-domain input of 1.5 periods duration. Hence, all input waveforms must be of equal duration when transformed to yield correct results.

4. Many fast Fourier transform algorithms expect  $2^N$  time-domain points to be present. Although the sampling oscilloscope typically produced samples of this length, the length of a single period—which was the usual interval of interest—corresponded to a fewer number of time-domain points.

To surmount these problems, a set of waveform editing and interpolation procedures were developed to insure correct signal processing. Additionally, all measurements were taken in sets — short cable, long cable, and sample — at each frequency to insure correct periodicity. Mismatches due to time delay were eliminated by *adjusting the triggering control* of the oscilloscope so that all signals were captured on their leading edge. To overcome random errors in the measurements, provisions were made in the editing and re-interpolation steps to average a number of similar measurements. The averaging process was employed since averaging tends to reduce the amplitude of individual noise components, while it tends to reinforce the true underlying signal waveform (90:169-170).

Comprehensively, the de-cabling process is summarized as follows:

1. Measurements were collected from the *short cable configuration* using the procedure outlined in Appendix C.
2. Measurements were collected with the same pulsed-waveform input from the *long cable configuration* (measurement configuration with no test structure).
3. Measurements were collected with the pulsed-waveform input utilizing the *test wafer structure measurement configuration*.

4. Each of the waveforms collected above were edited using a spreadsheet program, with each waveform truncated as nearly as possible to one period duration.
5. The truncated waveforms were saved and re-sampled so that each would occupy 1024 time-voltage pairs. This re-sampling was done with a dedicated linear interpolation program. After the interpolation is performed, redundant data sets are averaged. It is necessary to perform the averaging process *after* interpolation, since the truncated waveforms may not have identical numbers of time-voltage pairs.
6. The spectrum of each signal was extracted through an FFT algorithm using either MATRIX, MathCad, or Mathematica. Only one of these programs were used for a particular set of data, since differences existed between the FFT algorithms used by the programs.
7. The cable inversion filter  $C^{-1}(\omega)$  was formed with Equation 3.29.
8. The cable inversion filter was applied to the spectra of appropriate subject measurements.
9. The time-domain response of the filtered (de-cabled) signal was recovered through an inverse FFT.

### *Summary*

This chapter outlined the metrics used to analyze the test wafers evaluated in this research effort. The measurands included electrical continuity, characteristic impedance, coupling gain, and transmission gain. To verify the last three of these measurands, theoretical techniques were developed and outlined. For the characteristic impedance, several of the expressions presented in Chapter 2, along with finite-difference and LINECALC estimates, were used to provide a theoretical basis for comparison. For coupling and transmission gain estimates, LIBRA models and two analytic methods were discussed as verification methods. The first analytic



model was based on a simplified lossless analysis, for which closed-form, analytic expressions could be used to estimate coupling and transmission levels. The other analytic method considered the solution of multi-conductor transmission line equations for similar estimates.

Qualitatively, a set of pulsed-input response measurements were proposed. For these measurements, no previous prediction techniques were performed. The goal of these measurements was to show how pulsed-signal inputs, such as those used in digital logic circuits, would be affected by their propagation through WSI interconnections.

## *IV. Results and Analysis*

### *Overview*

The goals of measurement analysis in this research effort were to provide a correlation between the characteristic impedance measurements and the established theory. Additionally, an analysis was undertaken to provide insight into the performance of WSIC interconnections when impressed with digital signals. The results and findings of both the analytic projections and the measurements associated with the wafer scale interconnections are presented in this chapter. First, the physical observations related to the subject wafers tested are discussed. The simple dc continuity tests were considered to be an integral part of this physical characterization. Consequently, these findings are presented in the context of physical observations. Next, the frequency-domain metrics of characteristic impedance, coupling gain, and transmission gain are discussed. When possible, correlations are provided. Otherwise, the results and their associated interpretations are presented. Finally, findings from the time-domain, pulsed-signal response measurements are presented.

Due to the large number of structures on each wafer and the number of measurement categories (continuity, characteristic impedance, coupling gain, transmission gain, and pulsed-signal response), an exhaustive measurement exercise was considered to be beyond the scope of this research effort. Accordingly, a limited number of structures were measured. In some measurement categories, such as continuity measurements, many more measurements were taken, since the range of possibilities for interpretation were small, and the measurements were themselves simple to perform. However, for other categories, such as the pulsed-signal measurements, fewer measurements were conducted, due to the more robust analytic complexity. The balance between time available for measurement versus the time required for analysis necessarily resulted in further limitations in scope, and an equitable mixture was sought to provide a comprehensive analysis for a few of the most relevant structures on the test wafers.

### *Physical and Continuity Measurement Findings*

This section presents the physical observations and the results of continuity measurements performed on the three test wafers available for study in this thesis. For convenience during data collection, the measurements performed on the 10 cm structures were divided into "near end" measurements, which were performed on only one side of the transmission structure, and "far end" measurements, which were performed on both sides of the structure at the same time.

*Physical Observations.* Optical measurements were performed during the experimental phase of this research in conjunction with the electrical measurements. The bulk of this work was done with the optical microscope assembly on the wafer probing station. Scanning electron microscopy (SEM) was not performed on the wafers that were electrically measured; the charge storage mechanism present in the dielectrics of the wafers prevented this investigation. Several proposed methods to overcome this problem, including the application of a thin film conductive coating and the destructive examination of the wafers were considered but not pursued. The following paragraphs summarize the physical and optical characterization of the test wafers.

*PIQ Wafers.* Two PIQ wafers were examined and electrically measured. The PIQ dielectric is a polyimide; hence, polyimide material parameters were assumed in the subsequent analysis. The PIQ dielectric was applied to form layers which were specified to be 6  $\mu\text{m}$  thick between each metal level. According to the Polycon Corporation (80), the thickness variation of this material across the wafer was within 10%. An additional thickness variability of 10% was assigned to account for profile variations across the wafer due to the technique used to apply the dielectric.

The physical continuity on the lines of almost every structure appeared to be relatively straight, regular, and aligned in accordance with the prescribed design.

According to Polycon design guidelines (76), the resolution of the lithography process was approximately two microns. Thus, diagonal geometries (which are referred to as non-"manhattan" directions in VLSI layout design) would, under sufficient magnification, reveal the coarseness of lithographic definition. Close examination of sloping surfaces on the test wafers, in particular the sloping walls of the coplanar waveguide structures, revealed the limitations of the lithography, as shown in Figure 4.1.

In a few cases, the appearance of a physical anomaly could be correlated with an electrical performance problem. For example, on the second PIQ wafer, several conductor leakage paths were visible on several conductors, as shown in Figure 4.2. In other cases, the physical appearance of the transmission line structures did not indicate electrical performance problems. Nevertheless, these problems were discovered after electrical measurements were conducted.

Several structures were physically impossible to examine. On the first PIQ wafer, the 54th transmission line structure was not measurable due to a large, gouge at one end. This physical defect did not appear to be fabrication-related, but rather as an accidental scratch which occurred some time after fabrication. The structures at either end of the 10 cm block (the 1st and the 123rd structures) on each wafer were unsuitable for electrical measurements. A visual inspection of these structures revealed that the probing pads and transmission line "active" conductors for these structures were missing, although the meshed ground plane portions of the structures appeared to be intact. These later defects appear to be fabrication-related, but were not surprising, since it is difficult to achieve the higher quality fabrication work on the outermost edges of a wafer in practice. However, this indication of reduced process quality on the wafer's periphery implies that the edges of the interconnection networks on actual WSI systems must be carefully quantified.

An inspection of the second PIQ wafer revealed leakage paths on several of the transmission line structures, in particular, on those structures which were closely



Figure 4.1. Detailed view of coplanar waveguide, revealing definition of lithography.

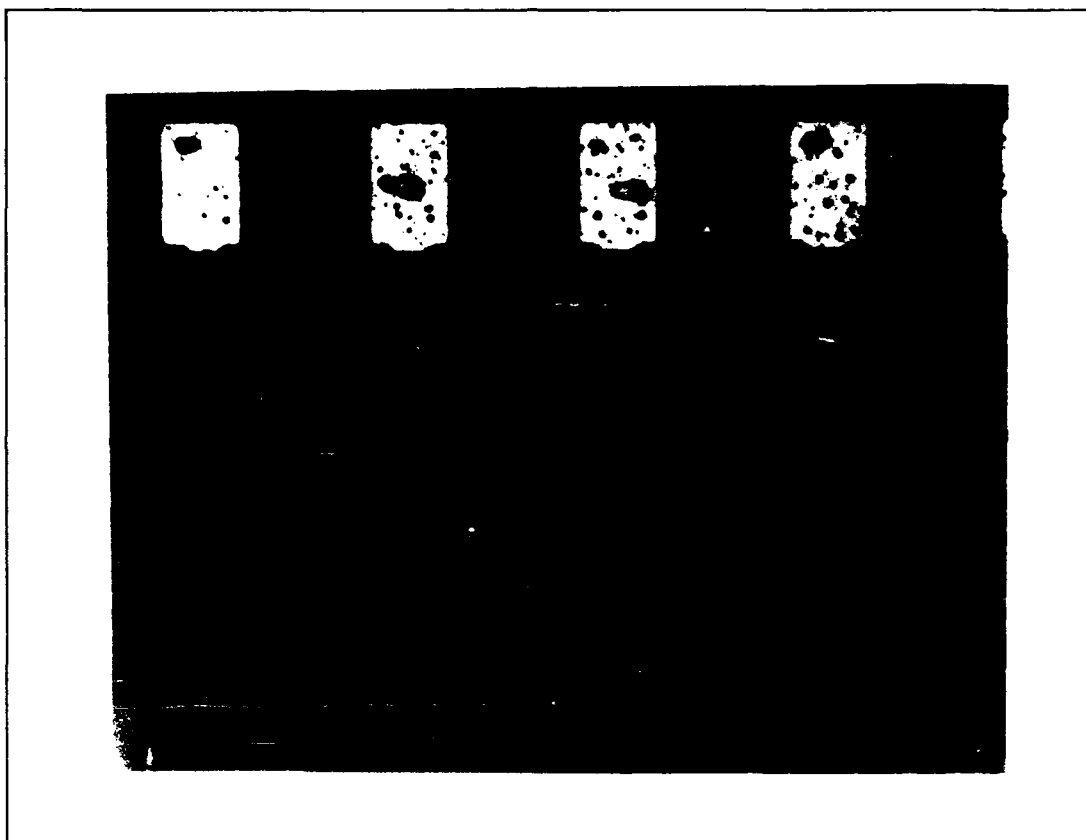


Figure 4.2. Leakage defect from one of the test wafers.

spaced ( $10\text{ }\mu\text{m}$ ), which included the set of structures numbered 65-80 in the 10 cm block. The leakage paths appeared as filamentary conducting conduits between adjacent conductors. An example of the anomaly is shown in Figure 4.2. As shown, these filamentary paths bridged across the structure at the point where the  $45^\circ$  bend furthest from the input pads occurred. Additionally, this wafer experienced the same fabrication quality problems on its periphery as the first wafer.

*BCB Wafers.* Although two different wafers with a BCB dielectric were examined, only one wafer was suitable for electrical measurement. The input pads of the structures on the first BCB wafer examined had a blackish coating, which was originally believed to be an oxide. It was found that by sufficiently abrading a conductor pad, an underlying, reflective metal surface was exposed. With the recommendation of the Polycon Corporation (82), two repetitions of a simple etch procedure were implemented on this wafer in an attempt to remove the coating. The etch procedure consisted of immersing the wafer in a solution of 90% phosphoric acid, 5% nitric acid, and 5% de-ionized water, heated to  $40^\circ\text{C}$ , for ten seconds, followed by an immediate immersion in a cascaded bath of de-ionized water for several minutes. After each etch was performed, the wafer was optically inspected. These inspections did not reveal any change in appearance (the coating was still present), even after two etch cycles. Figure 4.3 illustrates the appearance of two structures from the "coated" BCB wafer, compared to corresponding structures from one of the PIQ wafers. The wafer was subsequently inspected by the Polycon Corporation after both etches were performed. Their inspection of the wafer revealed no traces of oxide, so further characterization work was attempted on the wafer.

Most of the structures present on the BCB wafer were regular in appearance, consistent with those of the two PIQ wafers. The thickness of the BCB dielectric layers between metal levels was reported by the Polycon Corporation to be thicker (80); each dielectric layer was designed to be  $8\text{ }\mu\text{m}$  thick. The thickness variability was assumed to be the same percentage as that reported for the PIQ wafer. The appearance

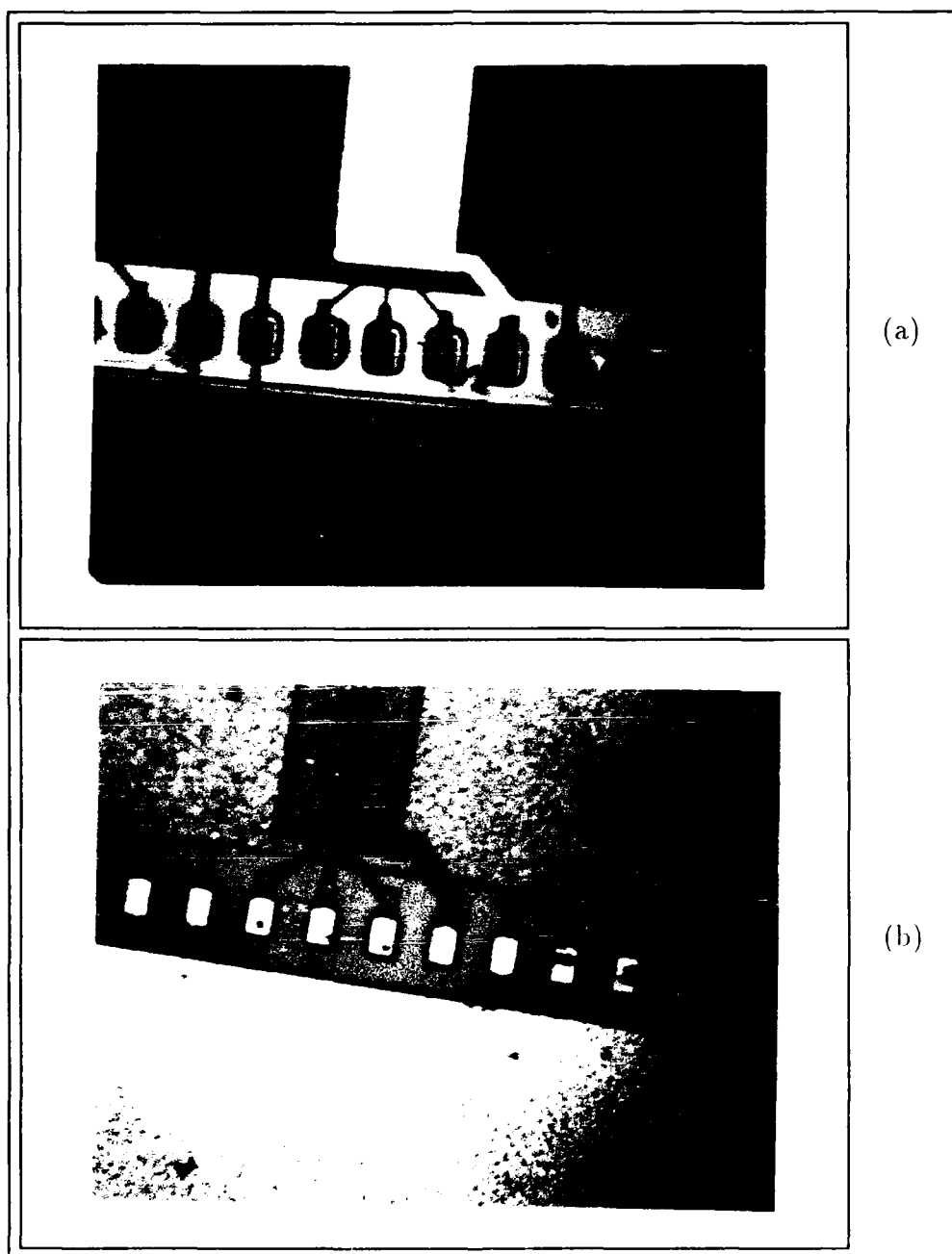


Figure 4.3. Appearance of the contact pad "blackened" surfaces of the BCB wafer compared to those of normal (PIQ) wafer. (a) BCB wafer. (b) Normal wafer (PIQ).



of pads which seemed to be eroded were noted. In some cases, the erosion was severe enough to cause electrical problems. Unfortunately, due to the extra processing procedures carried out on this wafer, it is not possible to conclude whether this erosion was caused by the etching or whether it was present during fabrication. The highest probability was assigned to the former possibility, since no conductors on any of the other wafers displayed these characteristics. Some of the structures possessed filamentary shorts between conductors, identical to those described for the second PIQ wafer.

The thickness of the BCB dielectric posed some problems with probing operations. The input pads were accessed by positioning a probe at the bottom of a trench-like or well-like structure (Figure 4.4a). The walls of the "trench" were formed by the superimposed thicknesses of the dielectric layers, totaling approximately  $26.5\ \mu\text{m}$ . The pad itself was a rectangular conductor ( $40\ \mu\text{m} \times 65\ \mu\text{m}$ ) located at the "bottom" of the "trench". Due to the deepness of this trench, the acceptable "angles of attack" required to insert a beam-like probe tip were more restrictive than for the corresponding "trenches" associated with the PIQ wafer pads, which were approximately  $6\ \mu\text{m}$  shallower. Many times, during probing operations, the probe tip would become wedged between the top of the "trench" and the bottom of the "trench" on the opposite side. From this arrangement, any additional motion, however imperceptible, would apply additional pressure to the probe tip, much like a lever against a wedge. The resulting force acted against the opposite wall of the dielectric, which was less capable of resisting pressure than was the tungsten-tipped probe. The brittleness of the BCB dielectric resulted in the ensuing action of a rather large section of dielectric being forcibly catapulted from the wafer's surface (Figure 4.4b). If the prying action was in the direction of an adjacent conductor pad, then the section of dielectric between the two pads was often ejected. An example of this effect is demonstrated in Figure 4.5. This phenomena did not occur in the PIQ wafers, since their corresponding conductor pad "trenches" were shallower. Furthermore,

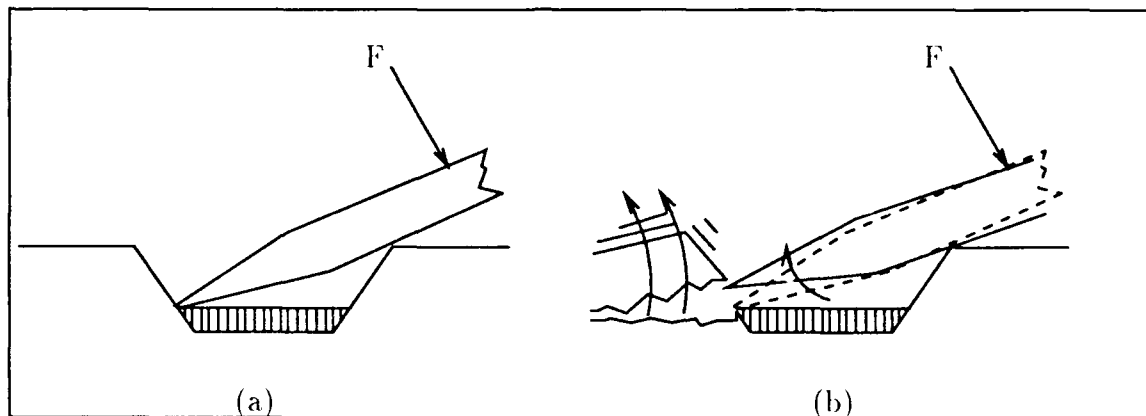


Figure 4.4. Depiction of problem encountered during probing. (a) Probe positioned in dielectric trench. (b) Result of the application of excessive force ( $F$ ) during probing.

the “taffy-like” consistency of the PIQ dielectric created a pliable surface which was more forgiving of probe slippage.

A second wafer with BCB dielectric was considered for electrical measurement. The input pads of this wafer did not have the appearance of a blackish coating, as did the first BCB wafer. However, when any probing operations were attempted on the pads of structures in the 10 cm block, the pads were severed from the structures altogether. It was found that the pads on the near end of all 10 cm structures were not physically connected to the dielectric beneath. Hence, any electrical probing was impossible, since the mechanical force exerted by a micro-manipulator arm during a routine probing operation detached these pads from the structure. However, the far end electrical pads on the same structures appeared to possess a reasonable degree of electromechanical integrity. This finding indicated that the adhesion problem was somewhat localized, perhaps only affecting one side of the wafer.

*Continuity Measurement Results.* Continuity measurements were performed to establish the electrical connectedness of individual conducting structures, while



Figure 4.5. Example of the physical (destructive) removal of the dielectric region adjacent to an input pad of a WSIC structure. The hazy appearance of the left contact pad is attributable to the fractured section of the dielectric.

the leakage measurements were used to determine the presence of undesired leakage conduction paths between presumably isolated conductors. The measurements performed revealed many open-circuit (continuity) failures and short-circuit (leakage) failures on the PIQ wafers, while the results for the BCB wafer were believed to be inconclusive.

Table 4.2 is a condensed summary of continuity measurement results for the test wafers. The measurements were performed in the manner described in Chapter 3 and were roughly divided into continuity measurements and leakage measurements. The table enumerates the number of structures for which failures were found; multiple occurrences of the same type on a particular structure are not listed. Although leakage results for the BCB wafers are presented, continuity measurements are not. The reason for the omission was that the many occurrences of continuity failures could not be resolved to be true continuity failures of the conductor or false indications caused by the interfering film present on the conducting pads.

*Leakage Measurements.* Leakage measurements were performed on approximately 50 structures of the first PIQ wafer, 120 structures on the second PIQ wafer, and approximately 50 structures on the BCB wafer. All of these leakage measurements were near-end measurements, taken from the top surface of the wafer. Leakage failures were found on each of the PIQ and BCB wafers that were examined electrically.

*PIQ Wafers.* The leakage mechanisms manifested themselves in apparently different ways on each of the PIQ wafers. The first wafer manifested leakage through paths which were not optically visible. Based on continuity measurements, the leakage paths appeared to pass through a ground node. For example, the 23rd structure of the first PIQ wafer displayed a dc resistance of  $151.8\ \Omega$  between the left and right conductors, but individually, each of these conductors displayed a resistance of approximately  $81\ \Omega$  to a common ground. Since the resistance of each conductor to ground was roughly one-half of the leakage resistance between

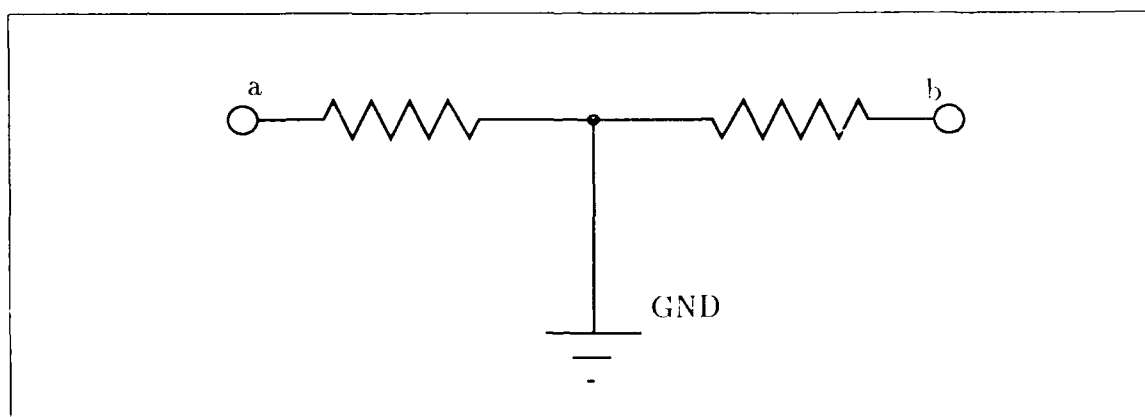


Figure 4.6. Leakage model for structures on first PIQ wafer.

the conductors, a likely model representing this leakage mechanism is shown in Figure 4.6. For the cases which appeared to follow this model, the leakage resistances were unusually low ( $< 100 \Omega$ ). However, not all leakage problems encountered on the first wafer were represented by the leakage model in Figure 4.6. For example, the 46th structure of the first wafer manifested a higher leakage resistance —  $171 \text{ K}\Omega$  — on only one conductor. Without exception, every occurrence of this particular type of leakage involved conductors at the Metal 2 level. These particular leakage problems appeared to be isolated with respect to the first PIQ wafer. None of the leakage problems encountered on the second wafer behaved like the Figure 4.6 model. As previously implied, several of the leakage problems encountered were related to the small, filamentary conduction paths between the conductors of certain structures on this wafer.

*BCB Wafer.* Due to the presence of some type of coating over the conductive pad and ground surfaces which were probed, the results of the continuity measurements for the BCB wafer were considered to be inconclusive, in general. The continuity measurements were necessary, nevertheless, so that structures with a high probability of electrical integrity could be identified. Of the two possible continuity measurement categories, four possible outcomes exist, as indicated in Table 4.1. (In this table, the terms “open” and “short” are symbolic and do not necessarily

represent infinite and zero resistance, respectively. The desirable outcomes are given by entries 1 and 4. However, when a questionable element is introduced into the continuity measurements, the meaning of the results in Table 4.1 is questionable. In particular, the questionable element affecting the continuity measurements of the BCB wafer was that which was caused by the blackish film which coated the conductor pads (Figure 4.3). The outcomes of Table 4.1 which were questionable were entries 1 and 3. That is, the presence of an open reading on a continuity measurement was questionable under these circumstances, since this outcome might have occurred due to poor electrical contact. Of course, the establishment of a proper contact could have been aggravated by the blackish film (which was obviously non-conductive) on the conductor pads of the BCB wafer. Although it might seem that continuity measurements under these circumstances were of little value, the measurements were important for the identification of "good structures" for subsequent measurements. "Good structures" were defined as those which performed satisfactorily with respect to entries 1 and 4 in Table 4.1 for each conductor in a given structure. For example, a three-conductor structure would not be considered "good" unless the measurements of all three conductors possessed the appropriate series conductivity value (entry 4), and simultaneously, that no leakage paths were found (entry 1). Although a false entry 3 outcome was possible due to the ambiguity of open continuity measurements, the occurrence of an entry 4 outcome was regarded as definite or conclusive for that conductor. Therefore, the probability that some structures eliminated by these measurements were actually "good" also existed. Similarly, for leakage measurements, the occurrence of leakage paths (entry 2 outcome) was considered to be definite or conclusive, while the occurrence of an entry 1 outcome was not. Therefore, the possibility of *not* screening out a leaky structure also existed. Hence, great care was exercised in subsequent measurements to identify leakage in the screened structures that was not detected in the initial continuity measurements.

Table 4.1. Continuity measurement outcomes.

#	Measurement category	Outcome	Desired?
1.	Leakage	Open	Yes
2.	Leakage	Short	No
3.	Continuity	Open	No
4.	Continuity	Short	Yes

*Continuity Measurements.* Continuity measurements were conducted on approximately 50 structures of the first PIQ wafer, 80 structures on the second PIQ wafer, and 50 structures on the BCB wafer. These measurements, as all others, were restricted to structures in the 10 cm block of each test wafer. Continuity measurements were far-end measurements, except for the meander structures, which began and terminated on the same side. Many continuity failures occurred on the two PIQ wafers. Some of the continuity data recorded were ambiguous due the presence of leakage, and the associated structures were screened accordingly. Based on an optical inspection of these structures, the failures did not appear to be related to structural integrity problems. Expected values of resistance for the aluminum conductors (which were used on both PIQ and BCB wafers) were based on the simple resistance formula:

$$R = \rho \left( \frac{L}{A} \right) \quad (4.1)$$

where  $\rho$  is the material's bulk resistivity (reciprocal of the conductivity  $\sigma$ ),  $L$  is the conductor's length, and  $A$  is the conductor's cross-sectional area. Based on values tabulated in Chapter 2 for resistivity, and assumed values of width (10  $\mu\text{m}$  and 25  $\mu\text{m}$ ) and thickness (2.5  $\mu\text{m}$ ), a 10 cm line of aluminum has a dc resistance of 106  $\Omega$  for a 10  $\mu\text{m}$  wide line and 40  $\Omega$  for a 25  $\mu\text{m}$  wide line. These values are considerably lower than those measured in any of the corresponding structures

on the test wafers. Many reasons for these differences exist, including the non-ideality of the transversal cross-section (non-rectangular), the contact resistance at the pads, the amorphicity of the materials (for example, grain boundary resistance), and the work function which exists between different metals at the contact points. As an arbitrary division, the structures were categorized as good, marginal, high resistance, and open. For the 10  $\mu\text{m}$  wide structures, the chosen dividing points were: good ( $< 400 \Omega$ ), marginal ( $< 5000 \Omega$ ), high resistance ( $< 20 \text{ M}\Omega$ ), and open ( $> 20 \text{ M}\Omega$ ). For the 25  $\mu\text{m}$  wide structures, the divisions were: good ( $< 300 \Omega$ ), marginal ( $< 2000 \Omega$ ), high resistance ( $< 20 \text{ M}\Omega$ ), and open ( $> 20 \text{ M}\Omega$ ).

Upon compilation of the data in Table 4.2, a trend involving the very high resistance continuity failures on the two PIQ wafers became apparent. That is, based on these findings, it appeared that most of the extremely high resistance and open failures occurred at the Metal 3 level, although no trends were evident regarding the resistances recorded as marginal.

#### *Frequency-Domain Computational and Measurement Findings*

This section considers the frequency domain analysis and measurements conducted for several representative wafer structures. The metrics selected for this work included the characteristic impedance, the coupling gain, the transmission gain, and the isolation gain. In each case, the analyses and measurements were pursued as swept-frequency investigations (where a signal with a single frequency component) was swept over the range of 1-700 MHz for the characteristic impedance investigation and over the range of 1-100 MHz for the other measurements. Representative structures of several geometric types and conductor linewidths (10  $\mu\text{m}$  and 25  $\mu\text{m}$ ) were investigated.

Simulations and other analytic methods applied values based on design information (82). In addition to these data, another parameter, the ground plane separation distance ( $b_1$ ), was estimated to be 20.5  $\mu\text{m}$  for the PIQ wafers and 26.5  $\mu\text{m}$  for the BCB wafers. These estimates were based on the Polycon Corporation design



Table 4.2. Results of the continuity and leakage measurements.

Type of Failure	Wafer	Number of observed occurrences	Metal Level
Leakage due to shorts	PIQ 2	8	2
Leakage due to shorts	PIQ 2	5	3
Leakage due to shorts	BCB-1	1	1
Leakage due to shorts	BCB 1	3	2
Other leakage--low resistance	PIQ-1	27	2
Other leakage--low resistance	PIQ 1	1	3
Other leakage--low resistance	PIQ 2	1	3
Other leakage--low resistance	BCB-1	1	2
Other leakage--high resistance	PIQ-1	5	3
Other leakage--high resistance	PIQ-1	1	2
Other leakage--high resistance	PIQ 2	1	2
Other leakage--high resistance	PIQ 2	1	3
Continuity opens	PIQ 1	2	3
Continuity opens	PIQ 1	1	2
Continuity opens	PIQ 2	20	3
Continuity opens	PIQ 2	1	2
Continuity--high resistance	PIQ 1	11	3
Continuity--high resistance	PIQ 2	3	2
Continuity--high resistance	PIQ 2	3	3
Continuity--marginal	PIQ 1	3	3
Continuity--marginal	PIQ 2	13	2
Continuity--marginal	PIQ 2	5	3

thicknesses of 6  $\mu\text{m}$  and 8  $\mu\text{m}$  between metal layers for the PIQ and BCB test wafers, respectively (80). To obtain the ground plane distances, the thicknesses were multiplied by three for the three dielectric layers between Metal 1 and Metal 4. Another 2.5  $\mu\text{m}$  was added to this value to account for the vertical displacement of the stripline active conductor. For the height above ground ( $h$ ), the design thicknesses were multiplied by the appropriate integer corresponding to the level of metal which contained the active conductors. Structures on the HDMI substrate without a ground plane possessed an inhomogeneous dielectric composition. Furthermore, the semi-conducting substrate did not possess the conductivity normally associated with a ground plane. Hence, due to the inhomogeneity, such structures were not strictly described by the specialized expressions in Chapter 2, nor were they correctly approximated by typical CAD programs, such as LINECALC. As an approximation, the structures were nevertheless modeled by those approaches, when possible. The height parameter used in these models was approximated by the vertical distance of the structures' active conductors above the semi-conducting substrate.

All analyses assumed perfect geometries; that is, the conductors were assumed to be perfectly rectangular. Also, the transversal cross-sections of structures were assumed to be invariant along their length. This assumption was necessary to implement a validation of the two-dimensional theoretical analyses. The theoretical analyses of the two-dimensional structures represent equivalent analyses of infinite length, three-dimensional structures. Therefore, structures which are not infinitely long are only approximately represented by two-dimensional solutions (85).

The following sub-sections discuss the detailed findings of the characteristic impedance analyses and measurements.

*Characteristic Impedance Results.* The list of structural classes for which characteristic impedance analyses and measurements were performed is shown in Table 4.3. The parameters  $b$  and  $h$ , omitted from the table, were assumed to be the same as discussed above.

Table 4.3. Structures for which characteristic impedance measurements were performed.

Structural Type	Linewidth	Spacing	Representative Structures
Two-line ECS	10 $\mu\text{m}$	38 $\mu\text{m}$	34-41
Two-line ECS	25 $\mu\text{m}$	22 $\mu\text{m}$	104-111
Three-line ECS	25 $\mu\text{m}$	14 $\mu\text{m}$	96-103
Coplanar waveguide	10 $\mu\text{m}$	18 $\mu\text{m}$ (gap)	62
Coplanar waveguide	25 $\mu\text{m}$	26 $\mu\text{m}$ , 18 $\mu\text{m}$ (gap)	33, 91

*Analytic Characteristic Impedance Results.* Several analytic methods were used to predict the characteristic impedance ( $Z_0$ ) for the structures in Table 4.3. First, a number of theoretically based calculations were performed, based on analytic expressions presented in Chapter 2. Next, the LINECALC program was used to estimate the characteristic impedance of several structures. As mentioned in Chapter 3, not all the structures were compatible with the LINECALC analysis repertoire, namely the three-conductor ECS structures and structures possessing inhomogeneous dielectric compositions. Finally, the finite difference implementation discussed in Chapter 3 and Appendix E was used to model some structures. The latter technique, as expected, proved to be the most general of these estimation techniques, since it could be readily adapted to provide analyses of most structural geometries. Additionally, the finite difference model was sufficiently flexible to evaluate different definitions of the characteristic impedance and capacitance coefficients.

A summary of the single-, two-, and three-conductor models is shown in Figure 4.7; Table 4.4 enumerates all definitions used for the characteristic impedance and capacitance coefficients. For the majority of cases, these definitions coincide with those given in Chapter 2 and Chapter 3. However, it was necessary to create some new characteristic impedance definitions to accommodate the measurement configurations associated with the two- and three-conductor structures. For example, with

a two-conductor structure, the even- and odd-mode characteristic impedances could not be measured with the Chapter 3 technique, since the voltage distribution on the conductors under which these modes are defined could not be created in the measurement environment. In fact, the only practical measurements which could be accomplished on the multi-conductor structures using the Chapter 3 technique were the driving-point impedance measurements. These measurements were made on one conductor, with the remaining conductor or conductors left unconnected ("floating"). To provide a basis of comparison for these measurements, impedance definitions were created which were compatible with the measurement configurations used. These definitions were then implemented in simulations.

Entries 13-16 in Table 4.4 provide such definitions. In the FDM approach used, a special technique was developed to model a floating conductor, since the normal FDM method expects Dirichlet boundary conditions, whereas floating conductors represent Neumann boundary conditions. This refinement is described in detail in Appendix E. These special characteristic impedance definitions were compatible with the measurement configurations for the multi-conductor structures. Entry 13 defines the characteristic impedance with respect to one conductor of a two-conductor transmission line, where the other conductor is left floating. Entries 14 and 15 are the corresponding definitions for a three-conductor transmission line. The second of these definitions apply to a three-conductor system where the center line is held to zero volts. The final entry (16) considers a characteristic impedance definition for a three-conductor system with respect to the center conductor, in which case, the conductors on either side are left floating.

The structures in Table 4.3 were analyzed using the closed-form expressions in Chapter 2, the LINECALC program, and FDM simulations. The resulting calculations for particular structural classes are discussed in the following paragraphs.

*Two-Conductor Structure Results.* The two conductor ECS structural models were based on ideal, rectangular stripline models. The lateral extent

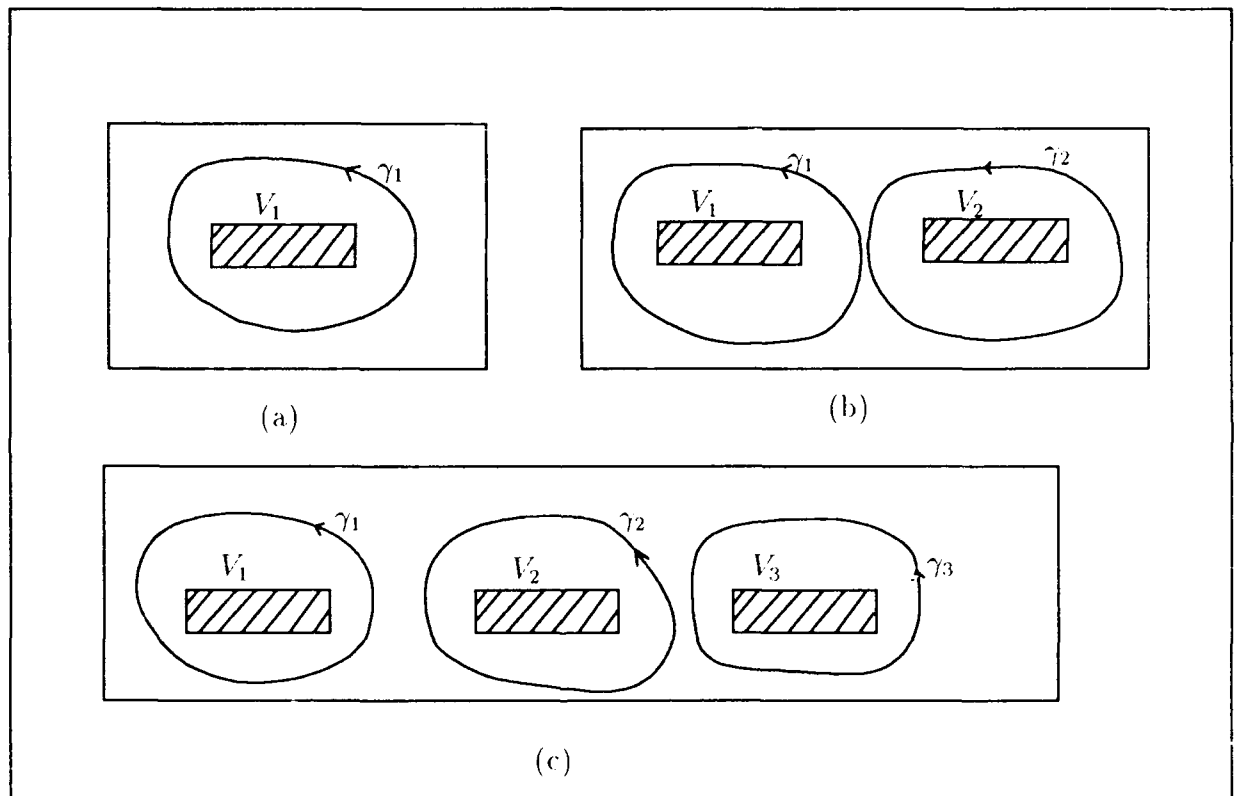


Figure 4.7. Finite-difference model cross-sections. (a) Single-conductor. (b) Two-conductor. (c) Three-conductor.

Table 4.4. Quantity definitions used in the finite-difference simulations.

	Quantity	Figure 4.7	$V_1$	$V_2$	$V_3$	$\int_x E_n \cdot ds$	Notes
1	$q_1$	a, b, c	Arb	Arb	Arb	$x = \gamma_1$	
2	$q_2$	a, b, c	Arb	Arb	Arb	$x = \gamma_2$	
3	$q_3$	a, b, c	Arb	Arb	Arb	$x = \gamma_3$	
4	$c_{11}$	a, b, c	1	0	0	$x = \gamma_1$	
5	$c_{22}$	b, c	0	1	0	$x = \gamma_2$	
6	$c_{33}$	c	0	0	1	$x = \gamma_3$	
7	$c_{21}$	b, c	1	0	0	$x = \gamma_2$	Not unique
8	$c_{23}$	c	0	1	0	$x = \gamma_3$	Not unique
9	$c_{31}$	c	1	0	0	$x = \gamma_3$	Not unique
10	$Z_O$	a	1	n/a	n/a	$x = \gamma_1$	
11	$Z_{even}$	b	1	1	n/a	$x = \gamma_1$	Also used $\gamma_2$
12	$Z_{odd}$	b	1	-1	n/a	$x = \gamma_1$	Also used $\gamma_2$
13	$Z_O$	b	1	Float	n/a	$x = \gamma_1$	Special definition
14	$Z_O$	c	1	Float	Float	$x = \gamma_1$	Special definition
15	$Z_O$	c	1	0	Float	$x = \gamma_1$	Special definition
16	$Z_0$	c	Float	1	Float	$x = \gamma_2$	Special definition

of the dielectric and ground plane in the transverse cross-section (Figure 3.2) was assumed to be infinite in both directions. Some of the actual structures possessed meshed ground planes, while the others did not possess *any* superficial ground plane. No attempts were made to simulate these variations in the analytic models. That is, only the ECS structures were modeled with the FDM approach. The other structures were assumed to approximate this behavior.

The resulting estimates for two representative ECS structures are presented in Tables 4.5-4.8. The results of Table 4.5 were based on the specifications associated with the PIQ wafer. Two particular structures were considered from the Table 4.3 list: the 36th structure and the 109th structure. This choice was made to simulate these structures since they most closely represent ECS structures. The 36th structure on the PIQ wafer was assumed to possess the following parameters:  $w=10\text{ }\mu\text{m}$ ,  $t=2.5\text{ }\mu\text{m}$ ,  $h=6\text{ }\mu\text{m}$ ,  $s=38\text{ }\mu\text{m}$ ,  $b=20.5\text{ }\mu\text{m}$ , and  $\epsilon_R=3.4$ . The 109th structure on the PIQ wafer was assumed to possess the following parameters:  $w=25\text{ }\mu\text{m}$ ,  $t=2.5\text{ }\mu\text{m}$ ,  $h=6\text{ }\mu\text{m}$ ,  $s=22\text{ }\mu\text{m}$ ,  $b=20.5\text{ }\mu\text{m}$ , and  $\epsilon_R=3.4$ . The results of Table 4.8 were based on specifications for the BCB wafer. These specifications were identical to those of the PIQ wafer, with the following exceptions:  $h=8\text{ }\mu\text{m}$ ,  $b=26.5\text{ }\mu\text{m}$ , and  $\epsilon_R=2.75$ .

A number of the calculations in Tables 4.5-4.8 were based on expressions for single microstrips and striplines. These expressions, although *not* representative of the coupled WSIC structures, were included for reference. For each PIQ structure, three of the characteristic impedance estimates were based on FDM simulations. The first FDM-based estimate was the result of two FDM simulations. These simulations created odd- and even-mode characteristic impedance estimates, as defined in Table 4.4. The resultant potential distribution of a typical FDM simulation in an odd-mode configuration is shown in Figure 4.8. The second FDM-based estimate was derived from a simulation based on definition 13 from Table 4.4. A final FDM-based estimate used an additional FDM simulation to produce the capacitance coefficients, comprising the matrix  $[C]$ , as required by Equations 2.29-2.30. Next,

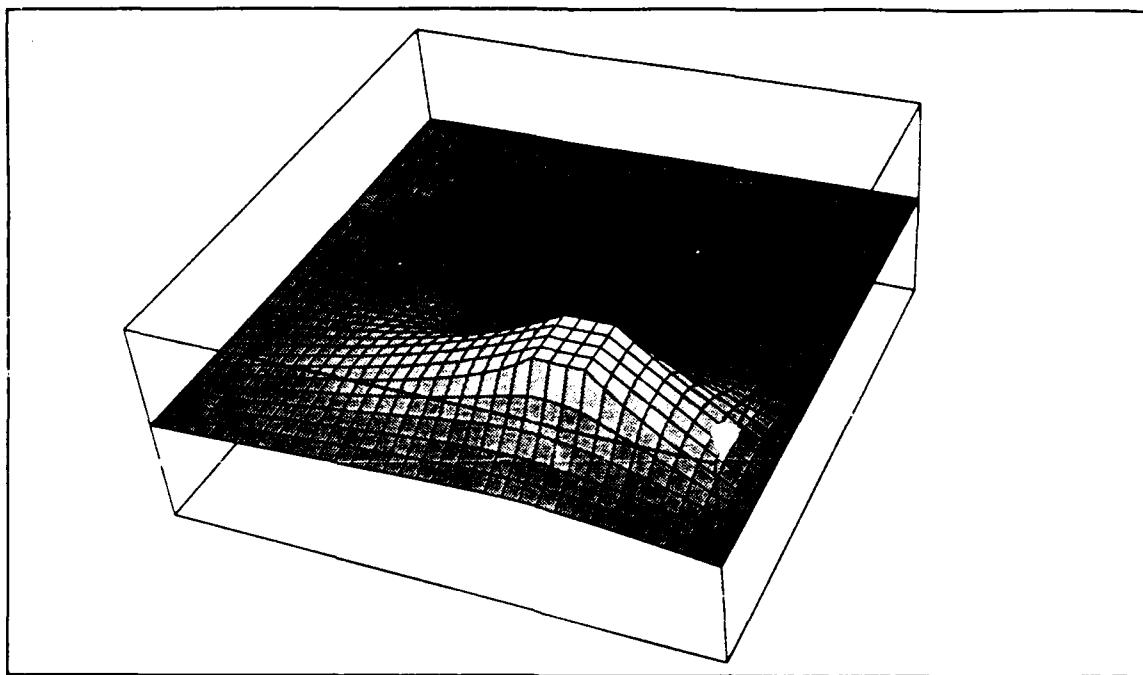


Figure 4.8. Voltage distribution in a convergent FDM simulation (odd-mode) for an ECS structure (number 48 from PIQ wafer).

these equations were solved using Mathematica routines as described in the subsequent characteristic impedance measurement results subsection. The appropriate current and voltage components from the matrix solutions were then combined to form the final FDM-based estimate of the characteristic impedance.

*Three-Conductor Structure Results.* The three-conductor structural models were based on assumptions similar to those used in the two-conductor case. However, unlike the two-conductor case, only the FDM method was used to produce an estimate of the characteristic impedance. For the FDM simulations, the 65th structure from the PIQ wafer and the 101st structure from the PIQ and BCB wafers were analyzed. The analysis was based on design specifications.

Based on design specifications, the 65th structure most closely resembled an embedded ECM, except that the dielectric composition was inhomogeneous (in accordance with Figure 3.1). The representative transverse cross-section for this



Table 4.5. Analytic characteristic impedance results for certain 10  $\mu\text{m}$  wide ECS structures from the PIQ wafer. All impedances are in ohms.

Structure	Technique	$Z_{O,even}$	$Z_{O,odd}$	$Z_O$
034-041	LINECALC	44.09	44.00	44.05
034-041	Equation 2.50	n/a	n/a	60.81
034-041	Equation 2.51	n/a	n/a	60.48
034-041	Equation 2.55	n/a	n/a	60.81
034-041	Equation 2.62	n/a	n/a	51.28
034-041	Equation 2.63	n/a	n/a	55.76
034-041	Equation 2.64	n/a	n/a	41.42
034-041	Equation 2.65	n/a	n/a	46.86
034-041	Equation 2.66	n/a	n/a	41.64
034-041	Equation 2.73	55.85	55.70	55.76
034-041	Equation 2.75	44.09	44.00	44.05
034-041	FDM	47.73	48.22	47.97
034-041	FDM <sup>1</sup>	n/a	n/a	48.44
034-041	FDM <sup>2</sup>	n/a	n/a	48.01

<sup>1</sup>Using special definition 13 from Table 4.4.

<sup>2</sup>Using definitions 4 and 7 from Table 4.4 in conjunction with Equations 2.29-2.30, subject to the appropriate boundary conditions, and Equation 2.35.

Table 4.6. Analytic characteristic impedance results for certain 25  $\mu\text{m}$  wide ECS structures from the PIQ wafer. All impedances are in ohms.

Structure	Technique	$Z_{O,even}$	$Z_{O,odd}$	$Z_O$
104-111	LINECALC	25.83	25.44	25.63
104-111	Equation 2.50	n/a	n/a	33.31
104-111	Equation 2.51	n/a	n/a	33.46
104-111	Equation 2.55	n/a	n/a	33.83
104-111	Equation 2.62	n/a	n/a	29.36
104-111	Equation 2.63	n/a	n/a	29.21
104-111	Equation 2.64	n/a	n/a	28.56
104-111	Equation 2.65	n/a	n/a	26.02
104-111	Equation 2.66	n/a	n/a	23.67
104-111	Equation 2.73	29.41	29.00	29.20
104-111	Equation 2.75	25.83	25.44	25.63
104-111	FDM	28.20	27.55	27.87
104-111	FDM <sup>1</sup>	n/a	n/a	27.96
104-111	FDM <sup>2</sup>	n/a	n/a	27.93

<sup>1</sup>Using special definition 13 from Table 4.4.

<sup>2</sup>Using definitions 4 and 7 from Table 4.4 in conjunction with Equations 2.29-2.30, subject to the appropriate boundary conditions, and Equation 2.35.

Table 4.7. Analytic characteristic impedance results for certain 10  $\mu\text{m}$  wide ECS structures from the BCB wafer. All impedances are in ohms.

Structure	Technique	$Z_{O,even}$	$Z_{O,odd}$	$Z_O$
034-041	Equation 2.50	n/a	n/a	77.82
034-041	Equation 2.51	n/a	n/a	77.19
034-041	Equation 2.55	n/a	n/a	77.78
034-041	Equation 2.62	n/a	n/a	66.90
034-041	Equation 2.63	n/a	n/a	71.85
034-041	Equation 2.64	n/a	n/a	50.59
034-041	Equation 2.65	n/a	n/a	61.65
034-041	Equation 2.66	n/a	n/a	52.75
034-041	Equation 2.73	72.18	71.52	71.85
034-041	Equation 2.75	57.68	57.15	57.41
034-041	FDM	62.10	60.95	61.31
034-041	FDM <sup>1</sup>	n/a	n/a	61.31
034-041	FDM <sup>2</sup>	n/a	n/a	68.21

<sup>1</sup>Using special definition 13 from Table 4.1.

<sup>2</sup>Using definitions 4 and 7 from Table 4.1 in conjunction with Equations 2.29-2.30, subject to the appropriate boundary conditions, and Equation 2.35.

Table 4.8. Analytic characteristic impedance results for certain 25  $\mu\text{m}$  wide ECS structures from the BCB wafer. All impedances in ohms.

Structure	Technique	$Z_{O,even}$	$Z_{O,odd}$	$Z_O$
104-111	Equation 2.50	n/a	n/a	45.28
104-111	Equation 2.51	n/a	n/a	45.15
104-111	Equation 2.55	n/a	n/a	45.02
104-111	Equation 2.62	n/a	n/a	39.73
104-111	Equation 2.63	n/a	n/a	39.56
104-111	Equation 2.64	n/a	n/a	37.56
104-111	Equation 2.65	n/a	n/a	35.98
104-111	Equation 2.66	n/a	n/a	31.91
104-111	Equation 2.73	40.28	38.81	39.54
104-111	Equation 2.75	35.85	34.52	35.17
104-111	FDM <sup>1</sup>	36.92	35.40	36.14
104-111	FDM <sup>2</sup>	n/a	n/a	40.250

<sup>1</sup>Using special definition 13 from Table 4.4.

<sup>2</sup>Using definitions 4 and 7 from Table 4.4 in conjunction with Equations 2.29-2.30, subject to the appropriate boundary conditions, and Equation 2.35.

structure is shown in Figure 4.9a. The following geometric dimensions were assumed:  $w=10\text{ }\mu\text{m}$ ,  $h=6\text{ }\mu\text{m}$  (measured with respect to the  $\text{SiO}_2$  interface),  $s=10\text{ }\mu\text{m}$ ,  $t=2.5\text{ }\mu\text{m}$ , the thickness of the  $\text{SiO}_2$  layer =  $1\text{ }\mu\text{m}$ , and the distance from the top of the active conductors to the atmospheric interface =  $18\text{ }\mu\text{m}$ . Even for representative three-conductor ECS structures (for example, the 72nd structure), no correlation with any Chapter 2 expression was possible, since these expressions did not treat three-conductor structures. Hence, numerical simulations were required to obtain estimates for the characteristic impedance.

The FDM simulation of the 65th structure considered only the PIQ wafer. In the FDM simulation of Figure 4.9, the conductivity of the the silicon substrate was assumed to be infinite; that is, the substrate was treated as a ground plane. The horizontal sidewalls were assumed to be of infinite extent, as were the vertical atmospheric interface. However, the numerical treatment of the two cases differed. For the horizontal sidewalls, the technique described in Appendix E was implemented. On the other hand, the vertical atmospheric interface was terminated in a Neumann boundary condition. In this case, a symmetry plane was assumed at the vertical end of the simulation domain. The effects of the resulting image were deemed to be negligible. The resulting FDM simulation possessed the appearance of Figure 4.9b.

Two different characteristic impedance simulations were performed with the Figure 4.9b model. The resultant characteristic impedances, presented in Table 4.9, were based on the Equation 2.22 definition of characteristic impedance. For the impedance defined on the left conductor, the associated values of  $C'$  and  $C_1$  were found to be  $9.985 \times 10^{-11}$  and  $3.000 \times 10^{-11}$  farads/m, respectively. For the center conductor, the values of  $C'$  and  $C_1$  were found to be  $9.379 \times 10^{-11}$  and  $2.836 \times 10^{-11}$  farads/m, respectively.

For the 101st structure on the PIQ wafer, the following parameters were assumed:  $w=25\text{ }\mu\text{m}$ ,  $h=6\text{ }\mu\text{m}$ ,  $b=20.5\text{ }\mu\text{m}$ ,  $s=11\text{ }\mu\text{m}$ , and  $\epsilon_R=3.4$ . The results of the FDM simulations are presented in Table 4.9. Unlike the 65th structure, the center

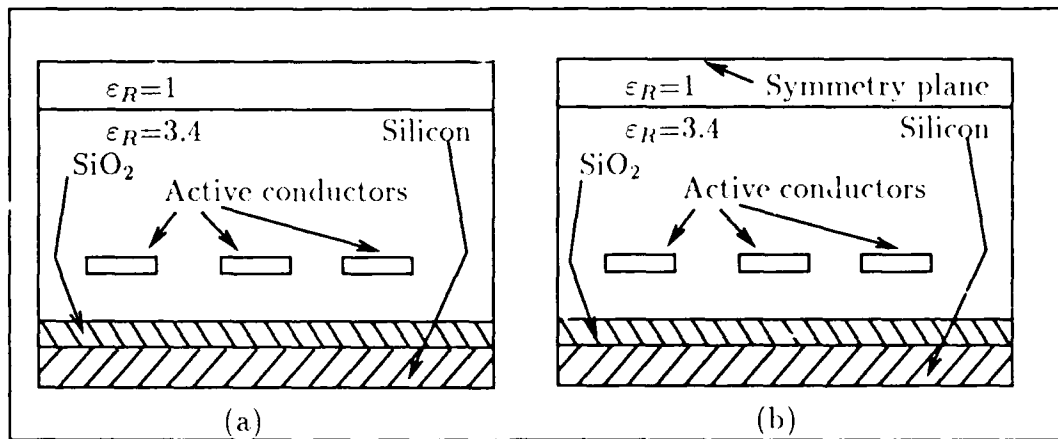


Figure 4.9. Transverse cross-section of the 65th structure from the PIQ wafer.

Table 4.9. Results of the FDM simulations for the three-conductor structures. All impedances are in ohms.

Structure	Table 4.4	$Z_0$ (PIQ)	$Z_0$ (BCB)
65 (left)	14	60.90	n/a
65 (center)	16	64.63	n/a
101	15	27.03	36.13

conductor of the 101st structure was fabricated as a ground conductor. That is, the center conductor of this structure was permanently connected to the ground plane. Hence, although the 101st structure possessed three conductors, only two of these were usable as active conductors.

*Coplanar Waveguide Results.* The coplanar waveguide structures were modeled using closed form expressions and the LINECALC program. FDM simulations were not attempted for the CPW structures. With the exception of the height ( $h$ ) above the substrate, the parameters used for the analyses were based on the design specifications. The analyses considered the structures numbered 33, 62, and 91 from the PIQ and BCB wafers. For the 33rd structure on the PIQ wafer,

the following specifications were assumed:  $w=25\text{ }\mu\text{m}$ ,  $t=2.5\text{ }\mu\text{m}$ ,  $h=7\text{ }\mu\text{m}$ ,  $s=26\text{ }\mu\text{m}$ , and  $\epsilon_R=3.4$ . For the 62nd structure on the PIQ wafer, the following specifications were assumed:  $w=10\text{ }\mu\text{m}$ ,  $t=2.5\text{ }\mu\text{m}$ ,  $h=7\text{ }\mu\text{m}$ ,  $s=18\text{ }\mu\text{m}$ , and  $\epsilon_R=3.4$ . For the 91st structure on the PIQ wafer, the following specifications were assumed:  $w=25\text{ }\mu\text{m}$ ,  $t=2.5\text{ }\mu\text{m}$ ,  $h=7\text{ }\mu\text{m}$ ,  $s=18\text{ }\mu\text{m}$ , and  $\epsilon_R=3.4$ . For the BCB wafers, the specifications of the respective structures were assumed to be identical, except that the height above ground plane was assumed to be  $h=9\text{ }\mu\text{m}$ , and the relative permittivity was assumed to be  $\epsilon_R=2.75$ . The results of these analyses are presented in Table 4.10. It is important to recognize that these analyses are approximate at best, since they are based on a homogeneous dielectric fill between the active conductor and upper ground plane, as well as the lower ground plane (one of the closed-form expressions does not consider even the existence of a ground plane below.) However, as shown in Figure 3.1, the homogeneous composition assumption is not correct, due to the  $\text{SiO}_2$  layer beneath the primary dielectric layer. Furthermore, the "ground plane" beneath the  $\text{SiO}_2$  dielectric layer is actually the semiconductor substrate, which does not possess the high conductivity normally associated with the ground plane materials. These restrictions were similarly applied to the other WSIC structures which did not have ground plane surfaces at the Metal 1 level. Unfortunately, the analytic results were varied and inconsistent for the CPW structures.

*Measured Characteristic Impedance Results.* The technique described in Chapter 3 for measuring the characteristic impedance was applied to the structures listed in Table 4.3. Using the HP 4191A impedance analyzer, the measurement data sets were collected over the frequency range spanning 1 MHz–700 MHz. For greater resolution, but over a narrower frequency range, the HP 4194A was used to gather data over the frequency range 1 MHz–13 MHz. The measurement structures were chosen from those screened in the initial continuity measurements, and they represent most of the structural types found on the test wafers.

The typical plot of a characteristic impedance magnitude and phase measurement

Table 4.10. Analytic characteristic impedance results for coplanar waveguide structures. All impedances are in ohms.

Structure	Technique	$Z_o(\text{PIQ})$	$Z_o(\text{BCB})$
33	LINECALC	38.92	50.46
33	Equation 2.67 with Equation 2.69	105.5	114.3
33	Equation 2.67 with Equation 2.70	139.7	139.4
33	Equation 2.67 with Equation 2.71	128.00	106.0
33	Equation 2.72	111.41	92.61
62	LINECALC	68.47	83.99
62	Equation 2.67 with Equation 2.69	124.4	134.8
62	Equation 2.67 with Equation 2.70	158.3	132.7
62	Equation 2.67 with Equation 2.71	99.56	83.16
62	Equation 2.72	81.56	68.24
91	LINECALC	38.28	49.43
91	Equation 2.67 with Equation 2.69	93.98	101.8
91	Equation 2.67 with Equation 2.70	122.0	121.8
91	Equation 2.67 with Equation 2.71	80.43	64.72
91	Equation 2.72	67.9	54.83



is shown in Figure 4.10. The structure used to obtain this plot was the 36th structure from the second PIQ wafer (two-conductor ECS). The measurement configuration used for this structure most closely resembled the Table 4.4, entry 13 definition. That is, one conductor of the structure was used for the measurement, while the other conductor was left floating. Unfortunately, the measurement technique used revealed a wide variance in the value of the characteristic impedance over the frequency range considered, much more than would be caused by any of the geometrical or material dispersion mechanisms discussed in Chapter 2.

The reason for the impedance variation with frequency was not immediately apparent. One suggestion, forwarded by Chipman, was that if the measurement frequency was too low, then the resultant values of  $Z_{SC}$  and  $Z_{OC}$  would fall outside the range where reliable measurements could be made. He further suggested that the measurements should be made at frequencies corresponding to odd-integer multiples of one-eighth of the transmission line's wavelength (16:134). Based on this guideline, and the definitions of  $\beta$  and  $\lambda$ , the following expression can be derived (as shown in Appendix G):

$$f_n = \frac{c}{4} \sqrt{\frac{n}{\pi \ell \epsilon_{R,eff}}} \quad (4.2)$$

where  $f_n$  is the frequency corresponding to the  $n$ th multiple of  $\lambda/8$  ( $n=1, 3, 5, 7, 9$ ). Using  $n = 1$ , the first applicable frequency for the PIQ ECS structures occurs at 72.6 MHz, and, for the BCB ECS structures, the first applicable frequency occurs at 80.0 MHz. These values correspond to the  $f_1$  frequency for the respective materials. Although the effective relative permittivity ( $\epsilon_{R,eff}$ ) varies among structural types, the  $f_1$  frequencies were taken as "guideline" frequencies for the other structures, including the coplanar waveguides. Based on Chipman's suggestion, measurements near  $f_1$ ,  $f_3$ ,  $f_5$ , and higher odd-integer multiples of  $\lambda/8$  would be more accurate, since the impedance values of  $Z_{OC}$  and  $Z_{SC}$  would be closer to the anticipated value of  $Z_0$ . Unfortunately, the Figure 4.10 plot and other measurements did not manifest stable values for  $Z_0$  at these frequencies.

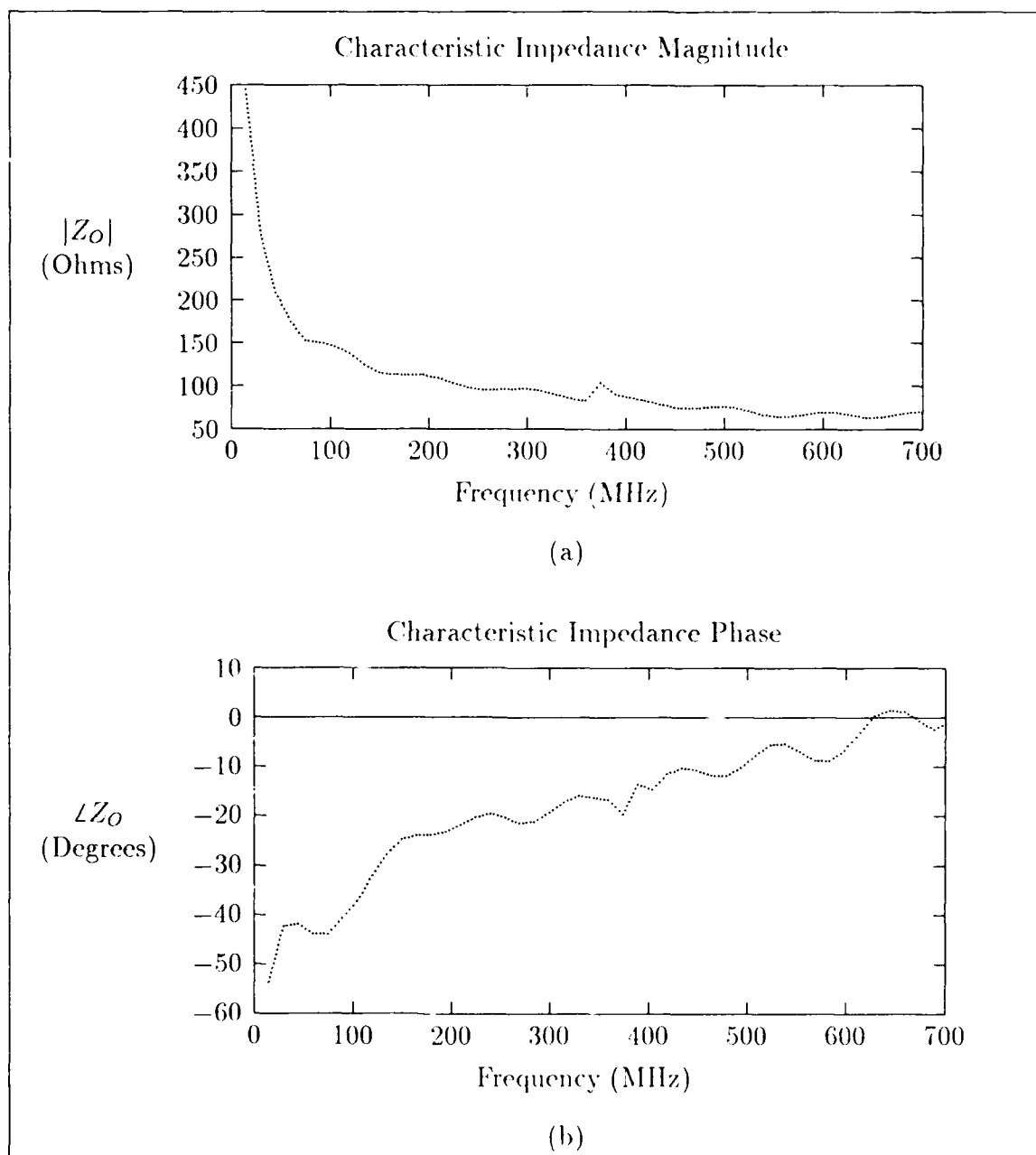


Figure 4.10. Magnitude and phase of characteristic impedance, measured from the 36th structure (two-conductor ECS, with  $w=10\ \mu\text{m}$ ,  $s=38\ \mu\text{m}$ ,  $b=20.5\ \mu\text{m}$ ) on the PIQ wafer. (a) Magnitude. (b) Phase.

A more critical examination of Equation 2.35 was undertaken in an attempt to improve the correlation between the theory and measurement of the characteristic impedance. From the relationships (16:134)

$$Z_{SC} = Z_O \tanh(\beta\ell) \quad (4.3)$$

$$\text{and } Z_{OC} = Z_O \coth(\beta\ell) \quad (4.4)$$

it is apparent that Equation 2.35 can be derived through direct multiplication:

$$Z_{SC} Z_{OC} = \tanh(\beta\ell) \coth(\beta\ell) (Z_O)^2 \quad (4.5)$$

By taking the square root of Equation 4.5, the original relationship (Equation 2.35) is derived. Of course, the  $\tanh(\beta\ell)$  term is undefined at dc, but it is apparently a removable discontinuity. Furthermore, if *ideal* short circuits and open circuits are not achieved at the ends of the line, then the measured values of the impedance are not reflected by Equations 4.3 and 4.4.

To further investigate the behavior of the characteristic impedance in its measurement configurations, a number of simulations were undertaken. The simulations were performed to determine the "looking-in" or driving point impedance of a WSIC transmission line structure over the frequency range of 1–700 MHz. Thus, the simulation was designed to coincide with the measurement configurations, and it was evaluated over the same frequency range. Each of the simulations were based on the solution of the multi-conductor telegrapher's equations (Equations 2.29 and 2.30), subject to the appropriate boundary conditions (as discussed in Appendix F). Each overall simulation separately considered two different measurement configurations (one to determine  $Z_{SC}$  and one for  $Z_{OC}$ ) and combined the results using Equation 2.35 to form the characteristic impedance. Common to all simulations were the  $[C]$ ,  $[L]$ , and  $[R]$  matrices. The  $[C]$  and  $[L]$  matrices were found by FDM simulations, while the  $[R]$  matrix was estimated using Equation 4.1.

The particular example considered was the 36th structure from the 10 cm block on the PIQ wafer. Through a finite difference simulation, the self-capacitance coefficients ( $C_{11} = C_{22}$ ) were determined to be  $1.281 \times 10^{-10}$  farads/m, and the off-diagonal coefficients ( $C_{12} = C_{21}$ ) were estimated as  $(-1.038 \times 10^{-12})$  farads/m. Given these values, the  $[C]$  and  $[L]$  matrices are uniquely determined. The diagonal components of the  $[R]$  matrix were estimated at  $1000 \Omega/\text{m}$ , based on the calculations described for the continuity measurement (using Equation 4.1).

Three simulations were attempted:

1. Lossless ( $[R] = [0]$ )
2. Lossless plus random noise (maximum noise amplitude  $1 \Omega$ ), where the noise was summed as:  $Z_{SC,eff} = Z_{SC} + \text{Random noise}$ .
3. Lossy.

The results of the first two simulations are shown in Figure 4.11. The first simulation revealed a constant characteristic impedance value of  $48.01 \Omega$ . Thus, consistent with the limiting behavior of Equation 2.35, the  $\tanh(\beta\ell)$  term was found to be constant as  $\beta \rightarrow 0$ . When random noise was introduced, as was done in the second simulation, the calculated value of  $Z_O$  was no longer constant across the frequency spectrum. The fluctuations in value across the frequency range revealed two features of possible interest. The first feature was an increase in the value of  $Z_O$  at lower frequencies. This increase reflected the trend found in the measurement data, although the magnitude of the increase was too small in the simulation to account for that found in the measurement data. The second feature was a resonance in the vicinity of 400 MHz. The frequency where the resonance occurs seems to coincide with the aberration in the measured  $Z_O$  magnitude data near the same frequency. Besides these features, no other systematic trends were evident in the random simulation.

However, in the third simulation, a systematic trend was found. The results of a lossy simulation are shown in Figure 4.12, along with those of the measured

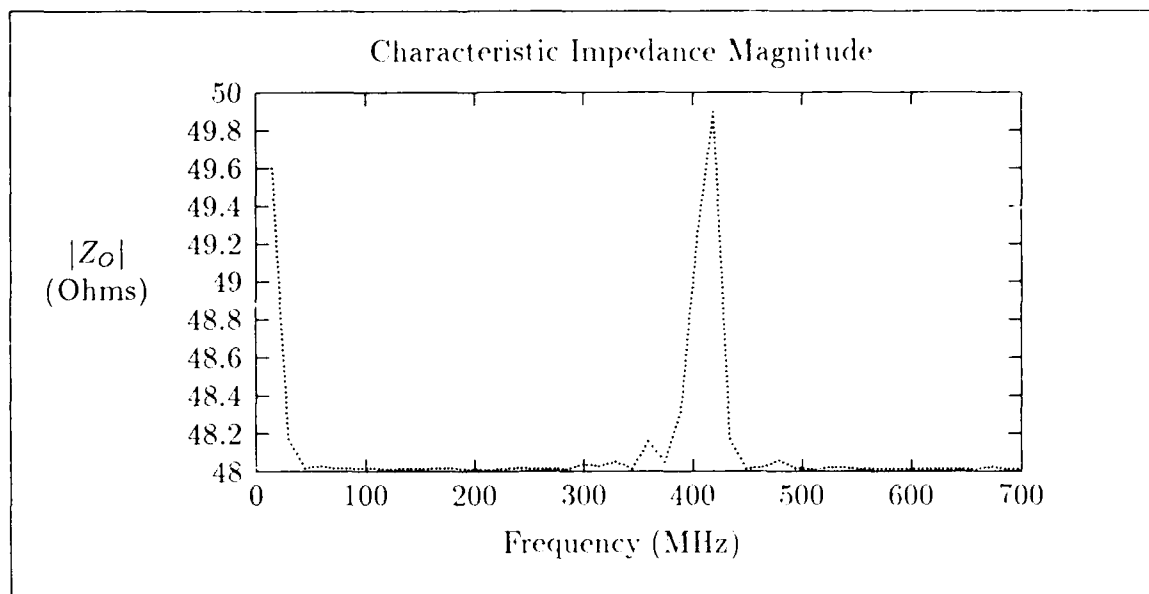


Figure 4.11. Results of two lossless simulations of the 36th structure from the PIQ wafer. The first simulation produced a constant  $48.01 \Omega$  across the frequency range (and is obscured by the second simulation), while the second produced an unusual variation across the frequency range.

characteristic impedance and those of the first simulation. As evident in this figure, the simulated characteristic impedance displays a behavior similar to that of the measurement, while neither the lossy simulation nor the measurement actually ever achieved the value of  $Z_C$  predicted by the lossless simulation. Apparently, the presence of loss in the transmission line created the behavior displayed in the measured data. In fact, it appeared that the lossless values of  $Z_O$  might be approached in a high-frequency limit, although this result would probably not be found in practice, due to skin effect losses and geometric dispersions, which were not considered by the simulations.

Thus, all other things being equal, the Chapter 3 measurement technique will not produce a constant value of  $Z_O$  for a lossy line over a given frequency range. Furthermore, the technique appears to produce values of impedance which asymptotically approach the characteristic impedance at a higher frequency. Unfortunately, the frequency at which the limiting behavior is sufficiently developed

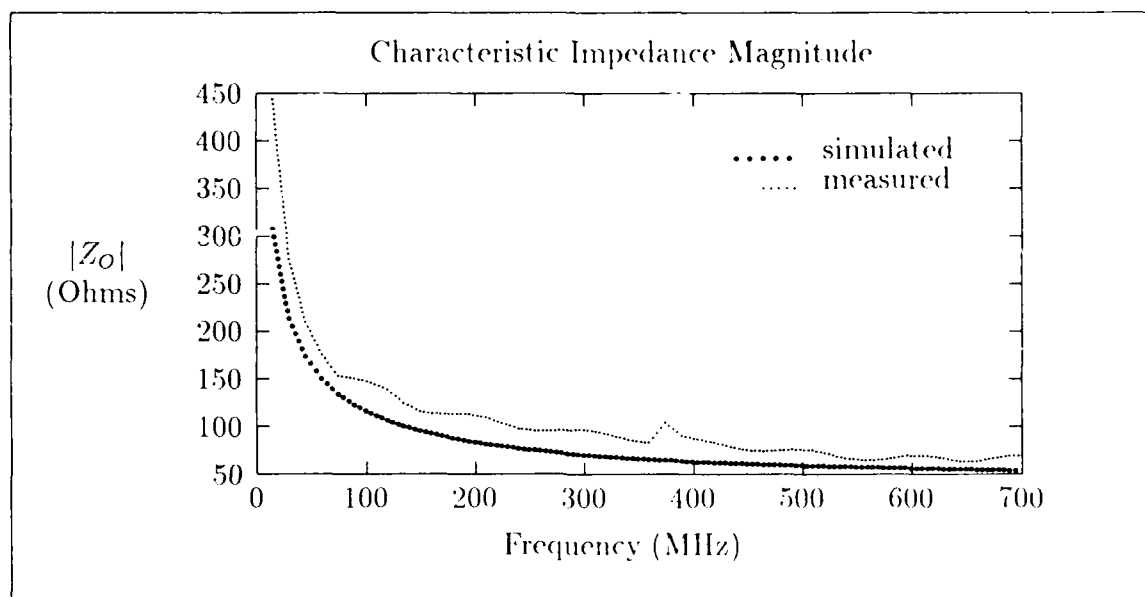


Figure 4.12. Results of a lossy simulation of the 36th structure compared with the measured values.

could not be measured with the available test equipment. In fact, it is not certain that an asymptotic value would be reached, even if such equipment were available, since other loss mechanisms may become dominant at these higher frequencies. In particular, the skin effect losses and geometric dispersion at these frequencies may further obscure such asymptotes.

As a further comparison, the measured and calculated values of the open-circuit ( $Z_{OC}$ ) and short-circuit ( $Z_{SC}$ ) driving-point impedances are shown in Figure 4.13. Apparently, the larger discrepancy occurred in the short-circuit measurement, which implies that the electrical measurement configurations which were previously assumed to have been short-circuits, were not. In fact, the measured values of  $Z_{SC}$  and  $Z_{OC}$  coincided over much of the frequency range. Only at frequencies below 200 MHz was a significant difference shown.

Although a true characteristic impedance was not found in the measurement process, a simple extrapolation procedure was applied to the measurement data to produce an estimation of the characteristic impedance. Since the lossy simulations

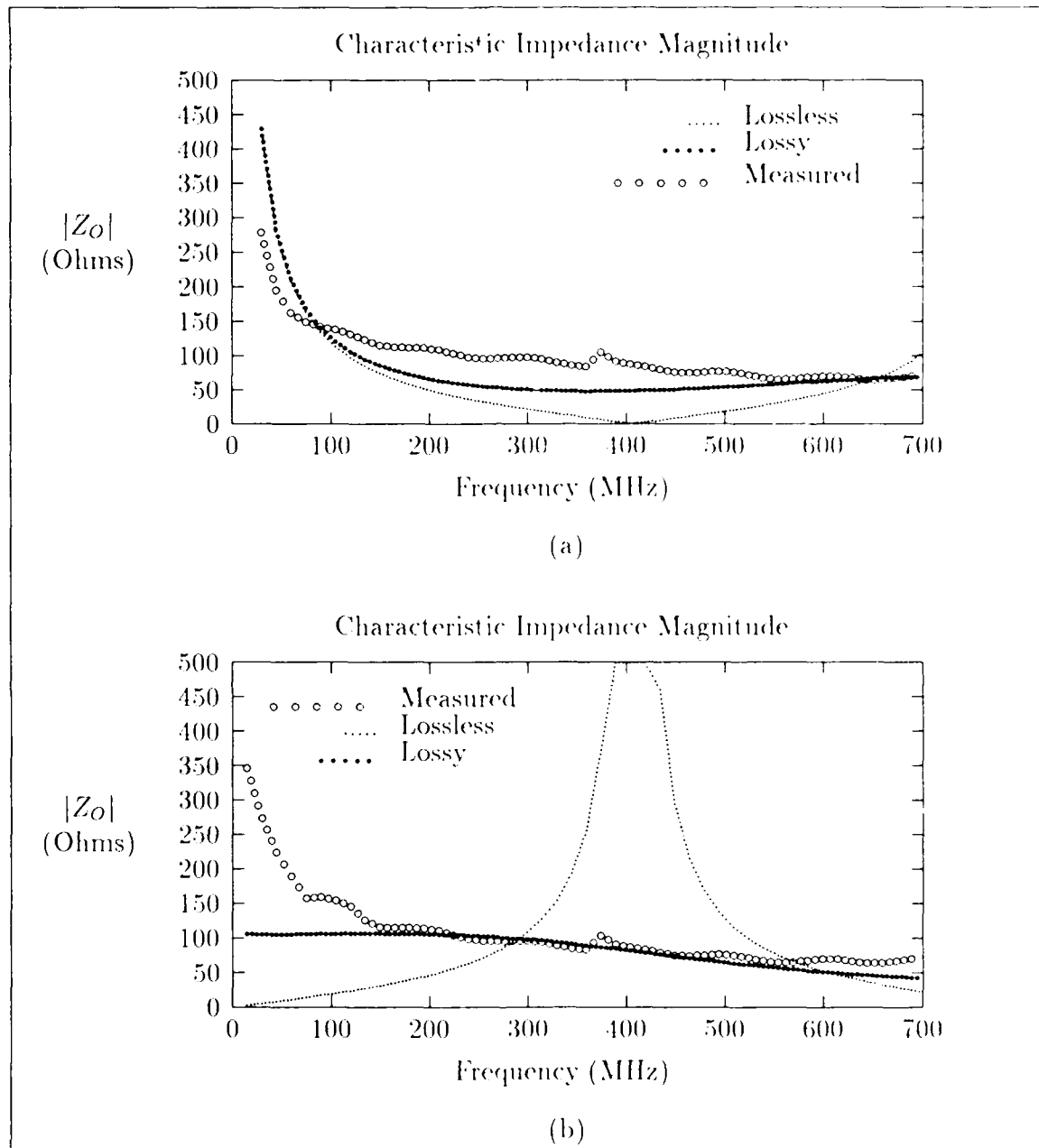


Figure 4.13. Comparisons between simulated and measured driving point impedances in open-circuit and short-circuit configurations. (a) Open-circuit configuration, illustrating lossless simulation, lossy simulation, and measured results. (b) Short-circuit configuration, illustrating lossless simulation, lossy simulation, and measured results.

produced a behavior similar to the measured lines, and since the lossless simulation produced a known characteristic impedance, the extrapolation technique was developed using the lossy simulation. If the data from the lossy simulation could be used to approximate the *known* value of the characteristic impedance from the lossless simulation, then the same technique could be applied to the measured data. The resulting approximation would then be considered to be the value of the characteristic impedance for the structure under consideration.

The extrapolation technique was based on a linear fit of the last twenty points of the data set (those points corresponding to the highest frequencies) in the lossy simulation. The number of points used was chosen arbitrarily. All frequency points of the simulation were not used, since the overall impedance curve was non-linear and would, therefore, introduce excessive error in the linear approximation. Using resident Mathematica curve-fitting routines, the linear model produced, using the last 20 points of data from the lossy simulation, the following result:

$$Z(f) = 73.8 - 0.0282f \quad (4.6)$$

where  $Z(f)$  is the impedance in ohms and  $f$  is the frequency in MHz. Using the known characteristic impedance from the lossless simulation ( $48.01 \Omega$ ), the frequency  $f$  where the linear model yields a match, was defined to be a "crossing frequency"  $f_{cross}$ . Solving Equation 4.6,  $f_{cross}$  was determined to be approximately 913 MHz. When the last 20 points of data from the measurement data were modeled with the Mathematica routines, the following model was produced:

$$Z(f) = 97.79 - 0.048f. \quad (4.7)$$

At 913 MHz, which was assumed to be the crossing frequency for the measurement data, the resulting approximation produced a value of  $54.079 \Omega$  for the characteristic impedance of the 36th structure on the PIQ wafer.



To validate such an approximation, several questions should be addressed:

1. What is being approximated?
2. How representative is the value of characteristic impedance of a lossless line to that of lossy line?
3. What other error sources are present in such measurements, and what are the resulting approximations which need to be used to produce a single, "boiled-down" value?

The first question is one of definition. As previously discussed, the characteristic impedance measured was not that which is typically described for ECS structures, but similar to that of a single stripline conductor. When the measurement was performed, the second conductor was left floating, and it was thereby excluded from electrical connection in the measurement configuration. However, the electrical interaction of the conductor affected the measurement, and it had to be accounted for. The definitions in Table 4.4 (entry 13, in particular) attempted to provide appropriate definitions for this measurement condition and similar ones for other structures.

The second question regards the approximation of a characteristic impedance value in a lossy line compared to the value computed for a lossless line. This application was necessary to implement the previously described extrapolation technique. The values of the characteristic impedance in both cases are not equal in a strict sense, as implied in the Equation 2.35 definition for single-conductor lines. Of course, as afforded by examination of Equation 2.35, the approximation becomes more accurate as the frequency of simulation is advanced. At sufficiently high frequencies, the lossy line is closely approximated by lossless line calculations. This implicit assumption was reinforced by LINECALC simulations of the transmission line structures described in the previous subsection. In each case, the introduction of the appropriate conductor and dielectric loss parameters did not produce a significant change in the estimated values of characteristic impedance. In fact, the asymptotic behavior is probably the strongest evidence that the characteristic impedance of a lossy

transmission line approaches that of a comparable lossless line at a sufficiently high frequency (skin effect losses and dispersion notwithstanding).

The third question applies to other errors which might have been present in the measurement, in the simulation, and in the ensuing approximations. The measurement errors involved could have come from a variety of sources: calibration, contact repeatability, and equipment accuracy. As discussed in Chapter 3, three calibrations, (zero  $\Omega$ ,  $\infty \Omega$ , and 50  $\Omega$ ), were used. These standards were based on a probe contacting an aluminum surface, a probe suspended in air, and a customized 50  $\Omega$  standard, respectively. Of course, the reliability of the first two calibrations might be questioned, since the aluminum surface has a non-zero resistance, and the suspended probe has a finite impedance at non-zero frequencies. However, since these calibrations were made in the same environment used for measurement, and they were performed to de-embed the environmental effects from the measurement device under test, the error associated with the calibrations was believed to be minimal. Unfortunately, none of the appropriate standard calibrations supplied with other microwave probes (such as the Cascade probes described in (78)) existed for the probes used in this research effort. The probing of contact pads introduced a small error, since no two probing operations occur in the same position with the same force. The lack of repeatability is further aggravated by the deformation of the contact pads after each probing operation. Again, the error associated with repeatability was believed to be small, since overall continuity of the contact could be verified prior to measurement through the use of a multimeter. Finally, the equipment itself could be expected to introduce measurement errors. Based on measurements performed on the 50  $\Omega$  standard after calibration, the impedance analyzer used was accurate to within one ohm. Hence, although several error sources existed within the measurement environment, the contributions of most of these sources was believed to be small. However, the error sources were impossible to quantify without a "probe-able" reference test structure.

Table 4.11. Results of the characteristic impedance measurements after processing.

Structure	Wafer	Table 4.4	$Z_0$
10 $\mu$ m CPW (33)	PIQ	10	31.05 $\Omega$
10 $\mu$ m ECS (36)	BCB	13	73.58 $\Omega$
10 $\mu$ m ECS (36)	PIQ	13	54.80 $\Omega$
10 $\mu$ m CPW (62)	PIQ	10	59.46 $\Omega$
10 $\mu$ m ECS (65)	PIQ	14	38.02 $\Omega$
10 $\mu$ m ECS (65)	PIQ	16	48.29 $\Omega$
25 $\mu$ m CPW (91)	BCB	10	45.54 $\Omega$
25 $\mu$ m CPW (91)	PIQ	10	37.05 $\Omega$
25 $\mu$ m ECS (100)	BCB	15	38.91 $\Omega$
25 $\mu$ m ECS (100)	PIQ	15	31.22 $\Omega$
25 $\mu$ m ECS (104)	PIQ	13	45.85 $\Omega$
25 $\mu$ m ECS (109)	BCB	13	53.82 $\Omega$

In addition to the example structure previously discussed, several other representative structures on the PIQ and BCB wafers were measured using the Chapter 3 technique. The aforementioned extrapolation procedure was similarly applied to these structures to obtain an estimate of the characteristic impedance for each structure. Table 4.11 summarizes the structures measured and their estimated characteristic impedances. The definition from Table 4.4 associated with the impedance measurement is also provided. The measured impedance curves for these structures appears in Appendix G. Since FDM simulations were not performed on a number of the structures in Table 4.11, the same frequency determined for the example structure (913 MHz) was used for the frequency in the linearized impedance approximations of the "static" characteristic impedance values. The following paragraphs provide further discussion for the particular structural classes measured.

*Two-Conductor Structure Results.* The two-conductor structures measured from the PIQ wafers were the 36th structure and the 104th structure. From the BCB wafer, the 36th structure and the 109th structure were measured. Based on the specifications, the 36th and 109th structures most closely represent the ECS structures, while the 104th structure more closely approximated an embedded, ECM structure. Both ground plane surfaces of the 36th and 109th structures were solid, while for the 104th structure, the ground plane below was meshed. In the FDM simulations undertaken, only the ECS structures were modeled.

The 36th structure was modeled in the previous section as an ideal ECS with ground planes of infinite extent. In most closed form expressions for striplines, the height parameter ( $h$ ) was seldom used. Rather, the ground plane separation distance was the more important parameter. The superficial ground plane was electrically isolated from the bottom ground plane. Electrical grounding of this plane was achieved by connecting a grounded, passive probe to the access pad, which was adjacent to the access pads of the active conductor.

Due to the measurement procedure used, the even- and odd- mode impedances could not be directly measured. Hence, the most approximate comparison was achieved by simulating the measurement configuration in the FDM simulations and applying an appropriate definition of the characteristic impedance. Thus, the results in Tables 4.5 and 4.7, which were believed to be most approximate, were those of the FDM simulations. As such, the measurements for the 36th structure were found to be 11.6 % higher than the special FDM analysis results for the PIQ wafer, and 7.3 % higher for the BCB wafer. Interestingly, the value of  $Z_0$  given by Equation 2.73 combined with Equation 2.35 formed a more accurate estimate for both wafers (within 1.75 % for the PIQ wafer and within 2.35 % for the BCB wafer), even though Equation 2.73 was based on a *zero-thickness* structure. For the 104th structure from the PIQ wafer, all analytic approaches produced characteristic impedance estimates much lower than the measured value of 45.85  $\Omega$ . A discrepancy *was* expected, since

the 104th structure was not a true ECS structure. For the 109th structure on the BCB wafer, which *was* much more representative of an ECS structure, the discrepancy between the analytic results and the measured results also existed. In all cases, the analytic values were lower than the value derived from the measurement. The difference ranged from 26.53 % to 34.65 % using the expressions based on odd- and even-mode impedances for the ECS structures.

Of course, the appropriate validation of these results hinged upon an accurate knowledge of the geometrical and material parameters. Without this data, the determination of error sources could not be established. The specification parameters were judged to be only certain to within approximately 20 %, due to expected fabrication tolerances. Since no destructive testing was undertaken to obtain the geometric dimensions, the associated specification parameters were not physically verified. The material parameters assumed were also uncertain since the dielectrics used did not have large databases of established characterization work as do some of the materials commonly used in microwave work. The appropriate characterization of the materials requires electrical measurements of special structures with closely controlled geometries. For example, several authors have discussed these types of measurements for ring resonators and linear resonators. Additionally, at least one author has suggested the measurement of a resonant cavity formed by plating a wafer of unknown dielectric material on both sides with a conductive film [(29:182-185),(41:28-35),(45:205-212),(68)].

*Three-Conductor Structure Results.* Two three-conductor structures from the PIQ wafers (structures numbered 65 and 100) and one from the BCB wafer (structure numbered 100) were measured. The 100th structure of the test wafers most closely resembled a three-conductor embedded ECM, which was treated as a three-conductor ECS in the previous analysis section. In both cases, the calculated values were lower than the measured results. For the PIQ wafer, the measured results differed from the calculated results by 21 %, while for the BCB wafer,

the difference was 7.7 %. This result follows intuition, since one would expect the impedance of an ECS structure to increase upon the removal of the superficial ground plane.

*Coplanar Waveguide Results.* The CPW structures proved to be the most difficult to correlate. The lack of correlation between analytic methods only exacerbated this problem. The measured results indicated that the CPW structures manifested a characteristic impedance lower than those predicted by any of the analytic methods described in the previous subsection. Of course, some error resulted in the approximation of the inhomogeneous dielectric structure with a homogeneous one. The CPW is not expected to be a prevalent structure in WSIC work, since the wirability goal of 400 lines/cm could not be achieved with such structures. As compared to other measured structures, the impedance was found to be lower across the measured frequency range. Hence, the matching termination for CPWs would necessarily be lower in impedance than those for the other structures.

*Coupling Results.* The gain-phase investigation considered coupling and transmission gain measurements for the various structures, using the Figure 3.16 configurations for analysis and measurement. The initial coupling analysis focussed on a relatively simple structure: the two-conductor ECS. The representative configuration used for the measurement scheme is that shown in Figure 3.16. By achieving a correlation between the theoretical and experimental results for this structure, an analysis of more complicated structures could then be considered. Of the several groups of two-conductor ECS structures, the set comprising the structures numbered 42-48 from the 10 cm block were selected for the initial attempt. The conductor widths ( $10\text{ }\mu\text{m}$ ) and spacings ( $18\text{ }\mu\text{m}$ ) associated with these structures closely approach those dimensions required to achieve the wirability limits identified by McDonald *et al.* (66). A reference structure, based on the Figure 3.20 model was programmed as a LIBRA circuit input file for simulation. Additionally, the multiconductor telegrapher's equations were solved with the appropriate boundary conditions. Of course,

the associated boundary conditions were those corresponding to the measurement configuration. A summary of general boundary conditions for two- and three-conductor structures is presented in Appendix F.

The initial analysis considered the backward-coupled configuration over the frequency range of 1–100 MHz. The measurements were performed using low-impedance ( $50\ \Omega$ ) settings on the HP 4194A input and output channels, producing the measurement configuration which is equivalently shown in Figure 3.16b.

*Analytic Coupling Results.* Several available analytic approaches were used to investigate the coupling gain of two-conductor structures. The first approach used the LIBRA circuit-modeling program to simulate representative ECS structures in their measurement configurations. The simulations were then swept across the frequency range of 1–100 MHz. The second approach was based on the closed-form expressions given in Chapter 3 for an ideal coupler (Equations 3.12–3.14). The final approach involved matrix solutions to the telegrapher's equations (Equations 2.29–2.30). Single-conductor structures, such as CPW structures, were not investigated, since the amount of coupling energy between these and other structures were believed to be very small. Three-conductor structures were also not investigated analytically, since the LIBRA program did not offer three-conductor structures (with the exception of microstrip structures), and no appropriate closed-form expressions were found. The analysis of these structures was feasible through matrix solutions of the associated telegrapher's multi-conductor equation system, although no simulations for three-conductor structures were undertaken.

*LIBRA Analysis.* Using LIBRA, an initial analysis revealed a coupling magnitude characteristic as shown in Figure 4.14. The reference simulation used for this analysis used the following distinguishing characteristics in a LIBRA program listed in Appendix B:

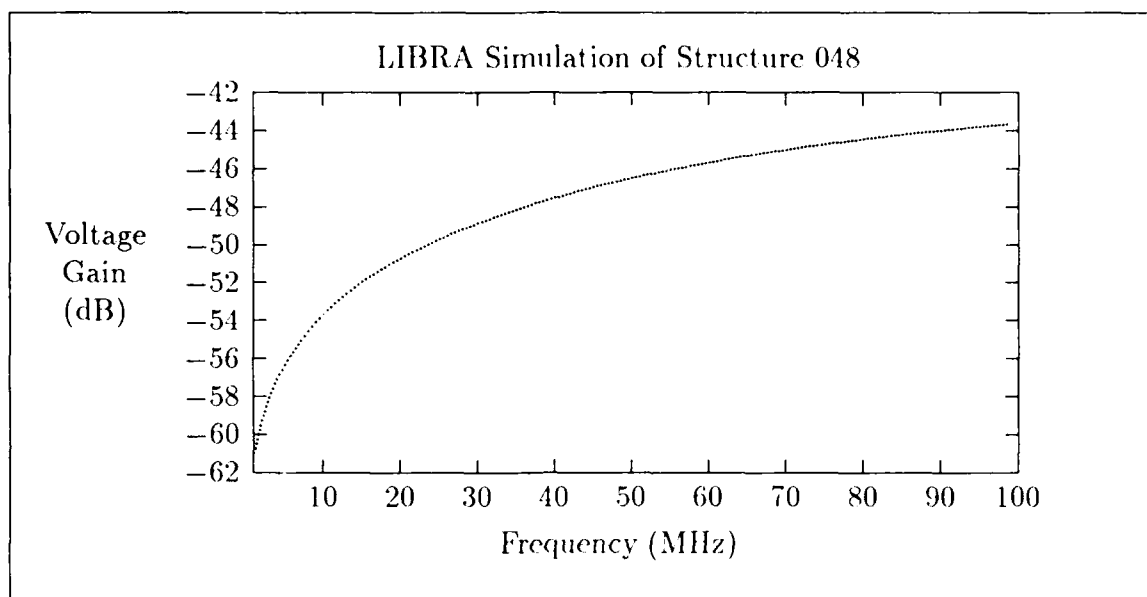


Figure 4.14. The reference LIBRA simulation

1. Conductor material: aluminum.
2. Dielectric relative permittivity ( $\epsilon_R$ ): 3.4.
3. Thickness of conductor ( $t$ ): 2.5  $\mu\text{m}$ .
4. Width of conductor ( $w$ ): 10  $\mu\text{m}$ .
5. Separation of ground planes ( $b$ ): 20.5  $\mu\text{m}$ .
6. Inter-conductor spacing ( $s$ ): 18  $\mu\text{m}$ .

With these parameters used in the Figure 3.20 model, the structures numbered 042–049 on the PIQ wafers were approximated. The simulation, by design, would be most approximate for the structures numbered 042 and 044, since these structures were those which most closely represented true ECS structures. To represent floating lines, terminations with very high impedances ( $> 10 \text{ M}\Omega$ ) were used. For both the source and load terminations, 50  $\Omega$  terminations were programmed to simulate the HP 4194A test channel impedance. The Figure 4.14 plot represents the voltage gain in decibels (dB) of the load compared to the source.



Table 4.12. Analysis of coupling sensitivity to various factors.

Item	"+" Deviation	"-" Deviation	Average	Maximum
$\epsilon_R$	11.8%	36%	2.61 dB	4.36 dB
Conductor thickness ( $\mu\text{m}$ )	20%	20%	0.438 dB	0.5 dB
Conductor width ( $\mu\text{m}$ )	10 %	10 %	0.551 dB	1.00
Ground Plane distance ( $\mu\text{m}$ )	19.4 %	13.9 %	9.27 dB	10.3 dB
Discontinuity Removal	n/a	n/a	<0.0034 dB	0.0034 dB
Ideal Line Model	n/a	n/a	3.46 dB	4.7 dB
Hand Calculation	n/a	n/a	1.48 dB	3.28 dB

The variation in backward-coupling due to differences in the ground plane separation (*b*) was deemed to be one of the most sensitive parameters in the simulation trials. This conclusion was based on a number of simulations which considered variations in relative permittivity of the dielectric, the thickness of the conductors, the width of the conductors, and the presence of discontinuities. Considering the effects of such differences on a simulation using the reference structure, a sensitivity analysis was undertaken. The results of this analysis are summarized in Table 4.12. In each applicable case, the differences in the coupling magnitudes between the two extremes were examined. Thus, the deviations shown constitute an error enveloped about the reference case. In the Table 4.12 entries, where the quantitative parameters were not considered, such as for discontinuities, the deviations are simply obtained as the difference in magnitude between the results of that case with the reference simulation.

The intent of the sensitivity analysis was to provide an insight into which geometrical and material parameters were most influential in changing the coupling gain of a reference structure.

The influence of changes in relative permittivity on the magnitude of the coupling gain were shown to be small. In simulations which varied the relative permittivity from  $\epsilon_R=2.2$  to  $\epsilon_R=3.8$ , the average difference of the coupling gain over the

considered frequency range was 2.61 dB. The dispersion in the dielectric constant of polyimides has been reported to be less than 0.2 over four orders of magnitude, although these results did not consider frequencies above 10 MHz (3:8). Nevertheless, even a dramatic change in dielectric permittivity (greater than 1.0) in the frequency range of 10–100 MHz creates a relatively modest departure from the reference simulation. Similarly, the introduction of small changes to the thickness or width of the conductors in a coupled stripline did not produce dramatic changes. These findings were based on simulations which considered ten percent variations of the width and thickness.

The effects of discontinuities in LIBRA simulations were shown to be small at the frequencies measured, as depicted in Figure 4.15. This observation was based on two LIBRA simulations, the first, using the reference model, and the second, using only a 10 cm long ECS, without pad structures. Even when the input pads were removed from the simulated structures, the large difference between the values of coupling gain across the frequency range was found to be small (0.034 dB). Of course, the ability of LIBRA to adequately model the true discontinuities involved with WSI structures is not really known.

To further explore modeling differences, another LIBRA model was prepared which consisted of an ideal, coupled transmission line pair. This model required an estimate of the even- and odd-mode characteristic impedances (furnished from of LINECALC or similar estimates), but did not otherwise regard any of the specific geometrical or material properties. When this model was simulated, the data seemed to correlate closely to the reference simulation, as shown in Figure 4.15, and the average deviation in magnitude between the two structures was found to be 3.46 dB. Of course, even though the ideal lossless model does not directly depend on material and geometrical parameters, the even- and odd-mode impedances are determined by them. For this simulation, the even- and odd-mode impedances were based on the results given by the LINECALC program, using the reference model parameters.

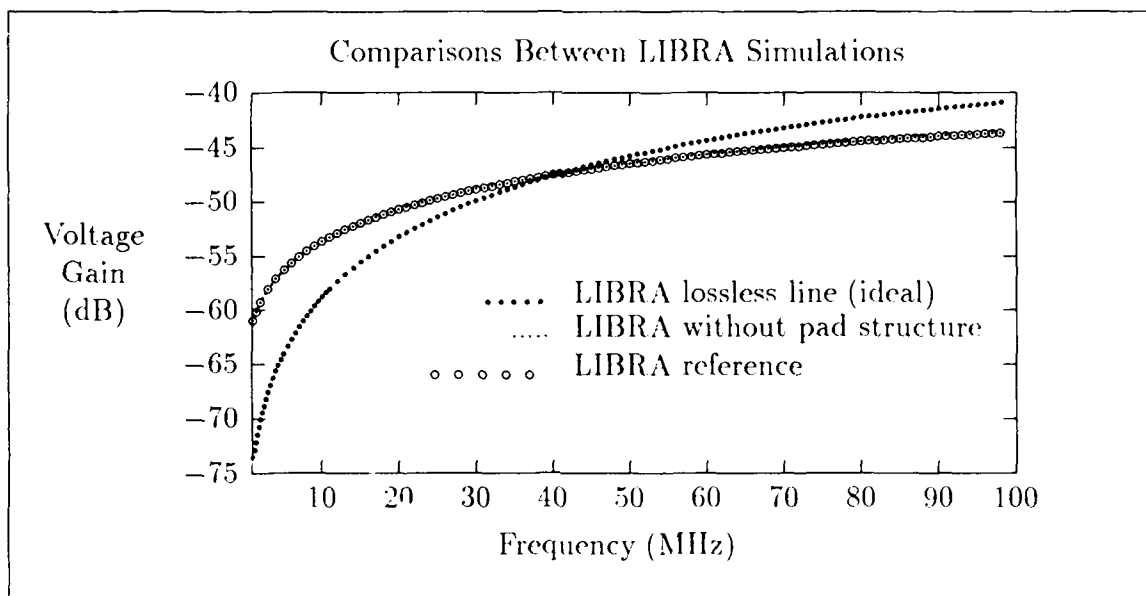


Figure 4.15. Variations of the reference simulation which considered the omission of discontinuities and a lossless model.

*Closed-Form Results.* Analysis based on the closed-form expressions (Equations 3.12–3.14) were undertaken. The results of the closed-form expressions for the 42nd structure are shown in Figure 4.16. The results of this simplified analysis, which assumed a lossless structure, produced results which were within  $\pm 5$  dB of the LIBRA reference simulation. The required even- and odd-mode characteristic impedances used for these expressions were provided by LINECALC simulations.

Strangely, these results seemed to be slightly more approximate to the LIBRA reference model than did the lossless line case. The second approach considered the solution of the multiconductor transmission line equations (Equations 2.29–2.30), as described in Chapters 2, 3, and Appendix F. As inputs, this model required the capacitance coefficients pertaining to the conductor system. These coefficients were estimated using the finite difference model. Creating the Figure 4.16 chart involved the solution of the Equations 2.29–2.30 system was formed at each of 100 frequencies, equally spaced between 1 and 100 MHz. To mechanize the process, solutions in MATRIXX and Mathematica were utilized.

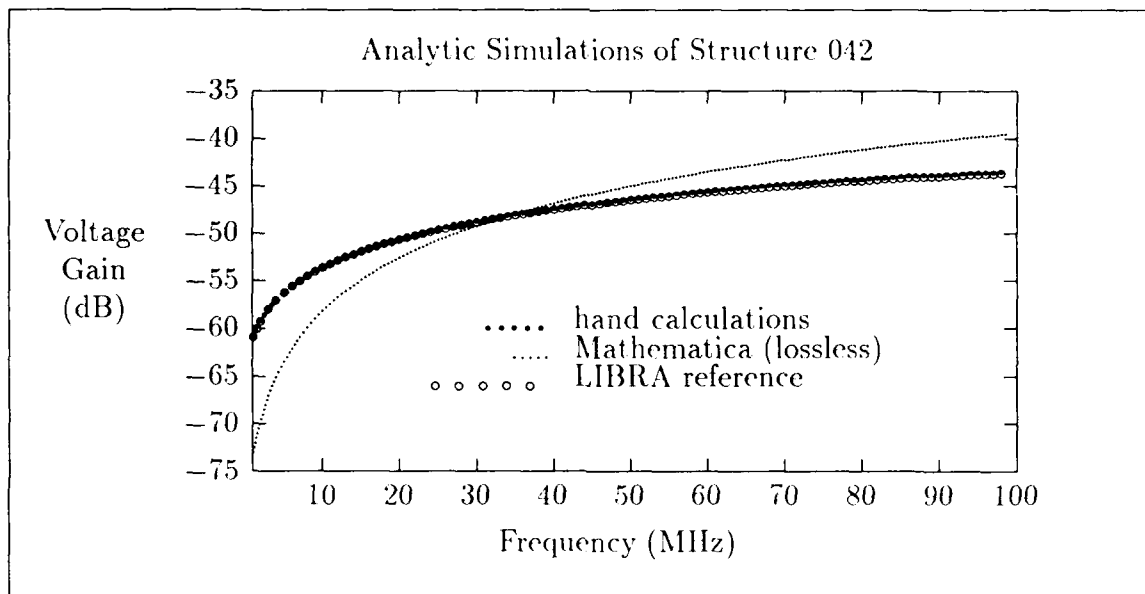


Figure 4.16. Other analytic estimates of the 42nd structure.

The LIBRA simulations did not reveal significant differences at lower frequencies when attenuation effects were modeled. The effects due to attenuation in the LIBRA reference simulation were more noticeable at higher frequency, but these differences did not improve the agreement between theoretical and experimental curves.

*Telegrapher's Equation Results.* The matrix solution of Equations 2.29–2.30, described in Appendix E, were solved using the boundary conditions specified in the coupling measurement. Since the solution of these equations was frequency-dependent, the solution for a range of frequencies was accomplished by “frequency-stepping”. That is, the equations were individually solved at each frequency of interest. The capacitance and inductance matrices required by Equations 2.29–2.30 were found using the FDM simulations. The initial telegrapher's solution considered a lossless line, producing the results shown in Figure 4.17. These results were very close to those produced with the aforementioned closed-form expressions. To model attenuation, a first-order calculation of the series resistance loss was determined through Equation 4.1. Dielectric conduction loss was assumed to be negligible. Based on these refinements, the Figure 4.17 results were produced. The

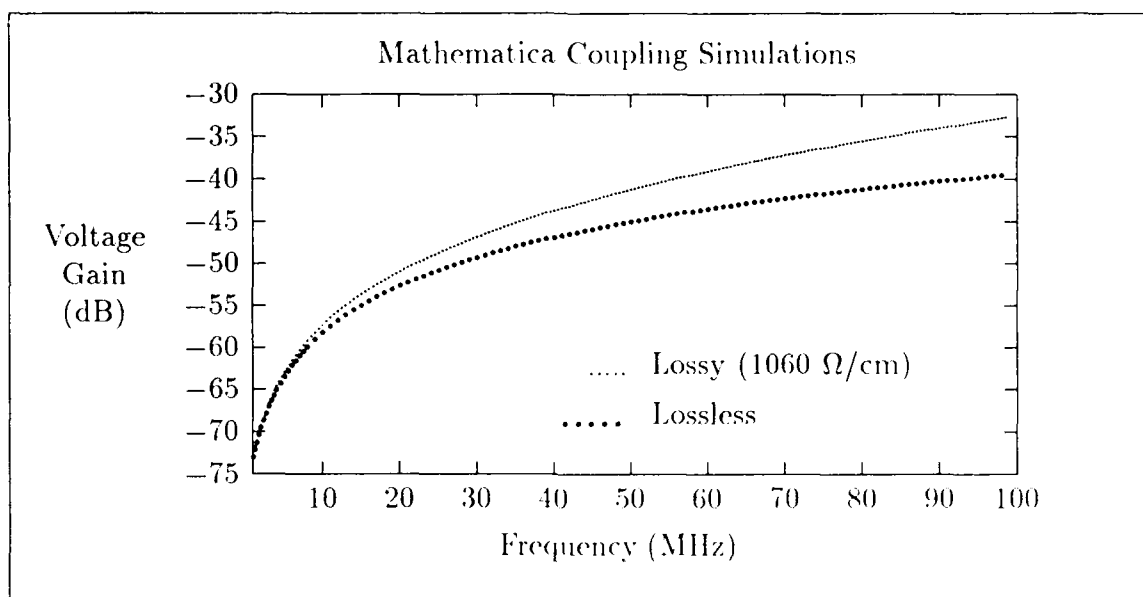


Figure 4.17. Results of lossless and lossy solutions to the telegrapher's equation.

introduction of loss produces a frequency-dependent departure from results of the coupled gain curve based on a lossless simulation.

*Measured Coupling Results.* The technique described in Chapter 3 for measuring coupling gain was applied to structures on each wafer. Most of the measurement plots are presented in Appendix H. Using the HP 4191A gain-phase analyzer, the measurements were collected over the frequency range 1–100 MHz. For most of these structures, only the backward-coupling gain was measured, while for other structures, the forward transmission gain and forward-coupling gain (isolation) was also collected.

The plot shown in Figure 4.18 presents measurements of the structures numbered 48 and 49 from the PIQ wafers, compared to the initial reference LIBRA simulation. Unfortunately, it was found after continuity screening that these were the only structures from the two PIQ wafers which were suitable for use in the initial coupling analysis. Also shown on this plot are the results of the reference LIBRA simulation.

For the 48th structure, which was an ECS with rectangularly gridded ground

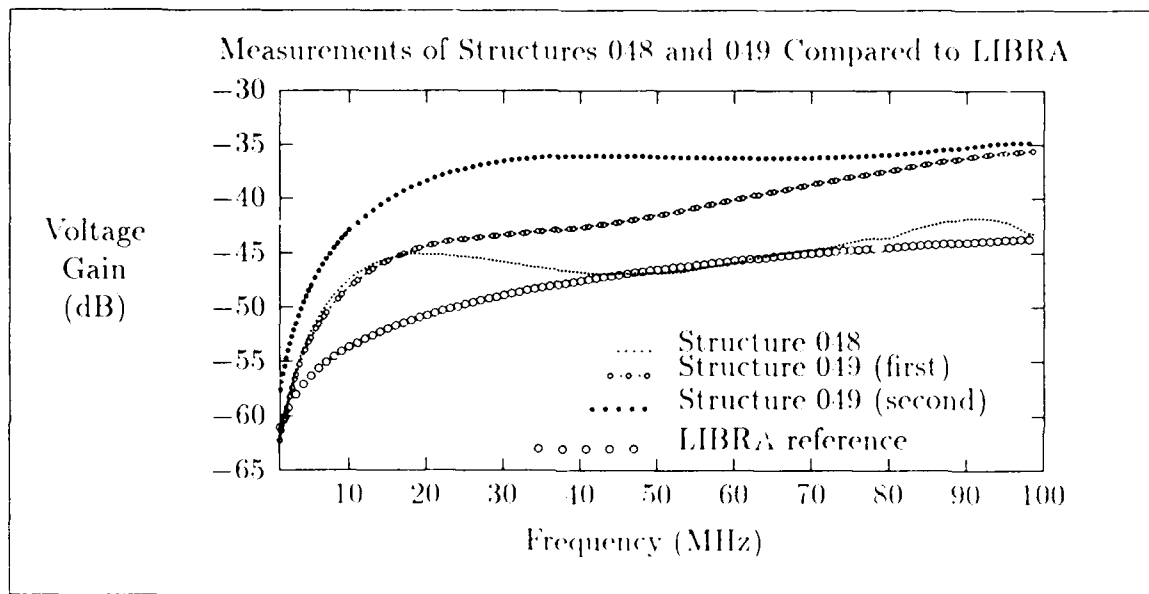


Figure 4.18. Coupling measurement of the 48th structure from the second PIQ wafer compared with two LIBRA simulations.

planes above and below, the LIBRA plot approaches the measurement values over several portions of the frequency range. The shapes are dissimilar, a peculiarity which may be attributed to electrical properties of gridded ground planes. It is believed that the particular case of gridded ground planes in striplines has not been addressed in the literature. Hence, no theoretical treatments exist which could predict the behavior of these structures. Although the fact that the measured and theoretical curves were close at some frequencies was promising, the difference in magnitudes between these curves at other point—greater than 5 dB at some points across the frequency range—was a disconcerting result.

The 49th structure, which has no superficial ground plane, is not a true stripline structure. The reference analysis is shown for comparison, since no other similar structural model exists in the LIBRA component library. The coupling for this structure was shown in both measurements to be higher than that predicted in results produced by the LIBRA simulations. Based on theory, the coupling for such a

structure should be higher, since no superficial ground exists to intercept the coupling field lines between the two structures. The backward coupling gain of the other two-conductor structures in both the 10  $\mu\text{m}$  and 25  $\mu\text{m}$  linewidths were measured. The general trend found for these structures was that the measured values for the backward coupling gains were larger than those predicted by any of the analytical approaches. The measurement results for the other structures revealed similar discrepancies, as shown in Appendix H.

A summary of the maximum coupling gains spanning 1-100 MHz for the measured structures is presented in Table 4.13. The actual measurement curves for the individual structures are presented in Appendix H. The results for the simulated structures are shown on the same plot as the measurement for the associated structures. For the simulated structures, the maximum coupling gain spanning 1-100 MHz for the two-conductor ECS structures is presented as a function of lateral inter-conductor spacing in Figure 4.19. Plots for both conductor linewidths (10  $\mu\text{m}$  and 25  $\mu\text{m}$ ) are presented. It is important to note that the maxima were taken over a limited frequency range; higher coupling levels are possible at frequencies above 100 MHz. For example, a simulation of the 48th structure (discussed previously) extending to 500 MHz (Figure 4.20) manifests higher coupling levels compared to any frequency below 100 MHz.

Despite the difficulty in achieving a good correlation in the theoretical and experimental results, it was found that the coupling never exceeded -20 dB. This finding is promising for digital system, provided that series signal attenuation is not severe. For lossy lines, the effect of attenuation will be to *increase* the effects of a given coupling gain specification. For example, if a transmission gain of -10 dB is found for a structure with a -20 dB coupling gain, then the effective coupling gain is -10 dB. This result simply implies that the coupling will increase due to the need to increase the input signal level in order to overcome attenuation loss. The increase in the input signal causes the level of coupling in the adjacent signal conductor to

Table 4.13. Measured maximum coupling gain spanning 1–100 MHz for the WSIC structures.

Structure	Wafer	Maximum coupling gain (dB)
36	BCB	-39.63
36	PIQ	-32.95
37	PIQ	-37.00
49	PIQ	-35.26
50	PIQ	-24.07
51	PIQ	-34.00
55	PIQ	-49.05
100	BCB	-45.70
100	PIQ	-34.77
104	PIQ	-28.98
109	BCB	-34.51



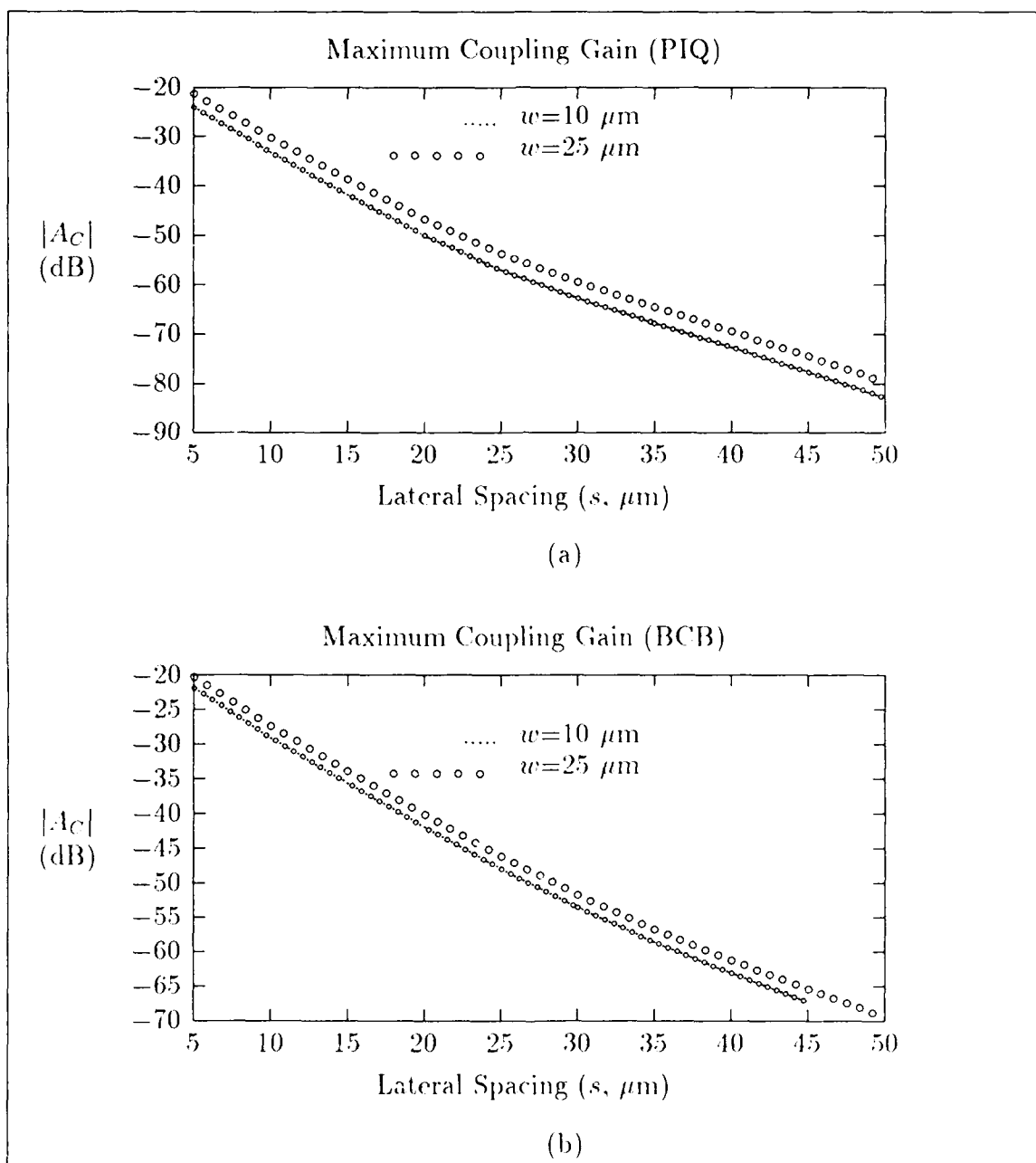


Figure 4.19. Maximum coupling gain spanning 1-100 MHz of the simulated two-conductor ECS structures as a function of lateral spacing between conductors. (a) For PIQ structures. (b) For BCB structures.

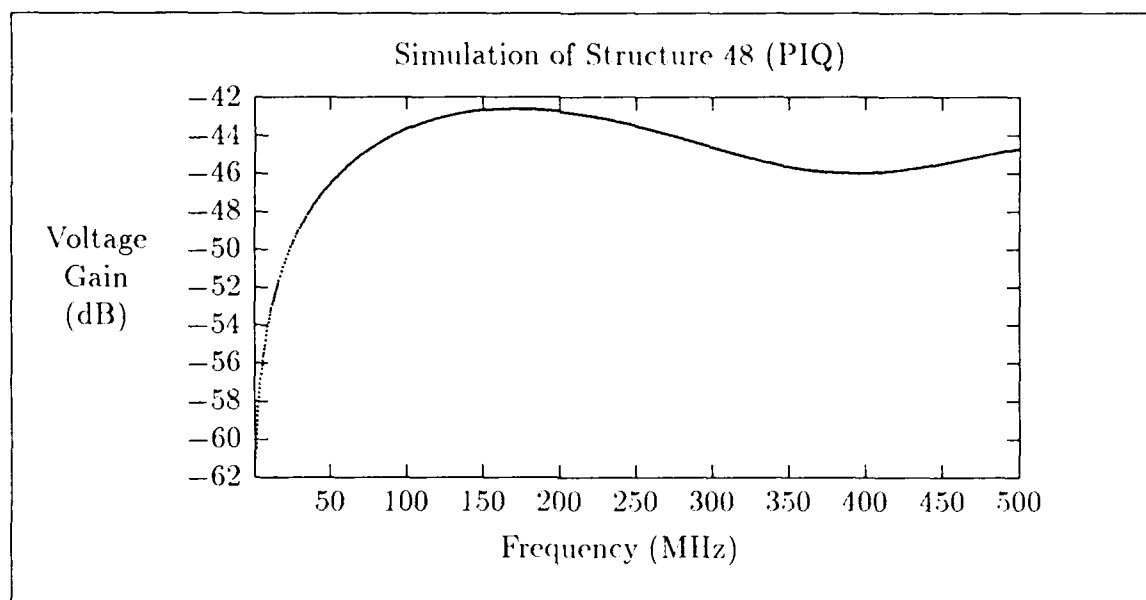


Figure 4.20. Extended frequency simulation of the 48th structure from the PIQ wafer.

increase. For example, in a structure with a maximum coupling gain of  $-20$  dB and a maximum transmission gain of  $-12$  dB has a net coupling gain of  $-8$  dB, based on this rule of thumb. In this context, the coupling effects are much more significant. Based on measurements associated with the  $10\text{ }\mu\text{m}$  wide structures,  $0.1\text{ m}$  in length and separated by  $18\text{ }\mu\text{m}$  of lateral distance, the maximum coupling gain was found to be  $-35$  dB. For a similar  $10\text{ }\mu\text{m}$  wide structure, the lowest transmission gain was found to be  $-11.4$  dB. Hence, by the above rule of thumb, the worst case net coupling gain would be  $-23.6$  dB. For a five volt input, this translates to a worst case coupling of  $0.33$  volts.

Using the net coupling gain concept, a set of design curves were constructed. These design curves predicted the noise margin for a digital system using  $0.1\text{ m}$  length structures with a known coupling gain and a  $5$  volt input. The design curves, presented in Figure 4.21, were based on the  $10\text{ }\mu\text{m}$  and  $25\text{ }\mu\text{m}$  linewidths. For the  $10\text{ }\mu\text{m}$  wide structure, the maximum conductor loss of  $-11.4$  dB (based on the transmission measurement of the 50th structure from the PIQ wafer) was used.

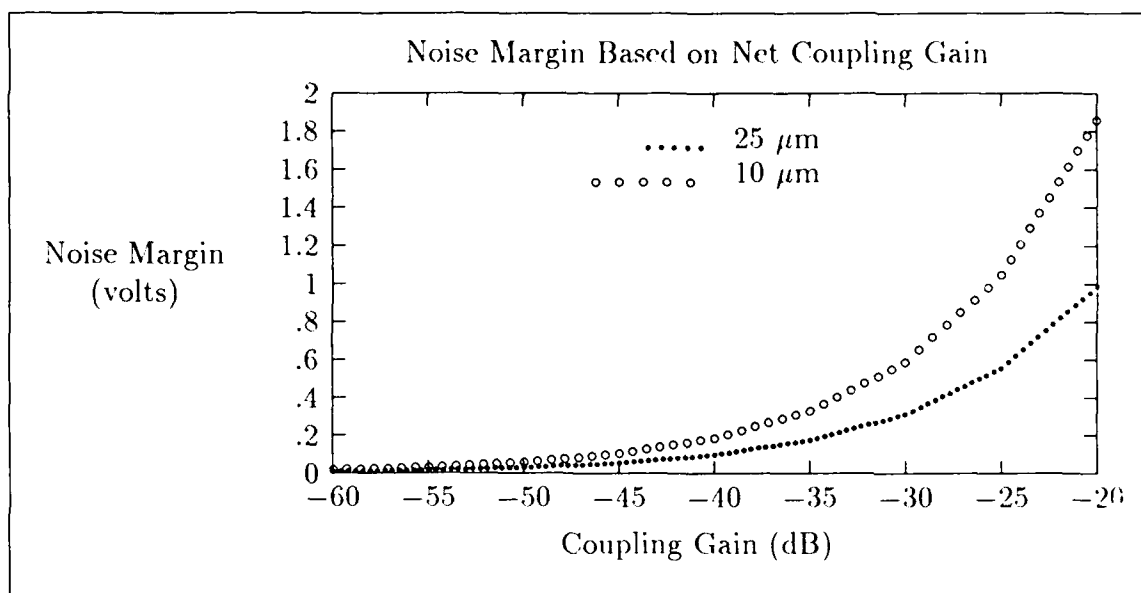


Figure 4.21. Predicted worst case coupling noise levels for the 10  $\mu\text{m}$  wide and 25  $\mu\text{m}$  wide structures (3.1 m length) based on five volt input signals as a function of the maximum coupling gain.

This value turned out to be 1.15 times larger than the  $-9.88$  dB of attenuation predicted for a similar structure using Equations 4.1 and 4.22. Since no transmission measurements were performed for the 25  $\mu\text{m}$  wide structures, an attenuation value was estimated using the 1.15 scaling factor, applied to the theoretically calculated attenuation of  $-5.11$  dB (the scaling factor was derived from the 10  $\mu\text{m}$  wide results). Thus, an attenuation of  $-5.87$  dB was assumed for the 25  $\mu\text{m}$  wide structures. The level of coupling noise measured for the WSIC structures was then calculated with the net coupling concept. After subtracting the maximum transmission loss from the maximum coupling gain, the worst case coupling noise levels were calculated for a system using five volt input levels.

*Transmission Results.* The transmission gain for WSIC structures was analyzed with simple, lumped-element circuit theory. Measurements were performed on several structures, including meander lines of 10  $\mu\text{m}$  and 25  $\mu\text{m}$  linewidths.

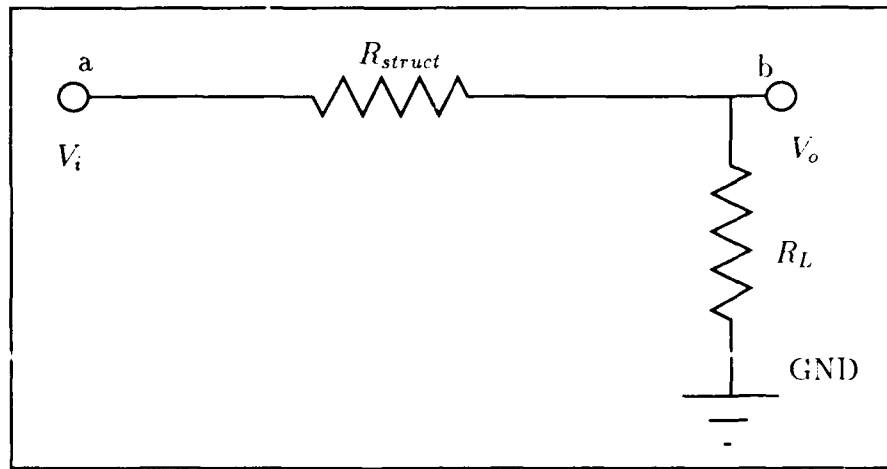


Figure 4.22. Simple transmission gain model.

*Analysis.* The transmission gain analysis of the WSICs was accomplished by the application of simple circuit theory. The transmission circuit of a conductor can be modeled as a voltage divider, as shown in Figure 4.22. The structural series resistance ( $R_{struct}$ ) was based on the series resistances calculated from Equation 4.1. From Figure 4.22, the voltage transmission gain is given by:

$$A_T = \frac{V_o}{V_i} = \frac{R_L}{R_L + R_{struct}} = 20 \cdot \log \left( \frac{R_L}{R_L + R_{struct}} \right) \text{ dB.} \quad (4.8)$$

Based on 50  $\Omega$  terminations and the previous Equation 4.1 results, the transmission gain for several WSIC structures were calculated. For 0.1 m long structures, the transmission gain was calculated as -9.88 dB for aluminum conductors with a 10  $\mu\text{m}$  linewidth and -5.1 dB for aluminum conductors with a 25  $\mu\text{m}$  linewidth. Clearly, for low impedance terminations, the 25  $\mu\text{m}$  wide structures possess the advantage of lower attenuation. The attenuation calculated for the meander lines was expectedly higher: -17.4 dB for a 25  $\mu\text{m}$  wide (0.6 m long) structure and -28.4 dB for a 10  $\mu\text{m}$  wide (1.2 m length) structure.

*Measurements.* The transmission gain of several structures were measured over the frequency range of 1–100 MHz using the HP 4194A gain-phase analyzer. A representative measurement of a WSIC structure with a 10  $\mu\text{m}$  linewidth and 0.1 m length is shown in Figure 4.23. Several other measurements which were performed are presented in Appendix II. Based on these measurements, the corresponding WSIC structures manifested a loss slightly greater than that predicted in the analysis. Furthermore, the loss varied slightly with frequency. Of course, since the analysis was based on dc resistances, the variance of resistance with frequency was not considered.

A more accurate measurement of attenuation was obtained by examining meander structures. The larger resistance which they manifested tended to reduce the measurement errors due to contact resistance. The measurement results for a 12-section (1.2 m length), 10  $\mu\text{m}$  wide meander line is shown in Figure 4.24. The measured transmission response of these two structures were sharply resonant near 55 MHz, and the response of another structure was resonant near 70 MHz. This resonance was undoubtedly a manifestation of the tightly coupled meander line, rather than a “long-line” property. As the frequency increased above the resonant point, it approached the calculated value based on Equation 4.1 and Equation 4.8. A similar result was obtained when the 25  $\mu\text{m}$  linewidth meander lines were characterized. The measured results of an 8-section (0.8 m length), 25  $\mu\text{m}$  wide meander line is shown in Figure 4.25.

The high attenuations manifested by the longer meander lines are obviously undesirable for lines terminated in low impedances, especially for the narrower conductor linewidths. Even for the 0.1 m length lines, which are more likely to find applications in practical WSICs, a 5 dB attenuation may not be acceptable for some logic types.

*Isolation Results.* Isolation gain measurements were performed on the 50th PIQ structure (three-conductor, edge-coupled, embedded microstrip). This structure

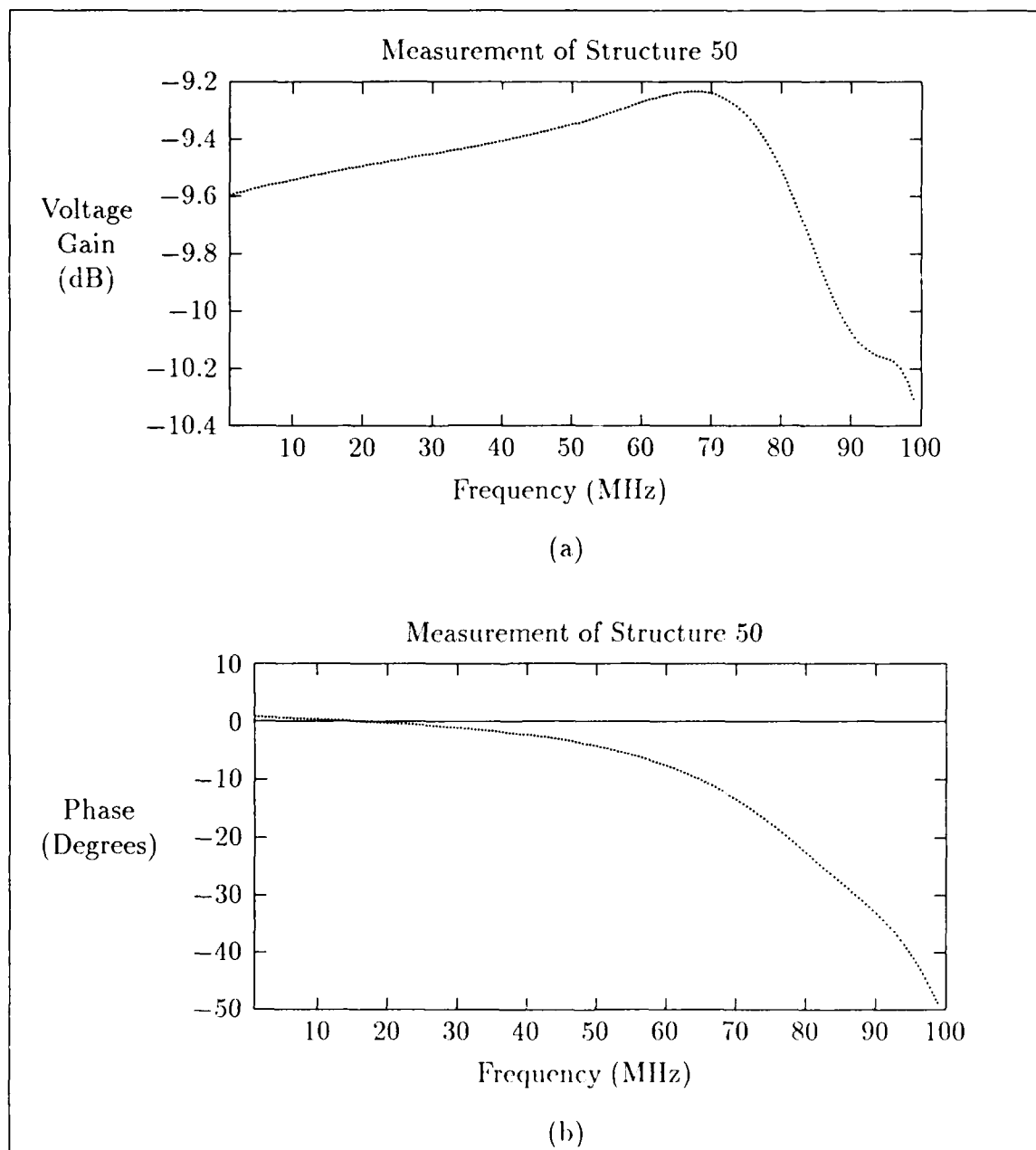


Figure 4.23. Measured transmission gain of structure 50 (three-conductor ECS, right conductor) from the PIQ wafer. (a) Magnitude. (b) Phase.

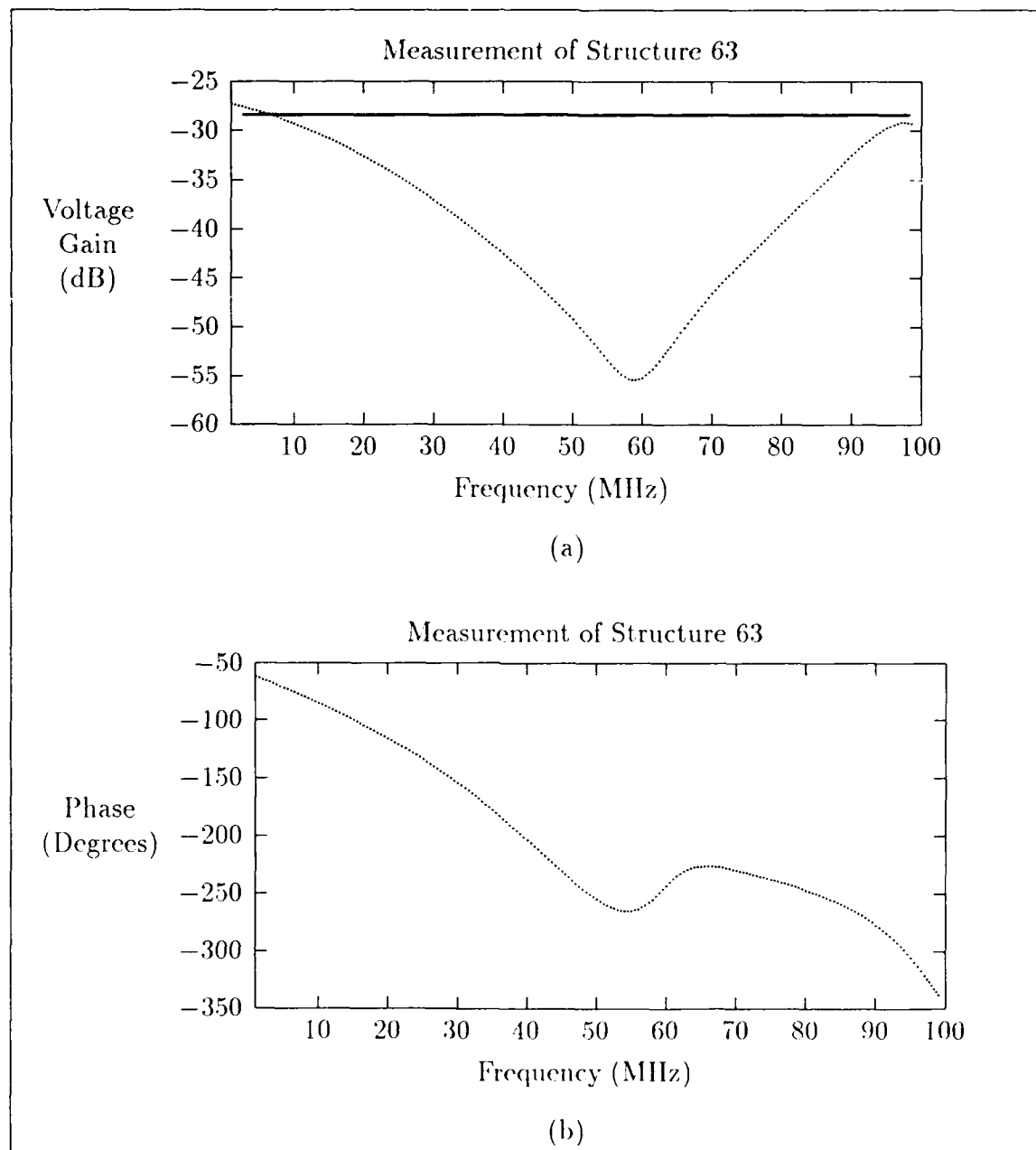


Figure 4.24. Measured transmission gain of structure 63 (1.2 meter length, 10  $\mu\text{m}$  wide meander) from the PIQ wafer. (a) Magnitude (straight line is the theoretical value based on Equation 4.1). (b) Phase.

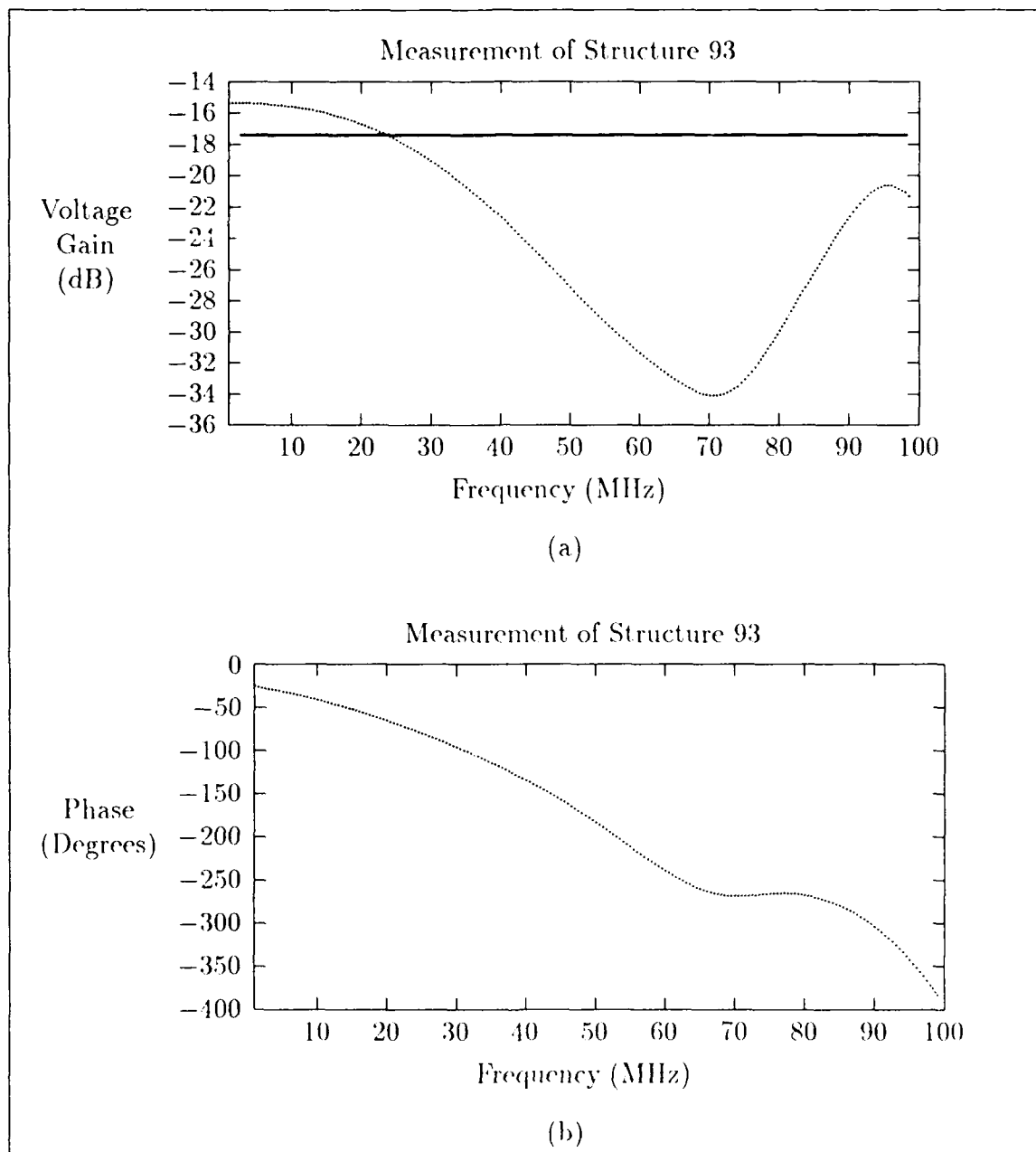


Figure 4.25. Measured transmission gain of structure 93 (0.8 meter length,  $25\mu\text{m}$  wide meander) from the PIQ wafer. (a) Magnitude (straight line is the theoretical value based on Equation 4.1). (b) Phase.



appeared to manifest a maximum forward-coupling gain of slightly greater than -25 dB, as shown in Appendix II. The analysis of isolation gain was not formalized for this structure.

### *Time-Domain Measurement Findings*

This subsection describes the results of the time-domain measurements performed for this research effort. The pulsed-signal response of several structures from the PIQ and BCB wafers were measured in the Figure 3.16d configuration, with  $R_S$  and  $R_L$  approximately 50  $\Omega$  in magnitude. The de-cabling technique described in Chapter 3 was applied to many of the measurements. The propagation delay was not measured for these structures due to the lack of resolution in the pulse generation and measurement equipment.

*De-Cabling Technique Results.* The results of the intermediate processing steps which were required to achieve a de-cabled signal are further illustrated by Figures 4.26–4.29. Specifically, these figures depict the application of the de-cabling technique to an actual measurement. Signal processing algorithms were developed with Mathematica software on a Sun workstation and with MathCad on a personal computer. An example of an “as measured” response is shown in Figure 4.26a. This measurement was taken from the 63rd structure (12-section, 1.2 m length, 10  $\mu\text{m}$  wide meander line) of the first PIQ wafer. The spectrum of the “as measured” response is shown in Figure 4.26b. The pulsed-signal input used for the measurement was a 5 MHz square wave. The corresponding short-cable and long-cable measurements are shown in Figures 4.27 and 4.28. To achieve the approximate impulse response of the cable, the Fourier coefficients of the long-cable spectrum were divided by those of the short-cable spectrum. The de-cabling filter is an inversion of this response and was formed by reciprocating each of the Fourier coefficients of the approximated cable impulse response. The resulting filter was then applied to the measurement spectrum, which revealed the Figure 4.29 filtered (de-cabled) response.

The time-domain representation of the filtered (de-cabled) signal was achieved via the inverse Fourier transform operation.

The filtered signal displayed features which were not present in the measured signal. These were the expected effects of the de-cabling process. Also expected was the introduction of low-level noise in the treated signal. To reduce noise contributions, all signals were averaged after measurement. For this reason, the changes in the signal after filtering are not likely to be artifacts of the de-cabling process. However, in most cases, the de-cabling process did not add any new information to the measurements, especially at lower frequencies. A marked annunciation or ringing of the leading and trailing edges of fast signals was observed in the filtered responses. This ringing was concluded to be the well-known Gibbs phenomenon associated with functional approximations. Despite the large number of Fourier coefficients used in the overall process (up to 1024), the approximated responses displayed this phenomenon when reconstructed. In smoother waveforms, particularly those at higher frequencies, the Gibbs phenomenon was not found to be significant.

Eventually, six de-cabling filters were synthesized, each corresponding to frequencies selectable on the HP 8082 pulse generator. In order to minimize phase errors to the maximum extent possible, the waveform acquisition was performed with the leading edges of the signals being synchronized to the extreme left of the oscilloscope display. The triggering levels upon which this synchronization was based were derived from autoscale operations in the long- and short-cable configurations. As described in Chapter 3, only one period of the signals measured were processed in this manner. One disadvantage was noted with this procedure. Occasionally, a low-level feature present in the initial leading edge of the measured signal was obscured when the triggering level was too high. Although such features were visible when multiple periods were observed, a single period measurement sometimes omitted them.

After the de-cabling filters were generated, they were routinely applied to most of the subsequent measurement data. The pulsed-input signal response near 5 KHz,

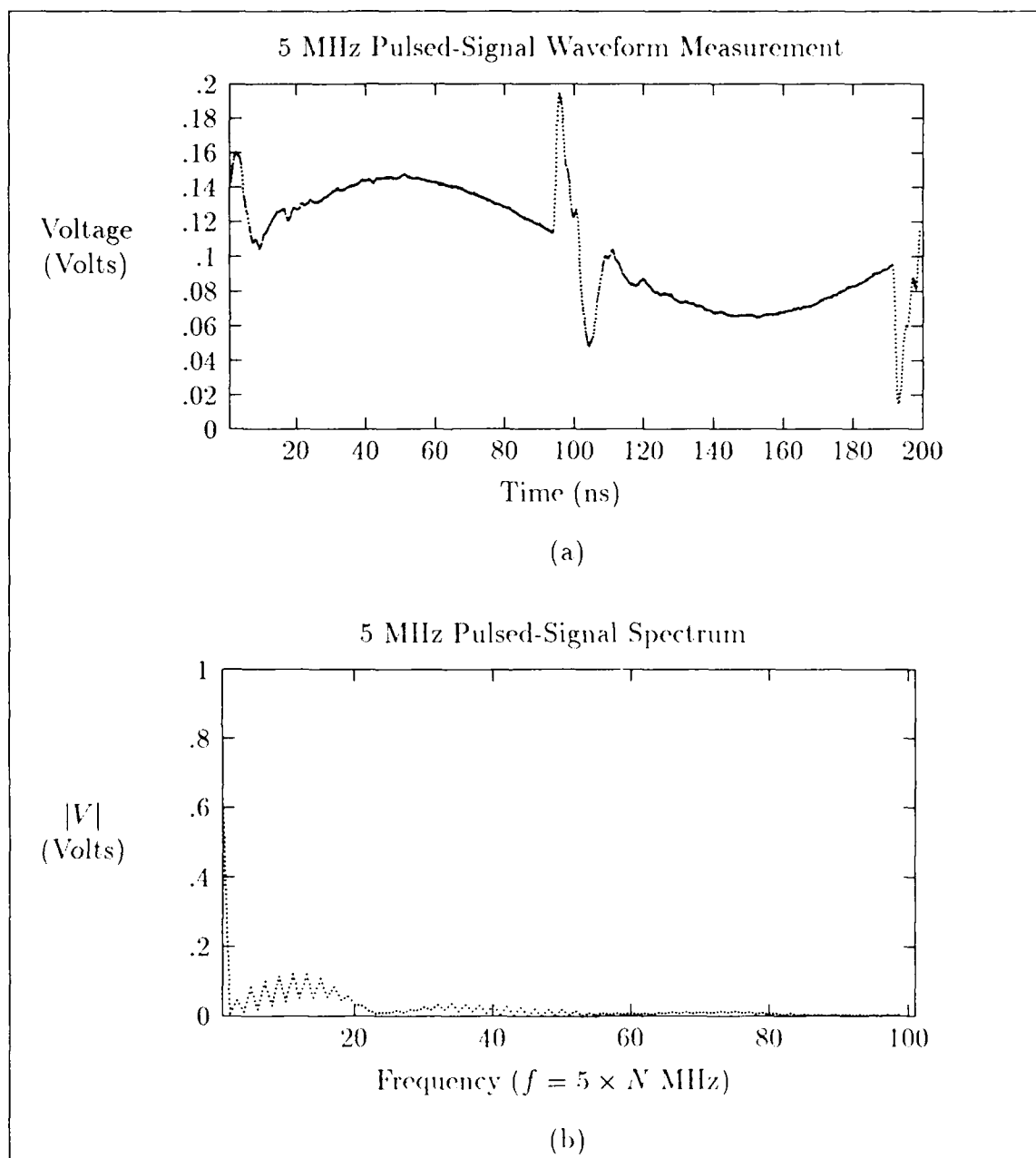


Figure 4.26. A representative pulsed-signal measurement of a  $10\text{ }\mu\text{m}$  wide,  $1.2\text{ m}$  length meander structure at  $5\text{ MHz}$ . (a) Measurement. (b) Spectrum. (Input voltage =  $5\text{ volts}$ ).

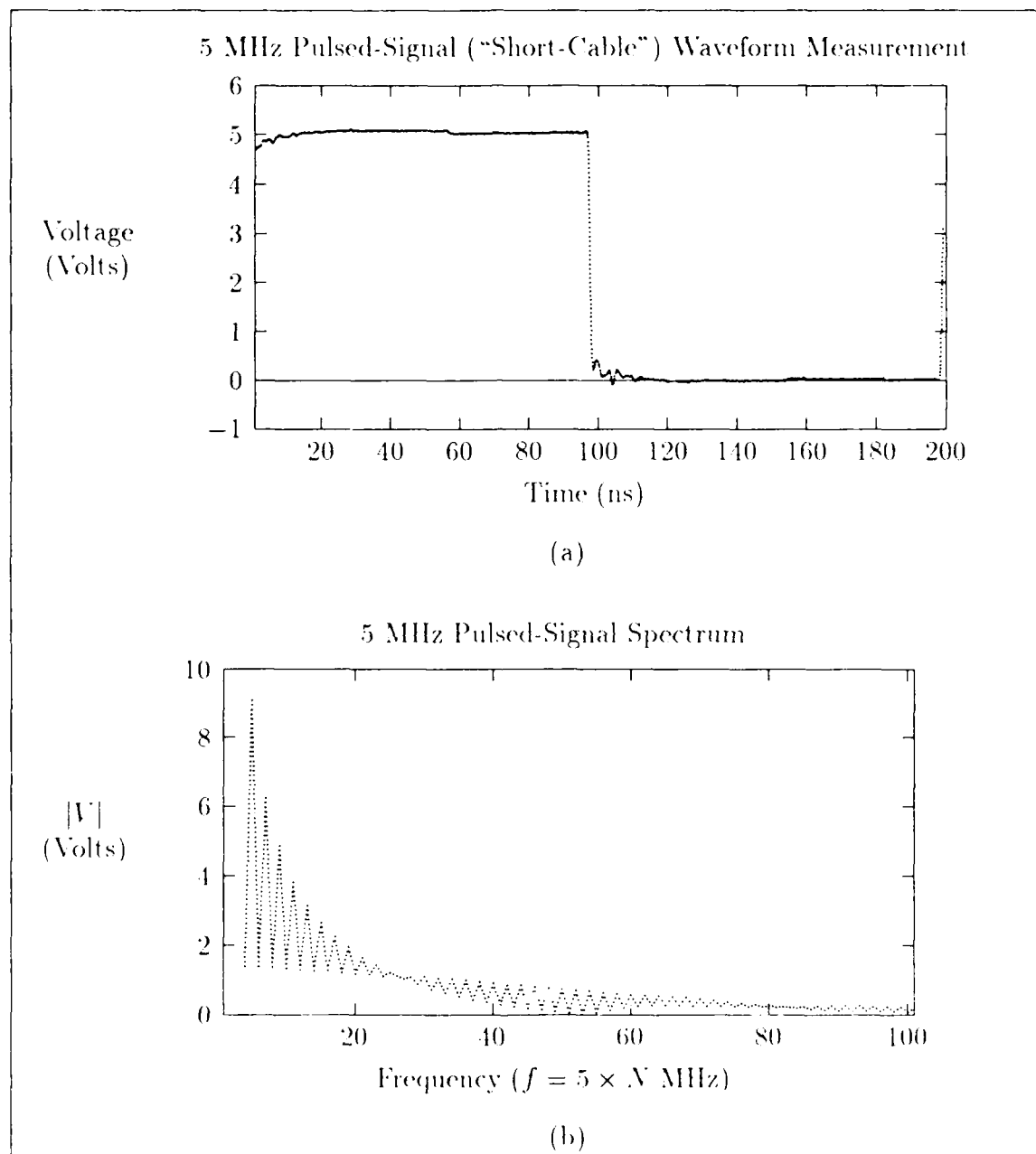


Figure 4.27. Short-cable, pulsed-signal measurement at 5 MHz. (a) Measurement. (b) Spectrum. (Input voltage = 5 volts).

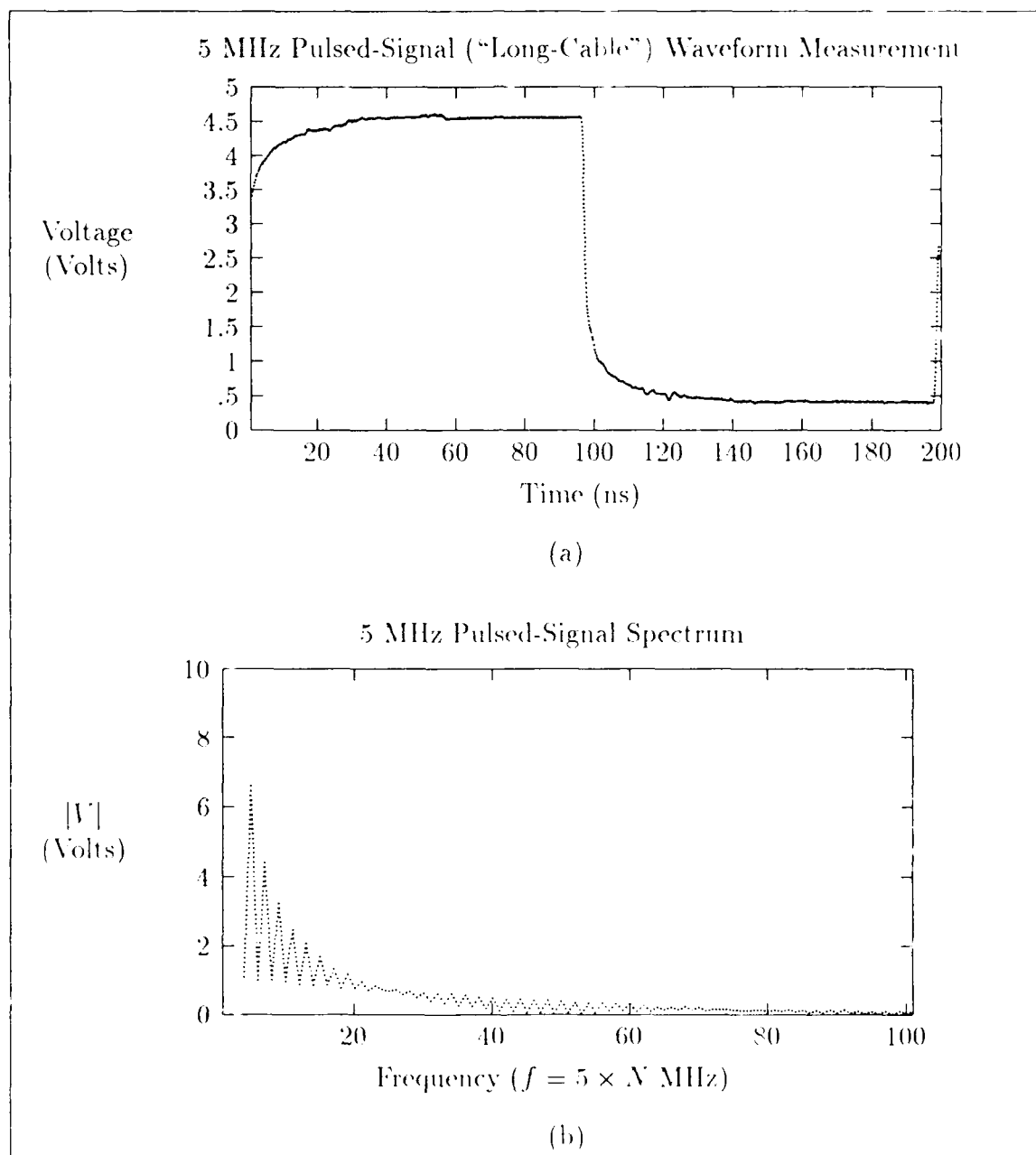


Figure 4.28. Long-cable, pulsed signal measurement at 5 MHz. (a) Measurement. (b) Spectrum. (Input voltage = 5 volts).

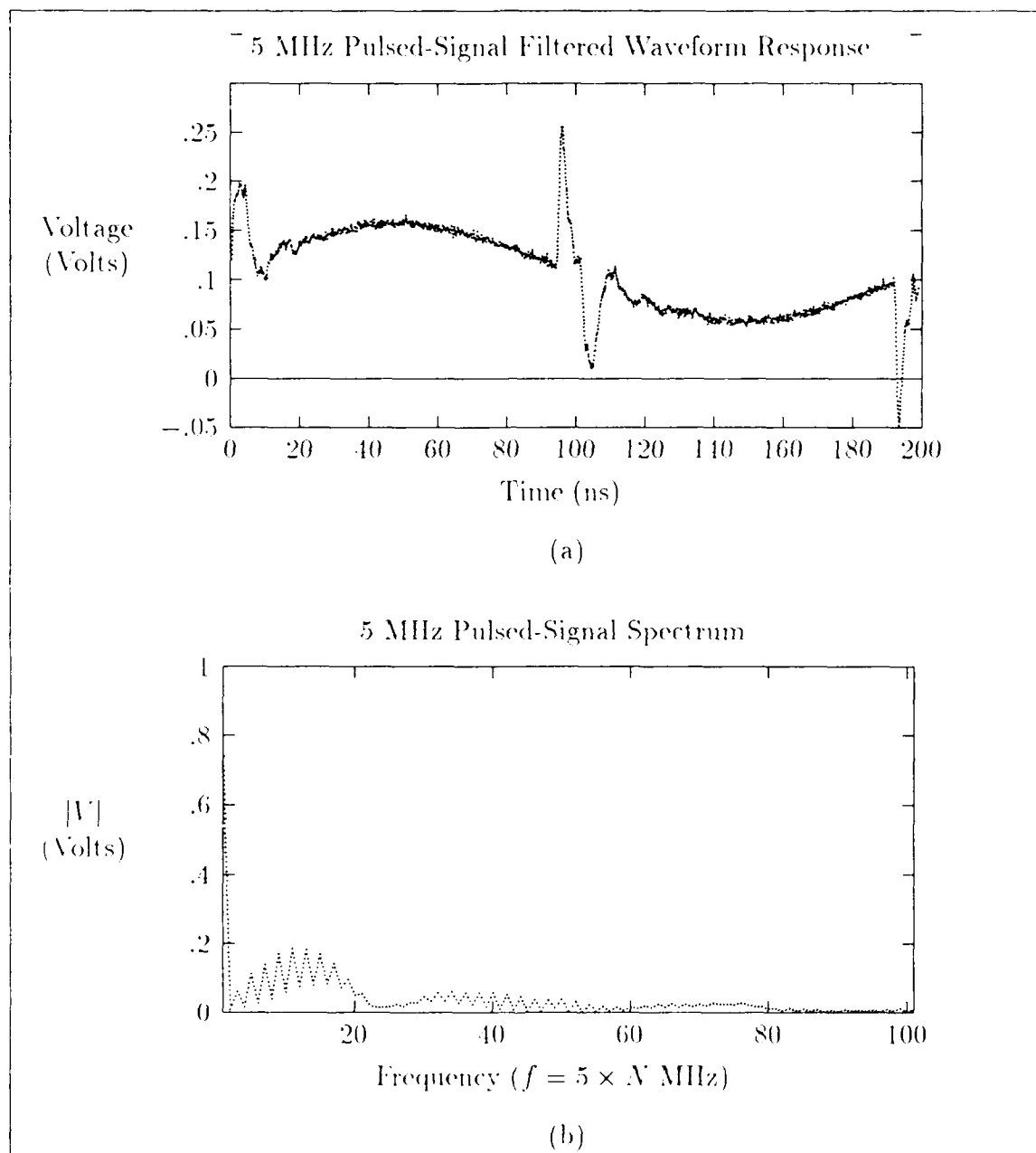


Figure 4.29. Signal after de-cabling processing. (a) Time-domain representation. (b) Frequency-domain representation. (Input voltage = 5 volts).

50 KHz, 500 KHz, 5 MHz, 50 MHz, and 200 MHz were utilized as shown in Figure 4.27 and Figures 4.30–4.34. Although the unprocessed measurements typically consisted of multiple periods of the pulsed signal, all filtered responses were composed of a single period of the pulsed waveform. The resulting waveforms for the meander structure are shown before and after de-cabling processing for each of the fixed frequencies in Figures 4.36–4.40. In some cases, the processed response of certain signals was excessively noisy (as shown in Figure 4.38), even when a known “good” filter was used for the de-cabling processing. This observation applied to most of the waveforms measured with high-impedance terminations, as well as for many of the signals near 5 MHz with both low- and high-impedance terminations. In these cases, only the unfiltered response was retained in the subsequent analysis.

*Input Signal Waveforms.* The input signals used for the pulsed-signal response measurements are shown in Figures 4.30, 4.31, 4.32, 4.27, 4.33, and 4.34, for the frequencies near 5 KHz, 50 KHz, 500 KHz, 5 MHz, 50 MHz, and 200 MHz, respectively. As described in Chapter 3, a pulse generator with six selectable frequencies were used as an input source. When measured, these frequencies were found to be 5.519 KHz, 43.48 KHz, 392.1 KHz, 5.025 MHz, 64.23 MHz, and 217.4 MHz. Each of the waveforms possessed a measured rise time of 3.0 ns, except for the latter frequency, which displayed a rise time of 1.23 ns.

*Meander Structure Results.* For the meander structure used in the previous example, the resulting filtered responses at the measurement frequencies other than 5 MHz are shown in Figures 4.36–4.40. In these figures, the predicted voltage levels of the resultant square waves is given by Equation 4.22. For the particular meander structure illustrated, the measured dc resistance of 1.81 K $\Omega$  was used to estimate the peak voltage of the square wave as 0.131 volts. Since the voltages associated with the actual measurements ranged from 0.18–0.20 volts, the actual series resistance appeared to be lower than that measured at dc. In fact, based on Equation 4.22 with  $V_{out} = 0.185$  volt, the series resistance was evaluated to be

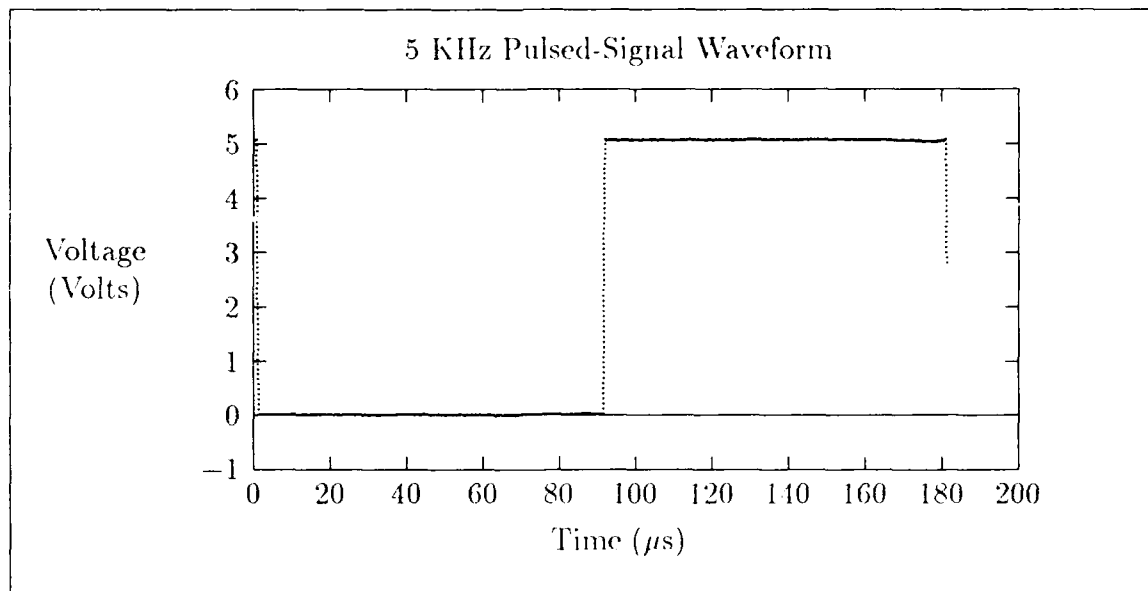


Figure 4.30. Pulsed-signal input for the short-cable configuration at 5 KHz.

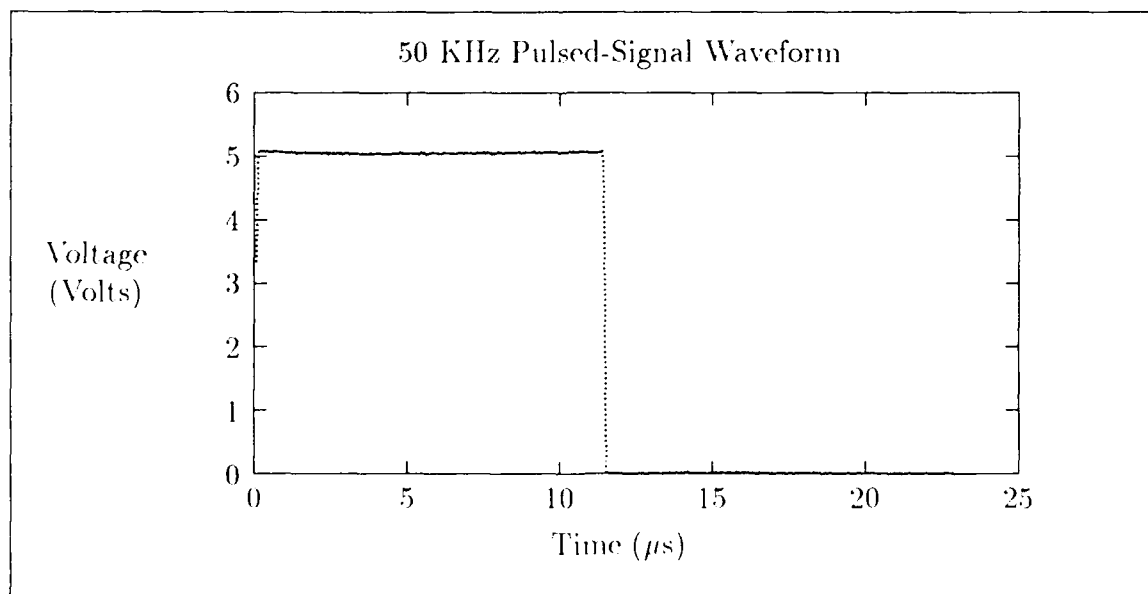


Figure 4.31. Pulsed-signal input for the short-cable configuration at 50 KHz.



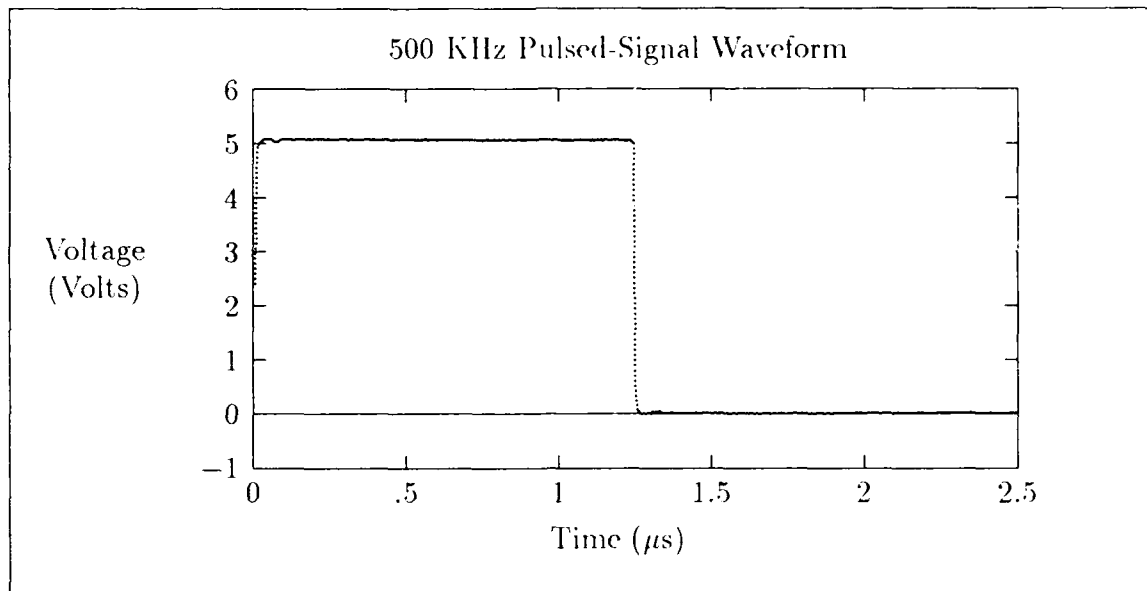


Figure 4.32. Pulsed-signal input for the short-cable configuration at 500 KHz.

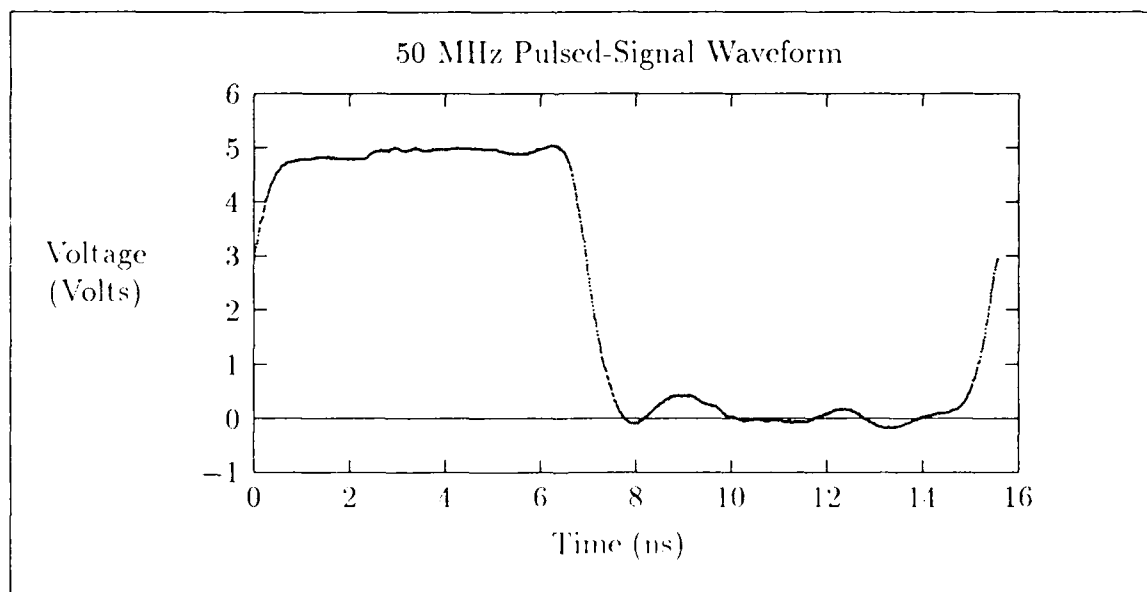


Figure 4.33. Pulsed-signal input for the short-cable configuration at 50 MHz.

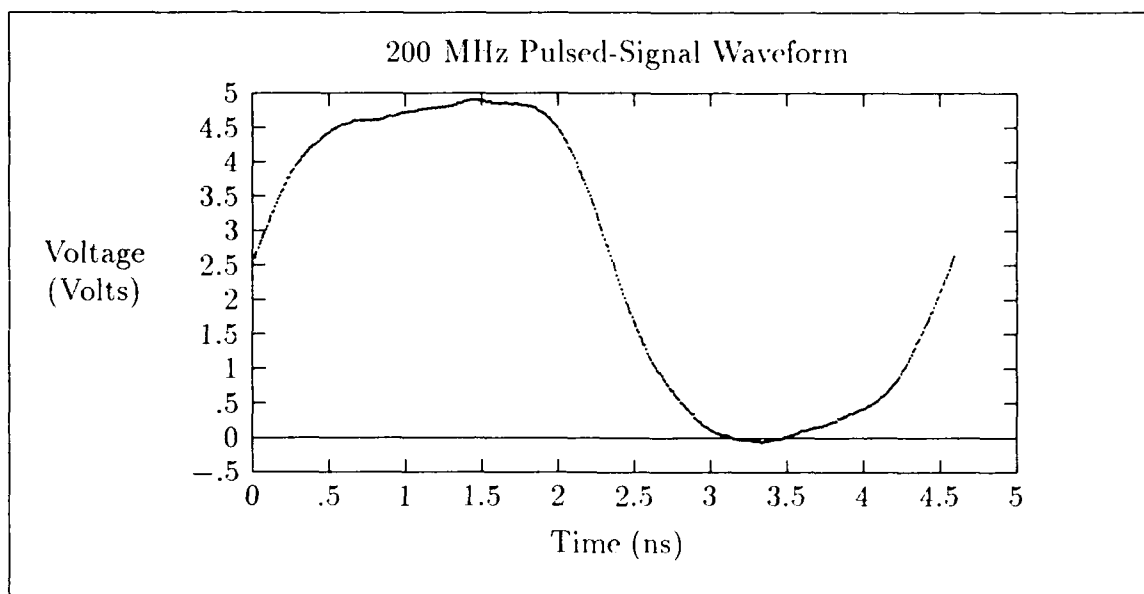


Figure 4.34. Pulsed-signal input for the short-cable configuration at 200 MHz.

1301  $\Omega$  , which is much closer to the 1271  $\Omega$  predicted by Equation 4.1 for a 1.2 m length line. As reinforced by the previous transmission measurements, an obvious observation with the use of very long lines, such as this 1.2 m length structure, is that a significant attenuation is created with low-impedance terminations, due to voltage divider losses.

For the meander structures, a small feature in the leading edge of the signal was present. This feature, evident in the "as measured" waveform displayed in Figure 4.35, appeared as a small pedestal of short duration which preceded the onset of the "main" portion of the pulsed-signal's leading edge. The source of this feature appears to be a reflection.

Another obvious question remains concerning the pulsed-signal response of the meander structures. Why does the response of the meander structure appear more degraded at 5 MHz compared to its frequency response either an order of magnitude below or above this frequency (at 500 KHz and 50 MHz)?

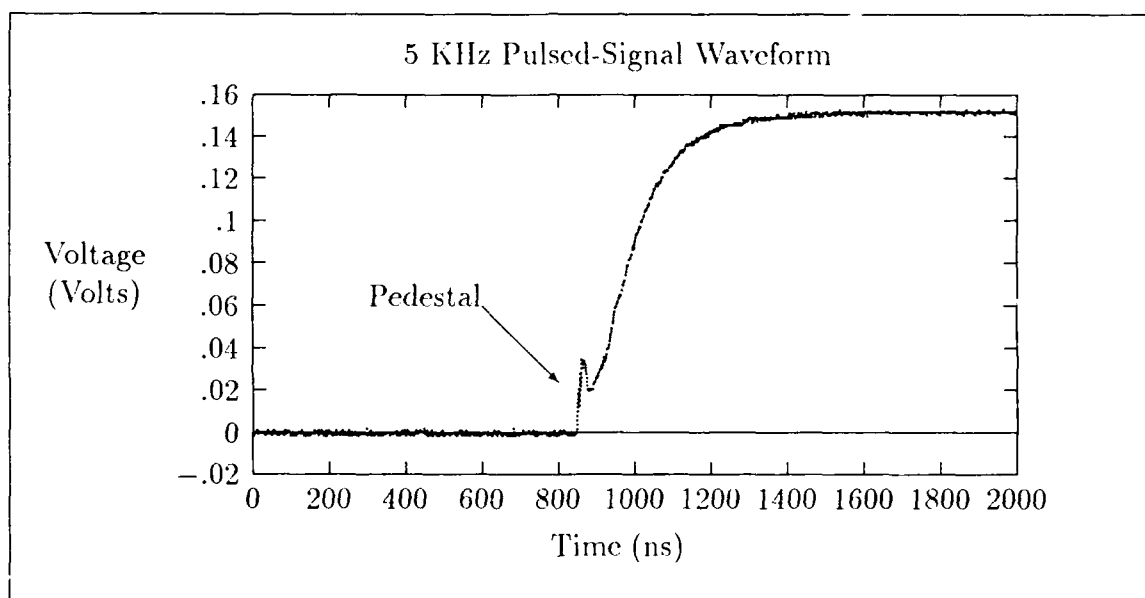


Figure 4.35. Pulsed signal response of meander structure, revealing small pedestal in waveform's leading edge.

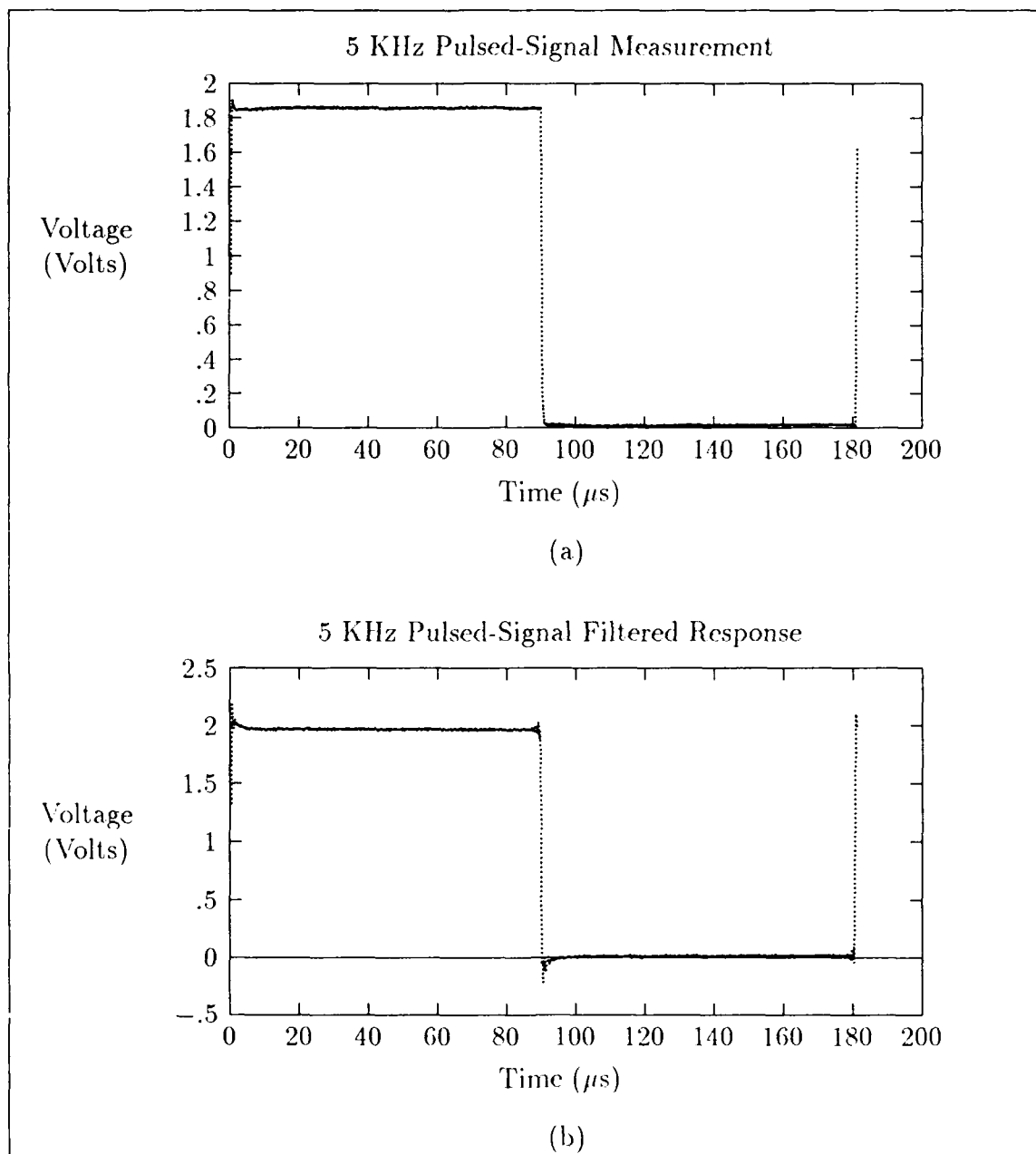


Figure 4.36. Pulsed signal response of the meander line at 5 KHz. (a) Unfiltered signal. (b) Signal after filtering.

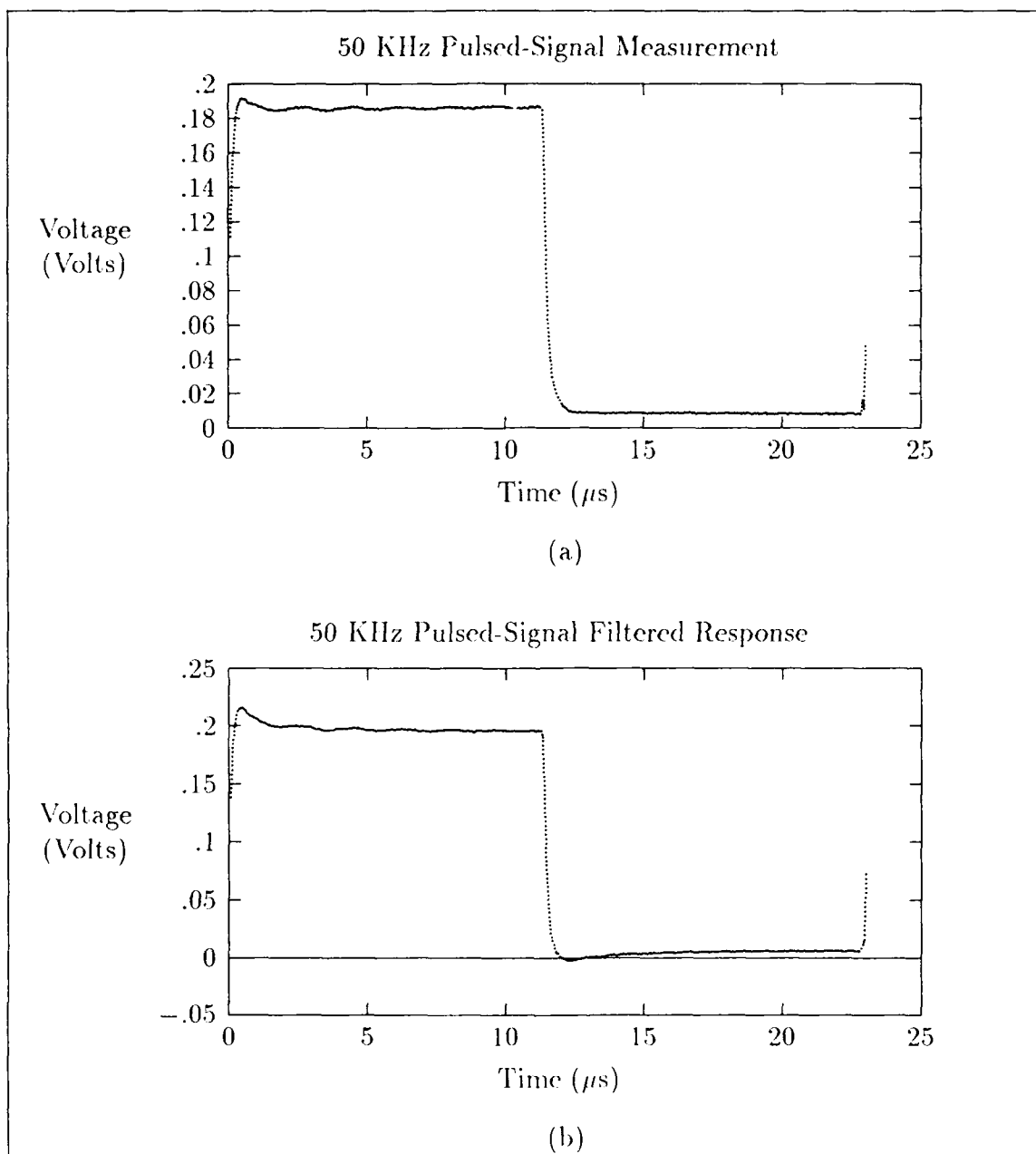


Figure 4.37. Pulsed signal response of the meander line at 50 KHz. (a) Unfiltered signal. (b) Signal after filtering.

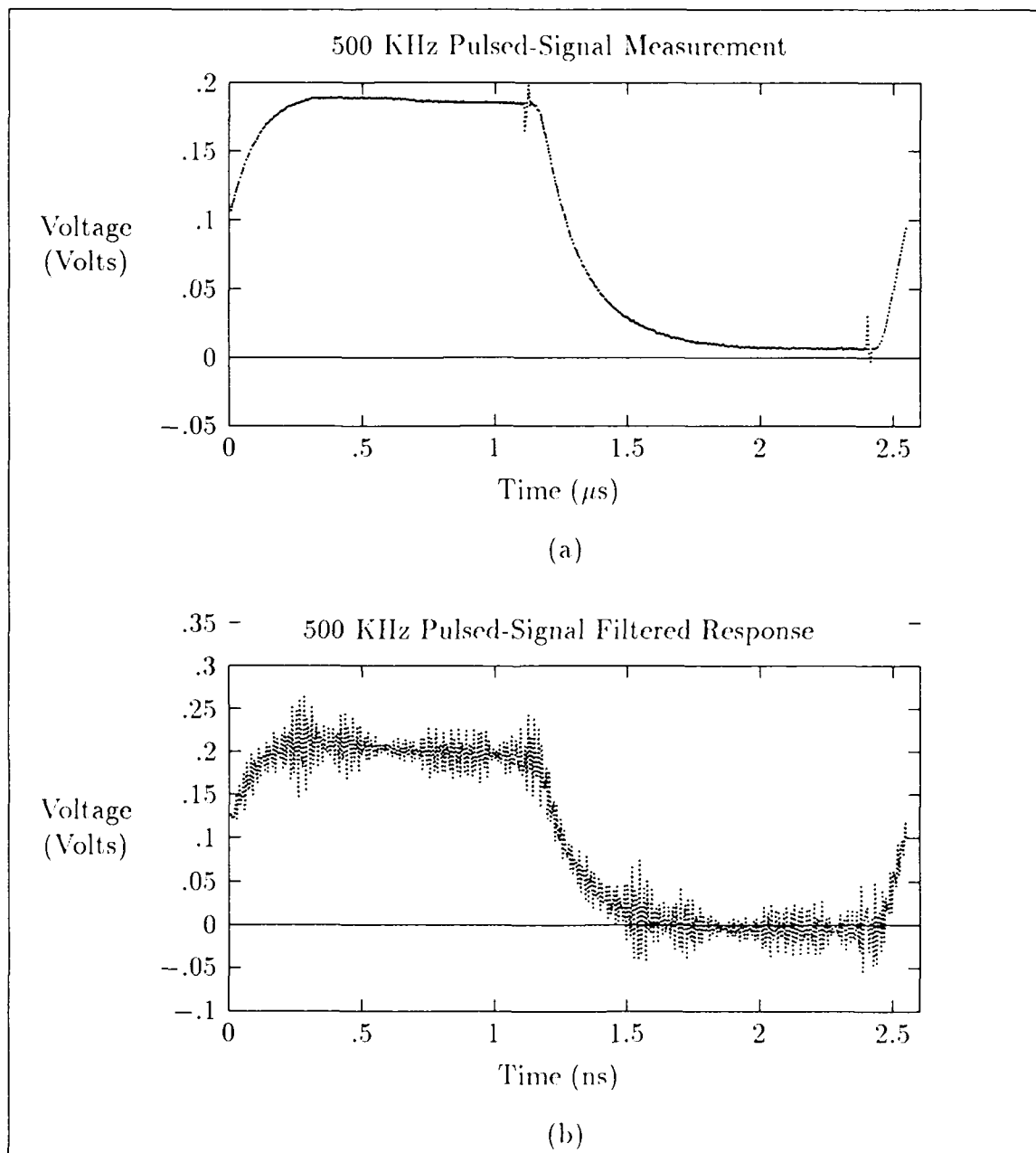


Figure 4.38. Pulsed signal response of the meander line at 500 KHz. (a) Unfiltered signal. (b) Signal after filtering.

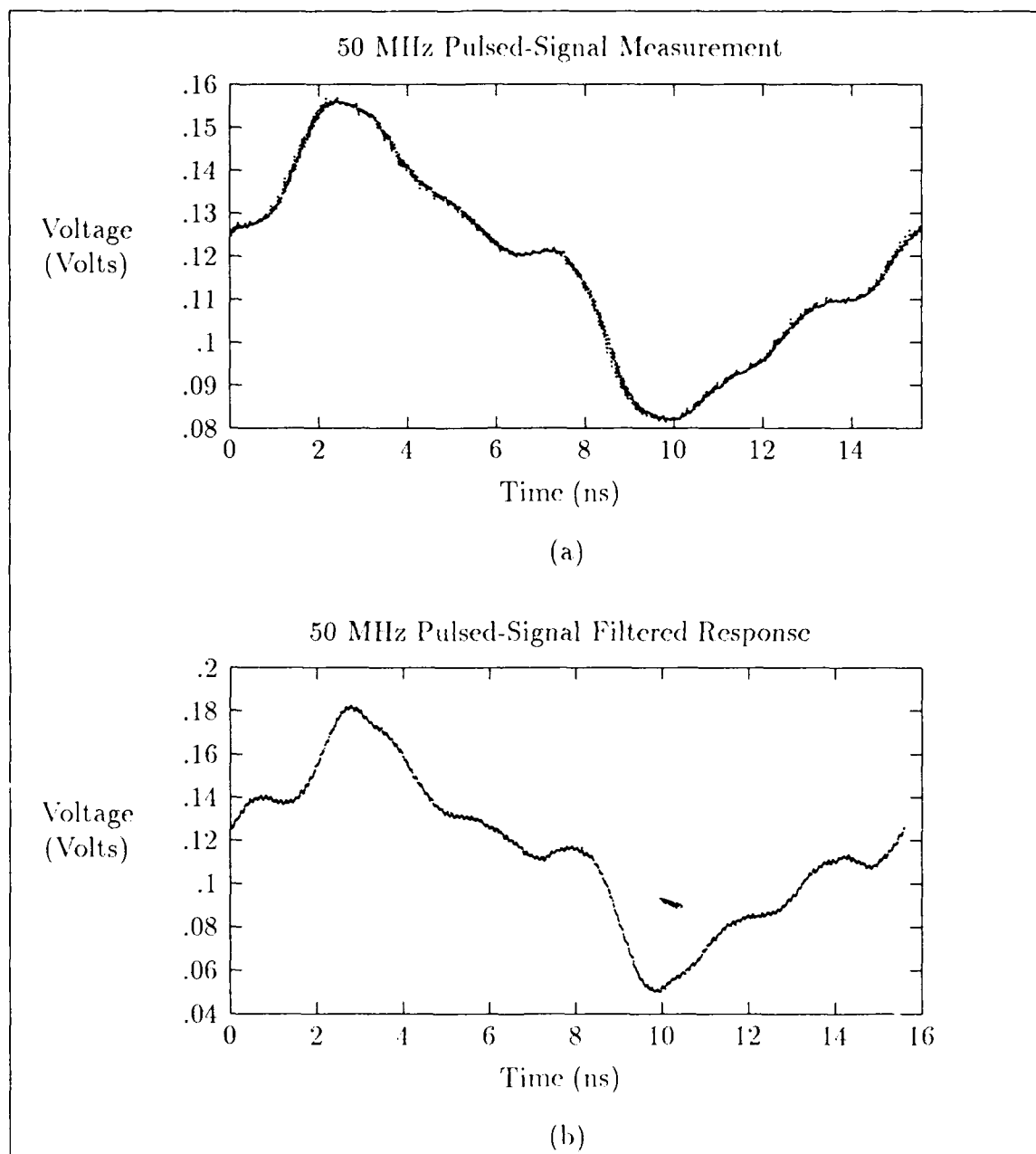


Figure 4.39. Pulsed signal response of the meander line at 50 MHz. (a) Unfiltered signal. (b) Signal after filtering.

The most likely possibility was concluded to be the filter-like behavior which was observed in the previous subsection for meander structures. This obvious frequency-dependent behavior would explain the preferential attenuation of the 5 MHz waveform. One problem evidenced by this measurement which complicates the analysis of pulsed-signal waveforms is the presence of many frequency components. Thus, to isolate the frequency-dependent behavior of these structures, a frequency-domain analysis must be undertaken in conjunction with the time-domain analysis.

*Dual-Line Structure Results.* The pulsed-signal response of several dual conductor WSI structures were measured (structures numbered 36 and 49 from the PIQ wafers and structures numbered 36 and 109 from the BCB wafer) in the transmission gain configuration (Figure 3.16d). Of course, in this schematic, the pulse generator represented the source, while the oscilloscope represented the load. Two circuit configurations were considered. The first configuration was identical to Figure 3.16d with source and load terminations of  $50\ \Omega$ . The second configuration was similar to the first except that the load termination was a larger impedance ( $> 1\ \text{M}\Omega$ ).

For these and the other 10 cm-length structures, the predicted attenuated output levels, based on 5 volt inputs, for the  $10\ \mu\text{m}$  wide structures were 1.6 volts using the theoretically predicted  $106\ \Omega$  conductor resistance and 0.7 volts using a resistance of  $300\ \Omega$ . For the  $25\ \mu\text{m}$  wide structures, the corresponding output levels were calculated as 2.78 volts based on the theoretically predicted  $40\ \Omega$  conductor resistance, and 1.0 volt based on the larger,  $200\ \Omega$  resistance. For a 2 volt input signal, the predicted voltages of the responses were similarly calculated as: 1.111 volts for  $40\ \Omega$ , 0.64 volts for  $106\ \Omega$ , 0.4 volts for  $200\ \Omega$ , and 0.286 volts for  $300\ \Omega$ .

The measurements made with low-impedance terminations revealed an attenuation comparable to that predicted by Equation 4.22 for the two linewidths ( $10\ \mu\text{m}$  and  $25\ \mu\text{m}$ ). The attenuation was significant in either case, but not nearly as great as that displayed by the longer meander lines. However, for these shorter



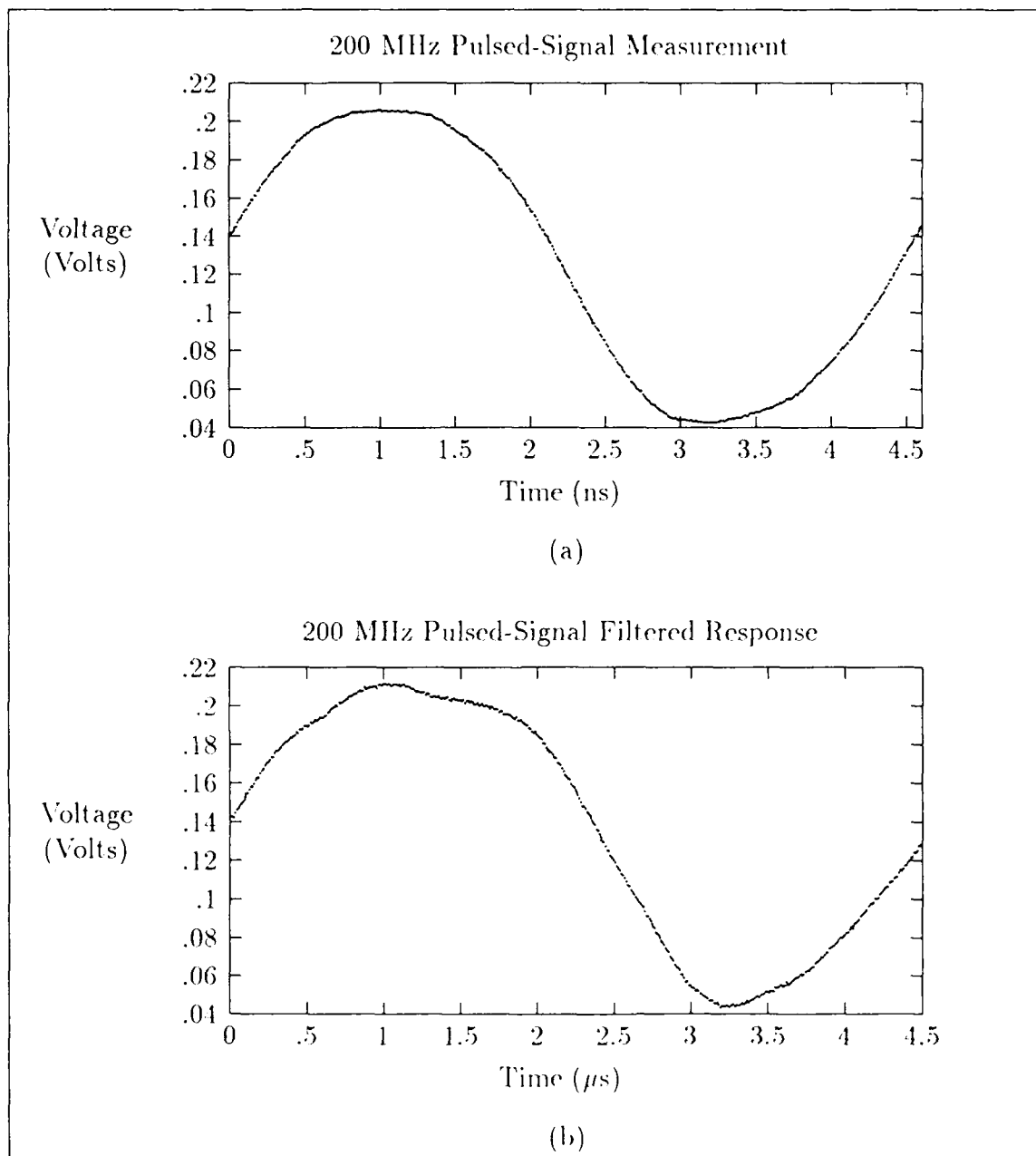


Figure 4.40. Pulsed signal response of the meander line at 200 MHz. (a) Unfiltered signal. (b) Signal after filtering.

structures, the *relative* attenuation was greater. The values obtained were usually more in agreement with the results obtained in the continuity measurements, rather than Equation 4.1. This result is in contrast with that observed for the meander measurements. Of course, any measurement of attenuation is more accurate in the longer structure, since any fixed, residual measurement bias errors are less significant. In the second configuration (high impedance), the attenuation displayed on the lines of structures measured was found to be insignificant, except at higher frequencies. As previously discussed, the de-cabling techniques were much less successful for measurements made in the high impedance configuration. Hence, the cable loss was not compensated for in the measurement data. Notwithstanding this attenuation source, the magnitudes of the voltages measured on these structures at higher frequencies appeared to be on the order of that produced by the source. In other words, the attenuation of the signals measured at higher frequencies were not believed to be due to resistive losses.

*Coupling.* Several coupling measurements were made with pulsed-input signals on a two-conductor ECS from the PIQ wafer (structure 49). In particular, isolation measurements (Figure 3.16c) were performed with low-impedance and high-impedance terminations (the source resistance was  $50\ \Omega$ , as in all other measurements). Additionally, several transmission measurements were made in the transmission configuration with sources impressed upon the isolated line. This latter measurement used high impedance load terminations on the distant end of both lines. At times, grounding and coupling problems were encountered, leading to erroneous coupling signals. When it was possible to identify and eliminate these signals, the resultant coupling signals were found to be relatively small. During some early measurement sessions, the grounding problems could not be eliminated, and it was not possible to isolate coupling sources. The largest obvious sources of these problems were found to be the lack of "ground-ability" of the perceived reference ground planes, and inter-conductor coupling between the cables in the

instrumentation arrangement. When the perceived ground plane was treated as a non-zero potential and measured, a non-zero potential was found during some measurement sessions. The most direct solution to this problem was achieved -- not always successfully -- by connecting the reference ground plane to a common system ground directly through an additional microprobe. The interline coupling was effectively eliminated by physically isolating the lines. Even these precautions were not always sufficient, and various results were obtained at different times. The most reliable results, and the only ones considered critically, were those obtained when a preliminary ground plane measurement revealed extremely low (less than 5 millivolts) potentials. Measurements made under these circumstances revealed peak coupling amplitudes of less than 0.06 volts. These results were obtained when five-volt, pulsed-signals of selected frequencies were impressed on the adjacent lines of the 49th structure on the PIQ wafer.

When interfering signals were placed on the adjacent line (5 volts in amplitude), no measurable difference was found in the signal transmitted. In other words, the independent digital pulse train of a neighboring conductor did not create any perceivable interference on a similar pulse train impressed on the conductor of this ECS. The pulse train of the neighboring line was produced by a second pulse generator, which was slaved to the first. Three particular cases were examined. The first case examined the pulse train transmitted on one line with the second generator suppressed. The second case examined the same pulse train when the second generator was activated with an amplitude of five volts and a relative phase shift of about 12 ns (corresponding to the internal path delays between the synchronization hardware of the two function generators). The final case was the same as the second case, except that an additional 180° phase shift was introduced. No difference was observed in the measured waveform of the first line in any of the three cases. The resultant waveforms of a typical coupling measurement are presented in Appendix I.

*Triple-Line Structure Results.* The pulsed-signal response of several three-conductor WSI structures were measured using a transmission gain configuration, similar to that shown in Figure 3.16, except that an additional line was included. Structures numbered 54 and 100 from the PIQ wafers, and structure 100 from the BCB wafer were characterized. Several coupling measurements were performed on the 100th structure on one of the PIQ wafers, similar to those described for the two-conductor structure. In this structure, the center conductor was electrically connected to ground during fabrication, so the isolation and transmission measurements were made with the conductors on either side. The results obtained were very similar to those obtained in the two-conductor case. Thus, under these circumstances, the use of an isolating conductor between active conductors did not seem to provide a significant advantage compared to the two-conductor case.

*Coplanar Waveguide Results.* The pulsed-signal response of several coplanar WSI structures were measured using a transmission gain configuration, similar to that shown in Figure 3.16, except that only one transmission line was included. Structures numbered 31, 62, and 91 from the PIQ and BCB wafers were characterized.

A representative measurement from the 62nd structure at 50 KHz is shown in Figure 4.41. As evident in the figure, severe ringing occurs coincident with the pulse edges. At 500 KHz (Figure 4.42) and 5 MHz (Figure 4.43), the ringing phenomenon is significantly exacerbated. The amount of overshoot on the falling edge at 500 KHz approaches levels which are sufficient to possibly cause false triggering in some logic families. The jagged "teeth" in the 5 MHz waveform are indicative of individual reflections reverberating back and forth along the 10 cm length transmission line. The larger flat plateaus correspond to cable bounce, based on the time duration of these features.

At higher frequencies, the response is further degraded, as evidenced by Figures 4.44, taken at 50 MHz. Under these conditions, the pulse response cannot be

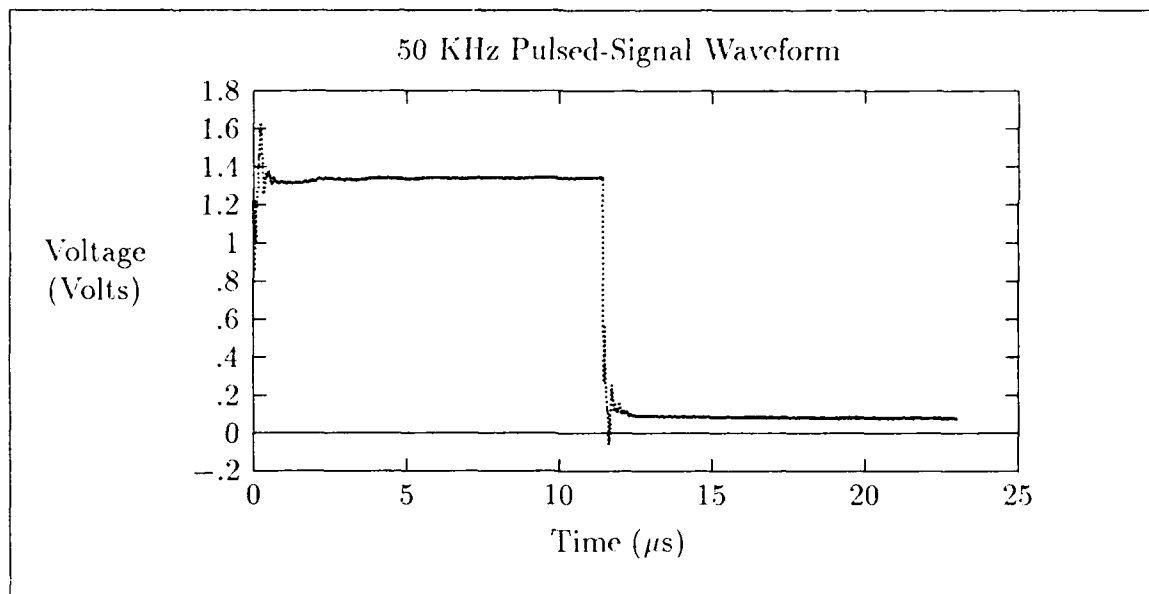


Figure 4.41. Pulsed-signal response of the 62nd structure from the PIQ wafer at 50 KHz (unfiltered).

truly considered as useful, due to the obvious lack of fidelity manifested in the pulsed-signal response. The causes of this distortion include impedance mismatches between the cabling and the transmission line structure and possibly dispersion of the signal within the structure. The latter effect is more difficult to verify, since frequency domain measurements were not made in the appropriate transmission configurations above 100 MHz. Hence, no dispersion data was available, and the multiple reflection environment under which the signal was measured made isolation of individual distortion effects impractical.

### *Summary*

Three wafers were investigated: two fabricated with PIQ as an intermetal dielectric and one fabricated with BCB. The investigation was restricted to the major grouping of the 10 cm transmission line structures, identically patterned onto each wafer. A relatively small subset of these structures were studied. The structures studied were screened based upon initial measurement results and the goal to explore at least one structure from each major structural category. The categories of

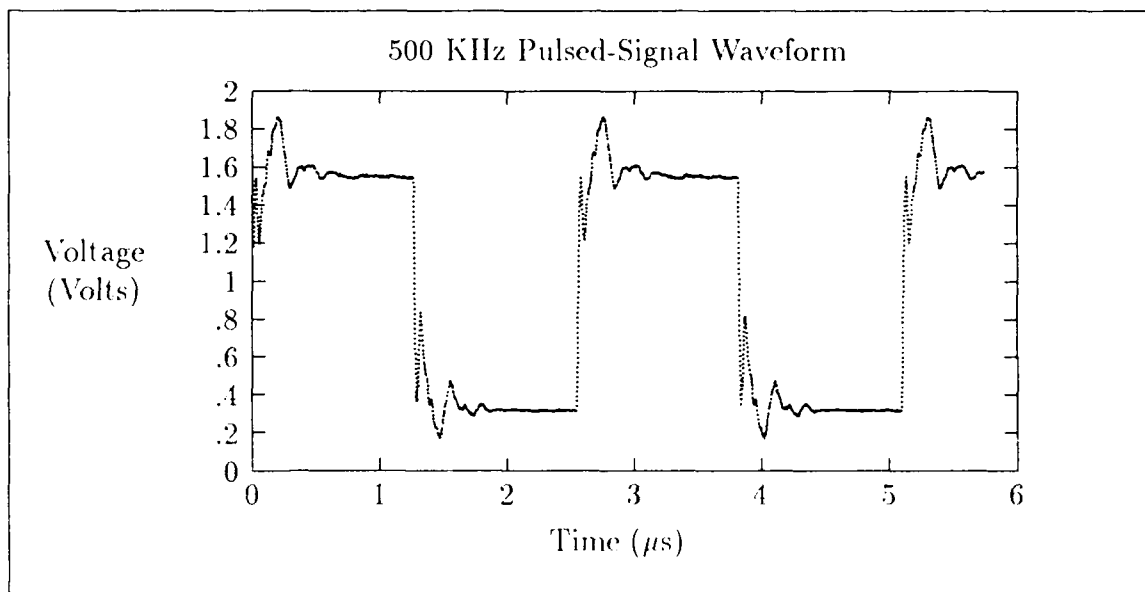


Figure 4.42. Pulsed-signal response of the 62nd structure from the PIQ wafer at 500 KHz (unfiltered).

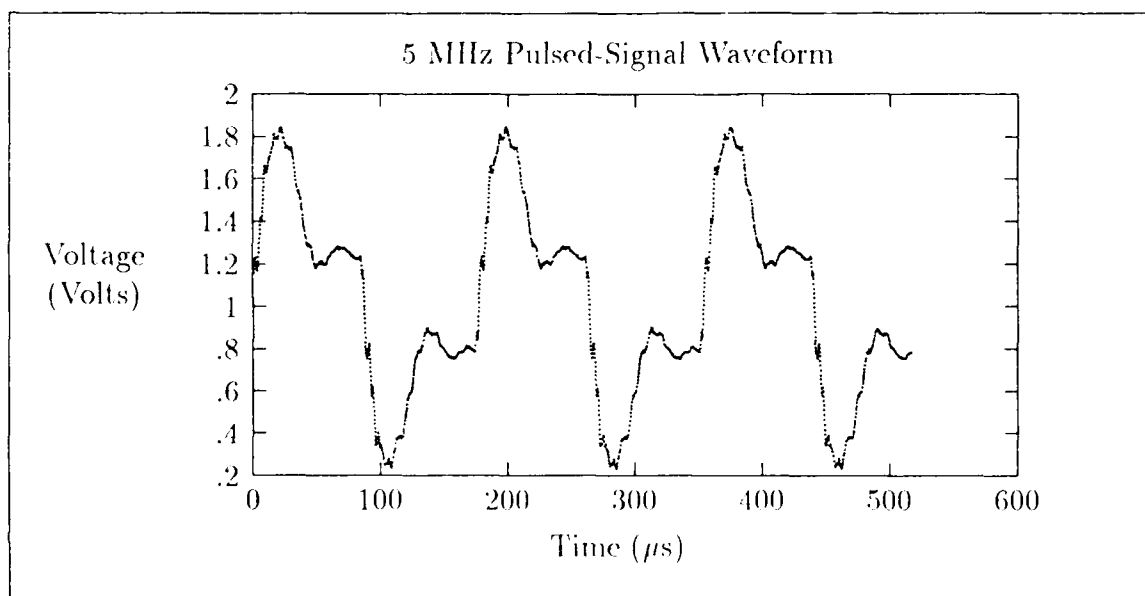


Figure 4.43. Pulsed-signal response of the 62nd structure from the PIQ wafer at 5 MHz (unfiltered).

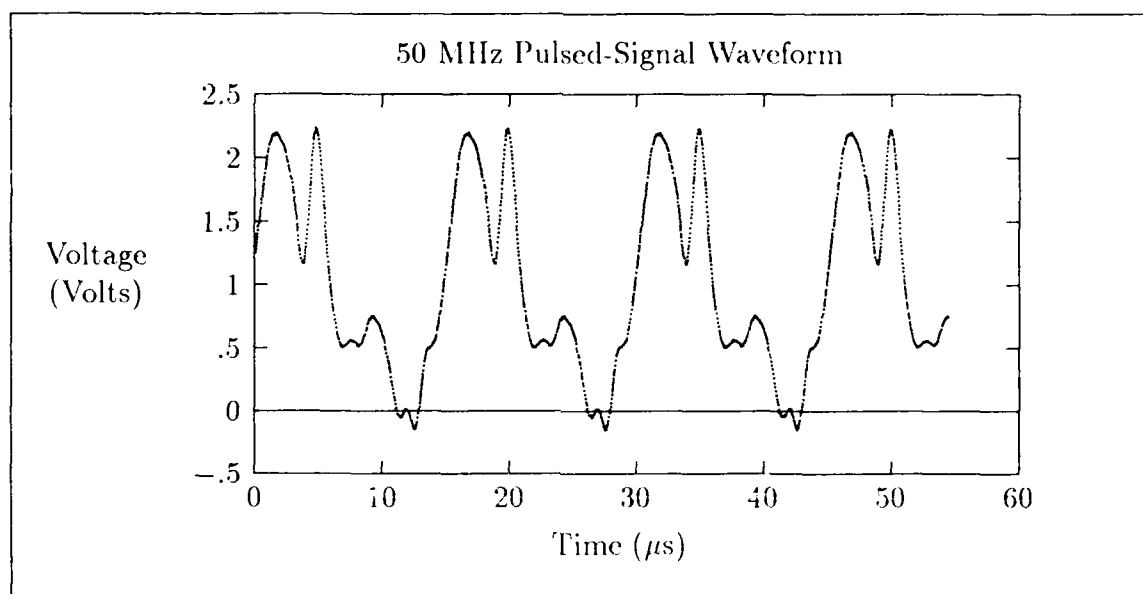


Figure 4.44. Pulsed-signal response of the 62nd structure from the PIQ wafer at 50 MHz (unfiltered).

structural types included two- and three-conductor ECS structures, coplanar waveguides, and meander lines. The investigations were roughly categorized as physical observations, frequency-domain measurements, and time-domain measurements. The physical observations consisted of the optical examination and dc continuity measurements. The frequency-domain measurements consisted of single-port measurements spanning 1–700 MHz that were utilized to estimate the characteristic impedance and two-port measurements spanning 1–100 MHz that were utilized to determine the transmission, coupling, and isolation gains. Finally, the time-domain measurements consisted of sets of pulsed-signal response measurements spanning 5 KHz–220 MHz which qualitatively examined the response of these structures to pulsed, voltage excitations of the type used in digital systems.

The optical observations revealed positive results regarding the photolithography of the various WSIC structures. However, dc continuity measurements revealed many continuity and leakage defects on structures from the PIQ wafers. These problems were also apparent on the BCB wafer, although more difficult to quantify, due

to the presence of a non-conductive (blackened) film on the exposed electrical contact surfaces. Significant abrasion was required for routine probing, and the diagnosis of continuity faults was inconclusive due to these electrical contact difficulties.

The characteristic impedance measurement analysis revealed the existence of loss in the WSIC structures which manifested themselves as specific frequency dependencies in the measured driving point impedances. In every case, the curves generated by the swept-frequency measurements spanning 1–700 MHz produced impedance curves which tended towards infinity at decreasing frequencies, and asymptotically appear to approach the theoretical value of  $Z_0$  at higher frequencies. In practice, however, the measurements did not consistently tend towards this theoretical value. As an approximation, the last 20 points of each curve were linearized and extrapolated to a crossing frequency  $f_{cross}$  where the anticipated value of  $Z_0$  would be attained. When compared with the various analytic projections, which were based on closed-form approximations, LINECALC program estimates, FDM simulations, and solution of the multi-conductor telegrapher's equations, the resulting correlation of measurements were varied. The correlation accuracy was seldom within 10 percent. However, the manifestation of transmission line behavior in the WSIC structures was clearly obvious, based on comparison of the swept frequency measurements with simulations. Furthermore, the establishment of the analytic characteristic impedance estimates were based on assumed geometric parameters which could not be verified. The uncertainty of at least one geometric parameter, the vertical separation between ground planes, was as much as 20 percent.

The bulk of the gain-phase measurements performed were those used to obtain the backward-coupling gain. Again, a common frequency-dependent behavior was identified in the various WSIC structures via the swept frequency measurements spanning 1–100 MHz. Simulations were performed on several ECS structures. The differences between the measured and simulation results were sometimes large — as much as a 20 dB difference throughout the measured range — but the general



shapes of the curves were very similar. Thus, the differences were mostly translational. Again, the dependencies observed were strongly indicative that the WSIC structures behave very much like transmission lines. Transmission measurements revealed significant attenuations in matched loads, especially in the structures having 10  $\mu\text{m}$  linewidths. Isolation performance measurements were conducted on one structure. The results of these measurements compared roughly to the backward-coupling case.

The results of the time-domain measurements were varied. For lower frequency pulses (at or below 50 KHz), the most important and obvious result found was that the pulse amplitude was attenuated for a 50  $\Omega$  termination, and it was relatively unattenuated for high impedance loads. However, at higher frequencies, the reflections caused by high-impedance loads were disastrous in certain structures. The worst distortions were observed in the CPW structures. These structures manifested significant signal distortion, even at frequencies as low as 50 KHz. It was concluded that these distortions were the result of reflections occurring due to impedance mismatches. Furthermore, even though the 50  $\Omega$  terminations produced relatively small reflections in the stripline structures, a more disrupted signal response was evident at higher frequencies. Some of the measured responses would be considered unacceptable even for digital systems. However, signal coupling in digital signals do not appear to pose a problem in these structures, based upon the time-domain measurements.

## *V. Conclusions and Recommendations*

### *Overview*

#### *Summary of the Research Effort*

The overall goal of this research was to identify and characterize the transmission line behavior in wafer scale integrated circuit (WSIC) interconnection structures through quantitative analysis and measurement. In particular, the undesired transmission line effects associated with reflection, coupling, and attenuation were a critical consideration. A topic of special interest, the performance of pulsed-signal waveforms on representative WSIC structures, was pursued as a qualitative investigation. Another topic of importance, the yield of WSIC interconnections, was not considered, due to the small number of samples available for investigation.

The theory underlying transmission line structures with geometries similar to those of WSIC structures was investigated in a literature review. Originally, it was not recognized that a large body of material existed to adequately treat WSIC structures. However, assuming that these structures behaved as transmission lines, it was evident that, in fact, many significant facets pertaining to the analysis and design *had* been addressed in the literature. These treatments were quite specific and did not explicitly treat WSIC structures in particular, but they instead addressed the general subject area of rectangular transmission line structures. The primary issues involving those structures assumed to be representative of WSIC structures were the transmission line properties of characteristic impedance, coupling, and attenuation.

Several substrates, designed at AFIT and manufactured by the Polycon Corporation, were utilized in a series of measurements. Three wafers were used: two wafers with a PIQ intermetal dielectric and one wafer with a BCB dielectric. The measurement approach itself required definition and the instrumentation configurations had to be devised. Appropriate metrics were chosen to exploit transmission line characteristics of the passive WSIC interconnections. The measurements were categorized as physical, frequency-domain, and time-domain measurements. The

physical measurements included physical observation and continuity probing measurements. The frequency-domain measurements included single- and dual-port, swept-frequency measurement techniques. The single-port measurement technique consisted of a two-part, driving-point impedance measurement intended to estimate the characteristic impedance of a particular WSIC structure. The two-port measurement technique pursued the coupling, transmission, and isolation measurements. The coupling and isolation measurements were defined and were only performed on multi-conductor structures. The final measurement category, the time-domain measurements, consisted of pulsed-signal response measurements. The performance of each category involving electrical measurement was both simulated and measured for the test structures, except for the time-domain measurements, which were not simulated. These pulsed-signal measurements were strictly qualitative in nature. The measurements were subsequently compared to the results theoretically projected, as appropriate.

Visually, the wafer fabrication results appeared to agree with the design specification. However, the dc continuity measurements revealed a significant number of series-continuity and parallel-leakage defects on each wafer.

The characteristic impedance measurements revealed a frequency-dependent behavior that was successfully simulated. Analytic characteristic impedance values did not systematically correlate with values derived from the measurements. The two-port measurements implied that the attenuation in WSIC interconnections were significant when 50  $\Omega$  terminations were used with the interconnection structures. The coupling between structures measured (some with interline spacings as close as 18  $\mu\text{m}$ ) were verified to be less than -20 dB. The measurement and analysis curves were similar in shape, but the measured coupling was always greater than the analytically predicted coupling. The difference was as much as 20 dB across the frequency range (1-100 MHz). Similar measurements were performed for isolation gain.

The time-domain, pulsed-signal response measurements indicated that, at least below 100 MHz, it was possible to achieve signal fidelity or high signal amplitudes, but not both, except at very low frequencies (below 500 KHz). Signal fidelity for most structures was adequate for applications where 50  $\Omega$  loads may be used (provided that the associated technology possesses adequate noise margins). However, these low-impedance loads caused significant signal attenuation in the 0.1 m long transmission lines. When the more practical high impedance terminations were used, signal level was preserved at the expense of signal fidelity. The impedance mismatch between the WSIC interconnection structure and the termination created reflections, which caused this distortion. For certain structures, significant signal distortions were obtained at frequencies higher than 500 KHz, even when 50  $\Omega$  terminations were used.

*Research Objectives.* As implied in Chapter 1, the research objectives of this thesis were to address the transmission line properties of WSI interconnection structures. These WSI structures, as extensions of the interconnections between circuit elements on an integrated circuit die, were primarily treated as lumped-circuit interconnections. However, as microwave designers are acutely aware, these interconnections represent much more than that. This research effort evolved as an elaboration on the concept that WSIC interconnections *do* behave like transmission lines. Following this tenet, the questions of "How much are they like transmission lines?" and "When are they like transmission lines?" were natural consequences. These particular questions were enumerated in the problem statement of Chapter 1, and they represent refinements of these basic questions, except for the last question — the pulsed-signal response, which emerged as a topic of special interest. After all, the main impetus of WSI research is from VLSI work, which is predominantly digital in nature.

*Research Methodology.* The research methodology was directly driven by the problem statement. The first question:

1. Do currently established and proposed models for calculating the characteristic impedance, coupling, dispersion, and attenuation adequately characterize WSI interconnects so that designers may continue to use them?

involved the consideration of four elements: characteristic impedance, coupling, dispersion, and attenuation. For each element, a literature search and the selection of an appropriate measurement technique was performed. For the characteristic impedance, a relatively simple technique was selected. According to Equations 3.1 and 3.2, the characteristic impedance of a transmission line can be obtained by examining its driving point impedance twice. First, the impedance is measured when the load end of the transmission line is short-circuited; second, it is measured when the load end of the transmission line is open-circuited. These measurements were pursued over the frequency range of 1–700 MHz. The second element, the coupling between conductors of a multi-conductor structure, was readily measured by treating the WSIC structure as a two-port network and performing a gain-phase measurement in the appropriate configuration. These measurements were conducted over the frequency range of 1–100 MHz. The third and fourth elements, dispersion and attenuation, were explored through continuity measurements, transmission measurements (using a gain-phase measurement spanning 1–100 MHz), and the time-domain, pulsed-signal response measurements.

The second question from the problem statement addressed the coupling problem more specifically:

2. Is the electrical coupling in representative WSI interconnections so severe as to render them useless in digital and analog system applications?

To answer this question, the measured coupling levels were examined in the context of applications for these systems.

The final question:

What performance can be expected from a typical WSI network when digital signals are impressed upon it?

was approached qualitatively. The performance of WSIC structures was pursued by examining their pulsed-signal response at select frequencies spanning 5 KHz-220 MHz.

*Research Findings.* The following findings pertain directly to the topics addressed in the problem statement and the research objectives.

*Transmission Line Properties: Characteristic Impedance, Coupling, Dispersion, and Attenuation.* The literature review uncovered many closed form expressions for the characteristic impedance ( $Z_0$ ). Several of the closed form expressions were applied to the WSIC structures. Additionally, a commercial CAD program (LINECALC) was used to model these structures. It was apparent, even before this modeling was complete, that most of the WSIC structures were non-traditional. The presence of nonstandard ground planes or the absence altogether of ground planes made categorization difficult. Nevertheless, the structures were approximated with models for standard structures. The measurement of the characteristic impedance created other problems. As a consequence of the measurement configuration used, new definitions of  $Z_0$  were created to account for the presence of floating conductors. Consequently, finite difference models were generated to provide estimates of  $Z_0$  for these new definitions.

The standard Equation 3.1 approach did not directly produce the desired static value of the characteristic impedance. Rather, the measurements all displayed a common frequency-dependent behavior. That is, at low frequencies, the characteristic impedance magnitude increased towards infinity, while at high frequencies, the impedance magnitude asymptotically approached a single value. This asymptote turned out to be the static characteristic impedance, as supported by the simulations.

It was shown that Equation 3.1 produced static values of the impedance *only* for lossless lines. Hence, for any real line (which possesses loss), the characteristic impedance can be estimated only by examining the high-frequency limit behavior. The simple linear model used to extract the static values produced mixed results. Most of the structures exhibited characteristic impedances near  $50\ \Omega \pm 20\Omega$ . The basic trends of the measurements followed the theoretical predictions. The impedances of the BCB structures were slightly greater than those for the corresponding structures on the PIQ wafers. As expected, the impedances of the  $25\ \mu\text{m}$  linewidths were smaller than the impedances of  $10\ \mu\text{m}$  linewidths. The CPW structures on the test wafers were found to manifest a lower characteristic impedance than did the corresponding ECS and ECM structures.

The coupling of dual-conductor structures was explored by simulation and measurement. The simulations were provided by LJBRA models and numeric simulations based on the solutions of the multi-conductor telegrapher's equations. The simulations were swept in frequency over the range of 1–100 MHz, which corresponded to the measurements. For the coupling measurements, only low impedance terminations were used on the terminals involved in the two-port measurement, while the remaining terminals of the four- or six-port structures (corresponding to two-conductor and three-conductor structures, respectively) were left in a floating, high-impedance state.

The simulation and measurement curves were generally similar in shape. However, large translational differences existed in the two sets of curves; sometimes this difference was as large as 20 dB across the entire frequency range. As in the case of the characteristic impedance evaluation, the introduction of loss in the simulation made a difference, more notably in the latter simulation method. In all cases, the magnitude of the measured coupling exceeded that of the simulated coupling.

The effects of dispersion were not modeled in the characteristic impedance directly, but were displayed in the corresponding swept-frequency curves. Apparently,

the geometric dispersion effects widely discussed in the literature do not occur until the higher frequencies are encountered (well above 2 GHz). In terms of transmission, only the meander structure displayed a marked frequency dependent behavior (as large as a 25 dB variation). This variation undoubtedly created the dispersion manifested in the time-domain plots for these structures (for example, Figure 4.26). For other structures, the variation in transmission gain was much lower (typically less than 2 dB). Transmission measurements performed on one ECS-like structure revealed less than 2 dB of change across the frequency range of 1-100 MHz. Therefore, dramatic changes in the resulting waveforms of time-domain measurements were observed, these distortions were probably not dispersive. Rather, these distortions were probably due to reflections which resulted from an impedance mismatch. With respect to coupled signals, the dispersion effects were more evident, as shown in Appendix I. Since the coupling gain varied so widely with frequency, the appearance of dispersion was not surprising. The overall waveforms suffered severe attenuations, except for the higher-frequency components. (Of course, the WSIC designer, who wishes to treat neighboring conductors as isolated, would prefer that severe attenuations would occur at all frequencies for coupled waveforms.)

The attenuation due to conductor resistive losses was greater than expected in continuity measurements. Clearly, the presence of attenuation effects all other transmission line parameters, as was dramatically indicated in the characteristic impedance simulations.

*Coupling Effects.* Clearly, the presence of coupling was found in multi-conductor structures, both in theory and measurement. Although the translational correlation did not agree well between the two methods, the maximum measured coupling was found to be consistently less than -20 dB for frequencies less than 100 MHz. This finding is encouraging for digital applications, since this rather low level of noise can usually be tolerated.



*Pulsed-Signal Performance.* For low frequencies ( $<500$  KHz), the WSIC structures generally performed well (with the exception of the CPW structures), both in the low-impedance and the high-impedance loading terminations. Of course, at these low frequencies, the reflections of the high-impedance termination die relatively rapidly. The low-impedance terminations indicated a marked attenuation, due to voltage divider losses. At higher frequencies, as expected, the signal distortions increased, most notably in the high-impedance terminations, although several of the structures with low-impedance terminations all displayed severe distortion. The distortion problems were most severe in the meander and CPW structures. In the case of the meander structure, the resonances were most likely responsible for the distortion, since the performance actually improved in these structures at higher frequencies (above the resonance points observed in the frequency-domain, transmission measurements). For the CPW structures, the jagged appearance of the waveforms was strongly indicative of reflections. The severe reflections could have been a consequence of the low impedances which were observed for these structures.

### *Conclusions*

The following conclusions were made regarding the findings of this research effort.

*Transmission Line Behavior and Modeling.* Clearly, the WSIC structures behave like lossy LC transmission lines, based on the similarity of measured and simulated impedance and coupling responses. The ability of current models to do the necessary characterization is questionable, simply due to the non-standard geometries of the WSIC structures on the test wafers. When these geometries were approximated with conventional structures, the results tracked qualitatively, but the error between measurement and theory were still large, especially in the coupling investigation. No satisfactory source of the discrepancy was found for this difference, but grounding problems could be a possibility. Additionally, the approximations used for

the theoretical projections were based on assumed, but otherwise unverified design specifications.

As a design tool, the LIBRA and LINECALC models produce approximate performance results for the WSIC structures. For systems with wide bandwidths, a more in-depth investigation, perhaps including electrostatic analyses and numeric solutions to Equations 2.29 and 2.30 should be considered. At frequencies above 100 MHz, more investigations of the type conducted in this thesis are required.

*Coupling Effects.* As indicated in Chapter 4, both the series transmission gain and the coupling gain of a structure must be considered for a prospective application. Even though the coupling levels were found to be low ( $< -20$  dB) at low frequencies ( $< 100$  MHz) in representative WSIC structures, the transmission gain may also be low (as low as  $-11.4$  dB for a  $10\text{ }\mu\text{m}$ ,  $0.1\text{ m}$  structure at  $100\text{ MHz}$ ). As a rough rule of thumb, the coupling should be estimated by subtracting the transmission gain from the coupling gain. For example, in a structure with a maximum coupling gain of  $-20$  dB and a maximum transmission gain of  $-12$  dB, a net coupling gain of  $-8$  dB results based upon this rule of thumb. In this light the coupling effects are much more significant. Based on measurements associated with the  $10\text{ }\mu\text{m}$  wide structures  $0.1\text{ m}$  long and separated by  $18\text{ }\mu\text{m}$  of lateral distance, a maximum coupling gain was found to be  $-35$  dB. For a similar  $10\text{ }\mu\text{m}$  wide structure  $0.1\text{ m}$  long, the lowest transmission gain was found to be  $-11.4$  dB. Hence, by the above rule of thumb, the net coupling gain would be  $-23.6$  dB. For a five volt pulse input, this translates to a worst case coupling of  $0.33$  volts. (Design curves based on the this type of rationale were presented in Chapter 4 for the  $10\text{ }\mu\text{m}$  and  $25\text{ }\mu\text{m}$  linewidths for other values of the coupling gain).

*Pulsed-Signal Performance.* At frequencies below  $500\text{ KHz}$ , most structures performed acceptably. However, one problem observed with low-impedance terminations was that significant attenuation occurred. The use of high impedance terminations solves this problem. However, at higher frequencies, the impedance

mismatches between the line and the termination create extraordinary distortions. Creating a higher line impedance might provide some marginal benefits. In this case, a termination with higher impedance could be used. However, the ability to produce a characteristic impedance greater than  $125\ \Omega$  would be physically difficult, as discussed in Chapter 2. Even this improvement would not provide a dramatic reduction in attenuation.

Low impedance terminations improved signal fidelity, in general. However, even for low-impedance terminations, certain structures, such as the CPW structures, were plagued with reflection problems at high frequencies. At frequencies above 50 MHz, all structures seemed to distort the pulsed signals. However, it is difficult to conclude that the structures would not work effectively at these frequencies, since even the pulse generators used did not produce "good" pulse trains. At 50 MHz, most of the ECS and ECM structures on the PIQ and BCB wafers appeared to produce usable pulsed-signal waveforms when compared to the input signal. On the other hand, the meander structures, due to their resonant nature, produced terrible results at certain frequencies. The coplanar waveguides generally manifested poor signal fidelity at frequencies above 500 KHz. A possible source of the problem for the CPW structures is their impedance mismatch with the  $50\ \Omega$  load termination.

#### *Recommendations for future research*

This section outlines suggested recommendations pertaining to this research effort. The recommendations are divided into two separate categories. The first pertains directly to the extension of this research. The second category provides suggestions pertinent to the design support for WSIC interconnect characterization. The final category provides recommendations regarding the electrical design of hybrid WSI systems.

*Extension of Current Research.* This research effort was merely a scratch on the surface of what remains to be explored on the AFTT/Polycon test wafers. As

previously stated, only the 10 cm block of structures were considered, leaving at least eight other blocks which contain groupings of interconnections which were not examined. These groupings include shorter transmission line structures, various capacitors, and yield-related structures, such as via chains. In addition to the extra structures, several other prospective frontiers of special interest remain, which include:

1. Continued low-frequency work
2. Extended frequency-domain evaluation
3. Extended time-domain evaluation
4. Yield performance evaluation
5. Additional dielectric and conductor materials evaluation
6. Electromagnetic structural evaluation.

*Continued Low-Frequency Work.* Several resultant mysteries, such as the coupling gain discrepancy, should be followed up. Additionally, when the leakage and continuity problems are resolved, more parametric measurements should be accomplished. The test wafer was designed such that if all structures were measured, design curves could be produced. For example, the spacing of particular coupled structure types were varied across the wafer. By measuring each variation for a particular structural class (for example, 10  $\mu\text{m}$  2-conductor ECS structures), a design curve of a given measurand versus the parameter of lateral spacing could be generated. Unfortunately, due to the aforementioned continuity problems, it was not possible to measure a sufficient number of similar structures to produce these design curve plots.

*Extended Frequency Evaluation.* The measurements and analysis of the WSIC test wafers at higher frequencies would also be beneficial. Although some of the pulsed-signal response and impedance measurements were performed at

frequencies as high as 220 MHz and 700 MHz, respectively, the bulk of the evaluations performed in this research effort focussed on frequencies at and below 100 MHz. In particular, the coupling gain of these structures are expected to increase slightly at frequencies above 100 MHz. Additional measurements are required at these higher frequencies to verify this trend.

The evaluations should also continue at even higher frequencies. While many of the current silicon-based applications can be accommodated at frequencies well below 1 GHz, a large base of microwave applications could take advantage of hybrid WSI approaches if such an evaluation could be accomplished. As implied in Chapters 2 and 3, both the analysis and the measurement evaluations would be necessarily involved. For example, the simulations might require full-wave solutions, instead of the quasi-static approximations used. The effects of discontinuities would be more pronounced and could not be neglected. Additionally, the dispersion mechanisms and conductor skin effect loss mechanisms would provide further complications in the analysis. The measurements at frequencies above 2 GHz would require different probes, since the inductance of the coaxial probe, the discontinuities at the connector joints, and the transition formed at the probe tip would introduce significant if not insurmountable measurement challenges. More importantly, higher frequency test equipment, such as the HP 8510 network analyzer, would be required for the characterization work.

*Extended Time-Domain Evaluation.* Several powerful time-domain techniques, including time-domain reflectometry (TDR) and time domain transmission (TDT), would provide valuable insight into the electrical performance of the WSIC test structures. With these techniques, it is possible to determine the characteristic impedance of wafer structures and the physical position of discontinuities within the structure. The techniques would be most beneficially applied to the longer test structures, such as those found within the 10 cm block. Even for these longer structures, very fast equipment is required for adequate analysis. Special TDR/TDT

equipment is available, although reasonable results can be obtained with a relatively simple equipment configuration, consisting of a high-speed pulse generator and storage oscilloscope [(11),(61),(95)].

*Yield Evaluation.* The demonstration of high yield is essential for WSI. This line of research is important to pursue, and several via test chains are provided among the test structures on each wafer. Yield determination is necessarily a statistic process; hence, the evaluation should encompass as many different wafers as possible. Eventually, a yield model, similar to those discussed in Chapter 2, could be produced.

*Additional Dielectric and Conductor Materials Evaluation.* Another important line of potential research would be the characterization of different combinations of dielectrics and conductors. Other dielectrics, even within the categories of polyimides and BCBs, exist which could be evaluated. Since only aluminum conductors were evaluated in this effort, the exploration of structures using copper conductors would be an interesting extension to the characterization work accumulated for aluminum conductors. Of course, the implementation of this conductor in a WSIC substrate would also be of interest from a fabrication technology standpoint.

*Electromagnetic Structural Evaluation.* Many of the special structures contained on the test wafers have not been analytically treated in the literature, nor were they contained in model libraries of the LIBRA CAD program. Examples of these structures include the embedded two- and three-conductor ECMs, the meander structures, and structures of inhomogeneous dielectric composition above a semi-conducting substrate. Another very important potential line of work is the characterization of meshed ground planes, since these are more desirable to use in WSIC implementations. The characterization of these structures through a detailed, electromagnetic analysis should be performed. These analyses would lead to the generation of more accurate models which may more closely correlate to measured results.

*WSIC Design Support.* The following recommendations pertain to the WSIC test substrates and to the measurement and analysis of these substrates:

1. Inclusion of test standards.
2. Measurement of dielectric properties.
3. Grounding modifications.

*Inclusion of Test Standards.* The inclusion of several additional standards are recommended for the test wafers. Although some of the available commercial coplanar test probes are equipped with reference substrates, many test probes do not have a calibrated set of standards. The inclusion of test standards or calibration standards could improve measurement efficiency and could provide additional useful information about the test wafer. Several suggested additions are shown in Figure 5.1. The recommended additions include: a test short, multiple test opens, and two special transmission line structures.

The calibration short and open standards are patterned after those used in the impedance standard substrates supplied with some of the commercial coplanar probes (78). The calibration short would be useful in impedance short and transmission through calibrations. The calibration open would serve two purposes. As a calibration, it would provide greater accuracy than afforded by suspending the probe tip above the wafer, as was done in this research effort. The second purpose for the calibration would be for the attachment of chip resistors with known values ( $50\ \Omega$ , for example). Thus, at least two of the open standards would be required on each wafer: the first, for the open termination; the second, to accommodate a fixed resistance calibration. Finally, two transmission line structures are recommended for inclusion as calibration structures. The first transmission line structure would be shorted on one end to a reference ground plane, while the second transmission line would be left open at both ends. The transmission line structures would have solid ground planes above and below and would be sufficiently separated to minimize

coupling effects ( $s > 100 \mu\text{m}$ ). Hence, these structures would closely match the performance of a stripline, which can be categorized using the Chapter 2 expressions. As such, the transmission line pair would be directly configured for the driving-point impedance measurements, described in Chapter 3, which were used to estimate characteristic impedance in this research effort. While the resulting curves were shown to display the characteristic impedance only at high frequencies, the geometries are very well-studied, and the asymptotic behavior could be characterized empirically. After several wafers are successfully characterized, these particular structures would display differences in ground plane separation, attenuation, and dielectric constant from wafer to wafer. Hence, such a structure could be used as a quality control check to determine the variability of these parameters from wafer to wafer. Unfortunately, the stripline structure is not particularly sensitive to conductor height above ground plane. To alleviate this deficiency, other structures without the superficial ground plane could be placed on the wafer. Although the resultant embedded microstrip structure is less established in the literature, it could be characterized empirically.

*Measurement of Dielectric Properties.* To measure the dielectric properties of test wafer materials, it is recommended that special substrates be formed. These special substrates would be similar to those which contain test structures, except that solid ground planes would be extended across the entire wafer at metal levels one and four, and that the space between the planes would be homogeneously filled in the desired dielectric. Then, a technique for measuring the dielectric constant of wafers described in (68) could be used. Since this approach may be impractical due to the mechanical stresses induced by temperature coefficient mismatches, an alternate approach would consist of the forming of a linear or circular resonator as a regular structure on the test wafer. As shown in Figure 5.2, these resonators would be gap-coupled to striplines. Both the resonator and the coupling lines should be embedded inside the dielectric between the ground planes. If microstrip or embedded microstrip structures are used, then the resultant resonances will correspond to



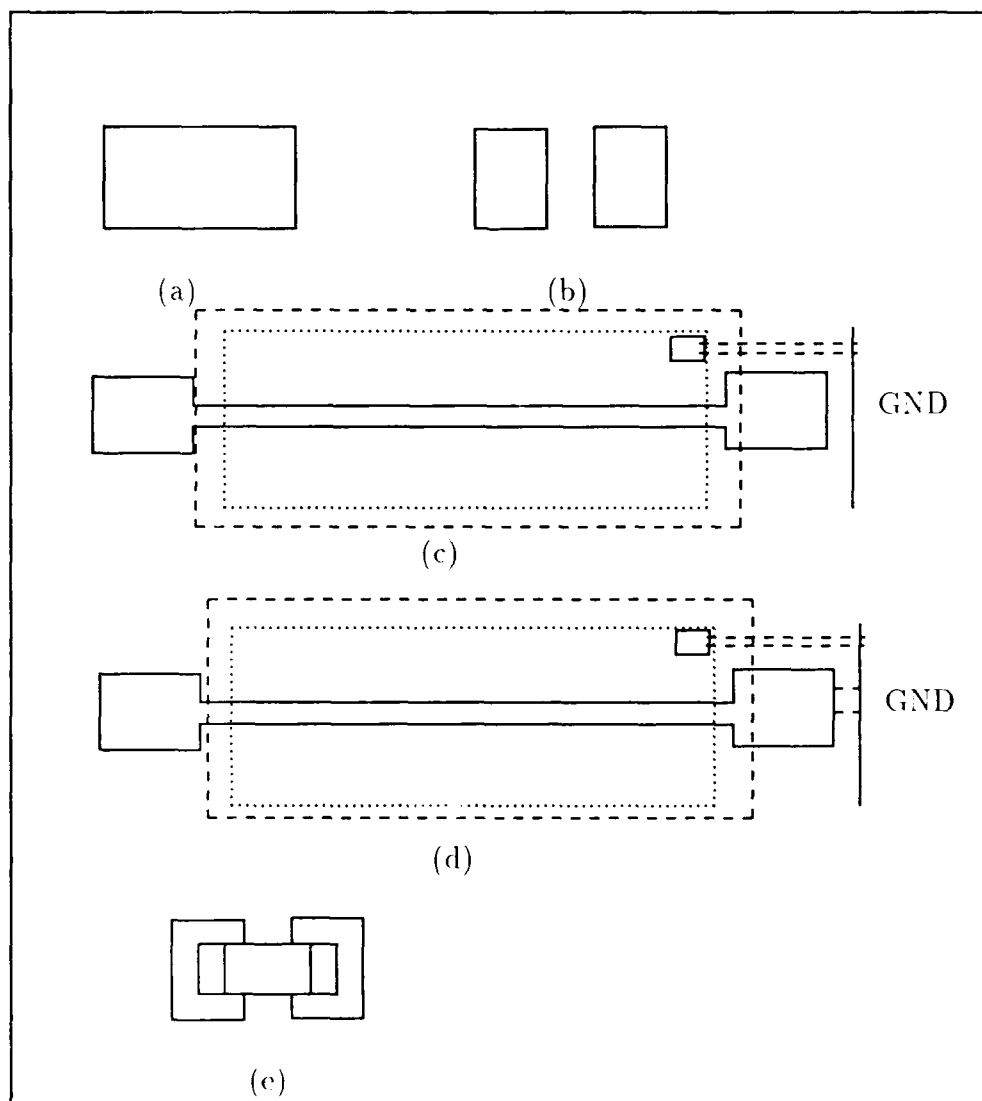


Figure 5.1. Suggested additional standards for future test wafers. (a) Short. (b) Open. (c) Transmission line (ECS) with shorted end. (d) Transmission line (ECS) with open end. (e) Suggested use of open from (b) as a resistive (or other lumped element) test standard.

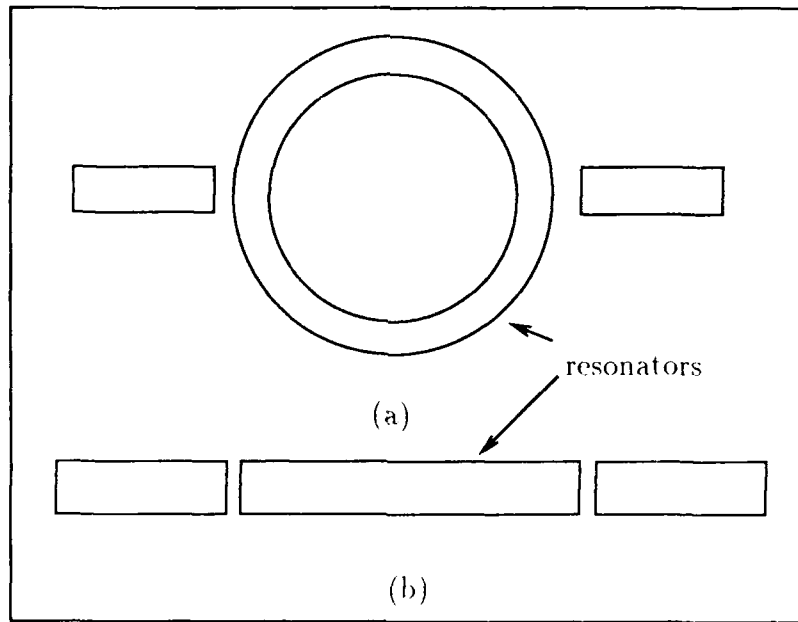


Figure 5.2. Ring and linear resonators. (a) Ring resonator. (b) Linear resonator. After (11).

the effective dielectric constant ( $\epsilon_{R,eff}$ ), rather than the relative dielectric constant ( $\epsilon_R$ ). The dielectric constant is calculated based on resonances of these structures, using techniques described in (41:33).

*Grounding Modifications.* Grounding and shielding was found to be a significant problem in this thesis. To minimize these problems, closely placed reference grounds were found to be essential. For the structures in the 10 cm block, the laterally-placed ground structures served this purpose, although it was sometimes necessary to place an additional grounding probe near the point where measurements were taken. For other test structures, such as the 1 cm and 2 cm blocks of test structures, no such reference plane is provided. It is recommended that the test wafer be modified to include a "probe-able", lateral ground plane for other structures, inasmuch as possible.

*Recommendations Regarding Future Hybrid WSI Systems.* Clearly, the design of a high-frequency hybrid WSIC system will involve many compromises. These compromises involve the length of interconnections, their width, and the separation distance between conductors.

If the length of an interconnection is excessive, then the line will behave as a transmission line. For this circumstance, high impedance terminations are unacceptable. However, conductor losses will promote attenuation when low-impedance, matching terminations are used, due to voltage divider losses. Using wider conductor lines will provide some reduction in attenuation, but the termination will also be affected. With wider lines, the characteristic impedance is decreased. Hence, the voltage divider losses are increased. Thus, the attenuation problem will not be sufficiently treated by merely increasing linewidths.

Another problem with increasing linewidths is the corresponding decrease of the wiring densities. Obviously, fewer lines/cm can be accommodated by wider lines. Additionally, the coupling gain of edge-coupled structures are increased when the width of the conductors is increased. To preserve noise margins, the inter-conductor lateral spacing must be increased, resulting in a further degradation of the wiring density.

Hence, wider lines produce quickly diminishing returns. Narrower lines are also bad. In order to increase the value of termination loads, one might consider narrower lines a good idea, since the characteristic impedance is increased. However, in no event is it likely that the characteristic impedance will increase above 115  $\Omega$ . Furthermore, the series attenuation of the conductor is increased.

Between the two conductor linewidths used in this work, 10  $\mu\text{m}$  and 25  $\mu\text{m}$ , the 25  $\mu\text{m}$  wide structure provides less attenuation for a fixed termination. Besides the attenuation, the 10  $\mu\text{m}$  wide structure provides comparable performance. However, in either case, the attenuation is unacceptable in conventional digital systems for the line lengths studied. To resolve this problem, the use of shorter interconnections

will be necessary. The conventional rules of thumb for interconnection design in larger circuits appear to be appropriate. One such rule of thumb, as indicated in Chapter 2, suggests the use of interconnections which are shorter than 1/15th of the wavelength of any signal applied to them. For such interconnections, the reflections due to mismatch are expected to decay before a significant portion of the input waveform appears on the line. These trends were reflected in the low-frequency (5 KHz), pulsed-signal responses presented in Chapter 4 for several structures. In these circumstances, high frequency terminations may be used. When the frequency is higher for a given line or when the interconnection is longer with respect to a given frequency, the time required for the reflections to decay become more significant and can noticeably affect signal fidelity. In these cases, the use of line terminations are required.

Based on these observations, an obvious question arises: How can a WSIC design be implemented which requires the use of long lines? It appears that one solution can be achieved through the use of non-standard buffer-driver devices. These buffer-drivers would provide a match to the transmission line, while providing amplification to the signal sufficient for driving conventional digital logic. An obvious final requirement of such a driver would be physical compatibility with the dimensions of the input pads of the integrated circuit die placed in the die sites of a prospective hybrid WSI system.

Figure 5.3 illustrates the application of this buffer-driver. The use of buffer drivers are limited to the periphery of die sites in a hybrid WSI substrate where long signals are to be propagated, as shown in Figure 5.3a. Depending on the frequencies involved, conventional drivers could be used for short runs. The actual configuration of such a driver, as shown in Figure 5.3b, could potentially be a simple dual-stage driver implemented in a MOSFET technology, designed to have an input impedance nominally equal to the characteristic impedance of the WSIC. Digital signal performance comparable to that achieved in this research effort would be obtained with a

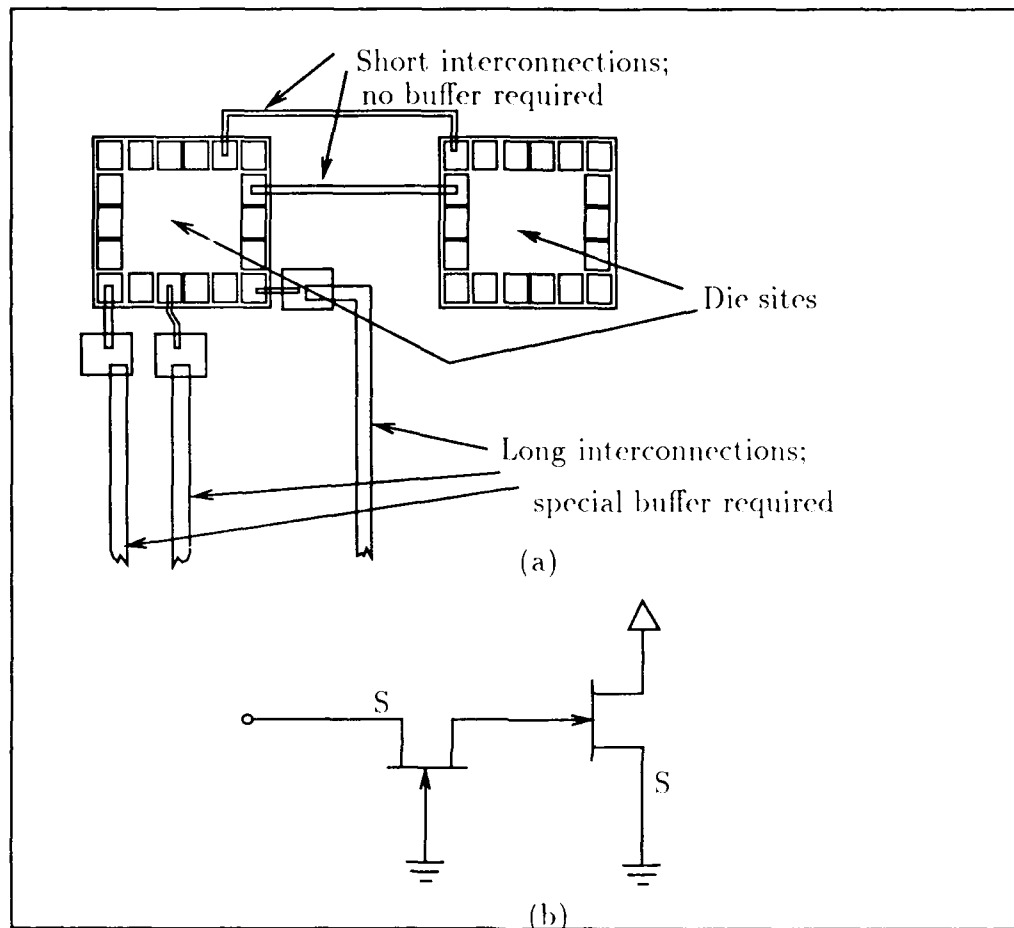


Figure 5.3. Application and configuration of a matching buffer-driver.

50  $\Omega$  input impedance. Unfortunately, since the input impedance of such a driver is proportional to the inverse of the device's transconductance (74), the implementation of a device in VLSI dimensions may be difficult, if not impractical. However, such devices are needed in order to accomplish practical long distance transmission lines for hybrid WSI at high frequencies. Hence, pursuit of the development of this special low impedance driver is recommended for future research.

### *Summary*

The results of Chapter 4 directly imply that transmission line behavior is manifested in WSIC interconnections. Although significant discrepancies between theory and measurement were found in the characteristic impedance and coupling of these structures, the behavioral traits were very similar. The coupling gains of these structures were found to be sufficiently low such that, with care, digital systems could be implemented and operated with relative immunity from coupling noise. The requirement imposed on such applications is that the associated fabrication technologies allow for sufficient noise margins. Time-domain performance indicated that reasonable propagation of high-speed pulse signals (up to 250 MHz) is possible in certain WSIC structures. Proper termination of the structures was found to be vital in achieving any semblance of signal fidelity at the higher frequencies. However, such terminations created great signal attenuation in 0.1 m length structures, even with the wider 25  $\mu\text{m}$  linewidths. For certain structures, including CPW structures, poor pulsed-signal response was evident, even at frequencies below 5 MHz.

Recommendations for further research included more in-depth evaluations of particular WSIC structures at the frequencies used in this research effort and at higher frequencies as well. Additionally, recommendations were made regarding design enhancements of the test wafers used in this research effort. Finally, the development of special drivers with high gain and low input impedance were recommended. Such drivers could be placed around the die sites in prospective hybrid WSI systems where long signal paths would be encountered.

## Appendix A. *Numerical Simulation Programs and Data*

The program listings used for the numerical analysis in this research effort are documented in this appendix, with the exception of the finite difference method simulations. Since the finite difference method was implemented through the Lotus 1-2-3 spreadsheet, no program listing (in the conventional sense) is available. However, details of the approach used are described in Appendix E.

### *Characteristic Impedance Formulas*

Most of the characteristic impedance formulas from Chapter 2 were implemented as a Mathematica listing. The program listing used follows:

#### *Program Listing.*

```
(* CHARACTERISTIC IMPEDANCE CALCULATION FORMULAS *)
(*)
(*) STRUCTURAL CLASSES: (*)
(*)   Microstrip-      Wheeler's (*)
(*)                   Schneider's (*)
(*)                   ChangSingle (*)
(*)                   Getsinger's (*)
(*)   Stripline-      Ober (*)
(*)                   Chatterjee (*)
(*)                   Wheeler's (*)
(*)                   Chang Double (*)
(*)   Coplanar Waveguide- (*)
(*)                   Gupta (zero thickness) (*)
(*)                   Gupta (non-zero thick) (*)
(*)                   Hoffman (infinite slab) (*)
(*)                   Hoffman (zero thickness) (*)
(*)   Coplanar Strip- Non-Grounded (*)
(*)   Coplanar Strip- (*)
(*)                   Gupta (zero thickness) (*)
(*)                   Gupta (non-zero thick) (*)
(*)   Edge-Coupled Striplines- (*)
(*)                   Hoffman (zero thickness) (*)
(*)                   Gupta (non-zero thick) (*)
(*)   Edge-Coupled Microstrips- (*)
(*) (*)
(*) (*)
(*) Default parameters: (*)
(*)   height: h1,h2    06.0 um (*)
```

```

(*)          width: w1,w2    10.0 um    *)
(+)          thickness: t1,t2  2.5 um    *)
(*)          spacing: s1,s2   18.0 um    *)
(*)          relative perm:epsr  3.4      *)
(*)          ground plane separation:    *)
(*)              b      20.5um          *)
(*)                                          *)
Get["useful"]
defaults:=(h1=6; h2=6; w1=10; w2=10; t1=2.5; t2=2.5; s1=18;
s2=18; epsr=3.4; e0=8.85*10^-12; mu=1.256*10^-6;
c=3*10^8);
defaults::usage = "The default parameters are h1=6; h2=6; w1=10; w2=10;
t1=2.5; t2=2.5; s1=18; s2=18; epsr=3.4; e0=8.85*10^-12;
c=3*10^8; and mu=1.256*10^-6"
eps:=epsr*e0;
(* Create a help file which is invoked by ?Help *)
(* from the console during a Mathematica session *)
help:="Type ?help for help"
help::usage="The following routines are available for
characteristic impedance calculations:
For more detailed help on an item, type ? followed by the name
of the feature.
"
help
(*)                                          *)
(* Now explicitly declare the defaults and set *)
(* the electric permittivity, which is defined as *)
(* epsr*e0, as shown above *)
defaults;
eps;
(*)                                          *)
(* Standard Formula for characteristic impedance *)
(*)                                          *)
stdZ01[cap_,v_]:=1/(cap*v);
stdZ01::usage="Standard definition (one of several) for characteristic
impedance. Syntax: stdZ01[C,v], where C is capacitance, and v is
phase velocity. This function is called by other formula, which supply
capacitance values (e.g., ChangEmbeddedMicrostrip[w,h,er,t] and
ChangStripline[w,h,er,t,b].)"
vp[er_]:=c/Sqrt[er];
vp::usage=" This function simply computes the phase velocity by dividing
the speed of light (c) by the square root of the relative permittivity (er),
which for microstrips and certain other transmission line geometries is
not necessarily the material relative permittivity. Syntax: vp[er]."
```

```

(*)                                          *)
(* Microstrip-- Wheeler's formula *)
(*)                                          *)
Wheeler[w_,h_,er_]:= (120/Sqrt[2*(er+1)]*(Log[4*h/w+Sqrt[16*(h/w)^2+2]]-
(er-1)/(2*(er+1)))*(Log[Pi/2]+Log[4*Pi/er]))
/(w/h)<=3.3)
Wheeler[w_,h_,er_]:= (60*Pi/Sqrt[er]*(w/(2*h)+Log[4]/Pi+(er+1)/(2*Pi*er))*

```



```

(Log[Pi*Exp[1]/2]+Log[w/(2*h)+0.94]))+
(er-1)*Log[Exp[1]*Pi^2/16]/(2*Pi*er^2))^(-1)
/;(w/h)>3.3)

```

Wheeler::usage = " The popular formula by Wheeler for microstrip, derived from a conformal transform technique. The calling syntax is as follows:

```
Wheeler[w,h,er],
```

where w is width, h is height, and er is the relative permittivity. The microstrip is assumed to have zero thickness, although it is possible to create effective height, width, and/or relative permittivity definitions such that thickness corrections can be approximated.";

```

(*)
(* Microstrip - Schneider's Formula
(*)
(* see Hoffman,p 147-148
(*)
(*)
Schneider[w_,h_,er_] := (60*Log[8*h/w+w/(4*h)]/Sqrt[er] /;(w<h))
Schneider[w_,h_,er_] := (120*Pi/(w/h+2.42-0.44*h/w+(1-h/w)^6)/Sqrt[er]
/;(w>=h))

```

Schneider::usage = " Formula developed by Schneider, based on asymptotic expansions of solutions obtained through conformal mapping. Syntax is as follows:

```
Schneider[w,h,er]
```

where w is width, h is height, and er is the EFFECTIVE permittivity. To use Schneider's formula as originally intended, the effective permittivity SchneiderPerm[w,h,er] must be used in the er position of the Schneider impedance function. Hence, the correct call would be

```
Schneider[w,h,SchneiderPerm[w,h,er]]
```

where in this case, er is the RELATIVE permittivity. The Schneider characteristic impedance model is implemented in this manner to permit the use of other effective permittivity models."

```

(*)
(*Schneider Effective Permittivity Model for zero *)
(*Frequency
(*)
(*)
SchneiderPerm[w_,h_,er_] := .5*((er+1)+(er-1)/Sqrt[1+10*h/w])
SchneiderPerm::usage = "The effective permittivity model developed by
Schneider provides a geometrically-based dispersion
correction for a given relative permittivity
in a special, conformally-transformed domain. Syntax is:
SchneiderPerm[w,h,er], where w is width, h is height, and er is relative
permittivity."
(*)
(*) SchneiderMicrostrip
(*)

```

```

SchneiderMicrostrip[w_,h_,er_] := Schneider[w,h,SchneiderPerm[w,h,er]];
SchneiderMicrostrip::usage="syntax:
SchneiderMicrostrip[w,h,er], where w is width, h is height, and er is
the relative permittivity."
(* *)
(* Hammerstad et al. *)
(* see Hoffman, p 149 *)
Hammerstad[w_,h_,er_] := (f1=6+(2*Pi-6)*
    Exp[-(30.66*h/w)^0.7528];
    60*Log[f1*h/w+Sqrt[1+(2*h/w)^2]]/Sqrt[er])
HammerstadPerm[w_,h_,er_] := (a=1+1/49*Log[((w/h)^4+(w/(52*h))^2)/
    ((w/h)^4+0.432)]+1/18.7*Log[1+(w/18.1/h)^3];
    ub=0.564*((er-0.9)/(er+3))^0.053;
    (er+1)/2+(er-1)/2*(1+10*h/w)^-(a*ub))
HammerstadMicrostrip[w_,h_,er_] := Hammerstad[w,h,HammerstadPerm[w,h,er]]
HammerstadMicrostrip::usage="Syntax: HammerstadMicrostrip[w,h,er], where
w is width, h is height, and er is the relative permittivity."
(* *)
(* *)
(* Getsinger formulas *)
(* *)
GetsingerWidth[w_,h_,t_] := ((w+1.25*t/Pi*(1+Log[4*Pi*w/t]))
    /;(w/h)<=1.57;
    (w+1.25*t/Pi*(1+Log[2*h/t]))
    /;(w/h)>1.57 )
GetsingerWidth::usage = "This formula supplies an effective width, which
is based on the thickness of a microstrip. The resultant effective width
is then used in an appropriate zero-thickness formula. Syntax is:
GetsingerWidth[w,h,t], where w is width, h is height, and t is thickness."
(* *)
Getsinger[w_,h_,er_,t_] := (wx=GetsingerWidth[w,h,t];
    60/Sqrt[er]*Log[8*h/wx+0.25*wx/h] /;(w/h)<=1;
    120*Pi/Sqrt[er]*(wx/h+1.393+0.667*
    (wx/h+1.444))^-1 /;(w/h)>1;)
Getsinger::usage="This formula calculates the characteristic impedance
of microstrips with non-zero thickness using Getsinger's formula. The
program actually uses a zero-thickness formula, and the width used is an
effective width. The effective width is calculated with GetsingerWidth, and
it is based on the thickness of the microstrip. The syntax is
given as: Getsinger[w,h,er,t] where w is the width, h is the height, er is
the EFFECTIVE relative permittivity, and t is the thickness. The user can
invoke one of the standard effective permittivity models or use a customized
model."
(* *)
GetsingerPermCorrection[w_,h_,er_,t_] := (er-1)*t/h/(4.6*Sqrt[w/h]);
GetsingerPermCorrection::usage="This formula provides a delta correction
for effective permittivity models which cannot model non-zero thicknesses.
The syntax is: GetsingerPermCorrection[w,h,er,t], where w is width, h is height,
t is thickness, and er is the relative permittivity. An example of how this
feature is used is shown in the following example where it is desired to
compute the characteristic impedance of a microstrip which is 2um thick,

```

```

10um wide, and is 18um above a ground plane, resting on a dielectric slab
with a permittivity of 3.4:
Z0=Getsinger[10,18,(SchneiderPerm[10,18,3.4] +
GetsingerPermCorrection[10,18,3.4,2]),2]."
```

```

(*)
(*) GetsingerMicrostrip
(*)
GetsingerMicrostrip[w_,h_,er_,t_] := ( Getsinger[w,h,(SchneiderPerm[w,h,er] +
GetsingerPermCorrection[w,h,er,t]),t]);
GetsingerMicrostrip::usage="Syntax:
GetsingerMicrostrip[w,h,er,t], where w is width, h is height, er is
the relative permittivity, and t is thickness."
(*)
(*) Yamashita's Effective Permittivity Model
(*)
Yamashita[w_,h_,er_,eff0_,f] := (
  F=4*f*h*Sqrt[er-1]*(1/2+(1+2*Log[1+w/h]/Log[10]))^2)/c;
  (Sqrt[eff0]+(Sqrt[er]-Sqrt[eff0])/(1+F^(-3/2)))^2 )
(*) If this message is still here, don't use Yamashita!*)
(*)
(*) Stripline Formula--Oberhetinger [Ober]
(*)
Ober[w_,er_,b_] := (k=Sech[Pi*w/(2*b)];
  kprime=Tanh[Pi*w/(2*b)];
  30*Pi*EllipticK[k]/(Sqrt[er]*EllipticK[kprime]) )
Ober::usage="This function computes the exact value for the characteristic
impedance of infinitesimally thin stripline. Syntax is given by:
Ober[w,er,b], where w is width, er is the relative permittivity, and
b is the ground plane separation distance. Note that a height specification
is not required"
(*)
(*) Chatterjee Stripline model for strips, non-zero*)
(*) thickness
(*)
Chatterjee::invalid = "Expression outside of valid range"
Chatterjee[w_,er_,t_,b_] := (If [(t/w)>0.5 || (t/w)<.05,
  Message[Chatterjee::invalid],
  94.15/(Sqrt[er]*(w/b+0.45+1.18*t/w))] )
Chatterjee::usage="Although the formula was not originated by Chatterjee, this
formula calculates the characteristic impedance of a stripline with
non-zero thickness. Syntax: Chatterjee[w,er,t,b], where w is width, er is
the relative permittivity, t is thickness and b is the ground plane
separation.
A warning is printed if the inputs fall outside the
range of validity 0.05<(t/w)<0.5"
(*)
(*) Wheeler's formula for stripline
(*)
WheelerStripline[w_,er_,t_,b_] := (x=t/b;m=2*(1+2/3*x/(1-x))^-1;
delw=(b-t)*x/(Pi*(1-x))*(1-.5*Log[(x/(2-x))^2 +
(0.0796*x/(w/b+1.1*x)^m)]);

```

```

wprime=w+delw;
30/Sqrt[er]*Log[1+4/Pi*(b-t)/wprime*
(8/Pi*(b-t)/wprime+Sqrt[(8/Pi*(b-t)/w)^2+6.27]] )
WheelerStripline::usage="This equation estimates the characteristic
impedance for a stripline which has non-zero thickness. Syntax:
WheelerStripline[w,er,t,b], where w is width, er is the
relative permittivity, t is the thickness, and b is the ground
plane separation.
"
(* *)
(* Gupta--Coplanar waveguide *)
(* *)
elliptic[k_] := (kp=Sqrt[1-k^2];
(1/Pi*Log[2*(1+Sqrt[kp])/(1-Sqrt[kp])])^-1
/(0<=k && k<=0.7));
elliptic[k_] := (1/Pi*Log[2*(1+Sqrt[k])/(1-Sqrt[k])]) /;
(0.7<=k && k<=1);
ellipK[k_] := EllipticK[k]/EllipticK[Sqrt[1-k^2]];
Oberhettinger[k_] := ellipK[k];
GuptaPermCPS[h_,w_,er_,s_] := (k=s/(s+2*w);
(er+1)/2*(Tan[0.775*Log[h/w]+
1.75]+k*w/h*(0.04-0.7*k+0.01*
(1-0.1*er)*(0.25+k))));
GuptaPermCPW[h_,w_,er_,s_] := GuptaPermCPS[h,s,er,w];
GuptaThinCPW[h_,w_,er_,s_] := (k=w/(w+2*s);
30*Pi/Sqrt[GuptaPermCPW[h,w,er,s]]/
ellipK[k])
GuptaThinCPW::usage= "This equation estimates the characteristic
impedance for an infinitely thin coplanar waveguide. Syntax:
GuptaThinCPW[h,w,er,s], where h is distance above ground plane, w is
the width of the center conductor, er is the relative permittivity, and
s is the gap spacing."
(* *)
(* Gupta-- Coplanar strips, zero thickness *)
(* *)
GuptaThinCPS[h_,w_,er_,s_] := ( k=s/(s+2*w);
120*Pi/Sqrt[GuptaPermCPS[h,w,er,s]]*
ellipK[k])
GuptaThinCPS::usage= "This equation estimates the characteristic
impedance for an infinitely thin coplanar strip transmission line. Syntax:
GuptaThinCPS[h,w,er,s], where h is distance above ground plane, w is
the width of the center conductor, er is the relative permittivity, and
s is the gap spacing."
(* *)
(* Gupta-- Coplanar waveguide, finite thickness *)
(* *)
GuptaCPW[h_,w_,er_,t_,s_] := (del=1.25*t/Pi*(1+Log[4*Pi*w/t]);
weff=w+del;
seff=s-del;
k=w/(w+2*s);
ke=weff/(weff+2*seff);

```

```

u=1/ellipK[ke];
v=1/ellipK[k];
eff=GuptaPermCPW[h,w,er,s];
efft=eff-0.7*(eff-1)*t/s/(v+0.7*t/s);
30*Pi*u/Sqrt[efft])
GuptaCPW::usage= "This equation estimates the characteristic
impedance for a coplanar waveguide transmission line. Syntax:
GuptaCPW[h,w,er,t,s], where h is distance above ground plane, w is
the width of the center conductor, er is the relative permittivity, t is
thickness, and s is the gap spacing."
(*                                     *)
(*Gupta-- Coplanar strips, finite thickness *)
(*                                     *)
GuptaCPS[h_,w_,er_,t_,s_]:= (del=1.25*t/Pi*(1+Log[4*Pi*s/t]));
weff=w+del;
seff=s-del;
k=s/(s+2*w);
ke=seff/(seff+2*weff);
u=1/ellipK[ke];
v=1/ellipK[k];
eff=GuptaPermCPS[h,w,er,s];
efft=eff-1.4*(eff-1)*t/s/(v+1.4*t/s);
120*Pi*u/Sqrt[efft])
GuptaCPS::usage= "This equation estimates the characteristic
impedance for a coplanar strip transmission line. Syntax:
GuptaCPS[h,w,er,t,s], where h is distance above ground plane, w is
the width of the center conductor, er is the relative permittivity, t is
thickness, and s is the spacing between conductors."
(*                                     *)
(*Hoffman-reported for non-grounded CPW *)
(*                                     *)
HoffmanZO[k_,er_]:=120*Pi/(4*Sqrt[er]*ellipK[k]);
HoffmanZO::usage= "This formula is very common in Hoffman's text and is
used in the characteristic impedance estimates for coplanar waveguides and
edge-coupled striplines. The calling syntax is: HoffmanZO[k,er], where
k is a special geometric factor that varies between structural types and er
is the effective permittivity."
HoffmanCPW[w_,er_,s_]:= (k=w/(w+2*s);HoffmanZO[k,er])
HoffmanCPW::usage= "This equation predicts the characteristic impedance
for coplanar waveguides. The conductors
are furthermore assumed to be infinitely thin. Syntax:
HoffmanCPW[w,er,s], where w=width, er=EFFECTIVE permittivity, and s=gap
spacing. Suitable models for effective permittivity include
HoffmanPermCPW1[er] for coplanar waveguides with infinitely thick
dielectrics and infinitely thin conductor. For a dielectric with
finite thickness and infinitely thin conductors,
HoffmanPermCPW2[h,w,er,s] is appropriate."
(*                                     *)
HoffmanPermCPW1[er_]:= (er+1)/2;
HoffmanPermCPW2[h_,w_,er_,s_]:= (q=(Sinh[Pi*w/(4*h)])^2/
(Sinh[Pi*s/(2*h)]*Sinh[Pi*(w+s)/(2*h)]));

```

```

k=w/(2*s+w);
k1=Sqrt[1/(1+q)];
kprim=Sqrt[1-k^2];
k1prim=Sqrt[1-k1^2];
1+((er-1)*EllipticK[k1prim]+EllipticK[kprim])/
(2*EllipticK[k1]*EllipticK[k]) )
(* From the green book, p. 275 *)
GuptaPermCPW3[h_,w_,er_,s_] := (k=w/(w+2*s);
(er+1)/2*(Tanh[1.785*Log[h/2]+1.75]+
k*w/h*(0.04-0.7*k+0.01*(1-0.1*er)*
(0.25+k))) );
(* *)
(* Hoffman-reported formula for edge-coupled *)
(* stripline *)
(* *)
HoffmanStripZOEEven[w_,er_,s_,b_] := (k=Tanh[Pi*w/(2*b)]*
Tanh[Pi*(w+s)/(2*b)]);
kprime=Sqrt[1-k^2];
HoffmanZO[k,er]);
HoffmanStripZOEEven::usage = "This formula calculates the even-mode
impedance for an edge-coupled stripline. A zero thickness is
assumed. Syntax:HoffmanStripZOEEven[w,er,s,b], where w is width,
er is relative permittivity, s is inter-conductor spacing, and
b is the ground plane separation distance."
HoffmanStripZOOdd[w_,er_,s_,b_] := (k=Tanh[Pi*w/(2*b)]*
Coth[Pi*(w+s)/(2*b)]);
kprime=Sqrt[1-k^2];
HoffmanZO[k,er]);
HoffmanStripZOOdd::usage = "This formula calculates the odd-mode
impedance for an edge-coupled stripline. A zero thickness is
assumed. Syntax:HoffmanStripZOOdd[w,er,s,b], where w is width,
er is relative permittivity, s is inter-conductor spacing, and
b is the ground plane separation distance."
HoffmanStripCoupled[w_,er_,s_,b_] := (even=HoffmanStripZOEEven[w,er,
s,b];
odd=HoffmanStripZOOdd[w,er,s,b];
Sqrt[even*odd]);
HoffmanStripCoupled::usage = "This formula calculates the characteristic
impedance for an edge-coupled stripline. A zero thickness is
assumed. Syntax:HoffmanStripCoupled[w,er,s,b], where w is width,
er is relative permittivity, s is inter-conductor spacing, and
b is the ground plane separation distance."
(* *)
(*Gupta, coupled striplines with finite (non-zero)*)
(* *)
GuptaCf[t_,b_] := 2*Log[(b^2-t)/(b-t)]-t/b*Log[t*(2*b-t)/(b-t)^2];
GuptaECSForm[w_,er_,t_,b_,a_] := (30*Pi*(b-t)/(Sqrt[er]*(w+b*GuptaCf[t,b]/
(2*Pi)*a)));
GuptaECSEven[w_,er_,t_,s_,b_] := (Aeven=1+Log[1+Tanh[Pi*s/(2*b)]]/Log[2];
GuptaECSForm[w,er,t,b,Aeven]);
GuptaECSEven::usage = "This formula evaluates the even-mode characteristic

```

```

impedance for edge-coupled striplines (ECS). Syntax:
GuptaECSEven[w,er,t,s,b] where w is width, h is height, er is the relative
permittivity, t is thickness, s is spacing, and b is ground plane
separation. The range of validity are
t/b < 0.1 and w/b >= 0.35."
GuptaECSOdd[w_,er_,t_,s_,b_] := (Aodd = 1 + Log[1 + Coth[Pi*s/(2*b)]]/Log[2];
  GuptaECSForm[w,er,t,b,Aodd]);
GuptaECSOdd::usage = "This formula evaluates the odd-mode characteristic
impedance for edge-coupled striplines (ECS). Syntax:
GuptaECSOdd[w,er,t,s,b] where w is width, h is height, er is the relative
permittivity, t is thickness, s is spacing, and b is ground plane
separation. The range of validity are
t/b < 0.1 and w/b >= 0.35."
GuptaECS[w_,er_,t_,s_,b_] := Sqrt[GuptaECSEven[w,er,t,s,b]*
  GuptaECSOdd[w,er,t,s,b]];
GuptaECS::usage = "This formula evaluates the characteristic
impedance for edge-coupled striplines (ECS). Syntax:
GuptaECS[w,er,t,s,b] where w is width, h is height, er is the relative
permittivity, t is thickness, s is spacing, and b is ground plane
separation. The range of validity are
t/b < 0.1 and w/b >= 0.35."
(* *)
(* Chang's formulas *)
(* *)
(* Formula #1: single ground plane *)
ChangSingle[w_,h_,er_,t_] := (bb = 1 + t/h;
  p = 2*bb^2 + Sqrt[(2*bb^2 - 1)^2 - 1] - 1;
  eta = (p^.5*(Pi*w/(2*h) + ((p+1)/(2*p^.5)))*
    (1 + Log[4/(p-1)] - 2*ArcTanh[p^-.5]));
  del = Max[eta,p];
  rb = eta + ((p+1)/(2*p^.5))*Log[del];
  ra = -1 - Pi*w/(2*h) - ((p+1)/(p^.5))*
    ArcTanh[p^-.5] - Log[(p-1)/(4*p)];
  ra = Exp[ra];
  2*er*e0/Pi*Log[2*rb/ra])
(* *)
ChangSingle::usage = "ChangSingle is the formula used to calculate
capacitance of a rectangular conductor of non-zero thickness over a ground
plane. Syntax: ChangSingle[w,h,er,t], where w is width, h is height, er is
relative permittivity, and t is thickness.
It is most approximate for (w/h) > 1."
(* *)
(* Formula #2: ground plane placed vertically above *)
(* *)
ChangDouble[w_,h_,er_,t_,b_] := (alpha = b/h; gamma = (b-t-h)/h;
  q = .5*(alpha^2 - gamma^2 - 1 + Sqrt[(alpha^2 -
    gamma^2 - 1)^2 - 4*gamma^2]);
  p = q^2/gamma^2;
  rb = (gamma^(-1)*(Pi*w/(2*h) + 2*alpha*
    ArcTanh[Sqrt[1/(1+q)/(p+q)]]) + gamma*
    Log[p-1]/4 - 2*ArcTanh[p^-.5]));

```

```

        rb=Exp[rb];
        ra=(-Pi*w/(2*h)-2*alpha*ArcTanh[Sqrt[
(p+q)/(p*(1+q))]]+2*gamma*ArcTanh[p^-.5]
+Log[4*p/(p-1)]]);
        ra=Exp[ra];
        2*er*e0/Pi*Log[rb/ra]);
ChangDouble::usage = "This formula calculates the capacitance of
rectangular conductors of non-zero thickness which are placed between two
vertically separated ground planes. Syntax:
ChangDouble[w,h,er,t,b], where w is width, h is height, er is relative
permittivity, and t is thickness. The formula is
most approximate for the cases where (w/h)>=.5 and (b-t-h)/h >=.5. "
(* *)
(*Chang's Embedded Microstrip formula *)
(* *)
ChangEmbeddedMicrostrip[w_,h_,er_,t_] := stdZ01[ChangSingle[w,h,er,t],vp[er]]
ChangEmbeddedMicrostrip::usage = "This formula estimates the capacitance
of an embedded microstrip (non-zero thickness), based on Chang's
conformal mapping analysis for
capacitance calculations and the standard definition of characteristic
impedance stdZ01[C,v]. Syntax:
ChangEmbeddedMicrostrip[w,h,er,t], where w is the width of the microstrip,
h is the height above the ground plane, er is the relative permittivity of
the dielectric surrounding the conductor, and t is the thickness of the
conductor. The approximation is based on an infinitely thick slab of
dielectric material, and is most accurate for w/h > 1."
(* *)
(*Chang's Stripline Formula*)
(* *)
(* *)
ChangStripline[w_,h_,er_,t_,b_] := stdZ01[ChangDouble[w,h,er,t,b],vp[er]];
ChangStripline::usage = "This formula estimates the capacitance of
a stripline which has thick conductors. The formula is based on
Chang's conformal mapping calculations of the capacitance, which is
used in the standard definition of characteristic impedance stdZ01[C,v].
Syntax:
ChangStripline[w,h,er,t,b], where w is the width of the microstrip,
h is the height above the ground plane, er is the relative permittivity of
the dielectric surrounding the conductor, and t is the thickness of the
conductor, and b is the ground plane separation distance. The formula is
most approximate for the cases where (w/h)>=.5 and (b-t-h)/h >=.5.";

```

### *Telegrapher's Equation Solver.*

The multi-conductor telegrapher's equations (Equations 2.29 and 2.30) were used in this thesis effort to determine the terminal voltages and currents of transmission line structures. In theory, given the proper parameter matrices ( $[R]$ ,  $[L]$ ,



$[G]$ , and  $[C]$ ), these equations can be solved to determine most electrical quantities of interest, including the characteristic impedance, transmission gain, and coupling gain for structures of interest. The MATRIXX and Mathematica programs were used to solve Equations 2.29 and 2.30 for a variety of boundary conditions (the analytic development of these solutions are described in Appendix F.) Eventually, the MATRIXX approach was abandoned, and only the resultant Mathematica "code" is listed in this section. Sweep routines were additionally developed to construct swept-frequency solutions, corresponding to the swept-frequency measurements made in the laboratory. The reference in the Mathematica program to the routine "useful" refers to the Mathematica package containing the digital signal processing routines (described in the next section).

```
Get["useful"]
newco:=(
a=(Input["Enter self-capacitance coeff>"]);
b=(Input["Off-diagonal coeff>"]);
c=(Input["Series resistance>"]);
coup={{a,b},{b,a}};
mu=1.2566*10^-6;
coupinv=Inverse[coup];
eps=8.85*10^-12*3.4;
eta=(eps*mu);
f={{1},{0},{0},{0}};
R=c*IdentityMatrix[2];
)
newco::usage="Establishes information necessary for telegrapher's matrix
solution. Required prior to invocation of terminal gain evaluation's of
coupling, isolation, or transmission."
(* Define custom parameters *)
(* *)
(* Z1==> Impedance of the first line at z=0 *)
(* Z2==> Impedance of the second line at z=0 *)
(* Z3==> Impedance of the first line at z=1 *)
(* Z4==> Impedance of the second line at z=1 *)
Z1[w_]:=50;
(* terminate other ports with 10^-9 ohm + .1 pF cap in series *)
Z2[w_]:=10^-9-I*1/(w*10^-7);
Z3[w_]:=10^-9-I*1/(w*10^-7);
Z4[w_]:=10^-9-I*1/(w*10^-7);
(* Now define the forcing function vectors *)
(* *)
(* V1==> Voltage source on the first line at z=0 *)
```

```

(* V2==> Voltage source on the second line at z=0 *)
(* V3==> Voltage source on the first line at z=1 *)
(* V4==> Voltage source on the second line at z=1 *)
V1[u_]:=1;
V2[u_]:=0;
V3[u_]:=0;
V4[u_]:=0;
(* Now consider the end evaluation which is necessary to determine *)
(* the arbitrary constants in the solution of the matrix form of *)
(* the telegrapher's equations: *)
(*
TelegrapherEndEval[u_]:= (
w=u*2*Pi*10^-6;
gam=Sqrt[-w^2*eta*IdentityMatrix[2]+I*w*R.coup];
gaminv=Inverse[gam];
l=.1;
beta=(upper=Sinh[gam*l].gaminv.(R+I*w*eta*coupinv);
lower=Sinh[gam*l].gaminv.(I*w*coup);
cosh=Cosh[gam*l];
cosh={{cosh[[1,1]],0},{0,cosh[[2,2]]}};
u1=Flatten[{cosh[[1]],upper[[1]]};
u2=Flatten[{cosh[[2]],upper[[2]]};
u3=Flatten[{lower[[1]],cosh[[1]]};
u4=Flatten[{lower[[2]],cosh[[2]]};
{u1,u2,u3,u4});
z1=Z1[w];
z2=Z2[w];
z3=Z3[w];
z4=Z4[w];
s1=V1[w];
s2=V2[w];
s3=V3[w];
s4=V4[w];
)
(*Now define the sets of boundary conditions which apply to the *)
(*various configurations under consideration. The first set is a *)
(*custom boundary condition and is most general. It is capable of *)
(*handling arbitrary impedances at each port, and it will also *)
(*accommodate arbitrary voltage sources or forcing functions at *)
(*each of the four ports. *)
(*
CustomBC:={{1,0,z1,0},{0,1,0,z2},beta[[1]]+z3*beta[[3]],beta[[2]]+
z4*beta[[4]]};
CustomBC2:={{1,0,z1,0},{0,0,0,1},beta[[3]],beta[[4]]};
CustomFF:={{s1},{s2},{s3},{s4}};
BackCoupledBC:={{1,0,50,0},{0,1,0,50},beta[[3]],beta[[1]]};
TransmissionBC:={{1,0,50,0},{0,0,0,1},50*beta[[3]]-beta[[1]],beta[[4]]};
IsolationBC:={{1,0,50,0},{0,0,0,1},50*beta[[4]]-beta[[2]],beta[[3]]};
DrivePointOpenBC:={{1,0,50,0},{0,0,0,1},beta[[3]],beta[[4]]};
DrivePointShortBC:={{1,0,50,0},{0,0,0,1},beta[[1]],beta[[4]]};
Mag[x_]:=N[Abs[x],20];

```

```

MagLog[x_] := N[20*(Log[Abs[x]]/Log[10]), 20];
MagCoupledBack[u_] := (TelegrapherEndEval[u];
    gamma = BackCoupledBC;
    C = Inverse[gamma].f;
    N[20*(Log[Abs[C[[2]]/C[[1]]]]/Log[10]), 20])
MagTransmitted[u_] := (TelegrapherEndEval[u];
    gamma = TransmissionBC;
    C = Inverse[gamma].f;
    N[20*(Log[Abs[(beta[[1]].C)/C[[1]]]]/Log[10]), 20])
MagIsolated[u_] := (TelegrapherEndEval[u];
    gamma = IsolationBC;
    C = Inverse[gamma].f;
    N[20*(Log[Abs[(beta[[2]].C)/C[[1]]]]/Log[10]), 20])
MagDrivePointOpen[u_] := (TelegrapherEndEval[u];
    gamma = DrivePointOpenBC;
    C = Inverse[gamma].f;
    N[Abs[C[[1]]/C[[3]]], 20]);
MagDrivePointShort[u_] := (TelegrapherEndEval[u];
    gamma = DrivePointShortBC;
    C = Inverse[gamma].f;
    N[Abs[C[[1]]/C[[3]]], 20]);
(* Custom function is currently set to provide driving point *)
(* impedance with end open-circuited *)
Custom[u_] := (
    TelegrapherEndEval[u];
    gamma = N[CustomBC2, 20];
    ff = CustomFF;
    C = Inverse[gamma].ff;
    N[Abs[C[[1]]/C[[3]]], 20])
Sweep[a_, x_] := Flatten[Table[a[i*x], {i, 100}]];
SweepSI[a_, beg_, end_, step_] := Flatten[Table[a[i], {i, beg, end, step}]];
SweepCustom[x_] := Sweep[Custom, x];
SweepCustomSI[a, b, c] := SweepSI[Custom, a, b, c];
SweepBackCoupled[x_] := Sweep[MagCoupledBack, x];
SweepBackCoupledSI[a_, b_, c_] := SweepSI[MagCoupledBack, a, b, c];
SweepTransmitted[x_] := Sweep[MagTransmitted, x];
SweepTransmitted[a_, b_, c_] := SweepSI[MagTransmitted, a, b, c];
SweepIsolated[x_] := Sweep[MagIsolated, x];
SweepIsolatedSI[a_, b_, c_] := SweepSI[MagIsolated, a, b, c];
SweepDrivePointOpen[x_] := Sweep[MagDrivePointOpen, x];
SweepDrivePointOpenSI[a_, b_, c_] := SweepSI[MagDrivePointOpen, a, b, c];
SweepDrivePointShort[x_] := Sweep[MagDrivePointShort, x];
SweepDrivePointShortSI[a_, b_, c_] := SweepSI[MagDrivePointShort, a, b, c];
SweepZ0[x_] := (Flatten[Table[N[(Sqrt[MagDrivePointOpen[i*x]*
    MagDrivePointShort[i*x])], 20],
    {i, 100}]]);
SweepZOSI[a_, b_, c_] := (Flatten[Table[N[(Sqrt[MagDrivePointOpen[i]*
    MagDrivePointShort[i])], 20],
    {i, a, b, c}]]);
coupledgain[u_] := (ans = Custom[u];
    MagLog[ans[[2]]/ans[[1]]])

```

```

PhaseCoupledBack[u_] := (TelegrapherEndEval[u];
  gamma = BackCoupledBC;
  C = Inverse[gamma].f;
  N[Arg[C[[2]]/C[[1]]]*180/Pi, 20])
PhaseDrivePointOpen[u_] := (TelegrapherEndEval[u];
  gamma = DrivePointOpenBC;
  C = Inverse[gamma].f;
  N[Arg[C[[1]]/C[[3]]]*180/Pi, 20]);
PhaseDrivePointShort[u_] := (TelegrapherEndEval[u];
  gamma = DrivePointShortBC;
  C = Inverse[gamma].f;
  N[Arg[C[[1]]/C[[3]]]*180/Pi, 20]);
SweepZOPhaseSI[beg_, end_, step_] := (
  Flatten[Table[.5*(PhaseDrivePointOpen[i] +
    PhaseDrivePointShort[i]),
    {i, beg, end, step}]]])

```

### *Digital Signal Processing (DSP) Routines.*

The de-cabling filters used to process the pulsed-signal response measurements were developed using simple MathCad and Mathematica routines. The fast Fourier transform routines of the MathCad program could only accommodate data sets where the number of points coincide with an integral power of two (for example, 64, 256, 1024). The Mathematica fast Fourier transform routines proved to be more flexible, since they could accommodate sets with an arbitrary number of data points. Only the resultant Mathematica "code" is listed in this section. In addition to the DSP routines, other incidental utility functions were implemented in this package.

```

Mag[x_] := N[Abs[x], 20];
Threshold[a_, b_] := If[Mag[a] > Mag[b], 1, 0]
Denoise[a_, b_] := (n = Dimensions[a];
  Table[a[[i]]*Threshold[a[[i]], b], {i, n[[1]]}]);
MagLog[x_] := N[20*(Log[Abs[x]]/Log[10]), 20];
put[x_, test_] := (n = Dimensions[x];
  OpenWrite[test];
  Do[Write[test, x[[i]]], {i, n[[1]]}];
  Close[test])
Spectral[file_] := (x = Reverse[Flatten[Take[Transpose[ReadList[file, {Real, Real}]], -1]]];
  Fourier[x]
)
YankFirstColumn[file_] := (Flatten[Take[Transpose[ReadList[file, {Real, Real}]], -1]]);
)
SpectralRatio[a_, b_] := (n = Dimensions[a]; Flatten[Table[a[[i]]/b[[i]], {i, n[[1]]}]))

```

```

SpectralProduct[a_,b_]:= (n=Dimensions[b]; Flatten[Table[a[[i]]*b[[i]],{i,n[[1]]}]]);
spectrum[u_]:= (x=ReadList[u]; Fourier[x]);
Whats[x_]:= N[x,20];
Whats::usage = "Gives a numerical evaluation of argument to 20 decimal places."
space=" ";
huh:=Whats[%]
processtwocolumn[u_,y_,z_,j_]:= (v=spectrum[u];
                                ww=Get[y];
                                w=SpectralProduct[v,ww];
                                x=InverseFourier[w];
                                ww=Reverse[x];
                                w=Chop[ww];

                                n=Dimensions[w];
                                OpenWrite[z];
                                Do[(l=N[j/n*i,10];
                                Write[z,l[[1]],OutputForm[space],
                                w[[i]]]),{i,n[[1]]}];
                                Close[z])
process[u_,y_,z_]:= (v=spectrum[u];
                     ww=Get[y];
                     w=SpectralProduct[v,ww];
                     x=InverseFourier[w];
                     ww=Reverse[x];
                     w=Chop[ww];

                     n=Dimensions[w];
                     OpenWrite[z];
                     Do[( Write[z,w[[i]]]),{i,n[[1]]}];
                     Close[z])
Filter:=( u=(Input["Enter time-domain signal>"]);
          y=(Input["Enter appropriate filter name>"]);
          z=(Input["Enter result file>"]);
          j=(Input["Maximum time-scale value>"]);
          processtwocolumn[u,y,z,j];
          )
Decable[u_,cable_,z_]:= (w=spectrum[u];
                          v=SpectralProduct[w,cable];
                          x=InverseFourier[v];
                          ww=Chop[x];
                          w=Reverse[ww];
                          n=Dimensions[w];
                          OpenWrite[z];
                          Do[(Write[z,w[[i]]]),{i,n[[1]]}];
                          Close[z])
Decable::usage="Applies decabling filter to a signal. SYNTAX:
Decable[file1,cable,file2]. Read as: filter file1 with array cable,
then write results to file2."
juxtapose[u_,j_,z_]:= (v=ReadList[u];
                        OpenWrite[z];
                        n=Dimensions[v];
                        Do[(l=N[j/n*i,10];
                        Write[z,l[[1]],OutputForm[space],v[[i]]]),

```

```

        {i,n[[1]]});
        Close[z];)
justappend[u_,j_,z_]:= (v=ReadList[u];
    OpenWrite[z];
    n=Dimensions[v];
    Do[(Write[z,j[[i]],OutputForm[space],v[[i]]]),
        {i,n[[1]]});
        Close[z];)
affix:=(u=(Input["Enter file>"]);
    j=(Input["Maximum time-scale value>"]);
    z=(Input["Enter result file>"]);
    juxtapose[u,j,z];
)
affix::usage="tags a column of time-scale values to the left of each datum in
a single column file. NOTE: Answer ALL file queries with the arguments placed
inside of double quotations"
frip[u_,z_]:= (v=ReadList[u];
    OpenWrite[z];
    n=Dimensions[v];
    Do[( Write[z,v[[i]]]),
        {i,n[[1]],1,-1});
    Close[z];)
ListScaleTo[u_,scale_,z_]:= (v=ReadList[u];
    alpha=Max[v];
    beta=Min[v];

    n=Dimensions[v];

    s=scale/(alpha-beta);
    OpenWrite[z];

    Do[Write[z,N[(v[[i]]-beta)*s],10]],
        {i,n[[1]]});
    Close[z];)
LookAt[a_]:=ListPlot[ReadList[a]]

```

## Appendix B. *LIBRA Program Listing.*

This Appendix lists the LIBRA input program used to simulate two-conductor ECS structures. The results of these simulations are described in Chapter 4. In the program listing, the obvious material and geometrical parameters were altered as necessary to realize the different structures and to investigate the sensitivity of these parameters to minor changes.

### *Program Listing.*

```
!STRUCTURE SIMULATED: Two-conductor ECS
!LIBRA description of a two-line, edge-coupled .1 meter stripline
!line found on the test wafer.
!
!
DIM
  FREQ MHZ
  RES OH
  COND /OH
  CAP PF
  LNG UM
  TIME NS
  ANG DEG
VAR
  WLINE=11
  SPACE=18
EQN
  SP2=80+(40-WLINE)
  SAV=(80+SPACE)/2
CKT
  SSUB ER=3.4 B=20.5 T=2.5 RHO=1.64 RGH=0 !HDMI substrate
  TAND TAND=.002
!Now define a pad group structure, comprise of two input pads,
!and short lengths of coupled striplines
  SCLIN 1 3 4 2 W=40 S=80 L=65 !Input pads
!Step change in width
  SSTEP 2 5 W1=40 W2=26
  SSTEP 4 6 W1=40 W2=26
!Short length of coupled line (via section)
  SCLIN 5 6 8 7 W=26 S=SP2 L=40
!45 DEGREE BEND BEFORE TAPER DOWN TO LONG LINE PORTION
  SBEND 7 9 W=WLINE ANG=45 M=0
  SBEND 8 10 W=WLINE ANG=45 M=0
!TAPERED SECTION APPROXIMATED BY A COUPLED LINE PAIR WITH
!AVERAGE SPACING SAV
```

```

      SCLIN 9 10 11 12 W^WLINE S^SAV L=66
!45 DEGREE BEND BEFORE LONG LINE PORTION
      SBEND 11 14 W^WLINE ANG=-45 M=0
      SBEND 12 13 W^WLINE ANG=-45 M=0
!NOW DEFINE THIS WHOLE CONSTRUCT AS A FOUR PORT
      DEF4P 1 3 14 13 PADTYPE1
!END THE PAD DESCRIPTION
!
!
!BEGIN STRUCTURE DESCRIPTION
      PADTYPE1 1 2 3 4
!NOW THE MAIN LINE
      SCLIN 4 3 6 5 W^WLINE S^SPACE L=100000
      PADTYPE1 5 6 7 8
!
! NOW DEFINE THE STRUCTURE ENTIRELY AS A 4-PORT
!
DEF4P 1 2 7 8 TYPE1
!
!NOW, FOR OUTPUT PURPOSES DEFINE SOME 2-PORTS
!OF THIS STRUCTURE, TO EXAMINE FORWARD TRANSMISSION
!AND BACKWARD COUPLING, FOR EXAMPLE
!
TYPE1 1 2 7 8
RES 7 0 R=1000000000
RES 8 0 R=1000000000
DEF2P 1 2 BACKCOUP
!TYPE1 1 2 7 8
!DEF2P 1 8 STRAIGHT
!TYPE1 1 2 7 8
!DEF2P 1 7 FWDCOUP
OUT
      BACKCOUP DB[VG] GR1
      BACKCOUP ANG[VG] GR1A
FREQ
      SWEEP 1 100 1

```



## Appendix C. *Detailed Measurement Procedures*

This appendix outlines the detailed procedures used to conduct the measurements on the test wafer structures received from the Polycon Corporation (Ventura, CA). Each measurement was accomplished on the Micromanipulator wafer-probing station with the appropriate test equipment, probes, and properly configured computer-controller. The equipment list in Chapter 1 contains specific model and vendor information.

Before performing any measurements, the following preliminary steps were implemented:

1. (Required for wafers composed of hygroscopic materials, such as polyimide.) To remove humidity, soft-bake the subject wafer(s) at 140° C for about hour, and then allow them to cool in the oven for one hour.
2. Ultrasonically clean the electrical probe tips in methyl alcohol for 3 minutes.

### *Continuity Measurements*

#### *Required:*

1. Volt-ohm meter
2. Micromanipulator probing arms, fitted with probes that have tips which are connected to the volt-ohm meter. The electrical probe tips should have a tip radius compatible with the  $70\text{ }\mu\text{m} \times 65\text{ }\mu\text{m}$  test structure termination pads; that is, the tips should not be so large as to render the probing operation unreliable. The preferred probe styles for this operation are the model 44 probes equipped with a ground plane connector. If the model 44 probes are not available, most other probes may be used, although the use of active probes (such as the FET-1 probes) are not recommended.

*Procedure:*

1. When probes are used that have multiple tips (such as the model 44 Kelvin probes or the model 44 probes equipped with a ground plane connector), it is important to verify that the probe tips are planar. That is, it is essential that both probe tips contact the surface simultaneously in order to make a reliable measurement. To insure that the probes are "planarized," the probe placement operations outlined below should be practiced on some non-critical reference location of the wafer, such as the distant end of a large top-surface ground plane. When both tips of a probe are planarized, they will make similar abrasion patterns. If one tip of a multi-tipped probe makes a significant surface abrasion before the remaining tip, the probe should be lifted well above the test wafer, and the probe assembly should be slightly rotated in the proper direction to correct the mis-alignment. All probes should be planarized at the beginning of a fresh measurement sequence.
2. Position the micromanipulator probe arms at each position on the test wafer structure, insuring that proper reach and clearance can be obtained with the probes.
3. Carefully adjust the extension, horizontal, and vertical positions of the probes to bring the tip of the probe directly over, but not touching, the contact surface to be probed. The proximity of the probes can be ascertained by focusing the optical microscope to provide a sharp image of the surface to be probed. As the probes are brought near the contact surfaces, their image will be brought into sharp focus.
4. The physical connections between the probe arm and the volt-ohm meter should be established/verified, prior to the actual establishment of the electromechanical connection between the probe arm and the subject.
5. Carefully adjust the vertical height of the probe arm to lower it onto the contact surface(s). The microscope should be used during this adjustment. When

the probe makes contact, it will be sharply focused when viewed with the microscope. To insure integrity of the connection, it is necessary to further lower the probe vertically downward. After this procedure has been accomplished, the probe should be gently nudged forward. Especially with sharper probes (tip radius  $< 5 \mu\text{m}$ ), a minor destructive abrasion may occur. This abrasion does not radically affect the electrical properties of the measurement configuration, but excessive gouging will not only electrically alter the wafer test structure, but it could also obviously destroy it. Therefore, great care must be exercised in probe placement, especially when multiple contacts and reproducible measurements are desired.

6. After placement, the continuity between pads can be checked with the volt-ohm meter.

#### *Impedance Measurements*

##### *Required:*

1. An appropriate impedance analyzer (HP 4194A with type APC-7 connection port extension (5 KHz-13 MHz) or HP 4191A RF impedance analyzer (1-1000 MHz); one Micromanipulator, model 44 probe with ground plane connection. The model 44 probe is connected to the HP 4191A through a 1-meter long cable (the length includes the probe) to a BNC-to-type N and type N-to-type APC-7 connector.
2. A specially modified shorting probe, described in Chapter 3, is required.
3. Volt-ohm meter for continuity verification.
4. Z-248 computer connected to the analyzer through the HP-IB (IEEE-Std-488) interface bus.

##### *Procedure:*

1. Execute the appropriate software program to facilitate the measurements.

2. Planarize the probes, as discussed in the Continuity procedure.
3. Three calibrations should be accomplished prior to any measurement, which include a short-circuit, an open-circuit, and a 50  $\Omega$  load, respectively. For the short-circuit measurement, both probes are placed on a single, non-grounded pad of reasonable integrity (no serious gouges or obvious defects). For the open-circuit measurement, the probes are lifted above the wafer (free-space connection). For the 50  $\Omega$  load, the measurement probe is substituted with the special calibration probe. This probe has a 50  $\Omega$  termination mounted permanently at its end, and it is used specifically for the 50  $\Omega$  termination calibrations, and is otherwise identical to the measurement probe.
4. The software program is advanced to the measurement portion of its cycle. The open-circuit measurement is facilitated by connecting the probes to one end of the transmission line (the near end), and leaving the other end (the far end) open-circuited. The probe is positioned such that the active conductor portion of its tip contacts the active conductor of the transmission line, and the corresponding ground plane portion of the tip simultaneously contacts the corresponding WSIC ground plane structure. The measurement is then performed, and the data is sampled by the computer-controller.
5. A short-circuit measurement is initially accomplished. The near end connection made in the previous step is not altered. To facilitate the short circuit measurement, the modified probe assembly is positioned at the far end of the measurement assembly and brought into contact with both conductors, thereby creating a short-circuit. The integrity of this short circuit is verified with a dc continuity measurement between the shorting probe and each side of the near end of the transmission line. After verification of continuity and the short circuit measurement, an open-circuit measurement is similarly accomplished.
6. From the short and open circuit measurements, the computer program calculates the characteristic impedance as a function of frequency.

### *Coupling, Transmission, and Isolation Measurements*

This section describes the technique used in this research effort to perform two-port transmission measurements. The primary measurements done in this research effort were coupling gain measurements, although the following procedure may be generalized to many other two-port transmission measurements.

#### *Required:*

1. An HP 4194A gain-phase analyzer (5 KHz-100 MHz).
2. Two Micromanipulator, model 44 electrical probes, or one Micromanipulator, model 44 electrical probe and one Micromanipulator, FET-1 high-impedance probe, depending on the source and load conditions desired (as discussed in Chapter 3). Both probes are held by suitable micro-manipulator arms. The electrical connections for the probes are made through cables from the probes to the BNC connectors on the front panel of the HP 4194A.
3. Volt-ohm meter, for continuity verification.
4. Z-248 personal computer, connected to the analyzer through an IPIB (IEEE-Std-488) interface bus.

#### *Procedure:*

1. Connect equipment to match the Figure 3.13 configuration.
2. Execute the appropriate software program to facilitate measurements.
3. Planarize the probes, as discussed in the Continuity procedure above.
4. After the computer program is executed, a display prompt for compensation calibration will occur. At this point, the two model 44 probes are brought into contact with a non-grounded electrical conductor. An input pad on a test wafer is well-suited for this purpose. The continuity procedure may be applied, if necessary, to verify that an electrical connection exists. This step in the procedure provides a transmission reference to the gain-phase analyzer.

The gain-phase analyzer applies this compensation to the subsequent measurements, thereby eliminating the effects of the test equipment cabling from the test structure measurements.

5. After compensation, the program is advanced. Another display prompt will occur, this time for collecting the measurement data. A trial measurement is performed immediately after compensation, *without lifting the probes* from the previous step, as a calibration quality check. The IIP 4191A gain-phase display should not provide an indication of magnitude above 100 mdB. If this condition is not satisfied, the placement of the probes should be checked, and the measurement should be re-accomplished. Otherwise, the data collected during this particular trial should be aborted, and the measurement should be re-accomplished on the intended subject without re-calibration.
6. After the calibration quality is checked, the probes are positioned on a suitable structure for measurement. The program is advanced to facilitate the collection of data points representing the voltage gain magnitude in dB and phase in degrees across the chosen frequency range. A number of measurements may be gathered in succession, without recalibration. However, it is not advisable to collect more than five measurements without recalibration, since the quality of the contact surfaces, as well as other environmental parameters, may change with the time. To test the integrity of the current calibration, the original structure used for calibration can be re-measured. If this measurement is within 20 mdB of the original calibration measurement at every point across the measurement spectrum, the quality of the current calibration should be considered satisfactory. If this quality test fails (that is, if the re-measurement *deviates by more than 20 mdB at one or more points across the spectrum*), then a complete re-calibration should be performed.

### *Pulse Measurement Procedure*

#### *Required:*

1. HP 54100A digital sampling oscilloscope, with 50  $\Omega$  input modules installed in both channels.
2. An appropriate function generator, capable of generating square waves of high quality.
3. Two model 44 electrical probes, or one model 44 electrical probe and one FET-1 high-impedance probe, depending on the source and load conditions desired (as discussed in Chapter 3). Alternately, a high impedance module may be installed in the HP 54100A, in lieu of the FET-1 probe. Both probes are held by suitable micro-manipulator arms. The connections for the probes are made through cables from the probes to the BNC connectors on the front panel of the pulse generator and the HP 54100A.
4. Volt-ohm meter for continuity verification.
5. Z-248 computer connected to the analyzer through the HP-IB (IEEE-Std-488) interface bus.

#### *Procedure:*

1. Connect the equipment to match the configuration in Figure 3.14.
2. Execute the appropriate software program to facilitate the measurements.
3. Planarize the probes, as discussed in the above Continuity procedure.
4. Place the probes in a suitable measurement configuration.
5. Verify the continuity of the probes, either through continuity verification, or, if possible, through the oscilloscope display.
6. After the desired measurement pattern is obtained, the screen capture program is executed. Either or both of the channels may be specified, but the program will not capture both channels at the same time.

## Appendix D. *Control Programs for the Test Equipment*

In order to reduce the data-collection workload, a number of computer software programs were developed to semi-automate the collection and manipulation of data. In some cases, as with the Hewlett-Packard model HP 4191A gain phase analyzer and model HP 54100A digital storage oscilloscope, these programs were modified from the previous efforts of prior students [(83),(101)]. In other cases, such as for the Hewlett-Packard model HP 4191A, the programs were newly developed. Only the newly developed programs are listed in this appendix.

The following BASIC programs were developed to compute the characteristic impedance using the Hewlett-Packard model HP 4191A RF impedance analyzer and the Capital Equipment Corporation model PC488 interface card for the Z-248 computer.

Unless noted otherwise, the BASIC programs were coded using Microsoft QuickBasic 4.0, and the equipment servicing routines "SEND", "TRANSMIT", "RECEIVE", "TRANSMIT", "ENTER", and "SPOLL" require the use of QuickBasic library routines which have been modified by the Capital Equipment Corporation when a version number greater than or equal to 4.0 is used. The modified routines are supplied by the Capital Equipment Corporation with the hardware. The following QuickBasic 4.0 subprograms were either used directly or modified from demonstration programs supplied with the QuickBasic 4.0 software: "Filter," "StrTok\$," and "Parseline."

```
DECLARE SUB CollectData (StartFreq!, StepFreq!, StopFreq!, Elecln!, Number!,  
                        Frequency!(), Impedance!(), Phase!())  
DECLARE SUB OutputDecode (T$, A!, B!, C!)  
DECLARE FUNCTION StrTok$ (Srce$, Delim$)  
DECLARE SUB Parseline (Token$, Numwords!, x$())  
DECLARE SUB ENTER (TEMP$, Length%, ADDRESS%, Status%)  
DECLARE SUB Checkstat ()  
DECLARE SUB Send (ADDRESS%, CMD$, Status%)  
DECLARE SUB TRANSMIT (TEMP$, Status%)  
DECLARE FUNCTION Filter$ (Txt$, FilterString$)
```



```

DECLARE SUB Grabbaletter ()
DEF LARE SUB ASK (Prompt$, Default$, Result$)
DECLARE SUB ASKnum (Prompt$, Default$, Result!)
DECLARE FUNCTION StringRepOf$ (s!)
DECLARE SUB CMD (s$)
DECLARE SUB INIT (ADDRESS%, OTHER%)
DECLARE SUB RECEIVE (TEMP$, Length%, Status%)
DECLARE SUB SPOLL (ADDRESS%, poll%, Status%)
'This program estimates characteristic impedance
'from the 4191
    DIM SHARED A$, Status%, add%, r(1), delimiters$, Number$
    DIM Frequency(1000), ImpedOpen(1000), PhaseOpen(1000)
    DIM ImpedShort(1000), PhaseShort(1000)
    DIM ZOmaga(1000), ZOphase(1000)
    delimiters$ = ","
    Number$ = "0123456789.-+Ee"
    F$ = "##.#####~"
    MY.ADDR% = 21: add% = 19: SYSCON% = 0 ' AND EQUIPMENT
    DEF SEG = &HC400 ' ADDRESS OF GP-IB INTERFACE
    TRANSMIT "UNT UNL", Status%
    Checkstat
'Initialize the interface
    CALL INIT(MY.ADDR%, SYSCON%)

first:
'Opening menu
    PRINT
    PRINT "-----"
    PRINT
    PRINT "HP4191 Characteristic impedance calculation"
    PRINT "-----"
    PRINT "          OPTIONS"
    PRINT "-----"
    PRINT "(A)bort measurement in progress"
    PRINT "(C)ollect new measurements"
    PRINT "Other keys stop"
    PRINT
    Grabbaletter
    PRINT A$
    SELECT CASE A$
        CASE "A"
            CMD "AB"
        CASE "C"
            GOTO Collect
        CASE ELSE
            STOP
    END SELECT
    GOTO first

Collect:

```

```

'Start program by asking for sweep parameters
  ASKnum "START FREQUENCY (MHZ)", "13.98", StartFreq
  ASKnum "STEP FREQUENCY (MHZ)", "14.98", StepFreq
  ASKnum "STOP FREQUENCY (MHZ)", "700", StopFreq
  ASKnum "ELECTRICAL LENGTH (cm)", "00", Elecln
  PRINT
  PRINT "The 4191A should be in a calibrated condition. If this is not"
  PRINT "so, then type (A) at the prompt. Any other key continues"

'Now prepare to conduct sweeps
  CMD "I1" 'This places the 4191 into an interpolated mode (3-70)

,

'First, open-circuited....
  PRINT
  PRINT "Prepare open-circuited measurement."
  PRINT "Press (A) to abort; any other key to begin sweep"
  Grabballetter
  IF A$ = "A" THEN STOP
  CALL CollectData(StartFreq, StepFreq, StopFreq, Elecln, Number,
    Frequency(),
    ImpedOpen(), PhaseOpen())
'Then, short-circuited
  PRINT
  PRINT "Prepare short-circuited measurement."
  PRINT "Press (A) to abort; any other key to begin sweep"
  Grabballetter
  IF A$ = "A" THEN STOP
  CALL CollectData(StartFreq, StepFreq, StopFreq, Elecln, Number,
    Frequency(),
    ImpedShort(), PhaseShort())

'Now, form characteristic impedance magnitude and phase
  PRINT
  PRINT "NOW Calculating values of characteristic impedance over the"
  PRINT "frequency range "; StartFreq; " Mhz to "; StopFreq; " Mhz"
  FOR i = 1 TO Number
    ZOmag(i) = SQR(ImpedOpen(i) * ImpedShort(i))
    ZOphase(i) = .5 * (PhaseOpen(i) + PhaseShort(i))
    IF INT(i / 50) = i / 50 THEN
      PRINT i; "> Zo="; ZOmag(i)
    END IF
  NEXT i
  CALL Plotto(Frequency(), ZOmag(), Frequency(), ZOphase(), Number)
  ASK "Name of output file", "C:\JCL\4191.DAT", OUTPUTFILE$
  IF UCASE$(OUTPUTFILE$) = "ABORT" THEN END
  OPEN "O", #1, OUTPUTFILE$
  PRINT #1, "FREQUENCY          ";
  PRINT #1, "ZOMAG              ";
  PRINT #1, "ZOPHASE             ";
  PRINT #1, "OPEN-CKT IMPEDANCE    ";

```

```

PRINT #1, "OPEN-CKT PHASE      ";
PRINT #1, "SHORT-CKT IMPEDANCE ";
PRINT #1, "SHORT-CKT PHASE     "
FOR j = 1 TO Number
  PRINT #1, USING F$; Frequency(j) * 1000000!;
  PRINT #1, "      ";
  PRINT #1, USING F$; ZOmaga(j);
  PRINT #1, "      ";
  PRINT #1, USING F$; ZOphase(j);
  PRINT #1, "      ";
  PRINT #1, USING F$; ImpedOpen(j);
  PRINT #1, "      ";
  PRINT #1, USING F$; PhaseOpen(j);
  PRINT #1, "      ";
  PRINT #1, USING F$; ImpedShort(j);
  PRINT #1, "      ";
  PRINT #1, USING F$; PhaseShort(j)
NEXT j
CLOSE #1
PRINT
PRINT "(S)tart over, same (D)efaults, (Q)uit"
Grabbaletter
SELECT CASE A$
  CASE "S"
    GOTO first
  CASE ELSE
    END SELECT
END

SUB ASK (Prompt$, Default$, Result$)
PRINT Prompt$; "["; Default$; "]";
INPUT B$
IF B$ = "" THEN
  Result$ = Default$
ELSE
  Result$ = B$
END IF
END SUB

SUB ASKnum (Prompt$, Default$, Result)
ASK Prompt$, Default$, StringTemp$
Temp1$ = Filter(StringTemp$, Number$)
Temp2 = VAL(Filter(Default$, Number$))
IF Temp1$ = "" THEN
  Result = Temp2
ELSE
  Result = VAL(Temp1$)
END IF
END SUB

SUB CMD (s$)

```

```

Send add%, s$, Status%
Checkstat
END SUB

```

```

SUB CollectData (StartFreq, StepFreq, StopFreq, Elecln, Number, Frequency(),
    Impedance(), Phase())

```

```

'Estimate number of points to be collected
    Number = INT((StopFreq - StartFreq) / StepFreq + 1)

'Now set up 4191 for initial sweep
    CALL SPOLL(add%, poll%, Status%)
    CMD "A1B1T3"          'Z from A-side, Angle in degrees from
                          'the B-side, and Trigger is manual
    Step$ = "SF" + StringRepOf$(StepFreq) + "EN"
    Stop$ = "PF" + StringRepOf$(StopFreq) + "EN"
    Start$ = "TF" + StringRepOf$(StartFreq) + "EN"
    Length$ = "EL" + StringRepOf$(Elecln) + "EN"
    CMD Step$ + Start$ + Stop$

```

```

'Do sweep
    CMD "WU"
    i = 0
    CALL SPOLL(add%, poll%, Status%)      'MAKE SURE SRQ NOT SET
    DO WHILE flag <> 1
        i = i + 1
        T$ = SPACE$(47)
        ENTER T$, 1%, add%, Status%
        SPOLL add%, poll%, Status%
        IF poll% = 0 THEN flag = 1
        OutputDecode T$, Frequency(i), Impedance(i), Phase(i)
        PRINT i; ">"; Frequency(i), Impedance(i), Phase(i)
        IF flag = 1 THEN EXIT DO
        SPOLL add%, poll%, Status%
    LOOP
    Number = i

```

```

END SUB

```

```

FUNCTION Filter$ (Txt$, FilterString$) STATIC
,
, ===== FILTER =====
,     Takes unwanted characters out of a string by
,     comparing them with a filter string containing
,     only acceptable numeric characters
, =====
,
    TEMP$ = ""
    TxtLength = LEN(Txt$)

    FOR i = 1 TO TxtLength      ' Isolate each character in

```

```

        C$ = MID$(Txt$, i, 1)    ' the string.
        ' If the character is in the filter string, save it:
        IF INSTR(FilterString$, C$) <> 0 THEN
            TEMP$ = TEMP$ + C$
        END IF
    NEXT i

    Filter$ = TEMP$

END FUNCTION

SUB Grabballetter
1 A$ = INKEY$: IF A$ = "" THEN 1
A$ = UCASE$(A$)
END SUB

SUB OutputDecode (T$, A, B, C)
REDIM k$(10)
CALL Parseline(T$, m, k$())
IF m <> 3 THEN
    PRINT "DATA ERROR?!"
END IF
A = VAL(Filter$(k$(1), Number$))
B = VAL(Filter$(k$(2), Number$))
C = VAL(Filter$(k$(3), Number$))
END SUB

SUB Parseline (Token$, Numwords, x$())
REDIM x$(20)
' Invoke StrTok$ with the string to tokenize.
iWord = 1
x$(1) = StrTok$(Token$, delimiters$)
WHILE Token$ <> ""
    PRINT Token$
    ' Call StrTok$ with a null string so it knows this
    ' isn't the first call.
    iWord = iWord + 1
    Token$ = StrTok$("", delimiters$)
    x$(iWord) = Token$
WEND
Numwords = iWord - 1
END SUB

FUNCTION StringRepOf$ (s)
IF s >= 0 THEN
    s$ = RIGHT$(STR$(s), LEN(STR$(s)) - 1)
ELSE
    s$ = STR$(s)

```

```

END IF
StringRepOf$ = s$
END FUNCTION

FUNCTION StrTok$ (Srce$, Delim$)
STATIC Start%, SaveStr$

    ' If first call, make a copy of the string.
    IF Srce$ <> "" THEN
        Start% = 1: SaveStr$ = Srce$
    END IF

    BegPos% = Start%: Ln% = LEN(SaveStr$)
    ' Look for start of a token (character that isn't delimiter).
    WHILE BegPos% <= Ln% AND INSTR(Delim$, MID$(SaveStr$, BegPos%, 1)) <> 0
        BegPos% = BegPos% + 1
    WEND
    ' Test for token start found.
    IF BegPos% > Ln% THEN
        StrTok$ = "": EXIT FUNCTION
    END IF
    ' Find the end of the token.
    EndPos% = BegPos%
    WHILE EndPos% <= Ln% AND INSTR(Delim$, MID$(SaveStr$, EndPos%, 1)) = 0
        EndPos% = EndPos% + 1
    WEND
    StrTok$ = MID$(SaveStr$, BegPos%, EndPos% - BegPos%)
    ' Set starting point for search for next token.
    Start% = EndPos%
END FUNCTION

DECLARE FUNCTION GetFileName$ ()
DECLARE SUB ENTER (TEMP$, LENGTH%, ADDRESS%, Status%)
DECLARE SUB Send (ADDRESS%, CMD$, Status%)
DECLARE SUB Checkstat ()
DECLARE SUB DeviceCommand (ADDRESS%, CMD$, PARM%, Status%, OFFSET%)
DIM SHARED a$, Status%, add%, r(1)

SUB Checkstat
IF Status% <> 0 THEN
    PRINT "status error! #>"; Status%
END IF
END SUB

SUB Command (s$)
Send add%, s$, Status%
Checkstat
END SUB

SUB DeviceCommand (ADDRESS%, CMD$, PARM%, Status%, OFFSET%)

```

```

IF CMD$ <> "" THEN
    ' LOCATE MEMORY POINTER FOR R(1)
    STRPT = VARPTR(r(1))
    ' OBTAIN SEGMENT AND OFFSET FOR CMD$
    X& = VARPTR(CMD$)
    Y& = VARSEG(CMD$)
    ' READING IN THE STRING DESCRIPTOR FOR CMD$
    DEF SEG = Y&
    Q1 = PEEK(X&)
    Q2 = PEEK(X& + 2)
    Q3 = PEEK(X& + 3)
    ' CONSTRUCT A TEMPORARY STRING DESCRIPTOR
    ' WHICH MIMICS THE GW-BASIC STRING DESCRIPTOR
    ' (GW-BASIC USES A 3-BYTE, WHEREAS QB USES 4)
    Z& = VARSEG(r(1))
    DEF SEG = Z&
    POKE STRPT, Q1
    POKE STRPT + 1, Q2
    POKE STRPT + 2, Q3
END IF
' SET SEGMENT TO THAT OCCUPIED BY HPIB CARD
DEF SEG = &HC400
SELECT CASE OFFSET%
    CASE 0      'INITIALIZE
        CALL ABSOLUTE(ADDRESS%, PARM%, OFFSET%)
    CASE 3      'TRANSMIT
        CALL ABSOLUTE(r(1), Status%, OFFSET%)
    CASE 6      'RECEIVE
        CALL ABSOLUTE(r(1), PARM%, Status%, OFFSET%)
    CASE 9      'SEND
        CALL ABSOLUTE(ADDRESS%, r(1), Status%, OFFSET%)
    CASE 12     'SPOLL
        CALL ABSOLUTE(ADDRESS%, PARM%, Status%, OFFSET%)
    CASE 21     'ENTER
        CALL ABSOLUTE(r(1), PARM%, ADDRESS%, Status%, OFFSET%)
    CASE ELSE
        PRINT "AN ERROR HAS OCCURED. ILLEGAL OFFSET ADDRESS WAS SPECIFIED"
END SELECT
' RESTORE SEGMENT
DEF SEG
END SUB

SUB ENTER (TEMP$, LENGTH%, ADDRESS%, Status%)
DeviceCommand ADDRESS%, TEMP$, LENGTH%, Status%, 21
END SUB

FUNCTION GetFileName$ STATIC
,
' ===== GETFILENAME$ =====
'           Returns a file name from user input
' =====

```

```

PRINT "Enter file name>";
INPUT Ftemp$
GetFileName$ = Ftemp$
END FUNCTION

SUB Grabbakey
1 a$ = INKEY$: IF a$ = "" THEN 1
a$ = UCASE$(a$)
END SUB

SUB INIT (ADDRESS%, OTHER%)
DeviceCommand ADDRESS%, "", OTHER%, 0, 0
END SUB

SUB Query (s$, q)
CALL Send(b%, s$, Status%)
Checkstat
r$ = SPACE$(13)          'allocate receive buffer
CALL ENTER(r$, LENGTH%, b%, Status%)
Checkstat
q = VAL(r$)
END SUB

SUB RECEIVE (TEMP$, LENGTH%, Status%)
DeviceCommand 0, TEMP$, LENGTH%, Status%, 6
END SUB

SUB Send (ADDRESS%, CMD$, Status%)
DeviceCommand ADDRESS%, CMD$, 0, Status%, 9
END SUB

SUB SPOLL (ADDRESS%, POLL%, Status%)
DeviceCommand ADDRESS%, "", POLL%, Status%, 12
END SUB

SUB Stat
Checkstat
END SUB

SUB TRANSMIT (TEMP$, Status%)
DeviceCommand 0, TEMP$, 0, Status%, 3
END SUB

```



## Appendix E. *Finite Difference Method (FDM) Calculation Utilizing a Spreadsheet*

This appendix considers the application of two refinements of the finite difference method (FDM) discussed in Chapter 3 applicable to problems which require the calculation of potential distribution and dependent quantities in regions which are satisfied by Laplace's equation. The first refinement improves the voltage potentials estimated in a finite-difference simulation which requires semi-infinite extensions of a homogeneous region. The most important example of this contingency that was encountered in this research effort was situation where the microstrip-like conductors were embedded within homogeneous dielectric regions of semi-infinite extent. The second refinement allows the determination of the potential distribution on and about a "floating" ideal conductor which is embedded in a harmonic region. Calculations of this type were required in this research effort to represent a multi-conductor transmission line which possessed one or more active conductors in an unconnected or "floating" state. The Neumann boundary condition represented by this case, though commonly encountered, has been traditionally difficult to model with a finite-difference approach. Both these concepts were modeled using Lotus 1-2-3 spreadsheet simulations. This particular "coding" medium was selected by virtue of its convenience and rapid-prototyping capabilities.

### *Extension of Semi-Infinite Regions*

The concept of implementing techniques to artificially extend the finite "walls" of FDM simulations is not new, and the work of several researchers has been documented by Sandy *et al.* A representative problem, shown in Figure E.1, facilitates discussion of the semi-infinite problem. The domain of interest is defined by  $\Omega$ , and the origin of an  $x$ - $y$  coordinate system is defined as the center of a single conductor (this convention will also be invoked in several subsequent examples). This is the simulation "target," for which knowledge of a representative potential distribution

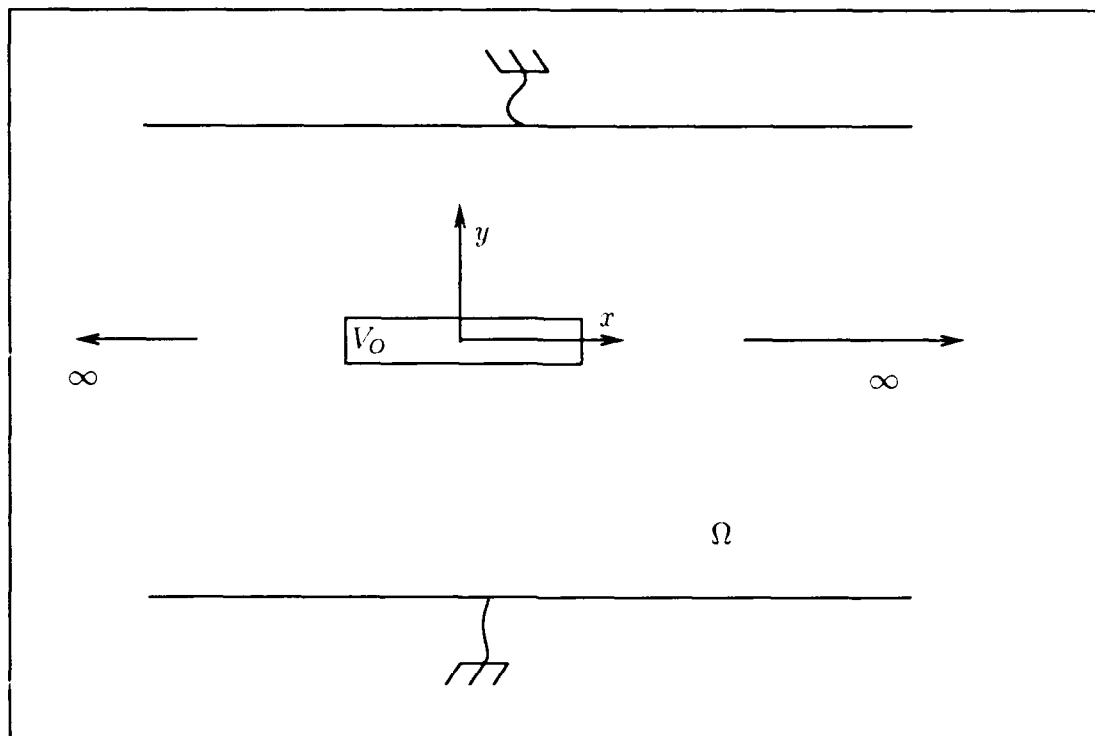


Figure E.1. Problem domain ( $\Omega$ ), representing the transverse cross-section of a stripline transmission line. Horizontal ground plane and dielectric structure extend semi-infinately.

is desired. For this problem, the center conductor is at a fixed positive potential, the boundaries above and below are perfect conducting ground planes, and the dielectric is homogeneous and horizontally infinite in spatial extent. The domain of the problem is defined to be the region  $\Omega$ .

A typical FDM representation of this model, which neglects the extended sidewalls of the target, is shown in Figure E.2. An obvious disadvantage of the Figure E.2 representation of the target model is that, not only are the horizontal boundaries truncated, but they are also fixed at zero potential. If the horizontal region is extended, as shown in Figure E.3, the effects of the truncation are lessened. As the horizontal sidewalls are extended to infinity, the model becomes more accurate, since the

potential distribution of any finite set of charges approaches zero at infinity. Hence, the horizontal extension of the Figure E.2 domain improves the model's accuracy. However, since computational resources are finite, and since most of the computational "investment" occurs far away from the usual region of interest, the overall improvements of this approach are marginal. Often in these simulations, the region of primary interest is centrally located. Hence, a more efficient technique would deal with a smaller spatial region, and also with more realistic boundary conditions. This refinement would then lead to a more accurate potential distribution with the region of interest. With the "virtual" boundary approach (Figure E.4), this compromise is pursued. The virtual boundary does not represent a physical boundary. Rather, it is a mathematical boundary possessing a potential that varies along the surface. The term "surface" will be used as a generality ( $n$ -dimensions), but in two-dimensional problems, the boundary surface is actually a curve. (In one-dimensional problems, it is a point!) As indicated by Sandy *et al.*, the FDM simulation will provide a correct potential distribution (within the resolution limits of the discretization scheme utilized) when the potentials on the virtual boundary are correctly selected. The potential at the virtual boundary is therefore chosen to be more approximate to that exhibited by the actual target simulation (85).

To provide estimates of the boundary potential, the technique of Sandy *et al.* used the free-space Green's function in an iterated scheme. The boundary potential distribution, as well as that of the interior nodes, converges towards the appropriate potential distribution as the number of iterations is increased. The boundaries equivalently represent self-adjusting Dirichlet conditions that asymptotically approach the distributions possessed by the associated surface inscribed within an equivalent interior, semi-infinite boundary problem. Therefore, in principle, the key to a virtual boundary method is the establishment of appropriate potential distributions on these virtual surfaces, which are fictitious as far as the physical problem is concerned, but are really the "edges" of a FDM model.

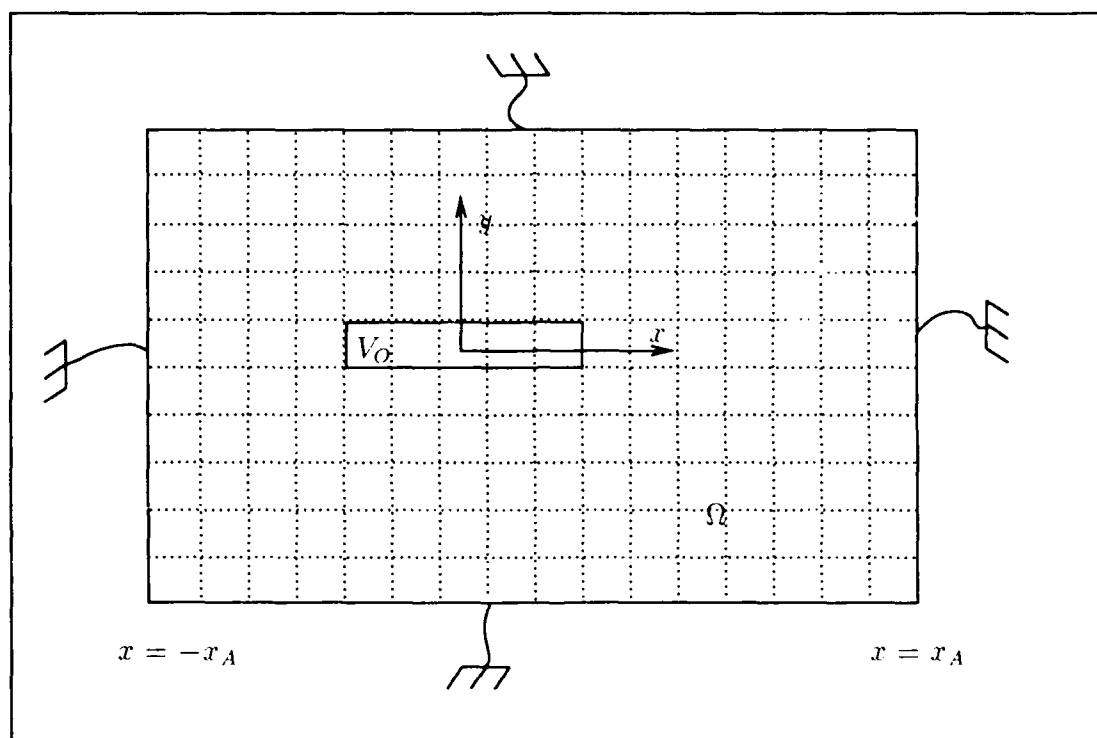


Figure E.2. Simple FDM model, illustrating the discretization of spatial domain  $\Omega$ . In addition to fixed boundaries in the  $y$ -dimension, fixed boundaries are present in the  $x$ -direction. The potential at all fixed boundaries is set to zero volts (which is only correct for the boundaries in the  $y$ -dimension).

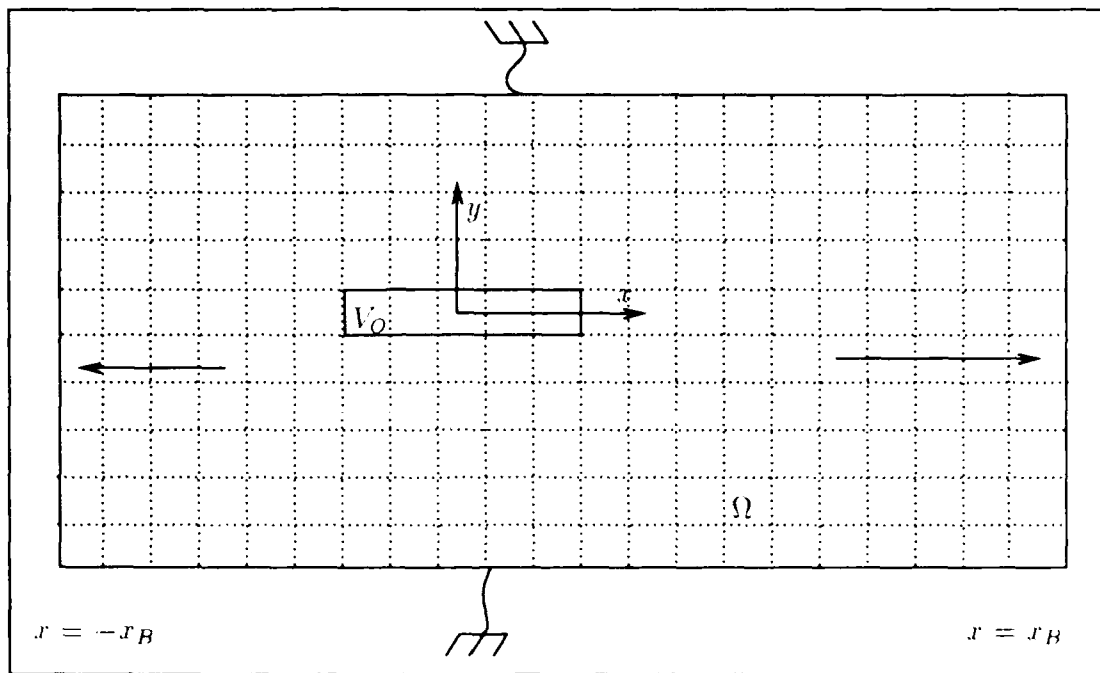


Figure E.3. Simple FDM model with an extended horizontal domain.

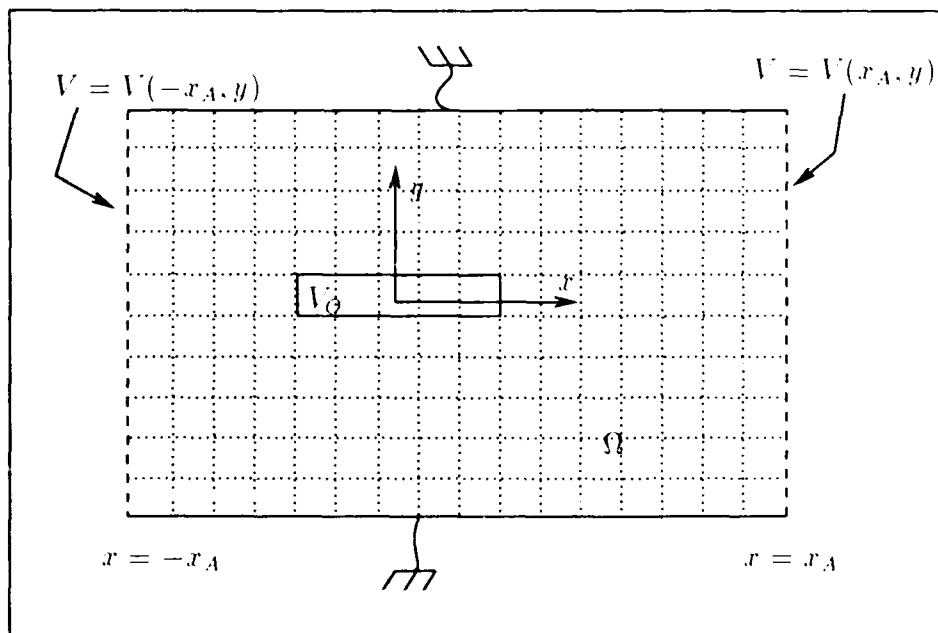


Figure E.4. FDM simulation with virtual boundaries.

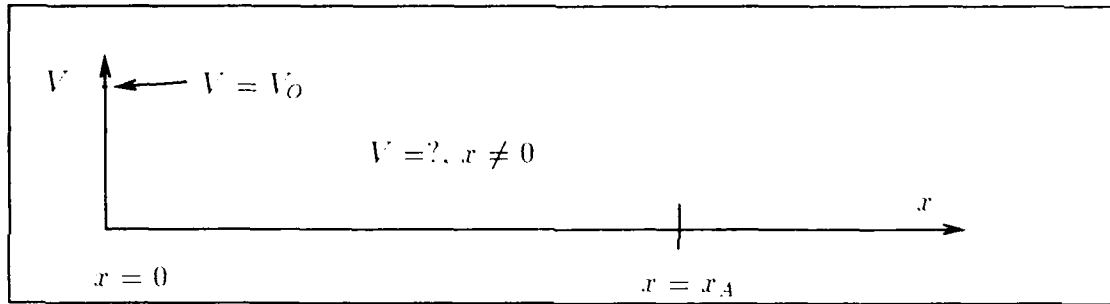


Figure E.5. One-dimensional example, illustrating the presence of a point voltage source  $V_0$  at  $x = 0$ .

Of course, the primary problem in an FDM simulation involving virtual surfaces is in determining the correct potential distribution on the boundaries. No analytic treatments exist that specify this distribution for any problem, although Sandy *et al.* use the  $\ln r$  dependence of the two-dimensional free-space Green's function to provide an estimate. The technique that is used must be relatively simple, so as to preserve the intrinsic simplicity of the FDM approach. For this research effort, a simple linear equation was used to model the potential distribution at the surface. The region interior to the virtual boundaries were modeled with conventional finite difference cells, as described in Chapter 3.

A discussion of the linear equation approach used to establish the potential at the virtual boundaries can be facilitated by considering a one-dimensional example. Figure E.5 represents such a problem. Figure E.5 depicts a point voltage source ( $V = V_0$ ) at  $x=0$ , placed in a domain for which a static potential distribution is sought. In this problem, the domain is semi infinite; that is,  $x$  may take on values over the interval  $[0, \infty)$ .

The potential is assumed to satisfy a one-dimensional version of Laplace's equation:

$$V_{xx} = 0 \quad (\text{E.1})$$

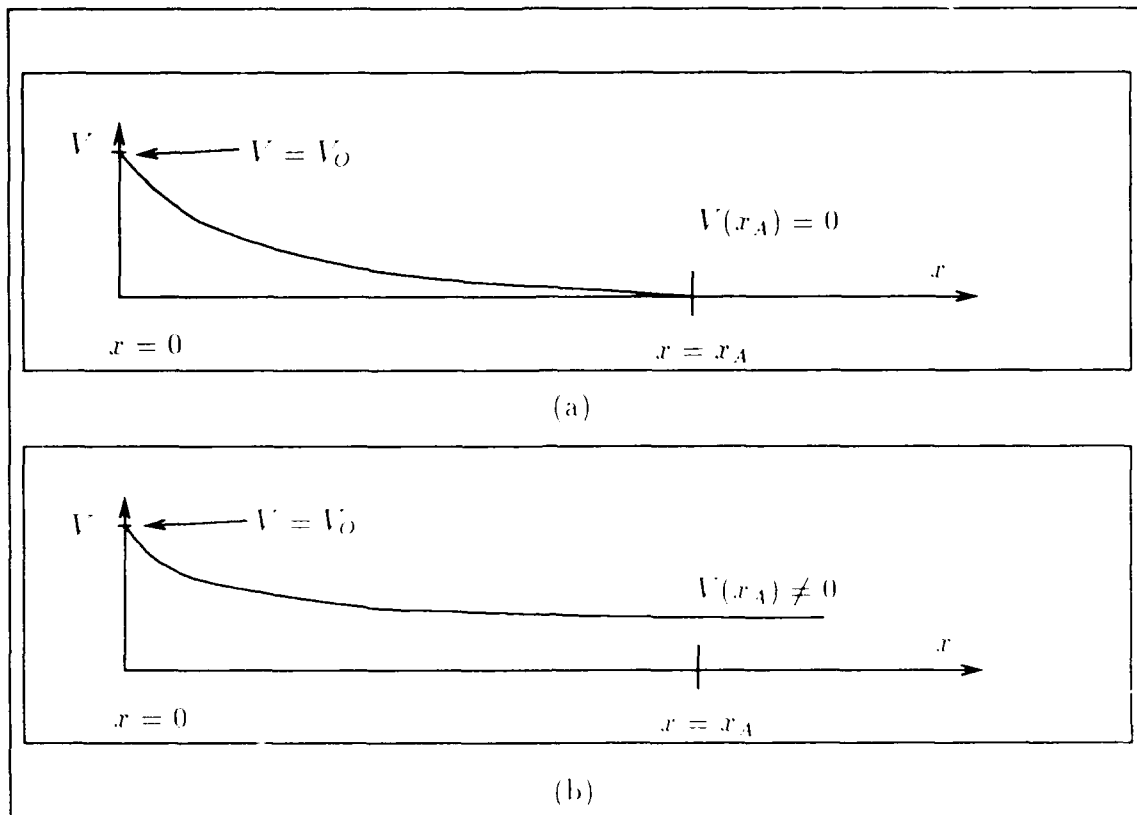


Figure E.6. One-dimensional point source distributions. (a) Based on  $V(x_A) = 0$ . (b) Correct potential distribution.

subject to the boundary conditions  $V(0) = V_0$  and  $V(\infty) = 0$ .

Since finite difference problems require finite domains, the arbitrary boundary  $x_A$  is selected for the horizontal boundary limit. In this one-dimensional problem, the point  $x = x_A$  constitutes the equivalent of a virtual surface. As in the higher dimensional problem, the potential  $V(x_A)$  is unknown. In the one dimensional version of Figure E.2,  $V(x_A)$  would be set equal to zero, producing the voltage distribution shown in Figure E.6a. This potential distribution is different from the correct voltage distribution shown in Figure E.6b (the differences are exaggerated for illustrative purposes). Clearly, based on Figure E.6b, the potential  $V(x_A)$  is not equal to zero.

As a refinement to the Figure E.6a results, the potential at  $x = x_A$  can be

estimated. The bounds on the estimate of this potential are:

$$0 < V(x_A) < V_O.$$

This result is based on the well-known maximum principle for elliptic partial-differential equations (21).

The estimated potential  $V(x_A)$  must be greater than zero, which is the minimum value of the potential, occurring at  $x = \infty$ . The estimate must also be less than  $V_O$ , the maximum value of potential, which occurs at  $x = 0$ . Since the two points ( $x=0$  and  $x = \infty$ ) are the boundaries of the problem's domain, the potential of any intermediate point must be bounded between zero and  $V_O$ . Another implication of the maximum principle is that the potential at  $x = x_A$  will be a minimum over the interval  $[0, x_A]$ .

The estimates for  $V(x_A)$  were formed by a linear equation:

$$V(x) = Mx + B \tag{E.2}$$

where  $M$  is the slope and  $B$  is the  $V$ -intercept. The value  $B$  corresponds to the value of  $x$  where the potential equals zero in Equation E.2. Consequently,  $B$  is always chosen to be greater than  $x_A$  ( Figure E.5a corresponds to  $x = x_A$ ). After  $B$  is chosen, the desired potential  $V(x_A)$  is determined.

Although no apparent advantage is evident from the linear equation, since now the intercept  $B$  must be estimated, this representation becomes advantageous for two-dimensional problems. For the two-dimensional problem (Figure E.1), Equation E.2 can be represented in the simulated representation (Figure E.4) as:

$$V(x, y) = M(y)x + B \tag{E.3}$$

where the slope  $M(y)$  depends on  $y$ . However, the  $y$ -intercept ( $B$ ) is fixed over the



range of  $y$  in the problem's domain ( $\Omega$ ). The advantage of using Equation E.3 is that the potential approximation relative to the virtual surfaces:

$$V(-x_A, y) = -M(y)x_A + B \quad (\text{E.4})$$

$$V(x_A, y) = M(y)x_A + B \quad (\text{E.5})$$

$$(\text{E.6})$$

is reduced to a *single* unknown ( $B$ ). It is important to note that this treatment is only approximate. For a sufficiently complicated problem with many sources, Equation E.3 would no longer apply, and a more general form:

$$V(x, y) = M(y)x + B(y) \quad (\text{E.7})$$

would be required. In that event,  $B(y)$  is also dependent on  $y$ , and there would be no advantage in attempting to estimate the boundary potential with a linear model. For the problems encountered in this research effort, the approximation in Equation E.2 was deemed to be sufficiently accurate.

The choice of the appropriate intercept  $B$  is approached in an iterative fashion, and it was found that an upper bound on the value of  $B$  could be determined graphically. For the two-dimensional problem representation in Figure E.4, this feature is demonstrated by examining the voltage profile along the  $x$ -axis for fixed values of  $y$  (in particular,  $y=0$ ). The resulting voltage profiles resemble the Figure E.5 plots for the one-dimensional case. For  $y=0$ , the voltage profile based on an initial estimate of  $B$  is shown in Figure E.7. However, upon inspection of the resultant profile and consideration of Equation 2.1, it is straightforward to conclude that the voltage distribution is incorrect in this case. Since the minimum of the profile does not occur at  $x = x_A$ , then the existence of another voltage source is implied. The existence of another potential source is necessary due to the change in concavity of the voltage profile that would be required at some  $x^* > x_A$  to produce  $V = 0$  at

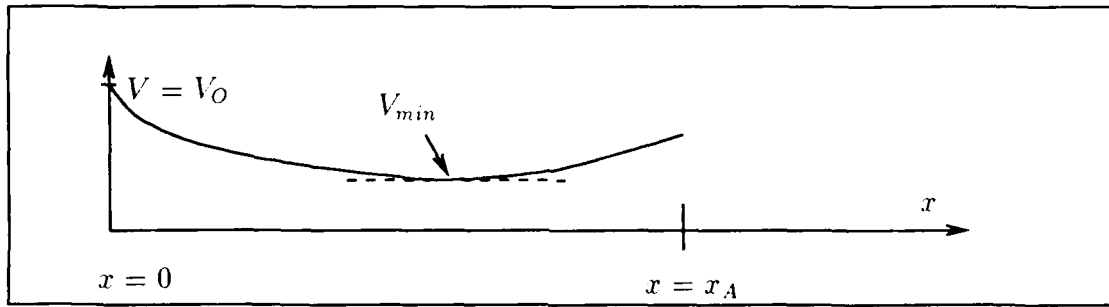


Figure E.7. Voltage profile along the  $x$ -axis for  $y=0$ .

$x = \infty$ . In other words, a local maximum at  $x^* > x_A$  is implied in Figure E.7. In the domain ( $\Omega$ ) of the two-dimensional problem, the application of Equation 2.1 around a contour ( $\gamma$ ) which encloses the local maximum produces a positive charge density. Hence, a charge or potential source is implied. However, this result is incorrect, since no other potential or charge source exists in the problem shown in Figure E.1. To remove this inconsistency, the estimated value of  $B$  must be increased to further extend the  $y$ -intercept of Figure E.3. This extension results in a reduction of potential on the virtual surface. Sufficient reduction will create a potential distribution in the profile that does not require a concavity change over  $x_A < x < \infty$ . Therefore, an upper bound for  $V(x_A, 0)$  exists. A similar argument exists for the potential surface  $V(-x_A, y)$ .

Based on this reasoning, a simple conclusion was reached: if any initial estimate for  $B$  produced a local minimum in the interval  $(0, x_A)$ , then the estimated value of  $B$  was too low.

Unfortunately, a similar result was not found for an upper bound on ( $B$ ); that is, no techniques for estimating the lower bound on the virtual surface potentials were found. Thus, it was impossible to determine a lower bound on the potential of the virtual surface greater than zero volts.

The existence of an upper bound on  $V(-x_A, y)$  and  $V(x_A, y)$  became the basis

of a manually-applied algorithm, which was used for most of the FDM simulations in this research effort. The resulting algorithm took advantage of the capability to detect an upper bound for the potential along virtual surfaces. The presence of an incorrect voltage distribution was concluded when the following inequality was satisfied:

$$\min_R V(x, y_o) < V(x_A, y_o); \quad R = \{(x, y) : 0 < x < x_A, (x, y_o) \in \Omega\} \quad (\text{E.8})$$

for the virtual surface along  $x = x_A$  and:

$$\min_R V(x, y_o) < V(-x_A, y_o); \quad R = \{(x, y) : -x_A < x < 0, (x, y_o) \in \Omega\} \quad (\text{E.9})$$

for the virtual surface along  $x = -x_A$ . An initial estimate on  $B$  for each virtual surface was supplied to the simulation prior to its execution. After several iterations of the FDM simulation (about 50 for the simulations in this research effort), the voltage profile corresponding to  $y=0$  in Figure E.1 was inspected. When a minimum was found that did not occur on the boundary, the simulation was adjusted such that lower potentials were produced on the virtual surface (by increasing the distance of the  $y$ -intercept ( $B$ ) from the origin). On the other hand, if the minimum occurred on the boundary, then the simulation was adjusted for higher potentials on the virtual surfaces (by decreasing the distance of the  $y$ -intercept  $B$  from the origin). This process was repeated until no change in the graph was evident between adjustments. Algorithmically, a convergence on the least upper bound of the surface potential was sought. Although it could not be shown that this least upper bound was identical to the correct potential distribution, it was assumed that the resulting potential was reasonably approximate. Typically, as stated before, the region of interest in many problems is not near the virtual surfaces. Rather, most of the field quantities will be derived from potential distributions that are closer to the active conductors. Since the magnitude of the potential at points near the virtual surfaces is small,

the associated error contribution to regions near the active conductors (where the potential and the change in potential is usually larger) is expectedly small. For this reason, an FDM simulation of the type illustrated in Figure E.2 is often used. The technique described in this appendix is merely an attempt to provide a further and more approximate refinement of these simulations. As in the Figure E.2 technique, the applications of this newer technique must be carefully considered, and further study of the application and further refinement of this technique are recommended.

### *Treatment of Floating Conductors*

The second extension of the basic FDM involved the modeling of a "floating conductor". This model was necessary for many simulations involved with this research effort. A *floating conductor* is defined as a conductor which is embedded in a dielectric region and electrically unconnected to any source or load. The conductors in this treatment are assumed to possess infinite conductivity. The floating conductor is represented by the Neumann boundary condition:

$$\frac{\partial V(x,y)}{\partial t} = 0 \quad (\text{E.10})$$

where  $t$  refers to the direction tangential to the surface of the conductor. The voltage on the conductor is constant, but unknown. The resulting FDM formulation was relatively simple. As shown in the reference model in Figure E.8, the floating conductor is represented with three basic cell types (for simplicity, the relaxation factor ( $\alpha$ ) is fixed at 0.25).

The first cell type used in the floating conductor simulations is the same type used for ordinary interior cells, identical to the type described in Chapter 3. Cells of the first type are placed *inside* the floating conductor region and beyond the interface region between the conductor and dielectric.

The second cell type is a modified interior node cell with an extended conductor reference node. This extended reference node is the unknown voltage of the floating



conductor. Each cell surrounding the floating conductor is specified by this cell type. The detailed example in Figure E.8 defines a dielectric which interfaces to the floating conductor on its top surface. Other orientations are described as simple permutations of the basic cell type. The " $V_x$ " nodes of all cells around a given conductor are referenced to the same (external) cell. This external cell constitutes the third cell type.

The third cell type is the computational cell for the voltage of the floating conductor. The cell is termed an "external cell", since it is not contained inside the simulation domain. The unknown voltage is formed from the average of the potential of all cells inside the floating conductor region. The resulting average voltage  $V_x$  is then the extended conductor reference voltage which is provided to the cells of the second type. Only one cell of the third kind is used for a given floating conductor. Multiple floating conductors are accommodated with separate cells of the third type, one for each floating conductor.

The combination of cells as shown in Figure E.8 satisfy the necessary boundary conditions of a floating conductor. However, no other sources describing a similar technique were found in the literature. Furthermore, no associated problem formulations which considered floating conductors were found. So, in a sense, this refinement of the basic FDM has not been verified. However, in a large number of simulations performed in this research effort, the floating conductor technique was applied. Nevertheless, the resulting potentials on these conductors satisfied both the boundary conditions of the problem and the maximum principle.

## Appendix F. *Solutions to the Matrix Representation of the Telegrapher's Equations*

This appendix considers the solution of the multiconductor telegrapher's equations (Equations 2.29–2.30) for transmission lines which are lossless, as well as those which possess resistive attenuation. The solution technique is then applied to several examples for two- and three-conductor lines, including backward- and forward-coupled gain configurations, transmission gain configurations, and driving point configurations. These solutions require knowledge of the capacitance matrix and, for lossy lines, a series resistance factor (with all quantities on a per meter basis). The coefficients of the capacitance matrix were determined by FDM analysis, as described in Chapter 3 and Appendix E.

The Chapter 3 numerical analysis discussion considered a special case of the telegrapher's equations applied to a lossless, two-conductor transmission line system. Although, in the context of Chapter 3, the problem was formulated for a two-conductor system, the Equation 3.19 matrix is general for an  $n$ -conductor lossless system. To further extend the generality of Equation 3.19, the introduction of series attenuation losses is readily introduced:

$$\begin{bmatrix} v' \\ i' \end{bmatrix} = \begin{bmatrix} 0 & [R] + j\omega[L] \\ j\omega[C] & 0 \end{bmatrix} \begin{bmatrix} v \\ i \end{bmatrix} \quad (\text{F.1})$$

where  $[R]$  is the series attenuation matrix (ohms/m) and, as before,  $[L]$  is the series inductance matrix (henries/m) and  $[C]$  is the capacitance matrix (farads/m). To simplify the subsequent analysis,  $[R]$  is assumed to be diagonal and symmetric; that is, it is assumed that  $[R] = r[I]$ , where  $r$  is positive and real, and  $[I]$  is the identity matrix of order  $N$ . The rank of the identity matrices utilized in this appendix will not be otherwise declared explicitly, but should be clear by context. The primed variables are differentiated with respect to  $z$ .

Several techniques exist to evaluate the solution of Equation F.1. When considering an eigenvalue-eigenvector approach, great care must be exercised, since repeated eigenvalues will occur when symmetric lines are considered (41:305-313). Some analytic packages, in particular MATRIXX, do not guarantee the generation of linearly independent eigenvectors when non-distinct eigenvalues occur (17). Physically, one would expect a duplicity of eigenvalues to occur for symmetric conductors in the lossless case, since these are, in fact, propagation constants of the transmission line system [(24),(26)]. Fortunately, a more direct approach for solving Equation F.1 is available (10:193). This approach completely circumvented the need to determine eigenvectors or eigenvalues. With the direct approach, the solution form of Equation F.1 becomes (10:193):

$$\begin{bmatrix} v \\ i \end{bmatrix} = e^{[A]z} [K] \quad (\text{F.2})$$

where, in this case,  $[K]$  is a  $[2N \times 1]$  matrix (column vector) of arbitrary constants and  $[A]$  is the  $[2N \times 2N]$  matrix on the right-side of Equation F.1, premultiplying the voltage-current column vector. The determination of the matrix  $e^{[A]z}$  can be approached through the power series expansion:

$$e^{[A]z} = 1 + [A]z + \frac{([A]z)^2}{2!} + \frac{([A]z)^3}{3!} + \frac{([A]z)^4}{4!} + \dots \quad (\text{F.3})$$

Next, the quantities  $[A]$ ,  $[A]^2$ ,  $[A]^3$ , ... are considered:

$$\begin{aligned} [A] &= \begin{bmatrix} 0 & [R] + j\omega[L] \\ j\omega[C] & 0 \end{bmatrix} \\ [A]^2 &= \begin{bmatrix} 0 & [R] + j\omega[L] \\ j\omega[C] & 0 \end{bmatrix} \begin{bmatrix} 0 & [R] + j\omega[L] \\ j\omega[C] & 0 \end{bmatrix} \end{aligned} \quad (\text{F.4})$$



$$= \begin{bmatrix} j\omega[C]j\omega\mu\epsilon C^{-1} + j\omega[R][C] & 0 \\ 0 & j[C]j\omega\mu\epsilon[C]^{-1} + j\omega[C][R] \end{bmatrix}. \quad (\text{F.5})$$

Since  $R = r[I]$ , then  $[C][R] = [R][C]$ , and  $[A]^2$  then becomes:

$$[A]^2 = (-\omega^2\mu\epsilon + j\omega[R][C])[I]. \quad (\text{F.6})$$

From  $[A]$  and  $[A]^2$ , the higher order products can be defined:

$$[A]^3 = [A]^2[A] = (-\omega^2\mu\epsilon + j\omega[R][C])[A] \quad (\text{F.7})$$

$$[A]^4 = [A]^2[A]^2 = (-\omega^2\mu\epsilon + j\omega[R][C])^2[I] \quad (\text{F.8})$$

$$[A]^5 = [A]^4[A] = (-\omega^2\mu\epsilon + j\omega[R][C])^2[A]. \quad (\text{F.9})$$

From the above progression, it is obvious that  $[A]^i$  can be expressed as:

$$[A]^i = \begin{cases} (-\omega^2\mu\epsilon + j\omega[R][C])^{(i/2)}[I], & i \text{ even} \\ [A]^{(i-1)}[A], & i \text{ odd.} \end{cases} \quad (\text{F.10})$$

This observation yields:

$$e^{[A]z} = [I] + [A]z + \frac{(-\omega^2\mu\epsilon + j\omega[R][C])z^2}{2!}[I] + \frac{(-\omega^2\mu\epsilon + j\omega[R][C])z^3}{3!}[A] + \frac{(-\omega^2\mu\epsilon + j\omega[R][C])^2z^4}{4!}[I] + \frac{(-\omega^2\mu\epsilon + j\omega[R][C])^2z^5}{5!}[A] + \dots \quad (\text{F.11})$$

Using the variable assignments  $[\gamma] = \sqrt{-\omega^2\mu\epsilon[I] + j\omega[R][C]}$  and  $[A] = [\gamma][B]$ , Equation F.11 may be written:

$$\begin{aligned} e^{[A]z} &= [I] + z[\gamma][B] + \frac{[\gamma]^2[I]}{2!}z^2 + \frac{[\gamma]^3[B]}{3!}z^3 + \frac{[\gamma]^4[I]}{4!}z^4 + \dots \quad (\text{F.12}) \\ &= \left[ [I] + \frac{[\gamma]^2[I]}{2!}z^2 + \frac{[\gamma]^4[I]}{4!}z^4 + \frac{[\gamma]^6[I]}{6!}z^6 + \dots \right] \\ &\quad + \left[ z + \frac{[\gamma]^3[B]}{3!}z^3 + \frac{[\gamma]^5[B]}{5!}z^5 + \dots \right]. \end{aligned}$$

The expansions can be written in terms of more familiar functions (1:85):

$$\begin{aligned} e^{[A]z} &= \text{Diag}(\cosh([\gamma]z))[I] + \sinh([\gamma]z)[B] \\ &= \text{Diag}(\cosh([\gamma]z))[I] + \sinh([\gamma]z)[\gamma]^{-1}[A] \end{aligned} \quad (\text{F.13})$$

where the notation,  $\text{Diag}()$ , implies a matrix which has diagonal elements specified as its argument, and zeros for all off-diagonal elements. The matrix form of Equation F.13 is:

$$e^{[A]z} = \begin{bmatrix} \text{Diag}(\cosh([\gamma]z)) & \sinh([\gamma]z)[\gamma]^{-1}([R] + j\omega\mu\varepsilon[C]^{-1}) \\ \sinh([\gamma]z)[\gamma]^{-1}j\omega[C] & \text{Diag}(\cosh([\gamma]z)) \end{bmatrix} \quad (\text{F.14})$$

The solution of Equation F.1 can be completed by considering the appropriate boundary conditions, which will allow the arbitrary constant column vector  $[K]$  to be determined. The remainder of this appendix considers several examples which were encountered in this research effort. For the two-conductor backwards coupling cases, MATRXXX and Mathematica programs were generated. Eventually, the MATRXXX approach was abandoned and subsequent developmental work was accomplished only for the Mathematica program. The program listing is provided in Appendix A.

Since only two evaluation points are considered in the solution of these problems ( $z = 0$  and  $z = \ell$ ), Equation F.13 need only be evaluated at these points. Further, since  $e^{[A]z} = [I]$  for any non-singular  $[A]$ , the only evaluation which actually requires computation is that for  $z = \ell$ .

### *Two-Conductor Backward Coupling Gain*

Assuming low impedance source and load terminations (as shown in Figure 3.16), the appropriate boundary conditions for the backward coupling gain configuration become:

$$v_1(0) = V_{source} - Z_S i_1(0) = 1 - 50i_1(0) \quad (\text{F.15})$$

$$v_2(0) = -Z_L i_2(0) = -50 i_2(0) \quad (\text{F.16})$$

$$i_1(\ell) = 0 \quad (\text{F.17})$$

$$\text{and } i_2(\ell) = 0 \quad (\text{F.18})$$

where the source voltage ( $V_{source}$ ) has been arbitrarily set to one volt and the source and load terminations are chosen to be  $50 \Omega$  (as commonly encountered with test instrumentation). The solution for this problem is achieved by considering evaluations of the system at  $z = 0$  and  $z = \ell$ . Of course, at  $z = 0$ , the voltage-current column vector is equal to the unknown constant vector  $[K]$ :

$$\begin{bmatrix} 1 - 50i_1(0) \\ -50i_2(0) \\ i_1(0) \\ i_2(0) \end{bmatrix} = [K]. \quad (\text{F.19})$$

As indicated earlier, this equation results from the fact that  $e^{[A] \cdot 0} = [I]$ . At  $z = \ell$ , the corresponding evaluation yields:

$$\begin{bmatrix} v_1(\ell) \\ v_2(\ell) \\ i_1(\ell) \\ i_2(\ell) \end{bmatrix} = e^{[A]\ell} [K]. \quad (\text{F.20})$$

Four equations in  $[K]$  can be extracted from these two independent evaluations:

$$1 - 50 \cdot K_3 - K_1 = 0 \quad (\text{F.21})$$

$$-50 \cdot K_2 - K_4 = 0 \quad (\text{F.22})$$

$$\left( e^{[A]\ell} \right)_3 [K] = 0 \quad (\text{F.23})$$

$$\text{and } \left( e^{[A]\ell} \right)_4 [K] = 0. \quad (\text{F.24})$$

The subscripted “ $K$ ” variables refer to the particular elements of column vector  $[K]$ , and the subscripts on the last two equations refer to particular rows of the matrix enclosed by parentheses. These expressions are easily represented in matrix form:

$$\begin{bmatrix} 1 \\ 0 \\ 0 \\ 0 \end{bmatrix} = \begin{bmatrix} 1 & 0 & 50 & 0 \\ 0 & 1 & 0 & 50 \\ \xi_{31} & \xi_{32} & \xi_{33} & \xi_{34} \\ \xi_{41} & \xi_{42} & \xi_{43} & \xi_{44} \end{bmatrix} \begin{bmatrix} K_1 \\ K_2 \\ K_3 \\ K_4 \end{bmatrix} \quad (\text{F.25})$$

where  $[\xi] = e^{[A]t}$ . This result may be abbreviated in a more compact form:

$$[f] = [\Gamma][K] \quad (\text{F.26})$$

for which  $[K]$  is solved by the inversion of  $\Gamma$ :

$$[\Gamma]^{-1}[f] = [K]. \quad (\text{F.27})$$

The coupled voltage gain, which is simply the ratio of load to source voltage, is directly obtained from  $[K]$ :

$$A_C = \frac{V_2(0)}{V_1(0)} = \frac{K_2}{K_1} \quad (\text{F.28})$$

which can also be expressed in decibels (dB):

$$A_C = 20 \cdot \log_{10} \left[ \frac{K_2}{K_1} \right]. \quad (\text{F.29})$$

The gain, when expressed in dB, provides a direct comparison to the measured results.

### Two-Conductor Configuration with Generalized Termination Conditions.

A more generalized approach for the two-conductor case can be considered, which allows arbitrary sources and loads to be modeled through boundary conditions. Furthermore, this generalized formulation can accommodate many different measurement quantities, including coupling gain, transmission gain, isolation gain, and driving point impedances. The various measurement configurations are readily simulated. Open end conditions are modeled with very high resistances shorting a given port to ground. A representative schematic of the most general case which such a treatment can be accommodated is shown in Figure F.1.

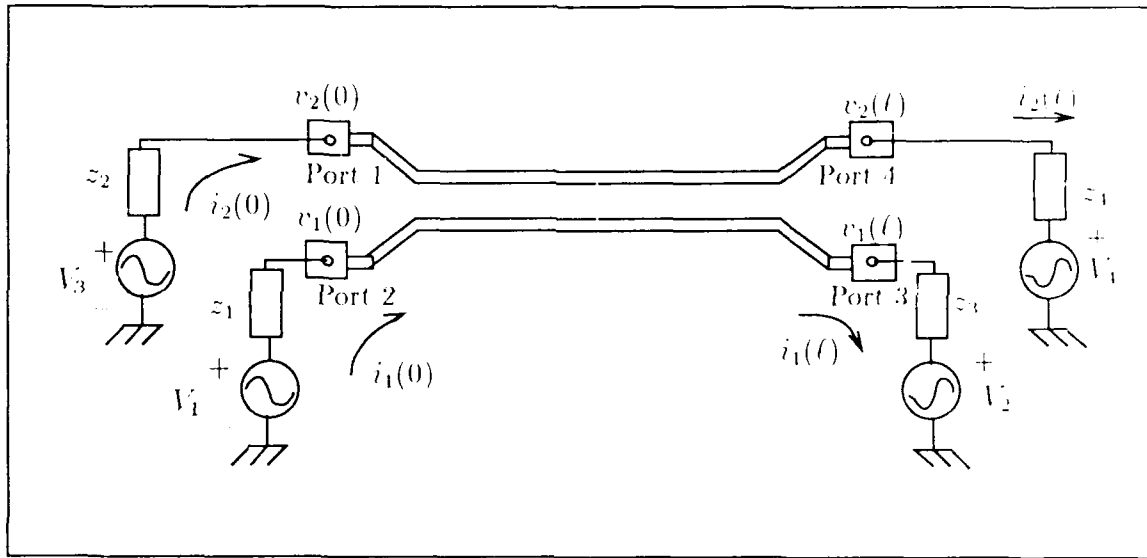


Figure F.1. Schematic of the general two-conductor configuration.

For the general case, the boundary conditions become:

$$-V_1 + z_1 i_1(0) + v_1(0) = 0, \quad \text{for port 1} \quad (\text{F.30})$$

$$-V_2 + z_2 i_2(0) + v_2(0) = 0, \quad \text{for port 2} \quad (\text{F.31})$$

$$V_3 + z_3 i_1(l) + v_1(l) = 0, \quad \text{for port 3} \quad (\text{F.32})$$

$$\text{and } V_4 + z_4 i_2(l) + v_2(l) = 0, \quad \text{for port 4} \quad (\text{F.33})$$

where  $V_1, V_2, V_3$ , and  $V_4$  are the voltage sources (forcing functions), and  $z_1, z_2, z_3$ , and  $z_4$  are the load impedances at ports 1, 2, 3, and 4, respectively. All of these quantities may be functions of frequency, and the port impedances may be complex.

The matrix formulations for these cases can be obtained by an analogous technique used in the special case of two-conductor backward coupling gain. The resulting matrix becomes:

$$\begin{bmatrix} 1 & 0 & Z_1 & 0 \\ 0 & 1 & 0 & Z_2 \\ \xi_1 & \xi_2 & \xi_3 & \xi_4 \\ \eta_1 & \eta_2 & \eta_3 & \eta_4 \end{bmatrix} [K] = \begin{bmatrix} V_1 \\ V_2 \\ -V_3 \\ -V_4 \end{bmatrix} \quad (\text{F.34})$$

where  $\xi$  and  $\eta$  are defined by:

$$\xi = [(\epsilon^{[A]\ell})_1 + z_3(\epsilon^{[A]\ell})_3][K] \quad (\text{F.35})$$

$$\eta = [(\epsilon^{[A]\ell})_2 + z_3(\epsilon^{[A]\ell})_4][K] \quad (\text{F.36})$$

As before, the  $(\ )_x$  notation refers to the  $x$ th row of the matrix argument. By defining the variable  $\Gamma$  as the matrix on the left side of Equation F.34 which premultiplies  $[K]$ , and defining the variable  $f$  as the forcing function column vector (the right side of Equation F.34), the solution for  $[K]$  is obtained through matrix inversion:

$$[K] = \Gamma^{-1}f. \quad (\text{F.37})$$

### *Three-Conductor Configuration with Generalized Termination Conditions.*

The treatment of a three-conductor structure with generalized end conditions (or an  $n$ -conductor structure) is a straightforward extension of the two-conductor case. The applicable schematic for this case is shown in Figure F.2.

For the general case, the boundary conditions become:

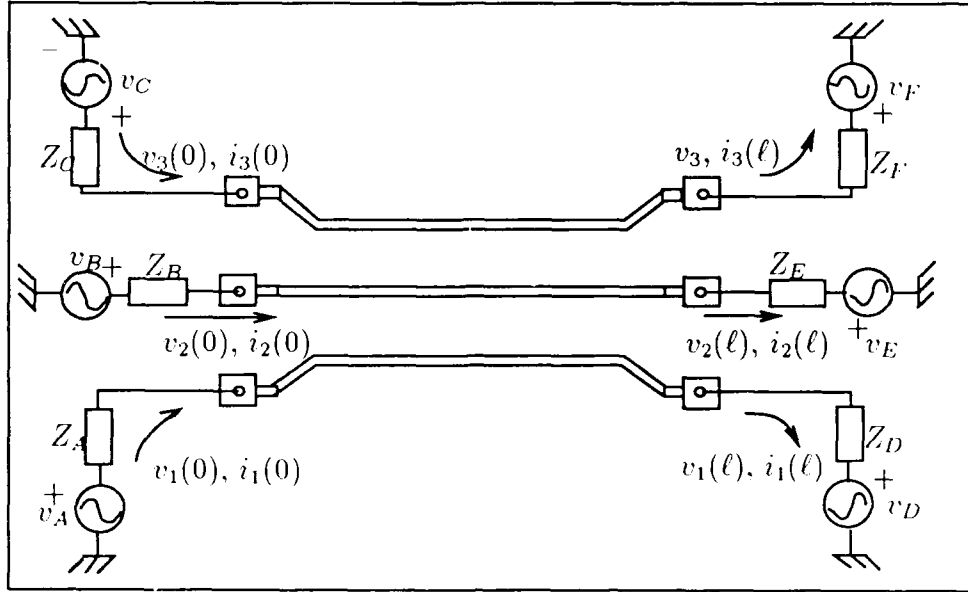


Figure F.2. Schematic of the general two-conductor configuration.

$$-V_A + z_A i_1(0) + v_1(0) = 0, \quad \text{for port A} \quad (\text{F.38})$$

$$-V_B + z_B i_2(0) + v_2(0) = 0, \quad \text{for port B} \quad (\text{F.39})$$

$$-V_C + z_C i_3(0) + v_3(0) = 0, \quad \text{for port C} \quad (\text{F.40})$$

$$V_D + z_D i_1(\ell) + v_1(\ell) = 0, \quad \text{for port D} \quad (\text{F.41})$$

$$V_E + z_E i_2(\ell) + v_2(\ell) = 0, \quad \text{for port E} \quad (\text{F.42})$$

$$\text{and } V_F + z_F i_3(\ell) + v_3(\ell) = 0, \quad \text{for port F} \quad (\text{F.43})$$

where  $V_A$ ,  $V_B$ ,  $V_C$ ,  $V_D$ ,  $V_E$ , and  $V_F$  are the voltage sources (forcing functions), and  $z_A$ ,  $z_B$ ,  $z_C$ ,  $z_D$ ,  $z_E$ , and  $z_F$  are the load impedances at ports A, B, C, D, E, and F, respectively.

The matrix formulations for these cases are obtained using a technique analogous to the two-conductor case:

$$\begin{bmatrix} 1 & 0 & 0 & Z_A & 0 & 0 \\ 0 & 1 & 0 & 0 & Z_B & 0 \\ 0 & 0 & 1 & 0 & 0 & Z_C \\ \xi_1 & \xi_2 & \xi_3 & \xi_4 & \xi_5 & \xi_6 \\ \eta_1 & \eta_2 & \eta_3 & \eta_4 & \eta_5 & \eta_6 \\ \psi_1 & \psi_2 & \psi_3 & \psi_4 & \psi_5 & \psi_6 \end{bmatrix} [K] = \begin{bmatrix} V_A \\ V_B \\ V_B \\ -V_D \\ -V_E \\ -V_F \end{bmatrix} \quad (\text{F.44})$$

where  $\xi$ ,  $\eta$ , and  $\psi$  are defined by:

$$\xi = [(\epsilon^{[A]\ell})_1 + z_D(\epsilon^{[A]\ell})_4][K] \quad (\text{F.45})$$

$$\eta = [(\epsilon^{[A]\ell})_2 + z_E(\epsilon^{[A]\ell})_5][K] \quad (\text{F.46})$$

$$\text{and } \psi = [(\epsilon^{[A]\ell})_3 + z_F(\epsilon^{[A]\ell})_6][K]. \quad (\text{F.47})$$

As before, the  $(\cdot)_x$  notation refers to the  $x$ th row of the matrix argument. By defining the variable  $\Gamma$  as the matrix on the left side of Equation F.44 which premultiplies  $[K]$ , and defining the variable  $f$  as the forcing function column vector (the right side of Equation F.44), the solution for  $[K]$  is obtained through matrix inversion:

$$[K] = \Gamma^{-1}f. \quad (\text{F.48})$$



## Appendix G. *Characteristic Impedance Results.*

This appendix presents the characteristic impedance measurement results for the structures discussed in Chapter 4. These structures were measured using the technique described in Chapter 3 based on Equation 2.35. Also presented in this appendix is a derivation of Equation 4.2, based on the criteria suggested by Chipman for performing these measurements most accurately near odd-integer multiples of  $\lambda/8$  (where  $\lambda$  is the wavelength of the transmission line structure.) Finally, the linearized models that were used to provide the Table 4.11 approximations to the static characteristic impedance are presented.

### *Characteristic Impedance Measurement Results.*

The data presented in Figures G.1–G.11 is summarized in Table G.1. For structures which were simulated using the multi-conductor telegrapher's equation solutions, the resulting impedance curve is plotted with the measurement curve of the associated structure.

Table G.1. List of characteristic impedance plots by structure and wafer type.

Structure	Wafer	Figure	Simulation
33	PIQ	G.1	no
36	BCB	G.2	Magnitude
36	PIQ	4.10	yes
62	PIQ	G.3	no
65	PIQ	G.4-G.5	no
91	BCB	G.6	no
91	PIQ	G.7	no
100	BCB	G.8	no
100	PIQ	G.9	no
104	PIQ	G.10	Magnitude
109	BCB	G.11	Magnitude

### *Estimation of "Good" Measurement Frequencies*

For the measurement of characteristic impedance using Equation 2.35, Chipman suggested frequencies near odd-integer multiples of  $\lambda/8$ , where  $\lambda$  is the wavelength for the transmission line under consideration, as discussed in Chapter 4. With this guideline, frequencies where the electrical length  $\theta$  is close to  $n(\lambda)/8$  are sought ( $n = 1, 3, 5, \dots$ ); that is:

$$\theta = \beta\ell = \frac{n\lambda}{8} \quad (\text{G.1})$$

From  $\beta = \omega/v_p$  and  $\lambda = (2\pi/\beta)$  [(4),(55)], it can be shown that:

$$\frac{\omega}{v_p} = \frac{n}{8} \frac{2\pi}{\beta} = \frac{n\pi}{4} \frac{v_p}{\omega}. \quad (\text{G.2})$$

Solving for  $\omega$ , Equation G.2 becomes:

$$\omega^2 = \frac{v_p^2}{\ell} \frac{n\pi}{4}. \quad (\text{G.3})$$

For the phase velocity, Equation 2.35 implies that:

$$\omega^2 = \frac{c^2}{\epsilon_{R,eff}} \frac{n\pi}{4\ell}. \quad (\text{G.4})$$

Thus,

$$\omega = \frac{c}{2} \sqrt{\frac{n\pi}{\epsilon_{R,eff}\ell}} \quad (\text{G.5})$$

or

$$f = \frac{c}{4} \sqrt{\frac{n}{\pi\epsilon_{R,eff}\ell}}. \quad (\text{G.6})$$

### *Linearized Impedance Approximations.*

A linearized estimation technique discussed in Chapter 4 was applied to the characteristic impedance measurement data. Since the magnitude of characteristic impedance appeared to asymptotically approach the value of a lossless structure, the linearized models provide a method of estimating this asymptote. To facilitate

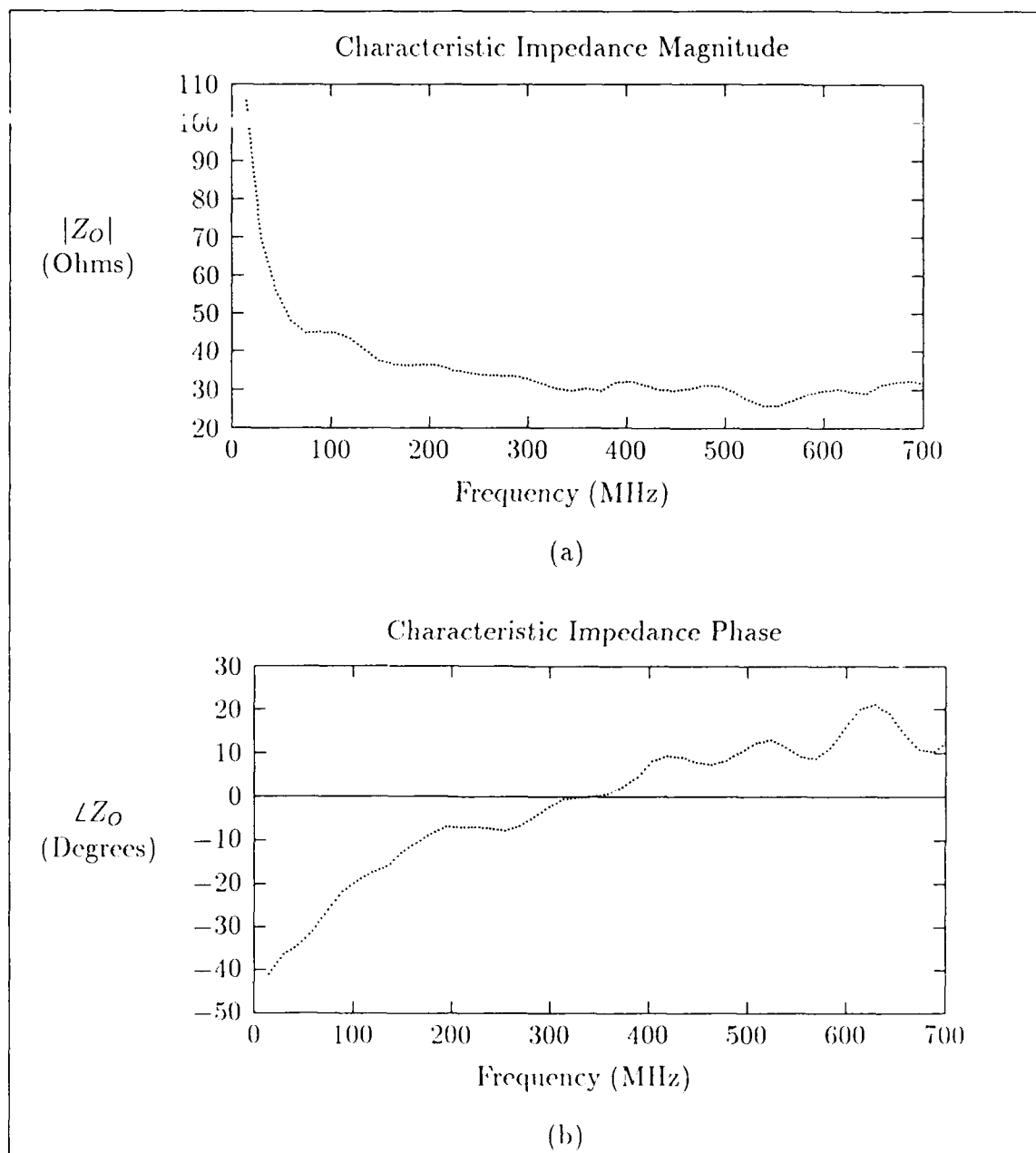


Figure G.1. Measured characteristic impedance of structure 33 (10  $\mu\text{m}$  wide coplanar waveguide) from the PIQ wafer. (a) Magnitude. (b) Phase.

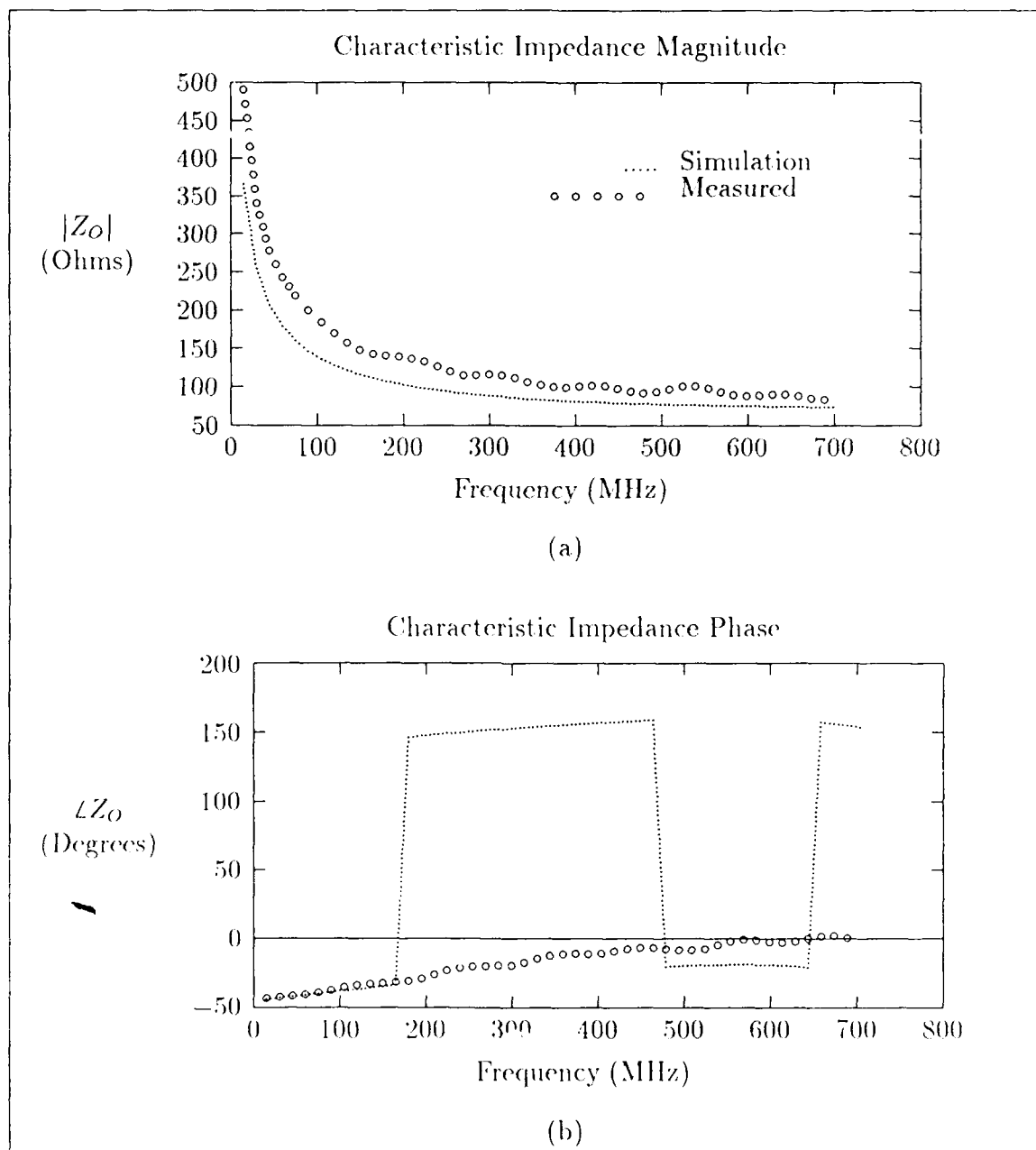


Figure G.2. Measured characteristic impedance of structure 36 (two-conductor, edge-coupled stripline) from the BCB wafer. (a) Magnitude. (b) Phase.

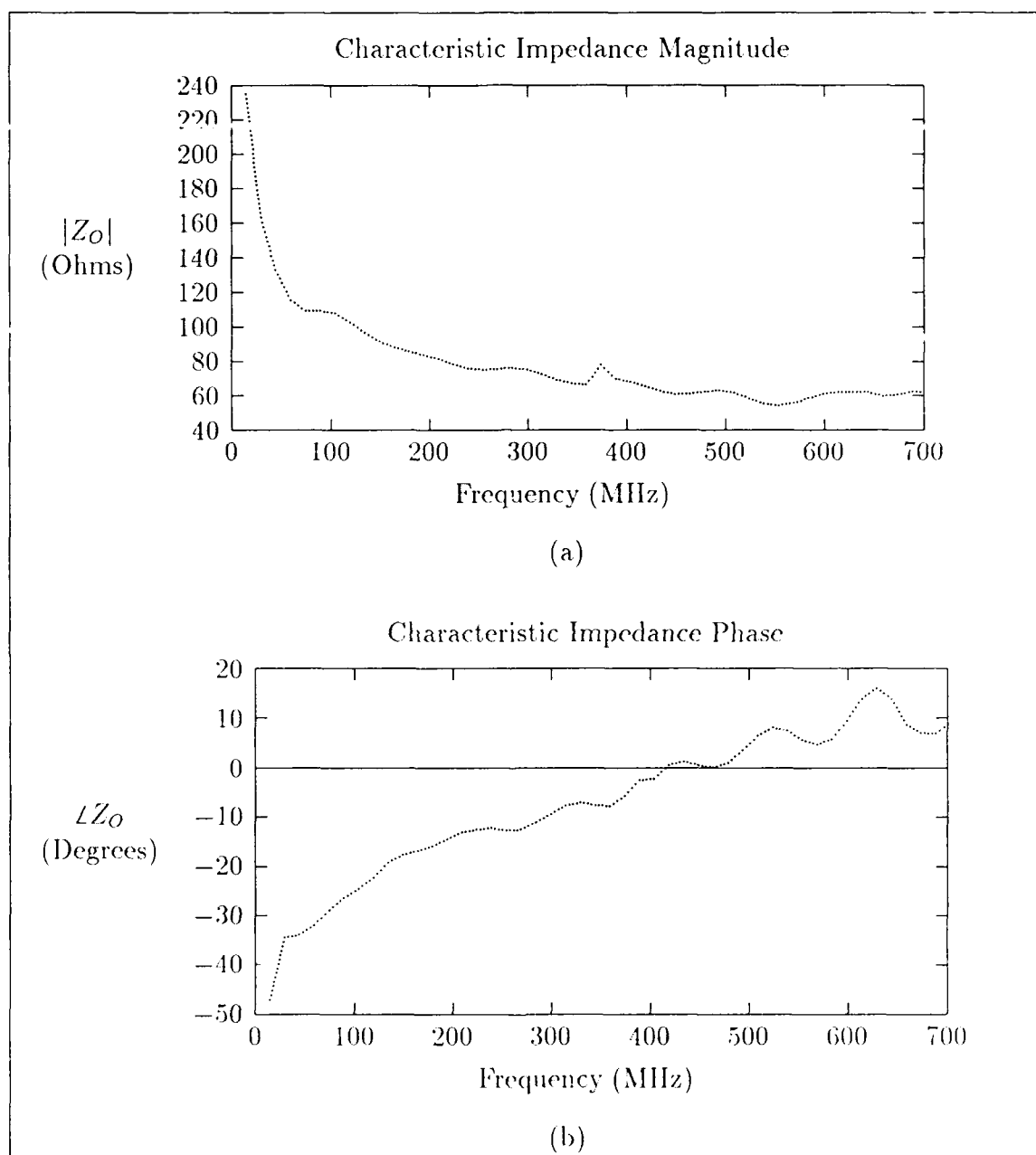


Figure G.3. Measured characteristic impedance of structure 62 (10  $\mu\text{m}$  wide coplanar waveguide) from the PIQ wafer. (a) Magnitude. (b) Phase.

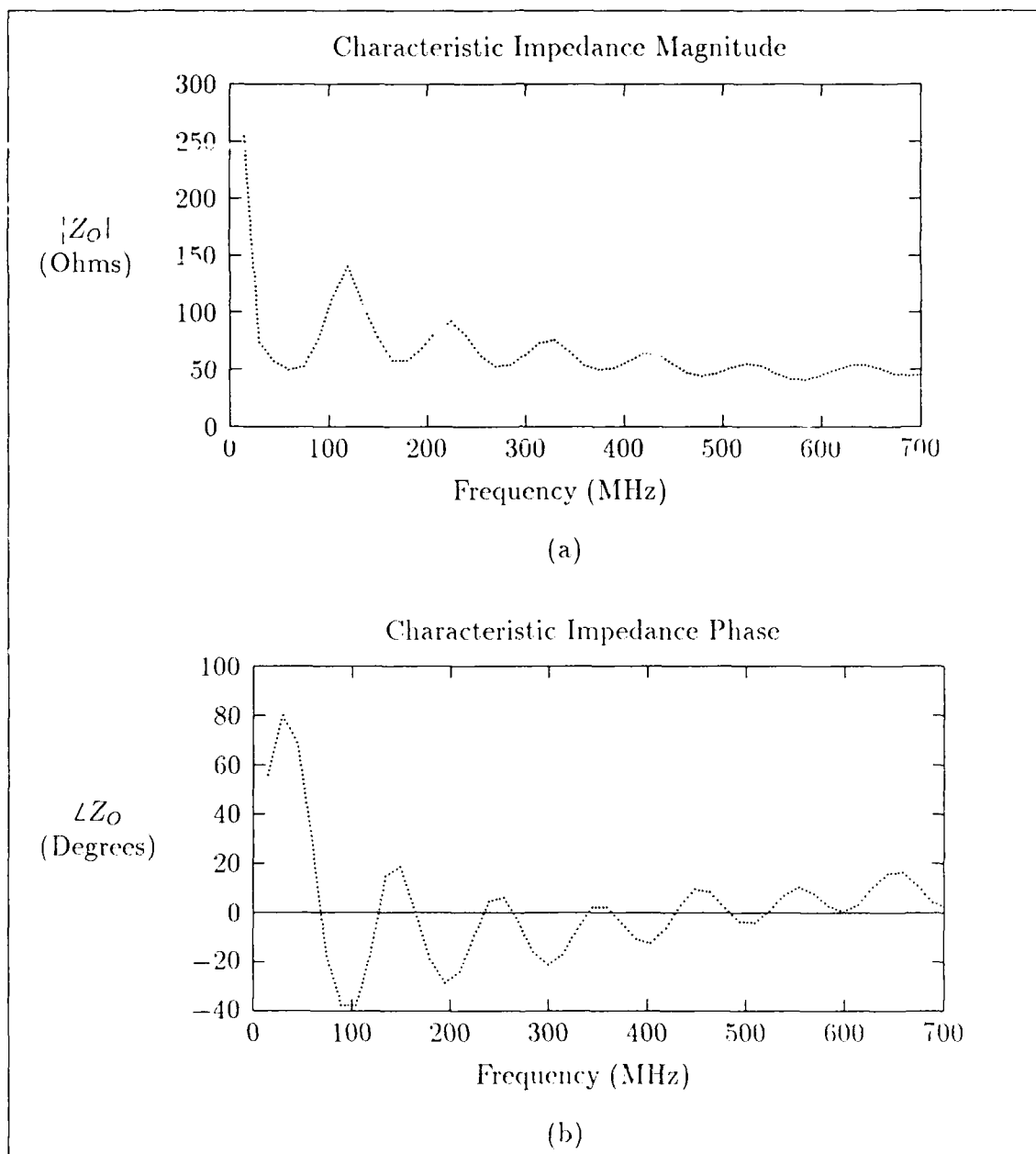


Figure G.4. Measured characteristic impedance of structure 65 (three-conductor, edge-coupled, embedded microstrip) from the PIQ wafer (left conductor). (a) Magnitude. (b) Phase.

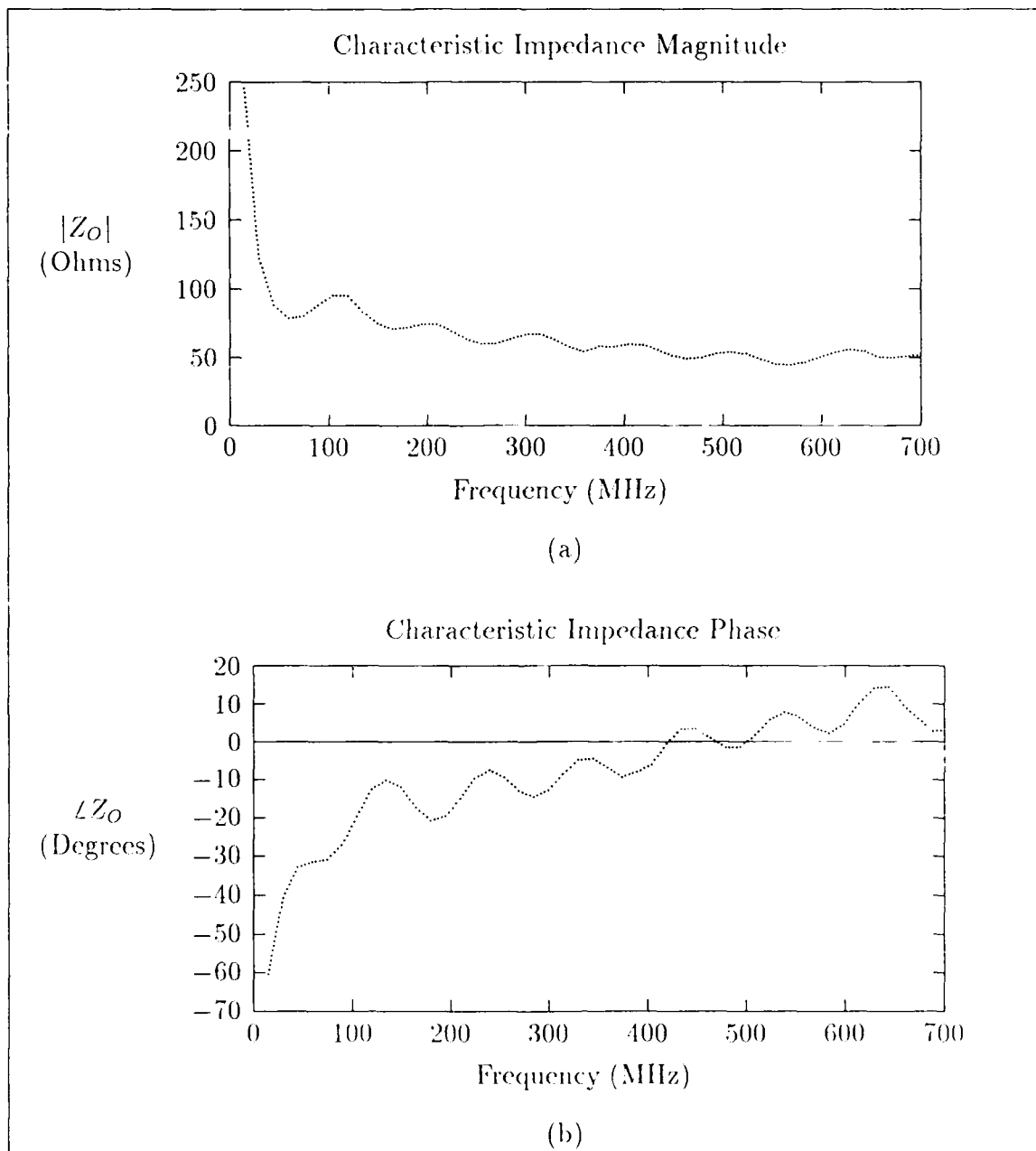


Figure G.5. Measured characteristic impedance of structure 65 from the PiQ wafer (center conductor). (a) Magnitude. (b) Phase.



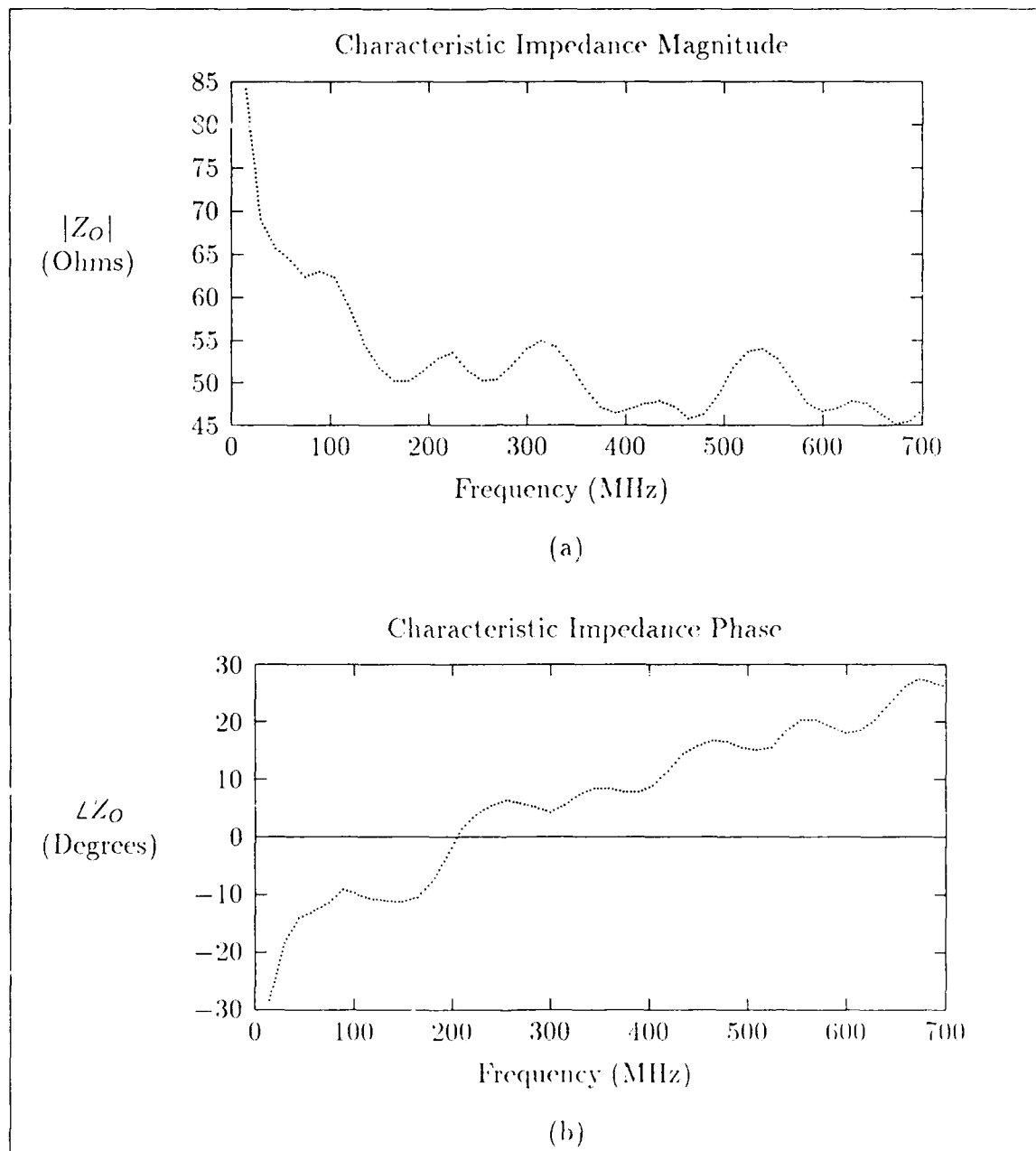


Figure G.6. Measured characteristic impedance of structure 91 (25  $\mu\text{m}$  wide coplanar waveguide) from the BCB wafer. (a) Magnitude. (b) Phase.

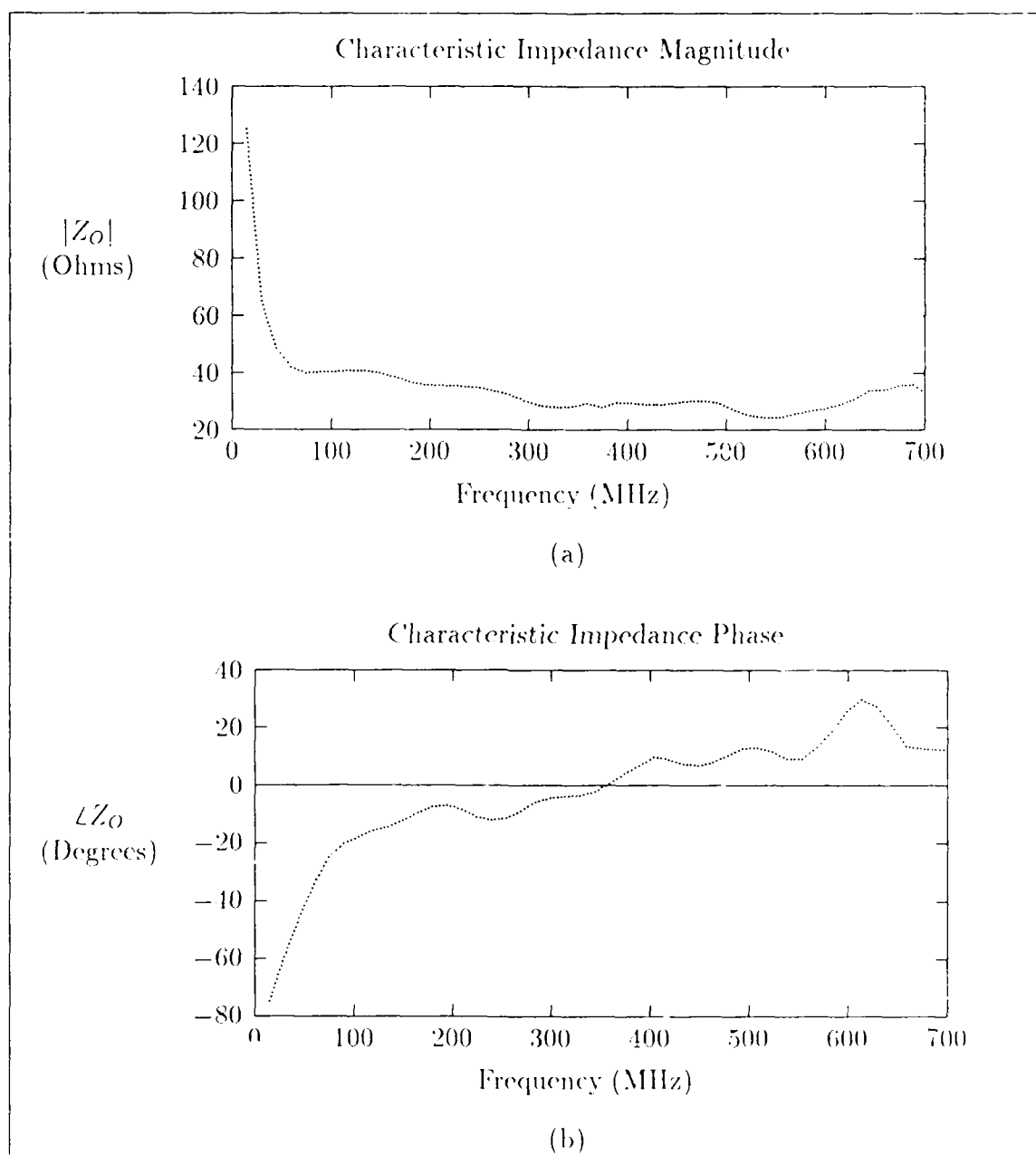


Figure G.7. Measured characteristic impedance of structure 91 (25  $\mu\text{m}$  wide coplanar waveguide) from the PIQ wafer. (a) Magnitude. (b) Phase.

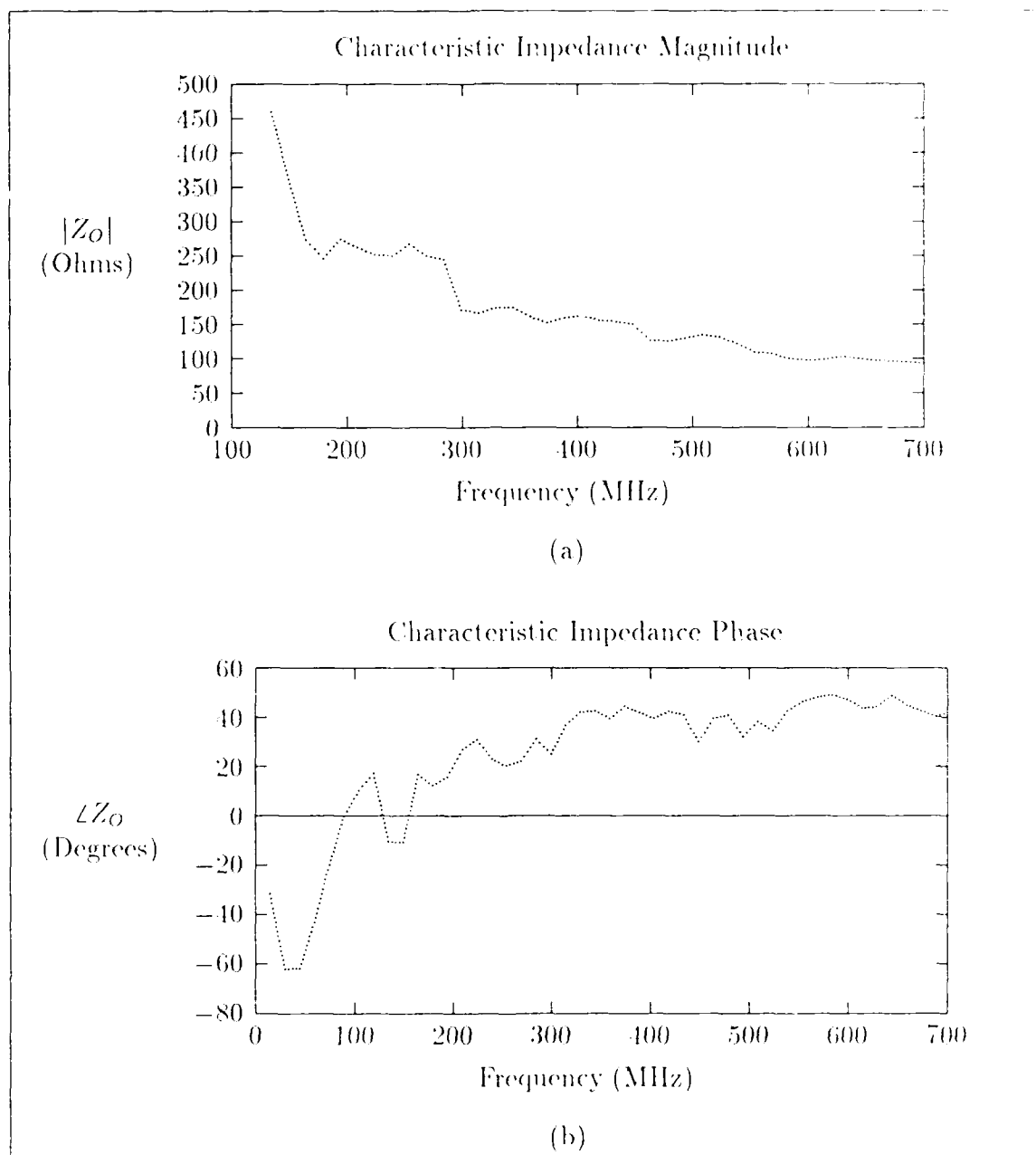


Figure G.8. Measured characteristic impedance of structure 100 (three-conductor, stripline-line, edge-coupled stripline with grounded center conductor) from the BCB wafer. (a) Magnitude. (b) Phase.

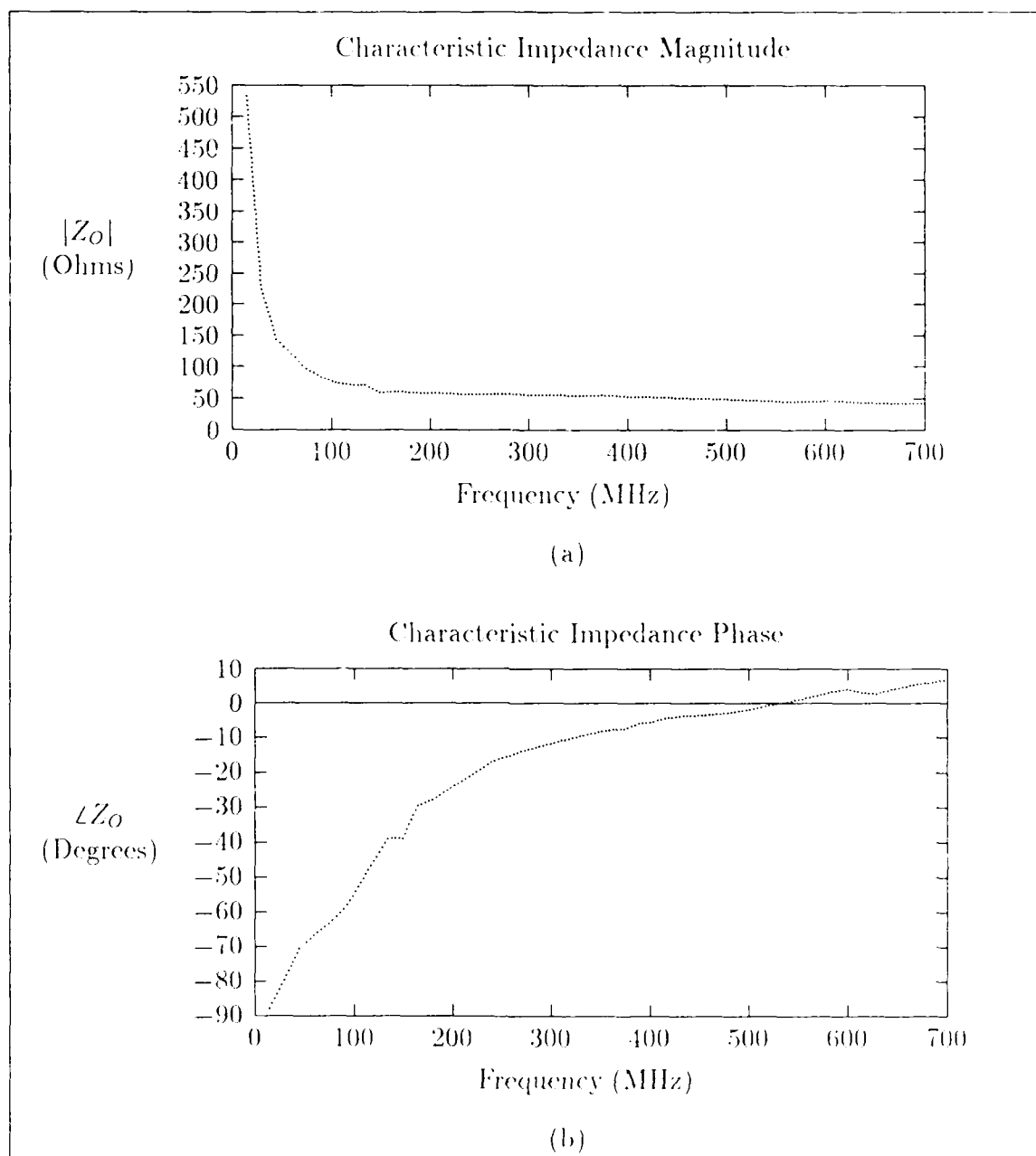


Figure G.9. Measured characteristic impedance of structure 100 (three-conductor, stripline-line, edge-coupled stripline with grounded center conductor) from the PIQ wafer. (a) Magnitude. (b) Phase.

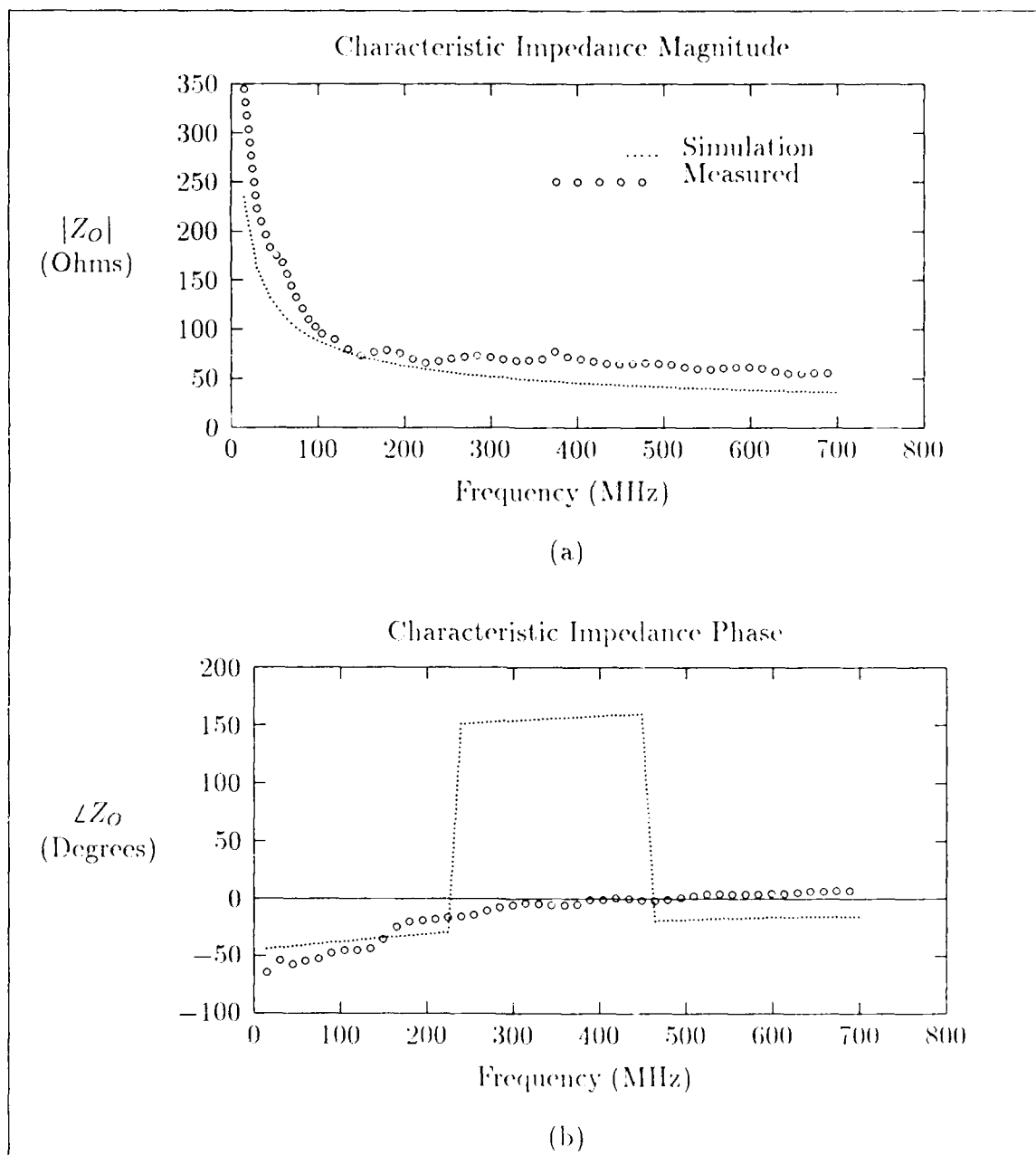


Figure G.10. Measured characteristic impedance of structure 101 (two-conductor, edge-coupled stripline-like structure) from the PIQ wafer. (a) Magnitude. (b) Phase.

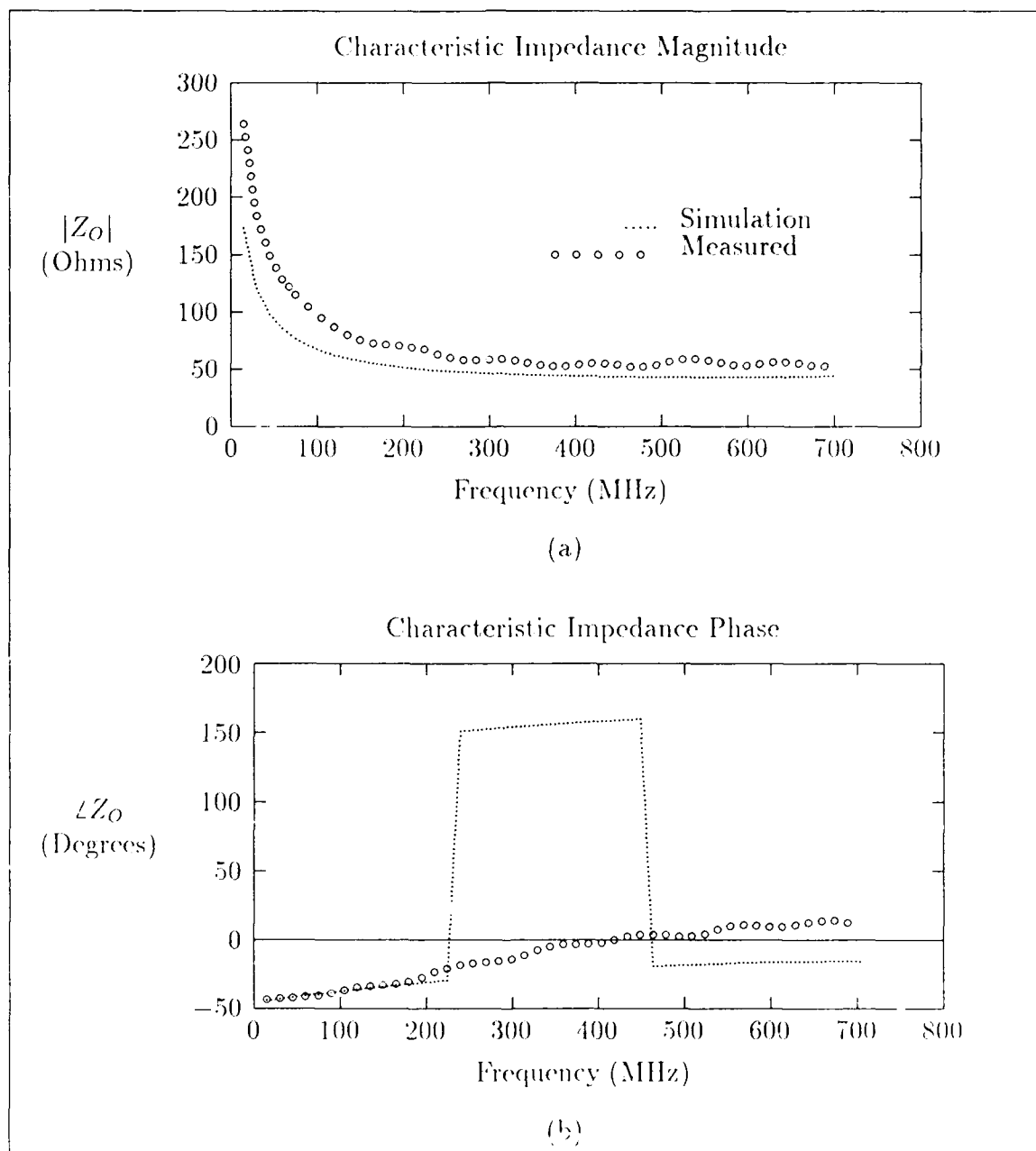


Figure G.11. Measured characteristic impedance of structure 109 (two-conductor, edge-coupled stripline) from the BCB wafer. (a) Magnitude, (b) Phase.

Table G.2. Linearized models of the characteristic impedance which are assumed to approximate the asymptotic values of the measured data when evaluated at  $f_{cross} = 913$  MHz.

Structure	Wafer	Linearized model
33	PIQ	$Z(f) = 27.57 + 0.0038f$
36	BCB	$Z(f) = 123.7 - 0.00235f$
62	PIQ	$Z(f) = 62.77 - 0.00363f$
65(left)	PIQ	$Z(f) = 69.40 - 0.0344f$
65(center)	PIQ	$Z(f) = 56.04 - 0.00849f$
91	BCB	$Z(f) = 52.754 - 0.00790f$
91	PIQ	$Z(f) = 17.41 + 0.0215f$
100	BCB	$Z(f) = 240.0 - 0.220f$
100	PIQ	$Z(f) = 66.54 - 0.0354f$
104	PIQ	$Z(f) = 84.65 - 0.0425f$
109	BCB	$Z(f) = 55.9719 - 0.00235f$

construction of the linear models, Mathematica polynomial fitting routines were used.

The linearized models for the simulated lossy structure and one of the measurements were presented in Chapter 4. For the other structures that were measured, the resulting linearized models are presented in Table G.2. In these expressions, the impedance ( $Z(f)$ ) is given in ohms and the frequency ( $f$ ) is given in MHz.

## Appendix H. *Gain Phase Measurement Results.*

This appendix presents the gain-phase measurement results for structures discussed in Chapter 4. The bulk of the measurements presented are the coupling measurements based on the conventions discussed in Chapter 3. The other measurement curves presented are transmission gain and isolation gain measurements.

The data presented in Figures H.1–H.11 are summarized in Table H.1.



Table H.1. List of coupling measurement plots by structure and wafer type.

Structure	Wafer	Figure	Type
36	BCB	H.1	Coupling
36	PIQ	H.2	Coupling
37	PIQ	H.1	Coupling
48	PIQ	4.18	Coupling
49	PIQ	4.18	Coupling
50	PIQ	H.3–H.4	Coupling
50	PIQ	H.12–4.23	Transmission
50	PIQ	H.13–H.15	Isolation
55	PIQ	H.7	Coupling
63	PIQ	4.24	Transmission
93	PIQ	4.25	Transmission
100	BCB	H.8	Coupling
100	PIQ	H.9	Coupling
104	PIQ	H.10	Coupling
109	BCB	H.11	Coupling

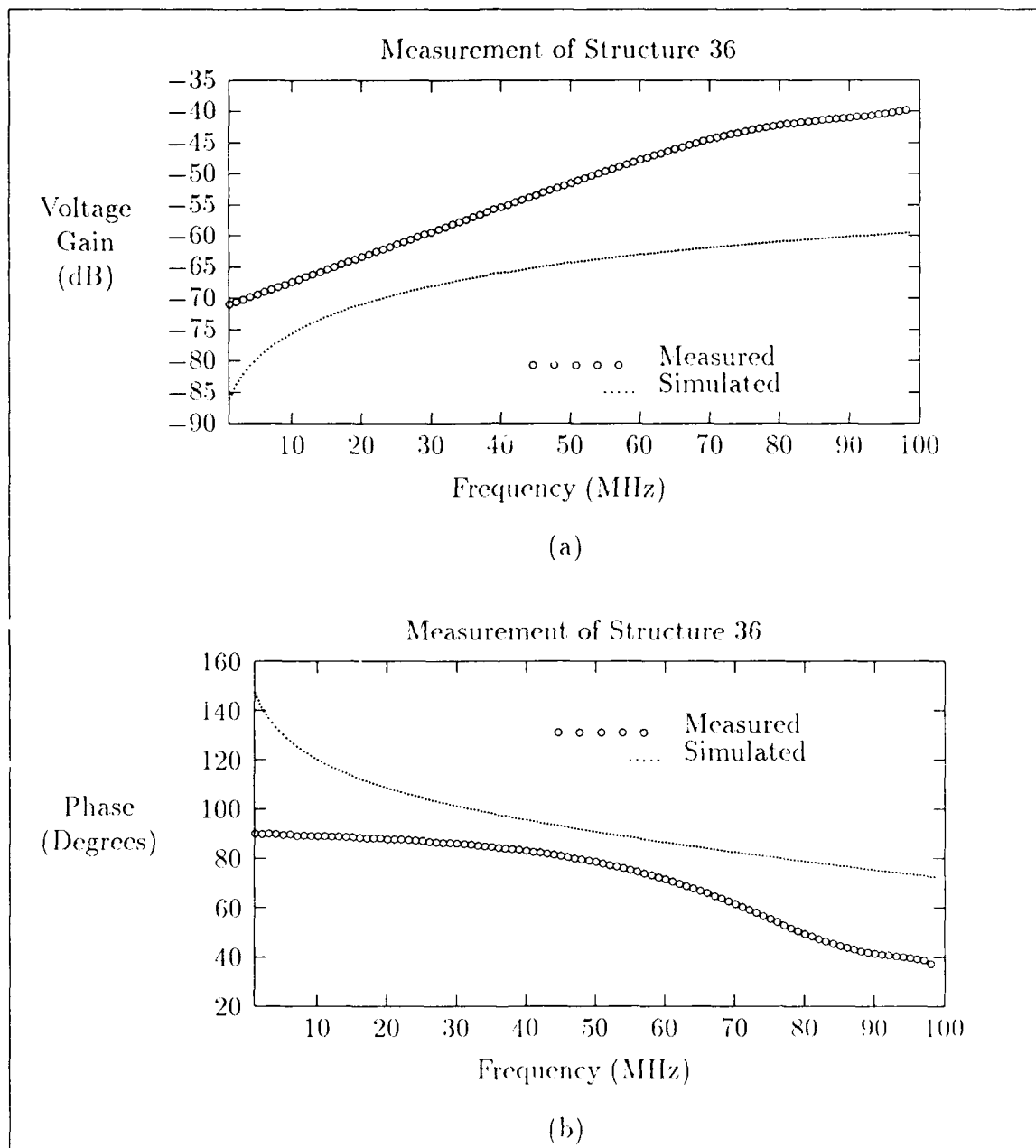


Figure H.1. Measured coupling gain of structure 36 (two-conductor ECS) from the BCB wafer. (a) Magnitude. (b) Phase.

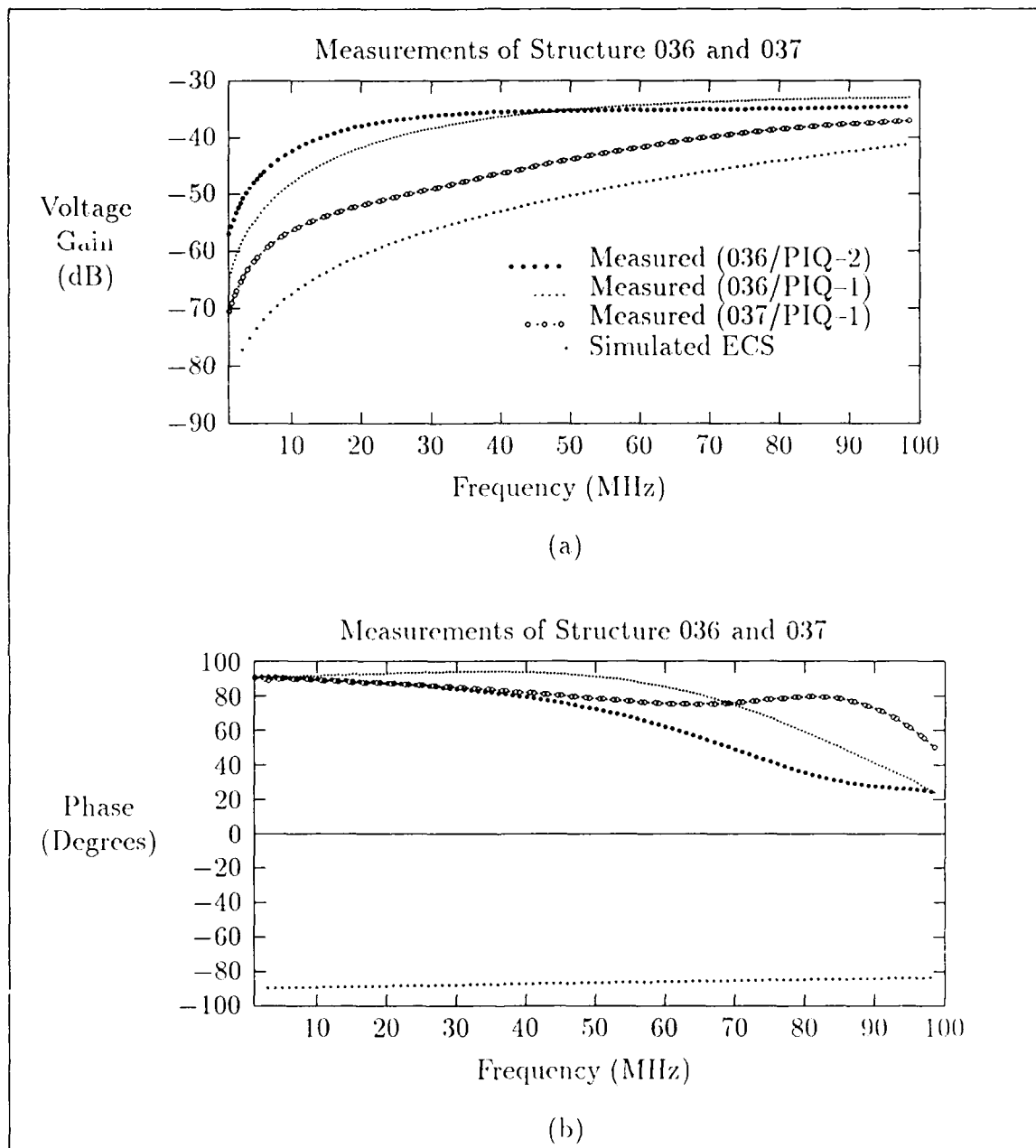


Figure II.2. Measured coupling gain of structure 36 (two-conductor ECS) and 37 (two-conductor embedded ECM) from the PIQ wafers. (a) Magnitude. (b) Phase (using same legend as above).

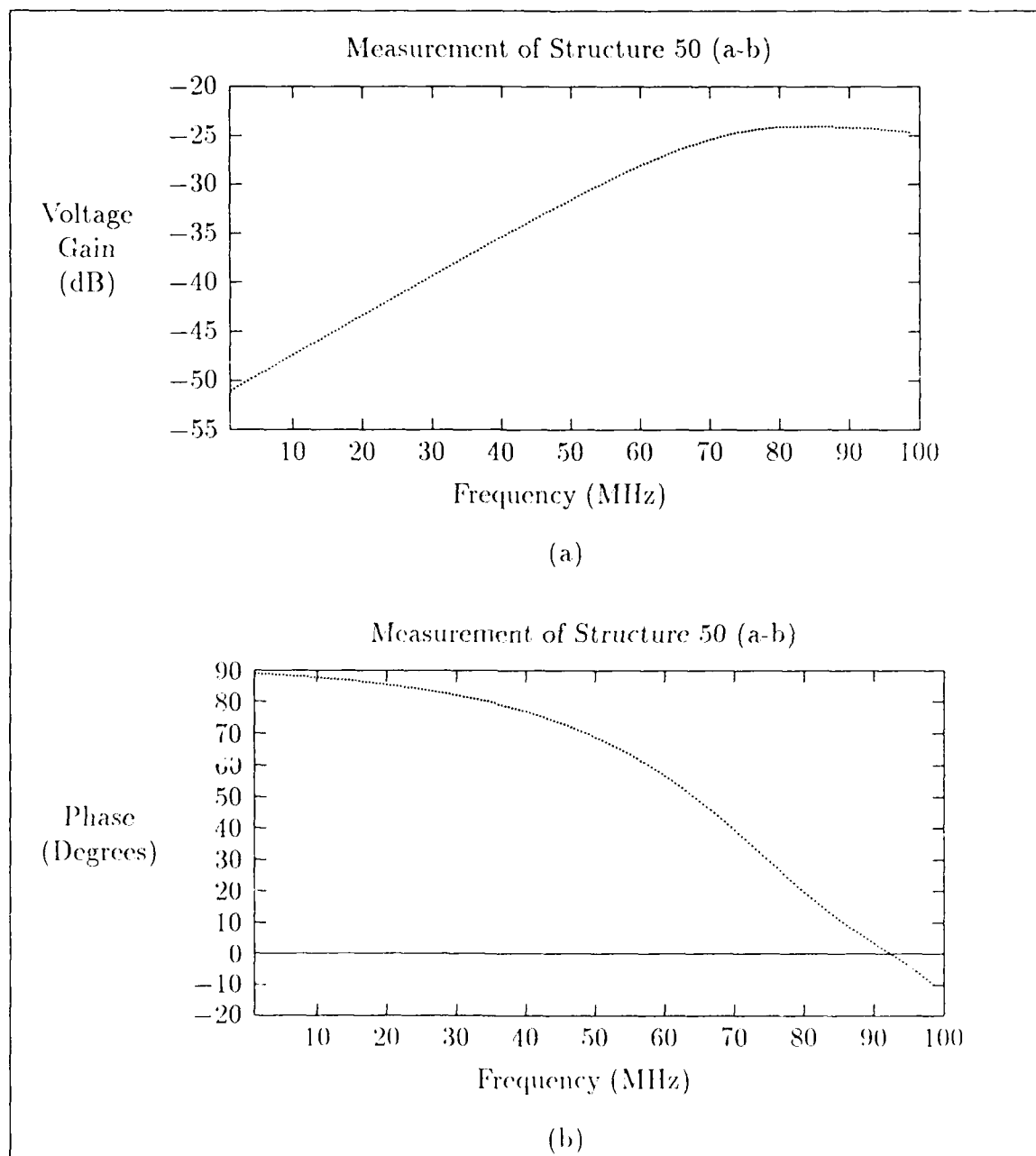


Figure H.3. Measured coupling gain of structure 50 (three-conductor ECS) from the PIQ wafer (measurement taken from a-b terminals).

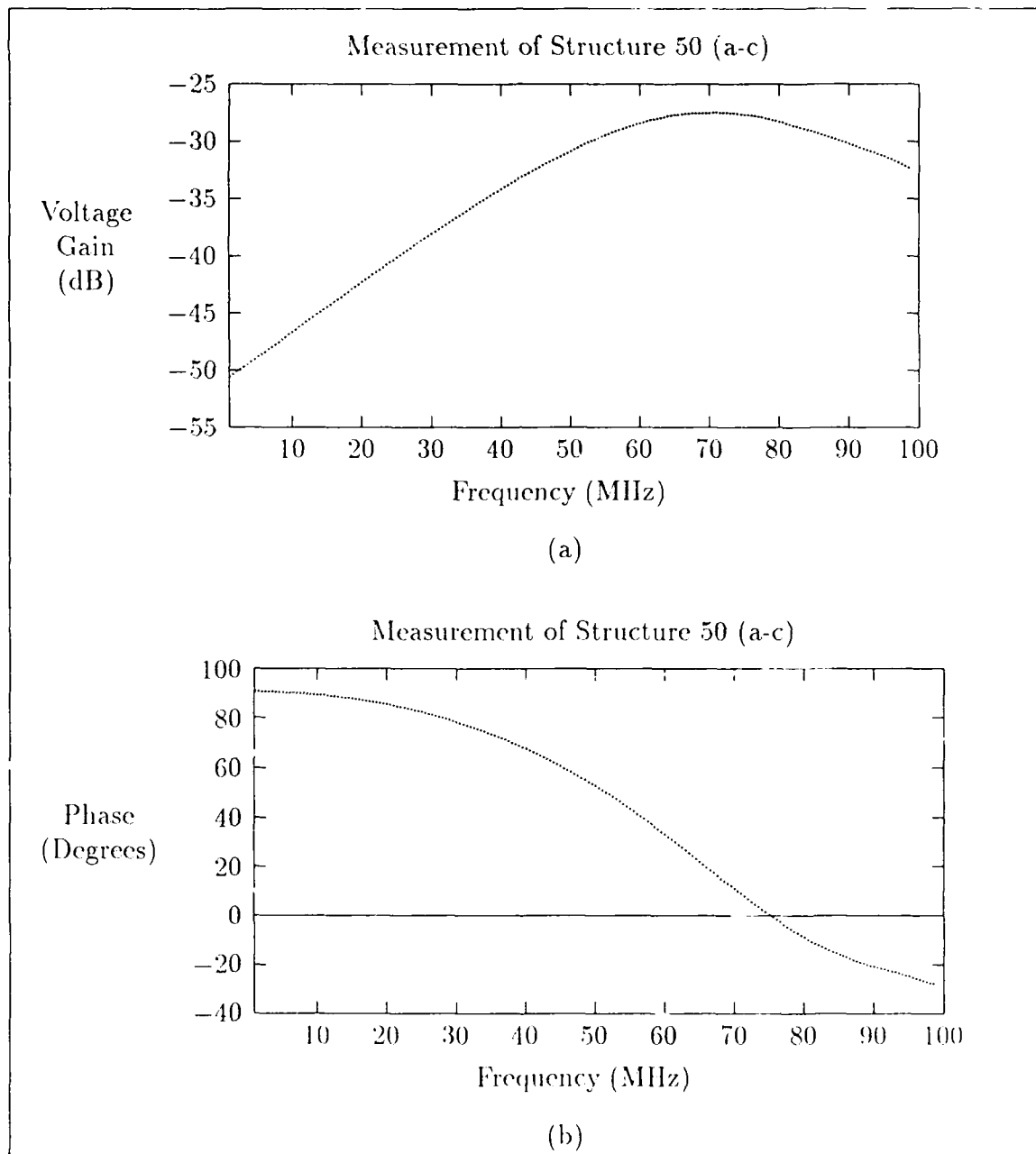


Figure II.4. Measured coupling gain of structure 50 (three-conductor ECS) from the PIQ wafer (measurement taken from a-c terminals).

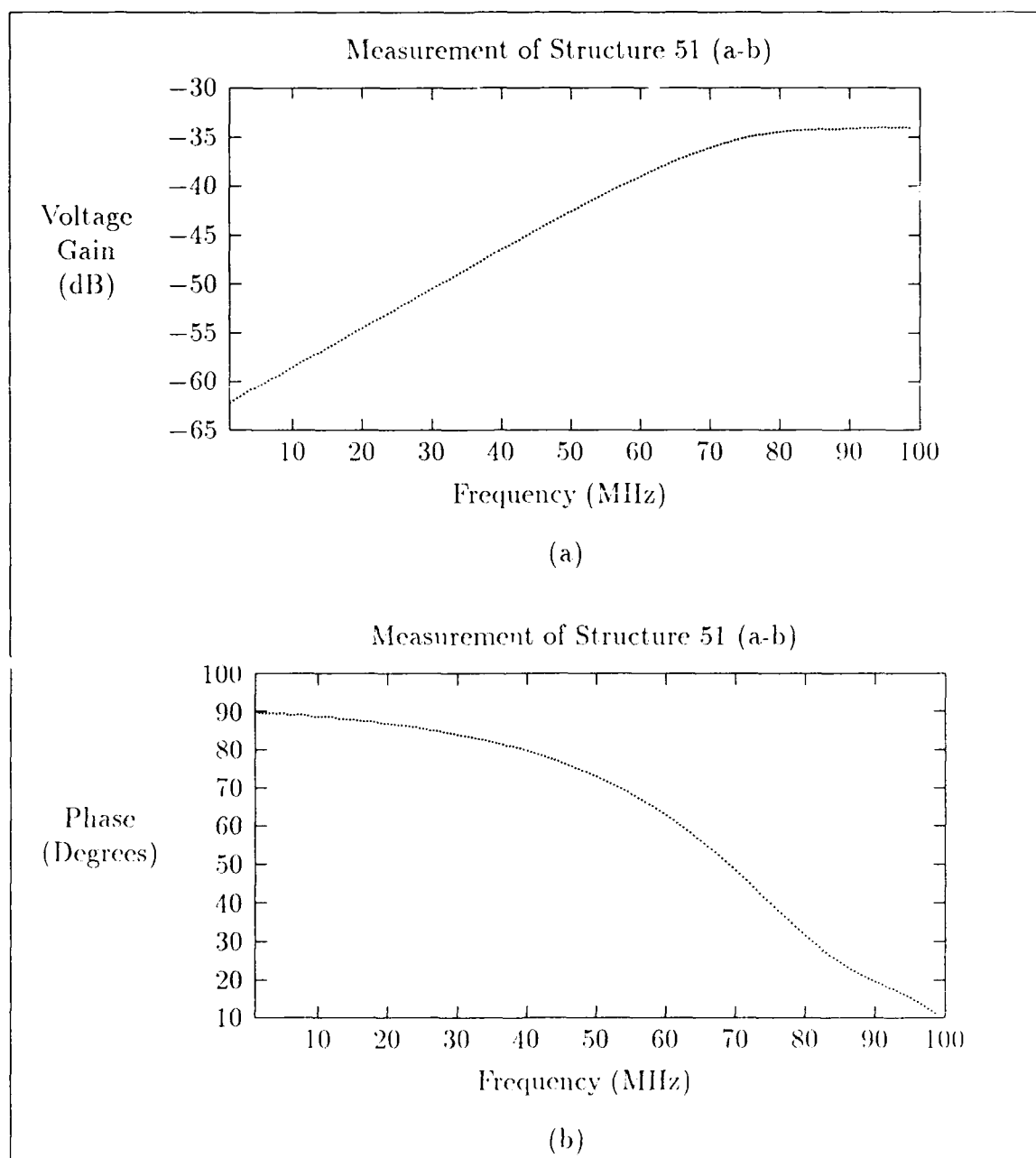


Figure II.5. Measured coupling gain of structure 51 (three-conductor embedded ECM) from the PIQ wafer (measurement taken from a-b terminals).

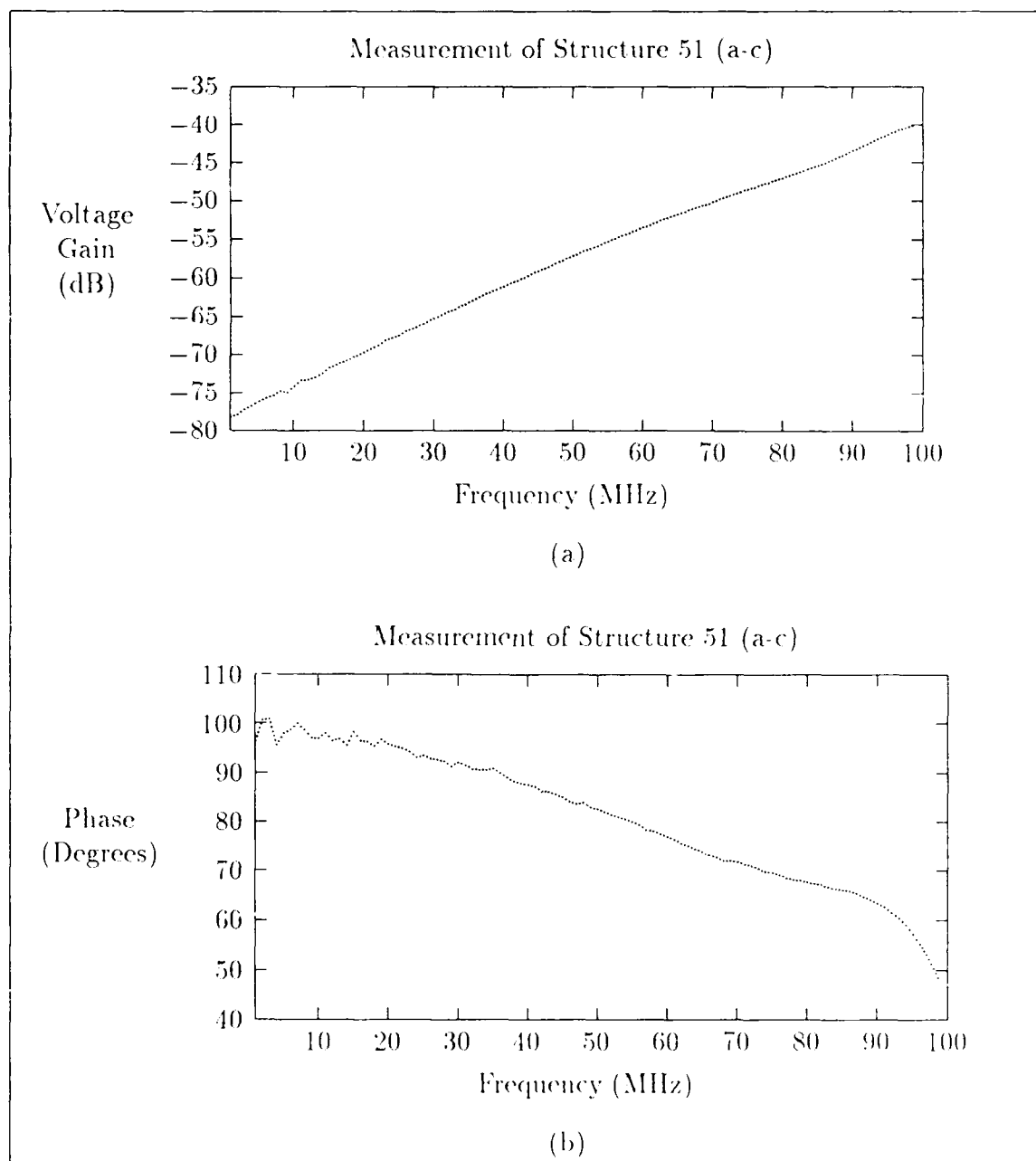


Figure II.6. Measured coupling gain of structure 51 (three-conductor embedded ECM) from the PIQ wafer (measurement taken from a-c terminals).

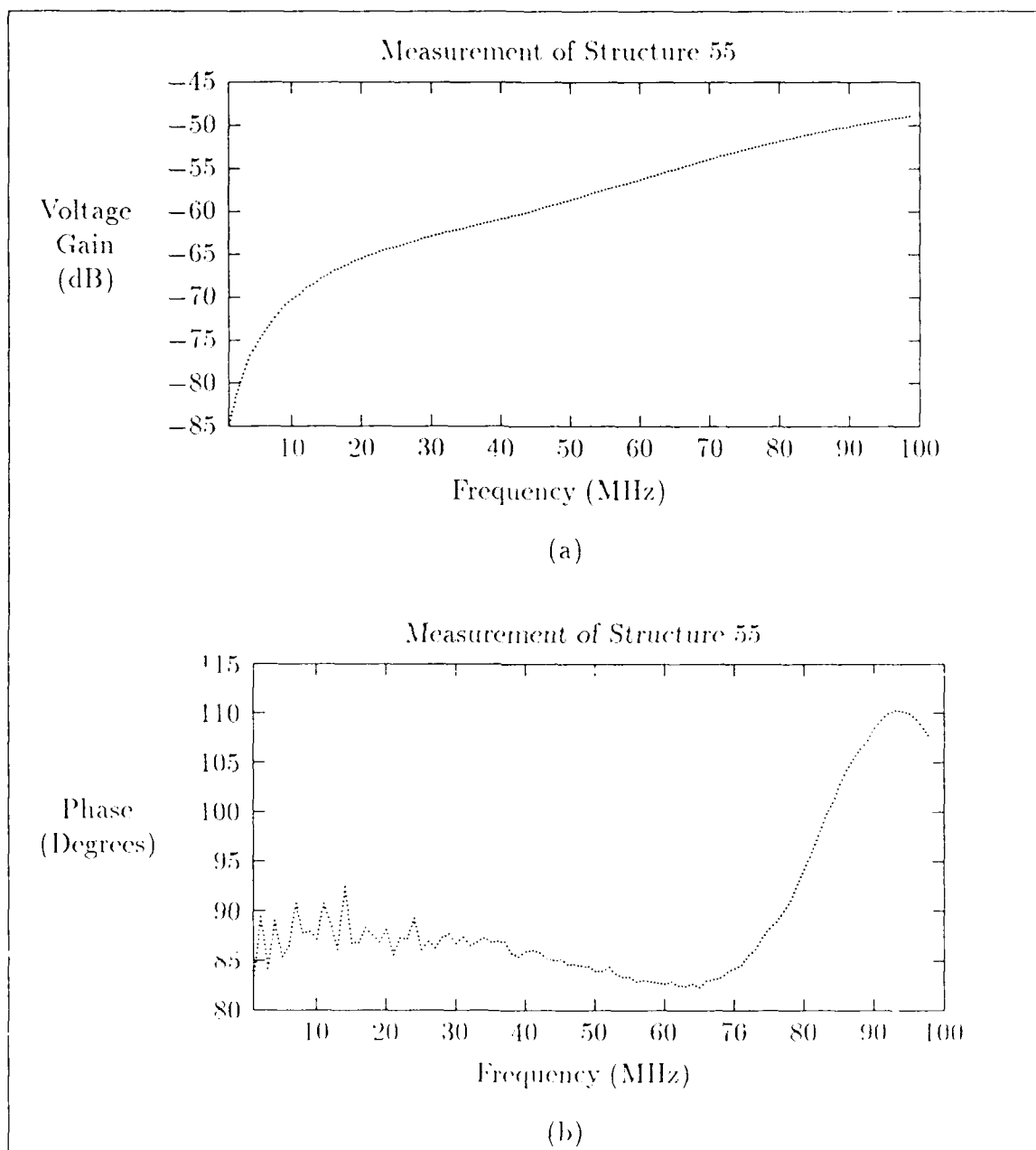


Figure II.7. Measured coupling gain of structure 55 (three-conductor embedded ECM, left conductor) from the PIQ wafer. (a) Magnitude. (b) Phase.



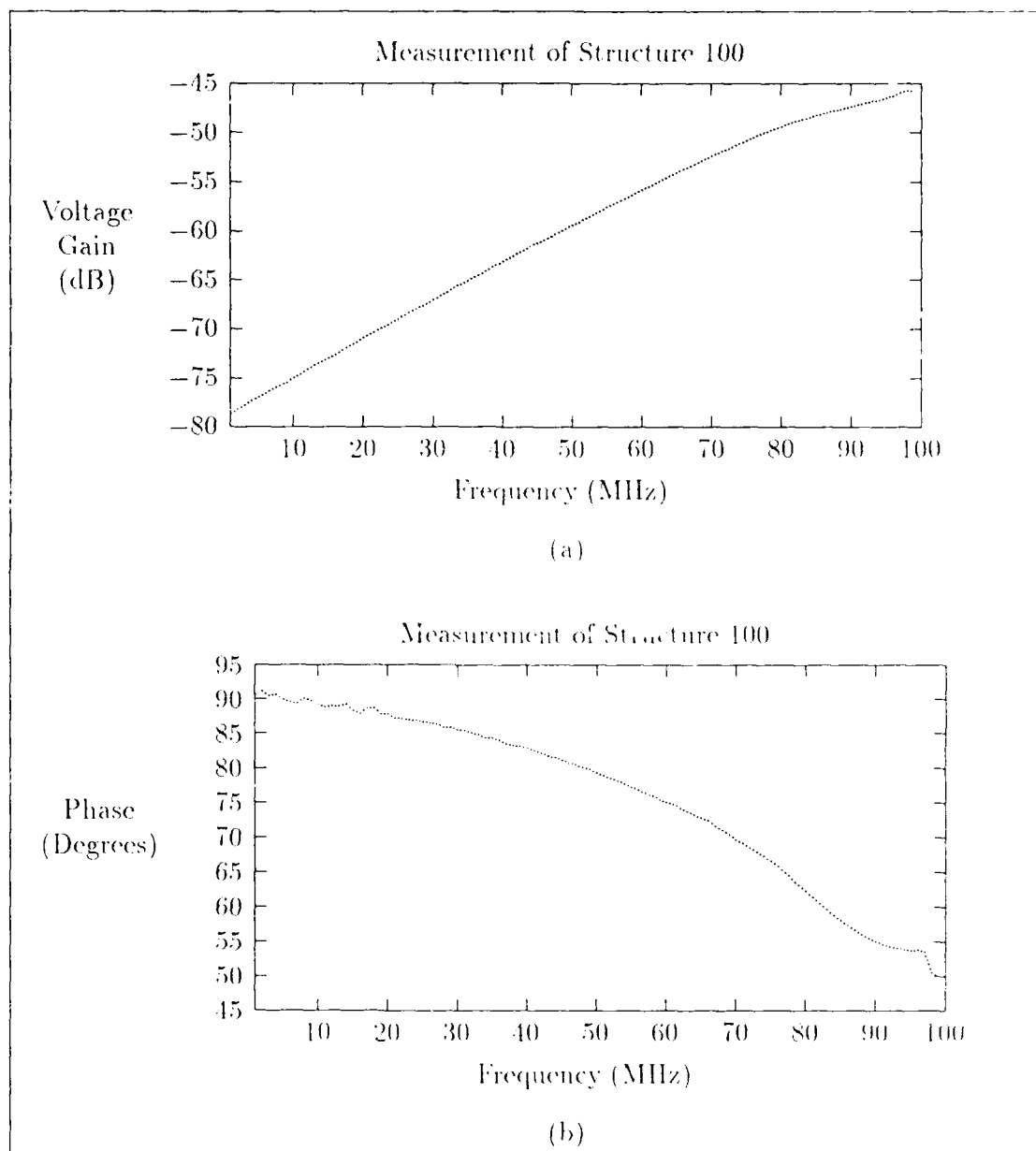


Figure H.8. Measured coupling gain of structure 100 (three-conductor embedded ECM) from the BCB wafer (measured from a-c terminals). (a) Magnitude. (b) Phase.

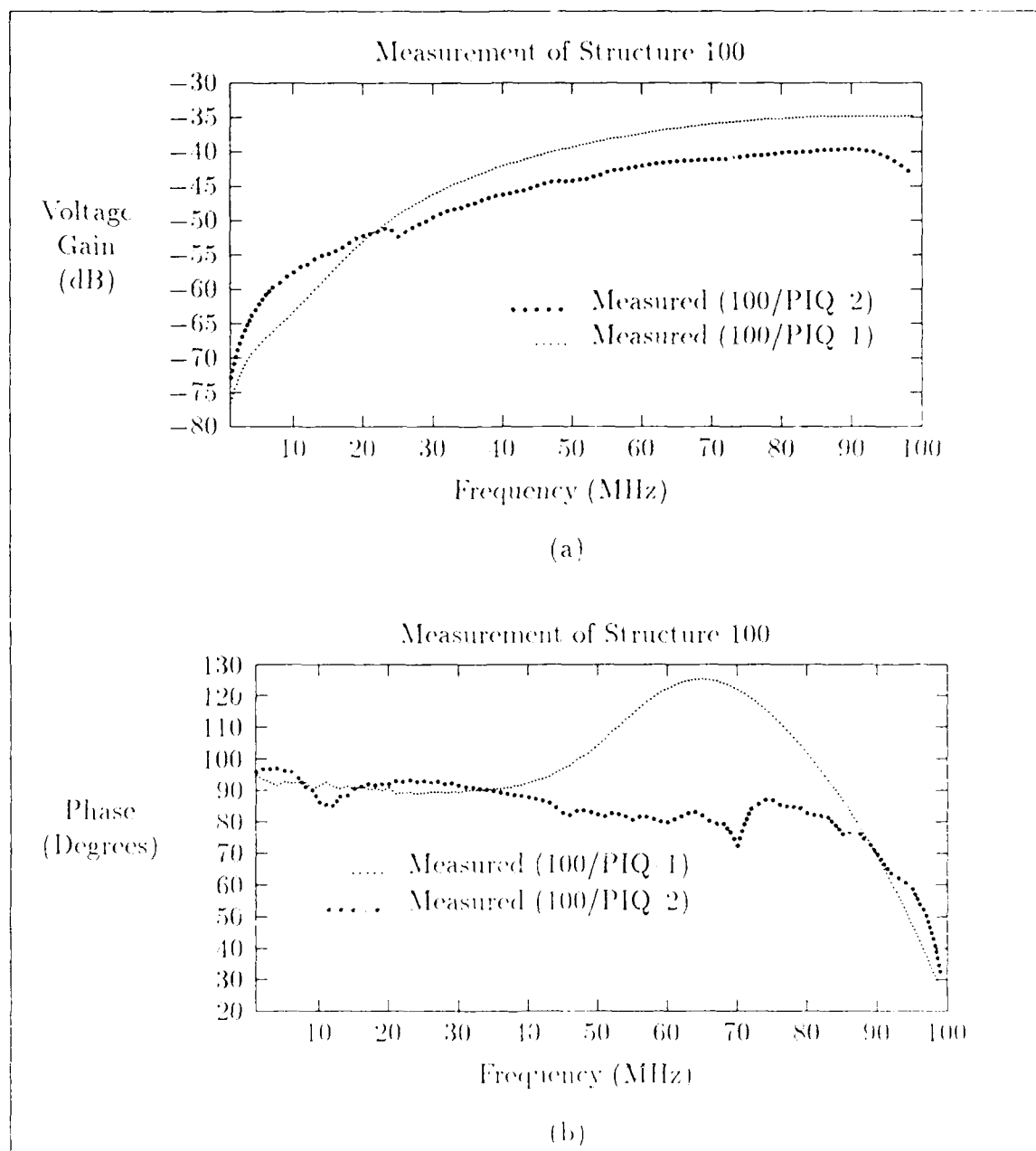


Figure H.9. Measured coupling gain of structure 100 (three-conductor embedded ECM) from the PIQ wafer (measured from a-c terminals). (a) Magnitude. (b) Phase.

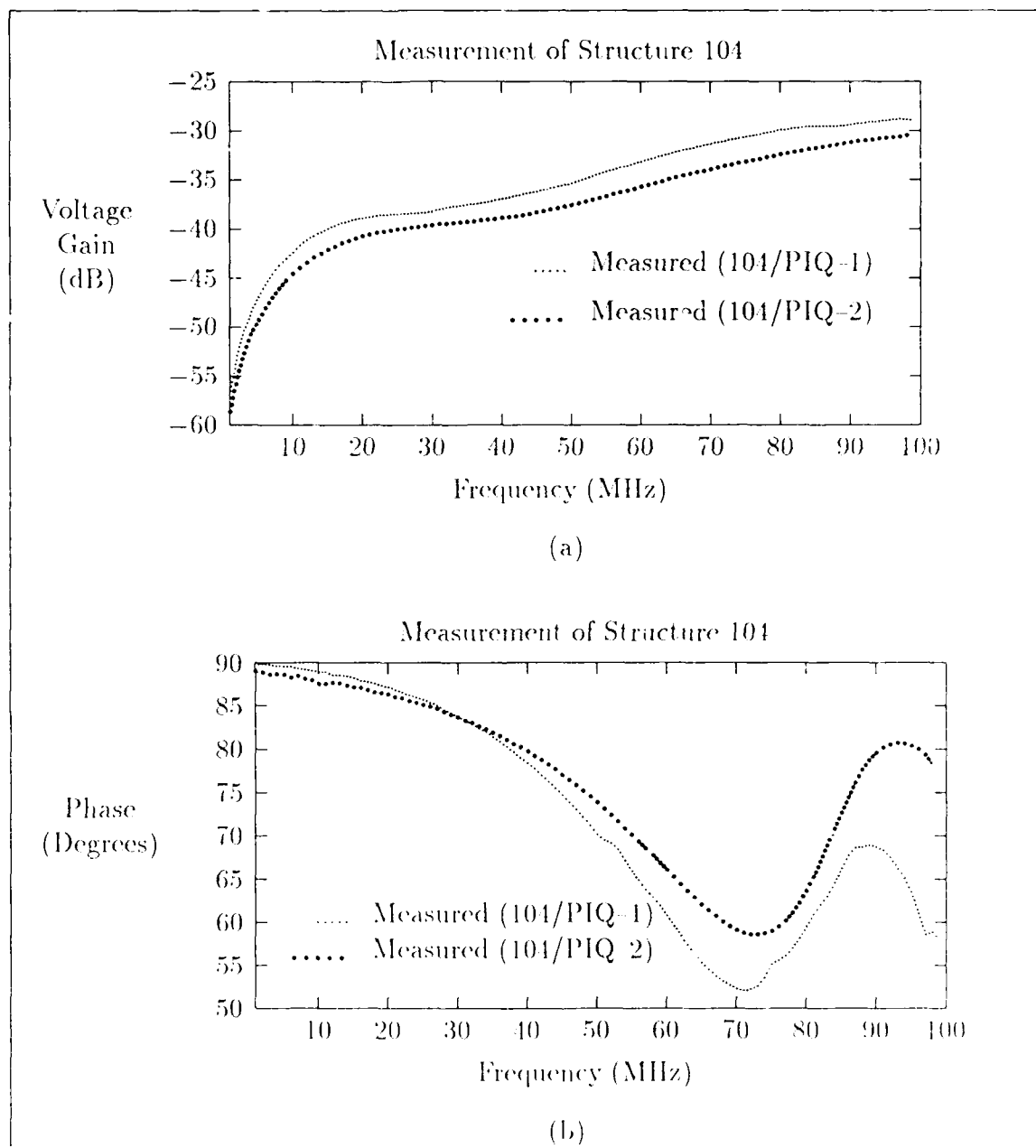


Figure II.10. Measured coupling gain of structure 104 (two-conductor embedded ECM) from the PIQ wafer. (a) Magnitude. (b) Phase.

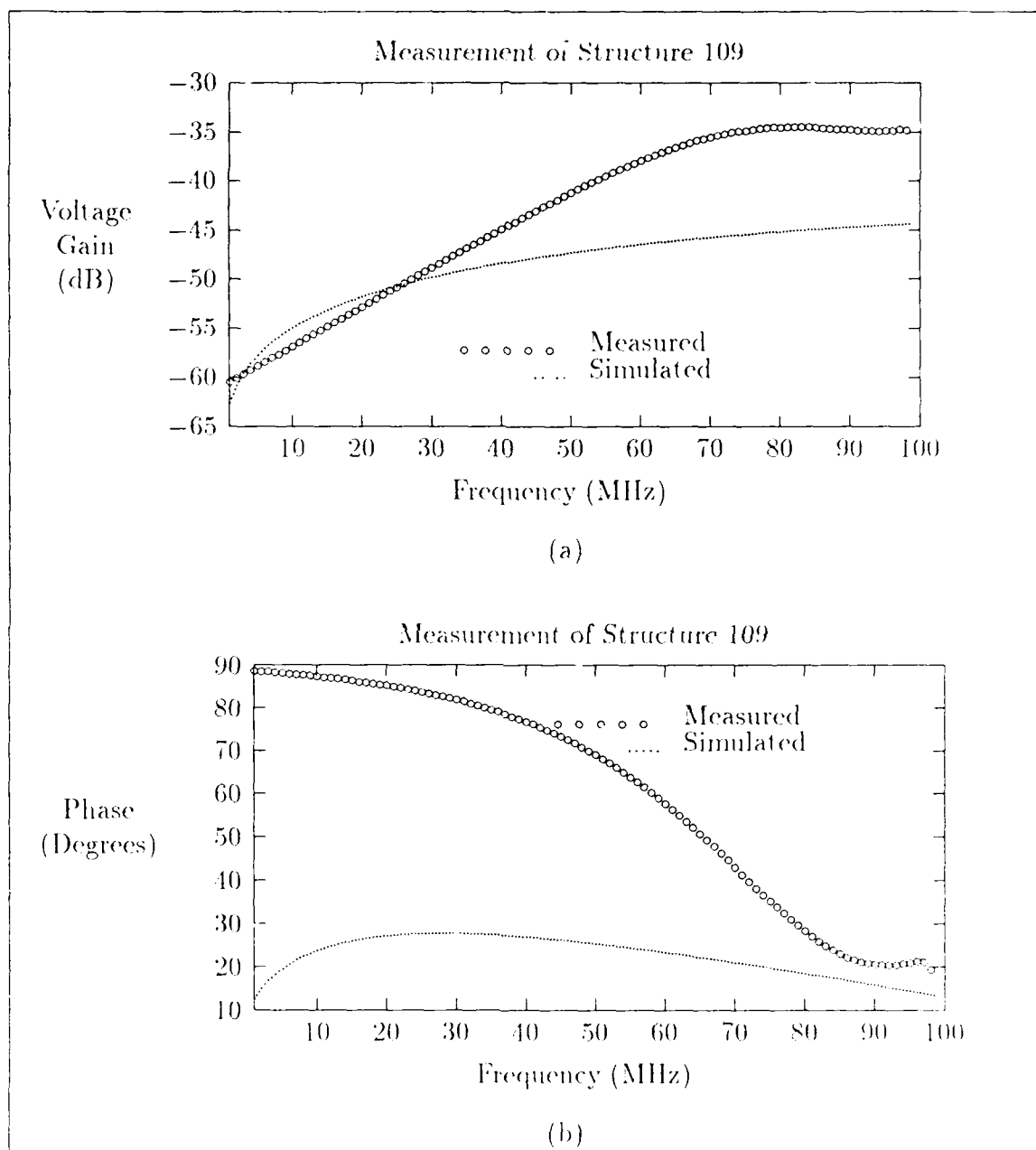


Figure H.11. Measured coupling gain of structure 109 (three-conductor ECS) from the BCB wafer. (a) Magnitude, (b) Phase.

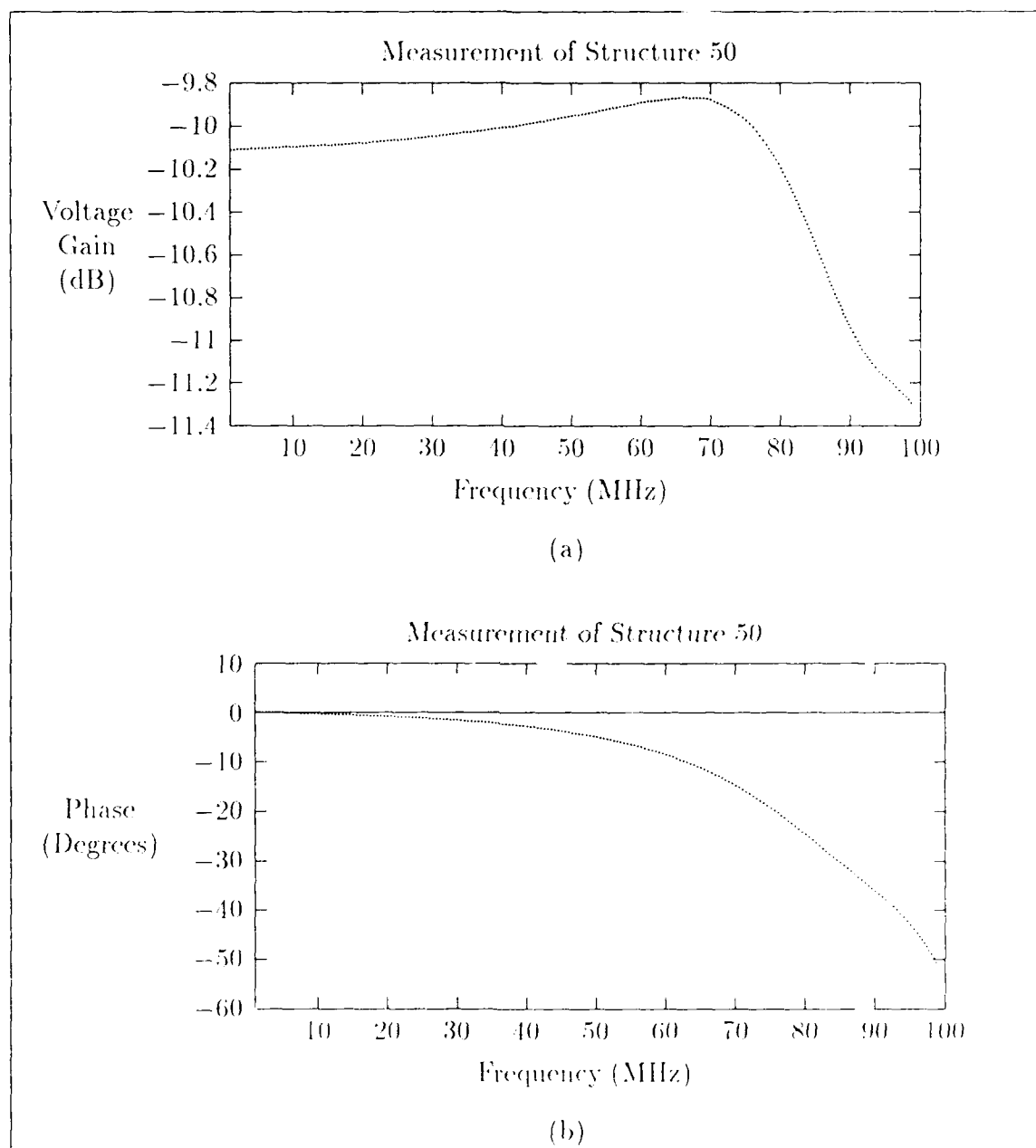


Figure II.12. Measured transmission gain of structure 50 (three-conductor ECS, left conductor) from the PIQ wafer. (a) Magnitude. (b) Phase.

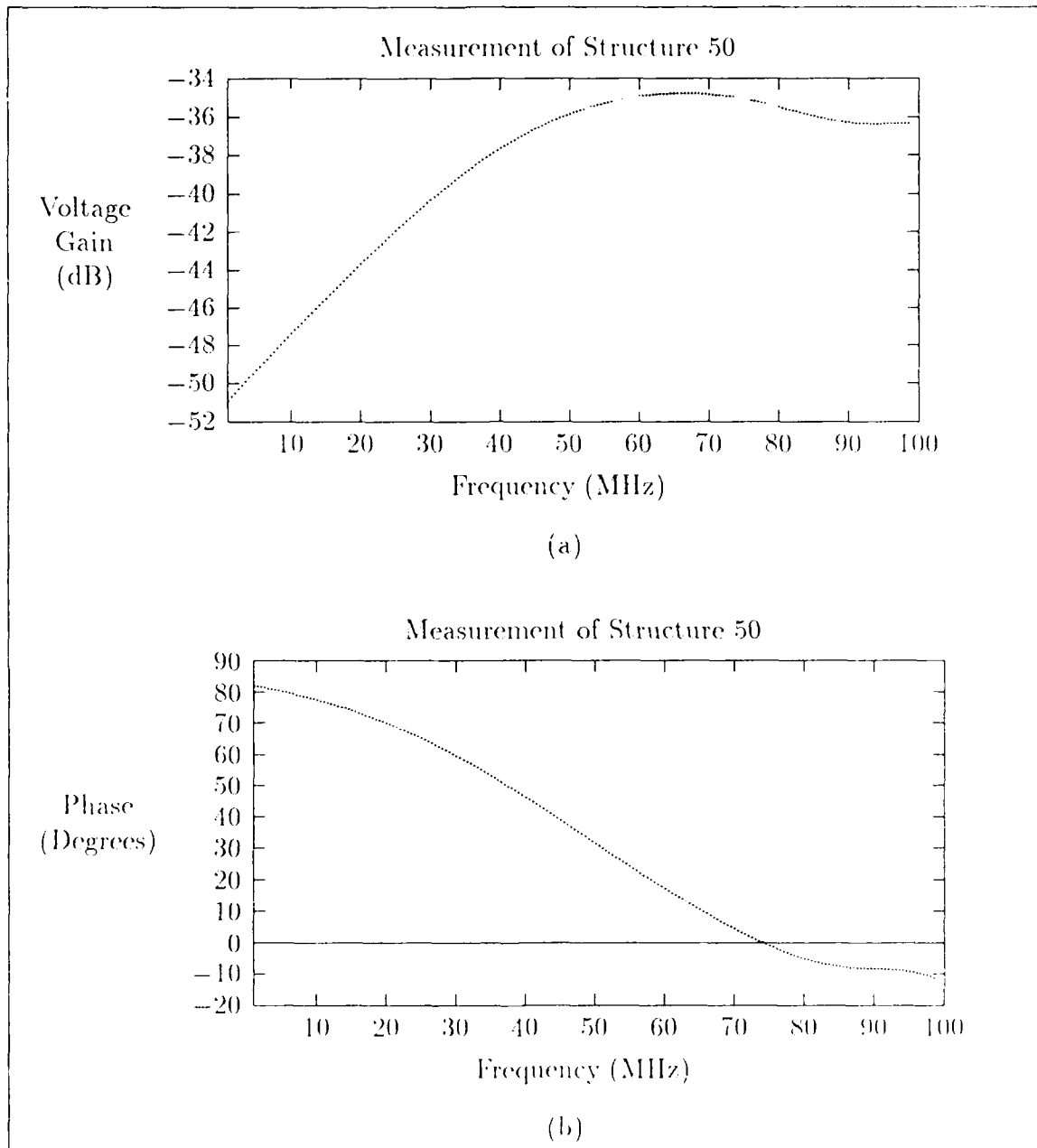


Figure II.13. Measured isolation gain of structure 50 (three-conductor ECS) from the PIQ wafer (measured from a-e terminals). (a) Magnitude. (b) Phase.

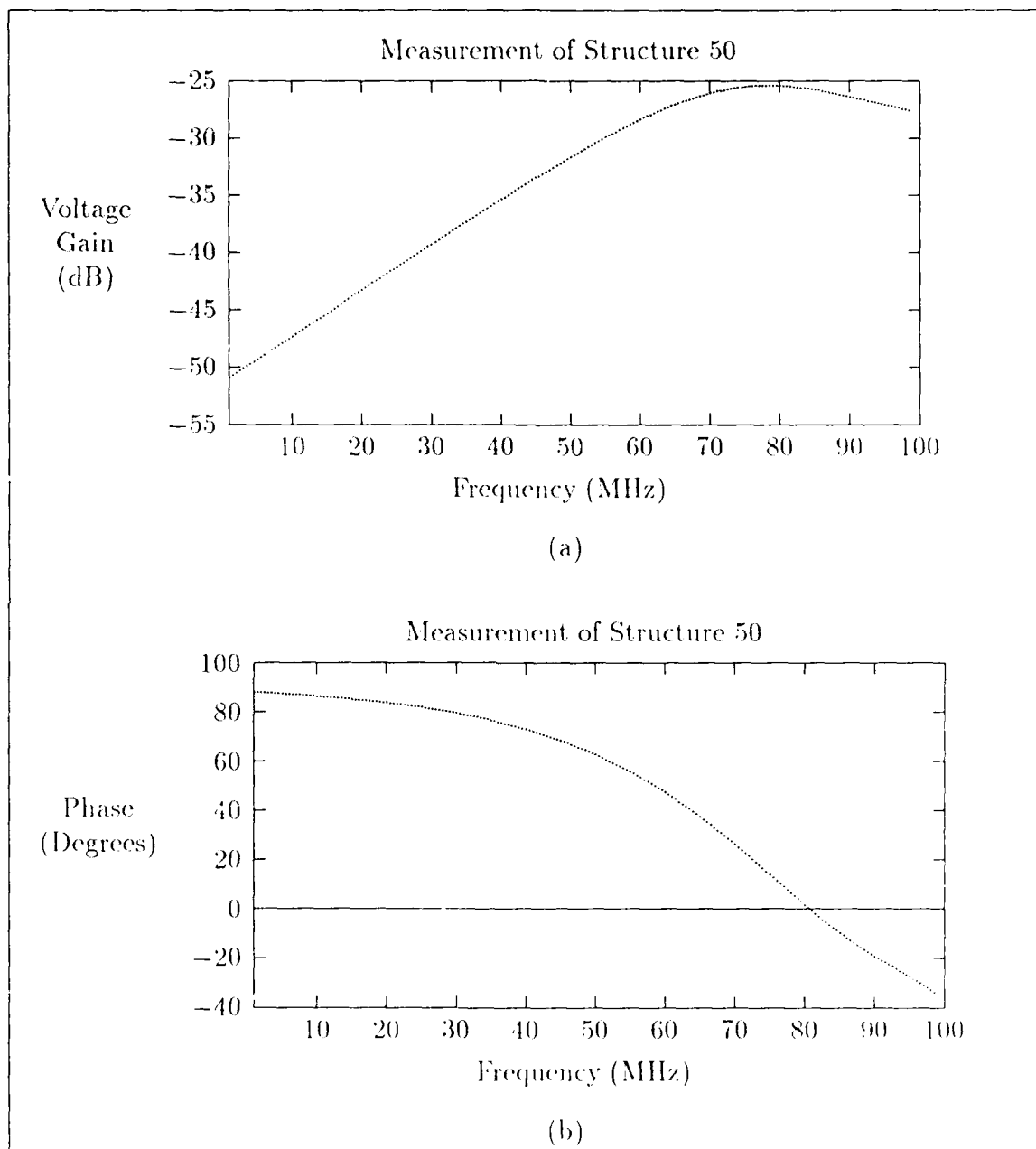


Figure II.14. Measured isolation gain of structure 50 (three-conductor ECS) from the PIQ wafer (measured from a-f terminals). (a) Magnitude. (b) Phase.

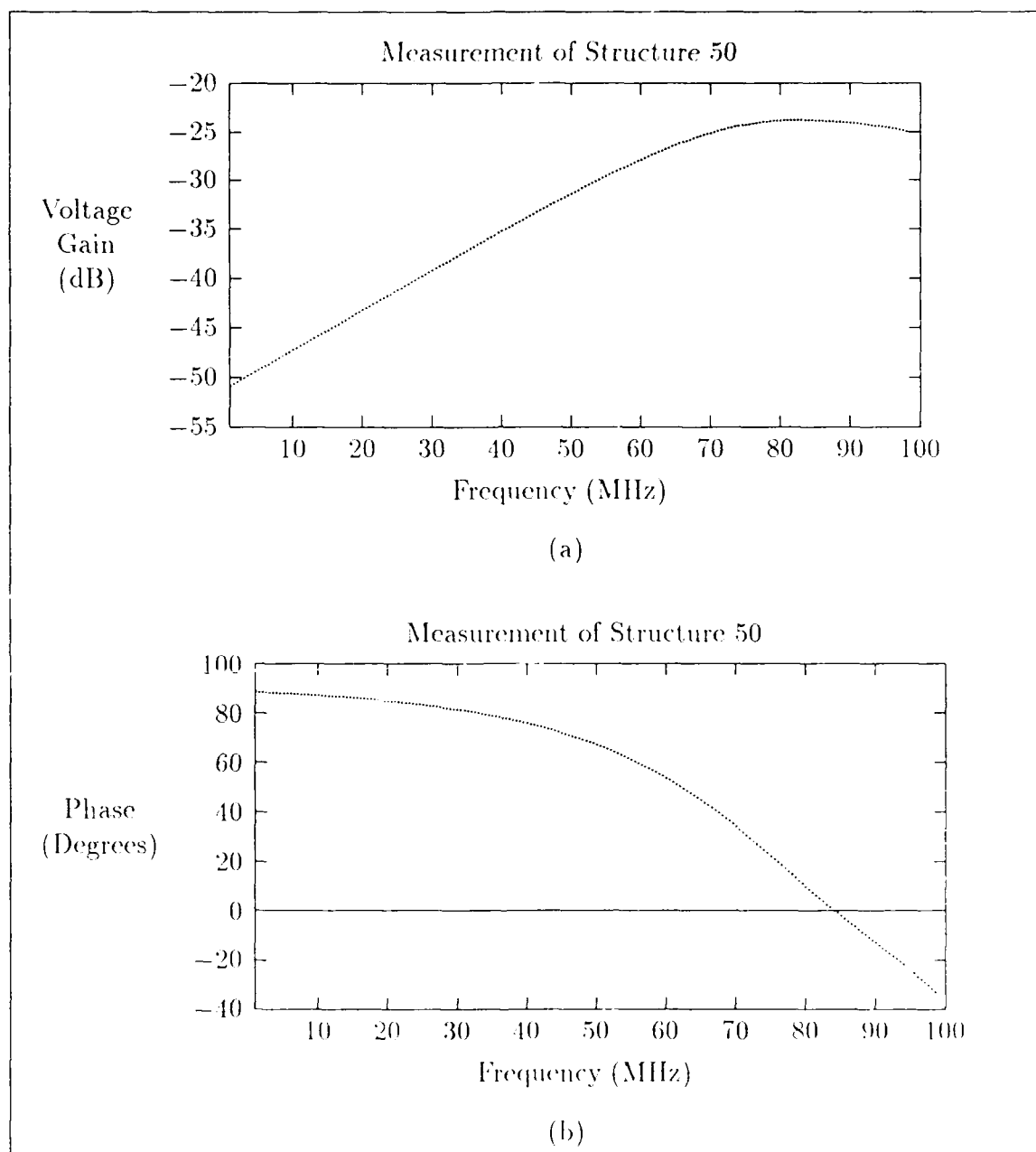


Figure II.15. Measured isolation gain of structure 50 (three-conductor ECS) from the PIQ wafer (measured from b-f terminals). (a) Magnitude. (b) Phase.



## Appendix I. *Pulsed-Signal Measurement Responses.*

This appendix presents the remaining pulsed-signal measurement responses for the structures discussed in Chapter 4. The data presented in Figures I.1–I.42 is summarized in Table I.1

Table I.1 List of time-domain response plots at 5 KHz.

Structure	Wafer	Figure(s)
36	BCB	I.1,I.6–I.7, I.11, I.17–I.18, I.28–I.29, I.36–I.37
36	PIQ	I.19
49	PIQ	I.12–I.13, I.20
54	PIQ	I.21, I.30, I.38
62	PIQ	I.1, I.22, I.31
63	PIQ	4.36–4.40,4.41–4.44
91	BCB	I.2–I.3, I.8, I.14, I.23–I.24, I.32, I.39
100	BCB	I.4,I.9, I.15, I.25–I.26, I.32, I.33–I.34, I.40
109	BCB	I.5, I.10, I.16, I.27, I.41–I.42 I.35

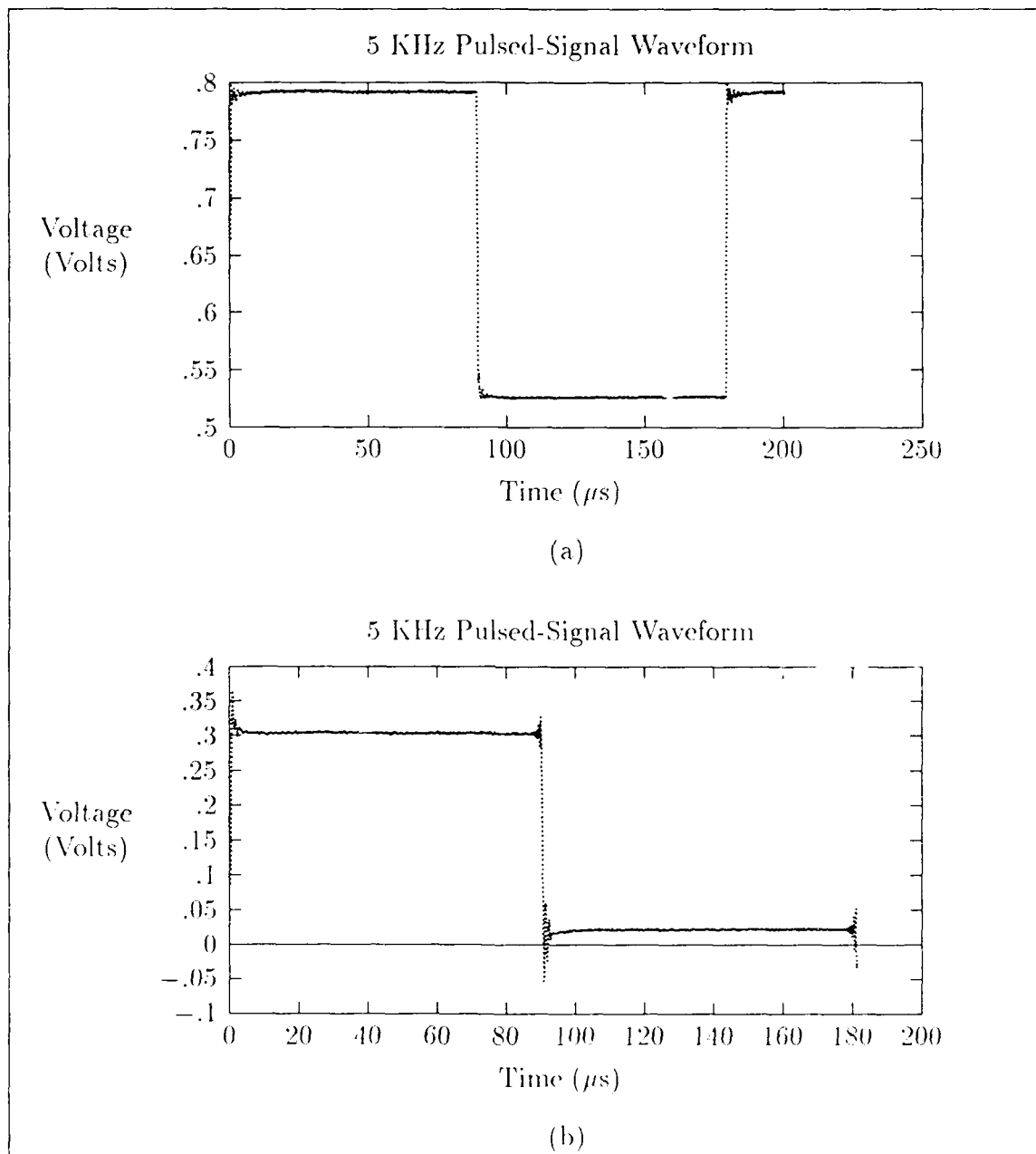


Figure 1.1. Pulsed-signal response of structure 62 ( $10 \mu$ m wide CPW) from the PIQ wafer at 5 KHz (low-impedance termination). (a) Untreated. (b) Filtered. (Input voltage = 5V).

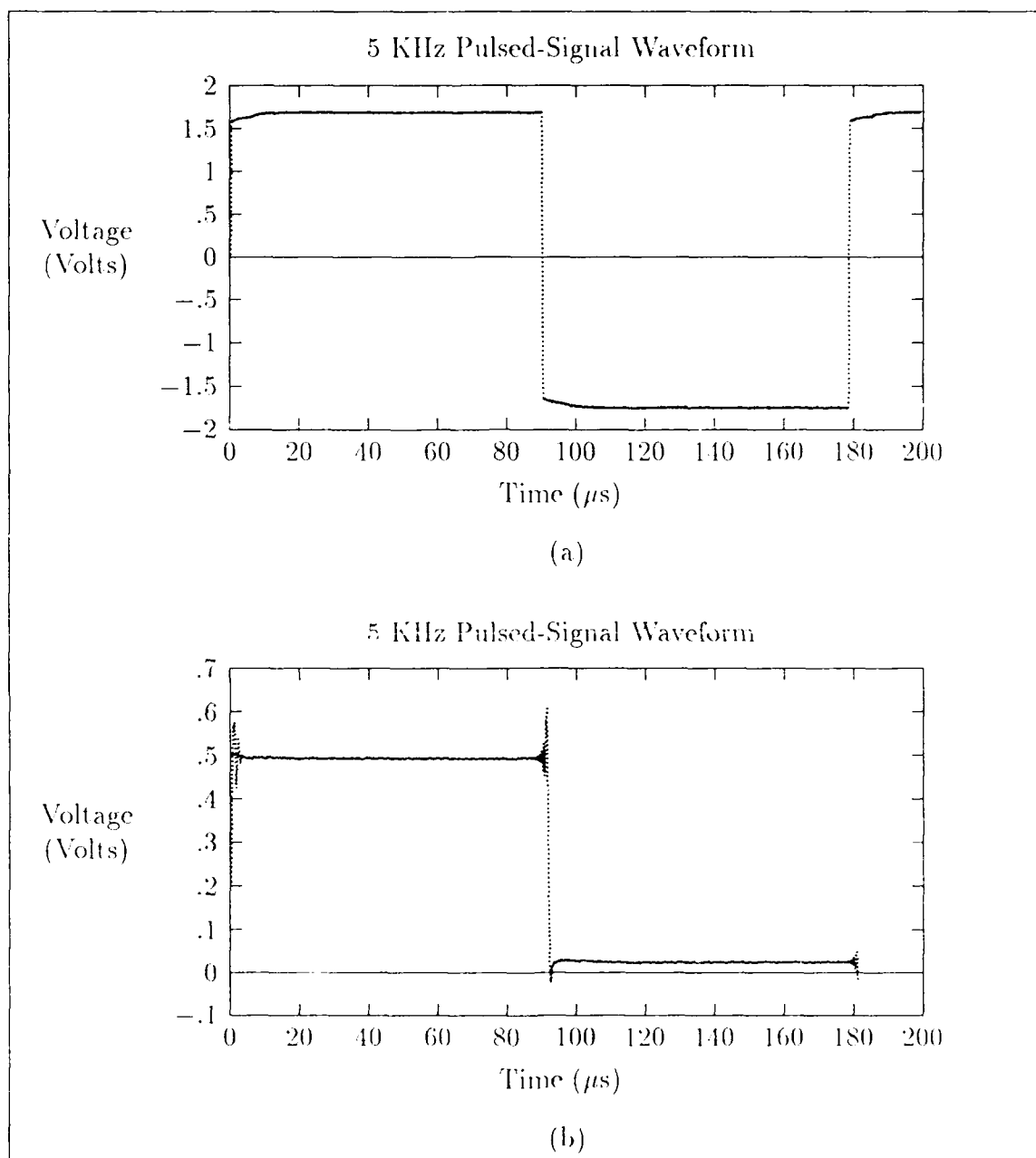


Figure I.2. Pulsed-signal response of structure 91 (25  $\mu$ m wide CPW) from the BCB wafer at 5 KHz (low-impedance termination). (a) Untreated. (b) Filtered. (Input voltage = 2V).

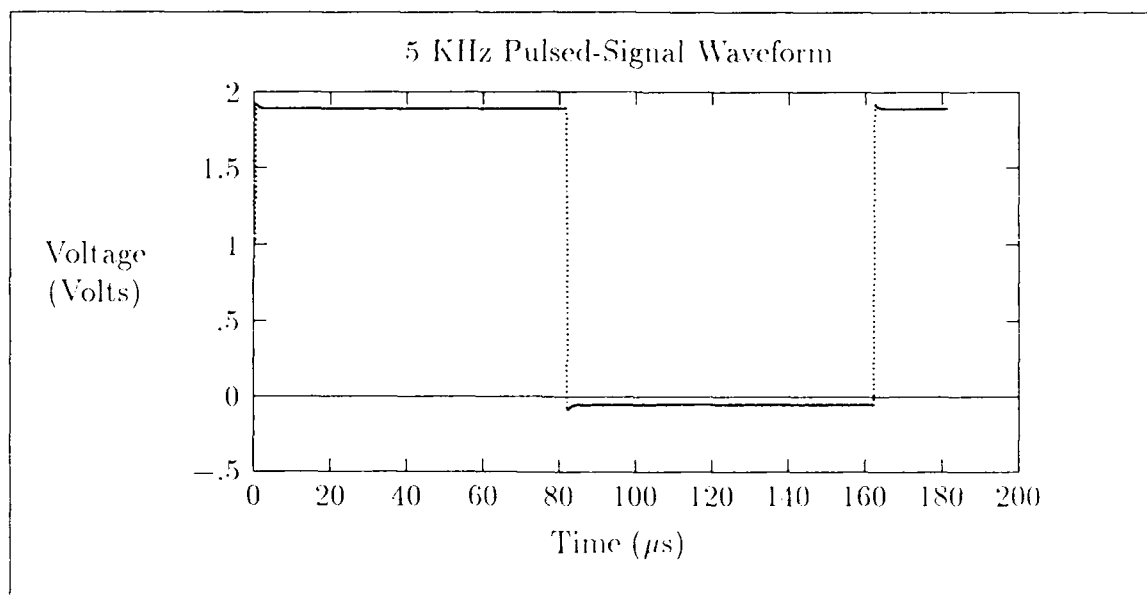


Figure I.3. Pulsed-signal response of structure 91 (CPW) from the BCB wafer at 5 KHz (high-impedance termination). (Input voltage = 2V).

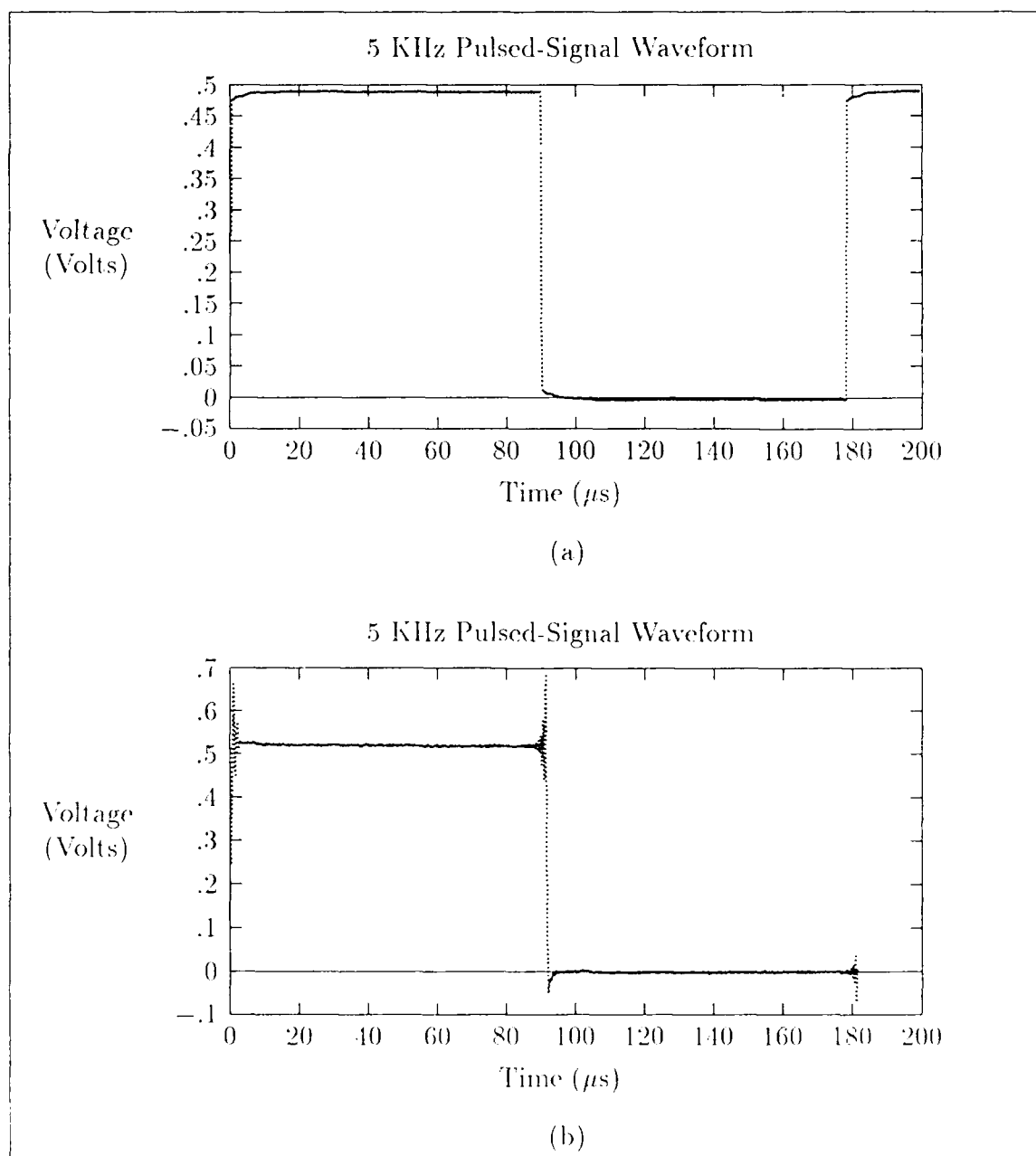


Figure I.1. Pulsed-signal response of structure 100 ( $25\text{ }\mu\text{m}$  wide, 3-conductor ECS) from the BCB wafer at 5 KHz (low-impedance termination). (a) Un-treated. (b) Filtered. (Input voltage = 2V).

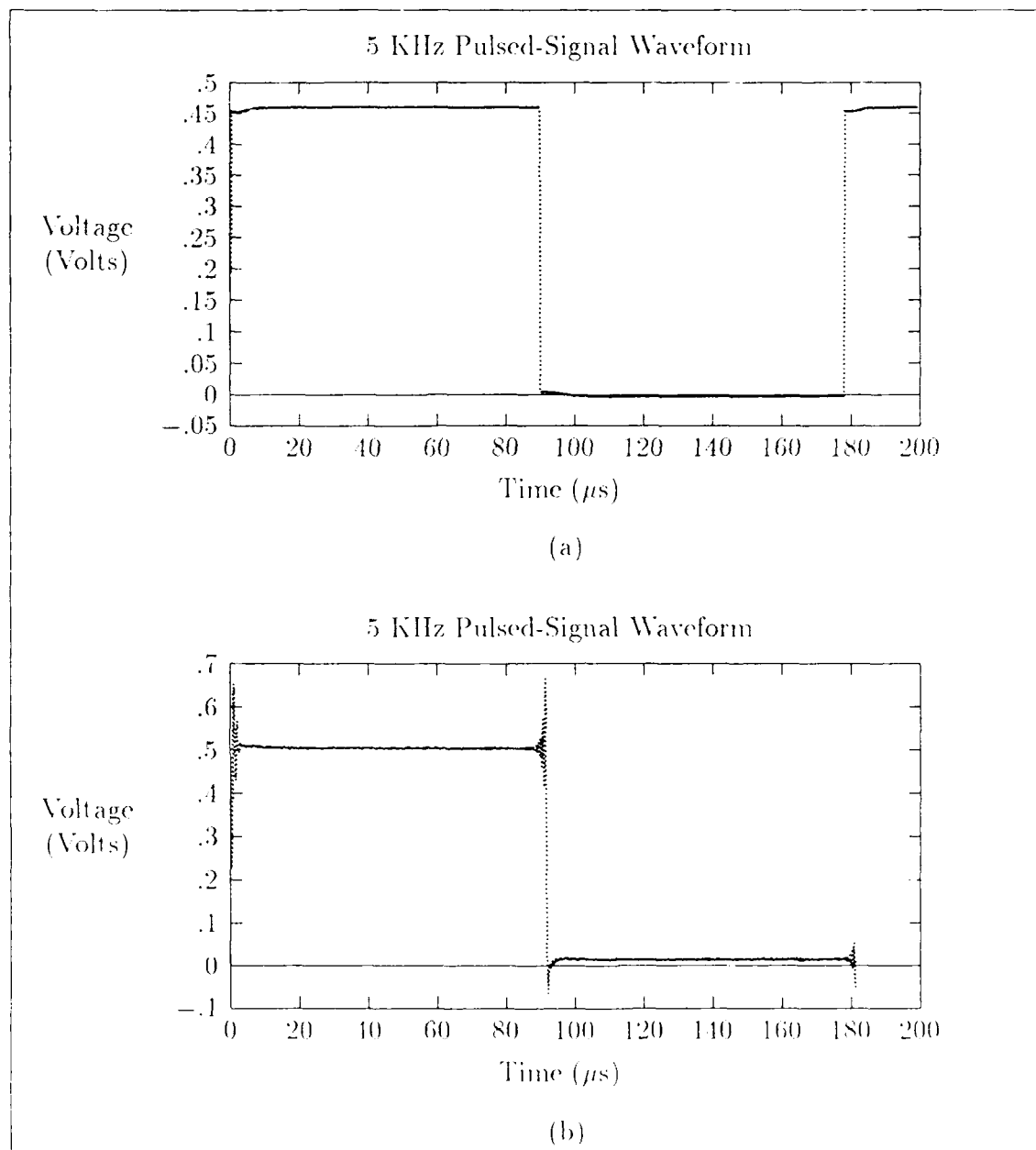


Figure I.5. Pulsed-signal response of structure 109 (25  $\mu m$  wide, 2-conductor ECS) from the BCB wafer at 5 KHz (low-impedance termination). (a) Untreated, (b) Filtered. (Input voltage = 2V).

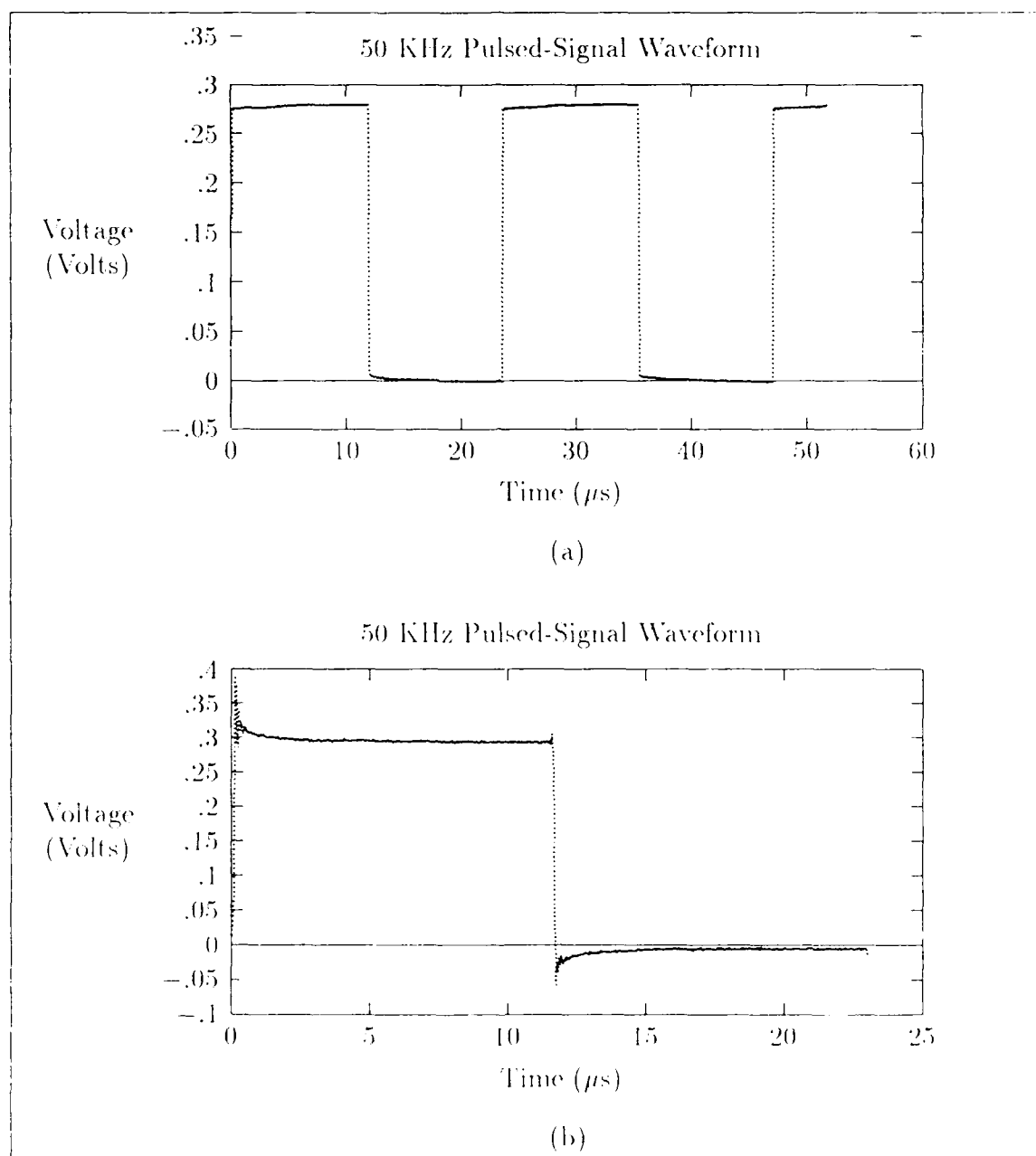


Figure 1.6. Pulsed-signal response of structure 36 ( $10\ \mu\text{m}$  wide, 2-conductor ECS) from the BCB wafer at 50 KHz (low impedance termination). (a) Untreated. (b) Filtered. (Input voltage = 2V).

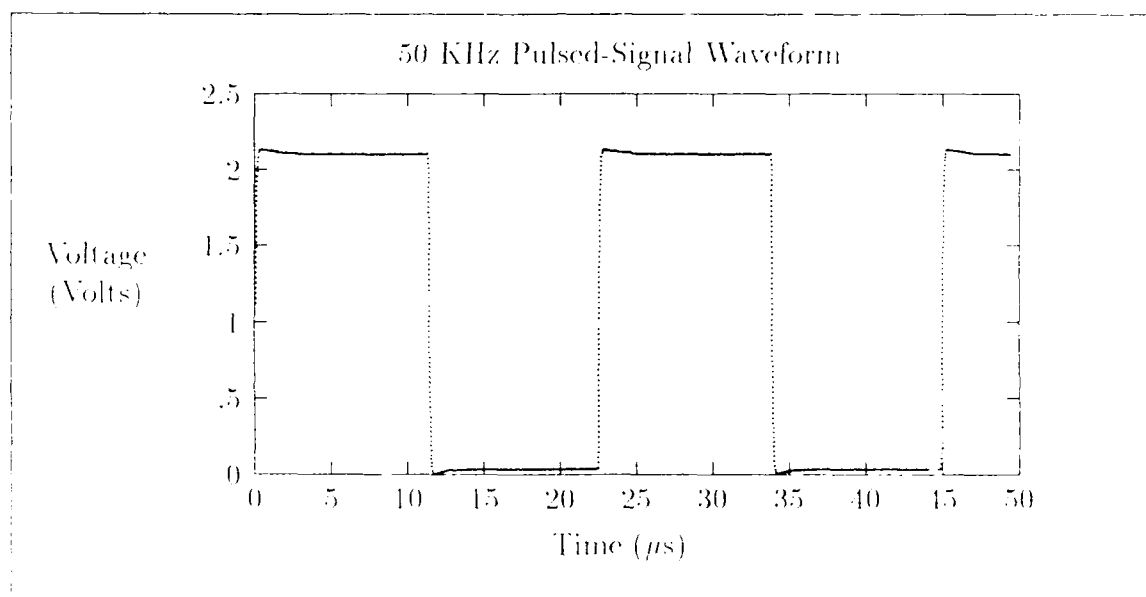


Figure E.7. Pulsed signal response of structure 36 (10  $\mu$ m wide, 2 conductor ECS) from the BCB wafer at 50 KHz (high-impedance termination). (Input voltage = 2V).



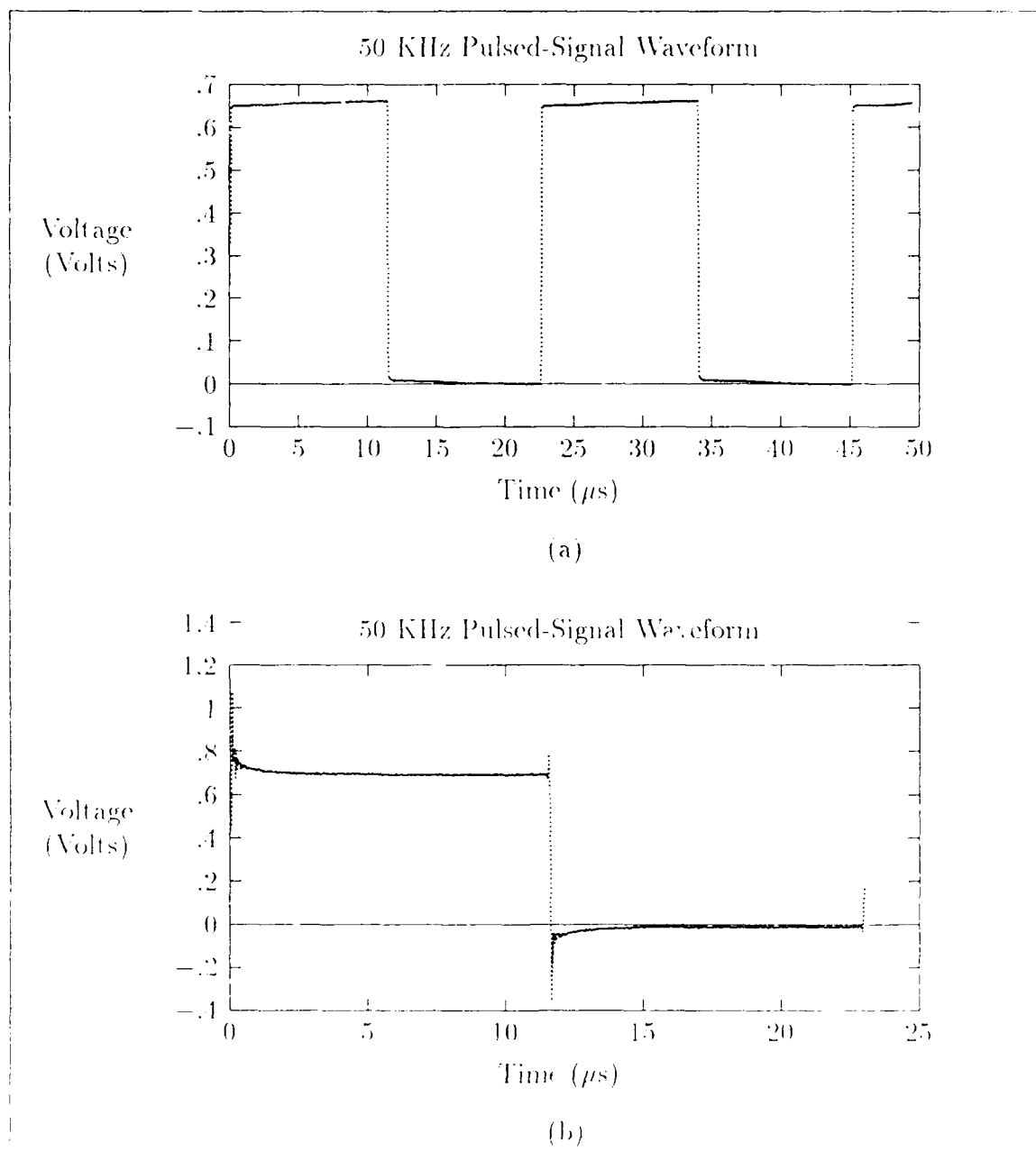


Figure 18. Pulsed-signal response of structure 91 (25  $\mu\text{m}$  wide CPW) from the BCB wafer at 50 kHz (low-impedance termination). (a) Untreated. (b) Filtered. (Input voltage = 2V).

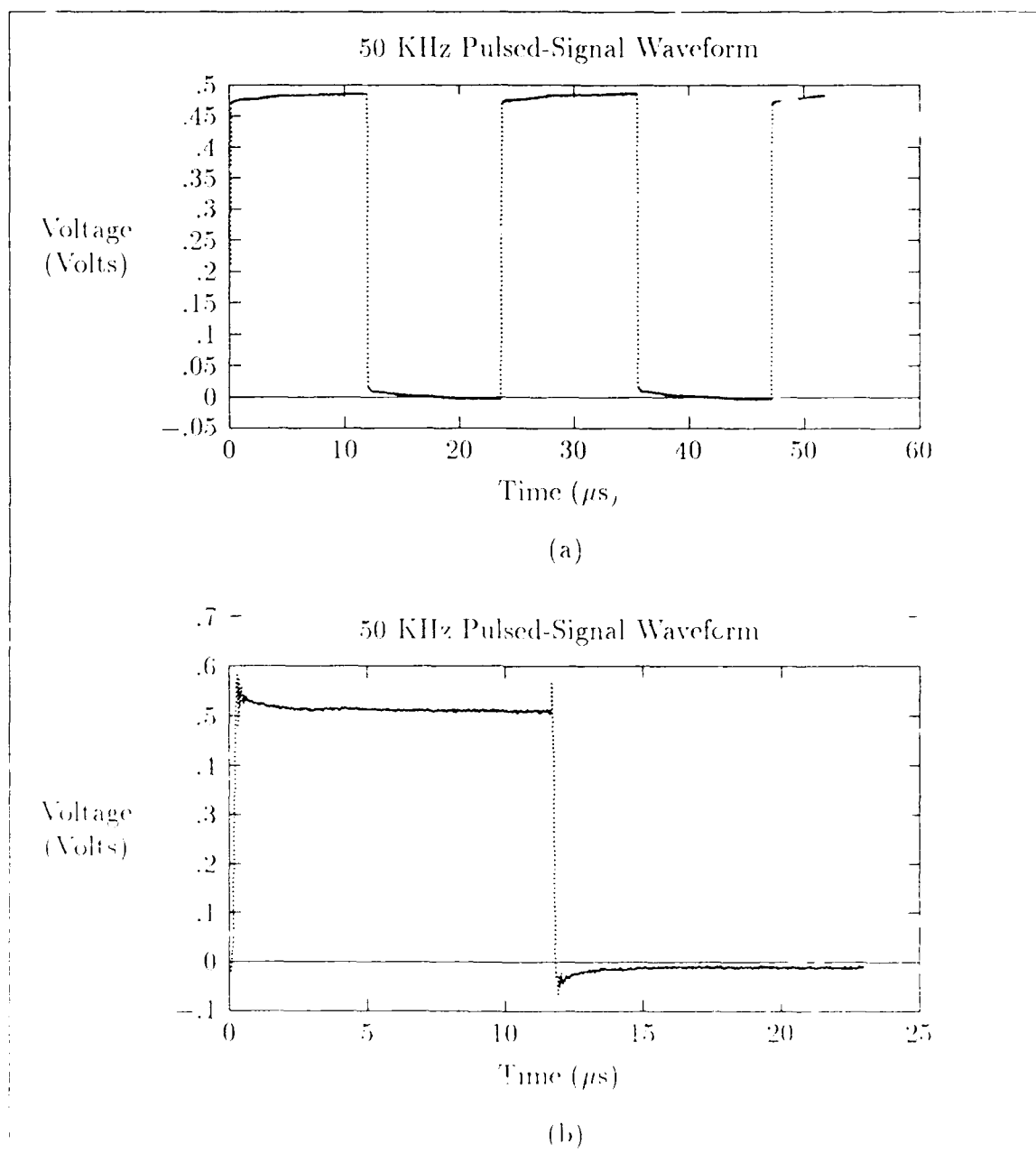


Figure 1.9. Pulsed-signal response of structure 100 (25  $\mu m$  wide, 3-conductor ECS) from the BCB wafer at 50 KHz (low-impedance termination). (a) Unfiltered. (b) Filtered. (Input voltage = 2V).

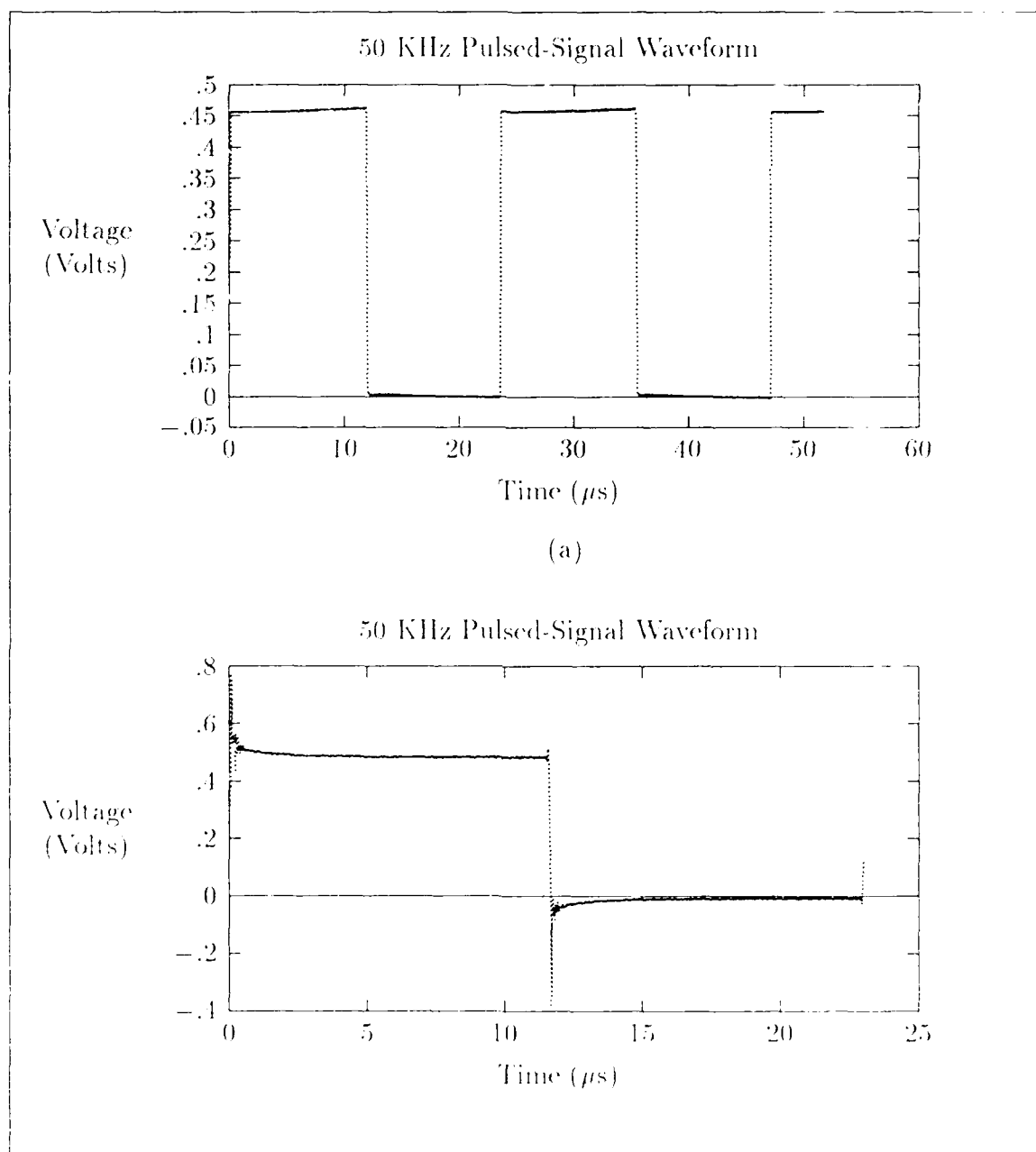


Figure I.10. Pulsed-signal response of structure 109 ( $25\text{ }\mu\text{m}$  wide, 2-conductor ECS) from the BCB wafer at 50 KHz (low-impedance termination). (a) Untreated. (b) Filtered. (Input voltage = 2V).

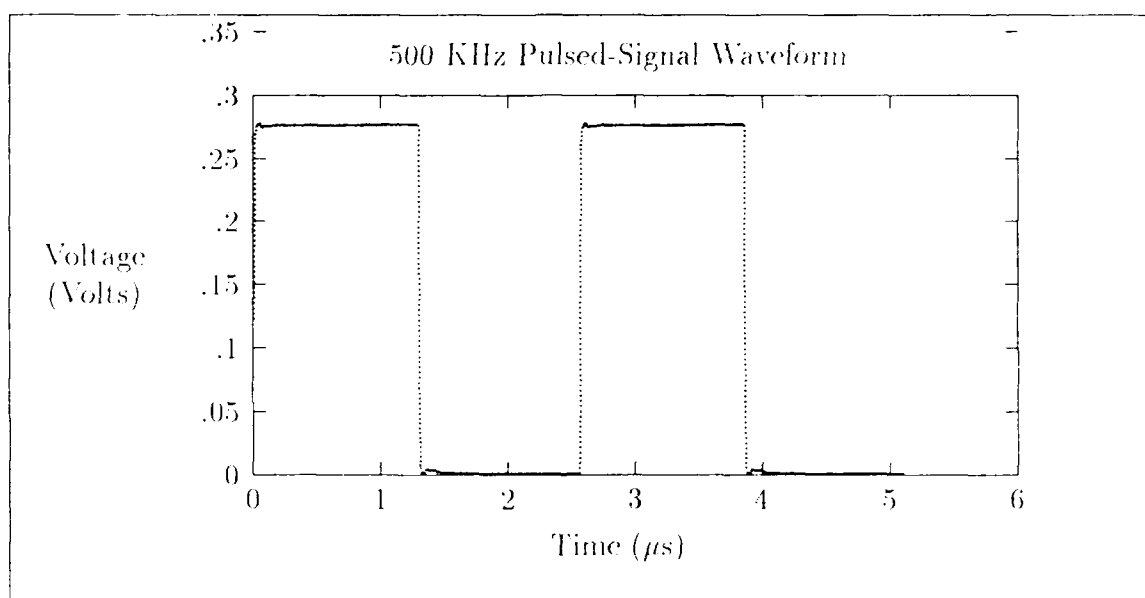


Figure I.11. Pulsed-signal response of structure 36 (10  $\mu$ m wide, 2-conductor ECS) from the BCB wafer at 500 KHz (low-impedance termination). (Input voltage = 2V).

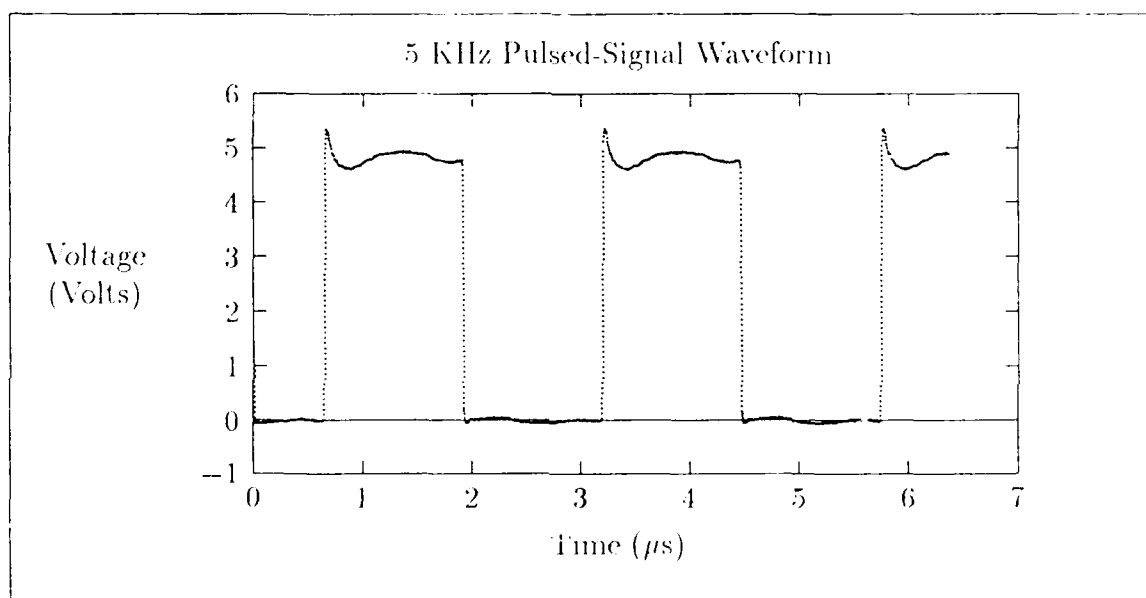


Figure I.12. Pulsed-signal response of structure 49 ( $10\ \mu\text{m}$  wide, 2-conductor ECS) from the PIQ wafer at 500 KHz (high-impedance termination). (Input voltage = 5V).

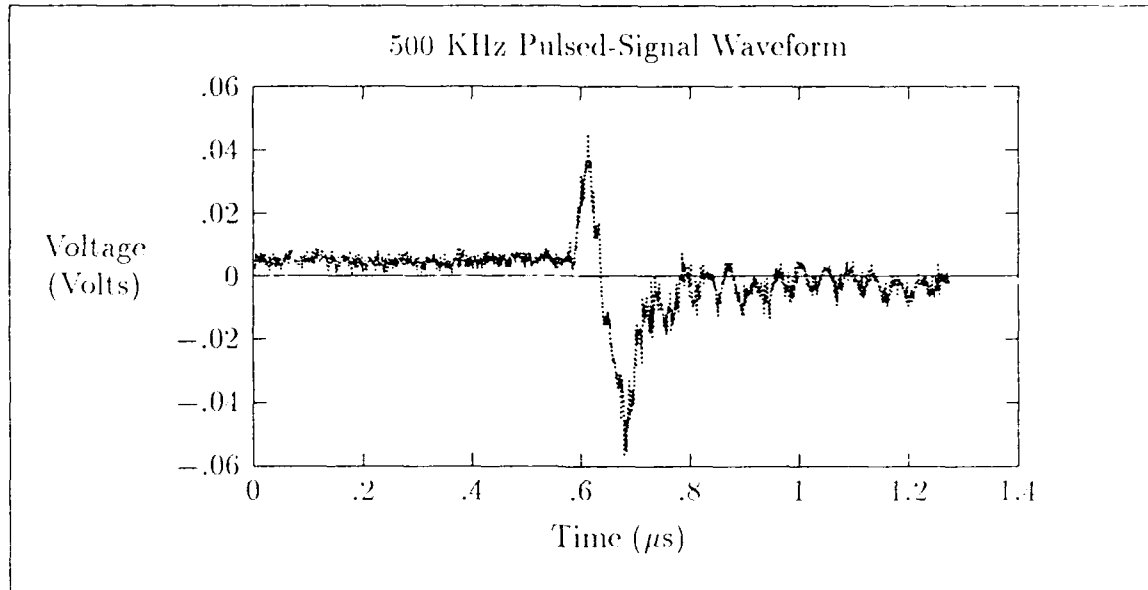


Figure I.13. Pulsed-signal response of structure 49 ( $10\text{ }\mu\text{m}$  wide, 2-conductor ECS) from the PIQ wafer at 500 KHz (high-impedance termination) from isolated conductor. (Input voltage = 2V).

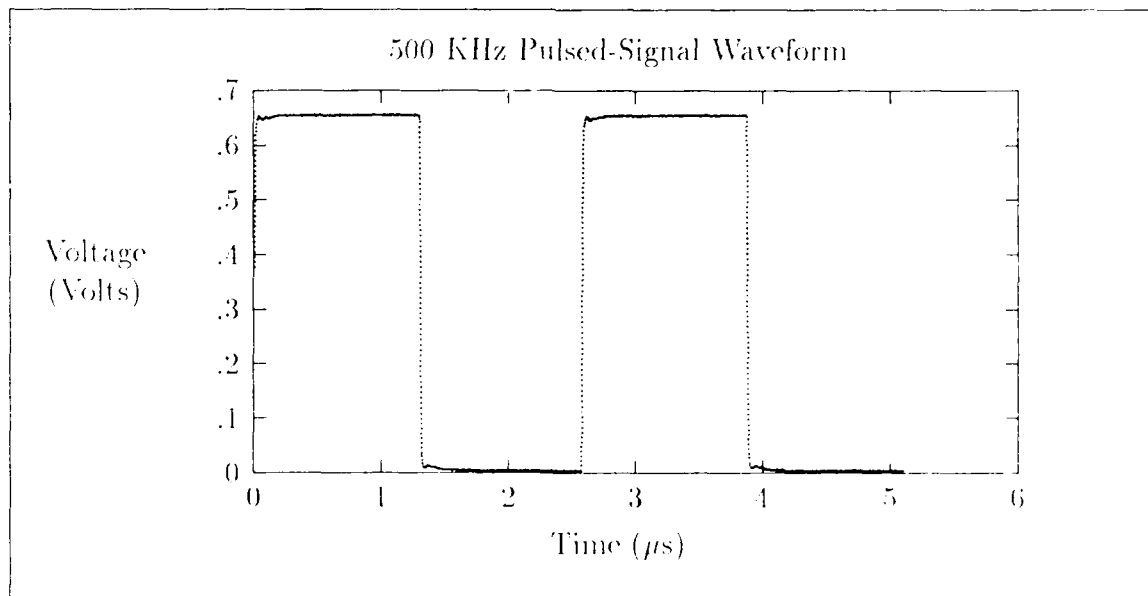


Figure I.14. Pulsed-signal response of structure 91 ( $25\text{ }\mu\text{m}$  wide CPW) from the BCB wafer at 500 KHz (low-impedance termination). (Input voltage = 2V).

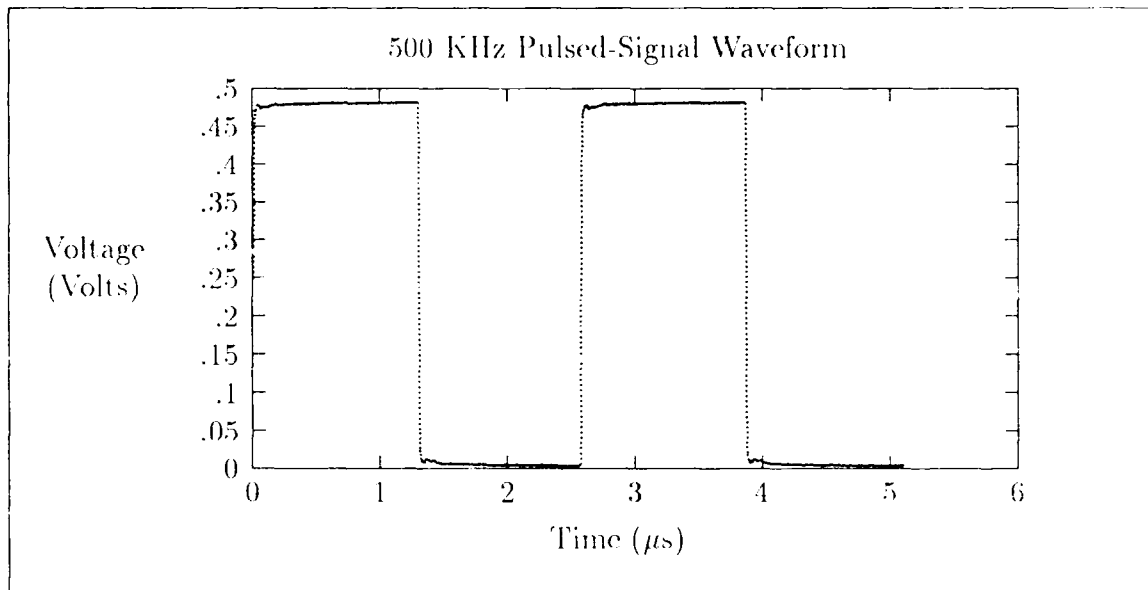


Figure I.15. Pulsed-signal response of structure 100 (25  $\mu m$  wide, 3-conductor ECS) from the BCB wafer at 500 KHz (low-impedance termination). (Input voltage = 2V).

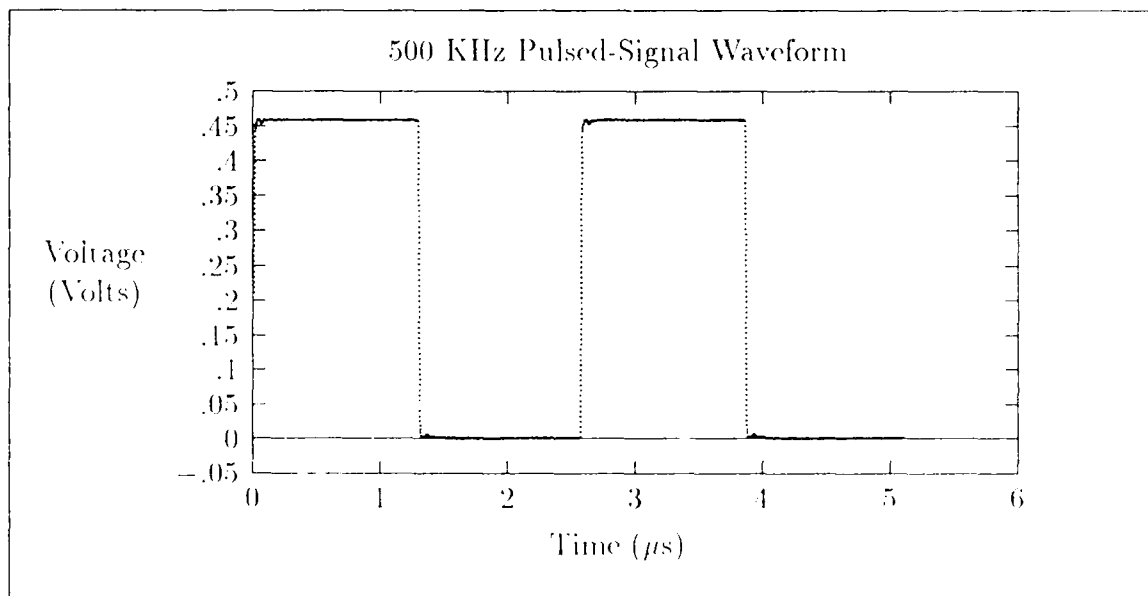


Figure I.16. Pulsed-signal response of structure 109 (25  $\mu m$  wide, 2-conductor ECS) from the BCB wafer at 500 KHz (low-impedance termination). (Input voltage = 2V).

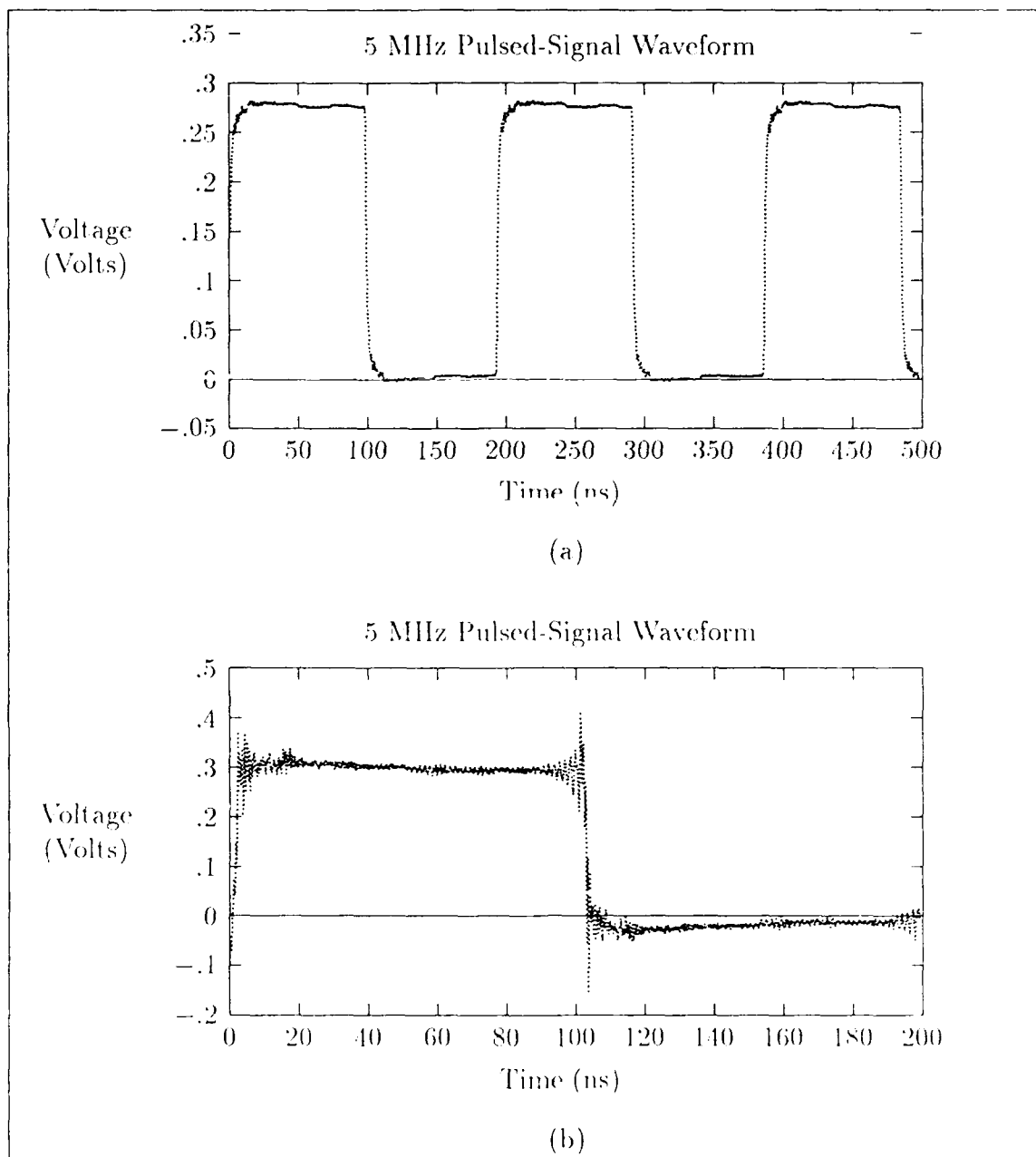


Figure I.17. Pulsed-signal response of structure 36 ( $10\ \mu\text{m}$  wide, 2-conductor ECS) from the BCB wafer at 5 MHz (low-impedance termination). (a) Un-treated. (b) Filtered. (Input voltage = 2V).



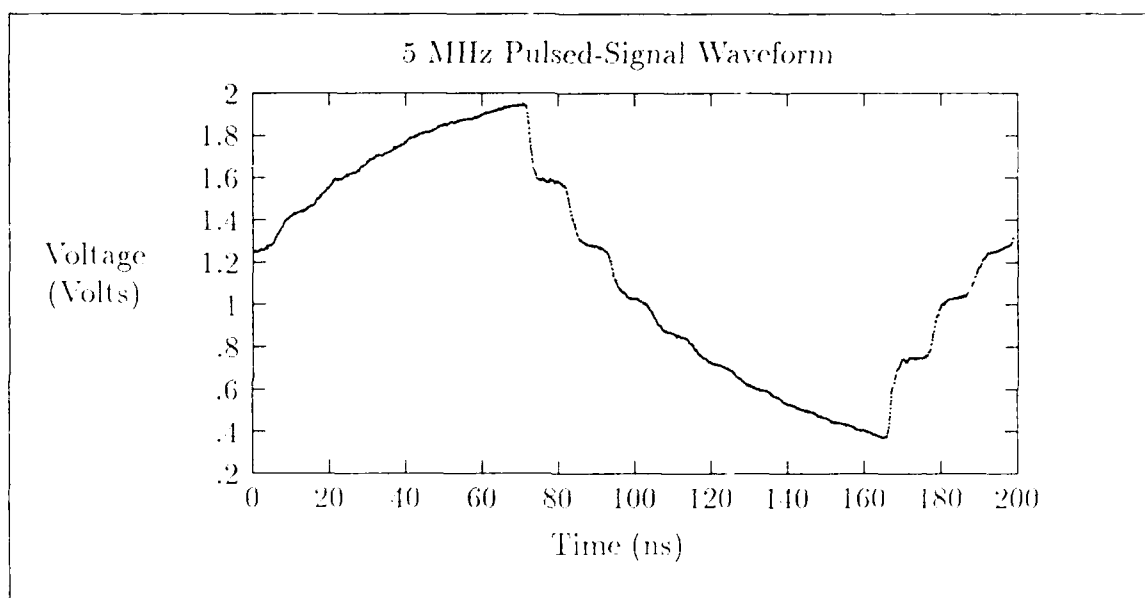


Figure I.18. Pulsed-signal response of structure 36 ( $10\text{ }\mu\text{m}$  wide, 2-conductor ECS) from the BCB wafer at 5 MHz (high-impedance termination). (Input voltage = 2V).

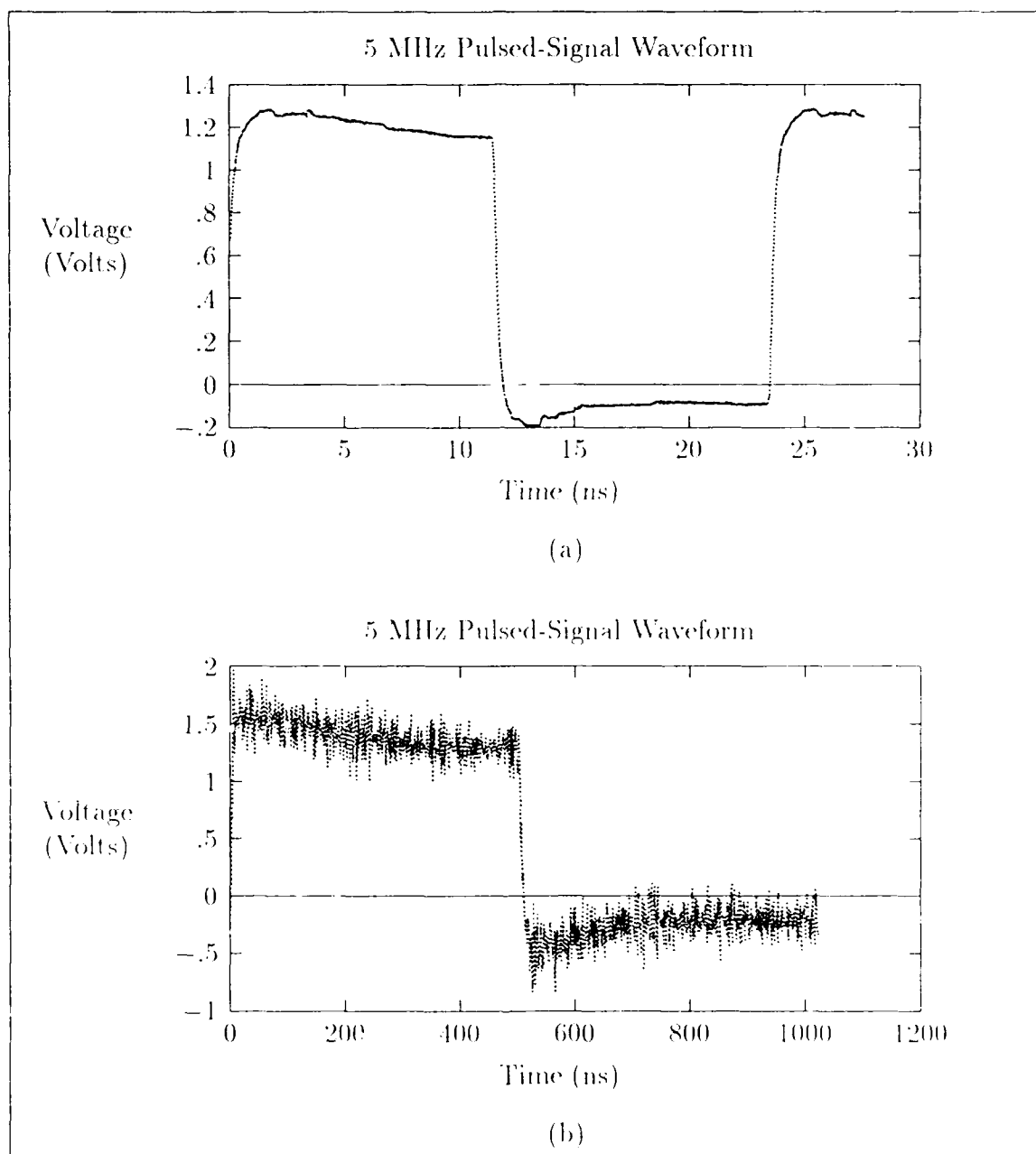


Figure I.19. Pulse-signal response of structure 36 ( $10\text{ }\mu\text{m}$  wide, 2-conductor ECS) from the PIQ wafer at 5 MHz (low-impedance termination). (a) Untreated. (b) Filtered. (Input voltage = 5V).

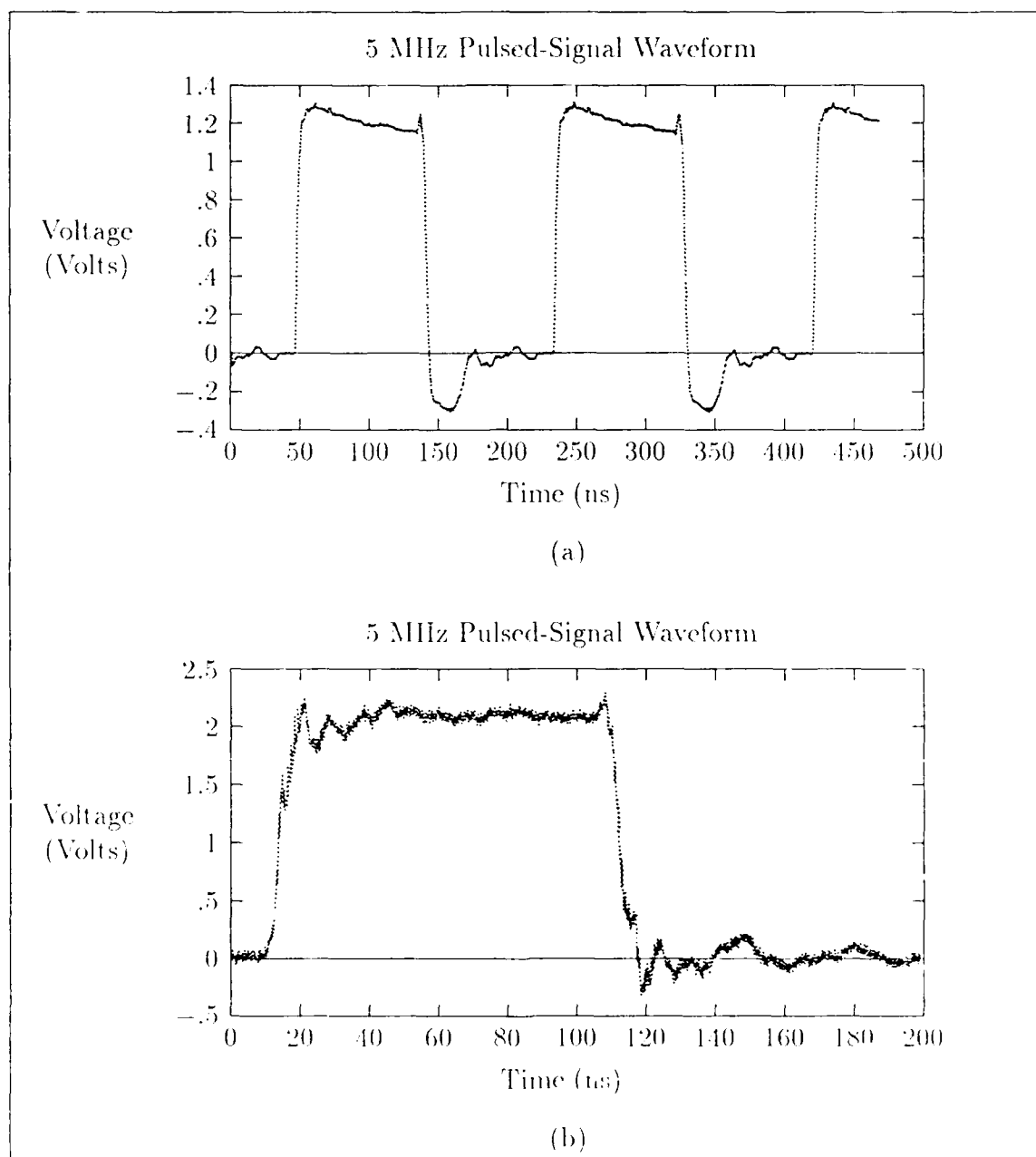


Figure L20. Pulsed-signal response of structure 49 ( $10\ \mu\text{m}$  wide, 2-conductor ECS) from the PIQ wafer at 5 MHz (high-impedance termination). (a) Untreated. (b) Filtered. (Input voltage = 2V).

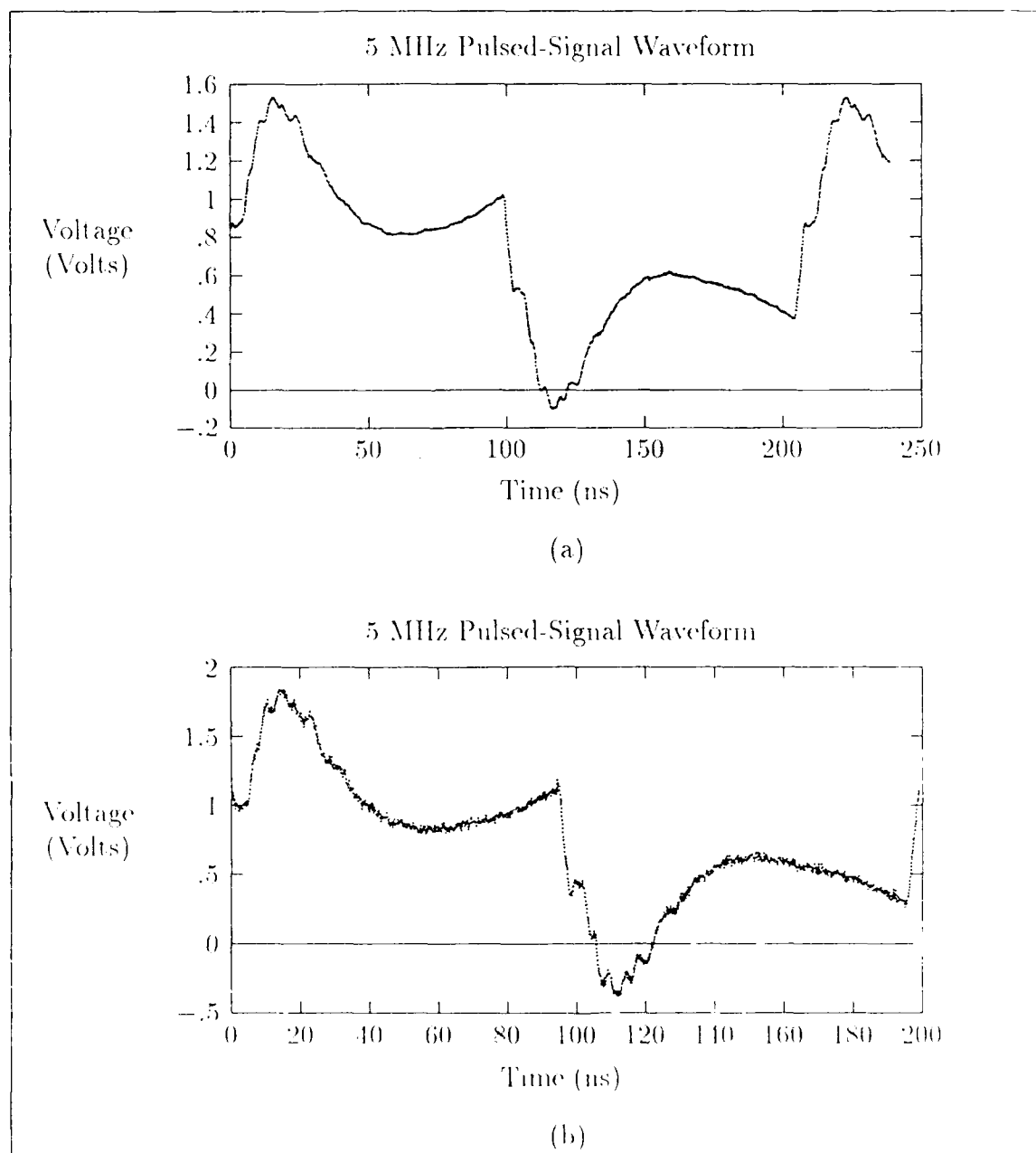


Figure I.21. Pulsed-signal response of structure 54 ( $10\ \mu\text{m}$  wide, 3-conductor ECS) from the PIQ wafer at 5 MHz (low-impedance termination). (a) Untreated. (b) Filtered. (Input voltage = 2V).

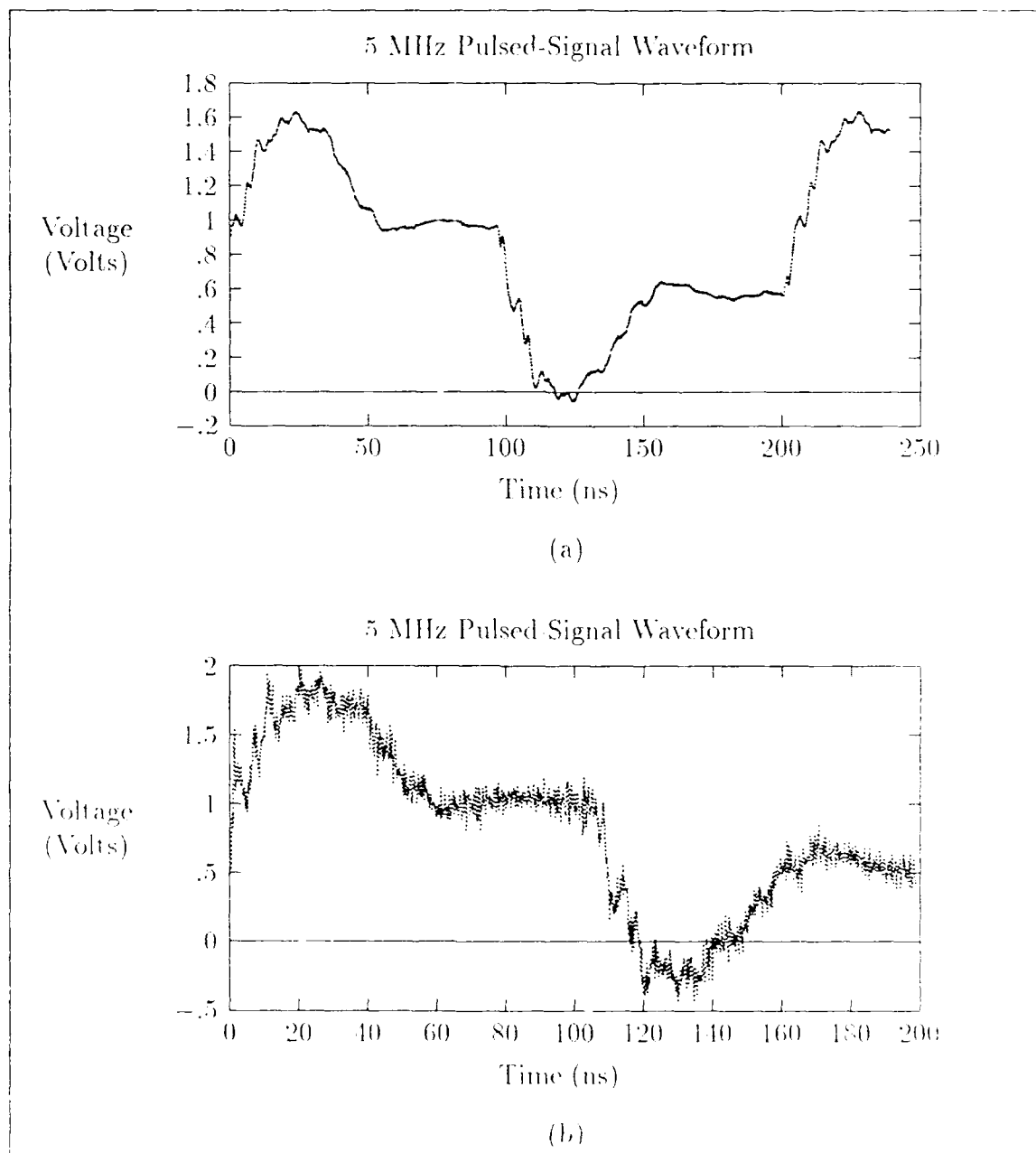


Figure I.22. Pulsed-signal response of structure 62 ( $10\ \mu\text{m}$  wide CPW) from the PIQ wafer at 5 MHz (low-impedance termination). (a) Untreated. (b) Filtered. (Input voltage = 5V).

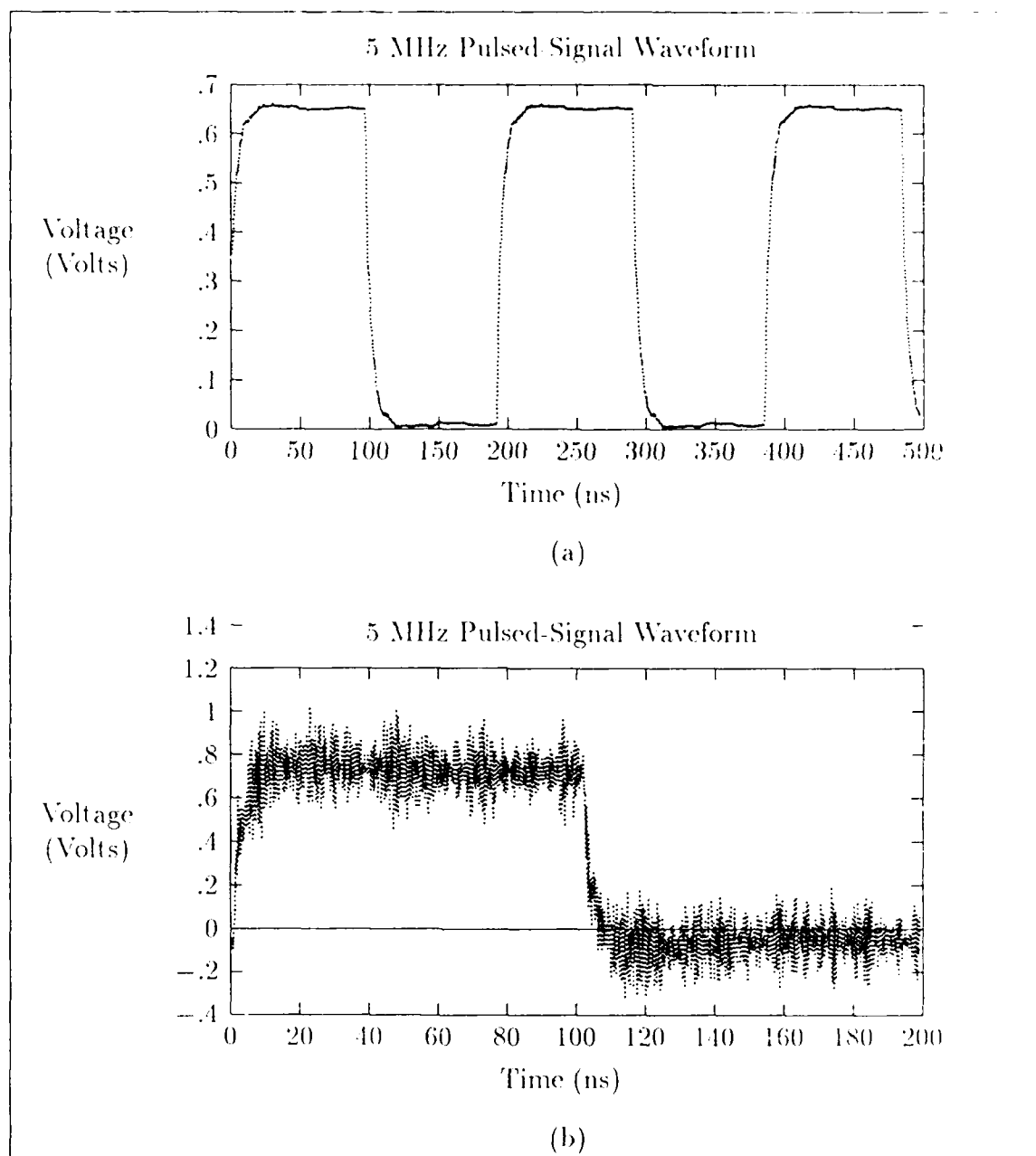


Figure 1.23. Pulsed-signal response of structure 91 ( $25\ \mu\text{m}$  wide CPW) from the BCB wafer at 5 MHz (low-impedance termination). (a) Untreated. (b) Filtered. (Input voltage = 2V).

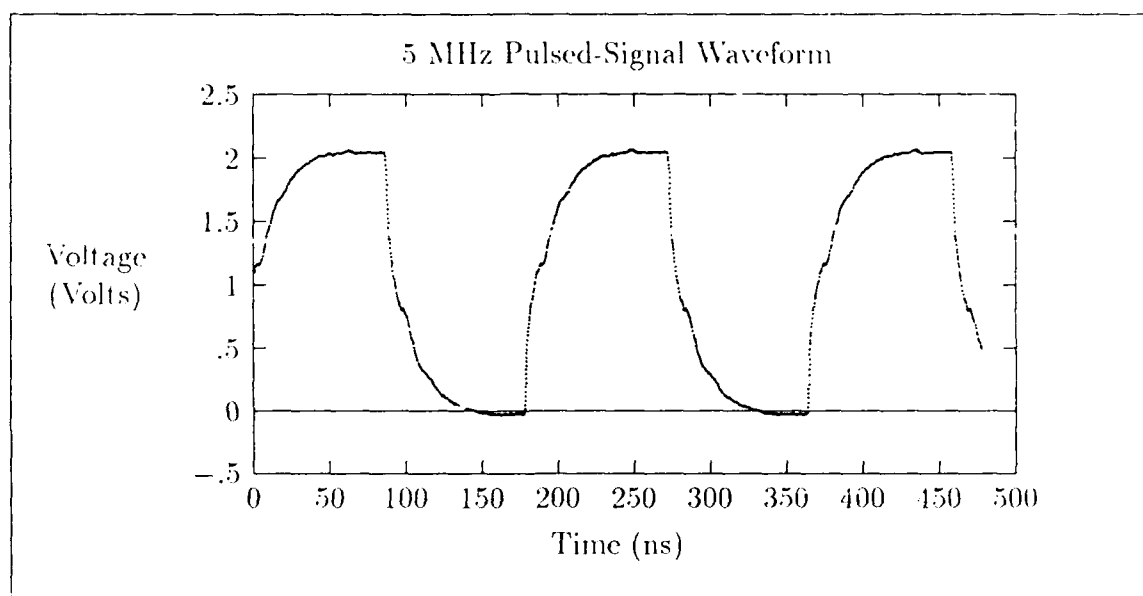


Figure I.24. Pulsed-signal response of structure 91 ( $25\text{ }\mu\text{m}$  wide CPW) from the BCB wafer at 5 MHz (high-impedance termination). (Input voltage = 2V).

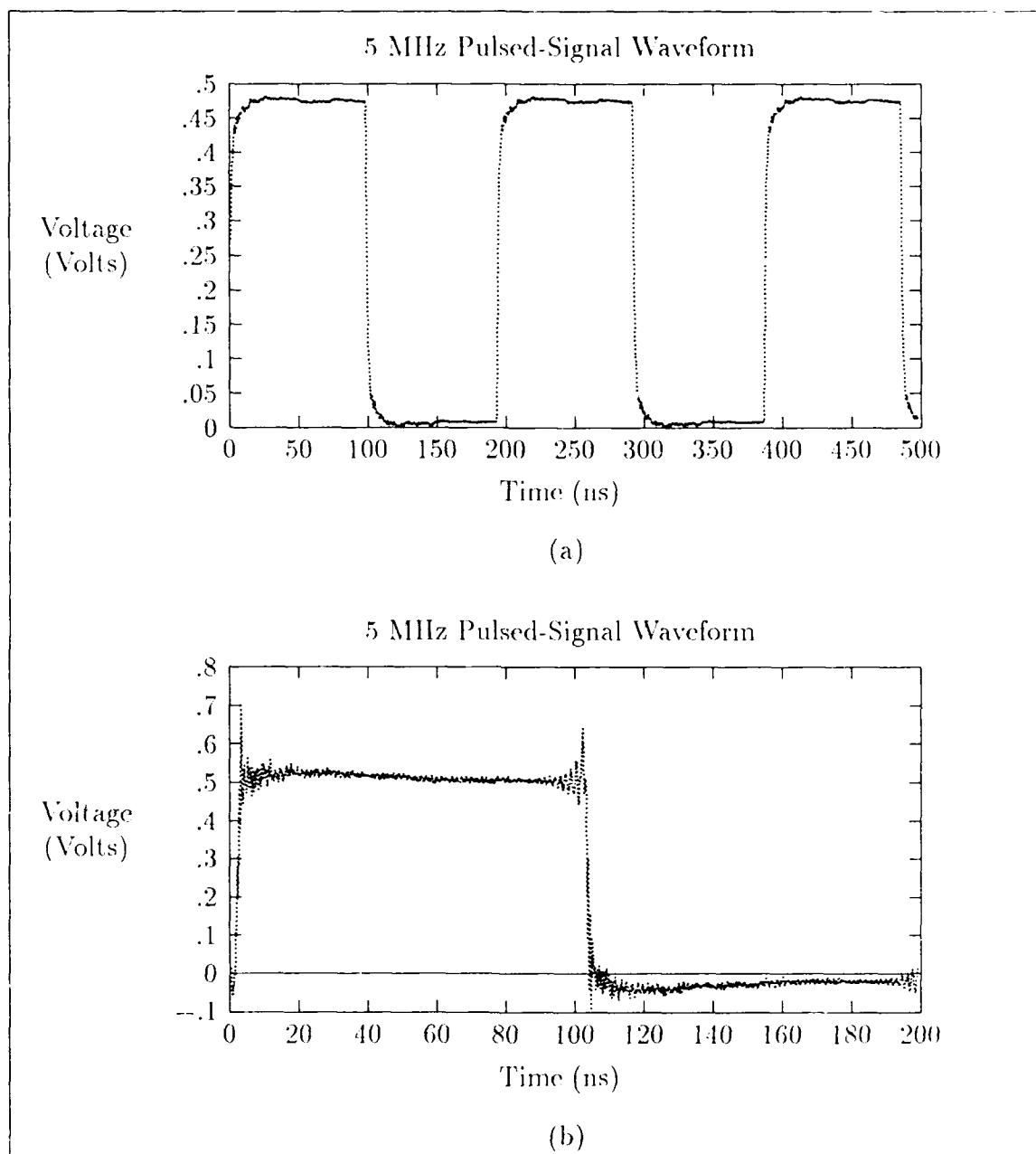


Figure I.25. Pulsed-signal response of structure 100 ( $25\text{ }\mu\text{m}$  wide, three-conductor ECS) from the BCB wafer at 5 MHz (low-impedance termination). (a) Untreated. (b) Filtered. (Input voltage = 2V).



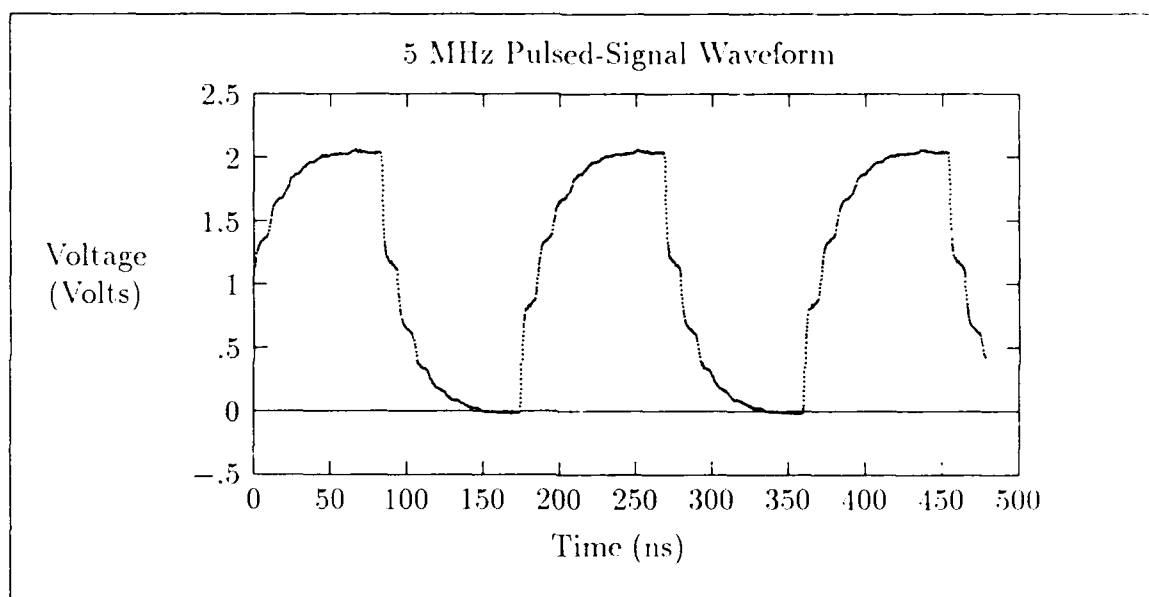


Figure I.26. Pulsed-signal response of structure 100 (25  $\mu\text{m}$  wide, three-conductor ECS) from the BCB wafer at 5 MHz (high-impedance termination).

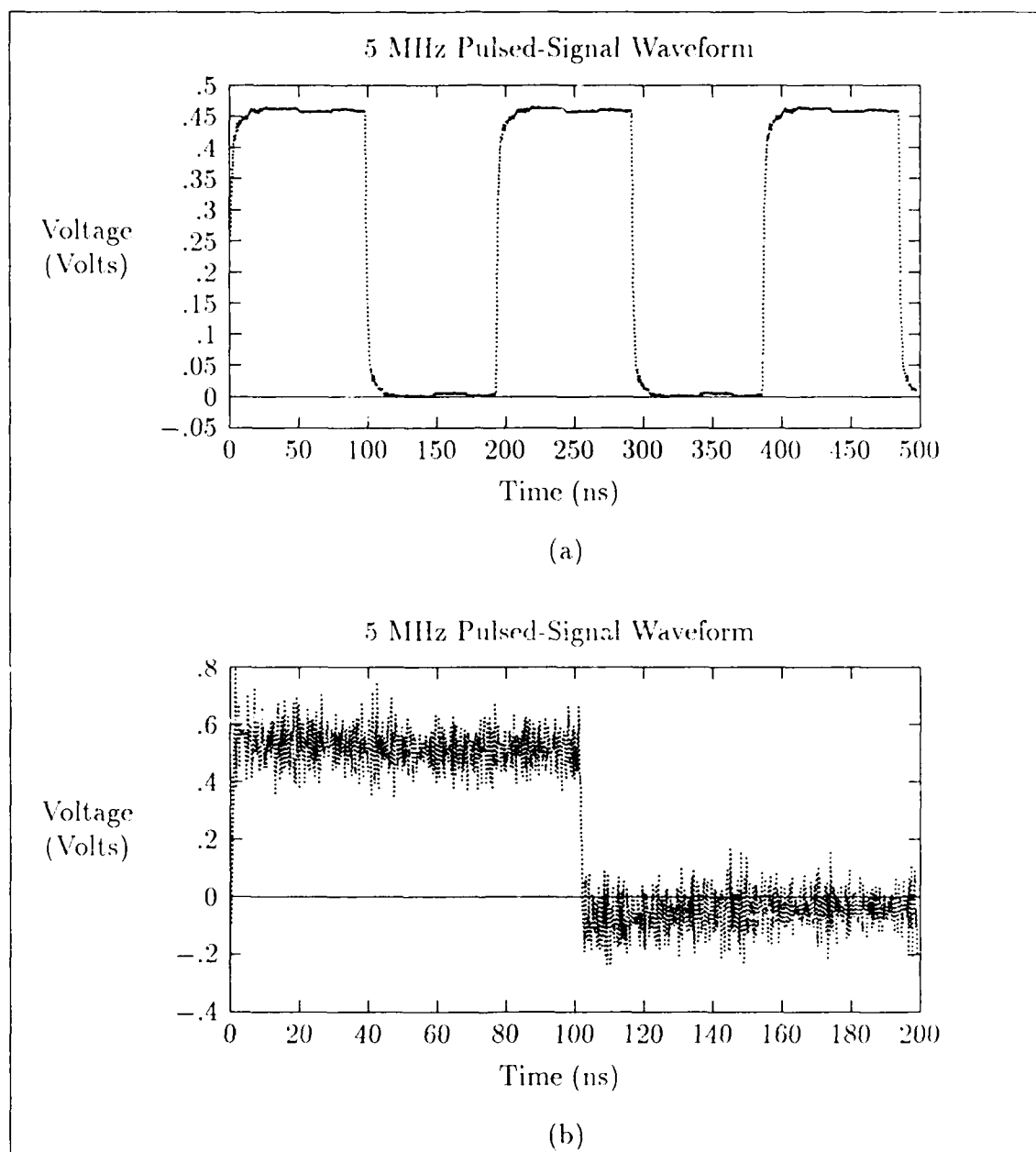


Figure I.27. Pulsed-signal response of structure 109 (25  $\mu\text{m}$  wide, 2-conductor ECS) from the BCB wafer at 5 MHz (low-impedance termination). (a) Untreated. (b) Filtered. (Input voltage = 9V).

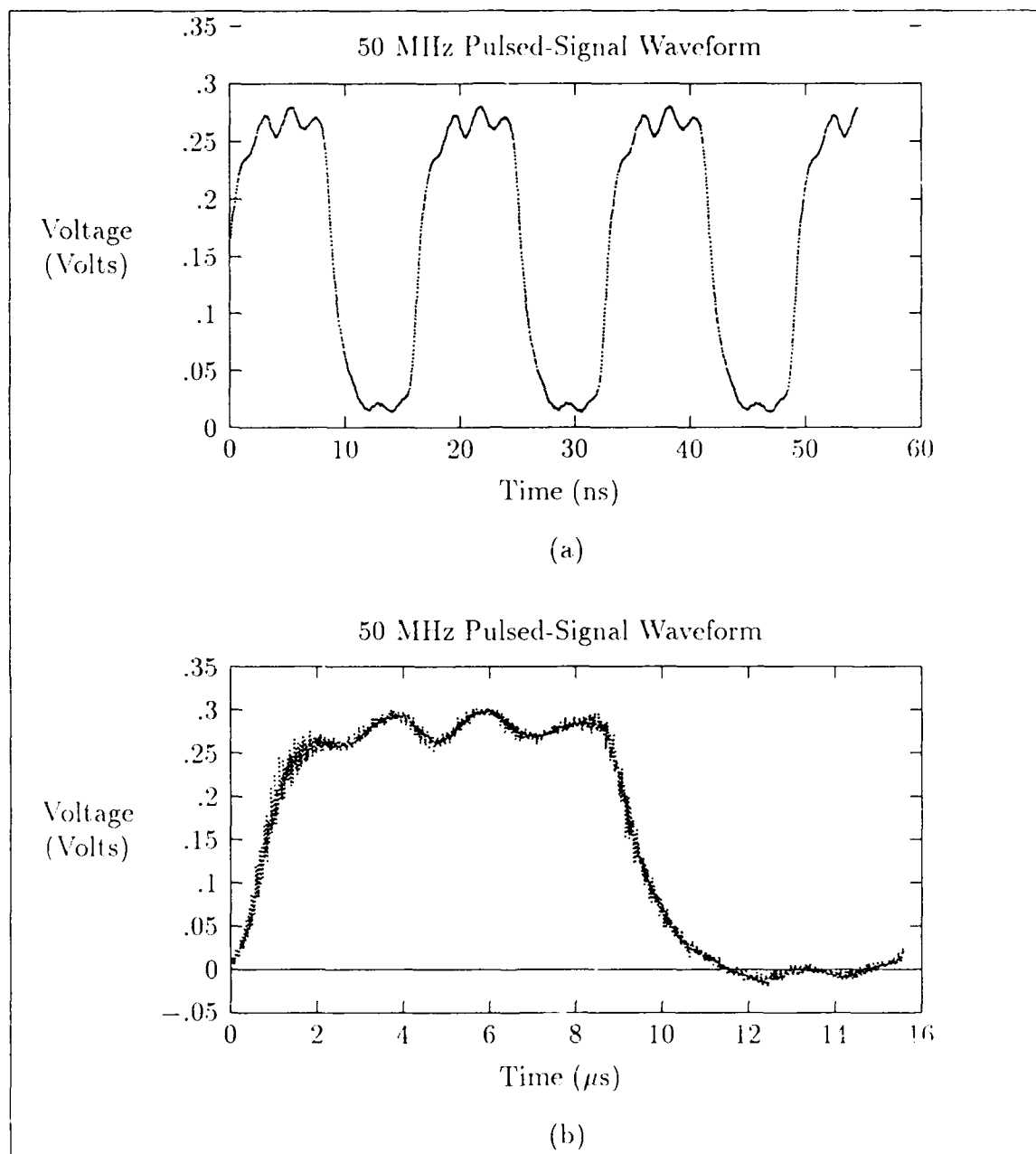


Figure I.28. Pulsed-signal response of structure 36 ( $10\text{ }\mu\text{m}$  wide, 2-conductor ECS) from the BCB wafer at 50 MHz (low-impedance termination). (a) Untreated. (b) Filtered. (Input voltage = 2V).

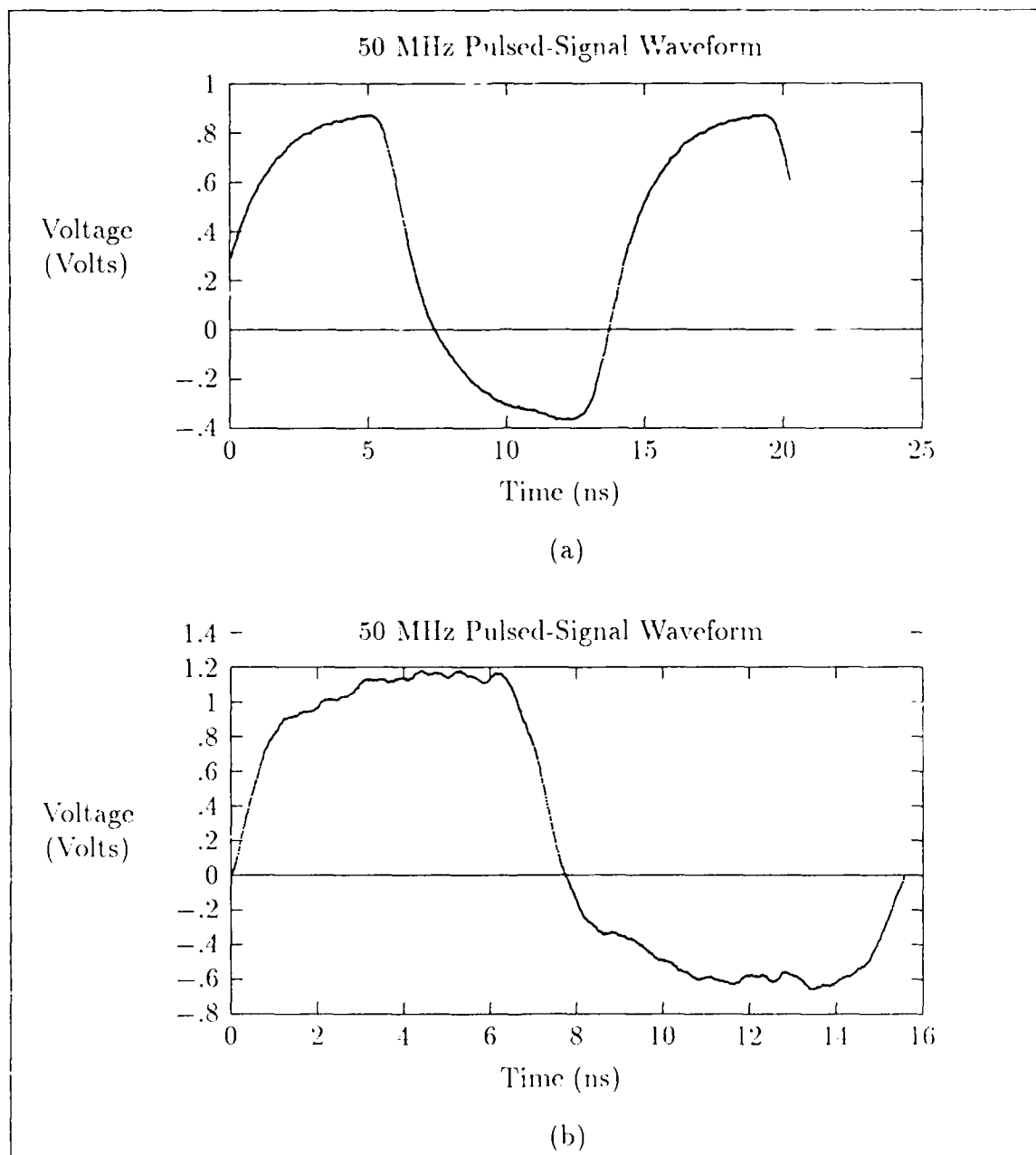


Figure I.29. Pulsed-signal response of structure 36 ( $10\ \mu\text{m}$  wide, 2-conductor ECS) from the PIQ wafer at 50 MHz (low-impedance termination). (a) Untreated. (b) Filtered. (Input voltage = 5V).

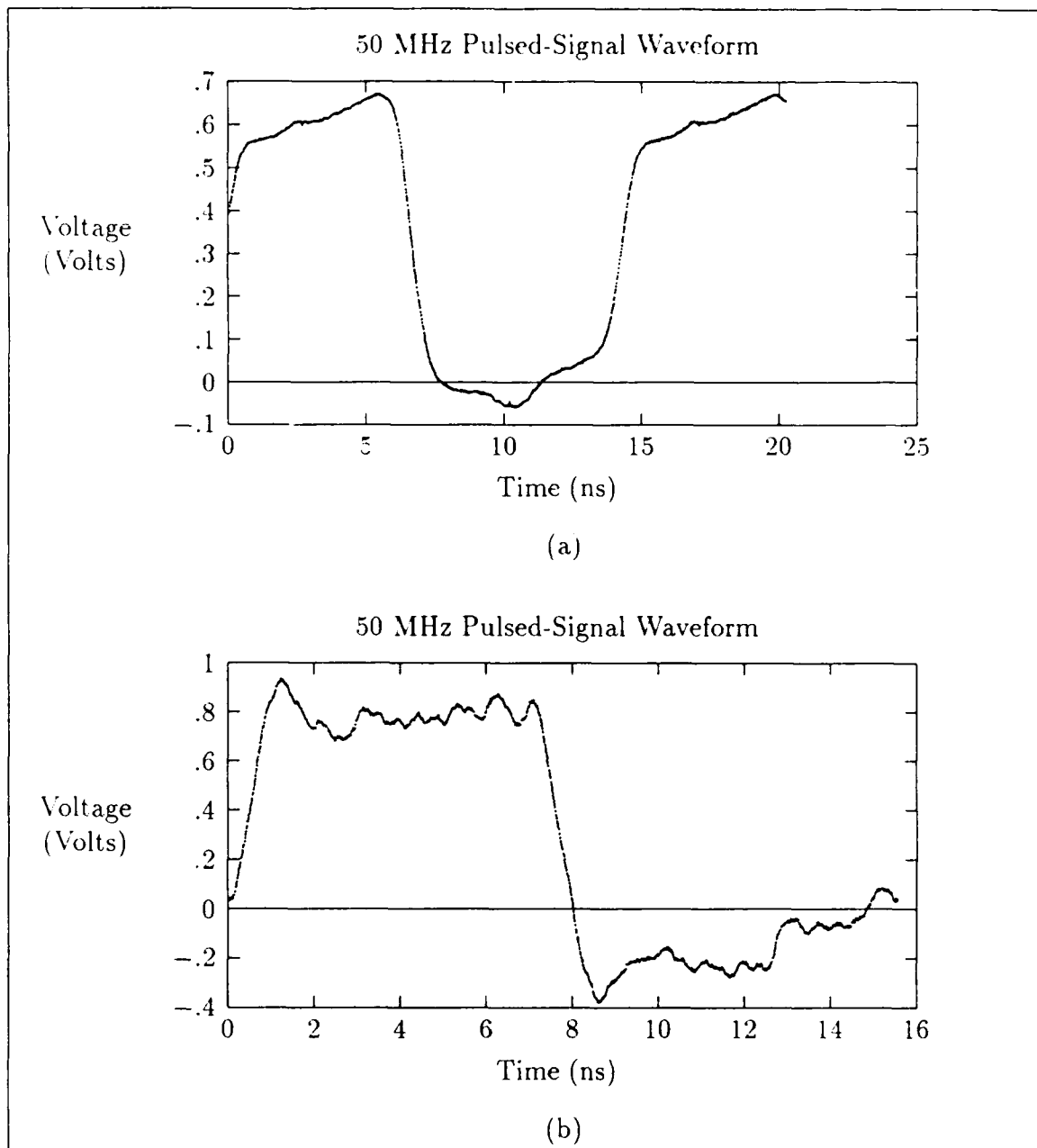


Figure I.30. Pulsed-signal response of structure 54 ( $10\text{ }\mu\text{m}$  wide, 3-conductor ECS) from the PIQ wafer at 50 MHz (low-impedance termination). (a) Un-treated. (b) Filtered. (Input voltage = 5V).

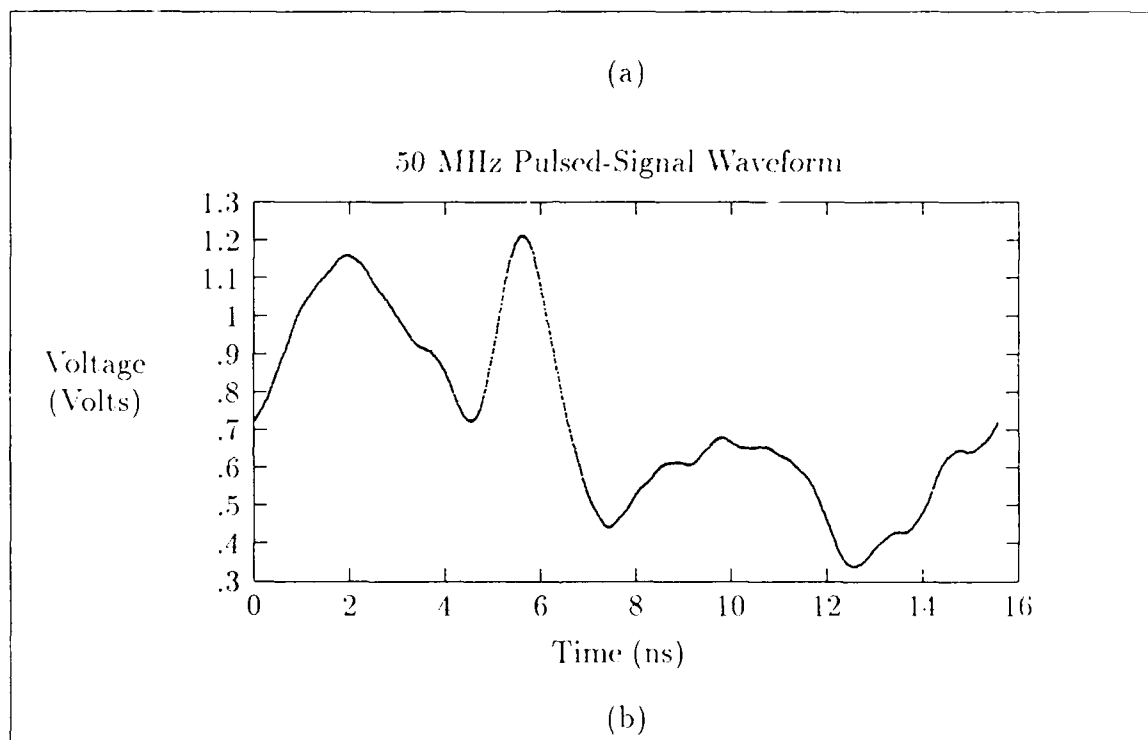


Figure I.31. Pulsed-signal response of structure 62 (10  $\mu\text{m}$  wide CPW) from the PIQ wafer at 50 MHz (low-impedance termination). (a) Untreated. (b) Filtered. (Input voltage = 2V).

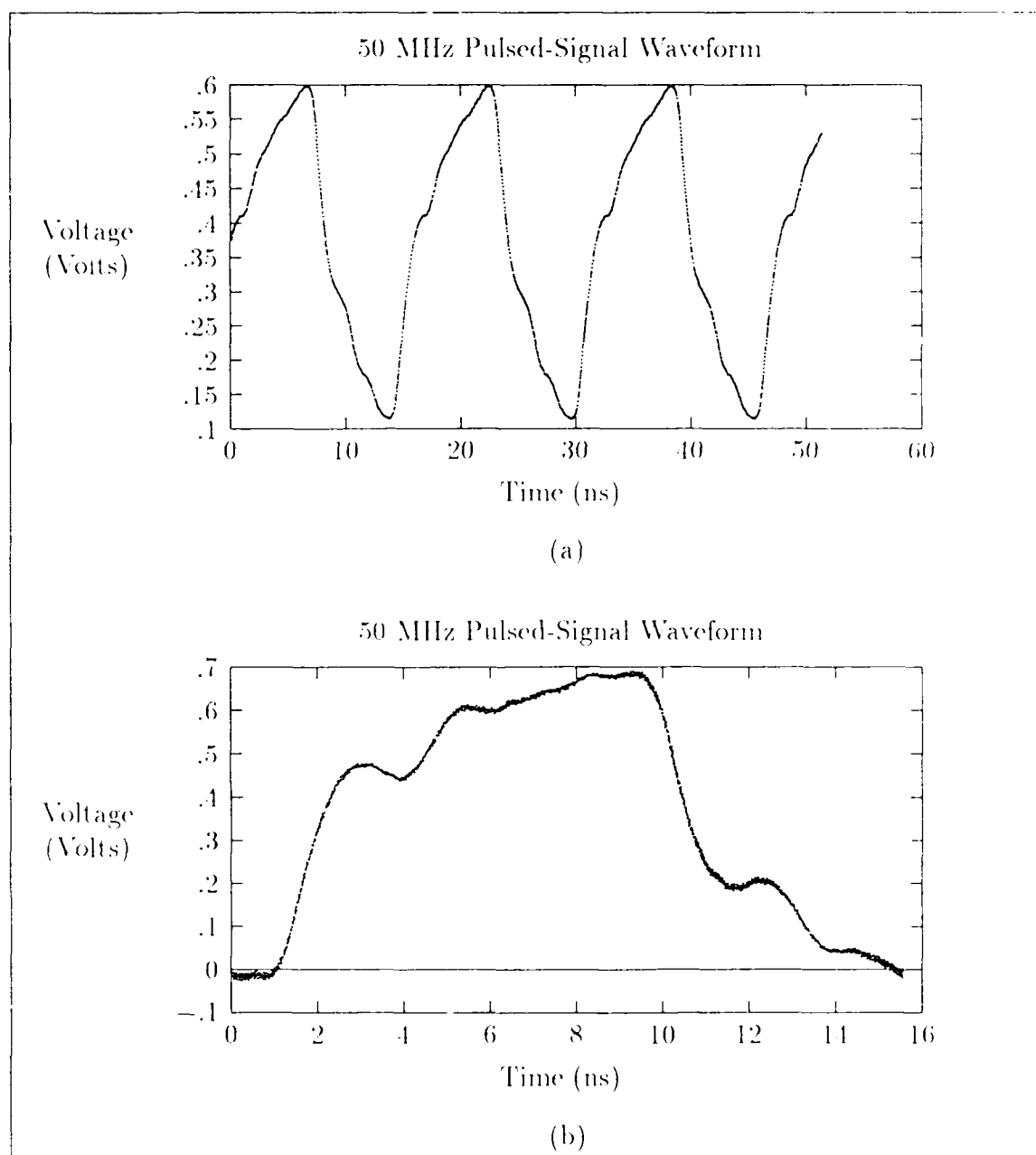


Figure L32. Pulsed-signal response of structure 91 ( $25\ \mu\text{m}$  wide CPW) from the BCB wafer at 50 MHz (low-impedance termination). (a) Untreated. (b) Filtered. (Input voltage = 2V).

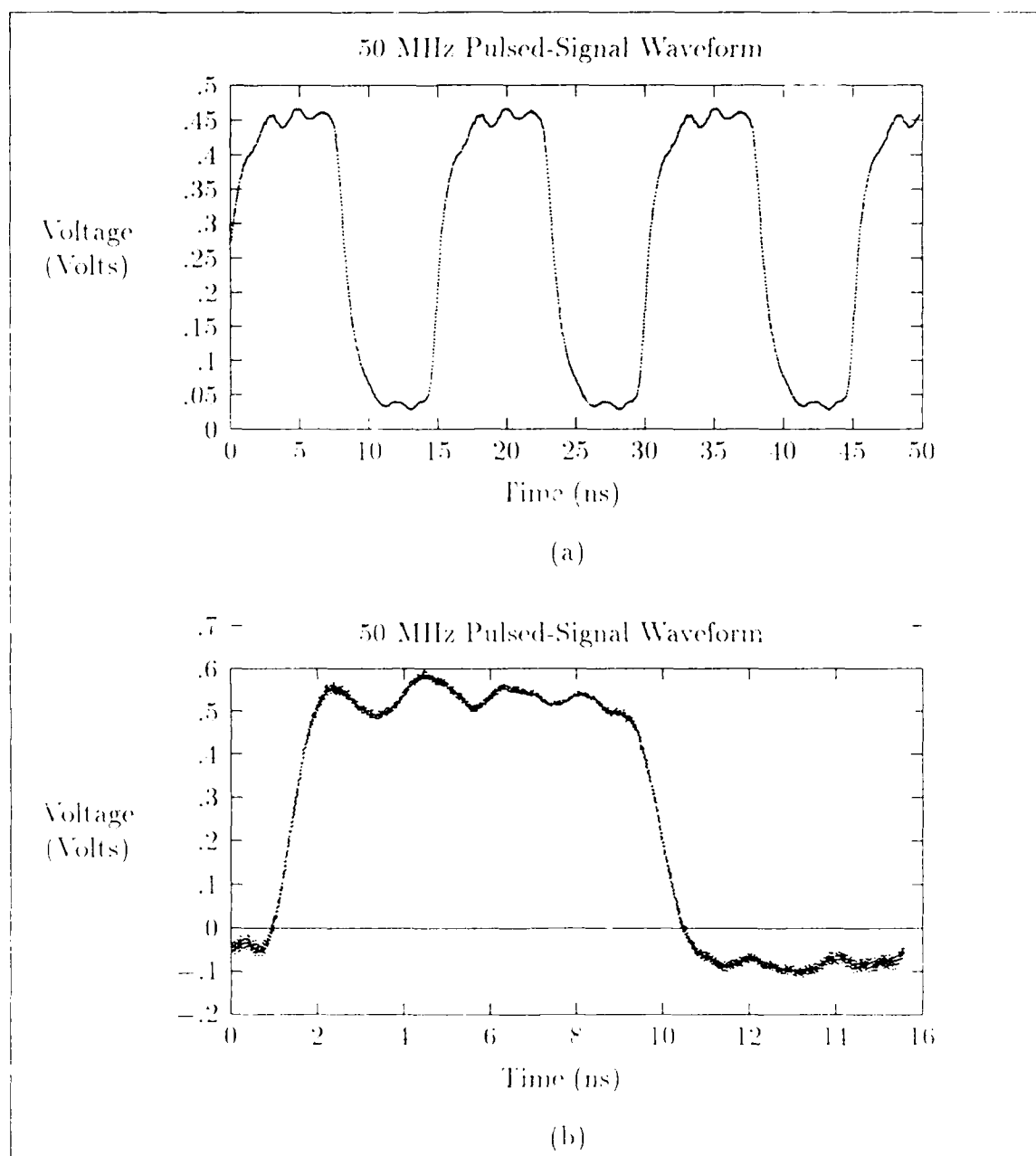


Figure I.33. Pulsed-signal response of structure 100 ( $25\ \mu\text{m}$  wide, 3-conductor ECS) from the BCB wafer at 50 MHz (low-impedance termination). (a) Untreated. (b) Filtered. (Input voltage = 2V).



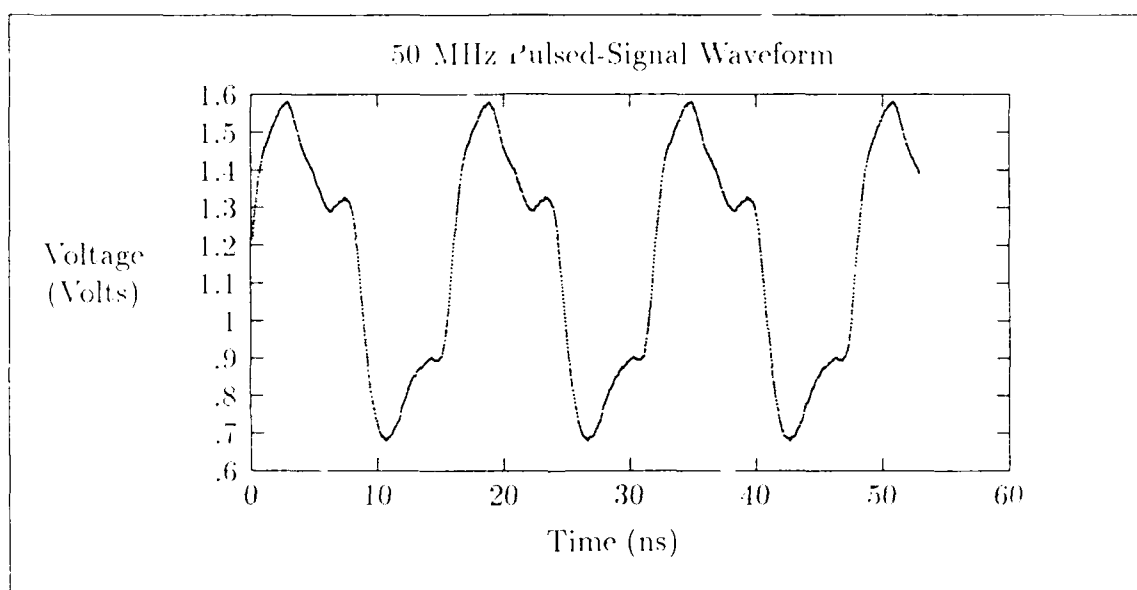


Figure I.31. Pulsed-signal response of structure 100 ( $25\text{ }\mu\text{m}$  wide, three-conductor ECS) from the BCB wafer at 50 MHz (high-impedance termination). (Input voltage = 2V).

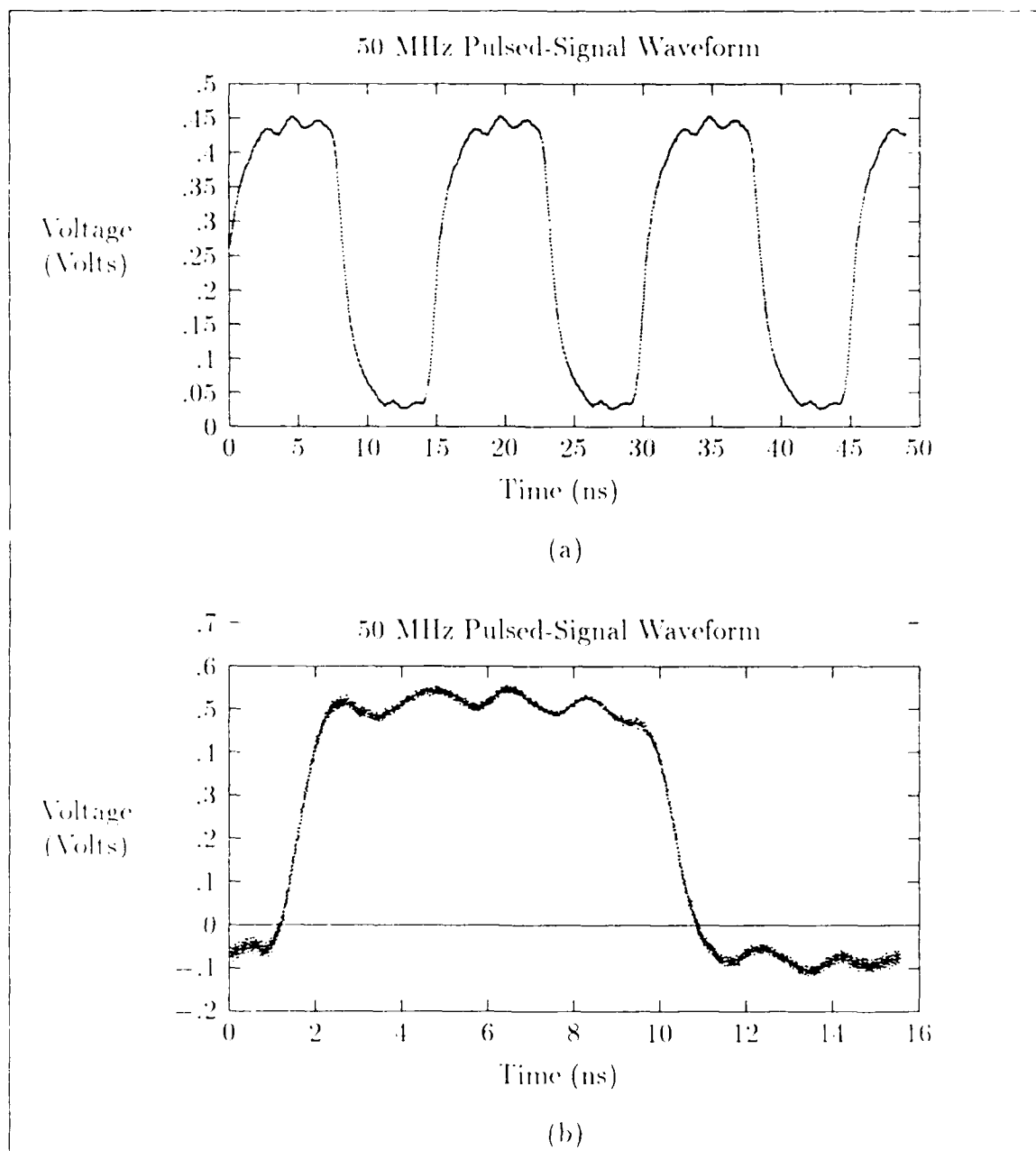


Figure L35. Pulsed-signal response of structure 109 ( $25\ \mu\text{m}$  wide, 2-conductor ECS) from the BCB wafer at 50 MHz (low-impedance termination). (a) Untreated. (b) Filtered. (Input voltage = 2V).

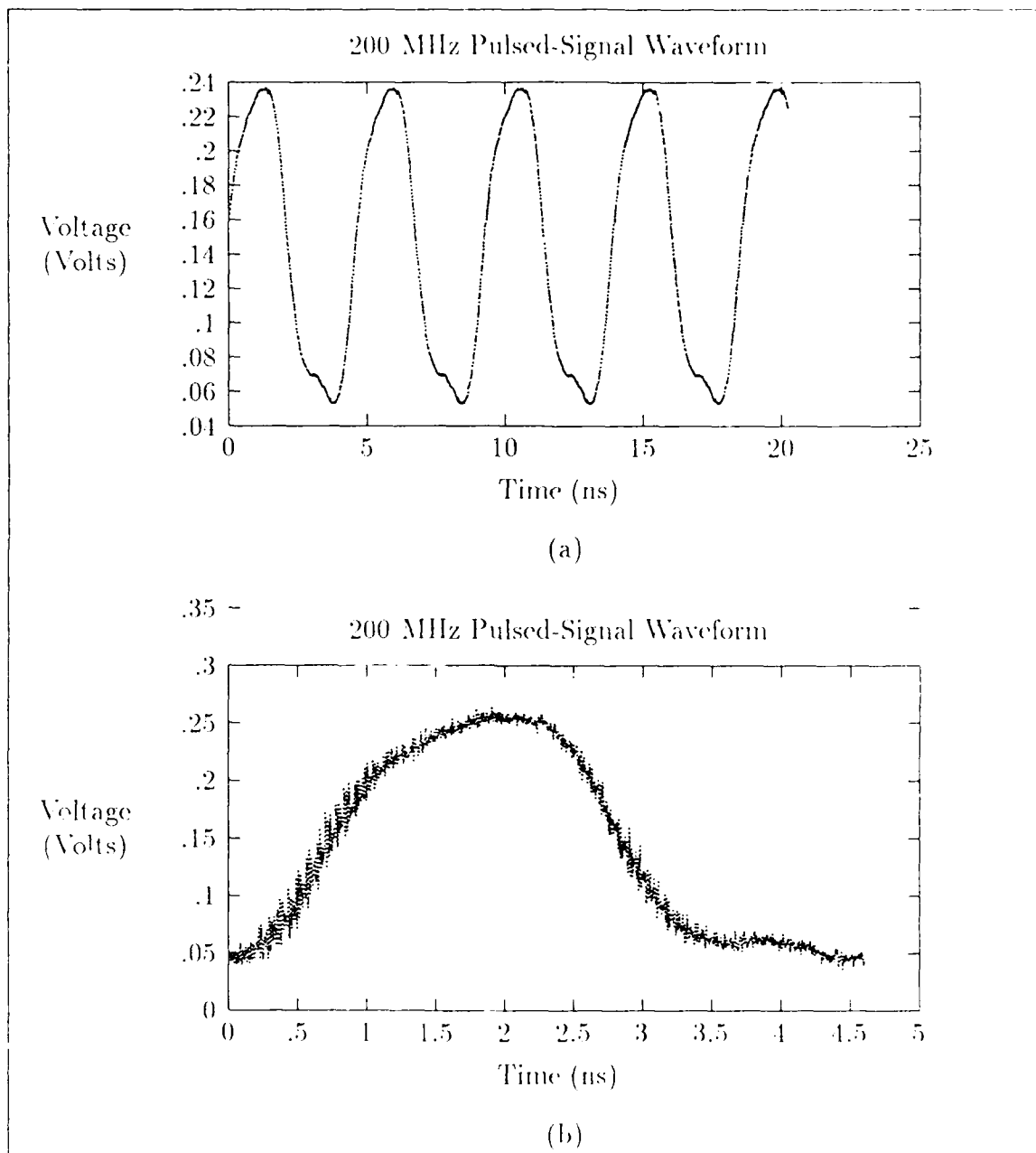


Figure I.36. Pulsed-signal response of structure 36 ( $10\ \mu\text{m}$  wide, 2-conductor ECS) from the BCB wafer at 200 MHz (low-impedance termination). (a) Untreated. (b) Filtered. (Input voltage = 2V).

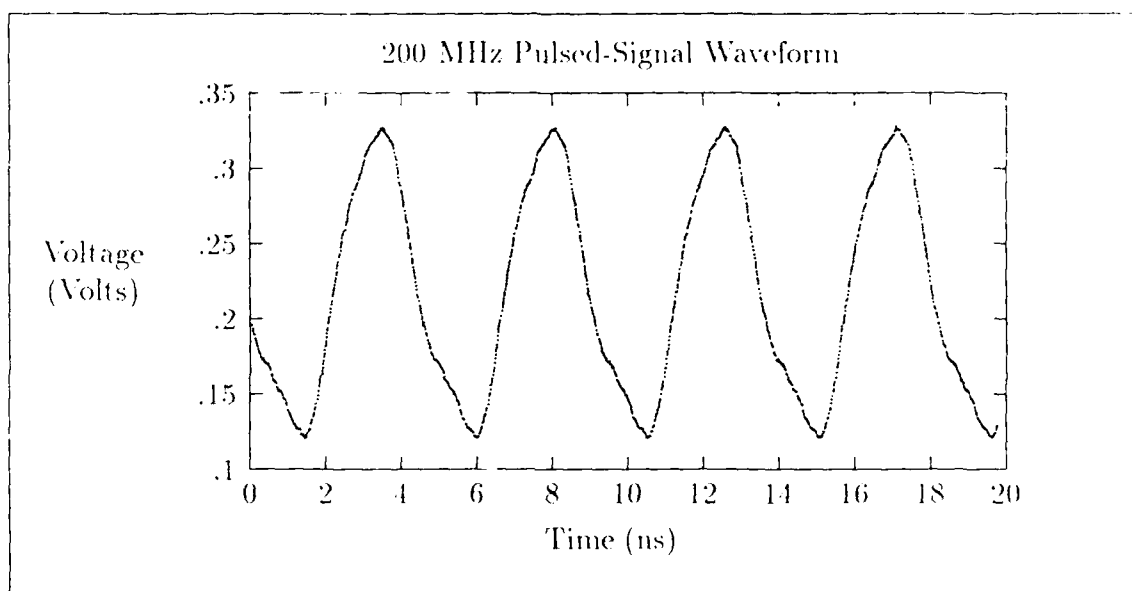


Figure I.37. Pulsed-signal response of structure 36 ( $10\text{ }\mu\text{m}$  wide, two-conductor ECS) from the BCB wafer at 200 MHz (high-impedance termination). (Input voltage = 2V).

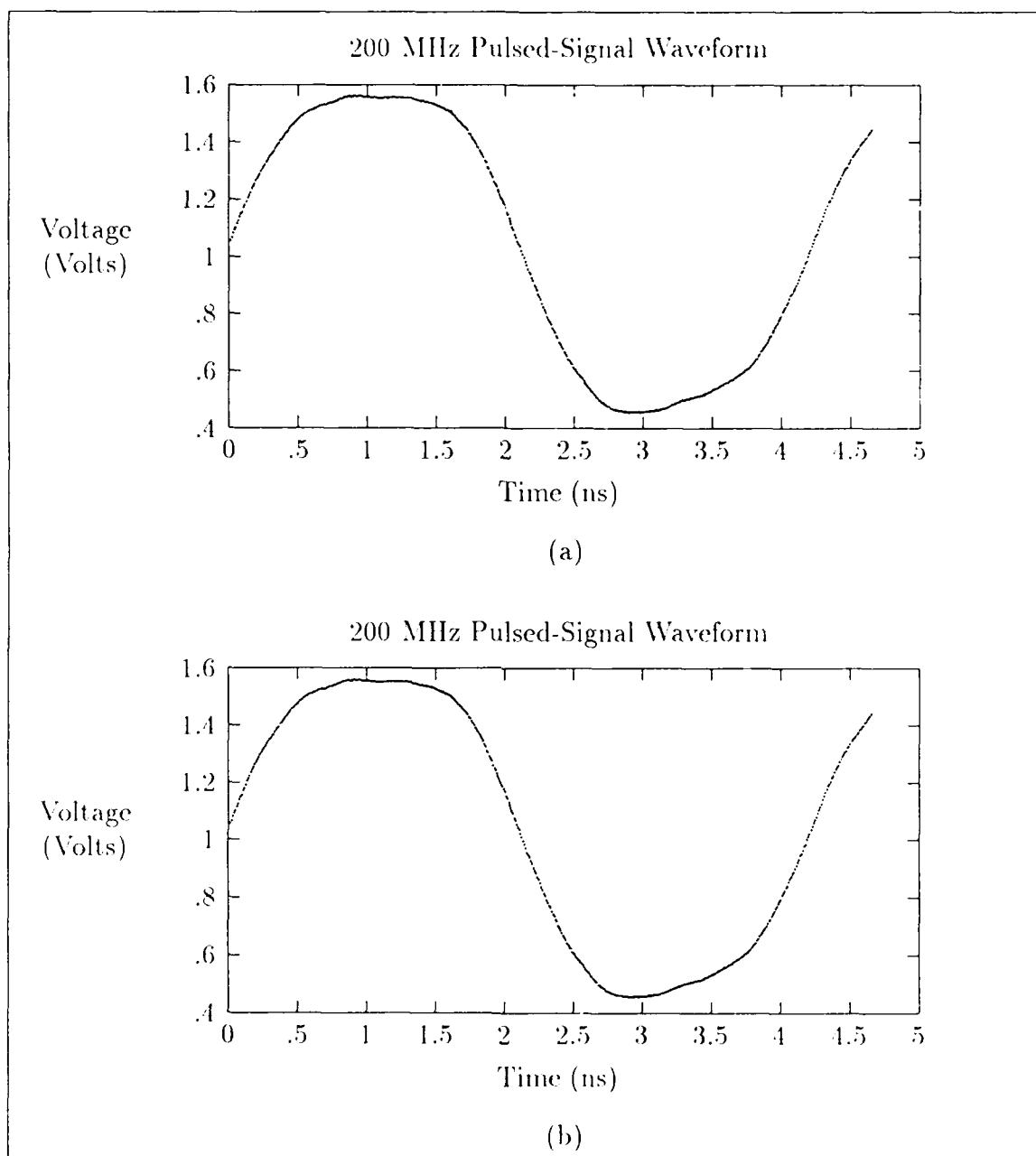


Figure L38. Pulsed-signal response of structure 54 ( $10\ \mu\text{m}$  wide, 3-conductor ECS) from the PIQ wafer at 200 MHz (low-impedance termination). (a) Untreated. (b) Filtered. (Input voltage = 5V).

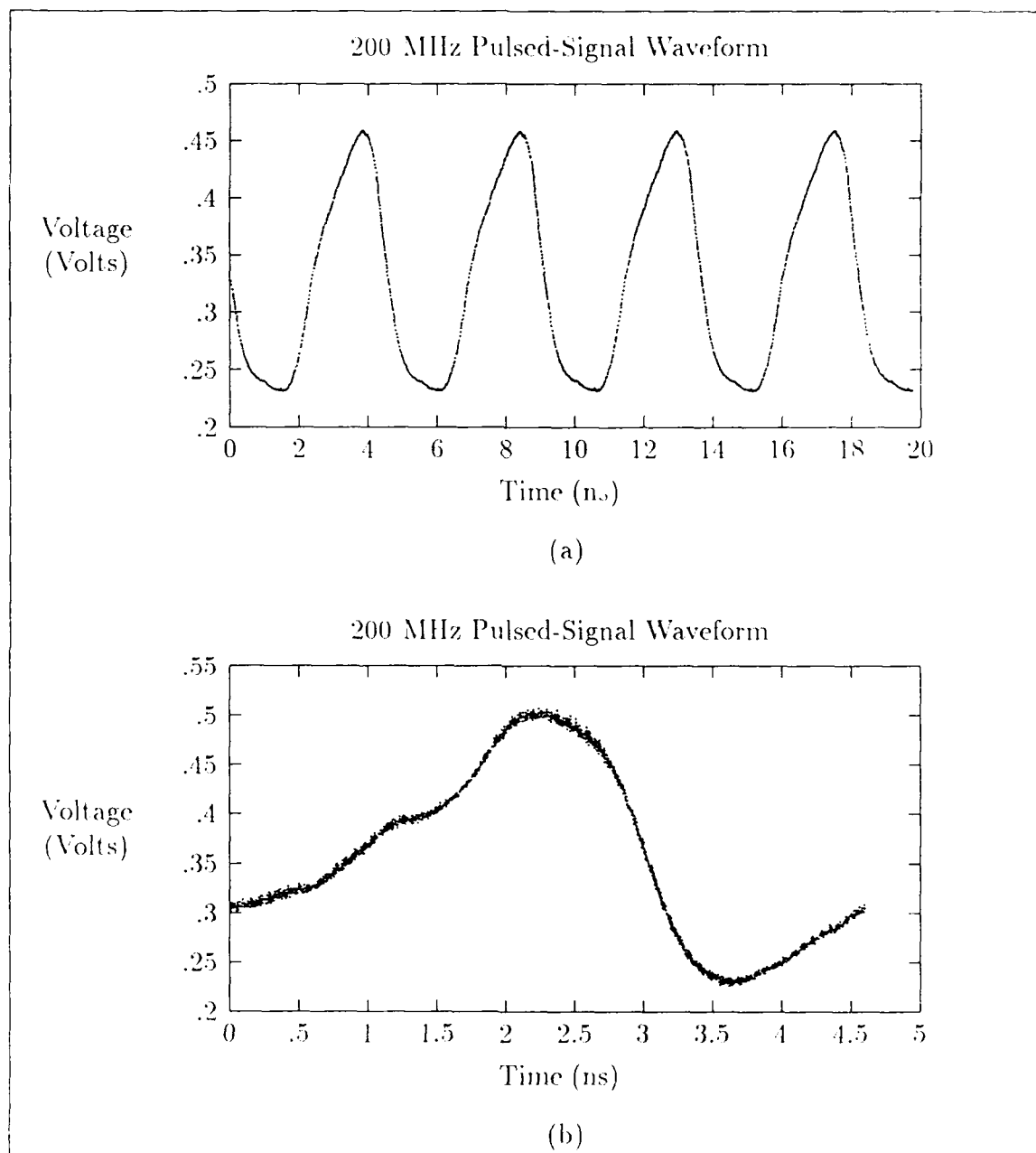


Figure I.39. Pulsed-signal response of structure 91 ( $25\text{ }\mu\text{m}$  wide CPW) from the BCB wafer at 200 MHz (low-impedance termination). (a) Untreated. (b) Filtered. (Input voltage = 2V).

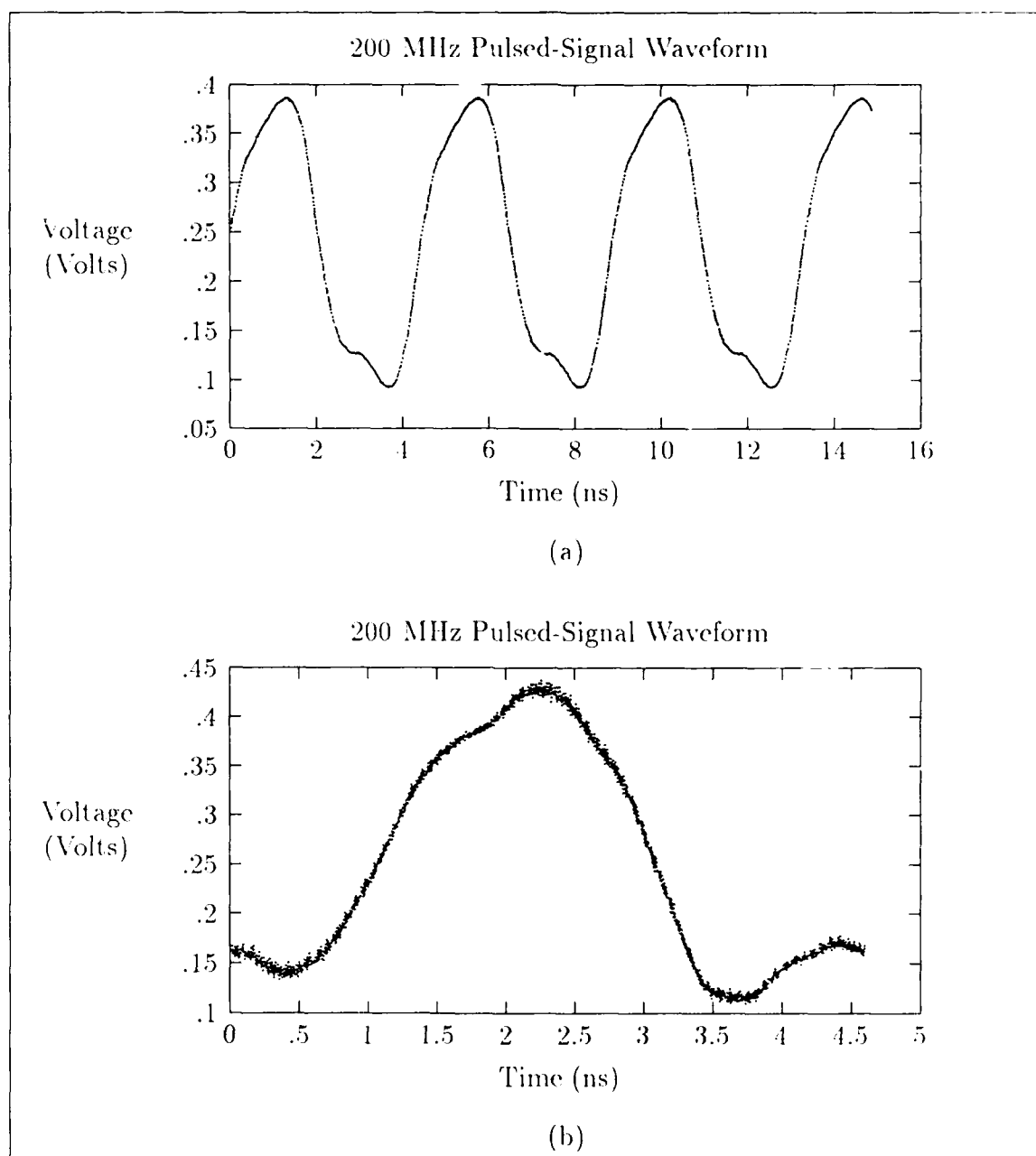


Figure I.40. Pulsed-signal response of structure 100 ( $25\text{ }\mu\text{m}$  wide, 3-conductor ECS) from the BCB wafer at 200 MHz (low-impedance termination). (a) Untreated. (b) Filtered. (Input voltage = 2V).

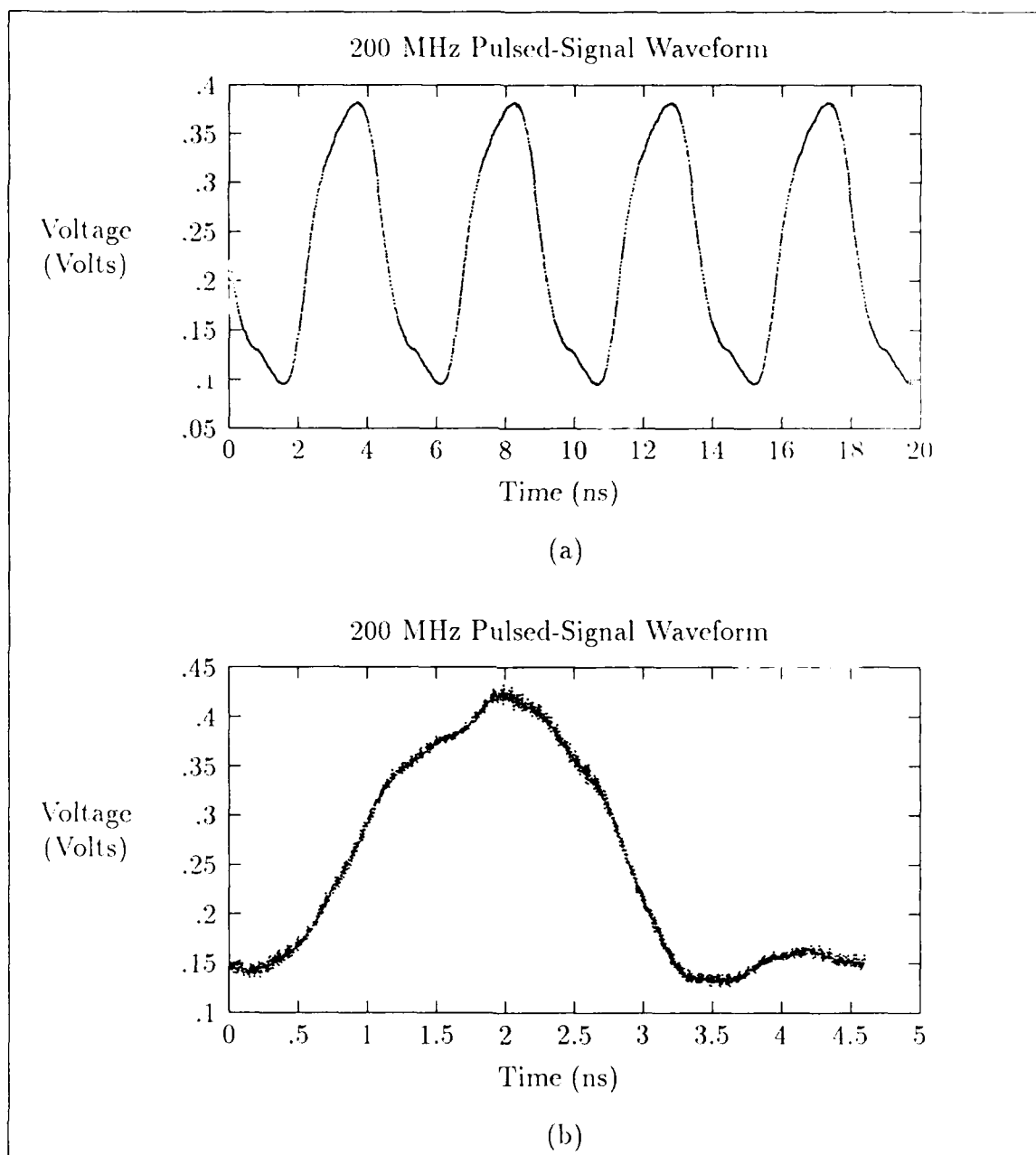


Figure I.41. Pulsed-signal response of structure 109 ( $25\ \mu\text{m}$  wide, 2-conductor ECS) from the BCB wafer at 200 MHz (low-impedance termination). (a) Untreated. (b) Filtered. (Input voltage = 2V).



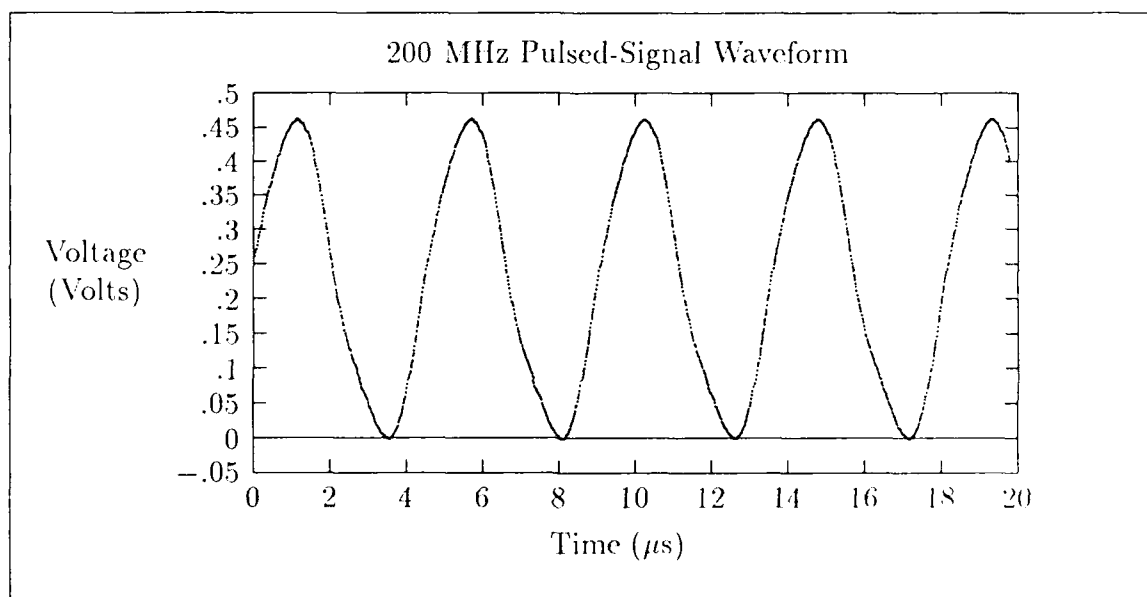


Figure I.42. Pulsed-signal response of structure 109 ( $25\text{ }\mu\text{m}$  wide, two-conductor ECS) from the BCB wafer at 200 MHz (high-impedance termination). (Input voltage = 2V).

## Bibliography

1. Abramowitz, M. *et al.* *Handbook of Mathematical Functions*. New York, NY: Dover, 1964.
2. Adam, S. F. *Microwave Theory and Applications*. Englewood Cliffs, NJ: Prentice-Hall, Inc., 1969.
3. Adams, A. C. *et al.*, "High Density Interconnect for Advanced VLSI Packaging." Presentation during the 1987 Karl Suss Seminar series, 1987.
4. Adler, R. B. *et al.* *Electromagnetic Energy Transmission and Radiation*. New York, NY: John Wiley and Sons, 1960.
5. Bakhru, B. S., "Discussions concerning benzocyclobutene based resins," April 1989. Informal meeting.
6. "Benzocyclobutenes for Thin Film, High Density Interconnect." Technical Report, February 1989. Dow Chemical Company, Plastics Group, Thermoset Applications, Midland, MI 48674.
7. Bhasin, K. B. "Monolithic Microwave Integrated Circuits -- Interconnections and Packaging Considerations." In *Proceedings of the 4th International Electronic Packaging Society*, 1984. Reprinted in (32).
8. Brews, J. R. "Characteristic Impedance of Microstrip Lines." *IEEE Transactions on Microwave Theory and Techniques*, MTT-35(1):30-34 (January 1987).
9. Brillouin, L. *Wave Propagation in Periodic Structures*. New York, NY: McGraw-Hill Book Company, 1946.
10. Bronson, R. *Modern Introductory Differential Equations*. New York, NY: McGraw-Hill Book Company, 1973.
11. Burton, E. A. "Transmission-Line Method Aid Memory-Board Design." *Electronic Design*, pages 87-91 (August 1988).
12. Cangellaris, A. C. "The Importance of Skin-Effect in Microstrip Lines at High Frequencies," *1988 IEEE Transactions on Microwave Theory and Techniques Symposium Digest*, pages 197-198 (1988).
13. Chang, W. H. "Analytical IC Metal-Line Capacitance Formulas," *IEEE Transactions on Microwave Theory and Techniques*, MTT-24(9):608-611 (September 1976).
14. "Characteristic Impedance Measurement of PC Board Circuit Patterns," June 1986. Application Note, A/N 339-2, Hewlett-Packard Inc.
15. Chatterjee, R. *Elements of Microwave Engineering*. New York, NY: Ellis Horwood Limited, 1986.

16. Chipman, R. A. *Theory and Problems of Transmission Lines (Schaum's Outline Series)*. New York, NY: McGraw-Hill Book Company, 1968.
17. "Class notes in Control Systems Summer Review." School of Engineering, Air Force Institute of Technology (AU), Wright-Patterson AFB, OH, June 1988.
18. "Class notes in EENG 524, Electromagnetic Waves I." School of Engineering, Air Force Institute of Technology (AU), Wright-Patterson AFB, OH, July 1988.
19. "Class notes in EENG 628, Intermediate Electromagnetic Waves." School of Engineering, Air Force Institute of Technology (AU), Wright-Patterson AFB, OH, March 1989.
20. "Class notes in Mathematics 505, Intermediate Differential Equations." School of Engineering, Air Force Institute of Technology (AU), Wright-Patterson AFB, OH, July 1988.
21. "Class notes in Mathematics 611, Introduction to Partial Differential Equations." School of Engineering, Air Force Institute of Technology (AU), Wright-Patterson AFB, OH, Winter 1989.
22. Cohn, S. B. "Characteristic Impedance of the Shielded-Strip Transmission Line," *Transactions of the IRE Professional Group on Microwave Theory and Techniques*, MTT-2(2) (September 1954).
23. Corr, D. G. *et al.* "Computer Analysis of the Fundamental and Higher Order Modes in Single and Coupled Microstrip," *IEEE Transactions on Microwave Theory and Techniques*, MTT-20(10):669-677 (October 1972).
24. Dalby, A. B. "Analysis and Synthesis of Coupled Microstrip Circuits with More Than Two Coupled Strips." In *7th European Microwave Conference*, pages 441-445, Microwave Exhibitions and Publications Limited, Sevenoaks, Kent, England, 1977.
25. Denlinger, E. J. "Losses of Microstrip Lines," *IEEE Transactions on Microwave Theory and Techniques*, MTT-28:512-522 (1980). Reprinted in (32).
26. Djordjevic, A. R. *et al.* "Analysis of Time Response of Lossy Multiconductor Transmission Line Networks," *IEEE Transactions on Microwave Theory and Techniques*, MTT-35(10):898-907 (October 1987).
27. Donlan, B. J. "WTM II Test Wafer Program." White Paper, AFIT/ENG, December 1988.
28. Donlan, B. J. *et al.* "The Wafer Transmission Module," *VLSI Design*, 7(1):54-58, 88, 90 (January 1986).
29. Edwards, T. C. *Foundations for Microstrip Circuit Design*. New York, NY: John Wiley and Sons, 1981.

30. Farr, A. *et al.* *Method of Moments Applications: Vol. VI-Matrix Methods for Static Microstrip.* Technical Report RADC-TR-73-217 Vol. VI, Rome Air Development Center, February 1975.
31. Frankel, S. *Multiconductor Transmission Line Analysis.* Dedham, MA: Artech House, 1977.
32. Frey, J. *et al.* *Microwave Integrated Circuits.* Dedham, MA: Artech House, 1985.
33. Gardiol, F. E. *Lossy Transmission Lines.* Dedham, MA: Artech House, 1987.
34. Getsinger, W. J. "Microstrip Dispersion Model," *IEEE Transactions on Microwave Theory and Techniques*, MTT-21:34-39 (1973). Reprinted in (32).
35. Getsinger, W. J. "Microstrip Characteristic Impedance," *IEEE Transactions on Microwave Theory and Techniques*, MTT-27(4):293 (April 1979).
36. Getsinger, W. J. "Measurement and Modeling of the Apparent Characteristic Impedance of Microstrip," *IEEE Transactions on Microwave Theory and Techniques*, MTT-31(4):624-631 (1983). Reprinted in (32).
37. Ghione, G. *et al.* "Modeling of Multiconductor Buses and Analysis of Crosstalk, Propagation Delay, and Pulse Distortion in High-Speed GaAs Logic Circuits," *IEEE Transactions on Microwave Theory and Techniques*, MTT-37(3):445-456 (March 1989).
38. Gilbert, B. K. *et al.* "The Application of Gallium Arsenide Integrated Circuit Technology to the Design and Fabrication of Future Generation Digital Signal Processors: Promises and Problems," *Proceedings of the IEEE*, 76(7):816-831 (July 1988).
39. Goossen, K. W. "Modeling of Picosecond Pulse Propagation in Microstrip Interconnections on Integrated Circuits," *IEEE Transactions on Microwave Theory and Techniques*, MTT-37(3):469-478 (March 1989).
40. Green, H. E. "The Numerical Solution of Some Important Transmission-Line Problems," *IEEE Transactions on Microwave Theory and Techniques*, MTT-13(5):676-692 (May 1965).
41. Gupta, K. C. *et al.* *Microstrip Lines and Slotlines.* Dedham, MA: Artech House, 1979.
42. Gupta, K. C. *et al.* *Computer-Aided Design of Microwave Circuits.* Dedham, MA: Artech House, 1981.
43. Higgins, D. F. "Calculating Transmission Line Transients on Personal Computers," *1987 IEEE International Symposium on Electromagnetic Compatibility*, pages 260-271 (1987).

44. Hill, Y. M., *et al.* "A General Method for Obtaining Impedance and Coupling Characteristics of Practical Microstrip and Triplate Transmission Line Configurations," *IBM Journal of Research and Development*, 13(3):314-322 (May 1969).
45. Hoffmann, R. K. *Handbook of Microwave Integrated Circuits*. Dedham, MA: Artech House, 1987.
46. Howe, H. *Stripline Circuit Design*. Dedham, MA: Artech House, 1971.
47. Izadian, J. S. *Microwave Transition Design*. Norwood, MA: Artech House, 1988.
48. Jayaraj, K. *et al.* "Performance of Low Loss, High Speed Interconnects for Multi-GHz Digital Systems." In *Proc. IEEE 1989 National Aerospace and Electronics Conference*, pages 1674-1681, 1989.
49. Johnson, D. D. "Laminate Spurs High-Speed Digital Processing," *Electronics Packaging & Production*, 27(2):80-82 (February 1987).
50. Johnson, W. R. *et al.* "Hybrid Silicon Wafer-Scale Packaging Technology," *IEEE Journal of Solid-State Circuits*, C-21(5):845-851 (October 1986).
51. Kirschning, M. *et al.* "Accurate Model for Effective Dielectric Constant of Microstrip with Validity up to Millimetre-Wave Frequencies," *Electronics Letters*, 18:272-273 (1982). Reprinted in (32).
52. Kolesar, E. S., "Hybrid-Wafer-Scale Microcircuit Integration." U.S. Patent Application, Application Letter No. 18432, December 1988. 43 pages.
53. Kozuch, J. J. "Controlled Impedance Packaging: A Comparison of Multiwire vs. Multilayer Technology," *Connection Technology*, 3(12):27-31 (December 1987).
54. Krage, M. K. *et al.* "Characteristics of Coupled Microstrip Transmission Lines I: Coupled-Mode Formulation of Inhomogeneous Lines," *IEEE Transactions on Microwave Theory and Techniques*, MTT-18(4):217-222 (April 1970).
55. Kraus, J. D. *Electromagnetics*, 3rd ed., New York, NY: McGraw-Hill, 1984.
56. Kreyszig, E. *Advanced Engineering Mathematics*. New York, NY: John Wiley and Sons, 1988.
57. Landau, L. D. *et al.* *Electrodynamics of Continuous Media*. New York, NY: Pergamon Press, 1984.
58. Lee, H. L. *Optimization of a Resin Cure Sensor*. MS thesis, Massachusetts Institute of Technology, 1982.
59. Lindell, I. V. *et al.* "Theory of Time-Domain Quasi-TEM Modes in Inhomogeneous Multiconductor Lines," *IEEE Transactions on Microwave Theory and Techniques*, MTT-35(10):893-897 (October 1987).

60. Lockyear, W. H. "Spreadsheets Cut Finite-Difference Computing Costs," *Microwaves & RF*, 27(12):99-108 (November 1988).
61. Lueker, J. "Differential Techniques Move TDR into the Mainstream," *EDN*, pages 171-178 (August 1989).
62. Lyman, J. "Silicon-on-Silicon Hybrids are Coming into Their Own," *Electronics*, 60(11):47-48 (May 1987).
63. Mainger, R. W. *Investigation of a Hybrid Wafer Scale Integration Technique that Mounts Discrete Integrated Circuit Die in a Silicon Substrate*. MS thesis, Air Force Institute of Technology (AFIT/GE/ENG/88M-7), March 1988.
64. Masi, C. G. (editor). "Solutions to Current Problems in ATE Fixturing," *Test and Measurement World*, 7(12):30-50 (December 1987).
65. McDonald, B. H. *et al.* "Finite-Element Solution of Unbounded Field Problems," *IEEE Transactions on Microwave Theory and Techniques*, MTT-20(12):841 (December 1972).
66. McDonald, J. F. *et al.* "Multilevel Interconnections for Wafer Scale Integration," *Journal of Vacuum Science and Technology, A* 4(6):3127-3138 (1986).
67. McDonald, J. F. *et al.* "Yield of Wafer-Scale Interconnections," *VLSI Systems Design*, 7(12):62-63, 65-66 (1986).
68. "Measuring the Dielectric Constant of Solid Materials," December 1987. Application Note, A/N 339-13, Hewlett-Packard, Inc.
69. Menzel, W. *et al.* "A Method for Calculating the Frequency-Dependent Properties of Microstrip Discontinuities," *IEEE Transactions on Microwave Theory and Techniques*, MTT-25(2):107-112 (February 1977).
70. Meyer, D. E. "Wafer Scale Integration? Time to Get Serious," *Semiconductor International*, 9(11):32 (November 1986).
71. Neugebauer, C. A. *et al.* "High Performance Interconnections between VLSI Chips," *Solid State Technology*, 31(6):93-97 (June 1988).
72. Ney, M. M. "Method of Moments as Applied to Electromagnetic Problems," *IEEE Transactions on Microwave Theory and Techniques*, 33(10):972-980 (October 1985).
73. Pavlidis, D. *et al.* "The Design and Performance of Three Line Microstrip Couplers," *IEEE Transactions on Microwave Theory and Techniques*, MTT-24(10):631-639 (October 1976).
74. Pierce, J. F. *et al.* *Applied Electronics*. Knoxville, TN: University of Tennessee, 1972.
75. Polivanov, K. *The Theory of Electromagnetic Fields*. Moscow, USSR: Mir Publishers, 1973.

76. "Polycon's High Density Multichip Interconnect Design Guidelines," June 1988. Polycon, Inc., 2686 B Johnson Drive, Ventura, CA 93030.
77. Pramanick, P. *et al.* "An Accurate Description of Dispersion in Microstrip," *Microwave Journal*, 26(12):89-93 (December 1983). Reprinted in (32).
78. Rabjohn, G. *et al.* "High-frequency Wafer-probing Techniques," *Canadian Journal of Physics*, 65(8):850-857 (August 1987).
79. Ramo, S. *et al.* *Fields and Waves in Communication Electronics*. New York, NY: John Wiley and Sons, 1965.
80. Reche, J. Telephone interviews from December 1988 to August 1989. Polycon, Inc., Ventura, CA 93030.
81. Reche, J. "Brief Review and Comments Concerning Lt James Lyke's Thesis Plan." Letter, March 1989.
82. Reche, J. "Polycon-AFIT High Speed Electrical Test Pattern." Polycon, Inc., 2686 B Johnson Drive, Ventura, CA 93030, 1989.
83. Reston, R. R. *Robotic Tactile Sensor Fabricated from Piezoelectric Polyvinylidene Fluoride Films*. MS thesis, Air Force Institute of Technology (AFIT/GE/ENG/88D-41), 1988.
84. Royle, D. "Designer's Guide to Transmission Lines and Interconnections (Parts I, II, and III)," *Electronic Design News*, 33(3):134-136, 143-148, 155-159 (June 1988).
85. Sandy, F. *et al.* "Use of Finite Difference Approximations to Partial Differential Equations for Problems Having Boundaries at Infinity," *IEEE Transactions on Microwave Theory and Techniques*, MTT-19(5):781 (May 1971).
86. Schelkunoff, S. A. "The Impedance Concept and its Application to Problems of Reflection, Refraction, Shielding, and Power Absorption," *Bell Systems Technical Journal*, 17(1):17-48 (January 1938).
87. Schneider, M. V. "Computation of Impedance and Attenuation of TEM-Lines by Finite Difference Methods," *IEEE Transactions on Microwave Theory and Techniques*, 13(6):793-801 (November 1965).
88. Schneider, M. V. "Microstrip Lines for Microwave Integrated Circuits," *Bell Systems Technical Journal*, 48(5):1421-1444 (1969).
89. Snook, J. B. "Substrates for Hybrid Microelectronic Applications," *MSN Microwave News & Communications Technology*, 2(2):26-31 (February 1988).
90. Stimson, G. W. *Introduction to Airborne Radar*. El Segundo, CA: Hughes Aircraft Company, 1983.
91. Stratton, J. A. *Electromagnetic Theory*. New York, NY: McGraw-Hill, 1911.

92. Sylvester, P. *et al.* "Microstrip Discontinuity Capacitances of Right-Angle Bends, T-Junctions, and Crossings," *IEEE Transactions on Microwave Theory and Techniques*, *MTT* 21:341-346 (1971). Reprinted in (32).
93. Sylvester, P. *et al.* "Equivalent Capacitances for Microstrip Gaps and Steps," *IEEE Transactions on Microwave Theory and Techniques*, *MTT* 20(11):729-733 (November 1972).
94. Takahashi, G. L. *Fabrication and Electrical Characterization of Multilevel Aluminum Interconnects Used to Achieve Silicon-Hybrid Wafer-Scale Integration*. MS thesis, Air Force Institute of Technology (AFIT/GE/ENG/87D-65), 1987.
95. Theorin, C. *et al.* "Differential TDR Testing Techniques," *Connection Technology*, 4(3):35-41 (March 1988).
96. Tripathi, V. K. "On the Analysis of Symmetrical Three-Line Microstrip Circuits," *IEEE Transactions on Microwave Theory and Techniques*, *MTT* 25(9):726-729 (September 1976).
97. Venkataraman, J. *et al.* "Analysis of Arbitrarily Oriented Microstrip Transmission Lines in Arbitrarily Shaped Dielectric Media over a Finite Ground Plane," *IEEE Transactions on Microwave Theory and Techniques*, *MTT* 33(10):952-959 (October 1985).
98. Warner, F. L. "Microwave Network Analysers." In *Microwave Measurements*, chapter 9, pages 171-194, London, UK: Peter Peregrinus Ltd., 1985.
99. Weeks, W. T. "Calculation of Coefficients of Capacitance of Multiconductor Transmission Lines in the Presence of a Dielectric Interface," *IEEE Transactions on Microwave Theory and Techniques*, *MTT*-18(1):35-43 (January 1970).
100. Wheeler, Harold, A. "Transmission-Line Properties of a Strip on a Dielectric Sheet on a Plane," *IEEE Transactions on Microwave Theory and Techniques*, *MTT* 25:631-647 (1977).
101. Wiseman, J. *Investigation of the Impedance Modulation of Thin Films with a Chemically-Sensitive Field-Effect Transistor*. MS thesis, Air Force Institute of Technology (AFIT/GE/ENG/88D-61), 1988.
102. Wu, T. T. "Theory of the Microstrip," *Journal of Applied Physics*, 28(3):299-302 (March 1957).
103. Yamashita, E. *et al.* "Strip Line with Rectangular Outer Conductor and Three Dielectric Layers," *IEEE Transactions on Microwave Theory and Techniques*, *MTT* 18(5):238-243 (May 1970).
104. Yasumura, G. "High-Speed ZIF Connectors Use Shape Memory Alloys and Flexible Circuits," *Connection Technology*, 3(12):40-44 (December 1987).



### *Vita*

PII Redacted

Captain James C. Lyke [REDACTED] [REDACTED] [REDACTED] [REDACTED], TN. He attended the University of Tennessee at Knoxville, where he received a Bachelor of Science in Electrical and Electronic Engineering in 1984. Having been accepted into the Air Force College Senior Engineering Program in 1984, Captain Lyke entered commissioned service with the Air Force upon completion of the Officer Training School program at Lackland AFB, Texas in April 1985. After his commission, he served as an avionics systems engineer with the Aeronautical Systems Division's Deputy for Engineering and the F-15 Systems Program Office at Wright-Patterson AFB, Ohio. His primary work involved the F-15 AN/APG-70 fire control radar system, which was his area of responsibility until he entered the School of Engineering, Air Force Institute of Technology, in May 1988.

PII Redacted

Per [REDACTED]  
[REDACTED]

REPORT DOCUMENTATION PAGE				Form Approved OMB No 0704-0188		
1a. REPORT SECURITY CLASSIFICATION UNCLASSIFIED			1b. RESTRICTIVE MARKINGS			
2a. SECURITY CLASSIFICATION AUTHORITY			3. DISTRIBUTION / AVAILABILITY OF REPORT  Approved for public release; distribution unlimited			
2b. DECLASSIFICATION / DOWNGRADING SCHEDULE						
4. PERFORMING ORGANIZATION REPORT NUMBER(S)  AFIT/ENG/GE/89D-27			5. MONITORING ORGANIZATION REPORT NUMBER(S)			
6a. NAME OF PERFORMING ORGANIZATION School of Engineering		6b. OFFICE SYMBOL (If applicable) AFIT/ENG	7a. NAME OF MONITORING ORGANIZATION			
6c. ADDRESS (City, State, and ZIP Code) Air Force Institute of Technology Wright-Patterson AFB OH 45433-6583			7b. ADDRESS (City, State, and ZIP Code)			
8a. NAME OF FUNDING / SPONSORING ORGANIZATION		8b. OFFICE SYMBOL (If applicable)	9. PROCUREMENT INSTRUMENT IDENTIFICATION NUMBER			
8c. ADDRESS (City, State, and ZIP Code)			10. SOURCE OF FUNDING NUMBERS			
			PROGRAM ELEMENT NO.	PROJECT NO.	TASK NO.	WORK UNIT ACCESSION NO.
11. TITLE (Include Security Classification)  SILICON HYBRID WAFER SCALE INTEGRATION INTERCONNECT EVALUATION						
12. PERSONAL AUTHOR(S) James C. Lyke, B.S.E.E., Capt, USAF						
13a. TYPE OF REPORT MS Thesis		13b. TIME COVERED FROM _____ TO _____		14. DATE OF REPORT (Year, Month, Day) 1989 December		15. PAGE COUNT 413
16. SUPPLEMENTARY NOTATION						
17. COSATI CODES			18. SUBJECT TERMS (Continue on reverse if necessary and identify by block number)			
FIELD	GROUP	SUB-GROUP	High Speed Interconnections Wafer Scale Integrati High Density Multilayer Interconnections			
09	01					
19. ABSTRACT (Continue on reverse if necessary and identify by block number)						
Thesis Advisor: Edward S. Kolesar Associate Professor Department of Electrical and Computer Engineering						
20. DISTRIBUTION / AVAILABILITY OF ABSTRACT <input checked="" type="checkbox"/> UNCLASSIFIED/UNLIMITED <input type="checkbox"/> SAME AS RPT <input type="checkbox"/> DTIC USERS			21. ABSTRACT SECURITY CLASSIFICATION UNCLASSIFIED			
22a. NAME OF RESPONSIBLE INDIVIDUAL Edward S. Kolesar, Assoc. Professor			22b. TELEPHONE (Include Area Code) (513) 255-3576		22c. OFFICE SYMBOL ENG	

This thesis considered the electrical characteristics of interconnections that have been proposed for use in silicon hybrid wafer scale integration (WSI) approaches. The study was based on a set of five-inch test wafers, containing various interconnection structures previously designed at AFIT. Two test wafers used a special polyimide dielectric, while a third was composed of a benzocyclobutene (BCB). The investigated structures represented 10 cm length aluminum, coupled, stripline-like transmission lines. The metrics used included continuity measurements, ac measurement of the characteristic impedance and coupling levels, and pulsed-signal response measurements. Continuity results indicated transmission and leakage failures in all wafers, although the failure mechanisms were sometimes wafer-specific. The characteristic impedance measurement technique was flawed, but revealed interesting information concerning the driving-point impedances of the structures. Most coupled structures manifested coupling responses which were consistent in shape with theoretical estimates, but higher in magnitude by 10-20 dB. All structures revealed coupling levels lower than -25 dB. Despite correlation difficulties, the results implied that transmission line behavior is manifested in WSIC interconnections. The measured coupling was determined to be sufficiently low to implement digital systems with adequate noise margins. Time domain performance indicated that pulsed signals up to 250 MHz could be propagated in certain WSIC structures. Proper termination of signals was found to be vital in achieving any semblance of signal fidelity at the higher frequencies. However, such terminations created great signal attenuation in 0.1 m length structures, even with 25  $\mu\text{m}$  linewidths. Recommendations for further research included: more in-depth and higher frequency evaluations of particular WSIC structures; design enhancements for future test wafers; and the development of special drivers with high gain and low input impedance for hybrid WSI systems.